TalentDetector

TalentDetector2026_Winter
INTERNATIONAL STUDENTS SCIENTIFIC CONFERENCE

Scientific editor:
Mirosław Bonek

Department of Engineering Materials and Biomaterials,
Faculty of Mechanical Engineering,
Silesian University of Technology
09 January 2026
Gliwice, Poland

Katedra Materiałów
Inżynierskich i Biomedycznych

Wydano za zgodą
Rektora Politechniki Śląskiej

Redakcja techniczna i skład komputerowy
dr h.c. dr hab. inż. Mirosław Bonek, prof. PŚ

Seria wydawnicza
Prace Katedry Materiałów Inżynierskich i Biomedycznych
Wydział Mechaniczny Technologiczny
Politechnika Śląska

ISBN 978-83-68390-55-1 Tom 1

INTERNATIONAL STUDENTS SCIENTIFIC CONFERENCE

TALENTDETECTOR2026_WINTER

SILESIAN UNIVERSITY OF TECHNOLOGY, GLIWICE, POLAND

09 JANUARY 2026

The International Student Scientific Conference TalentDetector2026_Winter aims to integrate the student and scientific community dealing with topics related to material technologies. It is a place that gives the opportunity to exchange experiences, knowledge, skills and present current scientific achievements, developing and expanding students' interests in the field of materials engineering, surface engineering, biomaterials and biomedical engineering, nanotechnology, pro-ecological technologies and computer materials science. The conference allows for the presentation of projects conducted with the industry as part of the activities of Student Scientific Circles, doctorates, projects implemented in the form of PBL - Project Based Learning as part of the Excellence Initiative - Research University at the Silesian University of Technology, projects in the framework of EURECA PRO/European University in Responsible Consumption and Production and international bilateral cooperation between Universities.

CONFERENCE ORGANIZER

Materials Science Circle of the Association of Alumni of the Silesian University of Technology, Gliwice, Poland

CONFERENCE CO-ORGANIZER

Department of Engineering Materials and Biomaterials, Faculty of Mechanical Engineering, Silesian University of Technology, Gliwice, Poland

INTERNATIONAL SCIENTIFIC COMMETTEE

ORGANIZING COMMETTEE

TalentDetector HISTORY

The International Student Scientific Conferences TalentDetector since 2018 have been a place for the exchange of experience, knowledge, skills and presentation of students' current scientific achievements in the field of materials engineering, surface engineering, biomaterials and biomedical engineering. As part of the conference, two international scientific monographs, TalentDetector_Summer and TalentDetector_Winter, are published annually, which already contain over 760 scientific articles resulting from the implementation of PBL, EURECA PRO, Students Scientific Cyrcles projects and projects with secondary school students with international authors. Participation in the form of presentations and posters in TalentDetector International Student Scientific Conferences allows members of the project teams to integrate the student and scientific community of the Silesian University of Technology as well as young staff from foreign research centres in Armenia, Austria, Brazil, China, Czech Republic, Ethiopia, Ghana, Georgia, Iran, Romania, Slovakia, South Africa, Ukraine and Turkey, dealing with topics related to materials technologies.
Scientific monographs are prepared based on articles, mostly with international authors, reviewed by an international scientific committee.
The initiative of the cyclical organization of the International Student Scientific Conference TalentDetector significantly expands activities in the field of student education, organizational and popularization activities for the scientific community related to materials engineering at the national and international level.
Thanks to extensive international cooperation, over 270 articles were published free of charge.

Number of cooperating universities: 17

City University Qatar, Doha, Qatar
Federal University of Rio Grande do Sul, Porto Alegre, Brazil
Gazi University, Ankara, Turkey
Gebze Technical University, Gebze, Turkey
Georgian Technical University, Tbilisi, Georgia
Khmelnitskyi National University, Khmelnitskyi, Ukraine
Laserinstitut Hochschule Mittweida, Mittweida, Germany
Pamukkale University, Denizli, Turkey
Silesian University of Technology, Gliwice, Poland
Slovak Technical University in Bratislava, Trnava, Slovakia
Stellenbosch University, Stellenbosch, South Africa
Technical University in Zvolen, Zvolen, Slovakia
University of Petroșani, Petroșani, Romania
University of Pristina, Pristina, Kosovo
University of Zilina, Zilina, Slovakia
Yanshan University, Qinhuangdao, China
Yerevan State University, Yerevan, Armenia

The history of TalentDetector in numbers:

2018
TalentDetector 2019 (Gliwice)
Number of articles: 59
Number of authors: 206
Number of countries: 1

2021
TalentDetector2021_Winter (Gliwice)
Number of articles: 37
Number of authors: 134
Number of countries: 2

TalentDetector2021_Summer (Zawiercie)
Number of articles: 57
Number of authors: 173
Number of countries: 3

2022
TalentDetector2022_Winter (Gliwice)
Number of articles: 79
Number of authors: 179
Number of countries: 4

TalentDetector2022_Summer (Wisła)
Number of articles: 79
Number of authors: 176
Number of countries: 4

2023
TalentDetector2023_Winter (Gliwice)
Number of articles: 73
Number of authors: 143
Number of countries: 6

TalentDetector2023_Summer (Brenna)
Number of articles: 105
Number of authors: 173
Number of countries: 9

2024
TalentDetector2024_Winter (Gliwice)
Number of articles: 82
Number of authors: 135
Number of countries: 7

TalentDetector2024_Summer (Gliwice-Zilina)
Number of articles: 84
Number of authors: 147
Number of countries: 8

2025
TalentDetector2025_Winter (Gliwice)
Number of articles: 95
Number of authors: 173
Number of countries: 9

TalentDetector2025_Summer (Brenna)
Number of articles: 87
Number of authors: 143
Number of countries: 10

TalentDetector2025_Yanshan (Gliwice)
Number of articles: 12
Number of authors: 29
Number of countries: 1

TalentDetector2025_Prom (Gliwice)
Number of authors: 15
Number of countries: 6

2026
TalentDetector2026_Winter (Gliwice)
Number of articles: 93
Number of authors: 184
Number of countries: 11

TalentDetector

9th January 2026
Gliwice, Poland

DEPARTMENT OF ENGINEERING MATERIALS AND BIOMATERIALS
FACULTY OF MECHANICAL ENGINEERING
SILESIAN UNIVERSITY OF TECHNOLOGY

INTERNATIONAL STUDENTS SCIENTIFIC CONFERENCE

Contents

VOLUME 1

VOLUME 2

TalentDetector
9th January 2026
Gliwice, Poland
DEPARTMENT OF ENGINEERING MATERIALS AND BIOMATERIALS
FACULTY OF MECHANICAL ENGINEERING
SILESIAN UNIVERSITY OF TECHNOLOGY
INTERNATIONAL STUDENTS SCIENTIFIC CONFERENCE

Energy Dispersive X-ray Spectroscopy Analysis of ZnO Dye Sensitized Solar Cells Photoanodes

Elizabeth Addae, Wojciech Sitek, Marek Szindler

Scientific and Didactic Laboratory of Nanotechnology and Material Technologies, Faculty of Mechanical Engineering, Silesian University of Technology, Towarowa 7 Str., 44-100 Gliwice, Poland; Elizabeth.Addae@polsl.pl; Wojciech.Sitek@polsl.pl; Marek.Szindler@polsl.pl

Abstract: Dye-sensitized solar cells (DSSCs) require efficient charge separation at the dye–semiconductor–electrolyte interface; however, electron back-transfer at the fluorine-doped tin oxide (FTO) substrate can significantly decrease device efficiency. Zinc oxide (ZnO) is commonly employed as a blocking layer because its wide bandgap, high electron mobility, and compatibility with low-temperature processing make it suitable for suppressing interfacial recombination. In this study, ZnO thin films were deposited onto FTO using 500 cycles of atomic layer deposition (ALD) at 100 °C, 200 °C, and 300 °C to examine the influence of deposition temperature on film characteristics. The ALD technique enabled accurate control over film thickness and produced chemically stable ZnO layers capable of operating under DSSC conditions. Following ZnO deposition, TiO_2 semiconducting films were screen-printed and sintered to fabricate complete electrode assemblies. Energy-dispersive X-ray spectroscopy (EDS) demonstrated distinct elemental separation between the TiO_2 layer, the ZnO interlayer, and the FTO substrate, indicating that the ZnO film was continuous and compositionally homogeneous. Morphological and compositional analyses collectively confirm the successful formation of high-quality ZnO by ALD. Overall, ZnO deposited at 300 °C exhibited the most favorable blocking properties, effectively reducing recombination and improving DSSC photoanode performance.

Keywords: Energy-dispersive X-ray spectroscopy (EDS), ZnO, Photoanode, Dye Sensitized Solar Cells

1. INTRODUCTION

Dye-sensitized solar cells (DSSCs) are considered promising third-generation photovoltaic technologies due to their strong power conversion capability under diffuse illumination, relatively low fabrication cost, and straightforward manufacturing processes [1]. Unlike conventional silicon-based solar cells, DSSCs operate through photoinduced charge transfer occurring at the interface between a dye-sensitized semiconductor and an electrolyte. The performance of this process is strongly influenced by the photoanode, which typically consists

of a transparent conducting oxide (TCO) substrate coated with a mesoporous titanium dioxide (TiO_2) layer [2].
Zinc oxide (ZnO) is regarded as one of the most suitable materials for the FTO blocking layer because its wide bandgap (≈3.3 eV), high electron mobility, and compatibility with low-temperature deposition allow it to effectively suppress interfacial recombination while maintaining optical transparency [3], [4]. ZnO forms a compact, uniform, and transparent film that minimizes charge losses and promotes efficient electron transport, aided by favourable conduction band alignment with both FTO and TiO_2. When engineered to overcome potential chemical instability in acidic dye environments, ZnO represents a cost-effective and scalable strategy to enhance interfacial properties and improve overall DSSC performance [5].
Atomic Layer Deposition (ALD) offers precise, atomic-scale control over the thickness and composition of ZnO films, enabling the fabrication of uniform blocking layers with finely tuned properties [6]. This level of precision is critical for optimizing the electrical behaviour of the blocking layer, directly influencing DSSC efficiency. Furthermore, ZnO films produced by ALD exhibit enhanced chemical stability in the acidic conditions typical of DSSC electrolytes, contributing to improved durability and long-term operational stability of the device [7].

2. MATERIALS AND METHODOLOGY

The FTO glass substrates were thoroughly cleaned to eliminate surface impurities that could compromise film adhesion or structural quality. Each substrate was subjected to sequential ultrasonic treatment in acetone, isopropanol, and deionized water, with each step lasting approximately fifteen minutes. Afterward, the substrates were dried and blown clean using nitrogen gas.

Atomic layer deposition (ALD) of ZnO was then carried out using a Picosun R-200 reactor. The process began by pulsing diethylzinc (DEZ) vapor into the chamber for roughly 0.1 seconds, allowing DEZ molecules to chemisorb onto available reactive sites on the FTO surface, forming the first half-reaction of the ZnO monolayer. A subsequent nitrogen purge lasting about four seconds removed excess precursor and gaseous byproducts, preventing parasitic reactions.

Next, water vapor was introduced for approximately 0.1 seconds to initiate the oxidation half-reaction. Interaction between water molecules and the adsorbed DEZ layer produced a uniform zinc oxide monolayer across the substrate. A second nitrogen purge eliminated residual reaction products and unreacted water, completing a full ALD cycle. This carefully controlled sequence of self-limiting reactions ensured consistent layer growth and high structural quality. The cycle was repeated 500 times at deposition temperatures of 100 °C, 200 °C, and 300 °C to obtain ZnO films with controlled thickness and properties.

For photoanode fabrication, TiO_2 films were deposited via screen printing. A mesh screen selected for controlled coating thickness was aligned over the ZnO-coated FTO substrate, and TiO_2 paste (18NR-AO Active Opaque Titania Paste, GreatCell Solar Materials, Australia) was uniformly distributed using an automated squeegee. The deposited films were dried at 100 °C for 10 minutes to evaporate solvents and enhance adhesion. Subsequent thermal annealing at 480 °C for 30 minutes in air removed organic components, promoted particle sintering and crystallization, and produced a mesoporous TiO_2 network favourable for electron transport and

dye adsorption. The samples were then slowly cooled to room temperature to prevent thermal stress. The resulting sintered TiO_2 layer served as the functional photoanode for further DSSC assembly. These steps for fabricating the photoanode is schematically demonstrated in Figure 1.

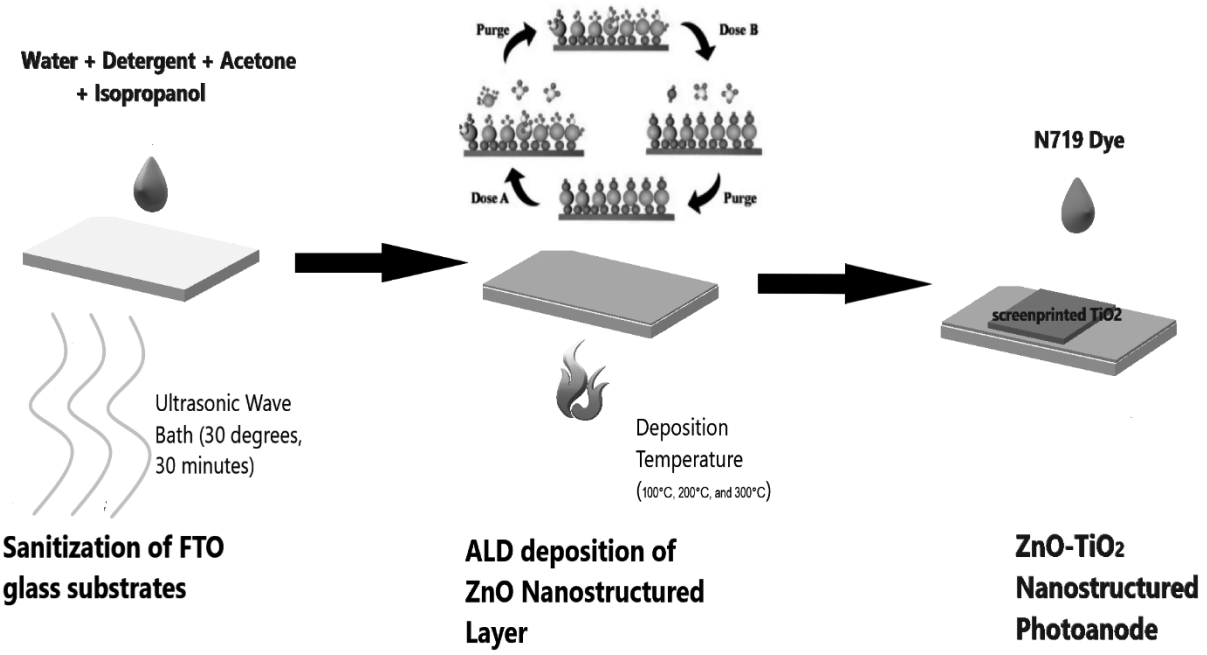

Figure 1. Schematic diagram of ZnO based DSSC Photoanode

3. RESULTS AND DISCUSSION

Energy-dispersive X-ray spectroscopy (EDS) was utilized to examine the elemental composition and spatial distribution of essential elements within the samples [8]. The analysis was performed using a scanning electron microscope (SEM) equipped with an EDS detector, enabling simultaneous correlation of compositional data with surface morphology. During EDS mapping, characteristic X-rays produced through interactions between the incident electron beam and the specimen were detected, providing semi-quantitative information regarding the identity and relative abundance of the elements present [9].

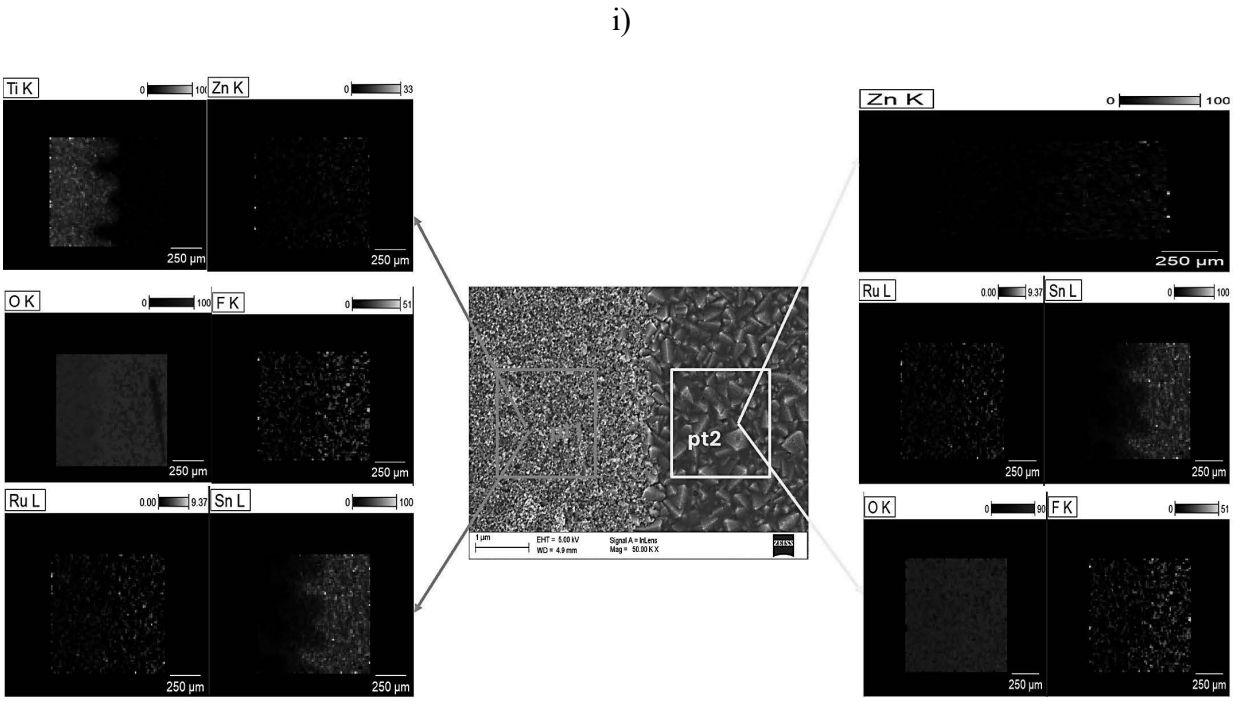

Figure 2. i) EDS images of the ZnO-TiO2 and FTO-ZnO interface of FTO-ZnO 500cycles-300°C photoanode ii) Elemental integral counts of a) Pure FTO-TiO2 (no dye) photoanode b) ZnO-TiO2-FTO 500cycles-100°C photoanode c) ZnO-TiO2-FTO 500cycles-200°C photoanode d) ZnO-TiO2-FTO 500cycles-300°C photoanode

Figure 2. i) shows the interfacial boundary between the ZnO-FTO (pt 2) and TiO_2-ZnO semiconductor layer (pt 1) of the photoanode deposited at 300°C and their corresponding elemental compositions.

In Figure 2 i), the cross-sectional microstructure clearly reveals a distinct and well-defined interface between the ZnO–TiO_2 composite region and the underlying FTO–ZnO layer. The FTO–ZnO region exhibits a highly compact, continuous, and morphologically uniform structure, indicating effective film consolidation during growth. In contrast, the ZnO–TiO_2 region displays comparatively greater heterogeneity in thickness and microstructural uniformity [10]. This difference is predominantly attributed to the contrasting fabrication techniques employed for each layer. The ZnO layer deposited via atomic layer deposition (ALD) at 300 °C undergoes sequential, self-limiting reactions that promote the formation of a dense, homogeneous, and conformal film with controlled thickness. Such growth characteristics significantly enhance interfacial continuity and reduce structural defects. Conversely, the TiO_2 layer prepared through screen printing inherently introduces microstructural variability due to paste rheology, mesh patterning, and the mechanical nature of the deposition process. As a result, the screen-printed TiO_2 film contains localized fluctuations in thickness and displays comparatively reduced compactness. These morphological trends are further supported by compositional analysis. Energy-dispersive X-ray spectroscopy (EDS) conducted on the 300_pt1 region identifies pronounced titanium (Ti) and zinc (Zn) particles, validating the presence of the TiO_2 overlayer above the ZnO interlayer. The dominance of Ti signals in this region reflects the relatively greater thickness of the TiO_2 coating [11]. In contrast, the spectrum obtained from the 300_pt2 region reveals strong tin (Sn) and zinc (Zn) peaks. The prominence of Sn is consistent with the proximity to the FTO substrate, where tin is a primary constituent. The simultaneous detection of Zn confirms the persistence of the ZnO blocking layer at this depth. Figure 2 ii) on the hand shows the total elemental intensity found with all samples. Figure 2 ii) d) displays the highest total integral count of Zn peaks as compared to Figure 2 ii) b) and c). This is possibly due to the slow grain growth at 300°C which ensures uniform compact ZnO nanolayers hence a stronger presence of the Zn element.

Overall, the combined structural and elemental observations demonstrate the successful formation of a dense ALD-grown ZnO film and highlight the inherent microstructural contrast introduced by the screen-printed TiO_2 layer.

4. SUMMARY AND CONCLUSION

Energy-dispersive X-ray spectroscopy (EDS) analysis confirmed both the elemental composition and spatial distribution of key constituents within the multilayer photoanode structure while correlating these results with the observed microstructural features. The cross-sectional observations demonstrated a distinct and continuous interface between the compact FTO–ZnO region and the comparatively less uniform ZnO–TiO_2 layer, reflecting the influence of their respective fabrication processes. The ALD-deposited ZnO film grown at 300 °C exhibited a dense, homogeneous, and conformal structure, whereas the screen-printed TiO_2 layer displayed greater thickness variation due to its deposition mechanism. Elemental mapping supported these morphological findings, with strong Ti and Zn signals detected in the TiO_2-rich (pt1) region and pronounced Sn and Zn peaks in the FTO-adjacent (pt2) region, confirming structural integrity and appropriate layer stacking. Furthermore, the higher integral Zn peak intensity observed for

samples processed at 300 °C suggests improved ZnO film quality, likely associated with slower, more controlled grain growth leading to compact nanolayer formation.
In conclusion, the combined EDS and microstructural analyses verify the successful formation of a chemically and structurally robust ZnO blocking layer produced by ALD at 300 °C, while simultaneously highlighting the intrinsic variability introduced by the screen-printed TiO_2 film. These results demonstrate that optimized ALD processing significantly enhances layer uniformity, elemental stability, and interface integrity, supporting improved functional performance of the DSSC photoanode.

BIBLIOGRAPHY

[1] J. B. Baxter and E. S. Aydil, "Dye-sensitized solar cells based on semiconductor morphologies with ZnO nanowires," *Solar Energy Materials and Solar Cells*, vol. 90, no. 5, pp. 607–622, Mar. 2006, doi: 10.1016/j.solmat.2005.05.010.

[2] E. Cahya Prima, H. Setyo Nugroho, Nugraha, G. Refantero, C. Panatarani, and B. Yuliarto, "Performance of the dye-sensitized quasi-solid state solar cell with combined anthocyanin-ruthenium photosensitizer," *RSC Advances*, vol. 10, no. 60, pp. 36873–36886, 2020, doi: 10.1039/D0RA06550A.

[3] N. I. Beedri, G. Dani, M. Gaikwad, H. M. Pathan, and S. Salunke-Gawali, "Comparative Study of TiO2, ZnO, and Nb2O5 Photoanodes for Nitro-Substituted Naphthoquinone Photosensitizer-Based Solar Cells," *ACS Omega*, vol. 8, no. 41, pp. 38748–38765, Oct. 2023, doi: 10.1021/acsomega.3c06271.

[4] D. Pugliese *et al.*, "A Chemometric Approach for the Sensitization Procedure of ZnO Flowerlike Microstructures for Dye-Sensitized Solar Cells," *ACS Appl. Mater. Interfaces*, vol. 5, no. 21, pp. 11288–11295, Nov. 2013, doi: 10.1021/am403527m.

[5] D.-I. Suh *et al.*, "The fabrication and characterization of dye-sensitized solar cells with a branched structure of ZnO nanowires," *Chemical Physics Letters*, vol. 442, no. 4, pp. 348–353, July 2007, doi: 10.1016/j.cplett.2007.05.093.

[6] E. A. Addae, W. Sitek, M. Szindler, M. Fijalkowski, and K. Matus, "Effects of ALD Deposition Cycles of Al2O3 on the Morphology and Performance of FTO-Based Dye-Sensitized Solar Cells," *Coatings*, vol. 14, no. 8, Art. no. 8, Aug. 2024, doi: 10.3390/coatings14081019.

[7] S. M. George, "Atomic Layer Deposition: An Overview," *Chem. Rev.*, vol. 110, no. 1, pp. 111–131, Jan. 2010, doi: 10.1021/cr900056b.

[8] L. Eftekhari and M. Ghasemi, "Analysing the surface morphology of annealed FTO/ZnS bilayer films: stereometric, fractal, and wettability approaches," *Sci Rep*, vol. 14, no. 1, p. 14262, June 2024, doi: 10.1038/s41598-024-65118-w.

[9] K.-M. Lee, V. Suryanarayanan, and K.-C. Ho, "The influence of surface morphology of TiO2 coating on the performance of dye-sensitized solar cells," *Solar Energy Materials and Solar Cells*, vol. 90, pp. 2398–2404, Sept. 2006, doi: 10.1016/j.solmat.2006.03.034.

[10] L. J. Antila *et al.*, "ALD Grown Aluminum Oxide Submonolayers in Dye-Sensitized Solar Cells: The Effect on Interfacial Electron Transfer and Performance," *J. Phys. Chem. C*, vol. 115, no. 33, pp. 16720–16729, Aug. 2011, doi: 10.1021/jp204886n.

[11] C.-Y. Cho, S. Baek, K. Kim, and J. H. Moon, "3D bicontinuous SnO2/TiO2 core/shell structures for highly efficient organic dye-sensitized solar cell electrodes," *RSC Adv.*, vol. 6, no. 78, pp. 74003–74008, Aug. 2016, doi: 10.1039/C6RA09810J.

TalentDetector
9th January 2026
Gliwice, Poland
DEPARTMENT OF ENGINEERING MATERIALS AND BIOMATERIALS
FACULTY OF MECHANICAL ENGINEERING
SILESIAN UNIVERSITY OF TECHNOLOGY
INTERNATIONAL STUDENTS SCIENTIFIC CONFERENCE

Recycling of multilayer polymer composites – verification of mechanical properties, prediction of application possibilities

Krystian Albrecht[a], Jakub Pyka [a], Agnieszka J. Nowak [b], Anna Krzak [b]

[a] Students of Silesian University of Technology, Faculty of Mechanical Engineering
email: ka303942@student.polsl.pl
[b] Silesian University of Technology, Faculty of Mechanical Engineering, Scientific and Didactic Laboratory of Nanotechnology and Material Technologies
email: agnieszka.j.nowak@polsl.pl

Abstract: Multilayer polymer composites are widely used in industrial applications due to their high strength-to-weight ratio and durability, but their thermoset-based structure limits conventional recycling routes. This study investigates the mechanical recycling of multilayer polymer composites derived from industrial waste streams and their reuse as a filler in new composite materials. Mechanical grinding and particle size classification were applied to obtain recycled composite powder. The morphology of the recycled material was analyzed using scanning electron microscopy, revealing irregular particles, resin-rich regions, and fragmented fiber remnants. Selected powder fractions were incorporated into an epoxy resin system to manufacture new composite specimens. The results demonstrate the feasibility of using mechanically recycled composite powder as a filler in polymer matrix composites and provide a foundation for further research on mechanical property verification and application potential.

Keywords: multilayer polymer composites, mechanical recycling, recycled filler scanning electron microscopy (SEM)

1. INTRODUCTION

Fiber-reinforced polymer composites have become one of the key groups of materials in modern engineering applications owing to their high specific strength, stiffness, corrosion resistance, and good fatigue performance. They are widely used in the automotive, aerospace, construction, and energy industries, where weight reduction and durability are essential. Consequently, the global production of fiber-reinforced polymer composites has systematically increased in recent decades [1]. However, the rapid growth in the use of these composites has led to a significant increase in the amount of composite waste generated during production and at the end of the product life cycle. Thermoset matrix composites pose specific environmental challenges. Owing to their cross-linked structure, thermoset resins cannot be remelted or remolded, making traditional recycling methods used for thermoplastics ineffective in their case [2].

Consequently, a significant portion of composite waste is currently disposed of in landfills or incinerated, which is inconsistent with the principles of sustainable development and circular economy [3]. To address this problem, various recycling technologies for polymer composites have been developed, including mechanical, thermal, and chemical methods of recycling. Among these, mechanical recycling is considered the most accessible and economically viable solution because it requires relatively simple equipment and low energy input. Nevertheless, mechanically processed materials usually exhibit reduced mechanical properties compared to virgin composites, which limits their potential applications [4].

Therefore, further research is necessary to better understand the properties of mechanically recycled composite materials and to identify potential application areas in which such materials can be reused. In this context, the present study focuses on the mechanical recycling of multilayer polymer composites obtained from industrial waste streams and the assessment of the properties of new materials containing recycled fillers.

This research was conducted as part of a PBL project, utilizing actual waste materials supplied by IZO-ERG Plastic Products Ltd. The main objective of this study was to evaluate the feasibility of using mechanically recovered composite powder as a filler in new polymer matrix composite materials and to determine the directions for future research aimed at maximizing the proportion of recycled materials while maintaining acceptable mechanical properties.

2. MATERIALS AND METHODS

2.1. Origin of composite waste

The studied materials consisted of multilayer laminates reinforced with glass fibers and an epoxy resin matrix. The composite waste originated from industrial production processes and was supplied by Zakład Tworzyw Sztucznych IZO-ERG Sp. z o.o., (Gliwice, Poland). The waste materials included scraps and rejected laminate components that could not be reused in their original forms. The waste underwent preliminary processing, involving mechanical shredding into smaller pieces, which facilitated further processing. Subsequently, these materials were thoroughly cleaned of contaminants and residues from other substances.

2.2. Mechanical recycling, sieving and fraction separation

Mechanical recycling was performed using a laboratory knife mill (TESTCHEM LMN 100). The grinding process was used to mechanically fragment the multilayer polymer composite laminates into smaller particles. Consequently, a heterogeneous powder comprising resin-rich regions and fiber-containing particles was obtained. During grinding, the entire material was collected and stored as a single bulk powder for further analysis. No classification or separation was performed at this stage. The purpose of the grinding process was solely to reduce the size of the composite material and obtain a particulate form suitable for subsequent particle size classification.

The ground composite powder was then used as the input material for further processing steps, particularly sieving and fractionation based on particle size, which enabled the separation of the recycled material into distinct size fractions for further characterization and composite manufacturing.

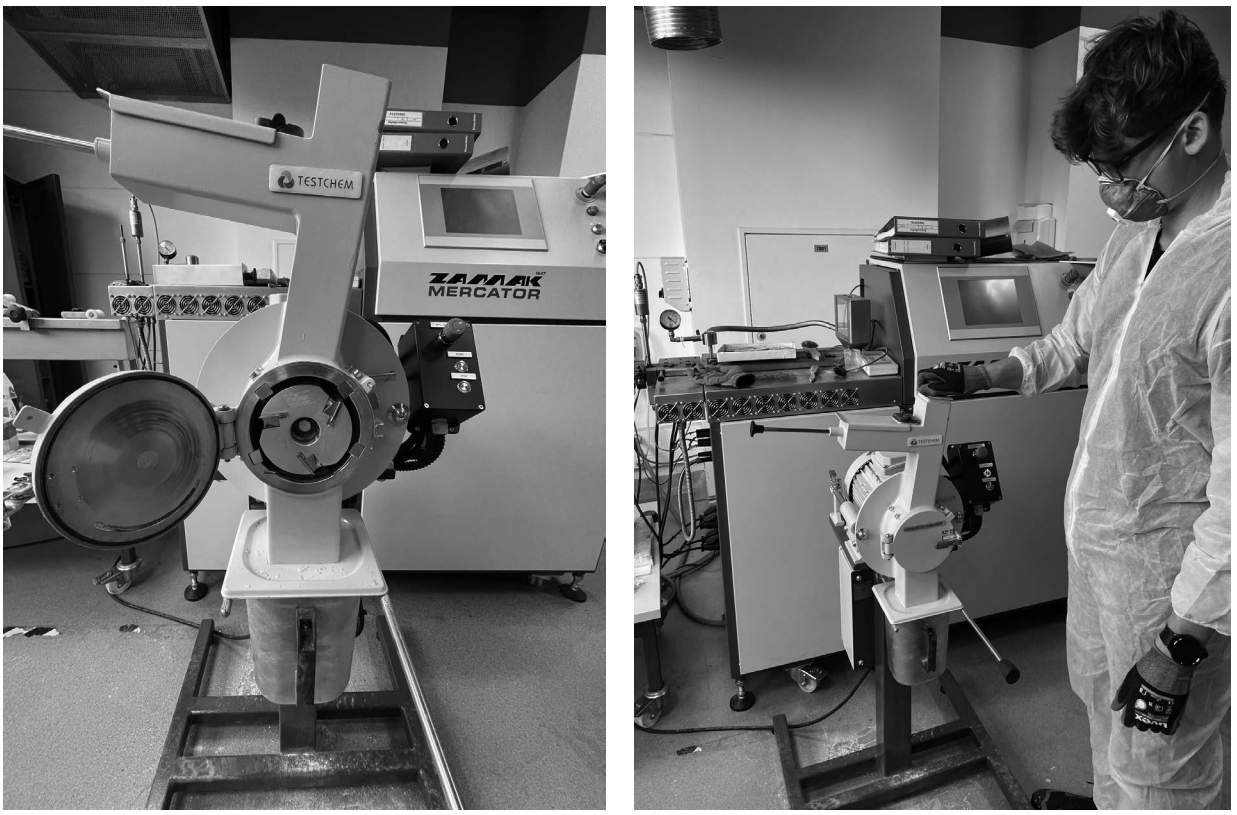

Figure 1. Laboratory knife mill (TESTCHEM LMN 100) used for grinding multilayer polymer composites [own study]

After grinding, the obtained composite powder was sieved using a set of laboratory sieves with controlled mesh sizes. This procedure enabled the separation of the material into fractions with different particle sizes. The classification of fractions allowed for a preliminary assessment of their morphology and potential suitability for further composite processing.

Figure 2. Separated powder fractions [own study]

2.3. Morphology of recycled powder and manufacturing of new composite materials

Prior to scanning electron microscopy, the recycled powder fractions were preliminarily examined using a stereoscopic optical microscope, which enabled a general assessment of the particle size distribution, agglomeration tendencies, and qualitative differences between the obtained fractions. Following the initial evaluation, detailed microstructural observations were performed using scanning electron microscopy (SEM). The morphology of the recycled composite powder was analyzed using a Zeiss Supra 35 microscope equipped with a GEMINI electron column. Before SEM analysis, the samples were coated with a thin gold layer to ensure adequate electrical conductivity of the samples. The SEM observations focused on the particle shape, fiber length, surface roughness, and presence of resin-rich regions within the individual powder fractions.

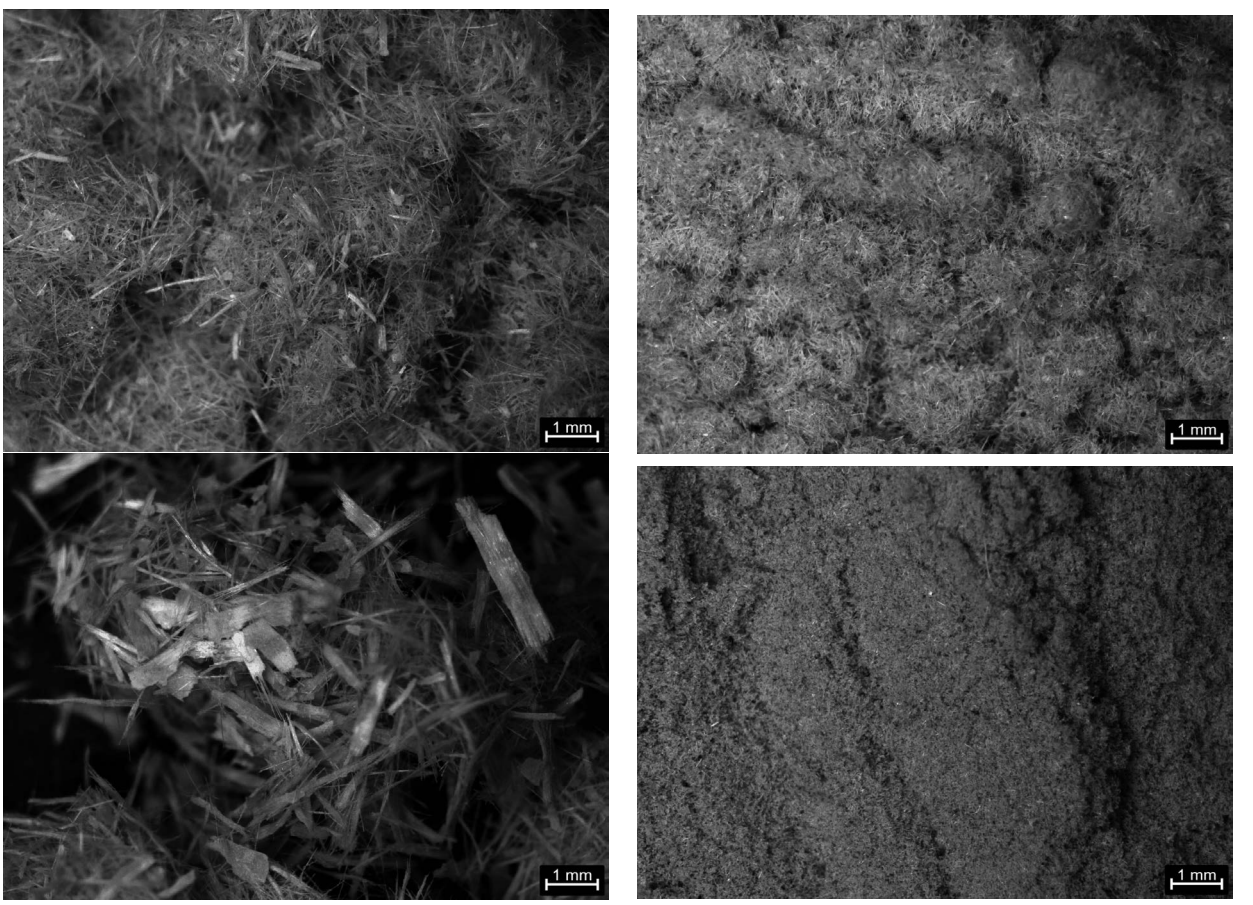

Figure 3. Optical stereomicroscope images of representative powder fractions at a magnification of 32× [own study]

The SEM image (Table 1) shows the diverse morphology of a mechanically recycled composite powder, consisting of particles with irregular shapes and a wide size distribution. Large, plate-like fragments with relatively smooth surfaces are attributed to resin-rich areas, while smaller, angular particles and agglomerates are also present. Fragments of fibers embedded in the polymer matrix can be observed, indicating simultaneous fracture of the matrix and reinforcement during grinding. The particle surfaces exhibit a rough texture and sharp edges, which is characteristic of mechanical fragmentation.

Table 1. SEM micrographs of recycled composite powder fractions obtained after mechanical recycling [own study]

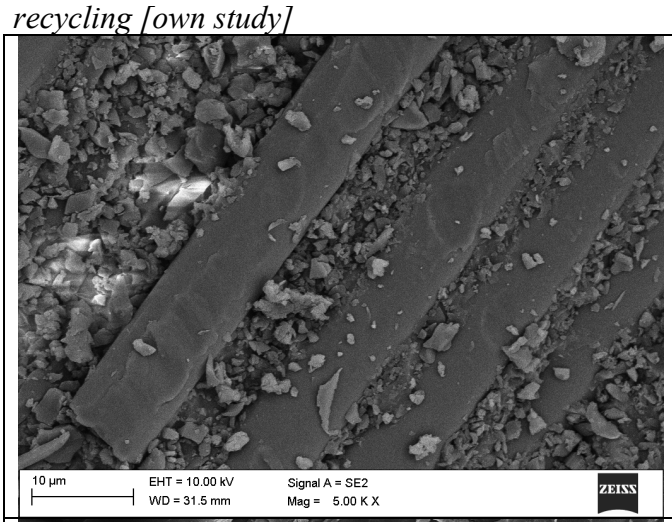	*SEM image of powder fraction 0,5*
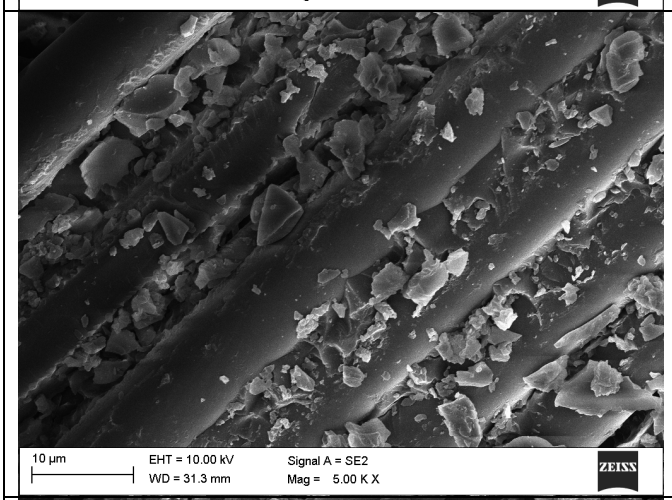	*SEM image of powder fraction 0,16*
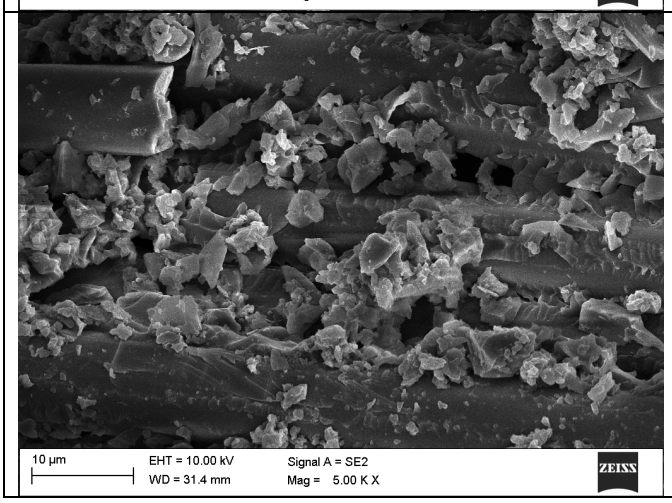	*SEM image of powder fraction >0,1*

Table 1 (continued).

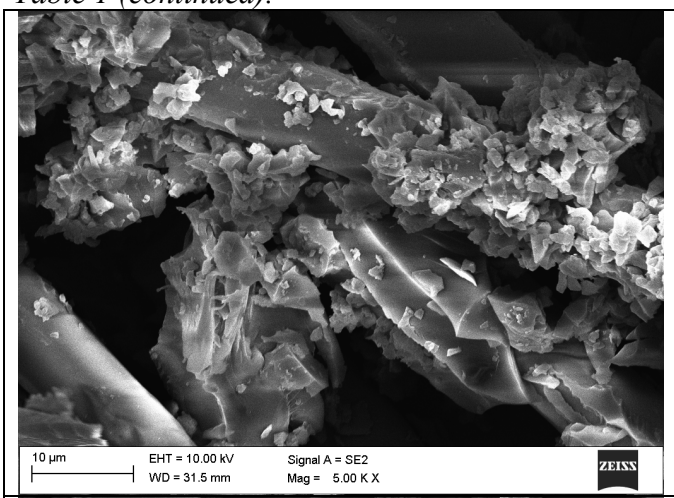	*SEM image of powder fraction >0,09*
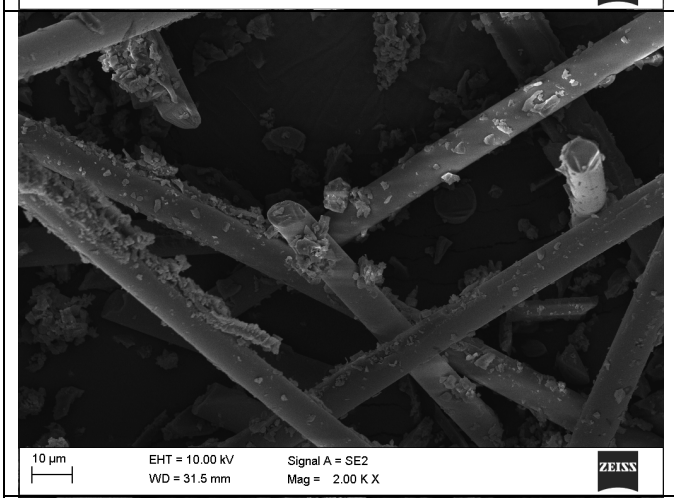	*SEM image of powder fraction >0,08*
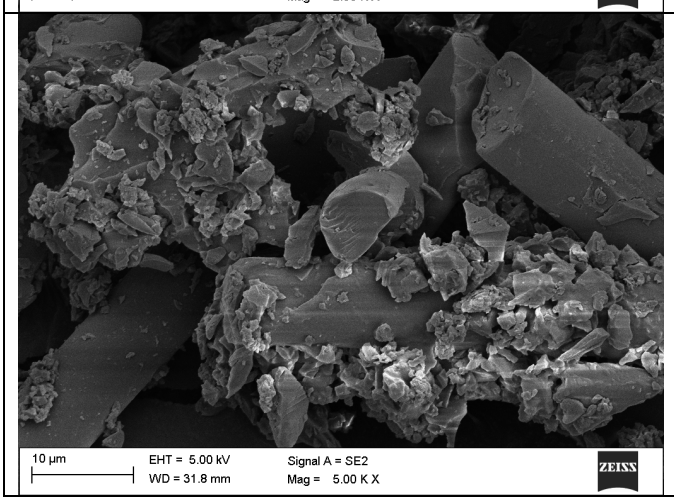	*SEM image of powder fraction <0,08*

New composite materials were manufactured by mixing selected powder fractions with an epoxy resin system (Epidian DECO) and a dedicated curing agent according to the proportions recommended by the manufacturer. The recycled powder was introduced as a filler into the resin matrix, and the mixtures were cast into molds to produce the test specimens. The curing process was performed under laboratory conditions at ambient temperature. The process of preparing new samples is presented in figure 4.

Figure 4. Preparation of composite specimens containing recycled fillers

3. RESULTS AND FUTURE WORK

The obtained powder fractions exhibited significant differences in morphology and fiber content. The coarser fractions contained longer fiber fragments and larger resin agglomerates, whereas the finer fractions consisted mainly of short fibers and resin-rich particles. SEM observations confirmed a progressive increase in fiber fragmentation with decreasing particle size.

These differences are expected to strongly influence the mechanical behavior of newly manufactured composites. Finer fractions may improve the matrix–filler interaction but can also lead to increased resin demand and potential processing challenges. Therefore, careful optimization of the fraction selection and filler content is required.

Future research will focus on improving the homogeneity of composite mixtures using a dedicated homogenization device. Additionally, systematic mechanical testing will be conducted to evaluate the influence of the recycled filler content on the strength, stiffness, and impact resistance. Particular attention will be paid to maximizing the recycled material content while maintaining acceptable mechanical performance.

4. CONCLUSIONS

This study demonstrates the feasibility of mechanically recycling multilayer polymer composites and reusing the obtained material as a filler in new composite systems. The applied approach, based on industrial waste materials and implemented within a PBL framework, highlights both the technical challenges and potential applications of recycled composite materials. An additional problem remains the lack of a developed market for recycled products and the high costs of implementing alternative recovery methods. Therefore, further intensive research and development are necessary to develop more sustainable composite materials that are easier to recycle, as well as the recycling technology itself. In response to these challenges, this project aimed to deepen students' knowledge of the possibilities of recycling composite materials, including their reuse.

ACKNOWLEDGEMENT

The present study was developed through the PBL project entitled. "Recycling of multilayer polymer composites – verification of mechanical properties, prediction of application possibilities" implemented under the Excellence Initiative - Research University program. Order No. 55/2020 of the Rector of the Silesian University of Technology. The work was carried out by members of the "HEAD TO HEAD" Student Scientific Circle of Plastics and Composites Processing, operating at the Scientific and Teaching Laboratory of Nanotechnology and Materials Technology at the Faculty of Mechanical Engineering.

HEAD TO HEAD

BIBLIOGRAPHY

1. Pickering S. J**.:** *Recycling technologies for thermoset composite materials – current status*, Composites: Part A, vol. 37, Elsevier, 2006, pp. 1206–1215.
2. Oliveux G., Dandy L. O., Leeke G. A.: Current status of recycling of fibre reinforced polymers: Review of technologies, reuse and resulting properties, Progress in Materials Science, vol. 72, Elsevier, 2015, pp. 61–99.
3. Pimenta S., Pinho S. T.: Recycling carbon fibre reinforced polymers for structural applications: Technology review and market outlook, Waste Management, vol. 31, Elsevier, 2011, pp. 378–392.
4. Job S., Leeke G., Mativenga P. T., Oliveux G., Pickering S., Shuaib N. A.: Composites Recycling: Where are we now?, Composites UK, University of Birmingham, University of Nottingham, University of Manchester, Report, 2016.

TalentDetector

9th January 2026
Gliwice, Poland

DEPARTMENT OF ENGINEERING MATERIALS AND BIOMATERIALS
FACULTY OF MECHANICAL ENGINEERING
SILESIAN UNIVERSITY OF TECHNOLOGY

INTERNATIONAL STUDENTS SCIENTIFIC CONFERENCE

Accuracy Assessment and Verification of the GOM ATOS 3D Optical Scanner Using Mitutoyo Reference Etalons

Drilon Bajgora[a], Vladimir Dukovski[b], Mitre Tomov[b], Afrim Gjelaj[c], Fatmir Azemi[a]

[a] University "Isa Boletini" in Mitrovica, Faculty of Mechanical and Computer Engineering email: drilon.bajgora@umib.net, fatmir.azemi@umib.net
[b] Ss. Cyril and Methodius University in Skopje, Faculty of Mechanical Engineering email: vladimir.dukovski@mf.edu.mk, mite.tomov@mf.edu.mk
[c] University of Prishtina "Hasan Prishtina", Faculty of Mechanical Engineering email: afrim.gjelaj@uni-pr.edu

Abstract: Dimensional measurement accuracy is critical in additive manufacturing (AM), where non-contact optical inspection enables reliable verification of complex geometries that are difficult or impossible to assess with tactile probes. This study evaluates the accuracy and repeatability of the GOM ATOS 5 using a Mitutoyo reference standard with well-defined nominal values and tolerance tables. Three repeated scans were acquired and aligned in GOM Inspect via Gaussian Best Fit; local deviations were quantified using Deviation Label. Accuracy was analyzed at two complementary scales: (i) global surface evaluation in four analysis planes reporting Sigma (σ), Residual, Max Deviation, Selected Points, benchmarked against a ±0.010 mm band; and (ii) local orthogonal sections (X +26.50 mm, Y +10.00 mm, Z +7.50 mm) with Max search distance = 0.01 mm and bilateral tolerance = ±0.10 mm. Results show high accuracy and excellent repeatability in well-sampled regions (e.g., Plane 1: σ≈0.0012 mm, Residual≈0.0009 mm, Max≈0.0089 mm, all within ±0.010 mm), whereas zones with low point density/coverage exhibit larger maxima (Planes 3–4). All features evaluated on the orthogonal sections fall within ±0.10 mm (dXYZ in −0.01…+0.01 mm), confirming conformity of critical profiles. Overall, the ATOS 5 demonstrates robust metrological performance when coverage and incidence are adequate.

Keywords: 3D Optical Scanning, GOM ATOS 5, Dimensional Accuracy, Measurement Verification, Additive Manufacturing

1. INTRODUCTION

Non-contact optical measurement technologies are increasingly recognized as a cornerstone of modern industrial metrology, particularly in Additive Manufacturing (AM). The growing demand for dimensional accuracy and surface integrity in AM exposes the limitations of conventional tactile methods when inspecting freeform surfaces, thin-walled geometries, and

delicate or inaccessible internal structures [1,2]. In contrast, optical 3D scanning enables rapid data acquisition, micron-level precision, and reliable digitization of complex parts for direct CAD comparison, supporting efficient deviation detection and process optimization [3,4].
The reliability of optical metrology systems depends on rigorous calibration and verification procedures to ensure accuracy, repeatability, and traceability. International standards such as ISO/IEC 17025 and ISO 3650 define laboratory competence requirements and the use of gauge blocks as fundamental length standards [5,6]. Accordingly, certified reference artifacts—including miniature step gauges and precision blocks—are widely applied to assess optical scanner performance under controlled and traceable conditions [1,4,7].
Recent studies confirm that advanced optical scanners, including the GOM ATOS series, achieve high accuracy in AM inspection tasks. Prior work demonstrates that calibration with reference standards validates scanner accuracy, supports systematic error identification, and ensures process reliability, particularly in critical sectors such as aerospace and biomedical manufacturing [1,2,6–8].
Building on this foundation, the present study investigates the accuracy of the GOM ATOS 5 3D scanner through direct comparison with a certified Mitutoyo reference standard. By integrating traceable calibration artifacts with Measurement System Analysis (MSA), the research provides a focused assessment of scanner performance and contributes to the advancement of optical metrology in additive manufacturing.

2.0 **MATERIALS AND METHODS**

This study was conducted at the Topomatika Institute in Zagreb under controlled laboratory conditions to minimize external influences and ensure measurement reliability. The experimental setup included a GOM ATOS 5 3D scanner, a non-contact optical measurement system widely used in industrial metrology and additive manufacturing, and a Mitutoyo certified setting ring (177-139) serving as the dimensional reference standard.
All measurements were conducted in accordance with established **metrological protocols**, including scanner configuration, the execution of scanning procedures, and subsequent data processing using **GOM Inspect software**. To evaluate measurement uncertainty and repeatability, multiple replicate scans were performed, and the deviations between the scanned datasets and the certified nominal dimensions of the etalon were analyzed.
The technical specifications of the Mitutoyo reference standard, as well as the operational characteristics of the GOM ATOS scanner, are detailed in this section. Additionally, calibration checks and preliminary testing were conducted prior to the measurement process to ensure full traceability and compliance with international quality standards.

2.1. Mitutoyo Etalon (177-139)

Certified dimensional artifacts are essential for ensuring traceability, accuracy, and repeatability in precision metrology [9]. In this study, a Mitutoyo Setting Ring (177-139), manufactured by Mitutoyo Corporation, was used as the certified reference standard for validating the performance of the GOM ATOS 5 3D optical scanner [10].
The etalon features precisely defined nominal dimensions, strict tolerance limits, and high geometric stability, ensuring compliance with ISO/IEC 17025 and ISO 3650 requirements [9–11]. *Figure 1* presents the reference artifact used in this research, while Table 1 summarizes its

principal specifications. The use of this certified standard established a traceable baseline for evaluating the accuracy and repeatability of the optical measurement system [12].

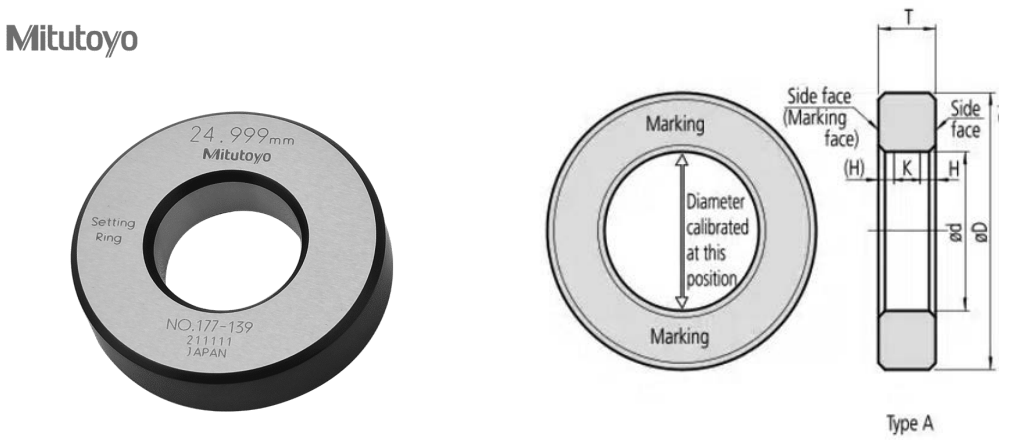

Figure 1. Mitutoyo Setting Ring (Model 177-139) is used as the certified dimensional reference standard.

The certified nominal dimensions and tolerance limits of the Mitutoyo Setting Ring (177-139), as specified by the manufacturer and compliant with ISO 3650 and ISO/IEC 17025 standards, are summarized in *Table 1.* These values were used as the reference for calibration and accuracy assessment of the optical measurement system.

Table 1. Technical specifications of the Mitutoyo Setting Ring (177-139).

Order No.	Dimensions (mm)				Type	Accuracy				
	Nominal size ød	øD	øE	T		Tolerance between the nominal size and the actual diameter (µm)	Uncertainty of marked diameter value (µm)*1	Roundness/ Cylindricity (µm)*2	Distance from the side face H (mm)	Size of warranted calibration surface K (mm)
177-177	16mm	45	–	10	A	±10	±1.5	1	2.0	6.0
177-133	17mm	45	–	10	A	±10	±1.5	1	2.0	6.0
177-285	18mm	45	–	10	A	±10	±1.5	1	2.0	6.0
177-286	20mm	45	–	10	A	±10	±1.5	1	2.0	6.0
177-139	25mm	53	–	15	A	±10	±1.5	1	3.2	8.6
177-288	30mm	71	–	15	A	±10	±1.5	1	3.2	8.6
177-140	35mm	71	–	15	A	±10	±1.5	1	3.2	8.6

.

2.2 3D Scanning Procedure Conducted at the Topomatika Institute, Zagreb

Accurate calibration of a 3D scanner is crucial to ensure high measurement accuracy and the reliability of the scanned data. Since 3D scanners can gradually lose accuracy and precision over time, regular calibration is necessary to maintain measurement integrity and ensure accuracy.[16,17]

The calibration of the GOM ATOS 5 3D scanner was performed at the Institute of Topomatics in Zagreb under controlled laboratory conditions to ensure high measurement accuracy and repeatability. The certified Mitutoyo setting ring (177-139) was used as a dimensional reference

standard, providing accurate calibration data for subsequent scanning operations. In *Figure 2a*, we present the placement of reference points on the surface of the standard before the scanning process. At this stage of the study, it is essential to perform this step. These points serve to ensure accurate spatial positioning of the object during scanning and enable precise focusing of the scanner beam on the target areas. This procedure contributes to improved dimensional accuracy and measurement repeatability. *Figure 2* b presents the standard during the preparation phase, where the placement of reference points can be observed, ensuring stable and precise scanning conditions.[14]

(a) (b)

Figure 2. (a) Calibration of the GOM ATOS 5 3D scanner. (b)Standard with reference points positioned for scanning.

Before scanning, the GOM ATOS 5 3D scanner was calibrated using predefined calibration points to ensure measurement accuracy and repeatability. The certified reference standard was prepared by applying reference points and a white matte spray to reduce optical reflections and improve data acquisition stability.
Three repeated scans of the reference standard were performed to assess measurement accuracy and repeatability. The acquired datasets were processed in GOM Inspect software, where the scanned geometry was compared with the reference model to support subsequent accuracy and deviation analysis.

3. RESULTS AND DISCUSSION

Based on the certified dimensional data of the Mitutoyo Setting Ring (No. 177-139), a high-accuracy 3D CAD model was generated in SolidWorks and used as the digital reference for the evaluation of the scanned data. The reference model includes nominal dimensions and tolerance limits (±10 μm), preserving full traceability to the manufacturer's specifications and serving as the metrological baseline for all subsequent analyses.
Figure 3 presents the CAD reference model with the principal geometric features used for inspection. This model was imported into GOM Inspect and employed as the reference geometry for alignment and deviation analysis of the scanned datasets.

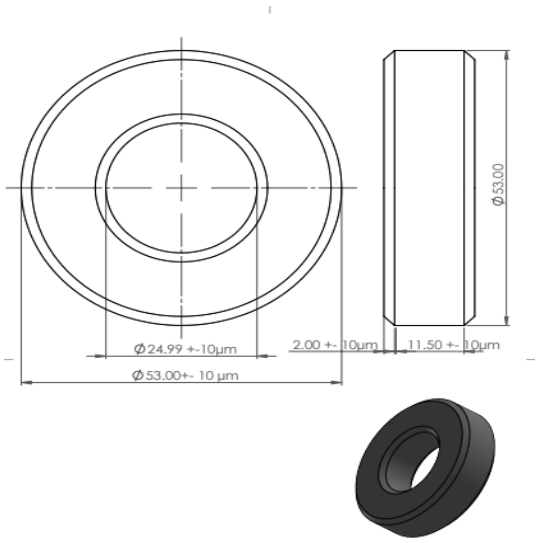

Figure 3. 3D CAD reference model of the Mitutoyo Setting Ring with nominal dimensions and tolerance limits.

The scanned STL data were imported into GOM Inspect and pre-aligned with the reference model using standard alignment procedures. *Figure 4* illustrates the inspection setup, including fitted geometric elements (inner and outer cylinders, distances, and angular features) together with Nominal–Actual–Deviation values and tolerance checks. The color-coded deviation map provides a visual representation of surface differences between the scanned model and the reference geometry, enabling rapid identification of local deviations.

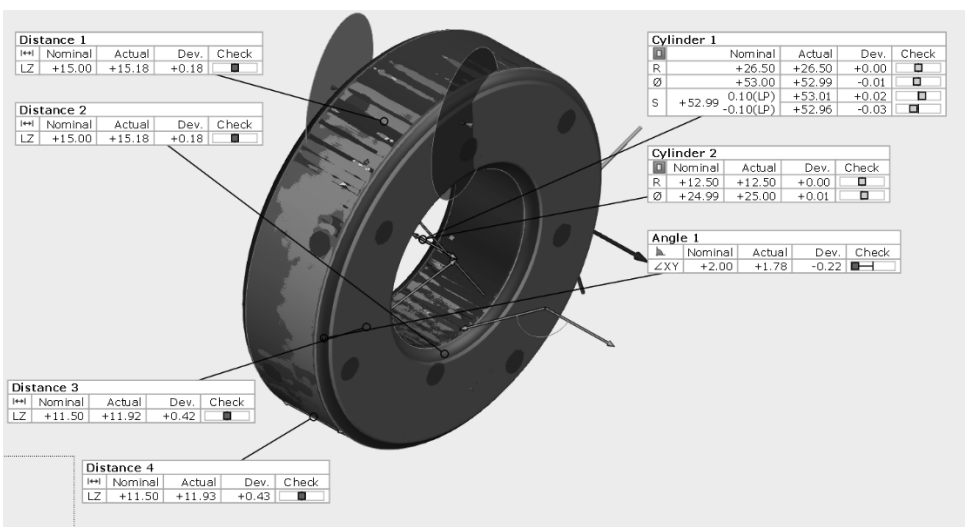

Figure 4. GOM Inspect inspection summary showing fitted features and Nominal–Actual–Deviation evaluatio

The numerical inspection results for the primary geometric features are summarized in *Table 2*. Cylindrical features show very small deviations and remain within the defined tolerance limits, indicating good geometric conformity. Larger deviations are observed for selected axial distance features, suggesting increased sensitivity to alignment conditions and surface quality. Fit-quality

indicators (Sigma, Residual, and Maximum Deviation) confirm stable fitting behavior in well-sampled regions, while areas with reduced point density exhibit increased scatter.

Table 2. Summary of GOM Inspect results for main geometric features.

PIP | Table | Diagram

Statistics Overview

Element	Property	Nominal	Actual	Tol -	Tol +	Dev	Avg
Cylinder 1	R	+26.50	+26.50	-0.10	+0.10	+0.00	+0.00
Cylinder 1	Ø	+53.00	+52.99	-0.10	+0.10	-0.01	-0.01
Cylinder 1	(I)	+52.99	+52.96 / +53.01	-0.10	+0.10	-0.03 / +0.02	-0.00
Cylinder 2	R	+12.50	+12.50	-0.10	+0.10	+0.00	+0.00
Cylinder 2	Ø	+24.99	+25.00	-0.10	+0.10	+0.01	+0.01
Angle 1	∠XY	+2.00	+1.78	-0.20	+0.20	-0.22	-0.22
Distance 1	LZ	+15.00	+15.18	+0.00	+0.00	+0.18	+0.18
Distance 2	LZ	+15.00	+15.18	+0.00	+0.00	+0.18	+0.18
Distance 3	LZ	+11.50	+11.92	+0.00	+0.00	+0.42	+0.42
Distance 4	LZ	+11.50	+11.93	+0.00	+0.00	+0.43	+0.43

Table 7. Dimensional repeatability results from three scans compared with nominal values.

Feature	Property	Nominal	Scan 1 Actual	Scan 2 Actual	Scan 3 Actual	Deviation Scan 1 (mm)	Deviation Scan 2 (mm)	Deviation Scan 3 (mm)	Avg Deviation (mm)	Max Δ Between Scans (mm)
Cylinder 1	Diameter	53.0	52.997	52.999	52.995	-0.003	-0.001	-0.005	-0.003	0.004
Cylinder 2	Diameter	24.999	25.019	24.999	24.998	0.02	0.0	-0.001	0.0063	0.021
Distance 1	Length	15.0	15.186	15.191	15.191	0.186	0.191	0.191	0.1893	0.005
Distance 2	Length	15.0	15.188	15.185	15.185	0.188	0.185	0.185	0.186	0.003
Distance 3	Length	11.5	11.68	11.3	11.3	0.18	-0.2	-0.2	-0.0733	0.38
Distance 4	Length	11.5	11.8	11.6	11.6	0.3	0.1	0.1	0.1667	0.2
Angle 1	Angle (°)	2.0	1.82	1.98	1.98	-0.18	-0.02	-0.02	-0.0733	0.16

To assess measurement repeatability, three independent scans of the reference standard were performed under identical conditions. The comparative results are summarized in *Table 3*. The deviations between scans are small for the cylindrical features, demonstrating high repeatability of diameter measurements. Larger variations are observed for axial distances and angular features; however, the maximum deviation between scans remains limited, indicating consistent measurement behavior across repeated acquisitions.

Local dimensional accuracy was evaluated using three orthogonal inspection sections in GOM Inspect at X +26.50 mm, Y +10.00 mm, and Z +7.50 mm, with a maximum search distance of 0.01 mm and a bilateral tolerance of ±0.10 mm. The consolidated deviation maps *(Figure 5)* indicate that all evaluated sections remain within the defined tolerance range, confirming high local dimensional accuracy and consistent measurement behavior across all spatial directions. The observed deviation distribution is uniform and stable, indicating good surface coverage and reliable data acquisition during scanning.

The alignment between the scanned data and the reference model was performed using the Gaussian Best Fit method, which minimizes the influence of local surface irregularities and outliers by optimizing the global fit between datasets. This approach enables a robust evaluation of overall dimensional accuracy and ensures reproducible alignment across repeated scans, thereby supporting a reliable assessment of scanner performance for precision inspection tasks.

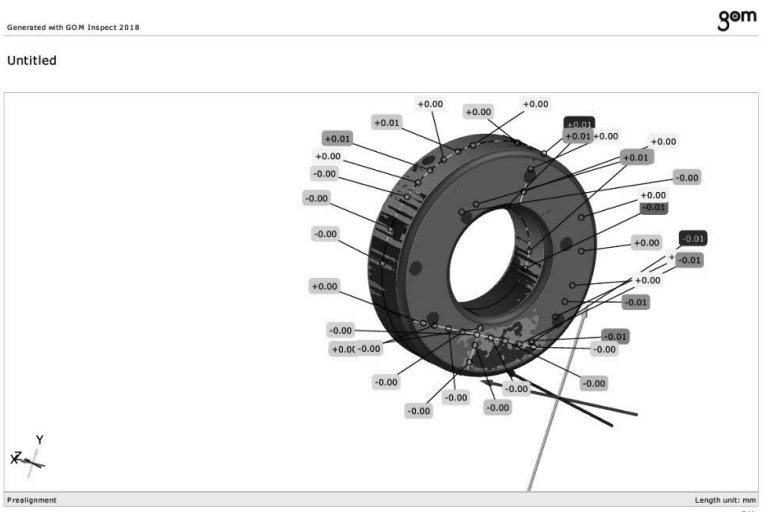

Figure 5. Orthogonal deviation sections at X +26.50 mm, Y +10.00 mm, and Z +7.50 mm (tolerance ±0.10 mm).

The authors gratefully acknowledge the SYNaM Research Group under the Horizon Europe Programme (HORIZON-MSCA-2022-SE-01-01, Grant No. 101129996) for research support.

CONCLUSION

In this study, a certified Mitutoyo reference standard was employed as a traceable benchmark to verify the dimensional accuracy and repeatability of the GOM ATOS 5 3D optical scanner. Three repeated scans were aligned in GOM Inspect using the Gaussian Best Fit method and evaluated through deviation analysis (dXYZ), including global metrics such as Sigma (σ), Residual, and Maximum Deviation, as well as local verification on orthogonal sections.

The results demonstrate that, in well-sampled regions, global accuracy reaches the sub-10 μm range, with maximum deviations remaining within or close to ±0.010 mm. Local orthogonal inspections (X, Y, and Z), performed with a maximum search distance of 0.01 mm and a bilateral tolerance of ±0.10 mm, confirmed that all evaluated features remained within the defined tolerance limits, indicating high local dimensional accuracy. Larger deviations were observed only in areas with reduced point density or challenging local geometry, suggesting that these effects are primarily related to measurement setup and surface coverage rather than limitations of the reference standard.

Overall, the results confirm that the GOM ATOS 5 combined with GOM Inspect provides a reliable and repeatable measurement chain for optical scanner verification and quality control. The use of a traceable Mitutoyo reference artifact together with repeated measurements establishes a robust Measurement System Analysis (MSA) approach, where Gaussian Best Fit ensures reproducible global alignment and deviation-based evaluation enables consistent local verification. This methodology is reproducible and directly transferable to industrial inspection and additive manufacturing quality assurance.
Non-contact 3D scanning enables fast, full-field and traceable verification of complex geometries, providing clear quantitative metrics for pass/fail decisions that are difficult to achieve with conventional tactile methods.

BIBLIOGRAPHY

1. M. G. Guerra, L. De Chiffre, F. Lavecchia, L. M. Galantucci, *Use of Miniature Step Gauges to Assess the Performance of 3D Optical Scanners and to Evaluate the Accuracy of a Novel Additive Manufacturing Process*, Sensors, Vol. 20, No. 3, 738, 2020.
2. C. Fang, S. W. Fu, Y. S. Leong, *Research on Optical Measurement for Additive Manufacturing Surfaces*, CIRP Proceedings, Vol. 60, pp. 362–367, 2017.
3. R. Leach, *Advances in Optical Surface Metrology*, Springer, 2018.
4. Mitutoyo Corporation, *Reference Gauge Blocks and Accessories*, Mitutoyo Corporation, 2020. Available online: https://www.mitutoyo.com/products/calibration-equipment/gauge-blocks/
5. ISO/IEC 17025:2017, *General requirements for the competence of testing and calibration laboratories*, International Organization for Standardization, Geneva, Switzerland, 2017.
6. ISO 3650:2017, *Geometrical product specifications (GPS) — Length standards — Gauge blocks*, International Organization for Standardization, Geneva, Switzerland, 2017.
7. R. Schmitt, M. Peterek, E. Morse, W. Knapp, M. Galetto, *Advances in Industrial Metrology for Additive Manufacturing*, CIRP Annals, Vol. 65, No. 2, pp. 729–752, 2016.
8. A. Thompson, N. Senin, I. Maskery, et al., *Topography of Selectively Laser Melted Surfaces: A Comparison of Different Measurement Methods*, CIRP Annals, Vol. 65, No. 1, pp. 543–546, 2016.
9. C. Fang, S. W. Fu, Y. S. Leong, *Research on Optical Measurement for Additive Manufacturing Surfaces*, Procedia CIRP, Vol. 60, pp. 362–367, 2017.
10. Mitutoyo Corporation, *Reference Gauge Blocks and Accessories*, Mitutoyo Corporation, 2020. Available online: https://www.mitutoyo.com/products/calibration-equipment/gauge-blocks/
11. JCGM 200:2012, *International Vocabulary of Metrology – Basic and General Concepts and Associated Terms (VIM)*, 3rd Edition, Joint Committee for Guides in Metrology, 2012.
12. BIPM, *Calibration and Measurement Capabilities in Metrology*, Bureau International des Poids et Mesures, 2019. Available online: https://www.bipm.org
13. D. Flack, *Fundamentals of Dimensional Metrology*, Cengage Learning, 2013.
14. Topomatika Institute, Zagreb, Croatia, *Calibration and 3D Scanning Laboratory Facilities*, Online resource. Available at: https://www.topomatika.hr (Accessed: October 2, 2025).

TalentDetector
9th January 2026
Gliwice, Poland
DEPARTMENT OF ENGINEERING MATERIALS AND BIOMATERIALS
FACULTY OF MECHANICAL ENGINEERING
SILESIAN UNIVERSITY OF TECHNOLOGY
INTERNATIONAL STUDENTS SCIENTIFIC CONFERENCE

Manual laser braze welding of galvanized automotive sheets

Sławomir Bensz[a], Sebastian Bartkowiak[a], Aleksandra Bodnar[a,*], Łukasz Chłud[a], Tomasz Harężlak[a], Katarzyna Jędrzejczyk[a], Piotr Karski[a], Igor Klima[a], Artur Czupryński[b]

[a] Student of Silesian University of Technology, Faculty of Mechanical Engineering
[b] Silesian University of Technology, Faculty of Mechanical Engineering, Department of Welding Engineering
* Corresponding e-mail address: alekbod982@student.polsl.pl

Abstract: The article describes research on the influence of parameters such as oscillation length and wire feed speed during manual laser braze welding of lap joints made of galvanized DC04+ZE steel with CuSi3 wire on joint quality and corrosion resistance.

Keywords: laser braze welding, galvanized steel, corrosion resistance

1. INTRODUCTION

Braze welding, referred to as non-capillary hard soldering, combines characteristics typical of both welding and soldering processes. In the brazing process, equipment and accessories used in conventional welding processes are employed. However, unlike in traditional welding, the edges of the joined components are not melted during braze welding. Instead, physical phenomena such as wettability and diffusion play a decisive role. The components to be joined are prepared for braze welding in the same manner as for conventional welding methods. The process temperature is lower than the melting point of the base materials, yet high enough to melt the filler material, allow it to wet the surfaces of the joined components, and activate diffusion processes. Braze welding methods are classified according to the heat source in line with the PN-EN ISO 4063:2011 standard. Laser braze welding involves melting the filler metal, supplied continuously in the form of wire, into the welding zone. The supplied heat enables activation of the surfaces of the joined materials, significantly improving wettability and the effectiveness of capillary processes. In the industry, solid-state lasers (fiber and disk lasers) as well as diode lasers are used as sources of laser radiation, due to requirements related to beam delivery to the processing head via optical fibers [1-5].

2. RESEARCH

2.1. Purpose and range of the research

The aim of this study was to determine the optimal parameters of the manual laser brazing process for galvanized DC04+ZE steel and to assess their influence on the quality and structure

of the joints, as well as on their mechanical properties and corrosion resistance. The scope of the work included:

- a literature review of the subject,
- preparation of lap joints of galvanized sheets using manual laser braze welding technology,
- metallographic examinations to assess the influence of process parameters on joint structure,
- hardness testing to evaluate the influence of process parameters on the mechanical properties of the joints,
- tensile and bending tests to assess the influence of process parameters on the mechanical properties of the joints,
- corrosion resistance tests to evaluate the joints' resistance to corrosive environments,
- metallographic examinations to determine the effect of corrosive exposure on joint structure,
- analysis of the obtained results.

2.2. Equipment and materials used to perform the operation

Lap joints of galvanized DC04+ZE steel were produced using laser brazing technology with the LightWeld XC laser source, which enables manual welding and brazing. Figure 1 presents the joint preparation process.

Figure 1. Manual laser braze welding process of lap joints and example joint

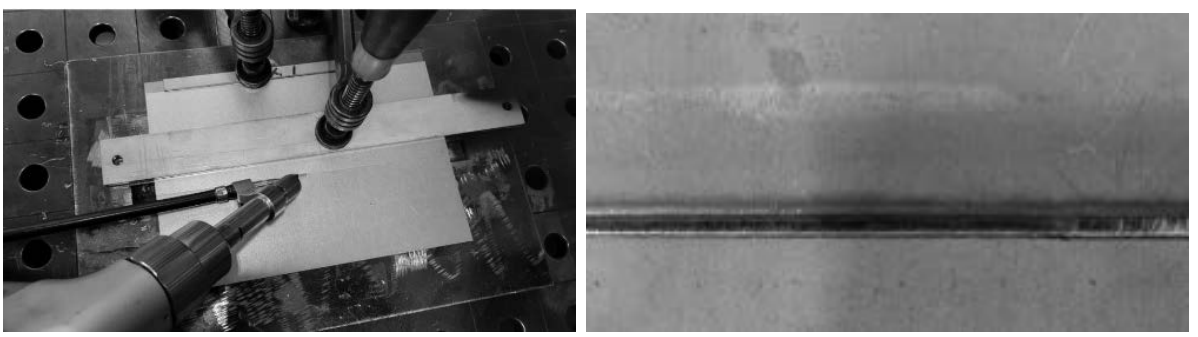

The chemical composition and mechanical properties of the joined sheets are presented in Tables 1–2. The thickness of the sheets was 0.9 mm. CuSi3 wire with a diameter of 1 mm was used as the filler material. The chemical composition and mechanical properties of the filler metal are presented in Tables 3–4.

Table 1. The chemical composition of DC04+ZE steel according to EN10130-2006

C max, %	P max, %	S max, %	Mn max, %
0.08	0.03	0.03	0.4

Table 2. Mechanical properties of DC04+ZE steel according to EN10130-2006

R_e, MPa	R_m, MPa	A_{80}, %
140 - 220	270 - 350	37

Table 3. The chemical composition of CuSi3 wire according to PN-EN 14640

Si, %	Mn, %	Cu, %	Fe, %	Zn, %	Sn, %
3.0	1.0	94.0	0.07	0.10	0.10

Table 4. Mechanical properties of CuSi3 wire according to PN-EN 14640

Re, MPa	Rm, MPa	A_5, %	KV, J (20°C)
>120	>350	>40	>60

2.3. Parameters and technique of braze welding

Before preparing the final test joints that were subjected to examinations, several technological trials were carried out to determine the optimal wire feeding speed ensuring process stability. The process parameters used for these trials are presented in Table 5.

Table 5. Process parameters used for the technological trials

Specimen number	Power [W]	Oscillation frequency [%]	Oscillation length [%]	f [mm]	Wire feeding speed [cm/min]
1	750	0	-40	10	40
2	750	0	-40	10	50
3	750	0	-40	10	60
4	750	0	-40	10	70
5	750	0	-40	10	80

Satisfactory face quality and process stability were achieved at a wire feeding speed of 70 cm/min. A feeding speed of 60 cm/min provided lower stability, while speeds below 60 cm/min resulted in an unstable process. Spatter occurred, as well as significant loss of the zinc coating on the sheet surfaces due to its evaporation. Increasing the wire feeding speed to 80 cm/min also led to reduced process stability.

After determining the optimal wire feeding speed, the final specimens intended for testing were prepared. The variable parameter was the oscillation length of the laser beam. The oscillation length at which the process remained stable was established. Subsequently, test joints intended for metallographic examinations and mechanical property testing (joints 22 and 23) were prepared. Table 6 presents the parameters used for producing each joint.

Table 6. Parameters used for producing joints *1-6, 22 and 23*

Specimen number	Power [W]	Oscillation frequency [%]	Oscillation length [%]	f [mm]	Wire feeding speed [cm/min]
1	750	0	-40	10	70
2	750	0	-40	10	70
3	750	0	-30	10	70
4	750	0	-20	10	70
5	750	0	-10	10	70
6	750	0	-50	10	70
22	750	0	-40	10	70
23	750	0	-30	10	70

2.4. Research methodology and results

2.4.1. Measurements of the zinc coating thickness”

Measurements of the electrolytically deposited zinc coating thickness were carried out for the test joints 1 – 6. The measurement results are presented in Table 7. The zinc coating thickness is uniform across the entire surface of the joined sheets and is approximately 7 μm.

Table 7. Results of zinc coating thickness measurements

Specimen joint number	1	2	3	4	5	6
Measurement 1	9	7	8	7	9	8
Measurement 2	8	7	7	8	8	8
Measurement 3	7	8	8	7	9	7
Measurement 4	6	9	6	6	8	7
Measurement 5	7	6	9	6	7	7
Measurement 6	9	7	7	7	7	8
Measurement 7	7	8	9	7	8	7
Measurement 8	7	8	7	7	7	8
Measurement 9	7	7	8	8	8	9
Measurement 10	7	7	7	6	8	7
Average	7.4	7.4	7.6	6.9	7.9	7.6

2.4.2. Visual and penetrant testing

Visual inspections were carried out in accordance with the PN-EN ISO 5817 standard. Slight melting of the upper sheet edges was observed in sample 4. Sample 5 exhibited numerous instances of edge melting on the upper sheet. Sample 6 exhibited insufficient weld groove filling.

Penetrant testing was performed in accordance with ISO 3452-2. All samples met the quality requirements according to acceptance level 2x, with no indications of nonconformities detected. Only false indications were observed, resulting from depressions as well as the start or end of the brazed joint.

2.4.3. Macro- and microscopic examinations

Specimens for macro- and microstructural examinations were taken from joints 22 and 23.

Macroscopic observations showed that the brazed joints exhibited a flat face without noticeable concavity or convexity, and their geometry was correct. Slight melting of the joined sheets was observed.

Microstructural analysis of the laser-brazed lap joints revealed a dendritic copper structure and a fine-grained ferritic structure of the base material. The transition line between the brazed joint and the base material is regular. Slight melting of the joined sheets was observed. No cracks were detected in either the base material or the brazed joint. Figure 2 presents representative microstructure of the joint.

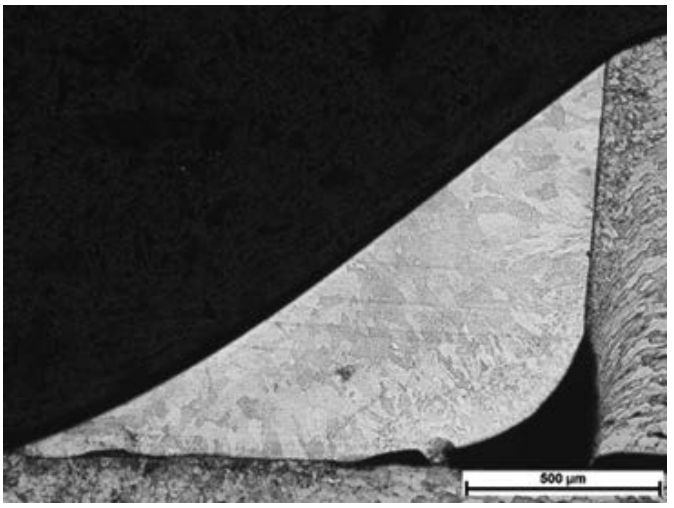

Figure 2. Representative microstructure of the joint

2.4.4. Microhardness testing

Microhardness measurements were carried out on specimens prepared for macro- and microstructural examinations. The measurements were performed using the Vickers method with a load of 50 gf and a dwell time of 12 seconds. Measurements were taken across the joint, both in the braze-welded material and the base material. The measurement line passed through braze-welded joint, heat-affected zone, and base material.

Table 8 presents the microhardness measurement results in the order of testing (from top to bottom). Slight hardening was observed in the heat-affected zone. The hardness in the HAZ is approximately 135 HV0.05 for samples 22.0 and 22.1. For samples 23.0 and 23.1, it is slightly higher, around 140 HV0.05. The hardness in the brazed joint is similar for all samples, approximately 123 HV0.05. In the base material, the hardness is also similar for all samples, around 130 HV0.05.

Table 8. Results of Vickers microhardness measurements performed with a 50 gf load and a 12 s dwell time

Sample number	22.0	22.1	23.0	23.1
Braze-welded joint	121	118	122	128
	126	124	123	125
	130	121	124	121
	120	126	119	124
	122	127	127	120
Average for braze-welded joint	123.8	123.2	123.0	123.6
HAZ	138	136	141	140
	132	135	147	139
Base material	126	131	132	130
	126	126	125	124
	122	124	124	126

2.4.4. Static tensile test of the joints

Specimens for the static tensile test were cut from test joints 22 (samples 22.1, 22.2) and 23 (samples 23.1, 23.2). The results of the static tensile test are presented in Table 9.

Table 9. Results of the static tensile test of laser braze-welded joints

Sample	m_E, GPa	$R_{p0.2}$, MPa	R_m, MPa	F_m, kN	A_g, %	A_{80mm}, %	S_0, mm^2
22.1	9.10	168.6	247.4	6.6	6.2	6.3	26.7
22.2	9.10	174.1	287.1	7.7	20.3	20.7	26.7
23.1	34.40	35.2	257.3	6.8	7.6	7.7	26.4
23.2	9.28	182.8	269.6	7.1	7.9	8.1	26.2

Figures 3 and 4 show the tensile curves of the individual samples. All tested joints failed in the brazed material. The tensile test results are similar for samples 23.1 and 23.2. The parameters Rm and A80 for these samples are approximately 260 MPa and 8%, respectively. In the case of samples 22.1 and 22.2, there are significant differences in the results. For sample 22.1, the tensile strength is about 250 MPa, while for sample 22.2 it is approximately 290 MPa. Similarly, the elongation for sample 22.1 is around 6%, whereas for sample 22.2 it is about 20%.

Figure 3. Tensile curves of samples 22.1 and 22.2

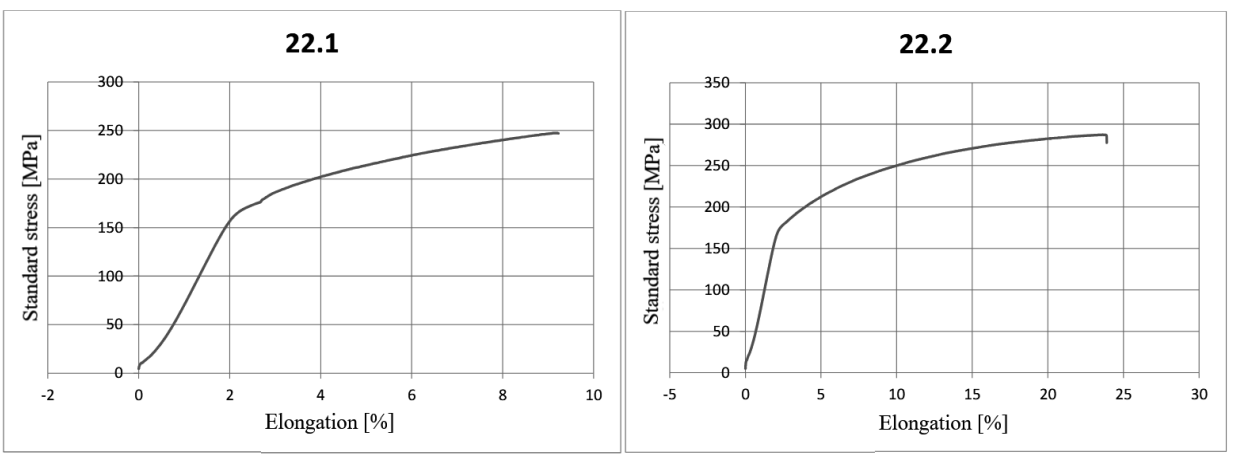

Figure 4. Tensile curves of samples 23.1 and 23.2

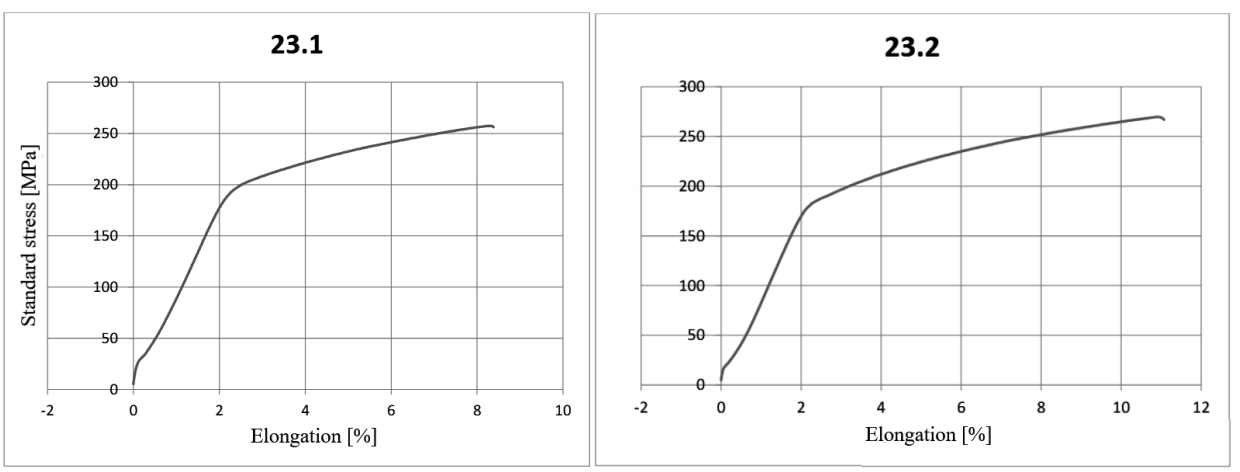

2.4.5. Bending test

Specimens for the bending test were taken from test joints 22 (samples 22.3, 22.4) and 23 (samples 23.3, 23.4). No cracks, delamination's, or tears were observed in the test joints.

2.4.6. Corrosion resistance testing

Corrosion resistance was evaluated using electrochemical and immersion methods.

For the electrochemical method, the prepared samples were immersed for 5 days in a 3% hydrochloric acid solution. The joint served as the anode, while austenitic steel was used as the cathode. The current density was 0.08 A/cm². The sample edges were protected with a paint coating. To determine the corrosion rate, mass measurements were performed on sample 1, which underwent corrosion, both before immersion in the electrolyte and after removal from the bath. Table 10 presents the average mass values of the sample prior to the test and upon its completion.

Table 10. Mass measurement results before and after the corrosion resistance test

Sample mass before immersion in the electrolyte, g	Sample mass after completion of the test, g	Mass reduction, g	Average mass reduction, g/day
97.03	83.32	13.71	2.74

After completing the corrosion process, metallographic examinations were carried out. Both macrostructural and microstructural analyses revealed material loss in the base metal and in the braze-weld metal. As a result of corrosive activity, complete separation occurred between the upper sheet and the brazed joint. Material loss was also observed at the interface between the braze-weld metal and the lower sheet, although to a considerably lesser extent.

In the immersion corrosion test, the corrosion resistance of the joints was evaluated by immersing the samples in a 6% hydrochloric acid solution. The test duration was 30 days. To determine the rate of corrosion progression, the mass of the sample was measured before the test and after its completion. The average measurement results are presented in Table 11.

Table 11. Results of the mass measurements before immersion in the corrosive solution and after removal from the bath

Sample mass before immersion in the solution, g	Sample mass after completion of the test, g	Mass gain, g
96.39	96.55	0.16

No corrosion products of the steel were observed on the sample surface. The slight mass gain after 30 days of immersion in a 6% hydrochloric acid solution may indicate the presence of corrosion products of the zinc coating - zinc oxides and hydroxides. This is supported by the appearance of a white deposit on the sample surface, characteristic of so-called white zinc corrosion.

2. SUMMARY

The conducted study on the influence of manual laser braze welding process parameters on the quality, mechanical properties, braze geometry, and corrosion resistance of lap joints made

of galvanized 0.9 mm thick automotive steel DC04+ZE using CuSi3 1 mm in diameter solid wire filler allows the following conclusions to be drawn:

- The oscillation length of the laser beam is a key parameter affecting the quality of laser-brazed joints. Increasing the oscillation length intensifies the evaporation of the zinc coating on the opposite side of the brazed sheet. This parameter also influences hardness in the heat-affected zone: for higher oscillation lengths, HAZ hardness is slightly increased. Excessive oscillation length leads to melting of the upper sheet edge, whereas too small a value results in insufficient filling of the weld groove.
- Based on the static tensile tests, the produced trial joints do not exhibit satisfactory mechanical properties, as failure occurred within the brazed material, meaning their tensile strength is lower than that of the base material. However, the joints demonstrated satisfactory bending performance. The bending tests did not reveal any tendency toward tearing or cracking.
- The results of the corrosion resistance tests are inconclusive. The immersion test confirmed satisfactory resistance of the joints to the corrosive environment. However, in the electrochemical test the joint underwent corrosion due to the action of the electrolyte and current flow. The discrepancies between the two methods may arise from the differing intensities of corrosion processes, which depend strongly on the specific test conditions.

BIBLIOGRAPHY

1. Pfeifer T., Stano S., Nowoczesne metody lutospawania w aspekcie jakości i właściwości połączeń, Przegląd Spawalnictwa, 2016, nr 88, s. 95 – 102,
2. Mirski Z., Wpływ czynników technologicznych w lutospawaniu płomieniowym na jakość złączy stalowych rur ocynkowanych, Seminarium Praktyczne Aspekty Zastosowania Lutospawania stali Trudno Spawalnych i z Pokryciami Ochronnymi, Gliwice, 2005,
3. Bunaziv I., Akselsen O., Ren X., Nyhus B., Eriksson M., Gulbrandsen-Dahl S., A Review on Laser Assisted Joining of Aluminium Alloys to Other Metals, Metals 2021, 11, 1680,
4. Reimann W., Pfriem S., Hammer T., Päthe D., Ungers M., Dilger K., Influence of different zinc coatings on laser brazing of galvanized steel, Journal of Materials Processing Technology, Vol. 239, pages 75-82, 2017,
5. Koltsov A., Bailly N., Cretteur L., Wetting and laser brazing of Zn-coated steel products by Cu-Si filler metal. J. Mater. Sci 45, 2118–2125, 2010.

The study was carried out as part of project-based learning (XIII Competition PBL) within the framework of the Excellence Initiative – Research University (IBUD) program, under the project entitled: „Verification of the technological capabilities of the innovative LightWELD and LightWELD Cobot welding systems in the laser braze welding process of thin corrosion-resistant sheets”.

TalentDetector

9th January 2026
Gliwice, Poland

DEPARTMENT OF ENGINEERING MATERIALS AND BIOMATERIALS
FACULTY OF MECHANICAL ENGINEERING
SILESIAN UNIVERSITY OF TECHNOLOGY

INTERNATIONAL STUDENTS SCIENTIFIC CONFERENCE

Modification of unmanned aerial vehicles for combat missions and increasing efficiency using modern technologies

Dima Beridze[a], Givi Sanadze[b]

[a] Georgian Technical University, Faculty of Transport Systems and Mechanical Engineering, Department of Mechanical Engineering and Industrial Technology, PhD Student
email: dima.beridze@gmail.com
[b] Georgian Technical University, Faculty of Transport Systems and Mechanical Engineering,Department of Mechanical Engineering and Industrial Technology, Professor
email: sanadzegivi05@gtu.ge

Abstract: The article addresses the strategic need to modify Unmanned Aerial systems (UAS) to perform combat missions beyond traditional intelligence, surveillance, and reconnaissance (ISR) functions. The main focus is on increasing their efficiency and survivability using post-2020 technological advances. Key areas discussed include structural and electronic adaptation of commercial platforms (e.g., First Person View (FPV) systems), integration of artificial intelligence (AI) for autonomous target recognition and navigation in GPS-deprived environments, and the implementation of coordinated swarm (Swarm) technology. The analysis highlights the emergence of kinetic warfare and the ongoing technological race against emerging counter-UAS (C-UAS) systems.

Keywords: Unmanned Aerial systems (UAS), Unmanned Aerial Vehicles (UAV), First Person View (FPV), Artificial Intelligence, Shield Technology, Electronic Warfare, Weapon Systems, Military Drone, Swarm Technology, Counter UAS

1. INTRODUCTION

Unmanned Aerial Vehicles (UAVs), commonly known as drones, have revolutionized the nature of military operations in recent years. From their initial reconnaissance functions, modern conflicts have clearly demonstrated the need for rapid and effective modification of drones into combat, strike platforms [3]. This phenomenon includes both the improvement of large military drones (MALE/HALE) and, more importantly, the adaptation of civilian and commercial multicomputer into inexpensive, mass-produced combat weapons [4].

The main goal of the modification is to improve the payload, accuracy, maneuverability and electronic protection parameters to ensure its effectiveness in a high-intensity combat environment. In modern warfare, the modification of UAVs is based on economic and tactical advantages: low cost and reduced human risks. The rapid development of UAVs requires

constant innovation in materials engineering and surface treatment. These systems allow small tactical units to confront and destroy expensive enemy armored vehicles and firing positions.

2. DIRECTIONS OF MODIFICATION FOR COMBAT MISSIONS

Modification to increase the combat potential of UAVs includes several main, technical aspects:

Structural adaptation of armament and payload: Structural modification of commercial drones involves strengthening the hull with lightweight composite materials and increasing the power of the engines, which is necessary for transporting combat loads [6]. It is necessary to simplify the logistics chain to ensure a constant supply of ammunition and spare parts. The integration of ammunition requires specially designed or 3D-printed suspensions (dropping mechanisms) that ensure the precise dropping or remote detonation of grenades, mines or small explosive devices.

Communication and electronic countermeasures: Signal protection is critical to maintaining control in electronic warfare (EW) conditions. This is achieved by integrating anti-jamming technologies. These include frequency hopping and encrypted data transmission methods that make it difficult for an adversary to gain control. It is also important to increase the control radius, which is achieved by using high-power amplifiers and directional antennas, which strengthen the signal and increase the range of the drone behind enemy lines.

FPV (First Person View) Technology: FPV drones are the most effective and inexpensive combat modification in recent years [8]. The operator controls the drone through virtual reality goggles, which provides maximum accuracy and maneuverability. The high maneuverability of FPV drones allows them to hit moving targets or penetrate small openings (e.g., through the hatch of a tank turret).

Most FPV drones are "kamikaze" type weapons, where the drone and ammunition form a single unit. Stealth and survivability modifications: Increasing the survivability of the UAV includes not only electronic protection, but also physical "stealth". This is achieved by reducing the thermal footprint: special materials and engine modifications reduce infrared radiation, making them difficult to detect with thermal cameras. Radar reflectivity reduction is also used - the use of certain materials that absorb radar waves to make the UAV a more difficult target for air defense systems [9]. It is also important to reduce the noise level, which is achieved by using special materials.

3. INCREASING EFFICIENCY WITH MODERN TECHNOLOGIES

It is impossible to increase the combat effectiveness of the UAV without artificial intelligence (AI) and network coordination [1].

Artificial intelligence (AI) and machine learning (ML): Artificial intelligence is a crucial factor in increasing the autonomy of the UAV and determines the future of warfare. Autonomous target recognition and tracking are carried out by ML algorithms that are based on real-time data.

The drones process visual and thermal sensor data. The drones automatically recognize and classify enemy equipment, which eliminates human error and increases the effectiveness of the strike. For navigation in GPS-unprotected environments, AI-based visual navigation systems

(VIO) and the use of an IMU (Inertial Measurement Unit) magnetic compass are used [12]. These systems allow the drones to maintain orientation and continue flying even when the GPS signal is suppressed. As for the autonomy of decision-making, the drones receive the right to independently complete the attack or change the route, which reduces the operator's reaction time and increases the chance of success [2].

Network operations (Swarm Technology): The highest level of efficiency is achieved by the group, coordinated use of drones - the so-called "shield" technology. According to the principle of Mesh Networking, drone groups function as a single network. They automatically exchange data (target location, threats) with each other in real time. "Shield" attacks involve a simultaneous, coordinated attack by many small UAS, aimed at overloading and neutralizing the enemy's air defense systems [5]. This approach is especially effective against heavily defended objects.

Integration with C4ISR systems: The full potential of modified UAS is realized through their integration into command, control, communications, computer, intelligence, surveillance, and reconnaissance (C4ISR) systems [10]. UAS become not just a weapon, but an integral part of the information and sensor network. This integration provides a complete picture at the operational level and accelerates the decision-making process.

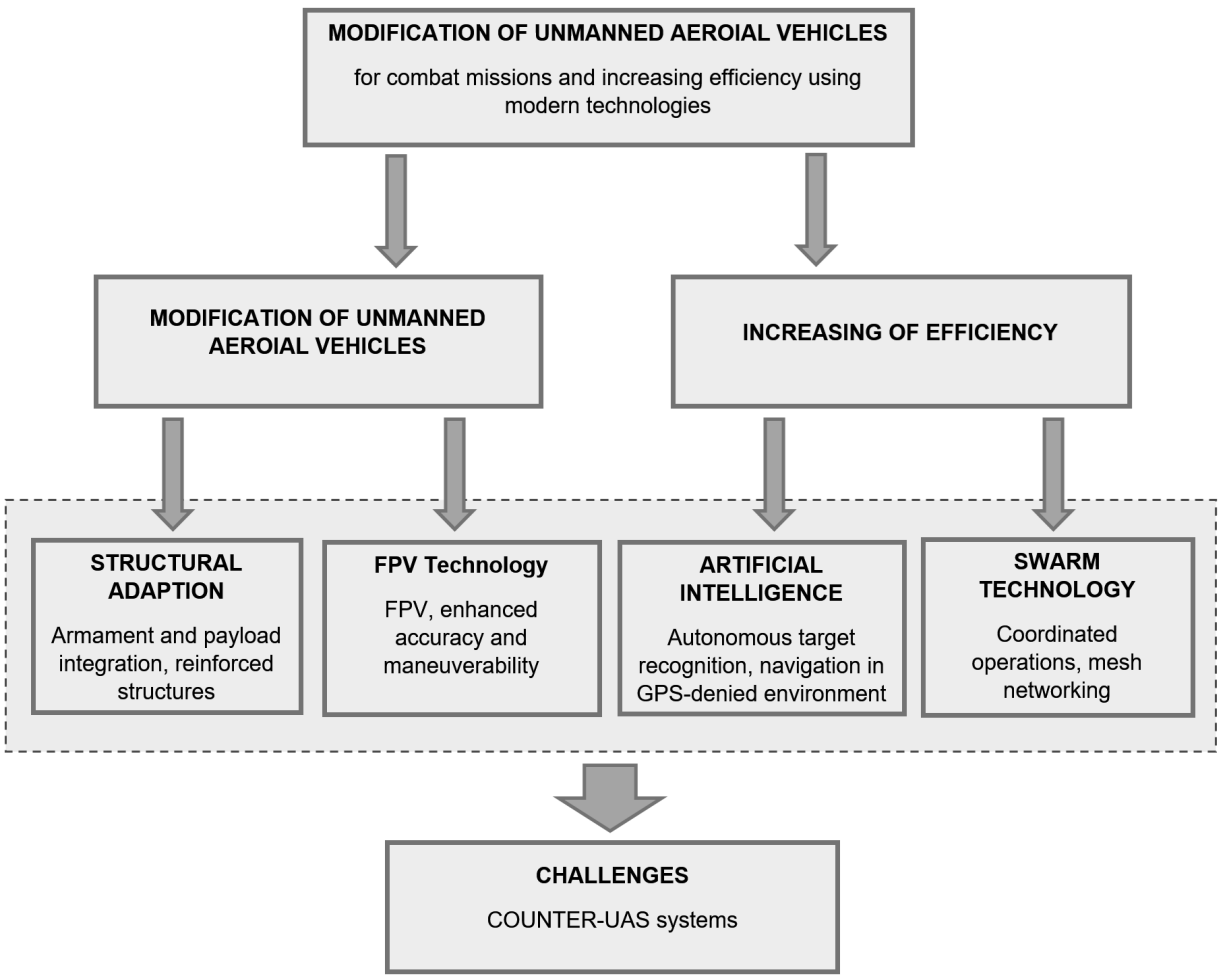

Figure 1. Modification of unmanned aerial vehicles

4. CHALLENGES AND COUNTERMEASURES

Despite the modification of UAS, there are serious challenges. Adversaries are actively developing counter-UAS (C-UAS) systems. Countermeasures include both kinetic (specialized bullets, missiles) and non-kinetic means (powerful jammers, laser weapons) [7]. In response, the modification of UAS must constantly take into account the development of the adversary's defensive technologies (Figure 1). The technological race becomes part of a constant race, where each improvement of UAS leads to the creation of new defensive technologies.

There are also ethical and legal regulations: the use of autonomous weapon systems (LAWS) requires international legal frameworks to reduce the risk of unauthorized using of UAS [11].

5. CONCLUSION

The modification of unmanned aerial vehicles has become a defining element of modern warfare, transforming UAVs from simple reconnaissance tools into highly adaptable combat systems. Structural upgrades, FPV platforms, and AI-driven autonomy now enable precise, low-cost, and flexible strike capabilities that can challenge far more expensive military assets. Swarm technologies further enhance operational effectiveness by enabling coordinated, resilient, and networked drone behavior on the battlefield.

At the same time, rapid advancements in counter-UAS systems highlight a continuous technological competition, where each improvement in UAV design prompts new defensive measures. Ethical and legal issues surrounding autonomous weapons add additional complexity and require clear international regulation.

Overall, UAV modification is reshaping military doctrine by expanding tactical options, reducing operational costs, and integrating intelligent systems into every layer of combat operations. As autonomy and coordination technologies mature, UAVs will play an increasingly central role in determining the outcome of future conflicts.

BIBLIOGRAPHY

1.Altmann, J. (2020). Implications of the Use of Armed Drones with Varying Degrees of Autonomy. Science and Global Security, 28(2), 118-135.
2.Gartzke, E., & Gerchenson, A. (2022). The Weaponization of Commercial Drones: Implications for State Conflict. Security Studies, 31(1), 1-28.
3.Horgan, J. (2023). The AI Revolution and the Future of Warfare. Journal of Contemporary Security Studies, 42(3), 400-415.
4. Johnson, R. (2023). Swarm Intelligence in Military Robotics: Challenges and Potential. IEEE Transactions on Cybernetics, 53(5), 2600-2612.
5. Jones, L. (2020). Counter-UAS Technology and the Arms Race in Airspace. Journal of Defense and Security Studies, 10(4), 112-130.
6. NATO Science and Technology Organization (STO). (2022). Exploiting Commercial Off-The-Shelf (COTS) UAS for Military Advantage. STO Technical Report.
7. Rumsfeld, D. (2020). Autonomous Navigation in GPS-Denied Environments for Tactical Drones. Journal of Navigation, 73(3), 321-338.

8. Schmitt, J. (2024). FPV Drones and Low-Cost Precision Strikes: A Tactical Revolution. Military Review Quarterly, 15(2), 70-85.
9. Smith, D. (2022). Integrating UAS into C4ISR Architecture: Data Fusion and Real-Time Combat Decisions. Defense Information Systems Journal, 12(3), 10-25.
10. Sparrow, R. (2021). Ethical and Legal Quandaries of Lethal Autonomous Weapon Systems (LAWS) in Drone Warfare. Journal of Military Ethics, 20(1), 5-25.
11. Williams, C. (2021). Materials Science and Stealth: Reducing the Radar Cross-Section of Small UAS. Aerospace Engineering Journal, 25(1), 45-60.
12. Zenko, M. (2021). The Drone Wars: The New Battlefield and the Geopolitics of Technology. Council on Foreign Relations.

TalentDetector

9th January 2026
Gliwice, Poland

DEPARTMENT OF ENGINEERING MATERIALS AND BIOMATERIALS
FACULTY OF MECHANICAL ENGINEERING
SILESIAN UNIVERSITY OF TECHNOLOGY

INTERNATIONAL STUDENTS SCIENTIFIC CONFERENCE

Analysis of the mechanical properties of biodegradable composite materials fabricated from components derived from renewable sources

Katarzyna Borowiecka[a], Agnieszka J. Nowak[b]

[a] Student of Silesian University of Technology, Faculty of Mechanical Engineering
email: kb303944@student.polsl.pl
[b] Silesian University of Technology, Faculty of Mechanical Engineering, Scientific and Didactic Laboratory of Nanotechnology and Material Technologies
email: agnieszka.j.nowak@polsl.pl

Abstract: In this study, concepts related to polymeric and composite materials derived from both renewable and non-renewable sources are presented. Composites based on biodegradable thermoplastic matrices reinforced with natural fillers were manufactured. The bioplastics GF 106/02 and GS 2189 were used, while the filling phase consisted of ground walnut shells and quercetin. Mechanical property tests were conducted.

Keywords: thermoplastic materials, composite materials, biodegradable materials, mechanical properties

1. INTRODUCTION

The growing environmental impact of conventional petrochemical-based polymers has intensified research into sustainable and biodegradable alternatives, particularly for applications in the packaging industry. Bioplastics derived from renewable resources offer significant ecological benefits; however, their relatively low mechanical performance often limits their practical use. One promising approach to overcoming these limitations is the development of composite materials in which biodegradable polymer matrices are reinforced with natural fillers. Such composites may provide an improved balance between mechanical properties, environmental impact, and production cost.

In this study, biodegradable thermoplastic bioplastics were used as matrix materials and reinforced with ground walnut shells and quercetin to develop fully biodegradable composite materials based on renewable resources.

The mechanical properties of the produced composites were systematically investigated using static tensile testing. The influence of filler type and content on the tensile strength, elastic modulus, and elongation at break was analyzed. The obtained results were compared with those of the unfilled bioplastics in order to assess the effectiveness of the applied reinforcements. Particular attention was given to evaluating whether the developed composites could achieve mechanical performance levels suitable for packaging applications.

2. COMPOSITES MATERIALS

Composite materials, alongside polymers, belong to a rapidly developing group of engineering materials. They are formed by combining at least two components that differ in their chemical and physical properties. These components do not completely dissolve in one another, resulting in a distinct phase boundary within the composite structure. The properties of the resulting material depend on the volume fraction of the individual constituents, which makes it possible to obtain characteristics derived from the component materials or to impart entirely new functional parameters to the composite [1-2].

A composite material consists of two main components. The first is the matrix, which is responsible for holding the reinforcement in place and transferring stresses to the reinforcing phase, which constitutes the second component of the composite. The reinforcing phase determines the mechanical properties of the material, such as tensile strength, hardness, and others [3-4].

Depending on the type of reinforcing phase, composites can be classified as continuously fiber-reinforced, particle-reinforced, and dispersion-strengthened materials. Continuous fibers, which usually constitute the largest volume fraction, provide the highest material strength. Particle-reinforced composites are strengthened by relatively larger particles, with the strengthening effect resulting from stress fields generated within the matrix. In dispersion-strengthened composites, very fine particles hinder the movement of dislocations in the matrix, leading to effective material strengthening [3-5].

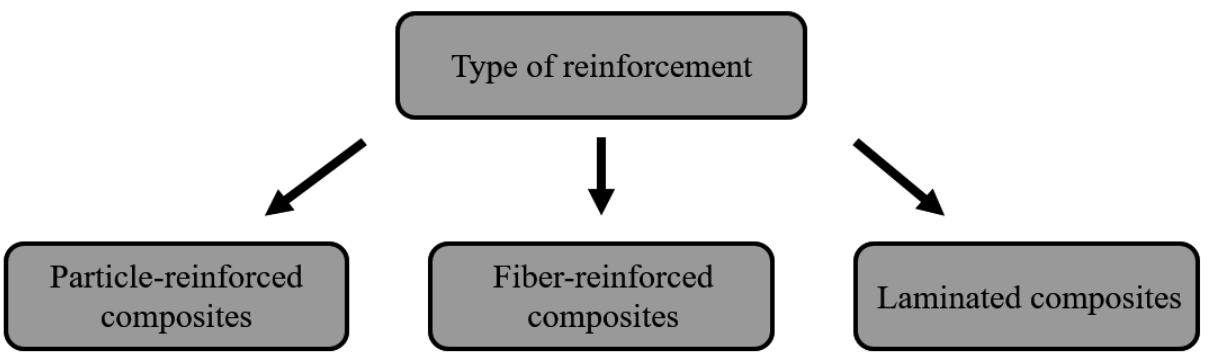

Figure 1. Classification of composites based on the type of reinforcement

3. EXPERIMENT

3.1 Used materials

During this experiment 20 composition of materials were created (Tab. 1). Firstly, the ingredients and their proportions were chosen. To create matrix of the composites biodegradable thermoplastic materials were used. BIOPLAST GF 106/02 and BIOPLAST GS 2189 are based on bio-derived raw materials.

Table 1. Percentage and mass share of individual components in the tested samples.

No.	Symbol of the sample	A, %	B, %	C, %	D, %	A, g	B, g	C, g	D, g
1.	A100	100	-	-	-	37,50	-	-	-
2.	B100	-	100	-	-	-	40,50	-	-
3.	A80 B20	80	20	-	-	30,00	8,10	-	-
4.	A60 B40	60	40	-	-	22,50	16,20	-	-
5.	A20 B80	20	80	-	-	7,50	32,40	-	-
6.	A40 B60	40	60	-	-	15,00	24,30	-	-
7.	A99 C1	99	-	1	-	33,75	-	0,48	-
8.	B99 C1	-	99	1	-	-	36,45	0,48	-
9.	A79 B20 C1	79	20	1	-	29,63	8,10	0,48	-
10.	A59 B40 C1	59	40	1	-	22,13	16,20	0,48	-
11.	A20 B79 C1	20	79	1	-	7,50	31,99	0,48	-
12.	A40 B59 C1	40	59	1	-	15,00	23,90	0,48	-
13.	A79 C1 D20	79	-	1	20	29,63	-	0,48	2,88
14.	B79 C1 D20	-	79	1	20	-	31,99	0,48	2,88
15.	A59 C1 D40	59	-	1	40	22,13	-	0,48	5,76
16.	B59 C1 D40	-	59	1	40	-	23,90	0,48	5,76
17.	A59 B20 C1 D20	59	20	1	20	22,13	8,10	0,48	2,88
18.	A20 B59 C1 D20	20	59	1	20	7,50	23,90	0,48	2,88
19.	A39 B20 C1 D40	39	20	1	40	14,63	8,10	0,48	5,76
20.	A20 B39 C1 D40	20	39	1	40	7,50	15,98	0,48	5,76

Legend to table 1:

- A - BIOPLAST GF 106/2;
- B - BIOPLAST GS 2189;
- C – quercetin;
- D - ground walnut shells.

The materials are characterized by good processability and stable processing behavior, which allows them to be formed using extrusion or injection molding technologies. Both bioplastics have a long shelf life while undergoing rapid biodegradation under industrial composting conditions. To provide mechanical properties, ground walnut shells were used as a reinforcement. Also a small amount of quercetin were added to provide antibacterial properties, which are necessary in packaging industry.

3.2 Fabrication of composite materials

First, the individual components of each composite material were weighed in accordance with Table 1. Next, the components were subjected to a homogenization process using a Zamak

Mercator VM-30 kneader. The process parameters were: stages 1 (Temp. 190°C/Blade rotational speed 5 obr./min/Mixing time 10 min.); stages 2 (Temp. 190°C/Blade rotational speed 10 obr./min/Mixing time 10 min.). As a result, homogeneous composite materials with specific contents of the matrix and reinforcing phases were obtained. The next step involved forming the material into standardized specimens for the static tensile test. Injection molding technology was used, employing a Zamak Mercator IM-15 laboratory injection molding machine. The process parameters were determined based on the walnut shell content in the material and are presented in Table 2. Representative specimens prepared for testing are shown in Fig. 2.

Table 2. Parameters of injection molding.

Type of material	Injection temperature, °C	Form temperature, °C	Pressure, bar	Injection time, s
Materials without walnut shells	190	40	4,5	3
Materials with walnut shells	195	40	4,5	3

Figure 2. Representative dumbbell shape of samples used for the static tensile test.

4. STATIC TENSILE TEST

The static tensile test was performed using a Shimadzu AGX-V universal testing machine in accordance with the requirements of the PN-EN ISO 527-2 standard. The test involved uniaxial stretching of the mounted specimen until failure. For each tested composite composition, three measurement repetitions were carried out. The tests were conducted at a tensile speed of 2 mm/min. Based on the obtained results, Young's modulus and tensile strength were determined (Tab. 4).

Table 3. Results of a static tensile test.

No.	Sample name	Young's modulus, GPa	Standard deviation	Tensile strength, MPa	Standard deviation
1.	A100	0,23	0,01	16,50	0,26
2.	B100	1,19	0,02	37,18	0,92
3.	A80 B20	0,77	0,19	16,30	2,52
4.	A60 B40	0,75	0,27	16,64	1,80
5.	A20 B80	2,25	0,52	30,46	0,64
6.	A40 B60	1,09	0,31	25,26	1,40
7.	A99 C1	0,30	0,11	14,53	0,43
8.	B99 C1	2,56	1,76	27,51	9,16
9.	A79 B20 C1	0,40	0,04	16,71	0,29
10.	A59 B40 C1	1,22	0,60	18,51	1,46
11.	A20 B79 C1	2,35	1,54	30,63	1,83
12.	A40 B59 C1	1,32	0,57	26,04	1,12
13.	A79 C1 D20	0,52	0,25	12,31	0,16
14.	B79 C1 D20*	-	-	-	-
15.	A59 C1 D40	0,55	0,39	12,30	0,14
16.	B59 C1 D40*	-	-	-	-
17.	A59 B20 C1 D20	0,82	0,50	14,97	0,10
18.	A20 B59 C1 D20	1,45	0,83	21,97	1,09
19.	A39 B20 C1 D40	0,74	0,12	15,34	0,40
20.	A20 B39 C1 D40	1,07	0,09	19,11	3,13

*- due to the applied technological process, manufacturing test samples was not possible.

The highest tensile strength was exhibited by the neat GS 2189 bioplastic, whereas the lowest value was recorded for GF 106/02 bioplastic containing 40% walnut shell filler and 1% quercetin. Among all modified materials, the most favorable results were obtained for the A20 B79 C1 composition. It was observed that an increase in walnut shell content led to a reduction in tensile strength, which can be attributed to oversaturation of the polymer matrix with the reinforcing phase and the formation of natural stress concentrators that disrupt structural continuity. The addition of quercetin resulted in only minor changes in composite properties, remaining within the measurement error of the testing equipment.

The highest Young's modulus was observed for the B99 C1 composition, while the lowest value was recorded for the neat GF 106/02 bioplastic. Increasing the walnut shell content caused a decrease in this property. Among the composites filled with walnut shells, the highest Young's modulus was obtained for the A20 B59 C1 D20 composite; however, its value was 24% lower than that of the B99 C1 material.

5. CONCLUSION

The conducted study demonstrated the mechanical properties of biodegradable thermoplastic materials and composites produced using these thermoplastics as the matrix and reinforced with ground walnut shells and quercetin. Among the fabricated biodegradable composite materials, the A20 B79 C1 formulation exhibited the greatest tensile strength. It can be concluded that polymers derived from renewable sources exhibit mechanical properties that are too low to replace widely used petrochemical-based polymers. However, through the use of composite materials, it is possible to achieve an appropriate balance between mechanical properties and production costs, enabling their application, among others, in the packaging industry.

ACKNOWLEDGEMENT

The present study was developed through the SKN project entitled. " Development of a manufacturing process for biodegradable composite materials reinforced with natural fillers used in the food industry " implemented under the Excellence Initiative - Research University program. Order No. 54/2020 of the Rector of the Silesian University of Technology. The work was carried out by members of the "HEAD TO HEAD" Student Scientific Circle of Plastics and Composites Processing, operating at the Scientific and Teaching Laboratory of Nanotechnology and Materials Technology at the Faculty of Mechanical Engineering.

BIBLIOGRAPHY

[1] Leszek A. Dobrzański, Podstawy nauki o materiałach, Wydawnictwo Politechniki Śląskiej, Gliwice 2012
[2] Leszek A. Dobrzański, Wprowadzenie do nauki o materiałach, Wydawnictwo Politechniki Śląskiej, Gliwice 2007
[3] J. Śledziona, Podstawy technologii kompozytów, Wydawnictwo Politechniki Śląskiej, Gliwice 1998
[4] G. Wróbel, Polimery i kompozyty konstrukcyjne, Wydawnictwo Politechniki Śląskiej, 2008
[5] Leszek A. Dobrzański, Niemetalowe materiały inżynierskie, Wydawnictwo Politechniki Śląskiej, Gliwice 2008

TalentDetector

9th January 2026
Gliwice, Poland

DEPARTMENT OF ENGINEERING MATERIALS AND BIOMATERIALS
FACULTY OF MECHANICAL ENGINEERING
SILESIAN UNIVERSITY OF TECHNOLOGY

INTERNATIONAL STUDENTS SCIENTIFIC CONFERENCE

Design and Construction of an Experimental Setup for Dry Particle Jet Erosion Testing of Materials

Daniel Bujara[a], Szymon Markocki[b], Bartłomiej Bodziach[b], Mikołaj Figołuszka[b], Łukasz Połap[b], Kacper Słania[c], Kamil Szałaśny[c], Marek Kremzer[d], Błażej Tomiczek[d]

[a] Student of Materials Engineering and Technologies, Silesian University of Technology
email: db303946@student.polsl.pl
[b] Student of Mechanics and Machine Design, Silesian University of Technology
email: sm307632@student.polsl.pl, bb307595@student.polsl.pl, mf309370@student.polsl.pl, lp309478@student.polsl.pl,
[c] Student of Production Engineering and Management, Silesian University of Technology
email: ks316724@student.polsl.pl, ks316726@student.polsl.pl
[d] Silesian University of Technology, Faculty of Mechanical Engineering, Scientific and Didactic Laboratory of Nanotechnology and Materials Technology
email: marek.kremzer@polsl.pl, blazej.tomiczek@polsl.pl

Abstract: The article presents the design, construction, and modernisation of a laboratory experimental setup dedicated to the erosion-resistance testing of engineering materials using abrasive air jets. The phenomenon of erosion, its formation mechanisms and key influencing parameters are discussed. Particular attention is paid to the decision-making process during the design of the experimental setup, including the development of the abrasive injection system, the automation of the flow control, and ergonomic improvements to the test chamber. The constructed setup enables controlled and repeatable erosion tests under laboratory conditions and may be used for comparative evaluation of materials and protective coatings.

Keywords: abrasive wear, erosion testing, abrasive jet, experimental setup,

1. INTRODUCTION

1.1. What is material erosion

Erosion is a surface-wear process involving the gradual loss of mass and degradation of the surface layer as a result of the action of a stream of solid particles, liquids, or a mixture of phases moving at high velocity relative to the examined surface [1, 2]. This phenomenon is one of the key degradation mechanisms of machine components in service, particularly in pneumatic conveying systems, turbines, heat exchangers, pipelines, and power engineering installations [3, 4].

In the relevant literature, erosion is classified according to the nature of the medium acting on the material surface. The following types are distinguished in particular: gas–solid erosion, liquid–solid erosion, and cavitation erosion [2, 5]. In slurry or particle-jet erosion, solid particles are transported by a gas or liquid stream and impact the material surface with high kinetic energy, causing local plastic deformation, cracking, and material chipping or removal [6]. The intensity of the erosive process depends on several factors, including stream parameters (velocity, density, particle concentration), abrasive properties (hardness, shape, particle-size distribution), and the mechanical properties of the substrate material [7]. For this reason, laboratory tests conducted under controlled conditions constitute the primary tool for assessing the erosion resistance of materials and protective coatings [3].

1.2. Mechanism of erosion formation

The mechanism of erosion formation is a complex physical phenomenon in which the kinetic energy of abrasive particles and the manner in which it is transferred to the material surface at the moment of impact play key roles [1]. Depending on the material characteristics and loading conditions, various erosion wear mechanisms can be distinguished, including micro-cutting, micro-impact, plastic deformation, crack initiation and propagation, and material chipping and spallation [6, 8]. For ductile materials, the dominant erosion mechanism is micro-cutting, in which abrasive particles act analogously to cutting tools, causing a gradual loss of material in the form of fine chips [2, 7]. In contrast, in brittle materials such as ceramics or specific protective coatings, erosion occurs primarily through localised cracking and material fragmentation induced by repeated particle impacts [4, 9].

One of the most important parameters determining erosion intensity is the particle impingement angle. Experimental studies show that for ductile materials, the maximum erosion rate typically occurs at intermediate angles (approximately 20–40°). In contrast, for brittle materials, erosion intensity increases with impingement angle and reaches a maximum near 90° [1, 3]. These relationships are widely described in testing standards and constitute the basis for the design of experimental setups that allow adjustment of the sample orientation relative to the erosive particle stream [10]. In addition, the literature emphasises the significant influence of particle velocity, with increased velocity leading to a nonlinear increase in erosion wear intensity. This justifies the necessity for precise control of flow parameters during laboratory erosion testing [5, 8].

2. CONCEPT OF THE EXPERIMENTAL SETUP

2.1. Conceptual design of the experimental setup

The experimental setup for jet erosion tests consists of a test chamber, a compressed air system, an abrasive injection system, an erosion nozzle, a sample holder with adjustable positioning, and an abrasive separator. Figure 1 shows a schematic diagram of the experimental setup with a side-mounted nozzle. The main components are: the testing chamber (1), the compressed air hose (2), the abrasive injection gun (3), the sample holder with adjustable angle (4), and the used abrasive separator with container (5). The testing chamber isolates the process from the surroundings and ensures user safety, while transparent structural elements allow observation of the experiment. The control system, based on a solenoid valve and a timer, enables automatic execution of test cycles.

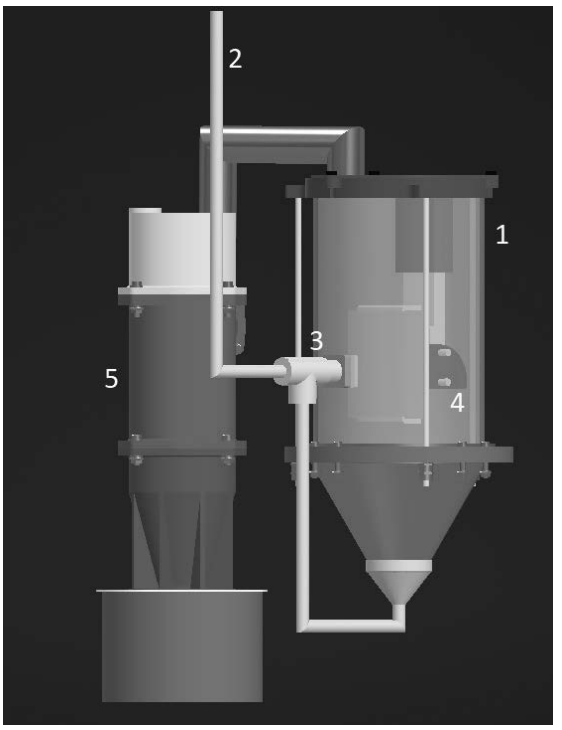

Figure 1. Schematic diagram of a jet erosion experimental setup

2.2. Design variants of the experimental setup

One of the key design assumptions was the complete elimination of manual operator intervention during the experiment. This requirement necessitated the integrated design of not only the mechanical and pneumatic subsystems, but also dedicated automation and control elements capable of ensuring stable and repeatable operating conditions. Particular emphasis was placed on achieving reliable abrasive transport, precise flow control, and long-term durability of system components under erosive operating conditions. During the design phase of the experimental setup, two alternative methods of abrasive supply to the erosion chamber were therefore analysed in detail. The objective of this analysis was to identify a solution that would ensure stable jet characteristics, minimise component wear, and maintain the overall tightness of the assembly, which is essential for both process stability and operational safety.

In the first concept, abrasive injection is achieved using an erosion gun positioned perpendicular to the cylindrical testing chamber (Figure 2a). In this configuration, the compressed air stream and the abrasive particle stream are supplied to the gun through separate channels, allowing controlled mixing of both media immediately upstream of the nozzle. Flow regulation is implemented via a solenoid valve located outside the direct particle impact zone, which significantly reduces erosive wear of the control components and increases their service life. The implementation of this concept required modification of a transparent mounting sleeve with an increased diameter, which serves both as a guiding element for the erosion gun and as an observation window for the mixing zone. Owing to the lack of a commercially available component with a suitably positioned technological opening, the sleeve was modified in-house by precise drilling. This approach enabled reliable abrasive delivery to the mixing zone while preserving visual process monitoring capabilities and maintaining the tightness of the system.

In contrast, an alternative abrasive supply method was considered as a contingency solution if the primary concept proved impractical. In this variant, abrasive material would be supplied to the chamber from above, while the erosion gun would be permanently mounted in the chamber's top cover at an angle of 38°, corresponding to the inclination of the test sample (Figure 2b). This configuration allows efficient use of the chamber's working space while maintaining a consistent jet–surface interaction geometry and enables easy disassembly of the gun for maintenance, supporting long-term usability of the experimental setup.

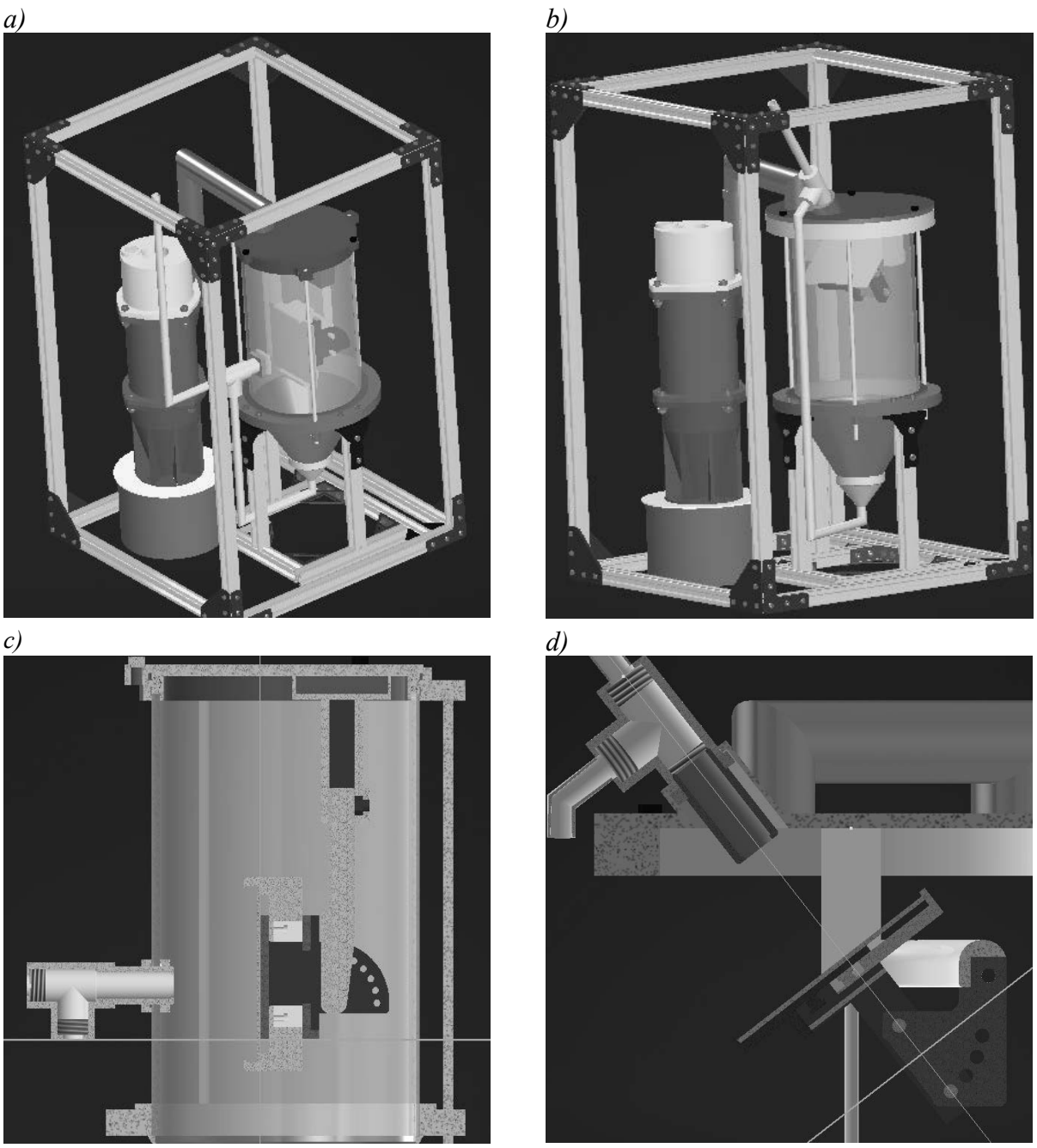

Figure 2. General views of the jet erosion experimental setup with a side-mounted nozzle (a) and a nozzle mounted in the chamber lid (b), along with cross-sectional views illustrating the erosion gun mounted in the side part of the sleeve (c) and in the chamber lid (d).

2.3. Abrasive Transport and System Tightness

The transport of abrasive powder in both considered variants is based on utilising the pressure difference within the system, resulting from the overpressure generated by compressed air and the local flow conditions inside the testing chamber. It was assumed that appropriately selected flow parameters would enable efficient transport of abrasive particles without the need for additional auxiliary components. The abrasive container is located at the lower part of the experimental setup as a funnel-shaped hopper, which allows gravity-assisted feeding of the powder into the system. This solution simplifies the setup design and reduces the number of components exposed to erosive wear. A crucial design aspect of the setup is ensuring complete system tightness. This is intended to prevent loss of working pressure and limit the escape of abrasive particles from the testing chamber. To achieve this, seals are used at the joints between components, enhancing user safety and stabilising the experimental process parameters.

2.4. Separator and Safety Components

The experimental setup is equipped with an abrasive separator, which separates solid particles from the air stream and allows their controlled collection. The separator operates on a centrifugal principle: the air–abrasive mixture enters the device tangentially, generating a vortex that forces heavier abrasive particles toward the separator walls, while the cleaned air exits through the central outlet. The collected particles are then directed to a container for reuse. The use of the separator reduces dust dispersion within the chamber and protects the pneumatic system components from excessive wear. Additionally, a safety valve is included in the system to protect the installation from uncontrolled pressure increases. This component plays a crucial role in ensuring the safe operation of the experimental setup.

2.5. The sample holder

The sample holder was designed as a spring-loaded mechanism, in which the sample is clamped by two movable elements that generate sufficient frictional force to securely fix it during testing. The design allows adjustment of the sample's inclination angle relative to the erosion stream. In the basic configuration, the sample can be set at angles of 0°, 15°, 30°, and 45°. An alternative holder concept was also considered, enabling adjustment over a broader range of 0°, 15°, 30°, 45°, 60°, 75°, and 90°. To better illustrate the operation of the holder, photographic documentation of the actual components produced using 3D printing was prepared (Figure 3). This presentation confirms the practical implementation of the designed solutions and emphasises the applied nature of the work. It should also be noted that the supply lines for the working medium, shown in the conceptual models in a simplified manner, will be implemented as flexible rubber hoses in the actual experimental setup construction, thereby improving the system's resistance to vibrations and facilitating assembly.

Figure 3. View of sample holder mechanism

3. CONCLUSIONS

The designed and upgraded experimental setup enables repeatable, well-controlled jet-erosion tests across a wide range of materials, ensuring high reproducibility of the experimental results. The implementation of an automated flow control system, combined with a carefully engineered abrasive feeding mechanism, has significantly enhanced the durability of critical components while improving the overall operational safety and reliability of the setup. The design allows precise and independent adjustment of key process parameters, including abrasive flow rate, nozzle position, and sample inclination angle, providing high experimental flexibility and facilitating systematic parametric studies under varying test conditions. Moreover, the modular and robust construction of the setup makes it a reliable and adaptable platform for further research, including the development of advanced erosion-testing methodologies, the evaluation and comparison of novel materials, and the optimisation of experimental procedures. Collectively, these features ensure that the experimental setup effectively supports both fundamental investigations of erosion mechanisms and applied studies of material performance in erosive environments.

ACKNOWLEDGEMENTS

This publication was supported under the "Excellence Initiative – Research University" program at the Silesian University of Technology, within the framework of the 13th Project-Based Learning (PBL) funding competition, entitled Design and Construction of a Experimental setup for Assessing the Erosion Resistance of Materials under Low-Pressure Conditions.

BIBLIOGRAPHY

1. T. Deng, Erosive Wear Mechanisms of Materials—A Review of Understanding and Progresses, Materials 18 (2025) 161
2. I. Hutchings, S. Philip. Tribology: friction and wear of engineering materials. United Kingdom: Matthew Deans 2017.
3. ASTM G76-18, Standard Test Method for Conducting Erosion Tests by Solid Particle Impingement Using Gas Jets, ASTM International.
4. R. Melentiev, Physical theories of solid particle erosion and abrasive jet wear, Journal of Manufacturing Processes 106 (2023) 422-452
5. G.W. Stachowiak, A.W. Batchelor (ed.) Engineering Tribology (Fourth Edition), Chapter 11 - Abrasive, Erosive and Cavitation Wear, Butterworth-Heinemann (2014) 525-576,
6. G. Sundararajan, The solid particle erosion of metallic materials: The rationalization of the influence of material variables, Wear 186 (1995) 129–144.
7. A. Devaraju, A critical review on different types of wear of materials, International Journal of Mechanical Engineering and Technology 6/11 (2015) 77-83.
8. A. Neville, T. Hodgkiess, J.T. Dallas, A study of the erosion-corrosion behaviour of engineering steels for marine pumping applications, Wear 186-187 (1995) 497-507
9. I. Finnie, Some observations on the erosion of ductile metals, Wear 19/1 (1972) 81-90.
10. ISO 16282:2015 Standart, Methods of test for dense shaped refractory products — Determination of resistance to abrasion at ambient temperature, International Organization for Standardization.

TalentDetector
9th January 2026
Gliwice, Poland
DEPARTMENT OF ENGINEERING MATERIALS AND BIOMATERIALS
FACULTY OF MECHANICAL ENGINEERING
SILESIAN UNIVERSITY OF TECHNOLOGY
INTERNATIONAL STUDENTS SCIENTIFIC CONFERENCE

The Role of Surface Engineering in Enhancing the Service Life and Performance of Mechanical Components

Saba Chakhaia

Georgian Technical University, Faculty of Transport Systems and Mechanical Engineering, Department of Mechanical Engineering
email: chakhaia.saba22@gtu.ge

Abstract: The performance and longevity of mechanical components heavily depend on their surface properties, which are directly exposed to friction, wear, corrosion, and other operating stresses. Surface engineering focuses on improving surface characteristics while keeping the bulk properties of the material unchanged, significantly improving component life and reliability. This paper provides an overview of common surface engineering methods, including thermal treatments, coatings, and mechanical surface modifications, and discusses their applications in industries such as automotive, aerospace, biomedical, and industrial machinery. The advantages and limitations of these methods are examined, highlighting the importance of surface engineering as a practical and cost-effective approach to enhancing the longevity and efficiency of mechanical components.

Keywords: surface engineering; wear resistance; corrosion resistance; coating technologies; mechanical surface treatments.

1. INTRODUCTION

In mechanical engineering, many components operate under conditions that involve friction, contact loading, and exposure to aggressive environments. Although the core material of a component provides strength and stiffness, the surface is the part that directly interacts with its surroundings. As a result, surface-related damage such as wear, corrosion, and fatigue cracks is a common cause of component failure.

Instead of replacing components with more expensive materials, engineers often modify only the surface to improve performance. This approach allows the bulk properties of the material to remain unchanged while significantly enhancing durability. Surface engineering has therefore become an important tool in modern mechanical design and maintenance. General overviews of these concepts are widely discussed in materials and surface engineering literature [1].

2. CLASSIFICATION OF SURFACE ENGINEERING METHODS

Surface engineering methods can be grouped based on how the surface is modified. In this paper, they are divided into thermal and thermochemical treatments, coating technologies, and mechanical surface modification methods.

2.1 Thermal and Thermochemical Treatments

These techniques modify surface properties by applying heat, often with chemical elements. Common methods include:

- Case hardening / Carburizing: Carbon is diffused into steel surfaces to improve hardness and wear resistance.
- Nitriding: nitrogen diffuses into the surface to form hard nitrides that improve wear and corrosion resistance.
- Induction hardening: Localized heating followed by rapid cooling increases surface hardness.

These techniques are commonly applied to gears, shafts, and similar machine elements that experience high contact stresses.

2.2 Coating Technologies

Coating technologies involve depositing an additional material layer onto the surface of a component in order to improve its functional performance. Unlike thermal treatments, coatings allow engineers to introduce entirely new surface properties that are not present in the base material.

- Physical Vapor Deposition (PVD): Produces thin, hard coatings, such as titanium nitride, for wear resistance.
- Chemical Vapor Deposition (CVD): Forms protective layers like diamond-like carbon.
- Electroplating: Adds metals such as nickel or chromium to improve corrosion resistance.
- Thermal spraying: Applies metallic or ceramic coatings for high-temperature or abrasive environments.

The effectiveness of coating technologies in improving wear and corrosion resistance has been demonstrated in numerous studies [2, 3].

2.3 Mechanical Surface Modification Methods

Mechanical surface modification methods improve surface performance by plastically deforming or texturing the surface layer. These methods do not involve material removal or the addition of coatings.

- Shot peening: small particles impact the surface, introducing compressive residual stresses that improve fatigue strength
- Laser surface texturing: Creates micro-scale patterns on the surface to reduce friction and enhance lubrication behaviour.
- Polishing and grinding: Refines surface finish to reduce wear in precision components.

Mechanical surface treatments are commonly used to control surface integrity and improve component reliability [4].

3. APPLICATIONS OF SURFACE ENGINEERING

Surface engineering finds applications across many industries:

3.1 Automotive Industry

In the automotive industry, components such as gears, camshafts, bearings, and suspension springs operate under high friction and repeated loading. Thermal treatments like carburizing are commonly used to improve wear resistance in transmission components, while shot peening is applied to suspension parts to enhance fatigue life. Coatings are increasingly used in engine components to reduce friction and improve fuel efficiency.

3.2 Aerospace Industry

Aerospace components are exposed to extreme temperatures, high stresses, and aggressive environments. Turbine blades and engine components often rely on thermal barrier coatings to protect against high-temperature oxidation and corrosion. Advanced laser-based surface treatments have also been used to improve fatigue resistance and surface durability in aeronautical materials [5].

3.3 Biomedical Engineering

In biomedical applications, surface engineering plays an important role in improving both durability and biocompatibility. Metallic implants such as hip and knee replacements require surfaces that resist wear while remaining compatible with human tissue. Surface treatments and coatings are commonly used to improve wear resistance and promote better integration between implants and bone [4].

3.4 Industrial Machinery

Industrial machinery components such as cutting tools, pumps, rollers, and molds benefit greatly from surface modification. Hard coatings produced by PVD and CVD are widely used to extend tool life, while thermal spraying is applied to protect components from wear, corrosion, and thermal damage in harsh operating environments [6].

4. ADVANTAGES AND LIMITATIONS

Advantages:

- Extended service life: Increases resistance to wear, corrosion, and fatigue.
- Cost-effective: Reduces the need for replacement or maintenance.
- Maintains bulk properties: Only the surface is modified.
- Versatile: Applicable to metals, ceramics, and composites.
- Performance improvement: Reduces friction and improves efficiency.

Limitations:

- Limited depth: Surface modifications affect only a thin layer.
- Complexity: Advanced techniques require specialized equipment.

- Potential surface defects: Improper processing may cause cracks or delamination.
- Environmental concerns: Some treatments involve hazardous chemicals.
- Application-specific limits: Not all methods suit every material or condition.

5. CONCLUSIONS

Surface engineering is an effective and practical approach for improving the performance and service life of mechanical components. By modifying surface properties through thermal treatments, coatings, and mechanical methods, engineers can significantly reduce surface-related failures such as wear, corrosion, and fatigue.

The wide range of applications in automotive, aerospace, biomedical, and industrial machinery demonstrates the importance of surface engineering in modern mechanical engineering. Although each method has its own limitations, proper selection and application of surface engineering techniques can lead to more reliable, efficient, and long-lasting components.

BIBLIOGRAPHY

1. Ramezani, M., Ripin, Z. M., Pasang, T., & Jiang, C.-P. (2023). *Surface Engineering of Metals: Techniques, Characterizations and Applications*. Metals, 13(7), 1299. doi:10.3390/met13071299
2. Wang, X., Zhao, W., Shi, T., Cheng, L., Hu, S., Zhou, C., Cui, L., Li, N., & Liaw, P. K. (2025). *A Review on Tribological Wear and Corrosion Resistance of Surface Coatings on Steel Substrates*. Coatings, 15(11), 1314. doi:10.3390/coatings15111314
3. Krella, A. (2020). *Resistance of PVD Coatings to Erosive and Wear Processes: A Review*. Coatings, 10(10), 921. doi:10.3390/coatings10100921
4. Santos, V., Uddin, M., & Hall, C. (2023). *Mechanical Surface Treatments for Controlling Surface Integrity and Corrosion Resistance*. Journal of Functional Biomaterials, 14(5), 242. doi:10.3390/jfb14050242
5. Wu, J., Zhou, Z., Lin, X., Qiao, H., Zhao, J., & Ding, W. (2023). *Improving the Wear and Corrosion Resistance of Aeronautical Component Material by Laser Shock Processing: A Review*. Materials, 16(11), 4124. doi:10.3390/ma16114124
6. AIMS Materials Science (2023). *Review of Effective Techniques for Surface Engineering Material Modification for a Variety of Applications*. AIMS Materials Science, 10(4), 652–692. doi:10.3934/matersci.2023037

TalentDetector
9th January 2026
Gliwice, Poland
DEPARTMENT OF ENGINEERING MATERIALS AND BIOMATERIALS
FACULTY OF MECHANICAL ENGINEERING
SILESIAN UNIVERSITY OF TECHNOLOGY
INTERNATIONAL STUDENTS SCIENTIFIC CONFERENCE

Influence of SLM process parameters on quality of Mediloy samples

Martyna Ciaś[a], Michalina Ziółkowska[a], Adam Popis[a], Magdalena Szindler[b], Mariusz Król[b], Wojciech Sitek[c]

[a] Student of the Silesian University of Technology
[b] Silesian University of Technology, Faculty of Mechanical Engineering, Department of Engineering Materials and Biomaterials
[c] Silesian University of Technology, Faculty of Mechanical Engineering, Didactic Laboratory of Nanotechnology and Material Technologies, Gliwice, Poland
email: magdalena.szindler@polsl.pl

Abstract: Selective Laser Melting (SLM) is a powder bed fusion process in which melting quality strongly depends on the spatial and temporal distribution of laser energy. Mediloy alloy, a Co-Cr-based dental material produced by BEGO GmbH, exhibits favorable mechanical properties and corrosion resistance suitable for biomedical applications. In point-wise scanning strategies, point distance and laser exposure time play a key role in controlling melt pool stability and densification, even at similar nominal energy densities. In this study, the influence of point distance and laser exposure time on the melting quality of Mediloy alloy manufactured by SLM was systematically investigated. Cubic samples were printed on a single build platform using constant laser power and layer thickness, while point distance and exposure time were varied within a controlled surface energy density range ensuring sufficient melting. Observations were performed on as-built surfaces using stereoscopic microscopy (Zeiss Axio Vision) at 25× and 100× magnification. The applied experimental design enabled the assessment of the individual and combined effects of discrete laser exposure parameters on densification and melting stability. The results highlight the limitations of energy density as a sole descriptor of melting quality and contribute to the identification of a stable process window for Mediloy alloy processed by point-wise SLM strategies.

Keywords: Mediloy alloy, Selective Laser Melting, Point Distance, Exposure Time

1. INTRODUCTION

Selective Laser Melting (SLM) is one of the most widely used metal additive manufacturing technologies, enabling the production of complex components with high geometrical accuracy and near-full density. Due to its capability to tailor microstructure and mechanical properties through process control, SLM has found extensive application in aerospace, automotive and biomedical engineering [1-3]. Despite significant technological progress, achieving stable melting conditions and reproducible quality remains a challenge, particularly for alloys characterized by narrow processing windows [1-6].

The quality of SLM printed parts is governed by the interaction between laser parameters, material properties and scanning strategy. Laser power, scanning speed, layer thickness and hatch spacing are commonly reported as the main process parameters controlling energy input into the powder bed [4-8]. Insufficient energy input may result in lack-of-fusion defects and high porosity, whereas excessive energy can lead to keyhole formation, spatter and evaporation-induced defects. Consequently, process optimization is often based on volumetric or surface energy density concepts [7-12].

However, in scanning strategies employing discrete laser exposure, such as point-wise or pulsed laser melting, additional parameters become critical. Point distance and laser exposure time directly control the overlap between consecutive laser spots and the duration of energy delivery at a given location. These parameters influence melt pool geometry, thermal gradients and solidification behavior, thereby affecting interlayer bonding and defect formation. Despite their importance, point distance and exposure time are frequently treated as secondary parameters or implicitly included in scanning speed calculations [9-18].

Mediloy alloy has recently attracted attention due to its favorable mechanical properties and potential suitability for biomedical applications [19,20]. Nevertheless, literature addressing the processing behavior of Mediloy under SLM conditions remains limited. Existing studies mainly focus on global parameter optimization using energy density approaches, while systematic investigations of discrete exposure parameters are scarce. As a result, the influence of point distance and exposure time on melting quality and densification behavior of Mediloy alloy is not yet fully understood. It should be noted that identical nominal energy density values can be achieved using different combinations of point distance and exposure time; however, such combinations may lead to significantly different melting behavior due to variations in energy distribution and melt pool dynamics. This observation suggests that energy density alone may be insufficient to describe melting quality in point-wise SLM scanning strategies [9-20].

The present study aims to systematically investigate the influence of point distance and laser exposure time on the melting quality of Mediloy alloy manufactured by Selective Laser Melting. By maintaining the surface energy density within a controlled range and varying the discrete exposure parameters, the individual and combined effects of point distance and exposure time on densification and melting stability are evaluated.

2. RESEARCH AND METHODOLOGY

All experiments were conducted using a Renishaw AM125 Selective Laser Melting system equipped with a fiber laser operating at a constant power of 200 W. The laser beam diameter was fixed at 80 μm, and the processing was carried out using a layer thickness of 30 μm and a hatch spacing of 70 μm. These parameters were kept constant throughout the entire build in order to isolate the influence of the investigated variables.

The printing process employed a point-wise laser exposure strategy, in which material consolidation is controlled by discrete laser pulses rather than continuous scanning. Within this strategy, Point Distance (Pd), defined as the spatial separation between consecutive laser exposure points, and Exposure Time (Et), defined as the duration of laser irradiation at each point, were selected as the primary variable parameters. In order to ensure comparable melting conditions, the printing parameters were selected so that the surface energy density delivered to the powder bed remained close to the value recommended by the material manufacturer. The surface energy density was calculated according to Equation (1):

$$E_s = \frac{P \cdot Et}{Pd \cdot h} \quad (1)$$

where: *P* is the laser power, *Et* is the exposure time, *Pd* is the point distance, and *h* is the hatch spacing. By adjusting Pd and Et, the energy input was maintained within a comparable range while enabling the assessment of their individual influence on melting quality.

A total of twelve 10×10×10 mm cubic samples were designed and arranged on the build platform, maintaining a 5 mm spacing to minimize temperature variability between samples. The Point Distance was varied in the range of 20–90 µm, while the Exposure Time ranged from 12 to 75 µs, resulting in different combinations of spatial and temporal energy input. The printing parameters were listed in the table 1.

Table 1. Summary of SLM process parameters applied for the fabrication of cubic samples

Sample No.	**Point Distance (µm)**	**Exposure Time (µs)**	**Laser power (W)**	**Layer thickness (µm)**	**Hatch spacing (µm)**
1.	70	60	200	30	70
2.		50			
3.		40			
4.	90	75			
5.		65			
6.		55			
7.	30	25			
8.		21			
9.		18			
10.	20	17			
11.		14			
12.		12			

Due to technical limitations of the Renishaw AM125 system, exposure times below approximately 15 µs could not be executed reliably. As a result, two planned samples with exposure times of 14 µs and 12 µs were not successfully printed because the laser did not activate at these settings. All remaining samples were printed under identical environmental and machine conditions, ensuring that observed differences in melting quality and consolidation behavior could be attributed primarily to variations in Point Distance and Exposure Time. Few representative printed samples are shown in figure 1.

a) 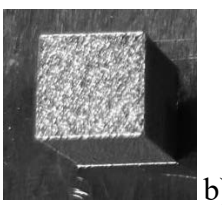 b) 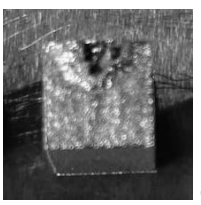 c) 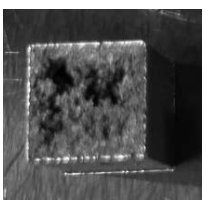

Figure 1. The Mediloy samples printed under varying SLM parameters (Pd and Et): fully consolidated (a); swollen and uneven (b); partially fused with powdery regions (c).

3. RESULTS AND DISCUSSION

The quality of the printed samples showed a strong dependence on the applied Point Distance (Pd) and Exposure Time (Et). Clear differences in consolidation behavior and surface morphology were observed across the investigated parameter combinations.

All samples were examined using a Zeiss Axio Vision stereoscopic microscope. Observations were performed at magnifications of 25× and 100×. The analysis was limited to the as-built surfaces of the samples, and no metallographic cross-sections were prepared or examined. Therefore, the observations presented in this study refer exclusively to surface-related melting features and consolidation behavior. Representative stereoscopic images obtained using the Axio Vision microscope are summarized and presented in the figures 2-11.

Samples prepared with moderate values of both Pd and Et exhibited the most favorable melting behavior. Samples 1 and 2 (Pd = 70 μm, Et = 60-50 μs) and Samples 4 and 5 (Pd = 90 μm, Et = 75-65 μs) showed continuous and relatively smooth surface morphology, indicating stable melt pool formation and sufficient overlap between consecutive laser exposure points. At all applied magnifications, these samples exhibited uniform melt features without visible signs of insufficient fusion. A different surface behavior was observed for Samples 3, 6, and 10, which were printed using reduced exposure times at comparable point distances. These samples exhibited a visibly swollen or uneven surface morphology. Microscopic observations revealed localized surface distortions and irregular melt features, suggesting melt pool instability or excessive local energy accumulation. Despite these surface irregularities, no extensive powdery regions were observed on the surface. In contrast, Samples 7, 8, and 9, produced with small point distances (Pd = 30 μm) and short exposure times (Et = 25-18 μs), exhibited insufficient surface melting. Although partial fusion was observed near the samples edges, large areas of the surface, particularly toward the center, appeared powdery and poorly bonded. The unmelted or partially melted powder particles and discontinuous melt features were visible, indicating inadequate surface consolidation. Two planned samples (Samples 11 and 12) could not be pronted due to technical limitations of the SLM system. Exposure times below approximately 15 μs could not be executed reliably, as the laser did not activate at these settings, preventing stable laser exposure.

a) b)

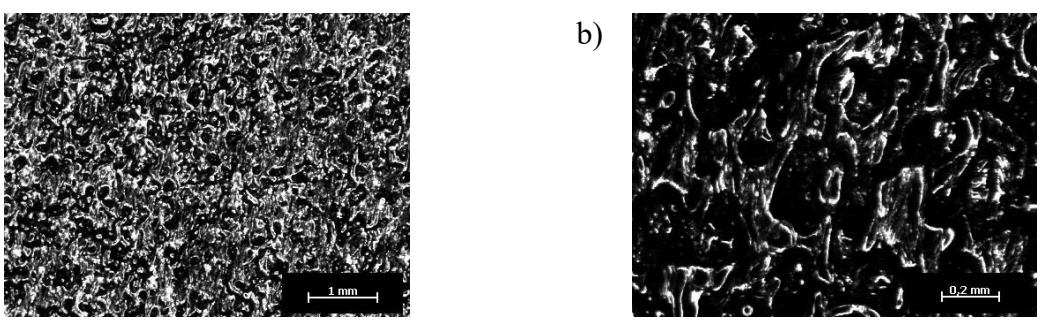

Figure 2. As-built surface morphology of Sample 1 (Pd = 70 μm, Et = 60 μs) observed by stereoscopic microscopy at: 25× magnification (a); 100× magnification.

a) b)

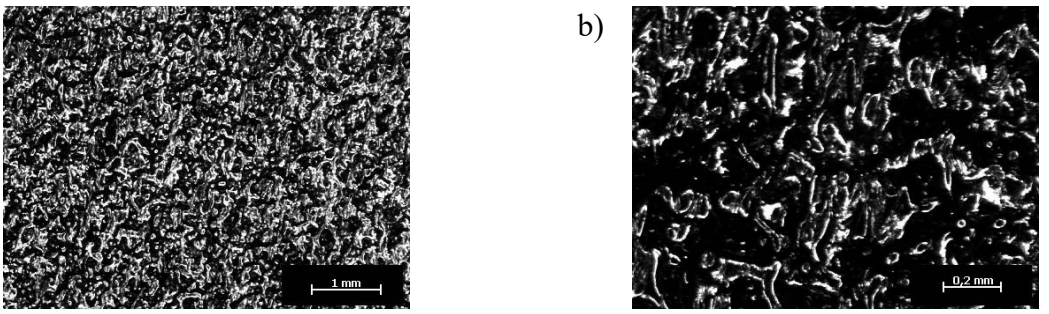

Figure 3. As-built surface morphology of Sample 2 (Pd = 70 µm, Et = 50 µs) observed by stereoscopic microscopy at: 25× magnification (a); 100× magnification.

a) b)

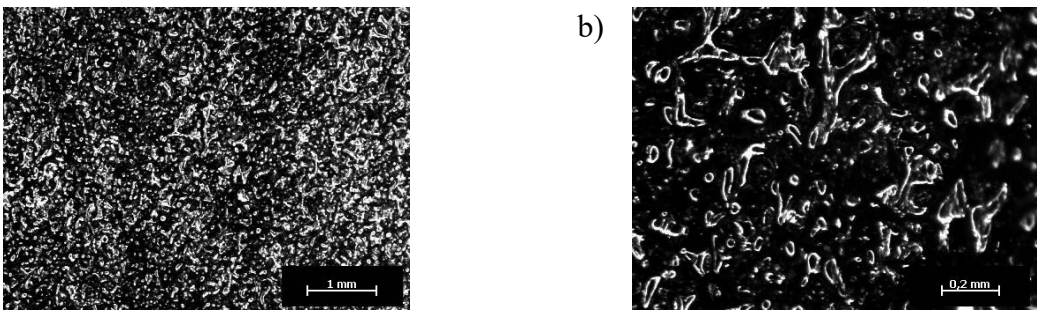

Figure 4. As-built surface morphology of Sample 3 (Pd = 70 µm, Et = 40 µs) observed by stereoscopic microscopy at: 25× magnification (a); 100× magnification.

a) b)

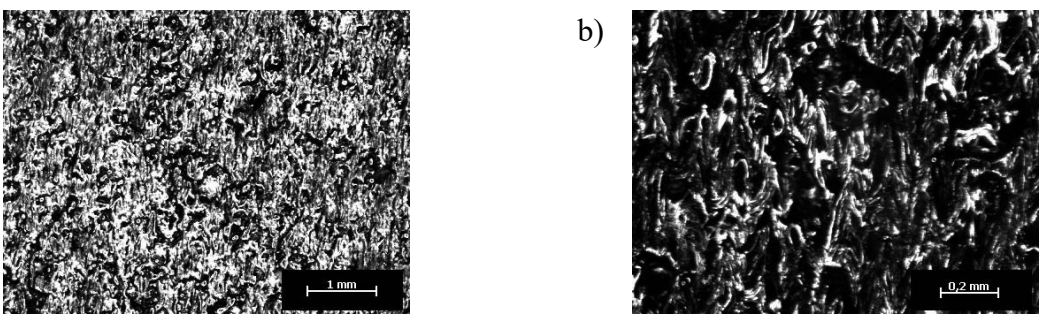

Figure 5. As-built surface morphology of Sample 4 (Pd = 90 µm, Et = 75 µs) observed by stereoscopic microscopy at: 25× magnification (a); 100× magnification.

a) b)

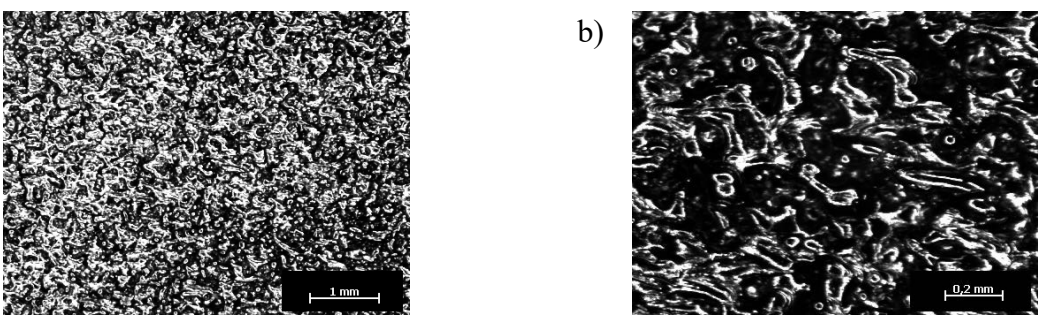

Figure 6. As-built surface morphology of Sample 5 (Pd = 90 µm, Et = 65 µs) observed by stereoscopic microscopy at: 25× magnification (a); 100× magnification.

a) b)

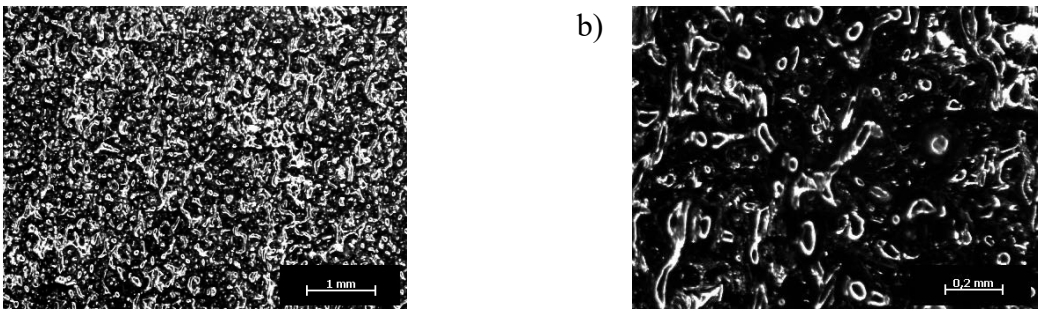

Figure 7. As-built surface morphology of Sample 6 (Pd = 90 µm, Et = 55 µs) observed by stereoscopic microscopy at: 25× magnification (a); 100× magnification.

a) b)

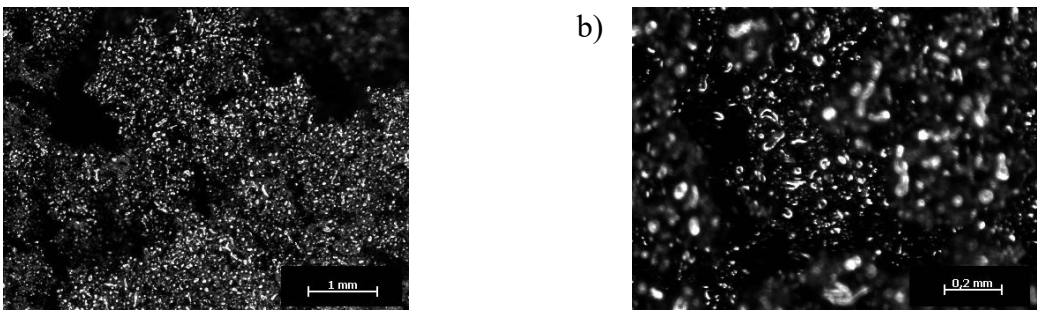

Figure 8. As-built surface morphology of Sample 7 (Pd = 30 µm, Et = 25 µs) observed by stereoscopic microscopy at: 25× magnification (a); 100× magnification.

a) b)

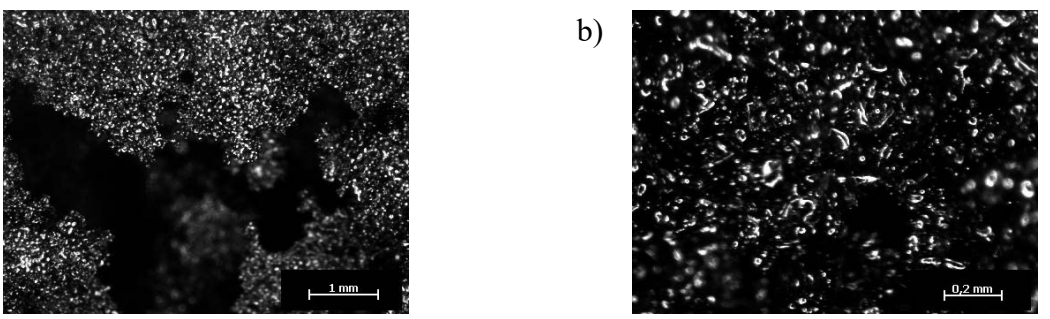

Figure 9. As-built surface morphology of Sample 8 (Pd = 30 µm, Et = 21 µs) observed by stereoscopic microscopy at: 25× magnification (a); 100× magnification.

a) b)

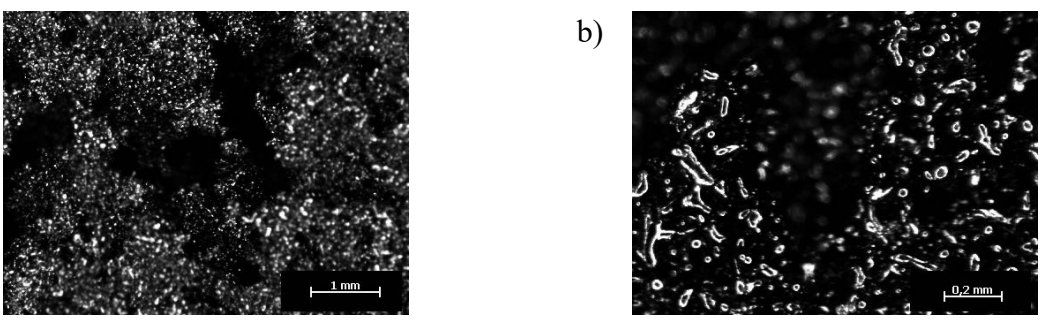

Figure 10. As-built surface morphology of Sample 9 (Pd = 30 µm, Et = 18 µs) observed by stereoscopic microscopy at: 25× magnification (a); 100× magnification.

a) b)

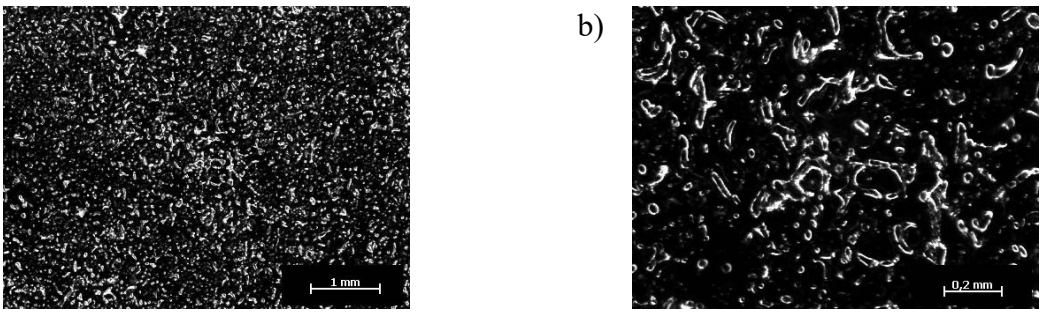

Figure 11. As-built surface morphology of Sample 10 (Pd = 20 µm, Et = 17 µs) observed by stereoscopic microscopy at: 25× magnification (a); 100× magnification.

4. CONCLUSIONS

The Point Distance (Pd) and Exposure Time (Et) significantly influence the surface melting quality of Mediloy® alloy in point-wise SLM. Optimal surface morphology was achieved at Pd = 70–90 µm and Et = 50–75 µs, while small Pd and short Et caused incomplete fusion, and long Et at large Pd led to surface swelling. Nominal surface energy density alone was insufficient to predict melting quality. Overall, the surface observations demonstrate that both Point Distance and Exposure Time must be carefully balanced to achieve stable surface melting and uniform morphology in point-wise SLM processing of Mediloy alloy. The results highlight that deviations from this balance lead to either surface deformation or insufficient surface consolidation, emphasizing the importance of optimized discrete laser exposure parameters.

REFERENCES

1. T. DebRoy, H.L. Wei, J.S. Zuback, T. Mukherjee, J.W. Elmer, J.O. Milewski, A.M. Beese, A. Wilson Heid, A. De, W. Zhang, Additive manufacturing of metallic components – process, structure and properties, Prog. Mater. Sci., Vol. 92, 2018, pp. 112–224.
2. D. Herzog, V. Seyda, E. Wycisk, C. Emmelmann, Additive manufacturing of metals, Acta Mater., Vol. 117, 2016, pp. 371–392.
3. W.E. Frazier, Metal additive manufacturing: a review, J. Mater. Eng. Perform., Vol. 23, 2014, pp. 1917–1928.
4. W.E. King, H.D. Barth, V.M. Castillo, A.J. Gallegos, J. Gibbs, T. Hahn, C. Kamath, A.M. Rubenchik, Laser powder bed fusion process mapping, Appl. Phys. Rev., Vol. 2, 2015, Article 041304.
5. H. Gong, K. Rafi, H. Gu, D. Starr, B. Stucker, Analysis of defect generation in SLM of metals, Mater. Des., Vol. 58, 2014, pp. 242–251.
6. F. Huang, H. Zhang, X. Gong et al., Influence of selective laser melting process parameters on the surface integrity of difficult-to-cut alloys: comprehensive review and future prospects, Int. J. Adv. Manuf. Technol., 2023.
7. S. Diegel, M.A. Masood, S. Singh, Influence of Selective Laser Melting Technological Parameters on the Mechanical Properties of Additively Manufactured Elements Using 316L Austenitic Steel, Mater. Sci. Eng. A, 2020.

8. Y. Zhang, C. Qiu, J. Liu et al., Effect of laser process parameters on the pores, surface roughness, and hardness of laser selective melting of dental cobalt-chrome alloys, J. Prosthodont. Res., 2024.
9. J.P. Kruth, P. Mercelis, J. Van Vaerenbergh, L. Froyen, M. Rombouts, Selective laser melting of iron-based powders, J. Mater. Process. Technol., Vol. 149, 2004, pp. 616-622.
10. M. Tang, P.C. Pistorius, Keyhole porosity in SLM of metals, Addit. Manuf., Vol. 18, 2017, pp. 49–56.
11. M.J. Matthews, G. Guss, et al., Defect formation mechanisms in SLM, Acta Mater., Vol. 114, 2016, pp. 33–48.
12. L. Thijs, F. Verhaeghe, T. Craeghs, J. Van Humbeeck, J.P. Kruth, Melt pool dynamics in pulsed SLM, Acta Mater., Vol. 58, 2010, pp. 3303–3312.
13. B. Zhang, J. Li, et al., Effect of laser spot overlap on SLM surface quality, Opt. Laser Technol., Vol. 120, 2019, Article 105699.
14. C. Li, W. Liu, et al., Influence of scanning strategy on melt pool behavior in SLM, Addit. Manuf., Vol. 31, 2020, Article 100980.
15. M. Król, T. Tański, Surface quality research for selective laser melting of Ti-6Al-4V alloy, Arch. Metall. Mater., Vol. 61, 2016, pp. 1291–1296.
16. L.A. Dobrzański, A.D. Dobrzańska-Danikiewicz, T. Gaweł, Computer-aided design and selective laser melting of porous biomimetic materials, Adv. Mater. Process. Technol., Vol. 3, No. 1, 2017, pp. 442–447.
17. A.D. Dobrzańska-Danikiewicz, L.A. Dobrzański, M. Szindler, A. Achtelik-Franczak, J. Dobrzański, Surface treatment of porous materials produced by selective laser sintering to enhance cell proliferation, in: Metalowe materiały mikroporowate i lite do zastosowań medycznych i stomatologicznych, Open Access Library, 2017, pp. 289-231.
18. A.D. Dobrzańska-Danikiewicz, A. Bączyk, A review of new Ti-based materials manufactured in situ for biomedical applications, Int. Sci. J. Mater. Manuf. Eng., Vol. 121, No. 2, 2023.
19. M. Soleimani, W. Sitek, M.M. Szindler, The influence of laser parameters in the selective laser melting on the properties of Co-Cr dental implants, in: XXIV Krajowa Konferencja Elektroniki, Program and Abstracts, 2025, pp. 273-275.
20. BEGO GmbH & Co. KG, Mediloy S-Co material data, 2013, https://www.bego.com

TalentDetector

9th January 2026
Gliwice, Poland

DEPARTMENT OF ENGINEERING MATERIALS AND BIOMATERIALS
FACULTY OF MECHANICAL ENGINEERING
SILESIAN UNIVERSITY OF TECHNOLOGY

INTERNATIONAL STUDENTS SCIENTIFIC CONFERENCE

How modern AI supports Power Line detection

Józef Cyran[a], Adam Brzezowski[b], Julian Koterba[c], Michał Sujkowski[d]

[a] Silesian University of Technology, Faculty of Automatic Control, Electronics and Computer Science, Department of Computer Graphics, Vision and Digital Systems, Student Research Club vFly, email: jozef.cyran@polsl.pl
[b] Silesian University of Technology, Faculty of Automatic Control, Electronics and Computer Science, Student Research Club vFly
[c] Silesian University of Technology, Faculty of Automatic Control, Electronics and Computer Science, Student Research Club vFly
[d] Silesian University of Technology, Faculty of Transport and Aviation Engineering, Student Research Club vFly,

Abstract: The paper presents a three-fold inspection of power line detection with the use of AI. Firstly, it examines the modalities and contrasts them with the use cases. Secondly, it describes common setups for visual input processing, examining the different pipelines employed. Thirdly, the paper explores the data-gathering problem of power line detection with particular focus on annotation and labelling.

Keywords: Power Lines detection, Deep-Learning, Convolutional Neural Networks, Multimodal-Imaging, Data-Annotation

1. INTRODUCTION

The transition from manual ground patrols to automated, AI-driven power line inspection is essential for maintaining modern grid reliability and safety. Therefore, in recent years a serious effort has been made to understand how various sensing modalities - including LiDAR for 3D geometry and infrared or ultraviolet imaging for fault diagnosis - can be used to successfully solve recognition tasks. In the following sections, we analyze deep learning frameworks, such as semantic segmentation and real-time detection pipelines, while addressing the significant operational bottleneck of expert-level data annotation. By evaluating unsupervised, weakly supervised, and human-in-the-loop paradigms, this study highlights how the field is moving toward multimodal integration, evolving automated systems from simple line detectors into comprehensive diagnostic tools for resilient infrastructure.

2. SENSING MODALITIES AND DATA ACQUISITION

In power line infrastructure recognition, sensing determines the structure of the data on which learning-based methods operate and, by extension, the formulation of the recognition task itself. Different sensors measure fundamentally different physical phenomena - reflected radiation, emitted radiation, geometric distance, or electromagnetic and acoustic signatures - and therefore produce data with distinct dimensionality, noise characteristics, and information content. As a consequence, identical inspection objectives may be expressed as two-dimensional image segmentation problems, three-dimensional geometric reconstruction tasks, or temporal signal analysis problems, depending on the sensing modality employed.

2.1 LiDAR-based sensing

LiDAR (Light Detection and Ranging) is an active sensing modality that directly measures distance through laser time-of-flight, producing dense three-dimensional point clouds. In power line inspection, LiDAR is primarily used not to discover the existence of infrastructure assets, but to recover accurate corridor geometry and spatial relationships between conductors, vegetation, terrain, and supporting structures. This role is explicitly emphasized in the literature. As noted in a widely cited overview of airborne LiDAR for transmission corridors, the 3d Point Cloud generated by LiDAR can be used for accurate extraction of power lines [1]. Such geometric information is central to right-of-way monitoring, clearance assessment, and vegetation encroachment analysis, where regulatory thresholds must be evaluated quantitatively rather than visually. Beyond detection, LiDAR enables reconstruction of conductor geometry and sag profiles along entire spans. Liang et al. explicitly frame LiDAR as a reconstruction tool [2].

Repeated LiDAR acquisitions further support change detection over time, enabling utilities to track vegetation growth, assess post-storm damage, and update corridor models. From a learning perspective, LiDAR data naturally leads to three-dimensional segmentation and reconstruction tasks operating on point sets or voxelized representations. However, while LiDAR provides precise spatial measurements, it carries little information about surface condition, thermal state, or electrical activity, motivating its integration with complementary sensing modalities.

2.2 Image-based sensing: visible and infrared

Visible-light (RGB) imaging remains the most widely used sensing modality in power line inspection due to its high spatial resolution and rich appearance information. RGB imagery supports detection and segmentation of conductors, poles or towers, insulators, and auxiliary components, as well as detailed visual inspection of surface-level defects. The suitability of visible imagery for detecting physical degradation is well documented. Faisal et al. mention in their comprehensive inspection study that visible light images are enough to detect external damage [3]. Because RGB images preserve fine texture and edge detail, they are particularly effective for identifying broken strands, damaged fittings, or foreign-object attachments. At the same time, RGB-based inspection is sensitive to illumination conditions, background clutter, and depth ambiguity, especially for thin structures such as conductors viewed against complex terrain.

Infrared imaging is therefore frequently employed as a complementary modality. In power line inspection, infrared sensing is most commonly used in the thermal infrared range, where sensors capture emitted radiation related to surface temperature. Thermal imagery is explicitly associated with fault detection rather than geometric reconstruction. Kähler et al. point out that thermal imaging is more useful for detecting wire faults than mapping [4]. Thermal cameras enable identification of abnormal heating caused by high resistance joints, loose connections, or overload conditions, and are largely invariant to visible illumination, allowing night-time operation. However, thermal images typically exhibit lower spatial resolution and weaker geometric detail than RGB images. Consequently, thermal data is often fused with visible-light imagery to combine condition awareness with precise localization.

2.3 Ultraviolet and non-visual sensing

Ultraviolet (UV) imaging is used to detect corona discharge and partial discharges on energized power line infrastructure. Unlike visible or thermal imaging, UV cameras capture optical emissions associated with electrical ionization processes, enabling early detection of insulation degradation and discharge activity before severe thermal or structural damage occurs [5]. UV inspection is typically performed from mobile platforms such as helicopters or UAVs in targeted missions, as the modality is sensitive to environmental conditions and requires controlled viewing geometry.

Beyond optical sensing, non-visual modalities such as acoustic or ultrasonic sensing have been investigated for partial discharge monitoring. These approaches treat discharge phenomena as temporal signals rather than spatial images, capturing mechanical vibrations or acoustic emissions produced by electrical activity. Du et al. described a multimodal setup employing voiceprint signals to detect mechanical vibrations and infrared images to find thermal anomalies [6]. Such signal-based methods provide valuable complementary information in low-visibility or enclosed environments, but typically offer limited spatial localization. As a result, acoustic and related non-visual sensing techniques are most effective when combined with image-based or LiDAR-derived geometric context.

3. COMMON PROCESSING SETUPS IN POWER LINE RECOGNITION

3. Common Processing Setups in Power Line Recognition

Practical systems adopt a small number of recurring processing setups that differ in how visual input is structured, processed, and transformed into usable outputs and typically operate on similar RGB imagery but diverge in architectural assumptions, intermediate representations, and post-processing strategies. This section summarizes the most common pipeline configurations observed in the literature and practice.

3.1 End-to-end segmentation pipelines (encoder–decoder networks)

One widely used setup formulates power line recognition as a dense semantic segmentation problem. In this configuration, an RGB image is processed by an encoder–decoder network that produces a pixel-level mask indicating the presence of power line structures. Architectures derived from the **U-Net family** are especially common, as their skip connections help preserve spatial detail that is critical for thin, elongated objects. In this setup, the encoder extracts multi-scale contextual features, while the decoder reconstructs high-resolution predictions.

Variants often incorporate attention mechanisms, auxiliary losses, or multi-scale feature aggregation to address severe class imbalance, since power line pixels occupy only a small fraction of the image [3]. The output is typically a binary or multi-class mask that can be further processed to extract line centerlines or connected components.

This pipeline is attractive for its conceptual simplicity and direct correspondence between input and output. However, it depends strongly on high-quality pixel-level annotations and may struggle with line continuity in cluttered backgrounds unless explicitly designed to enforce structural coherence.

3.2 Context-enhanced segmentation with dilated convolutions

A closely related but distinct setup extends the encoder–decoder paradigm by explicitly increasing the receptive field through dilated (atrous) convolutions. This approach is exemplified by architectures such as **D-LinkNet**, which augment a standard encoder–decoder backbone with a dilated convolution module at the bottleneck [7].

In this configuration, the dilated layers aggregate information over large spatial extents without reducing resolution, allowing the network to capture long-range continuity along conductors. The decoder then reconstructs the segmentation mask using skip connections similar to those in U-Net-like architectures.

3.3 Detection-first pipelines (object detection and instance segmentation)

Another common processing setup treats power lines as detectable objects rather than purely as pixel-level structures. In this approach, the input image is processed by an object detection or instance segmentation network that outputs bounding boxes, masks, or both. Single-stage detectors from the **YOLO family** are frequently adopted due to their favorable balance between accuracy and inference speed. In detection-first pipelines, the network learns to localize regions containing power line segments or spans, often at multiple scales. When segmentation outputs are available, they are typically associated with detected instances rather than produced as a global dense mask. This formulation naturally supports scenarios where multiple line segments must be distinguished and processed independently. Detection-based setups are particularly attractive for onboard UAV inspection, where real-time performance is critical. However, extremely thin or low-contrast conductors may be difficult to localize reliably unless high-resolution inputs, tiling strategies, or specialized loss functions are employed [3].

3.4 Hybrid pipelines combining deep learning and classical processing

Some systems adopt a multi-stage pipeline that combines classical image processing techniques with deep learning components. In such setups, the input image is first preprocessed using edge detection, thresholding, or filtering to emphasize linear structures. The resulting representations are then analyzed using convolutional networks to extract higher-level features. Examples of this approach include pipelines where CNN-based feature extraction is followed by classical classifiers or geometric post-processing, as in **RsurgeNet-style** or similar hybrid frameworks. Subsequent stages may apply line fitting or Hough-based methods to enforce structural consistency and suppress false positives. Hybrid pipelines are often used when training data is limited or when strong geometric regularity is expected. While they can be effective, they introduce additional design complexity and parameter tuning, and their performance depends on the interaction between learned and hand-crafted components.

3.5 Output representations and downstream use

Across all setups, outputs are ultimately transformed into representations suitable for inspection tasks. These include pixel-level masks, polylines representing conductor centerlines, detected line segments, or binary indicators of line presence. The chosen output representation determines how results are consumed by downstream stages, such as clearance computation, fault localization, or human review. Despite architectural differences, these processing setups reflect a shared design space shaped by thin-structure recognition challenges, annotation constraints, and operational requirements. Understanding these recurring configurations provides context for evaluating learning paradigms and performance trade-offs discussed in later sections.

4. LEARNING PARADIGMS AND THE ROLE OF ANNOTATION

In AI-based power line infrastructure recognition, the dominant constraint is annotation: its availability, cost, and structure. Inspection data can be acquired at a large scale using aerial or mobile platforms, yet converting this data into labelled training material typically requires expert knowledge and substantial manual effort. As noted in the Faisal *et al.* study human labour is a very substantial constraint, human agents are required for verification of labels [3].

4.1 Annotation granularity and task formulation

Labelling requirements vary significantly across inspection tasks and sensing modalities. Image-based detection tasks commonly rely on bounding-box annotations, which can be produced relatively efficiently and therefore dominate large-scale datasets. Tasks that involve geometric reasoning - such as conductor extraction, clearance analysis, or vegetation proximity assessment - depend on dense pixel-level or instance-level segmentation.

For thin structures such as conductors, precise segmentation is often essential for downstream analysis. At the same time, annotation is difficult due to low contrast, background clutter, and ambiguous boundaries. In LiDAR-based inspection, annotation challenges increase further. Labelling three-dimensional point clouds requires specialized tools and trained annotators, and scales poorly with dataset size. Industry analyses of data annotation practices consistently report that point cloud labelling is among the most costly and technically demanding forms of annotation, requiring greater expertise and longer processing times than image-based labelling [9].

4.2 Condition monitoring and event-level annotation

For condition-oriented inspection tasks, particularly those based on thermal infrared or ultraviolet sensing, annotation practices follow a different pattern. Annotations commonly describe the presence, type, or severity of an anomaly, with spatial delineation playing a secondary role. In industrial thermography practice, inspections are frequently reported using severity ratings aligned with established standards as stated in inspection guidelines. Publicly released datasets for power line anomaly detection reflect this approach. Labels are often provided at the image or event level and may include severity scores, mirroring operational inspection workflows [5]. This form of annotation emphasizes actionable diagnosis and influences the learning formulations used for condition assessment.

4.3 Weak supervision and Unsupervised learning

Given the cost of dense annotation, weakly supervised learning has emerged as a practical strategy for scaling inspection systems. In this setting, models are trained using coarse labels - such as image-level, patch-level, or span-level indicators - which reduces reliance on exhaustive manual annotation, as Choi proposes [8]. Recent surveys confirm that such methods enable broader use of available inspection data, particularly for screening and prioritization tasks. The resulting models typically sacrifice spatial precision, which limits their direct applicability in tasks that require accurate localization or geometric measurement. Unsupervised and semi-supervised learning approaches are primarily applied to anomaly detection, because traditional supervised methods often fail here [3].

In operational settings, outputs from unsupervised models rarely translate directly into maintenance actions. Industry experience emphasizes the necessity of expert validation. As one inspection provider describes, effective deployment relies on a human-in-the-loop (HITL) process where automated detections are reviewed and contextualized by specialists before decisions are made [9].

4.5 Implications for learning paradigms

Across sensing modalities and inspection objectives, the annotation strategy consistently shapes learning paradigms. Tasks that tolerate coarse labels favor weakly supervised or anomaly-based approaches, while geometry- and clearance-sensitive tasks remain dependent on high-quality dense annotations. Learning methods in this domain can therefore be interpreted as responses to labelling constraints, with supervision level acting as a key design parameter. This perspective motivates organizing the literature by task formulation and supervision level. The following section adopts this task-centric view to structure existing approaches.

5. CONCLUSION

Despite the maturity of single-sensor pipelines - especially RGB-based approaches that already achieve robust detection and segmentation in many field conditions - multimodal architectures remain an active and practical direction. Adding complementary sensors does not merely improve accuracy; it expands the task space a system can address, enabling a shift from “finding lines” toward broader inspection objectives such as condition assessment, safety screening, and corridor-level understanding. Across the reviewed works, convolutional networks remain the industry default for perception on visual inputs, with recurring architectural families including encoder–decoder segmentation networks (U-Net-like variants), context-augmented segmentation models (e.g., D-LinkNet-style designs with dilated convolutions), and detection-first pipelines (e.g., YOLO-family models). A consistent theme is that segmentation - particularly for thin, elongated structures - poses a central technical and practical challenge: architectures, losses, and post-processing steps are frequently adapted to preserve continuity, reduce fragmentation, and mitigate class imbalance.

Finally, unsupervised and semi-supervised learning emerges less as a competitor to supervised pipelines and more as a complementary capability, most naturally suited to anomaly detection. In inspection workflows, these methods provide a scalable way to flag deviations from normal patterns, while precise diagnosis and actionability still typically depend on downstream interpretation, task-specific validation, or human review. Overall, the field converges on a pragmatic design principle: strong single-modality baselines form the backbone

of deployment, while multimodality and label-efficient learning broaden coverage, robustness, and the operational relevance of automated power line inspection.

BIBLIOGRAPHY

1. A. Munir, M. Awrangjeb, B. Stantic, A Survey on LiDAR-Based Transmission Line Inspection, Remote Sensing, vol. 15, no. 4, art. 973(2023), doi: 10.3390/rs15040973.
2. Y. Ma *et al*., Enhanced Automatic Span Segmentation of Airborne LiDAR Point Clouds for Power Lines, Sensors, vol. 25, no. 20, art. 6448 (2025), doi: 10.3390/s25206448.
3. M. A. Faisal, I. Mecheter, Y. Qiblawey, J. Hernandez Fernandez, M. E. Chowdhury, S. Kiranyaz, Deep Learning in Automated Power Line Inspection: A Review, arXiv:2502.07826, 2025. (ar5iv HTML mirror.)
4. O. Kähler, S. Hochstöger, G. Kemper, J. Birchbauer, Automating Powerline Inspection: A Novel Multisensor System for Data Analysis Using Deep Learning, Int. Arch. Photogramm. Remote Sens. Spatial Inf. Sci. (ISPRS Archives), vol. XLIII-B4-2020,(2020) 747–754, doi: 10.5194/isprs-archives-XLIII-B4-2020-747-2020.
5. T. Santos *et al*., UAV Visual and Thermographic Power Line Detection Using Deep Learning, Sensors, vol. 24, no. 17, art. 5678 (2024), doi: 10.3390/s24175678.
6. X. Du, X. Lei, T. Ye, Y. Sun, Z. Shang, Z. Liu, T. Xu, A review of research on intelligent fault detection of power equipment based on infrared and voiceprint: methods, applications and challenges, Global Energy Interconnection, vol. 8, no. 5 (2025) 821–846, doi: 10.1016/j.gloei.2025.08.001.
7. L. Zhou, C. Zhang, M. Wu, D-LinkNet: LinkNet with Pretrained Encoder and Dilated Convolution for High Resolution Satellite Imagery Road Extraction, *Proc. CVPR Workshops* (2018).
8. H. Choi, G. Koo, B. J. Kim, S. W. Kim, Weakly supervised power line detection algorithm using a recursive noisy label update with refined broken line segments, Expert Systems with Applications, vol. 165, art. 113895 (2021), doi: 10.1016/j.eswa.2020.113895.
9. J. Plaza, Challenges in Training AI Models For Electric Grid Inspections, Commercial UAV News, 2025. https://www.commercialuavnews.com/challenges-and-solutions-in-training-ai-models-for-power-line-inspections

TalentDetector
9th January 2026
Gliwice, Poland
DEPARTMENT OF ENGINEERING MATERIALS AND BIOMATERIALS
FACULTY OF MECHANICAL ENGINEERING
SILESIAN UNIVERSITY OF TECHNOLOGY
INTERNATIONAL STUDENTS SCIENTIFIC CONFERENCE

Zdvíhacie mechanizmy do 3,5t pre parkovanie pod zemou

Sebastián Dlugosch[a], Matúš Vereš[b]

[a] Žilinská univerzita v Žiline, Strojnícka fakulta, Katedra materiálového inžinierstva, Univerzitná 8215/1, 010 26 Žilina, Slovak Republic
[b] Žilinská univerzita v Žiline, Strojnícka fakulta, Katedra konštruovania a častí strojov, Univerzitná 8215/1, 010 26 Žilina, Slovak Republic
email: dlugosch@stud.uniza.sk, matus.veres@fstroj.uniza.sk

Abstract: Cieľom príspevku je teoreticky popísať zdvíhacie zariadenia do 3,5t pre parkovanie pod zemou, ich charakteristika, rozdelenie, technologické trendy a inovatívne prístupy.

Keywords: zdvíhacie zariadenie, technické normy, skúšky zdvíhacích zariadení

1. ÚVOD

V dnešnom svete sa výroba áut pohybuje približne okolo 250 000 kusov za jeden deň. Najväčším producentom automobilov na svete je Čína, v ktorej sa vyrobí až 30 % z celkového počtu automobilov. Všetky vyrobené automobily je potrebné niekde skladovať, kým si ich zákazník nekúpi. Dnes automobilky a rôzne predajné bazáre využívajú parkovacie regály, ktoré však sú obmedzené ich výškou a výškou uskladňovacej budovy. Najčastejšie však nechávajú automobily zaparkované pred výrobnými halami, alebo predajnými centrami, čo má však negatívny vplyv na ich karosériu a pohonnú časť.

Jedným z riešení takejto situácie sú parkovacie výťahy do podzemných parkovísk. Podzemné parkoviská prinášajú nielen efektívne využitie priestoru ale aj ochranu vozidla pred počasím (sneh, námraza, UV žiarenie). Asi ich najväčšou výhodou je, že tieto parkoviská nie sú obmedzené výškou budovy, keďže pod zemou môže byť niekoľko poschodí takýchto parkovísk. Jediné čo stačí je nainštalovať zdvíhacie zariadenie, ktoré tieto automobily bude dopravovať do podzemných garáží, kde sú následne uskladnené.

Výhodou takýchto zdvíhacích zariadení je aj ich využiteľnosť v obytných budovách, keďže na povrchu zostáva miesto pre parky či zeleň, alebo detské ihriská.

2. ANALÝZA SÚČASNÉHO STAVU ZDVÍHACÍCH ZARIADENÍ

Zdvíhacie zariadenia sú technické prostriedky určené na zdvíhanie a manipuláciu s bremenami. Tieto zariadenia sú klasifikované do rôznych skupín a typov podľa ich funkcie, konštrukcie a nosnosti.

Na trhu existuje široká škála rôznych typov zdvíhacích zariadení, ktoré sa líšia konštrukciou a použitím, ako napr.:

- *Dvojstĺpové zdviháky*: ideálne využitie pre servisy a dielne zaoberajúce sa tuningom, montovaním autoalarmov a mechanických zabezpečovacích systémov, splynovačov, alebo ťažných zariadení (obr. 1).
- *Nožnicové zdviháky*: kompaktné a vhodné pre menšie alebo zložité priestory (obr. 2).
- *Jednostĺpové zdviháky*: poskytujú určitú flexibilitu pri manipulácií s bremenami.
- *Lanové navijaky a kladkostroje*: používajú sa pri manipulácií s ťažkými bremenami v priemysle.
- *Hydraulické zdviháky*: slúžia na zdvíhanie osobných, alebo malých úžitkových automobilov a tranzitov pri ich údržbe, oprave alebo kontrole. Na zdvih ťažkých bremien používajú hydraulickú kvapalinu.
- *Pneumatické zdviháky*: pomocou pneumatického systému zaručujú presnosť a spoľahlivosť.
- *Mechanické zdviháky*: zdvih bremena zaručujú ozubené kolesá, ktoré sa posúvajú po stĺpikoch s ozubením.

Obr.1 Dvojstĺpový zdvihák [1]
Figure 1. Duble-post lift [1]

Obr. 1 Nožnicový zdvihák [2]
Figure 2. Scissor lift [2]

3. TECHNOLOGICKÉ TRENDY A INOVATÍVNE PRÍSTUPY V OBLASTI ZDVÍHACÍCH ZARIADENÍ

V dnešnej dobe sa technológie vyvíjajú rapídnym tempom a výnimkou nie sú ani zdvíhacie zariadenia. Inovácie v zdvíhacích zariadeniach sa zameriavajú na zvýšenie efektivity, bezpečnosti a manévrovateľnosti, s dôrazom na inteligentné technológie, automatizáciu (ako autonómne vozíky), pokročilé materiály (ľahšie, pevnejšie), ergonómiu, dizajn, digitálne monitorovanie, alebo na prediktívnu údržbu [6], čo má za následok lepšie bezpečnostné normy a predpisy ich používania, prevenciu havárií a dlhovekosť zdvíhacích zariadení, kvalitnejšiu a

hlavne lacnejšiu výrobu a v neposlednom rade ich jednoduchšie ovládanie.

Tieto inovácie transformujú zdvíhacie zariadenia z jednoduchých strojov na inteligentné nástroje, ktoré integrujú digitálne technológie na optimalizáciu prevádzky v rôznych priemyselných odvetviach, nielen na parkovacie systémy.

Vo svete sa môžeme stretnúť s viacerými typmi inovácií zdvíhacích zariadení, ako napr.:

1. *Výťah na solárny pohon*
   TREVA ako prvá firma na Slovensku začala v roku 2015 vyvíjať výťah na solárnu elektrickú energiu. Vďaka vysokoúčinnému bez prevodovému stroju spotrebuje výťah relatívne málo elektrickej energie. Výťah bude vybavený komponentmi, ktoré eliminujú spotrebu takmer na minimum. O nižšie nároky na elektrickú energiu sa postarajú napr. riadiaca elektronika výťahu a výťahový stroj s najmodernejšou bez prevodovou technológiou. Výťah môže byť prevádzkovaný na solárnu energiu aj na energiu zo siete alebo môže byť napájaný obidvoma zdrojmi. V závislosti na konfigurácii a dostupnosti slnečného svetla je možná aj plne solárna prevádzka. Strešné solárne panely na pohon výťahu sú dimenzované podľa predpokladanej úrovne prevádzky danej budovy a plne postačujú pre napájanie výťahu aj počas dlhších období slabého slnečného svitu. Energia zachytená strešnými solárnymi panelmi môže byť použitá okamžite, môže byť uložená do batérií alebo ju možno dokonca predávať do siete či využiť na osvetlenie nebytových priestorov akými sú napríklad chodby a pivnice [3].

2. *Elektrický malý mobilný podlahový žeriav*
   Je navrhnutý na zlepšenie manévrovateľnosti a efektívnosti pri manipulácii s materiálom. S nosnosťou od 700 kg do 1 200 kg tento všestranný žeriav spĺňa rôzne prevádzkové potreby. Jednou z kľúčových vlastností je jeho schopnosť otáčať sa o 120 stupňov doľava a doprava. Táto schopnosť výrazne zlepšuje manévrovateľnosť a umožňuje presné a efektívne nakladanie a vykladanie ťažkých predmetov aj v stiesnených priestoroch. Takáto flexibilita je nevyhnutná v prostrediach, kde je obmedzený priestor a efektívnosť je prvoradá [4].

3. *Automatické paletové parkovacie systémy (obr. 3)*
   Na presun paliet s vozidlami využívajú vertikálne (centrálny výťah s extraktorom paliet) alebo horizontálne (kolieskové) dráhy. Vysokovýkonný priemyselný počítač zabezpečuje plne automatickú prevádzku a vyhľadáva najrýchlejšiu a najkratšiu cestu k vozidlu. Pre ľahší vjazd a výjazd je možná inštalácia otočnej platformy.

Obr. 3 Rotačný parkovací systém *Obr. 4 Zvislý parkovací systém [7]*
Figure 3. Rotary parking system *Figure 4. Vertical parking system [7]*

Jeho výhodou je najmenšia plocha pokrytia ako iné automatizované parkovacie systémy a až 10-krát väčšia úspora miesta v porovnaní s tradičným parkovaním.

4. PREHĽAD NORIEM A REGULÁCIÍ PRE ZDVÍHACIE MECHANIZMY

Pre navrhovanie technických zdvíhacích zariadení sa používajú nasledovné normy STN ako:

- **STN EN 13001-1**: - špecifikuje všeobecné zásady a požiadavky na konštrukčný návrh, aby sa predchádzalo mechanickým ohrozeniam pri zdvíhacích zariadeniach.
- **STN EN 12644-1+A1**: - špecifikuje požiadavky na vyhotovenie a obsah používateľskej príručky dodávanej výrobcom zdvíhacích zariadení.
- **STN EN 12999**: - špecifikuje minimálne požiadavky na navrhovanie, výpočet, skúšky a skúšky hydraulicky poháňaných nakladacích žeriavov a ich montáž na vozidlá alebo na statické základy.
- **STN EN 13155**: - špecifikuje bezpečnostné požiadavky na nasledujúce neupevnené prídavné zariadenia na zdvíhanie bremien pre žeriavy, zdvíhadlá a ručne ovládané zariadenia na manipuláciu s bremenami.
- **STN EN 14492-1+A1**: - je aplikovateľná pri návrhu, informáciách o používaní, údržbe a skúškach motorových vrátkov, pri ktorých je primárnou pohonnou jednotkou elektrický motor, hydraulický motor, motor s vnútorným spaľovaním alebo pneumatický motor.
- **STN EN 1494+A1:** - sa zaoberá všetkými významnými nebezpečiami vzťahujúca sa k mobilným, alebo premiestniteľným zdvihákom a súvisiacim zdvíhacím zariadením.
- **STN 27 0808**: - platí pre konštruovanie, výrobu a prevádzku skrutkových zdvihákov s elektrickým pohonom používaných na zdvíhanie dráhových vozidiel.
- **STN EN 1493**: - sa vzťahuje na stacionárne a mobilné zdvíhacie plošiny vozidiel, ktoré nie sú určené na zdvíhanie osôb, ale ktoré sú určené na úplné zdvíhanie vozidiel.
- **STN 27 0881**: - platí pre výpočty kovových konštrukcií zdvihákov, konštrukciu, výrobu, preberanie a dodávanie, ako aj prevádzkovanie, údržbu a skúšanie mechanických stojanových zdvihákov [5].

4.1 Skúšanie zdvíhacích zariadení

Podrobný predpis skúšok zdvíhacích zariadení ustanovuje norma STN 27 0142. Každý prevádzkovateľ zdvíhacieho zariadenia musí zaradiť svoje zdvíhacie zariadenie do príslušnej únavovej skupiny. Pri rozdeľovaní zdvíhacích zariadení do únavových skupín treba hodnotiť:

a) Počet pracovných cyklov za rok

$$Tr = n * t * \tau * Tn \quad [-]$$

kde: n - počet pracovných dní v roku, t - celková pracovná doba, τ - časové využitie zdvíhacieho zariadenia a T_n - počet pracovných cyklov za hodinu

b) Pomerné zaťaženie

$$q = \frac{Qp}{Qc} * 100 \ [\%]$$

kde: Q_p - priemerná hmotnosť nákladu, Q_c - nosnosť zdvíhacieho zariadenia

c) Dynamické účinky

Hodnotí sa pracovná rýchlosť pojazdu a pracovná rýchlosť zdvihu.

Pre každý z týchto troch parametrov norma určuje tzv. porovnávacie číslo a ich súčet zaraďuje zdvíhacie zariadenie do príslušnej únavovej skupiny.

Skúšky zdvíhacích zariadení sú:

1) Montážna skúška

Je predpísaná po dokončení montáže nových zdvíhacích zariadení po generálnej oprave alebo pri premiestnení zdvíhacieho zariadenia na iné pracovisko. Obsahuje významnú prehliadku I, funkčnú skúšku bez zaťaženia a funkčnú skúšku s hmotným bremenom. Pri druhej prehliadke je potrebné skontrolovať prístupy z hľadiska obsluhy, tesnosť hydraulických a pneumatických obvodov, bočné a zvislé vôle, značenia a nápis.

Pri skúške bez zaťaženia sa overuje funkcia všetkých pohyblivých a hnacích mechanizmov, pracovné rýchlosti, ovládacie prvky, hlavné vypínače, signalizácia a detekcia porúch.

Zaťažovacia skúška sa realizuje s bremenom prevyšujúcim hmotnosť o 10 %. S týmto zaťažením sa vykonávajú všetky pohyby najnižšími a najväčšími rýchlosťami vrátane skúšky bŕzd, nábeh do krajných polôh a funkcie preťažovacích poistiek.

Pri mostových a portálových žeriavoch sa meria aj priehyb mosta s týmto bremenom v najúčinnejšej polohe. Bremeno sa nechá zavesené 10 minút a priehyb nesmie prekročiť hodnoty prevádzky. Po realizácii skúšky technik urobí zápis do žeriavovej knihy.

2) Schvaľovacia skúška

Vykonáva sa po úspešnej montážnej skúške, prebieha v takom istom rozsahu ako montážna skúška, avšak skúšobné bremeno pri záťažovej skúške je o 25 % väčšie ako nosnosť zdvíhacieho zariadenia. Schvaľovaciu skúšku môže robiť len technická inšpekcia a príslušný technik, ktorý o výsledku skúšky vyhotoví osvedčenie o uvedení do prevádzky.

3) Pravidelné revízne skúšky

Vykonávajú sa v pravidelných obdobiach revíznym technikom. Dĺžka obdobia medzi revíznymi skúškami je stanovená podľa únavovej skupiny zdvíhacích zariadení. Rozsah revíznej skúšky je rovnaký ako pri montážnej skúške.

5. POSTUP PRI NAVRHOVANÍ ZDVÍHACIEHO ZARIADENIA

Pri návrhu zdvíhacieho zariadenia je dôležité:

1. *analyzovať mechanické zaťaženie a statickú analýzu konštrukcie, t.j.:*
   - Pevnostné výpočty konštrukcie - je potrebné stanoviť typ a rozmery nosných prvkov tak, aby uniesli vozidlo aj s rezervou.
   - Dynamické zaťaženie - pri zdvíhaní a spúšťaní dochádza k akceleráciám, ktoré spôsobujú dodatočné zaťaženie konštrukcie. Treba počítať s rázovými silami pri zastavovaní pohybu.
   - Rovnováha síl a momentov - pri zdvíhaní vozidla musí byť zabezpečená stabilita konštrukcie, aby nedošlo k prevráteniu alebo nerovnomernému zaťaženiu nosných prvkov.

2. *zvážiť spôsob ovládania a bezpečnostné prvky:*
   - elektromotory a riadenie - hydraulický pohon môže byť riadený elektromotorom s reverzným chodom, ktorý zabezpečí zdvíhanie aj spúšťanie.
   - bezpečnostné prvky - Dôležité sú koncové spínače, ktoré zastavia pohyb pri dosiahnutí maximálnej alebo minimálnej polohy.
   - automatizácia - Dajú sa využiť programovateľné riadiace jednotky (PLC) na ovládanie systému, čím sa zvýši bezpečnosť a pohodlie používania.
   - ovládanie na diaľku - Moderné systémy môžu byť ovládané pomocou diaľkových ovládačov alebo aplikácií v mobilných zariadeniach.

3. *Stavebná ochrana a bezpečnosť*

Zdvíhacie zariadenia sú umiestnené pod zemou, čo prináša špecifické konštrukčné požiadavky na ochranu a bezpečnosť, ktoré sú kľúčové pri návrhu zdvíhacieho zariadenia.

- Jednoduché ovládanie - Užívateľ by mal mať k dispozícii intuitívne ovládanie, napríklad prostredníctvom tlačidiel alebo dotykovej obrazovky.
- Ochranné mechanizmy - Je potrebné zahrnúť poistné ventily, mechanické západky alebo havarijné systémy, ktoré zabránia nekontrolovateľnému pádu vozidla.
- Normy a legislatíva - Návrh musí spĺňať príslušné normy
- Núdzové zastavenie - Každé zdvíhacie zariadenie musí mať tlačidlo núdzového vypnutia, ktoré okamžite zastaví pohyb v prípade nebezpečenstva.
- Ochrana proti preťaženiu - Elektronické alebo mechanické systémy, ktoré zabránia použitiu zariadenia nad jeho maximálnu nosnosť.
- Statické zaťaženie podlahy a okolitej konštrukcie - Nosnosť podlahy nad zdvíhacím zariadením musí byť dostatočná, aby uniesla ďalšie vozidlo alebo chodcov.
- Ochrana proti vode a vlhkosti - Podzemná šachta musí byť izolovaná proti vnikaniu podzemnej vody, napríklad hydroizolačnými materiálmi alebo drenážnym systémom.
- Vetranie a odvod vody - Dôležité pri dlhodobom parkovaní v podzemných priestoroch na zabránenie korózie a vzniku plesní.

POĎAKOVANIE

Príspevok vznikol v rámci riešenia spoločného slovensko-poľského projektu TalentDetector 2026 ako výsledok spolupráce medzi Politechnikou Slaskou, Gliwice a Žilinskou univerzitou v Žiline a projektu KEGA č. 033ŽU-4/2026.

BIBLIOGRAPHY

1. http://sk.daxmachinery.com/lift-parking-garage-product
2. http://sk.heshanindustry.com/underground-parking-car-scissor-lift-product
3. https://trevavytahy.sk/novinky/vytah-na-solarny-pohon
4. https://sk.cathaylift.com/info/innovations-in-industrial-lifting-equipment-e-96824765.html
5. https://revizie-technickych-zariadeni.dashofer.sk/onb/33/zoznam-vybranych-noriem-pre-technicke-zariadenia-zdvihacie-uniqueidmRRWSbk196FPkyDafLfWAKTY7gNHvWKAXo9Xv1WfYaoMO6VlftQMFg/
6. http://sk.liftawp.de/parking-lift/vertical-lifting-parking-system.html

TalentDetector
9th January 2026
Gliwice, Poland
DEPARTMENT OF ENGINEERING MATERIALS AND BIOMATERIALS
FACULTY OF MECHANICAL ENGINEERING
SILESIAN UNIVERSITY OF TECHNOLOGY
INTERNATIONAL STUDENTS SCIENTIFIC CONFERENCE

Studies of technological parameters of repid deformation processes

Olha Drobot[a], Oleh Polishchuk[b], Oleh Babak[c], Mirosław Bonek[d], Roman Cholovskij[e], Svitlana Pidgaichuk[f].

[a] Khmelnytskyi National University, Faculty of Mechanical Engineering, Transport and Architecture, Khmelnytskyi, Ukraine,
email: pion12208@gmail.com.
[b] Khmelnytskyi National University, Faculty of Mechanical Engineering, Transport and Architecture, Khmelnytskyi, Ukraine,
email: opolishchuk7l @gmail.com.
[c] Khmelnytskyi National University, Faculty of Mechanical Engineering, Transport and Architecture, Khmelnytskyi, Ukraine,
email: ang.babak:@gmail.com.
[d] Silesian University of Technology, Faculty of Mechanical Engineering, Department of Engineering Materials and Biomaterials, Gliwice, Poland,
email: miroslaw.bonek@polsl.pl.
[e] Khmelnytskyi National University, Faculty of Mechanical Engineering, Transport and Architecture, Khmelnytskyi, Ukraine,
email: romancolovskij@gmail.com.
[f] Khmelnytskyi National University, Faculty of Mechanical Engineering, Transport and Architecture, Khmelnytskyi, Ukraine,
email: svitlankayar@gmail.com.

Abstract. The paper presents examples of the use of high-speed video recording as a non-contact method for measuring dimensions and technological parameters. In this work we have overviewed an experience of implementation of a high speed video recording as a tool for the non-contact method of technological parameters measurement.

Keywords: high-speed video recording, video camera, recording frequency, technological parameters.

1. INTRODUCTION

The production of high-quality and reliable mechanical engineering products is based on the use of control and measuring equipment, which allows the use of direct and indirect methods of measuring dimensions and technological parameters. However, there are a significant number of processes whose parameters cannot be measured by existing instruments using developed methods and devices. A small number of researchers are engaged in improving existing ones

and developing new technical means that collect, process and analyze the obtained measurement results.

Therefore, today there is still not enough measuring equipment that would allow for quick and reliable control of the parameters of technological processes, such as pressure treatment, compressor operation, etc. In many cases, it is necessary to use non-contact measurement methods, which have a number of advantages, namely: they do not contact the parts that are the object of measurement, therefore they do not change their mass and do not affect their interaction. The paper describes examples of using a high-speed video camera to measure the parameters of fast-moving technological processes that occur during the operation of auto-balancing devices, compressors, automatic landing machines, etc.

The purpose of the work is to familiarize specialists in the field of metrology and measuring equipment, pressure processing technologists, and materials scientists with one of the non-contact methods for measuring fast-moving processes using high-speed video recording.

2. RESEARCH RESULTS

Example 1.

To study and analyze the operation of a hermetic rotary compressor, we used the method of film recording using a high-speed film camera SKS-1m, which provided shooting at a frequency of up to 4000 frames per second. The method of high-speed video recording belongs to non-contact measurement methods (Fig. 1).

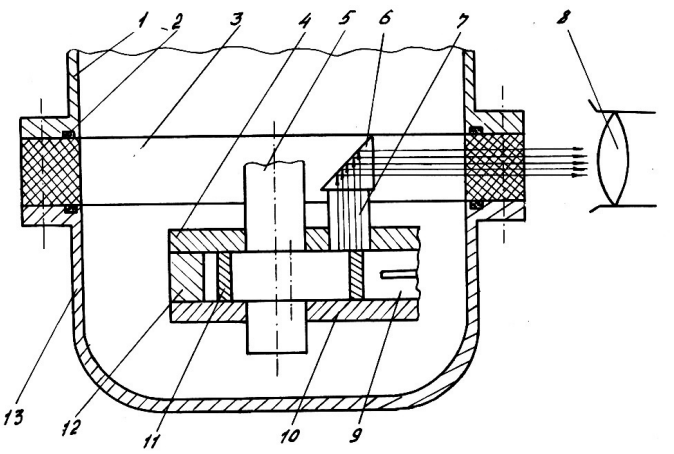

Figure 1 - Optical scheme of the installation for high-speed film shooting:
1 – housing; 2 – seal; 3 – light channel; 5 – roller; 6 – prism; 7 – light rays; 8 – lens; 9 – counter; 10 – housing; 11 – wall; 12 – damper; 13 – lower part of the housing.

The kinematics of the interaction of the elements of the FGr 500-1 refrigeration rotary compressor were investigated. The duration of the entire shooting and the shooting time of one frame were determined by the time counter. In addition, the speed of rotation of the electric motor shaft was recorded using a tachometer.

Analysis of the obtained film shooting results allowed us to identify the features of the compressor rotor movement. It turned out that the compressor rotor does not roll along the

cylinder, as was previously believed, but slowly slides, oscillating in both directions, while the resulting direction of the rotor movement depends on the pressure values in the supercharger. The moment of friction pairs seizing between the surfaces of the eccentric and the rotor was recorded, which is caused by an imperfect lubrication system for these surfaces. Thus, thanks to the obtained frames, the established opinion about the nature of the lubrication of the compressor friction pairs and the wear mechanism has changed. t was found that the wear of the compressor elements occurs not due to abrasive particles, but due to insufficient lubrication and imperfection of the kinematics of the movement mechanism. The nature of the interaction of the compressor elements when working with air and refrigerant was clarified. A significant number of measurements of the rotor speed were carried out, friction forces were calculated, which allowed us to develop a method for dynamic calculation of rotary compressors with a rolling rotor and to offer recommendations for improving its design [1].

Example 2.

When studying vibrations occurring during the manufacture and operation of radio-electronic components, devices are used that implement a method of non-contact measurement using ultrasonic, laser and other electromagnetic vibrations. However, they are difficult to maintain and also have significant limitations in determining such parameters as the amplitude of vibrations, speed of movement, etc. To simplify the process of studying object vibrations, a method has been developed by which vibration registration is carried out using high-speed video recording. This method allows studying vibrations of machines and units during operation, identifying the nature of vibrations and measuring their amplitude [2].

A video camera with an electronic image converter is capable of capturing a frame at a time from 1/50 to 1/8000 s. The captured material is processed on a computer, so each frame can be viewed and studied in detail without the “smearing” effect. The resulting video frames are recorded on a personal computer (PC) using a video card with video capture, which makes it possible to repeatedly view video frames with a record of the object’s movements and store individual fragments in the PC’s memory as graphic files. The received files are processed on a PC using special programs, the results of which determine the amplitude of the oscillations. The program for processing video images also allows you to determine the frequency of the object's oscillations based on the results of the video recording. Using such programs allows you to slow down the video recording to a speed at which it is convenient to count the number of oscillations of the object for a certain period of time. A simple calculation, taking into account the degree of slowing down the video recording, determines the nature and frequency of the oscillations and measures their amplitude. The method was tested when studying the oscillations of the electronic block boards of the shelf type on a vibration stand.

Thanks to high-speed video recording, we have identified the features of the operation of autobalancing devices (ABD), which are widely used in washing machines, separators, centrifuges, etc. To study these features, we conducted experimental studies to study the autobalancing of a horizontal rotor and the behavior of the fluid in the ABD chamber [3].

During the experiment, the rotor start-up was synchronized with the start-up of the loop oscilloscope and video camera. Processing of video recordings and oscillographic tapes allowed us to establish the efficiency of the UPS of an improved design, which provides radial partitions in the balancer, which is installed on a horizontal rotor. The partitions divide the UPS chamber into separate sectors (capacities), which are interconnected along the periphery by a thin channel.

During the video recording, an electronic clock was in the frame, so it was possible to record the time and determine the angular velocity of liquid capture by the ABP camera with and without partitions. A fragment of the video recording of liquid capture by the ABP camera with partitions is shown in Fig. 2.

The use of an autobalancer with partitions allowed to reduce the minimum angular velocity at which liquid capture occurs from W= $24s^{-1}$ to W = $19s^{-1}$, as a result of which the rotor acceleration time to operating speed decreased from 15 to 8 s. It was found that autobalancers with partitions undergo resonance with significantly less vibrations. Video recording allowed to establish that when passing through resonance, the liquid has not yet had time to settle opposite the imbalance, and in the presence of partitions, its uniform distribution along the circumference of the autobalancer is almost not disturbed (as in the case of an ABP without partitions) and does not affect the rotor vibrations.

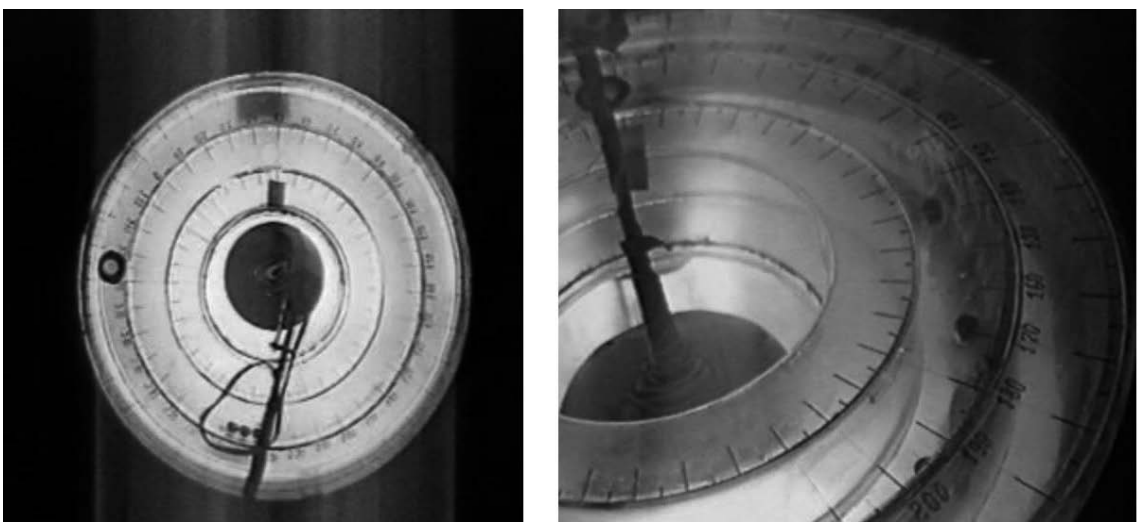

Figure 2 - Fragment of video recording of liquid capture by the ABP camera with partitions.

Example 3.

High-speed video recording was used in the study of the process of injection molding of polymeric materials. A method was developed to determine the velocity of the jet flow of the molding fluid when filling the working cavity.

Example 4.

The process of cold volumetric forming on cold-dropping machines when forming a nail head on a forging and pressing machine was also studied using high-speed video recording.

Cold volumetric stamping on cold-dropping machines is an economically advantageous way to obtain parts such as bolts, washers, nuts, rivets, nails. The complexity of manufacturing such parts lies in the fact that the technological process of their manufacture combines preparatory and production processes in one operation (preparation of the starting metal, manufacture of the blank, stamping (obtaining the finished part). At each of these stages, problems arise that worsen the quality of finished products. One of such problems arises during the operation of the forging and pressing machine (model AG 4116) when obtaining a nail head, which must be

symmetrical relative to the longitudinal axis of the nail, when the ratio of the length of the planted part of the workpiece to its diameter is more than 2 [4, 5].

A feature of the shooting was that the objects of research - wire, nails, nail cap - are small in size. The camera was installed at the smallest possible distance from the object of research. Video shooting was carried out at an exposure of 1/8000 second. The analysis of the obtained video recordings was carried out on a digital video recorder model AG DV 2700. The process of forming the nail cap was slowed down on a Pentium-713 computer.

When analyzing the obtained results, it was found that at the initial moment of forming the nail cap, the part of the rod that deforms into the head loses stability. The reason for this is the asymmetric application of force with which the punch hits the workpiece.

When viewing the results obtained by video recording in slow motion on a PC monitor (Fig. 3), it was possible for the first time to see the process of losing stability of the cantilevered part of the nail during the landing of the cap and to record the moment of impact, which led to a review of the current technological process, adjusting it to eliminate the defect in eccentricity.

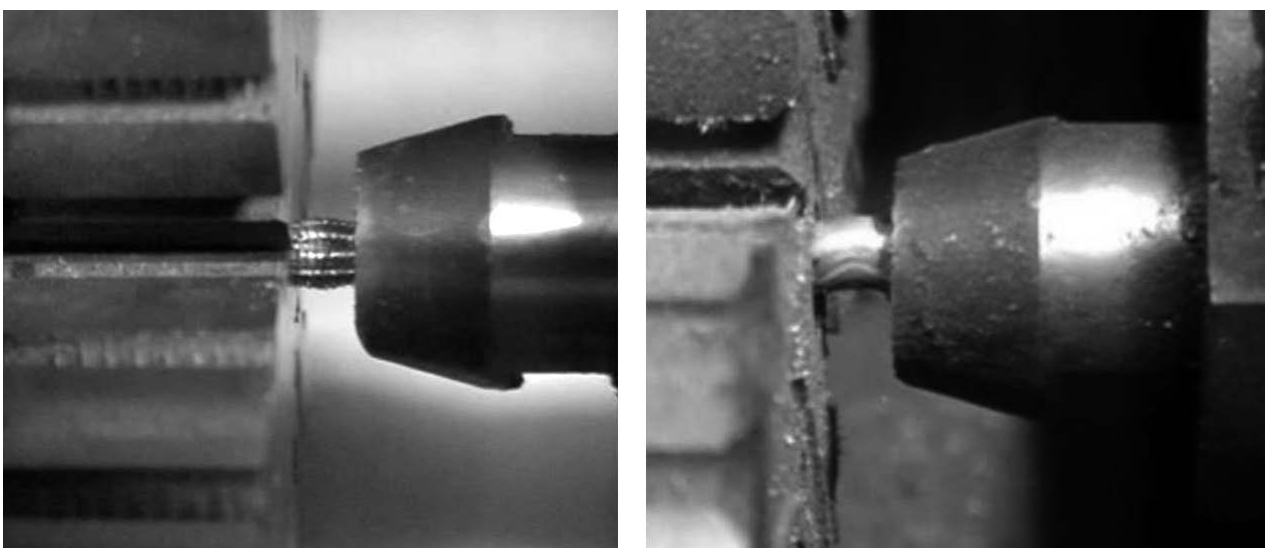

a b

Figure 3 - Frames of high-speed video recording of the deformation process during the landing of the nail cap: a - straight cut of the end; b - oblique cut of the end

It is shown that during deformation, when the applied force P approaches Pcr, the deflection of the workpiece increases sharply. It is established that the presence of an oblique end of the workpiece during cutting and sharpening of the nail is the cause of the eccentricity of the application of compressive forces. Examples of the use of high-speed video recording do not end there. This method has been successfully used in the study of the cooling capacity of liquid media during the quenching of steels to determine the duration of bubble boiling, which is especially necessary for the development of a technological process for step-by-step quenching of steel.

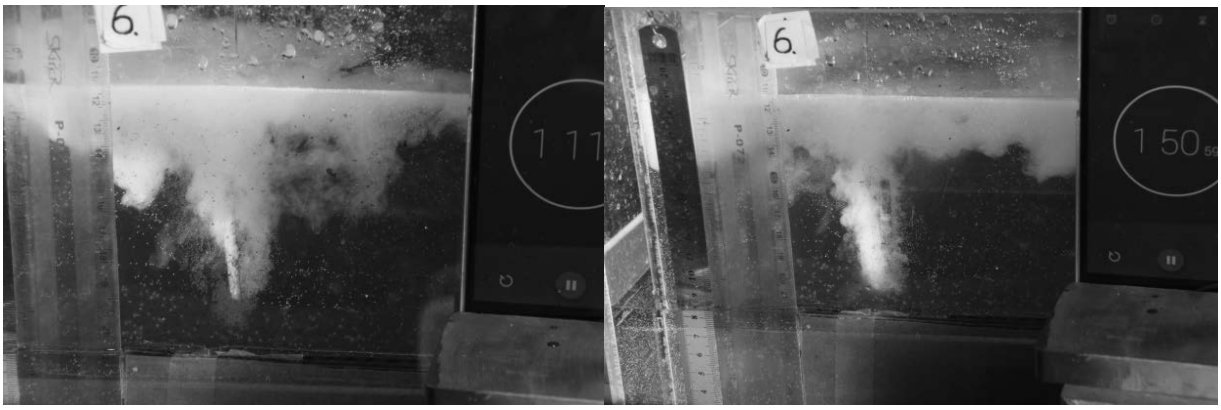

Figure 4 – Frames of a high-speed video recording of a sample cooling in water during quenching

3. CONCLUSION

The high-speed video recording method is a modern non-contact method for measuring technological parameters of fast-moving processes and studying the nature of the interaction of contacting bodies.

ACKNOWLEDGEMENTS

The work was created as part of project based learning - PBL, in the 13th competition under the Initiative of Excellence - Research University, Silesian University of Technology, Gliwice, Poland and as part of project of Students Scientific Circle of Laser Surface Treatment under the Initiative of Excellence - Research University, Silesian University of Technology, Gliwice, Poland.

BIBLIOGRAPHY

1. Nikitin O.O. , Oleksandrenko V.P., Drobot O.S. Experience in using high-speed video recording to determine technological parameters of fast-moving processes./ / O.O. Nikitin// Measuring and computing equipment in technological processes, No. 1, 2010 P. 122 – 124 / ISSN 2219-9365.
2. Patent 48774 A Ukraine, MPK G01N17/00. Method of non-contact measurement of vibration parameters and determination of object oscillation forms / Roizman V.P., Cholovsky R.G. Nikitin O.O.-2001128351; appl. 02/15/2001; publ. 08/15/2002, Bull. No. 8.
3. Roizman V.P. Results of application of liquid autobalancers on a rotor with a horizontal axis of rotation. /Roizman V.P. Tkachuk V.P. Nikitin O.O.//Collection of proceedings of the International Scientific and Technical Conference "Improving the quality, reliability and durability of technical systems and technological processes". Hurghada. Egypt, December 5-12, 2009.- Khmelnitsky- 2009.- P.19-22.

4. Analysis of the development paths of press machines for the production of wire products. // Vasilyshin S.A., Gural I.G., Veremeenko A.A. // Problems of tribology. 1999. - No. 3,4. – p. 101 - 123.
5. Investigation of the stress-strain state during the landing of nail heads on machines.// V.I. Steblyuk, S.A. Vasilyshin. // Problems of tribology.- 1999.-№3,4.-p.153-163.

TalentDetector
9th January 2026
Gliwice, Poland
DEPARTMENT OF ENGINEERING MATERIALS AND BIOMATERIALS
FACULTY OF MECHANICAL ENGINEERING
SILESIAN UNIVERSITY OF TECHNOLOGY
INTERNATIONAL STUDENTS SCIENTIFIC CONFERENCE

Passivation of 304 steel using nitric acid (V) and alternatively citric acid

Aleksandra Duda[a], Laura Junka[a], Marcin Magaczewski[a], Dawid Maliszak[a], Michał Mężyński[a], Arkadiusz Peczalka[a], Mikołaj Sas[a], Monika Kciuk[b], Monika Spilka[b]

[a] Student of Silesian University of Technology, Faculty of Mechanical Engineering, Department of Engineering Materials and Biomaterials
[b] Silesian University of Technology, Faculty of Mechanical Engineering, Department of Engineering Materials and Biomaterials
email: monika.kciuk@polsl.pl

Abstract: This article describes the passivation process of 304 stainless steel using nitric and citric acid. It presents the advantages and disadvantages of both acids and indicates future directions in the development of stainless steel passivation technology.

Keywords: austenitic stainless steel, passivation, nitric acid, citric acid

1. INTRODUCTION

Austenitic stainless steel (AISI 304), with the chemical composition given in Table 1, is the most widely used steel grade in various industrial sectors. It is characterized by high durability, strength at cryogenic temperatures and excellent corrosion resistance [1]. The corrosion resistance of 304 stainless steel is due to the presence of chromium, which forms a thin, passive oxide layer (Cr_2O_3) on the surface that limits oxidation and corrosion of the material. However, mechanical processing, contamination and oxidation at high temperatures may damage this layer, resulting in reduced corrosion resistance [3]. In such cases, chemical passivation is used, which involves the controlled removal of impurities and strengthening of the passive layer on the steel surface. Passivation involves immersing components in an acid solution, most commonly nitric acid (V), but alternatively, citric acid is increasingly being used, as it is considered more environmentally friendly and safer for humans [4,5].

Table 1. Chemical composition of AISI 304 steel [2]

C	Mn	Cr	Si	P	N	Ni	S	Fe
0.08	2.0	18-20	1.0	0.045	0.11	8-10.5	0.03	66.35-74

2. PASSIVATION OF STAINLESS STEELS

The most popular method of increasing the corrosion resistance of stainless steel is passivation, the mechanism of which comes down to enriching the surface layer with chromium and creating a thin, compact and continuous oxide layer that effectively limits the transport of oxygen and aggressive ions into the interior of the material [3-5]. The passivation process of stainless steels is carried out in several stages (Figure 1). It includes preliminary surface preparation, which consists of degreasing, i.e. removing residues of technological oils, abrasive particles and other contaminants generated during mechanical processing. Then the actual passivation takes place in a chemical solution, most often nitric acid (V) or citric acid, under specific time and temperature conditions. At this stage, free iron and its compounds are selectively dissolved from the steel surface. The final step is rinsing and drying to remove the remains of the passivating solution and stabilize the passive layer [7]. The resulting passive layer is characterized by a small thickness, about a few or a dozen nanometers, but it shows high chemical resistance and the ability to self-regenerate in the presence of oxygen. The quality of the passive layer is crucial for the corrosion resistance of stainless steel, especially in environments containing chloride ions [8]. In industrial practice, the effectiveness of passivation is assessed on the basis of corrosion resistance tests and compliance with applicable standards, such as ASTM A967 [9]. Passivation is usually a standard step in the final treatment of stainless steel components used in many industries.

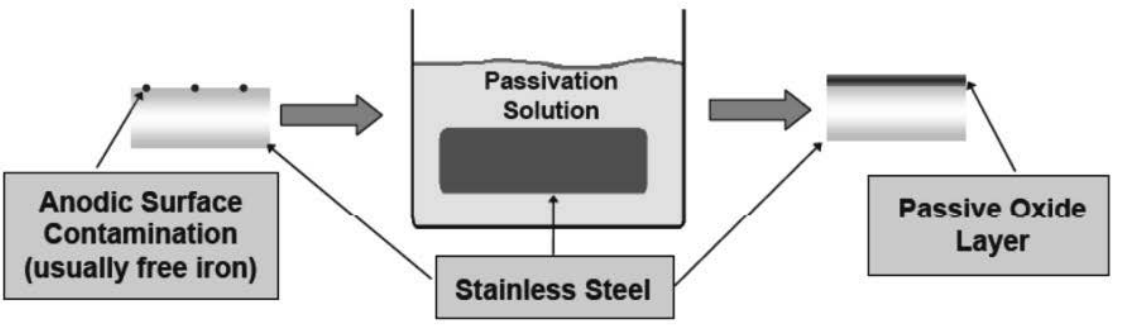

Figure 1. A schematic of the passivation process [6]

3. COMPARATIVE ANALYSIS OF 304 STEEL PASSIVATION IN NITRIC AND CITRIC ACID

Standards for the passivation of stainless steels allow the use of both nitric and citric acid, only specifying the process parameters for effective passivation (Table 2).

Table 2. Typical passivation parameters of 304 steel [9]

Parameter	Nitric acid (V)	Citric acid
Concentration	20-40%	4-10%
Temperature	49-60 °C	20-60 °C
Process duration	20-30 minutes	20-60 minutes
Chemical nature	Strongly oxidizing	Complexing (non-oxidizing)
Gas emissions	NO_x	-

Nitric acid has long been a classic method of passivating stainless steels, especially austenitic ones such as 304, acting as a strong oxidizing agent and effectively removing free iron and surface contaminants, accelerating the formation of a passive layer. The advantage of using nitric acid is primarily a short passivation time, even at low temperatures, and its high effectiveness in removing free iron. It has a wide range of applications. The disadvantage of this passivating medium is the high risk associated with ensuring occupational health and safety, as it is highly corrosive, produces toxic NOx oxides and requires the use of specialized ventilation and personal protective equipment. It also poses a burden on the environment because the waste produced is toxic and must be neutralized and subjected to costly disposal. Moreover, the use of nitric acid in the passivation of thin-walled elements carries the risk of excessive etching of the surface [10,11].

Citric acid, in turn, is used as a safe, biodegradable alternative to nitric acid because it does not produce toxic gases and can therefore be more easily removed and neutralized. This makes it widely used in the food and medical industries. Research shows that passivation with citric acid allows obtaining a passive layer with a similar or even higher Cr_2O_3 content than that obtained with nitric acid. The disadvantage of using citric acid may be the higher cost of organic solutions, although taking into account the cost of disposal, the total process costs may be lower. Another disadvantage of passivation in citric acid is the need for more precise control of process parameters (time and temperature), especially at lower concentrations [10-12].

When comparing both methods of stainless steel passivation, the key criteria are primarily the effectiveness of passivation, work safety, environmental impact, and process costs, as shown in Table 3.

Table 3. Comparison of passivation in nitric and citric acid [10-12]

Criterion	Nitric acid (V)	Citric acid
Fe removal efficiency	Very high	High
Occupational safety	Low	High
Environmental impact	Unfavorable	Friendly
Disposal costs	High	Low
Food industry applications	Limited	Very good
Etching risk	Occurs	Minimal

4. CONCLUSIONS

Passivation of 304 stainless steel is a commonly used method to ensure corrosion resistance and durability of components in many industrial applications. Nitric acid is typically used, which carries significant occupational health and safety as well as environmental risks. A safer and environmentally friendly alternative to nitric acid is citric acid, which is equally effective. Both nitric acid and citric acid effectively passivate 304 stainless steel, but through different mechanisms. Nitric acid forms a dense, chromium-rich passive layer with excellent corrosion resistance, making it ideal for industrial applications requiring fast and repeatable results. In turn, citric acid, by creating a thinner passive layer, increases the passivity of the surface by complexing the metal and enriching it with chromium, especially in conditions close to neutral. Its main advantages are biodegradability, low toxicity and environmental safety, which makes it a promising "green" alternative, although it may require longer processing time.

Further development of stainless steel passivation technology should aim towards environmentally friendly processes, characterized by less chemical aggressiveness and better control of the passive layer structure [13]. An important area of research remains the optimization of process conditions by shortening passivation time, lowering process temperature and minimizing chemical consumption, as well as the development of hybrid processes combining different passivation mechanisms [14].

BIBLIOGRAPHY

1. A. Kumar, R. Sharma, S. Kumar, P. Verma, A review on machining performance of AISI 304 steel, Materialstoday: Proceedings 56/5 (2022) 2945-2951.
2. https://304stainlesssteel.org/304-stainless-steel-composition/
3. S. Charazińska, A. Sikora, B. Malczewska, P. Lochyński, Reconstruction of the passive layer of AISI 304 and 316 steel after scratching, Materials 17/24 (2024) 6238.
4. Z.B. Zheng, Y.G. Zheng, Effects of surface treatments on the corrosion and erosion-corrosion of 304 stainless steel in 3.5% NaCl solution, Corrosion Science 112 (2016) 657-668.
5. Y. Zhang, J. Sun, H. Lei,·F. Jiao,·W. Niu, X. Xu,·X. Lin, Influence of citric acid passivation treatment on the marine atmospheric corrosion resistance of L80-13Cr stainless steel, Discover Applied Sciences 7 (2025) 226.
6. D. Yasensky, Citric acid passivation of stainless steel https://www.yumpu.com/en/document/read/7762473/citric-acid-passivation-of-stainless-steel-c3p, 2009.
7. ASTM A380/A380M-17. Standard Practice for Cleaning, Descaling, and Passivation of Stainless Steel Parts, Equipment, and Systems. ASTM International, 2017.
8. M.L. Banda, C.G. Tiburcio, P. Zambrano-Robledo, J.A. Cabral, F. Estupinán, M.A. Baltazar-Zamora, R. Croche, E. Vera, F. Almeraya-Calderón, Corrosion behaviour of 304 austenitic, 15-5PH and 17-4PH passive stainless steels in acid solutions, International Journal of Electrochemical Science 13 (2018) 10314-10324.
9. ASTM A967A967M-17. Standard Specification for Chemical Passivation Treatments for Stainless Steel Parts. ASTM International, 2017.
10. M.S. Narula, Passivation: to qualify equipment for installation qualification, IJRAR 7/1 (2020) 822-834.
11. R. Kremer, Developments in citric acid passivation of stainless steel, Plating&Surface Finishing (2008) 8-10.
12. P.L. Lewis, M. Kolody, J. Curran, Alternative to nitric acid for passivation of stainless steel alloys, https://ntrs.nasa.gov/citations/20140002809, 2013.
13. S. Parsons, O. Poyntz-Wright, A. Kent, M.C. McManus, Green chemistry for stainless steel corrosion resistance: life cycle assessment of citric acid versus nitric acid passivation, Materials Today Sustainability 3-4 (2019) 100005.
14. L. Zheng, H. Zang, Y. Liu, Y. Xiao, Y. Cong, Z. Cheng, G. Chen, Z. Xing, J. Pan, Q. Jiang, W. Chen, K. Yamanouchi, H. Xu, R. Li, Significant reduction of corrosion of stainless steel by strong-field laser surface passivation, Light Science&Applications 14 (2025) 352.

TalentDetector

9th January 2026
Gliwice, Poland

DEPARTMENT OF ENGINEERING MATERIALS AND BIOMATERIALS
FACULTY OF MECHANICAL ENGINEERING
SILESIAN UNIVERSITY OF TECHNOLOGY

INTERNATIONAL STUDENTS SCIENTIFIC CONFERENCE

Development of unmanned aerial vehicle control systems

Pavle Eprikian[a], Givi Sanadze[b]

[a] Georgian Technical University, Faculty of Transport Systems and Mechanical Engineering, Department of Mechanical Engineering and Industrial Technology, PhD Student
email: eprikyanpavle@gmail.com

[b] Georgian Technical University, Faculty of Transport Systems and Mechanical Engineering,Department of Mechanical Engineering and Industrial Technology, Professor
email: sanadzegivi05@gtu.ge

Abstract: Unmanned Aerial Vehicles (UAVs) are indispensable in both civilian and military operations. Regardless of configuration - fixed-wing, multirotor, or hybrid VTOL - UAVs demonstrate strongly nonlinear and under actuated dynamics, as well as high sensitivity to disturbances and parametric uncertainties. These traits demand advanced control strategies that ensure robustness, accurate tracking, and, in multi-vehicle missions, safe and coordinated behavior. This paper critically reviews two leading control paradigms for UAVs. First, Sliding Mode Control (SMC), including higher-order and super-twisting variants, is evaluated for its robustness against matched uncertainties, external disturbances, finite-time convergence, and relative ease of implementation. Recent progress in reducing chattering while upholding invariant manifold properties is also explored [5, 11, 14]. Second, Distributed Model Predictive Control (DMPC) frameworks are assessed for cooperative multi-UAV missions. We emphasize tube-based, dual-mode, and hierarchical MPC architectures that support scalability, recursive feasibility, and provable collision avoidance under communication and computational constraints [2, 6, 12, 17-19]. Critical challenges - such as non-convex constraints, real-time computational burden, and resilience to packet loss - are analyzed. Finally, we outline future directions toward fully autonomous UAV operations, focusing on the integration of learning-based methods (e.g., reinforcement learning, learning-MPC, neural-enhanced SMC) to enable adaptive, high-level decision-making in complex, unstructured, and adversarial environments [1, 3, 13, 20].

Keywords: Unmanned Aerial Vehicle (UAV), nonlinear control, robust control, sliding mode control (SMC), distributed model predictive control (DMPC), multi-agent systems, swarm coordination, learning-based control.

1. INTRODUCTION

Unmanned aerial vehicles (UAVs) are increasingly used across civilian and military applications, including agricultural spraying, infrastructure inspection, medicine delivery, filming, firefighting, and border patrol [1,7]. The platforms vary widely: fixed-wing, multirotor, or hybrid VTOL, each with distinct aerodynamic and mechanical properties [6,7]. Despite these differences, all UAVs share fundamental control challenges: strongly nonlinear and under actuated dynamics, sensitivity to wind gusts, payload variations, and model uncertainties [6,7,9].

For many years, commercial UAVs relied on cascaded PID controllers, which offer straightforward implementation and intuitive tuning [9]. While effective for calm, near-hover flight, PID performance degrades significantly under strong disturbances, aggressive maneuvers, or when operating far from linearization points [9]. This limitation has motivated research into more robust nonlinear control strategies capable of guaranteeing stability, precision, and safe operation even under uncertain conditions [5,6].

Two dominant families of advanced control methods have emerged over the past decade. Sliding Mode Control (SMC) and its modern variants exploit invariant manifold properties to reject disturbances and uncertainties while maintaining high tracking accuracy [5,11,14]. Model Predictive Control (MPC), particularly in distributed forms for UAV swarms, optimizes trajectory planning while explicitly enforcing physical and operational constraints, ensuring coordinated and collision-free flight [2,6,12,17-19].

This paper critically compares these two approaches, discusses their advantages and limitations, and explores recent trends integrating learning-based techniques to enhance UAV autonomy [1,3,13,20].

2. ANALYSIS OF GENERAL UAV DYNAMIC MODELS

Most UAVs, regardless of aerodynamic configuration, are modeled using six-degree-of-freedom (6-DOF) nonlinear kinematic and dynamic equations [6,7]. The inherent nonlinearity and strong state-input coupling pose significant challenges for control design. Common approaches to handle these nonlinearities include feedback linearization and geometric control formulated on SE (3) [10]. Both classical and advanced control strategies have been widely applied, including PID control, Sliding Mode Control (SMC), and Model Predictive Control (MPC). While PID controllers are simple and remain the industrial standard, they typically lack sufficient robustness when the system operates far from linearization points or under strong disturbances [9]. In contrast, SMC offers high robustness against model uncertainties and external disturbances [5], whereas MPC delivers optimal performance while explicitly enforcing physical and operational constraints (Figure 1) [6].

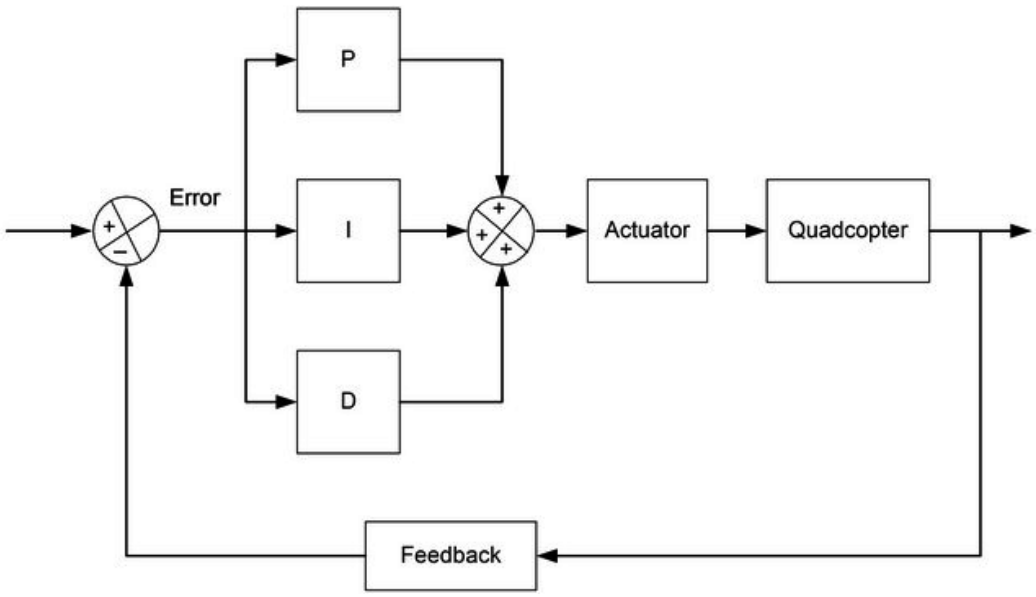

Figure 1. PID control scheme

Sliding Mode Control (SMC) is one of the most robust approaches, guaranteeing reliable performance under both model uncertainties and external disturbances (Figure 2) [5]. It has been effectively applied for precise positioning of multirotor UAVs as well as trajectory tracking of fixed-wing platforms [4,11]. Improved variants include Finite-Time SMC (FTSMC) [11], Non-Overshooting SMC (NOSMC) [4], and Adaptive SMC (ASMC), which can leverage learning-based techniques (e.g., neural networks) to estimate unknown dynamics and disturbances online [3,5].

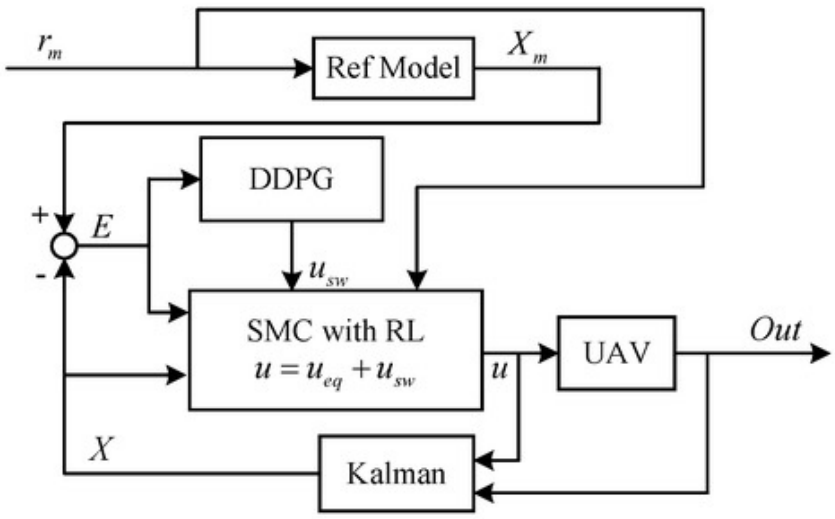

Figure 2. SMC control scheme

Model Predictive Control (MPC) is an optimization-based technique that predicts future behavior over a finite horizon and explicitly accounts for constraints and resource limitations (Figure 3) [6]. Distributed MPC (DMPC) enables scalable coordination in multi-UAV systems and swarms, where each vehicle plans its own trajectory while considering the intended motion

of neighboring agents [2,6]. DMPC naturally incorporates collision-avoidance constraints directly into the optimization problem, ensuring safe collective flight [12].

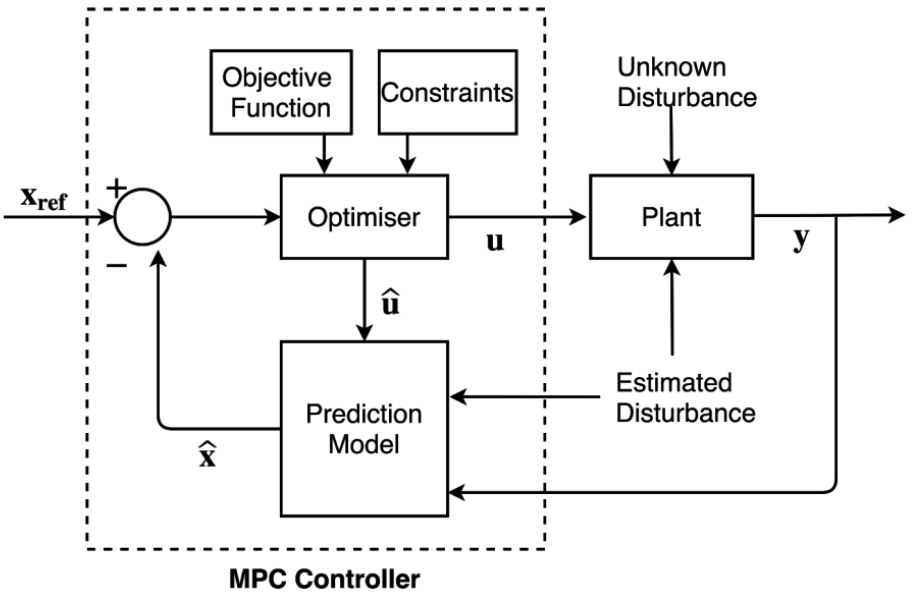

Figure 2. MPC control scheme

A particularly promising direction is the hybrid architecture, which combines the fast, robust disturbance rejection of SMC at the low level with the global optimal planning capabilities of MPC at the high level [13]. Future UAVs will require full autonomy, increasingly supported by advanced sensor fusion (GPS, inertial sensors, LiDAR, vision) and deeper integration of intelligent decision-making layers [1,3,13].

3. CONCLUSION AND FUTURE PERSPECTIVES

This paper has reviewed the principal control paradigms driving modern UAV development. For single-vehicle operations, Sliding Mode Control (SMC) and its contemporary variants continue to offer one of the most dependable solutions, delivering mathematically provable robustness, fast disturbance rejection, and excellent tracking accuracy despite considerable model uncertainty and external disturbances [5,11]. In team and swarm scenarios, Distributed Model Predictive Control (DMPC) stands out as the leading approach, achieving optimal resource use, guaranteed collision avoidance, and scalable coordination via constrained receding-horizon optimization [2,6,12].

Two major, mutually reinforcing trends will shape the near future of UAV control. First, adaptive and learning-based techniques will be increasingly fused with established robust frameworks. Neural networks and reinforcement-learning agents running in parallel with adaptive SMC or learning-enhanced MPC will provide real-time identification of unmodeled aerodynamic effects, wind fields, and component wear, dramatically raising performance beyond the limits of fixed models [1,3,13].

Second, hybrid hierarchical architectures that separate control timescales - rapid inner-loop SMC for attitude stabilization and aggressive maneuvering paired with higher-level DMPC for

global path planning and inter-agent negotiation - are quickly reaching maturity and consistently outperforming single-paradigm solutions in both simulation and real-world trials [13].

Collectively, these developments are bringing the field closer to truly autonomous UAV systems able to operate safely and effectively in complex, dynamic, and hostile environments with little or no human oversight. Full autonomy of this kind will greatly extend operational envelopes, improve mission success rates, and unlock entirely new civilian and defense applications for unmanned aerial vehicles.

BIBLIOGRAPHY

1. Chen, Y. (2025). Control Systems for Unmanned Aerial Vehicles: A Comprehensive Study (pp. 12–45).
2. Gräfe, A., Eickhoff, J., Zimmerling, M., & Trimpe, S. (2025). DMPC-Swarm: Distributed model predictive control on nano UAV swarms. *Autonomous Robots, 49*(2), 101–120.
3. Fatemi, M. M., & Akbarimajd, A. (2025). Adaptive Sliding Mode Control for Quadrotor UAVs Under Disturbances Using Multi-Layer Perceptron. *IEEE Access, 13*, 1500–1515.
4. Wang, X., & Mao, X. (2024). Non-overshooting sliding mode for UAV control. *The Aeronautical Journal, 128*(1312), 225–240.
5. Yesmin, A., & Sinha, A. (2023). Sliding Mode Controller for Quadcopter UAVs: A Comprehensive Survey. *Drones, 7*(3), 55–78.
6. Sharif Mansouri, S., Nikolakopoulos, G., & Gustafsson, T. (2016). Distributed Model Predictive Control for Unmanned Aerial Vehicles. *IEEE Transactions on Control Systems Technology, 24*(5), 1602–1616.
7. Zuo, Z., Liu, C., Han, Q.-L., & Song, J. (2022). Unmanned Aerial Vehicles: Control Methods and Future Challenges. *IEEE/CAA Journal of Automatica Sinica, 9*(6), 1012–1028.
8. Vititin, V., Kalyagin, M., & Kolesnichenko, V. (2023). Evaluation of Unmanned-Aerial-Vehicle-Integrated Control System Efficiency on the Basis of Generalized Multiplicative Criterion. *Inventions, 8*(5), 98–112.
9. Kiss, B., Ballagi, Á., & Kuczmann, M. (2025). PID Control and Alternative Control Approaches in UAV Systems. *Preprints.org, 7*(2), 45–60.
10. Oersted, H., & Ma, Y. (2024). Geometric and Feedback Linearization on UAV: Review. *Drones, 8*(1), 15–32.
11. Olguin-Roque, J., Salazar, S., González-Hernandez, I., & Lozano, R. (2023). A Robust Fixed-Time Sliding Mode Control for Quadrotor UAV. Algorithms, 16(7), 201–220.
12. Harun, M. H., Abdullah, S. S., Aras, M. S. M., Bahar, M. B., & Ali@Ibrahim, F. (2024). Recent Developments and Future Prospects in Collision Avoidance Control for Unmanned Aerial Vehicles (UAVS): A Review. International Journal of Robotics and Control Systems, 11(2), 75–94.
13. Abbas, N., Abbas, Z., Zafar, S., Ahmad, N., Liu, X., Khan, S. S., Foster, E. D., & Larkin, S. (2024). Survey of Advanced Nonlinear Control Strategies for UAVs: Integration of Sensors and Hybrid Techniques. Sensors, 24(5), 345–368.
14. Zoidze, M., Sanadze, G., Krakhmalyov, O., Zinchenko, O., & Brusentsev, V. (2021). Challenges and perspective with using a group of small combat unmanned aerial vehicles. *Incas Bulletin, 13*(Special Issue), 245–255.

TalentDetector
9th January 2026
Gliwice, Poland
DEPARTMENT OF ENGINEERING MATERIALS AND BIOMATERIALS
FACULTY OF MECHANICAL ENGINEERING
SILESIAN UNIVERSITY OF TECHNOLOGY
INTERNATIONAL STUDENTS SCIENTIFIC CONFERENCE

Evaluation of the Weldability of Armor Steel with Low Carbon Structural Steels

[a] Pakize Pınar Erbeyin, [a] Alara Aytekin, [a] Mert Cavus, [a]Cemal Meran, [a]Emre Korkmaz,
[b] Onur Celik

[a] Pamukkale University, Faculty of Engineering, Department of Mechanical Engineering, Denizli-Turkiye, email: cmeran@pau.edu.tr
[b] Askon Mechanics San. ve Tic. A.Ş., Denizli-Turkiye, email: info@askondemir.com

Abstract: This article investigates the weldability of armor steel joined with low-carbon structural steels such as S235JR and S355J2+N via gas metal arc welding. The research focuses on evaluating the mechanical performance and microstructural evolution of the dissimilar joints produced under varying process parameters. Systematic characterization, including hardness and toughness testing along with macro and microstructural analysis, was conducted to assess the integrity of the welds. Additionally, the joint quality was validated through both destructive testing.

Keywords: armor steel, weldability, GMAW, S235JR, S355J2+N

1. INTRODUCTION

The rapid evolution of defense technologies necessitates the use of high-performance materials that combine exceptional hardness with structural toughness. Armor steels, characterized by their tempered martensitic microstructure, are the primary choice for ballistic protection systems. However, integrating these high-strength alloys into larger structures often requires joining them with more ductile, low-carbon structural steels such as S235JR and S355J2+N.

The weldability of armor steel is inherently challenging. As shown in Table 1, their high carbon equivalent makes them susceptible to hydrogen-induced cold cracking (HICC) in the heat-affected zone (HAZ). Furthermore, the thermal cycle of the welding process typically leads to a localized reduction in hardness, known as "HAZ softening, [1,2]" which can compromise the ballistic integrity of the final product.

Table 1. The chemical composition of armor steel

C (max%)	Si (max%)	Mn (max%)	P (max%)	S (max%)	Cr (max%)	Ni (max%)	Mo (max%)	B (max%)
0.25	0,5	1,2	0,015	0,005	1	2	0,6	0,003

Previous research, [3] emphasizes that the phase transformations occurring during the rapid cooling of dissimilar joints are significantly influenced by the chemical composition of the filler metal and the cooling rate. This study aims to provide a comprehensive analysis of the mechanical and microstructural properties of armor steel when joined with S235JR and S355J+N steels using optimized gas metal arc welding (GMAW) parameters.

2. MATERIAL AND METHOD

The experimental phase utilized the thickness of 6.5 mm armor steel, which possesses a surface hardness of approximately 440 HBW. This plates were joined with S235JR and S355J+N structural steel grades. The chemical composition of armor steel includes alloying elements such as Cr, Ni, and Mo to ensure through-thickness hardening.

To prevent the risk of cracking and to manage the residual stresses arising from the dissimilar mechanical properties an austenitic filler wire (ESAB OK 16.95/307Si) was used. As provided in Table 2, the high nickel and manganese content of the 307Si wire increases its hydrogen solubility, thereby reducing the risk of cold cracking without the mandatory requirement for high preheating temperatures in structural joints.

Table 2. The chemical composition of filler metal- 307Si

Elements	C	Mn	Si	Ni	Cr	Mo
Composition (%)	0,08	7	0,9	8,1	18,7	0,2

The joints were prepared using the Metal Active Gas (MAG) process with Fronius TPS 500i Manual welding system. Single V-groove preparations were used to ensure full penetration. The shielding gas mixture was optimized at 80% Argon and 20% CO_2 to ensure arc stability and minimize spatter. The specific heat input was controlled through the following parameters, Table 3.

Table 3. The welding parameters

Pass Count	**Exp. No**	**Welding Current (A)**	**Voltage (V)**	**Welding speed (mm/min)**	**Heat Input (kJ/mm)**
Double-Pass Weld	S235JR-1	150	16,6	323 -313	0,36-0,38
	S235JR-3	175	17,2	323-318	0,45-0,46
	S235JR-5	200	20	437-362	0,32-0,42
Single Pass Weld	S235JR-2	150	16,6	161	0,74
	S235JR-4	175	17,2	172	0,84
	S235JR-6	200	20	291	0,65
Double-Pass Weld	S355J2+N -1	150	16,6	291-375	0,32-0,41
	S355J2+N -3	175	17,2	420-350	0,34-0,42
	S355J2+N -5	200	20	636-396	0.30-0,49
Single Pass Weld	S355J2+N -2	150	16,6	175	0,68
	S355J2+N -4	175	17,2	200	0,72
	S355J2+N -6	200	20	362	0,53

The heat inputs were calculated using the Eq. (1).

$$q = \eta IU60/v \quad (1)$$

where q, U, I, v and η are the heat input (kJ/mm), welding arc voltage (V), welding current (A), welding speed (mm/min) and the arc efficiency ($\eta = 0{,}8$), respectively.

Post-welding, samples were also sectioned for metallographic examination. The metallographic specimen was prepared using conventional metallographic grinding and polishing methods. Microstructural analysis was performed using optical microscopy after etching with Nital (2%) and Adler's reagent. Hardness profiles were mapped across the base metal (BM), heat-affected zone (HAZ), and weld zone (WZ) using a microvickers hardness tester. For the testing, measurements were taken at 1 mm intervals across the joint, and dwell time 10 s, and also the applied weight 200 g.

3. RESULTS AND DISCUSSION

Fractures in welded joints between S235JR and armor steel pairs have mostly occurred on the S235JR side, where strength is lower. In some joints with insufficient penetration, the fracture naturally occurred in the weld bead. In S235JR and armor steel pairs, an average yield strength of 490 MPa, tensile strength of 517 MPa, elongation at break of 11%, notch impact toughness of 61 J, and bending force of 6,7 kN were obtained. Double-pass welds exhibit better expansion, and as shown in Table 4, their mechanical properties are superior to those of single-pass welds.

Table 4. The tensile, impact, and bending test results of welded joints

Pass Count	Exp. No	Yield Strength, Re, (MPa)	Tensile Strength, Rm, (MPa)	Elongation, A (%)	Charpy Impact Energy (J)	Bending Force (kN)	Fractured
Double-Pass Weld	S235JR-1	505	557	11	85	7,8	S235JR
	S235JR-3	444	460	15	81	7,3	S235JR
	S235JR-5	518	550	17	73	7,0	S235JR
Single Pass Weld	S235JR-2	514	532	9	45	5,7	Weld. bead
	S235JR-4	441	447	7	39	5,1	S235JR
	S235JR-6	532	559	7	43	7,2	S235JR
Double-Pass Weld	S355J2+N -1	503	559	10	53	6,4	S355
	S355J2+N -3	523	549	16	49	7,6	S355
	S355J2+N -5	436	484	14	49	5,0	S355
Single Pass Weld	S355J2+N -2	492	525	6	30	6,8	Weld. bead
	S355J2+N -4	311	334	4	35	4,4	Weld. bead
	S355J2+N -6	386	432	2	32	6,3	Weld. bead

In S355J2+N and armor steel pair welds, breaks in double passes mostly occurred on the S355 side, where strength was low, while in single passes, all breaks occurred on the S355 side. In some joints with insufficient penetration, fractures occurred in the welds due to the lack of penetration. In S355J2 and armor steel pairs where the fracture occurred in the steel material, an average yield strength of 487 MPa, tensile strength of 530 MPa, elongation at fracture of 13%, notch impact toughness of 50 J, and bending force of 6,3 kN were obtained.

Visual and macrostructural examinations revealed a defect-free fusion zone with no evidence of porosity or incomplete penetration, shown in Figure 1. The microstructural evolution across the dissimilar joint was systematically characterized to evaluate the metallurgical compatibility between the high-strength armor steel and the ductile structural steel. The investigation focuses on three primary zones.

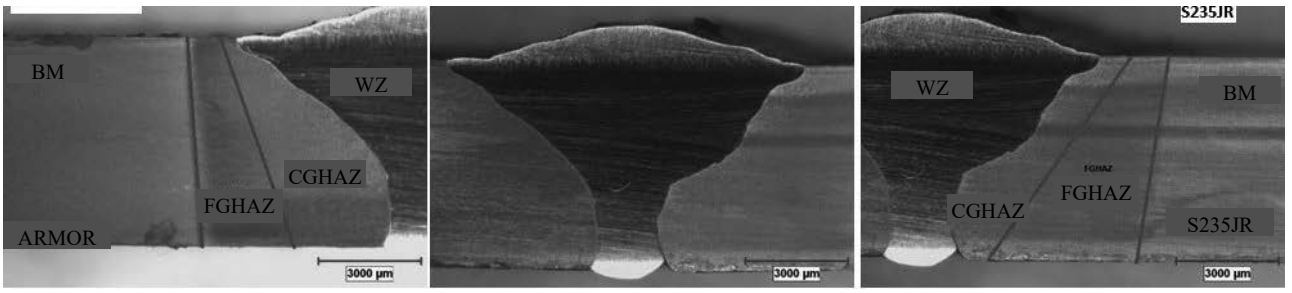

Figure 1. Macrostructure view of armor steel (left), weld zone (middle), and S235JR (right) of the welded joint.

The base metal of armor steel exhibits a fine-grained tempered martensitic structure, which is responsible for its high hardness and ballistic performance. The welding thermal cycle, however, induces significant transformations in this region. HAZ immediately adjacent to the fusion line, the peak temperature exceeded the transformation point, leading to significant austenite grain growth, Figure 2.

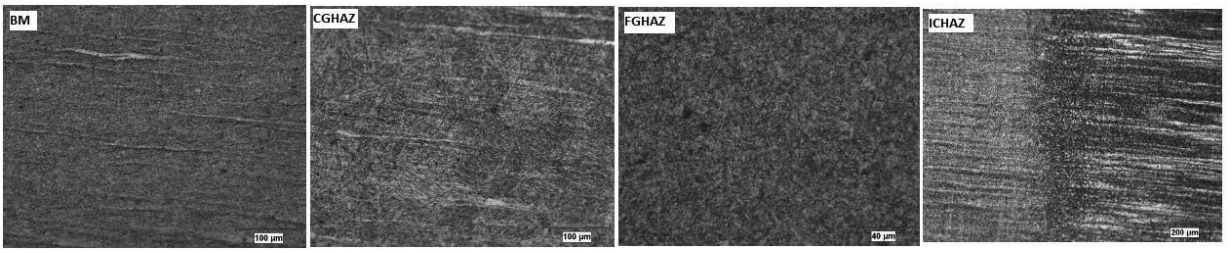

Figure 2: Microstructure of base material (BM), and heat affected zones (HAZ) welded joint

The fusion zone primarily consists of an austenitic matrix. This structure is highly beneficial for dissimilar joints as it provides high ductility and high hydrogen solubility, which effectively "shields" the armor steel from hydrogen-induced cold cracking. Within the austenitic grains, skeletal and lacy delta-ferrite formations were identified, presented in Figure 3. This 5-8% ferrite content is critical for preventing hot cracking during the solidification of the weld pool, as it restricts the segregation of low-melting-point impurities like sulfur.

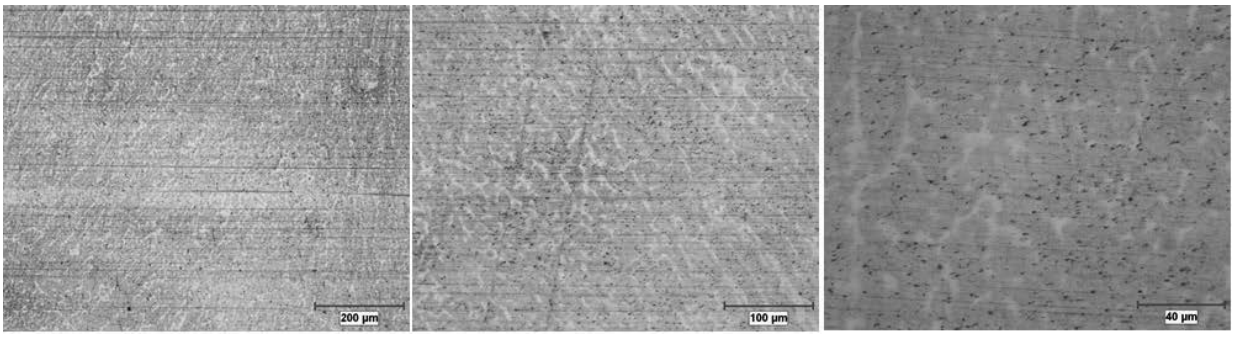

Figure 3. Microstructure view of WZ

In the Figure 4, the base metal displays a typical banded structure of pro-eutectoid ferrite (light) and pearlite (dark). In the HAZ of the S235JR side, the heat acted as a localized normalizing treatment. This led to a refinement of the ferrite grains near the fusion line, which explains the slight increase in hardness compared to the S235JR base metal and the subsequent failure of tensile specimens in the unaffected base metal zone.

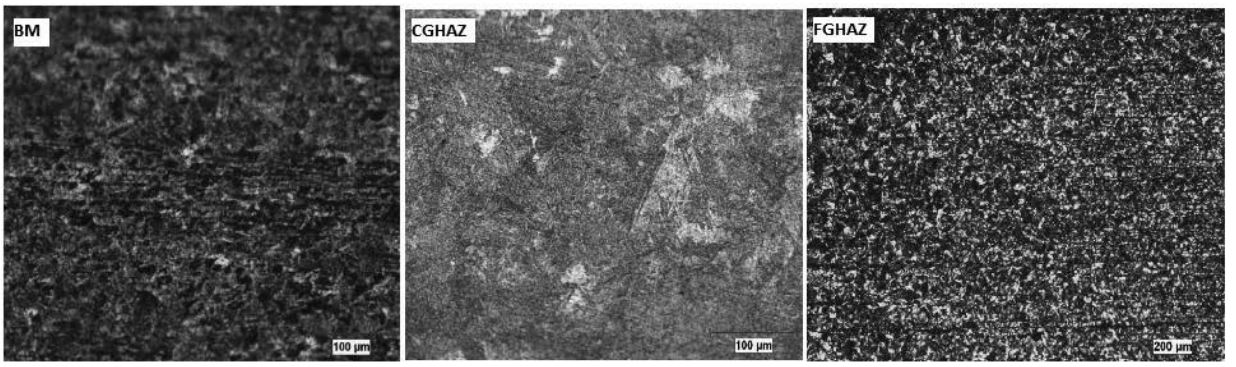

Figure 4. Microstructure of S235JR

The base material hardness of the armor steel was measured at approximately 620 $HV_{0.2}$. Hardness values for the armor steel decreased to approximately 580 HV in HAZ. This decrease was attributed to both the increase in grain size and the transformation of martensite into tempered martensite after slow cooling due to heat input. In the weld zone (WZ), the hardness values were measured at approximately 350 HV. The decrease in hardness in the weld zone was due to the use of a low-strength filler wire. Microhardness of the S235JR remained relatively uniform, with a slight decrease in the HAZ due to grain refinement. Vickers microhardness of welded sample shown in Figure 5.

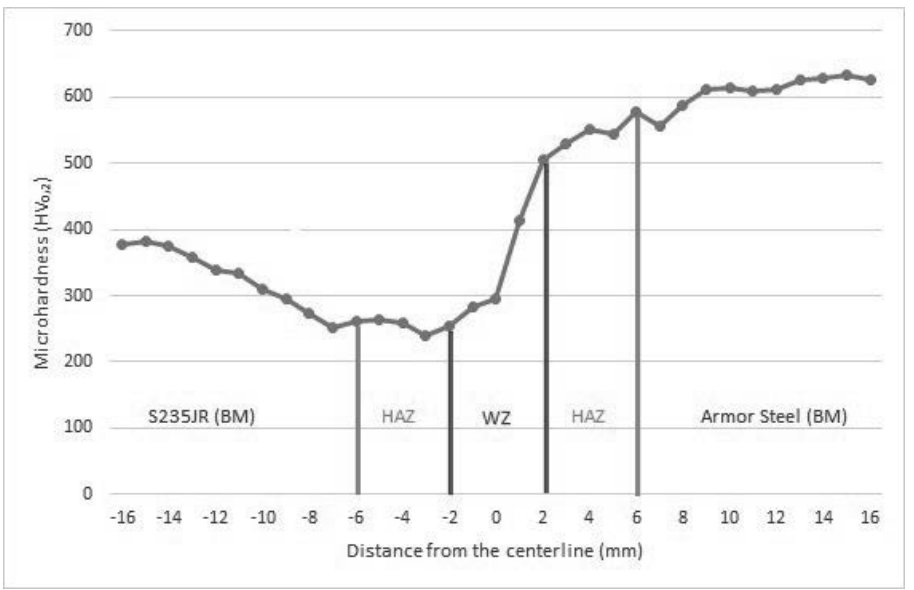

Figure 5. Vickers microhardness profile ($HV_{0.2}$)

The tensile tests demonstrated that the joints primarily failed in the structural steel base metal, rather than the WZ or heat-affected zone of the armor steel. This confirms that the joint efficiency is over 100% relative to the weaker base material and the 307Si filler metal provides

sufficient strength. In addition, tensile and hardness tests revealed significant differences between single-pass and multi-pass applications. The multi-pass welding strategy was found to be more reliable and mechanically superior for joining armor steels with dissimilar structural steels. The primary reason is the controlled heat input management. By distributing the thermal energy across multiple stages, the width of the "softened zone" in the Armor steel was significantly reduced. Furthermore, multi-pass welding enhanced the toughness of the fusion zone by preventing the formation of excessively coarse martensitic structures, thereby ensuring a better balance between hardness and ductility—a critical requirement for ballistic protection performance.

In bending testing, no surface cracks or discontinuities exceeding 3 mm were observed in either the face or root bend samples, demonstrating excellent fusion and ductility of the austenitic weld deposit. Furthermore, impact testing proved us the high toughness level is attributed to the austenitic microstructure of the 307Si filler, which effectively mitigates the risk of brittle fracture under dynamic loading conditions.

4. CONCLUSIONS

Based on the experimental investigation of dissimilar welding between armor and structural steels, the following conclusions were drawn:

The GMAW welding process with austenitic 307Si filler metal is an effective method for joining armor steel with S235 and S355 steels, providing crack-free joints without extensive preheating. The presence of delta-ferrite in the WZ plays a crucial role in ensuring the structural reliability of the dissimilar joint. While HAZ softening in the armor steel is inevitable with arc welding, it can be minimized by controlling the heat input within the 0.8–1.2 kJ/mm range. The joint efficiency is governed by the lower-strength structural steel, ensuring that the critical armor sections maintain their protective properties. The microstructural findings correlate perfectly with the hardness results. The loss of hardness in the HAZ is not a defect but a thermodynamic consequence of the welding thermal cycle on pre-tempered martensite. However, the use of 307Si filler ensures that the joint remains ductile enough to prevent catastrophic failure. Multi-pass welding was found to be superior to single-pass applications as it enhances fusion zone toughness and refines the martensitic structure. This optimized welding strategy ensures a critical balance between hardness and ductility, which is essential for maintaining the ballistic protection performance of the joint. This study proves that joining armor steel with affordable structural steel via multi-pass GMAW is a cost-effective alternative to full-armor designs. By using austenitic fillers that eliminate expensive preheating and post-weld heat treatments, production costs are significantly lowered. This approach allows high-cost ballistic alloys to be used only in critical areas, optimizing material expenses in large-scale defense manufacturing. In the next stage of our research, we plan to expand the investigation by testing a broader spectrum of heat input parameters to optimize the dissimilar joint performance further. Building upon our current findings, we will conduct advanced analyses on fatigue strength and material service life to ensure long-term structural reliability. Our goal is to translate these data into efficient, high-durability manufacturing processes specifically designed for large-scale production in the defense and mechanical industries.

BIBLIOGRAPHY

1. Korkmaz, E., & Meran, C. Gas metal arc welding of XPF800 steel for automotive industry: Microstructural evaluation and mechanical properties investigation. Proceedings of the Institution of Mechanical Engineers, Part L: Journal of Materials: Design and Applications, 236(4), 747-756, (2022).
2. Korkmaz, E., and Meran, C., "Mechanical properties and microstructure characterization of GTAW of micro-alloyed hot rolled ferritic XPF800 steel", Engineering Science and Technology, an International Journal 24, 503-513,DOI: 10.1016/j.jestch.2020.04.006, (2021).
3. Çelik, C., Göçmen, M., Çoban, O., Baykal, H., Gürol, U., & Koçak, M. (2023). Yüksek mukavemetli balistik zirh çeliklerinin kaynaklanabilirliği. Uludağ university journal of the faculty of engineering, 28(3), 1009-1028. https://doi.org/10.17482/uumfd.1333002

TalentDetector
9th January 2026
Gliwice, Poland
DEPARTMENT OF ENGINEERING MATERIALS AND BIOMATERIALS
FACULTY OF MECHANICAL ENGINEERING
SILESIAN UNIVERSITY OF TECHNOLOGY
INTERNATIONAL STUDENTS SCIENTIFIC CONFERENCE

Studies of the structure of food and spices using light, stereoscopic and scanning microscopy

Małgorzata Fligier[a], Lena Maksimowicz[a], Anna Włodarczyk-Fligier[b], Magdalena Polok-Rubiniec[b], Aneta Kania[b]

a Student of the 5th General Secondary School in Gliwice
email: gosiafligier@gmail.com
b Silesian University of Technology, Faculty of Mechanical Engineering, Department of Engineering Materials and Biomaterials
email: anna.wlodarczyk@polsl.pl

Abstract: This article presents the results of a comparative analysis of the possibilities of using light and scanning microscopes to observe the structure and morphology of objects selected for their originality from the group: food and spices. Selecting appropriate research methodology and comparing the imaging quality of the same objects required combining knowledge and skills in its practical application in the fields of physics, biology, chemistry, and materials science.

Keywords: light microscopy, scanning microscopy, samples, magnification

1. INTRODUCTION

A light microscope, also known as an optical microscope, is one of the fundamental research tools used in the natural sciences, materials science, medicine, and teaching. Its operating principle is based on the use of electromagnetic radiation in the visible light range, encompassing wavelengths from approximately 400 to 700 nm, to illuminate a sample and obtain a magnified image. The image is created by the interaction of light with the specimen, while its magnification and reproduction are achieved using a system of glass lenses specifically designed to focus and refract light rays.

Compared to electron microscopes, light microscopes are characterized by their small size, lower weight, and ease of use. They do not require a vacuum environment or complex laboratory infrastructure, making them portable and practical for everyday research applications.

The process of preparing a specimen for observation in a light microscope is relatively simple. Samples can be stained with appropriate dyes to enhance the contrast between individual structures, but in many cases, observations can be conducted without the use of additional chemicals. Unlike electron microscopy, specimens do not require dehydration,

fixation, or metal coating, significantly simplifying the sample preparation process and shortening analysis time.
The magnification capacity of light microscopes depends on the type of lenses used and typically ranges from 40× to 1500×.
There are two basic types of microscopes:
• simple microscope – uses a single converging lens, allowing for low magnification; used primarily for educational or reference purposes.
• compound microscope – equipped with two or more lens systems (objective and eyepiece), allowing for much higher magnifications and the observation of subcellular structures.

The optical system of a microscope is designed to refract and focus light rays, ensuring the highest possible image sharpness and contrast. Focus is adjusted by mechanically moving the stage or objective relative to the sample. The image can be observed directly through the eyepiece or, in modern designs, recorded with a digital camera and analyzed by a computer [1-5].

2. RESEARCH METHODOLOGY

Sample surface examinations were performed using a SteREO Discovery V12 (ZEISS) stereoscopic microscope with a magnification range of 10×–100×. This microscope enables three-dimensional observation of the examined objects and assessment of their topography in natural light, which is particularly useful when analyzing the surfaces of materials with complex structures.
A Leica DVM6 A digital light microscope was also used for detailed surface observations, equipped with three interchangeable objectives for macro and microscopic observations. The objectives differ in their magnification range and field of view, allowing for flexible adaptation of the device configuration to the type of sample being analyzed:
• low-magnification objective – used for observing the entire sample surface and initially locating areas of interest. Maximum magnification is 190×, with a field of view of 43.75 mm.
• medium-magnification objective – designed for analyzing fine structures within the sample. The magnification range is 46–675x, with a field of view of 12.55 mm.
• high-magnification objective lens – enables the observation of very small surface details, with a resolution of up to 425 nm. Maximum magnification reaches 2350x, with a field of view of 3.6 mm.
An additional advantage of the Leica DVM6 A microscope is its head tilt function within a range of ±60°, which allows for the analysis of samples from various angles. Combined with the ability to rotate and move the microscope stage, this solution enables the observation of difficult-to-access fragments and structures with complex geometry, such as corrosion spots in metals or the irregular surfaces of engineering materials.
The DSM 940 OPTON microscope is a classic scanning electron microscope (SEM), used in materials, biological, engineering, and technological research. This device enables detailed analysis of the morphology, topography, and chemical composition of sample surfaces using the DSM 940 OPTON scanning electron microscope, operating at an accelerating voltage of 20 kV and at maximum magnifications of 1000x and 2000x, using reflected and secondary electron detection.

3. EXPERIMENTAL RESULTS

The study conducted a comparative analysis of the potential use of light and scanning microscopes to observe the structure and morphology of objects (macro and micro) selected for their originality from the food and spices group (e.g., salt, black and white pepper). The results of the observations are presented in Figure 1.

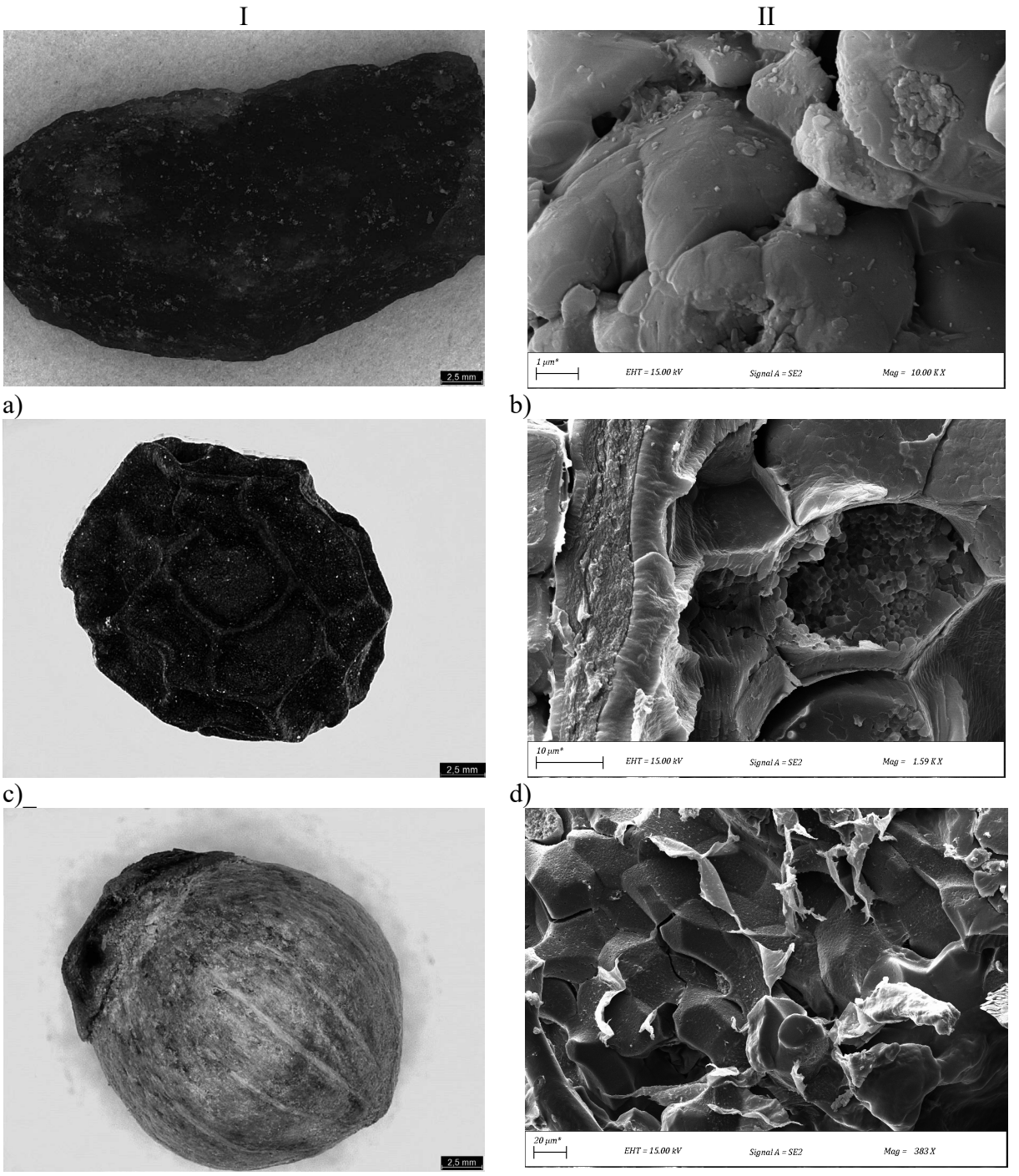

Figure 1. Surface of grains: a, b) salt, c, d) black pepper, e, f) white pepper, I. light microscope, II. scanning microscope.

Thanks to the use of higher magnifications in the Leica DVM6 A microscope, it was possible to precisely reproduce small surface structures (anise, tea, linden leaves and flowers, sunflower sprout, cauliflower leaves) (Fig. 2).

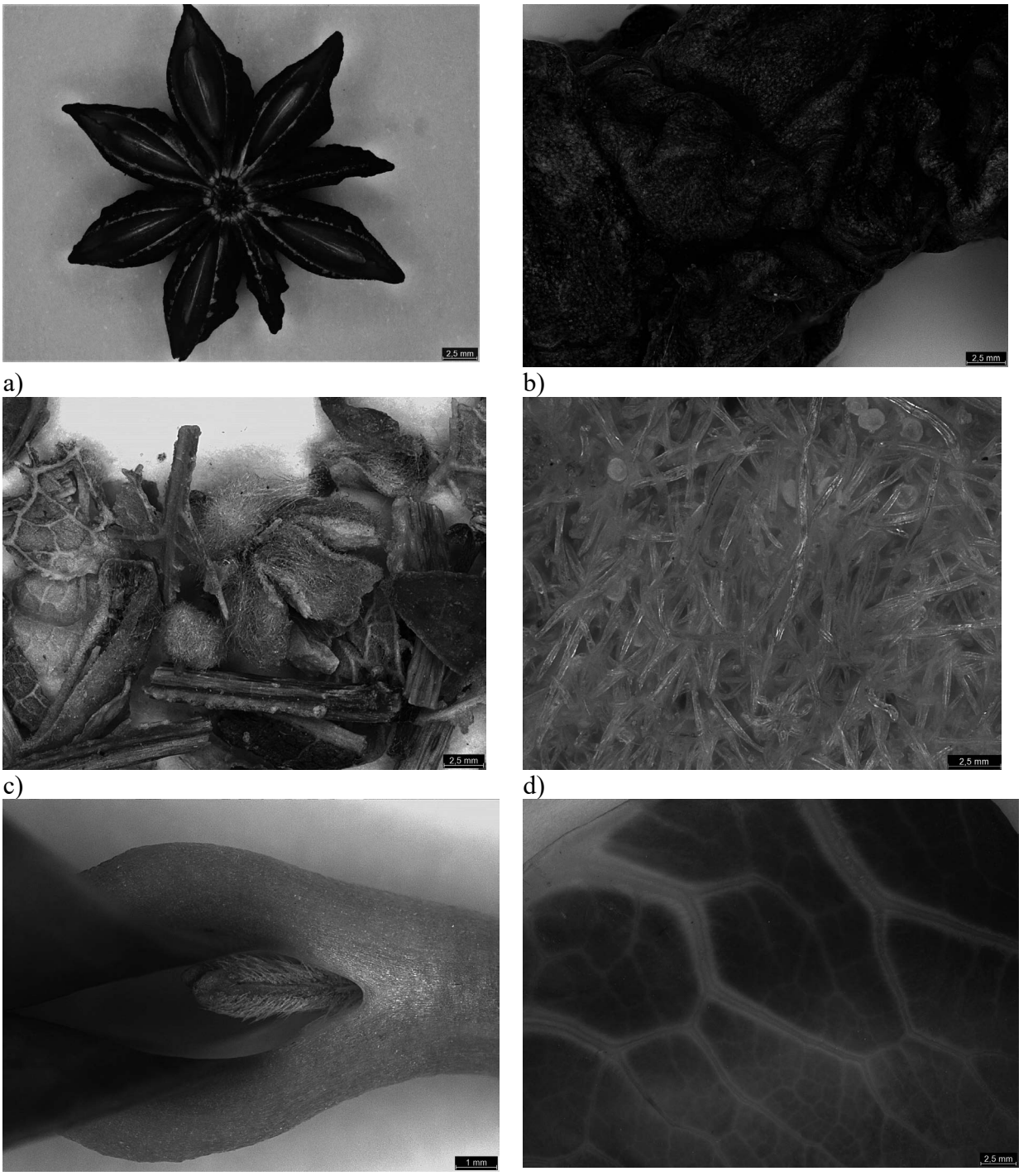

Figure 2. Surface of grains: a) anise, b) tea, c,d) linden leaves and flowers, e) sunflower sprout, f) cauliflower leaves, light microscope.

The obtained results confirm that the digital microscope enables a more detailed analysis of the microstructure of samples, while maintaining high contrast and depth of field.

4. CONCLUSIONS

Phenomena and processes occurring at the microscopic scale are crucial for understanding the nature of matter. Many of the most fundamental physical, chemical, and biological processes occur at dimensions invisible to the human eye. This fact is a key premise for the continuous development of observational technologies, including modern microscopy methods, which enable increasingly detailed understanding of the micro- and nanostructure of the world around us.

The use of light microscopy in scientific and engineering research allows for non-invasive observation of biological and material samples, without the need for complex preparation or interference with the structure of the object being studied.

A comparison of the capabilities of stereoscopic and digital microscopes revealed that modern digital microscopes offer significantly higher image quality, a wider range of magnifications, and more precise reconstruction of surface topography. Additional features, such as head tilt, automatic focusing, and high-resolution image capture, enable detailed analysis of difficult-to-access sample areas, as well as their three-dimensional visualization.

BIBLIOGRAPHY

1. M. Pluta, Mikroskopia optyczna, Wydawnictwo UJ, Kraków, 2005.
2. W. Sawicki, J. Malejczyk, Histologia. Mikroskop i technika histologiczna, WUM, Warszawa, 2024.
3. L. Błaż, Instrumentalne metody badawcze. Mikroskopia świetlna, AGH, Kraków, 2018.
4. A. Kawaska, Mikroskopia świetlna – budowa i zasada działania, kawaska.pl, 2023.
5. Helpi Optics, Mikroskopia świetlna – fundament nowoczesnych badań i edukacji, helpi-optics.pl, 2023.

This paper is the result of a project carried out with secondary school students, entitled Investigations of the materials structure from the student's environment using electron and light microscopes.

TalentDetector

23th-25th June 2025
Gliwice-Brenna, Poland

DEPARTMENT OF ENGINEERING MATERIALS AND BIOMATERIALS
FACULTY OF MECHANICAL ENGINEERING
SILESIAN UNIVERSITY OF TECHNOLOGY

INTERNATIONAL STUDENTS SCIENTIFIC CONFERENCE

Selection of control devices and 3D printing technology in an automated greenhouse project

Maurycy Frydecki [a], Karol Tkałka [a], Magdalena Koźlik[b], Kacper Strukowski[b], Kamil Kołodziej[b], Marcin Jaroszek[b], Mariusz Król[c], Marcin Bilewicz[c], Vojtěch Macejko[d], Eliška Posmyková[d]

[a] Silesian University of Technology, Faculty of Mechanical Engineering, Mechanical engineering
[b] Silesian University of Technology, Faculty of Mechanical Engineering, Automation and Industrial Robotics
[c] Silesian University of Technology, Faculty of Mechanical Engineering, Department of Engineering Materials and Biomaterials, e-mail: mariusz.krol@polsl.pl
[d] Department of Machining Assembly and Engineering Metrology, Faculty of Mechanical Engineering, VSB – Technical University Ostrava, Ostrava, Czech Republic.

Abstract: The article presents an overview of automatic greenhouse control solutions and the selection of 3D printing technologies for the production of non-standard components, focusing on DIY (do it yourself) solutions. The control overview includes a description of Arduino and identifies the main differences compared to industrial controllers. This is followed by a comparison of other solutions available on the market and a brief discussion of their advantages and disadvantages. The second part focuses on 3D printing technologies that can be implemented on commercially available printers, with particular emphasis on the thermal resistance of components that come into contact with the heating system.

Keywords: Arduino, 3D printing, FDM, automatic greenhouse

1. INTRODUCTION

At the end of the first half of the 20th century, the first computers began to appear. At the very beginning, they were huge cabinets that took up entire rooms, consumed enormous amounts of electricity, and required an experienced team of operators.
With the invention and miniaturization of transistors, computers began to consume less and less energy and became smaller and more common. It was during this period that electronics began to become a hobby for many people. Magazines provided the necessary schematics, specialized stores sold the necessary components, and enthusiasts could prepare and assemble a circuit board and then solder everything together. Any enclosures were usually made of wood. The process was quite long and required a considerable amount of knowledge at the outset. At

around the same time, automation was entering the industry, where it manifested itself in the form of control cabinets with a large number of contactors and relays. Changes in control systems proved to be a major problem, as they usually involved dismantling and reassembling the entire cabinet. PLC controllers proved to be a breakthrough, as in the event of a change in control, the connections to the controller could remain the same, and only the software part of the controller was changed. Although such solutions were becoming increasingly popular, their application was practically limited to industrial use. It then turned out that engineers did not have to design entire cabinets or electronic systems from scratch, but could use ready-made modules. In such cases, part of the control and logic is performed by a microcontroller, thanks to which weeks of designing electronics can be replaced by a day of writing a program. It was not until the 21st century that a company emerged that made it possible to reduce the time spent on tinkering on an unprecedented scale and allowed virtually anyone to start their adventure with electronics and programming in an affordable way.

A few years later, 3D printing became widely available, allowing anything that could be modeled on a computer to be printed. This was another convenience for all electronics enthusiasts, as they could model enclosures, handles, or actuators themselves in CAD software and then print the necessary parts with little effort. There are many printers and filaments available on the market. Depending on the application, the printed detail has different properties.

2. WHAT IS ARDUINO??

Arduino is a microcontroller, i.e., a small computer contained in a single chip and has the functionality of early home computers. It can run simple programs and is very energy efficient.

Arduino is a company in Italy that manufactures and sells boards that make microcontrollers very easy to use. The boards themselves are also called Arduino, and there are many types available. They are relatively inexpensive and sufficient for most projects. They allow you to control lighting, measure temperature, display anything you want on a connected display, and even control a simple robot. Arduino makes all its designs available under an open source license, which allows other manufacturers to make their own Arduino designs with the same functionality and expand them with new features. Other Arduinos have more advanced microcontrollers, built-in Ethernet or WiFi ports, Bluetooth modules, SD card readers, or Jack outputs. In addition, there are shields on the market, which are additional circuits on a board that plug directly into the Arduino pins and extend the capabilities of the original board. For example, to control a servo drive, without having to design the entire system, which significantly reduces the entry point.

Arduino has an integrated development environment called Arduino IDE. It simplifies the process of programming and uploading programs. You don't need to remember all the commands, worry about registers, or have a special programmer to upload code to the processor. Arduino has all of this integrated into the ArduinoIDE environment, which is available for all operating systems. All you need to do is connect the board to your computer via USB and upload the program you have written. The programming language itself is similar to C and C++. It is one of the easiest languages to learn. There are also many tutorials, ready-made codes, and a huge community on the internet that can help with any problems. There are also ready-made libraries for individual sensors, making the entry level very accessible.

In terms of hardware, the most important component is the microcontroller itself. In the original Arduino UNO, it is an ATmega AVR manufactured by Atmel. It contains built-in processor and memory circuits and supports the electronics necessary to operate input/output ports. It is one of the simplest, easiest, and most enjoyable microcontroller families. Of course, other versions of Arduino or products from other manufacturers may be controlled by other microcontrollers, but from a programming perspective in ArduinoIDE, it makes no difference. The microcontroller itself can also be used without a board, but this would require additional knowledge, resources, and soldering, which is an obstacle for novice DIYers.

Most boards, both original and "clones," have a similar design. A quartz resonator is connected to the microcontroller, generating 16 million pulses per second in the case of Arduino UNO, where the microcontroller performs one mathematical operation per pulse. To upload the program to the board, there is a separate second microcontroller responsible for communication between the board and the computer via a USB interface. These are usually USB Type B, USB micro B, or USB Type C ports. The board itself can be powered directly via USB, but in the case of Arduino UNO, it can also be powered by a 9V battery, for which there is a separate connector and a voltage stabilizer that reduces it to 5V. The board itself has a "reset" button and a built-in LED connected to one of the output pins. This LED is used to check the operation of the microcontroller with the "Blink" program without having to connect anything to the board outputs. There is a VIN power connector to which an external power supply can be connected. Pin 5V for 5V output, e.g. to power sensors, 3.3V for 3.3V voltage, and GND pins for grounding. There are also analog outputs connected to an analog-to-digital converter in a microcontroller with 10-bit resolution (from 0 to 1023). There are usually more digital outputs, and they allow for a state of 0-1. These pins also enable communication with sensors using various protocols, such as I2C. Documentation and schematics for the board itself can be found on the manufacturer's website [1, 2].

3. ARDUINO AND PLC CONTROLLER

At first glance, it may seem that Arduino and PLC controllers are practically the same thing. And theoretically, they can perform similar tasks. However, the difference lies primarily in safety and reliability. For hobbyist DIY projects or prototyping, this is not very important. The difference in purpose stems from the fact that PLC controllers are designed for industrial installations and must meet higher safety standards and operate continuously. Another important difference is the programming language, where controllers use LD, FBD, or ST languages, while Arduino uses a language similar to C++. The differences in technical parameters are presented in Table 1.

Focusing on hobbyist applications, Arduino is smaller, consumes less power, and has more inputs/outputs. Communication methods are adapted to popular sensors available for such projects, while PLC controllers use communication methods used in industry. For small and medium-sized projects, the memory offered by Arduino is more than sufficient. For logger-type applications, you can connect a module with an SD card or send data via another module over WiFi to a server. The biggest advantage of Arduino, as seen by DIY enthusiasts, is its price. And while its service life is shorter, the purchase price in such projects definitely favors the Arduino solution.

Table 1. Comparison of Arduino UNO with Siemens S7-1200 controller [2-5]

	Arduino UNO R3	Siemens S7-1200 1212C
	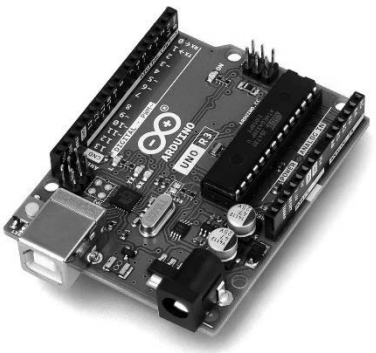	
Dimensions [mm]	69x53x12	100x90x75
Digital inputs/outputs	14	8 inputs 6 outputs
Analog inputs/outputs	6 putputs	2 inputs
PWM pins	6	6 (only for DC/DC/DC)
Communication	UARC, I2C, SPI	PROFINET, PROFIBUS, AS-i, S7 communication
Memory	2KB SRAM, 32KB FLASH, 1KB EEPROM	50 KB work memory, 1 MB load memory, 10 KB retentive memory
Power consumption	Up to 5W	Up to od 10 W
Price	120 zł	3700 zł

4. OTHER SOLUTIONS

In addition to the official Arduino series, we also have several other solutions. These include ESP microcontrollers and Raspberry Pico microcontrollers. An overview of the technical parameters for popular solutions is provided in Table 2. In fact, boards that use popular platforms have already been designed for most applications. This simplifies the entire design process, as you can choose the control system for a specific task.

5. SELECTION OF CONTROL DEVICE

Depending on the project, different Arduino models will have their advantages or disadvantages. Therefore, it is worth writing down the assumptions and requirements of the project at the beginning. For most beginner projects, Arduino UNO will be a perfectly sufficient solution.

For applications with a larger number of supported sensors and a large number of zero-one components such as buttons or independent LEDs, the Arduino Mega solution will be better.

If you need to distribute sensors in several locations and collect data from them, or serve only a few wireless outputs, the ESP solution has a built-in WiFi module. Additionally, you can create a simple HTTP page to display data or a control panel that will be accessible to all devices on the network. Furthermore, they can be programmed in both ArduninoIDE and LUA.

The Raspberry Pico solution can be useful when the program is already highly developed and we use many different sensors with different communication protocols. There are also variants with WiFi and low energy Bluetooth modules. In this case, the board is even more similar to the ESP solution. One advantage may be the default programming language, micro python, which is a stripped-down version of python. It is also possible to upload the appropriate libraries to the IDE environment and use it to program the board.

Table 2. Comparison with other microcontrollers [6-11]

	Arduino Mega 2560 Rev3	ESP8266 NodeMCU v3	Raspberry Pi Pico 2
			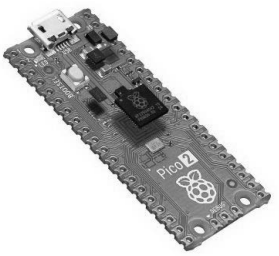
Digital inputs/outputs	54	10	26
Analog inputs/outputs	16	5	3
PWM Pins	15	10	24
Communication	4xUARC, I2C, SPI	I2C, 1-Wire, wbudowany moduł WiFi	2× UART, 2× I2C, 2× SPI
Memory	8KB SRAM, 256KB FLASH, 4KB EEPROM	4 MB FLASH	520KB SRAM, 4MB FLASH
Price	200zł	30 zł	25 zł

Regardless of which microcontroller you choose for DIY applications, it will be much easier than designing electronics from scratch. And the low cost makes it accessible to everyone.

For the planned greenhouse, a total of several digital sensors are planned, each requiring several wires for communication. And two limit switches that output a 0-1 signal. In addition, several outputs, some of which will be connected to a contactor to supply the receivers with more current. Wireless communication is desirable. In the case of fewer inputs/outputs, the ESP solution would be chosen. However, in order to connect all sensors and actuators and ensure future expansion, it was decided to use Arduino Mega. WiFi communication is solved by a separate module, which also requires pins for connection.

6. SELECTION OF MANUFACTURING TECHNOLOGIES AND MATERIALS

6.1. Requirements analysis for mechanical components

The automated greenhouse project involves specific environmental requirements. Structural elements must be resistant to changing weather conditions, including high humidity and exposure to UV radiation. An additional engineering challenge is the need to manufacture components with non-standard geometries that are difficult to obtain using subtractive methods, such as dedicated enclosures for electronic and heating systems.

6.2. Justification for choosing FDM technology

Two leading additive technologies were analyzed in the decision-making process: FDM/FFF (Fused Deposition Modeling) and SLA (Stereolithography). Ultimately, it was decided to use FDM technology. The main factors behind this choice were:

– Wide availability of engineering materials (thermoplastics) with diverse properties.
– Low cost of rapid prototyping and short model production time [12].

SLA technology was rejected due to the lower impact strength of resins and higher operating costs.

6.3. Criteria for selecting materials (filaments)

In order to select the appropriate materials, a comparative analysis of popular materials was carried out in terms of their performance in greenhouse conditions. The properties are summarized in Table 3 [13, 14].

Table 3. Comparison of popular materials

Filament	Resistance to UV	Temperature resistance [°C]	Required chamber	Tensile strength	Impact resistance	Price for 1 kg [zł]
PLA	Poor	~60	No	Medium	Poor	80
ABS	Poor	~100	Yes	Medium	Poor	110
ASA	Good	~105	Yes	Medium	Medium	140
PET-G	Good	~80	No	Good	Medium	80

Based on the above analysis, the following material classification was made:

1) PLA: Used for frame connectors and elements not subjected to thermal loads due to its ease of printing and low cost.

2) PET-G: Selected for the heating element housing. The decision was dictated by its higher softening temperature (resistance to approx. 80°C) [15], resistance to UV radiation and

chemicals, as well as the lack of need for a closed working chamber, which is required for ABS/ASA.

6.4. Design process and optimization (Rapid Prototyping)

Taking advantage of rapid prototyping, the heater housing design underwent four development iterations:

1) Base prototype: Verification of dimensions. At this stage, a geometric collision was identified—the heater chamber was too narrow, which prevented installation.

2) Tolerance correction: The processing shrinkage of the PET-G material was taken into account, and the fit of the mounting holes and heater socket was improved. A photo of the CAD model is shown below (Figure 1).

3) Function integration: An integrated mounting system was added, eliminating the need for additional brackets.

4) Print optimization: The geometry was modified to eliminate the need for support structures, which reduced printing time and improved aesthetics.

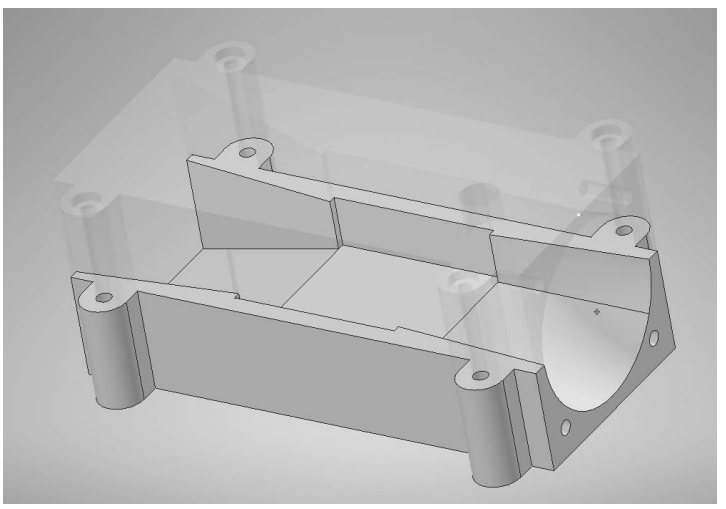

Figure 1. Heater housing render

Manufacturing process parameters: The final prints were made using the following settings (for PET-G material):

- Nozzle temperature: 240°C
- Work table temperature: 70°C
- Layer height: 0.2 mm
- Infill: 15% (pattern: Grid)
- Wall thickness: 3 layers
- Cooling: 20-50% (first 3 layers disabled)

7. EXPERIMENTAL VERIFICATION OF MATERIAL SELECTION

Two-stage thermal tests were conducted to confirm the safety of the structure.

7.1. Rated performance test

The system with the fan switched on was operated continuously for 2 hours. Thermal imaging camera measurements showed that the maximum temperature of the heating element was 75.2°C (Figure 2), the maximum temperature of the inner wall of the housing was 65.0°C (Figure 2), and the maximum temperature of the outer wall was 55.9°C (Figure 3).

The temperatures obtained are within the safe operating range of PET-G material (below the glass transition point), which confirms that there is no deformation of the housing during normal operation.

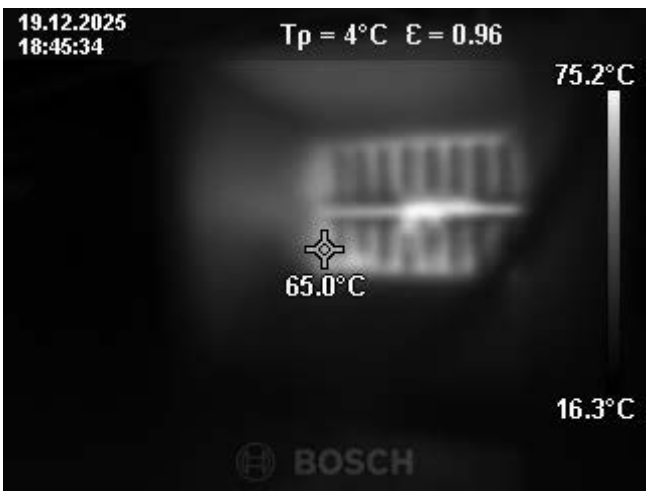

Figure 2. Internal wall temperature and maximum temperature during rated operation

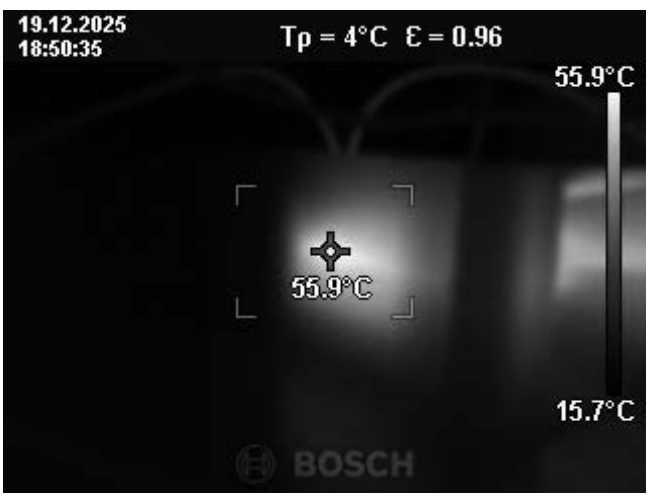

Figure 3. External wall temperature during rated operation

7.2. Emergency conditions test (cooling failure simulation)

In order to verify fire safety, a fan failure was simulated. In the absence of air flow, the heat sink temperature rose rapidly to 135.2°C (Figure 4), causing the thermal fuse to trip after 112 seconds.

Measurements showed the temperature of the enclosure wall to be 61.6°C (Figure 5). The thermal inertia of the plastic meant that the heat did not fully penetrate the wall before the power was turned off. After disassembly, only local plastic deformation was observed (reflection of the heat sink fin – Figure 6), but the structure of the casing was not broken or melted.

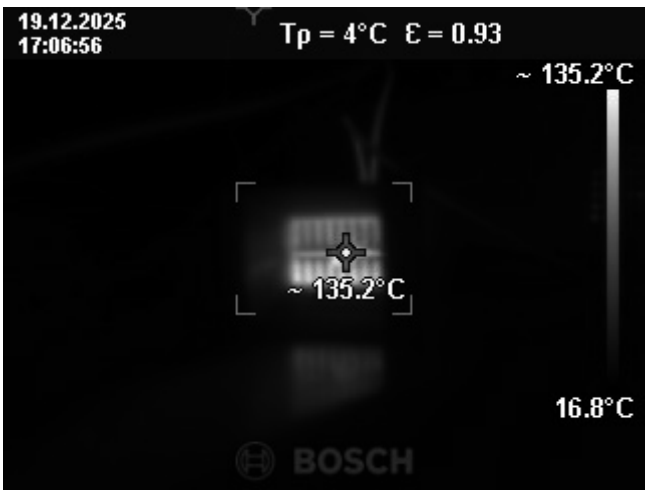

Figure 4. Maximum temperature on the heater when cooling is turned off

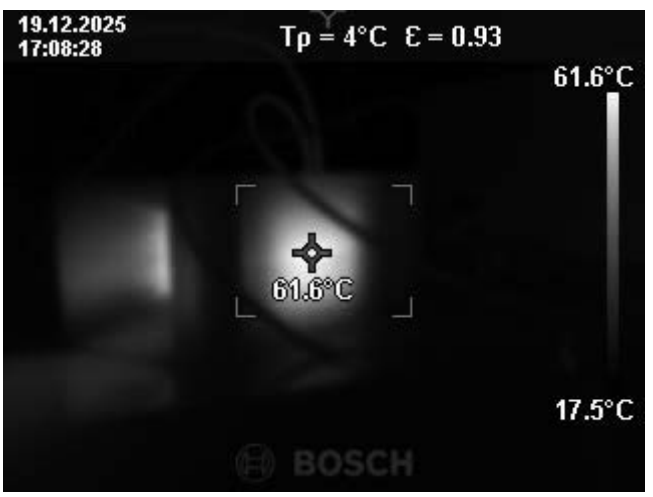

Figure 5. Side wall temperature with cooling turned off

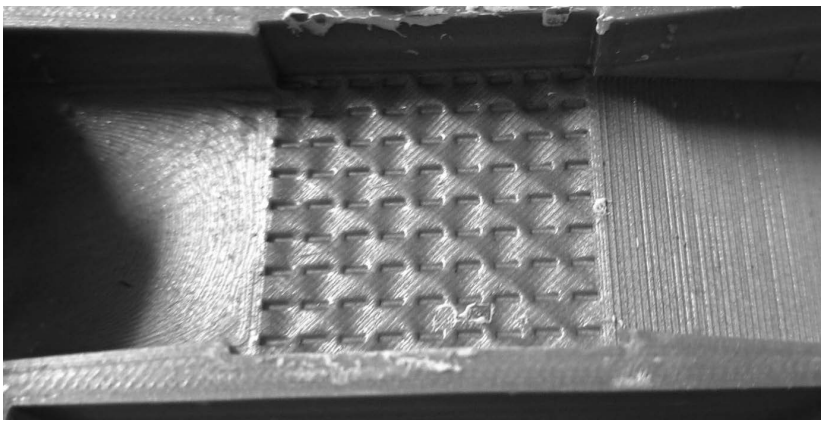

Figure 6. The lower part of the heater after testing with cooling turned off

8. SUMMARY OF THE SELECTION OF FRUKU 3D TECHNOLOGY

FDM technology combined with PET-G material is an economical and effective method of producing dedicated enclosures resistant to operating temperatures of up to 70-80°C.
The use of rapid prototyping allowed geometric errors to be eliminated in four design iterations without generating high molding costs.

Emergency tests have shown that the selected PET-G enclosure maintains its structural integrity even in the event of a cooling system failure (until the fuse is activated), which guarantees the safe use of the device.

ACKNOWLEDGEMENTS

The work was created as a result of a project carried out as part of project-based learning (PBL) in the 13th competition under the Initiative of Excellence – Research University program, Faculty of Mechanical Engineering, Silesian University of Technology.

BIBLIOGRAPHY

1. Banzi, M.; Shiloh, M. *Wprowadzenie Do Arduino, Wyd. II*; O'Reilly Media, 2022; ISBN 978-83-7541-492-9.
2. https://docs.arduino.cc/hardware/uno-rev3/ (dostęp z dnia 4.12.2025)
3. https://botland.com.pl/arduino-seria-podstawowa-oryginalne-plytki/1060-arduino-uno-rev3-a000066-7630049200050.html (dostęp z dnia 4.12.2025)
4. https://support.industry.siemens.com/cs/mdm/91696622?c=60466538379&dl=cs&lc=en-US (dostęp z dnia 5.12.2025)
5. https://publikacje.siemens-info.com/pdf/82/Pierwsze%20kroki%20z%20SIMATIC%20S7-1200%20-%20podr%C4%99cznik.pdf (dostęp z dnia 5.12.2025)
6. https://docs.arduino.cc/hardware/mega-2560/#tech-specs (dostęp z dnia 7.12.2025)

7. https://botland.com.pl/arduino-seria-podstawowa-oryginalne-plytki/1062-arduino-mega-2560-rev3-a000067-7630049200067.html (dostęp z dnia 7.12.2025)
8. https://randomnerdtutorials.com/getting-started-with-esp8266-wifi-transceiver-review/ (dostęp z dnia 8.12.2025)
9. https://botland.com.pl/moduly-wifi-esp8266/8241-modul-wifi-esp8266-nodemcu-v3-5904422300630.html (dostęp z dnia 8.12.2025)
10. https://www.raspberrypi.com/products/raspberry-pi-pico-2/ (dostęp z dnia 13.12.2025)
11. https://www.raspberrypi.com/documentation/microcontrollers/pico-series.html (dostęp z dnia 13.12.2025)
12. Chua, C.K; Leong, K.F; Lim, C.S. *Rapid Prototyping: Principles and Applications*; World Scientific Publishing, 2010; ISBN: 978-981-238-883-4
13. Redwood, B.; Schöffer, F.; Garret, B. *The 3D Printing Handbook: Technologies, design and applications*; 3D Hubs, 2017; ISBN: 978-908-274-850-5
14. https://anycubicofficial.pl/pages/filaments-performance-comparison (dostęp z dnia 20.12.2025)
15. https://nebulafilaments.com/en/product-line/premium/pet-g (dostęp z dnia 20.12.2025)

TalentDetector
23th-25th June 2025
Gliwice-Brenna, Poland
DEPARTMENT OF ENGINEERING MATERIALS AND BIOMATERIALS
FACULTY OF MECHANICAL ENGINEERING
SILESIAN UNIVERSITY OF TECHNOLOGY
INTERNATIONAL STUDENTS SCIENTIFIC CONFERENCE

Smart aquarium as an example of modern methods of water environment control

Maurycy Frydecki[a], Karol Tkałka[a], Magdalena Koźlik[b], Kacper Strukowski[b], Kamil Kołodziej[b], Marcin Jaroszek[b], Mariusz Król[c], Marcin Bilewicz[c], Vojtěch Macejko[d], Eliška Posmyková[d]

[a] Silesian University of Technology, Faculty of Mechanical Engineering, Mechanical engineering
[b] Silesian University of Technology, Faculty of Mechanical Engineering, Automation and Industrial Robotics
[c] Silesian University of Technology, Faculty of Mechanical Engineering, Department of Engineering Materials and Biomaterials, e-mail: mariusz.krol@polsl.pl
[d] Department of Machining Assembly and Engineering Metrology, Faculty of Mechanical Engineering, VSB – Technical University Ostrava, Ostrava, Czech Republic.

Abstract: The growing popularity of home aquariums necessitates ensuring stable environmental conditions in aquariums. Traditional water parameter control is mainly based on manual user operation, which makes it difficult to respond quickly to adverse changes. This article presents the concept of a smart aquarium based on Internet of Things (IoT) technology, enabling continuous monitoring of temperature, pH, and water turbidity. The use of sensors and a mobile application allows for ongoing supervision of the aquarium's condition, reducing the user's workload and increasing the safety of aquatic organisms.

Keywords: aquarium, mobile app, turbidity sensor, water pH sensor

1. INTRODUCTION

An aquarium is a closed ecosystem in which every change has an impact on the organisms living in it. Stable environmental conditions, including temperature, pH, and water turbidity, are fundamental to the health of the fish and plants living in this ecosystem. Fluctuations in these conditions have a negative impact on the organisms living in the aquarium, causing severe stress and disease. [1]

In traditional aquarium keeping, control of the tank's condition is largely based on manual intervention by the keeper [2], often based on a subjective, visual assessment of the aquarium rather than on ongoing analysis of actual water parameters. This approach increases the risk of delayed response to adverse changes in the aquatic environment.

The aim of this article is to present the concept of a smart aquarium that monitors and automatically corrects key parameters, providing real support in maintaining a stable and safe living environment for aquatic organisms.

2. THE CONCEPT OF A SMART AQUARIUM

In response to the problems inherent in traditional fish farming [2], the concept of a smart aquarium (Fig. 1) was developed, with the aim of automatically analysing and controlling the conditions surrounding the fish. The system ensures a safe environment for the animals with minimal user intervention.

The main design assumptions were: continuous monitoring of key water parameters, automatic system response to observed changes, and the possibility of remote supervision via an application.

The designed system was based on a scheme in which measurement data was obtained from sensors cooperating with a microcontroller. The obtained information was processed and transmitted to the cloud, creating a database enabling ongoing analysis and visualization of the achieved results in the application. If the set limit values were exceeded, the system was designed to activate warning signals in the form of LEDs, notifications in the application, or an LCD display. This solution assumed a quick response from the user to the problems that arose or the activation of appropriate automatic procedures.

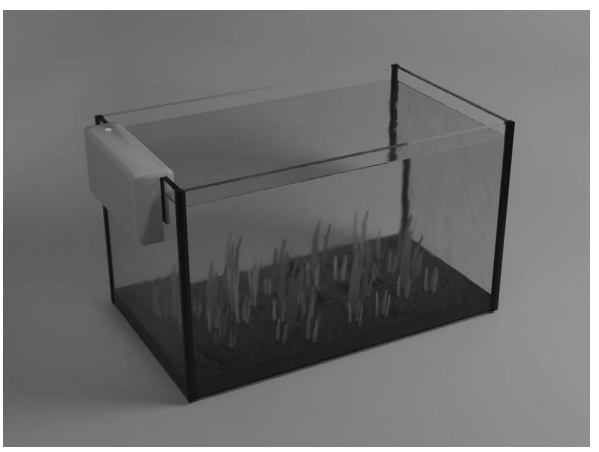

Figure 1. Smart Aquarium concept

3. WATER PARAMETER MONITORING SYSTEM

One of the key parameters of aquarium water is pH. Its optimal value varies depending on the organisms present in the aquarium, but the most common range is considered to be between 6.8 and 7.5. For some fish species, the appropriate pH value may vary, as is the case with some marine fish for which the optimal pH value ranges between 8.2 and 8.5. [3, 4]. A smart aquarium is based on the use of a photoelectric pH sensor (Fig. 2), which enables the measurement of water pH based on the analysis of changes in the optical properties of a medium that reacts to the concentration of hydrogen ions. Sensors of this type provide fast and

stable measurement across the entire pH range, making them useful in automatic water quality monitoring systems [6].

Figure 2. Photoelectric water pH sensor

Another important parameter in an aquarium is water temperature, where, similarly, the optimal value varies depending on the fish being bred. For most fish, the appropriate water temperature is in the range of ~24-28°C [5]. For the purposes of the project, it was proposed that temperature measurements be carried out using a waterproof probe with a DS18B20 sensor (Fig. 3) with an accuracy of ± 0.5°C, while water turbidity would be measured using an analog liquid turbidity sensor (Fig. 4). The sensor detects particles suspended in water by measuring light transmittance and propagation speed, which changes with an increase in the total amount of solid particles. The greater their number, the greater the level of turbidity [7].

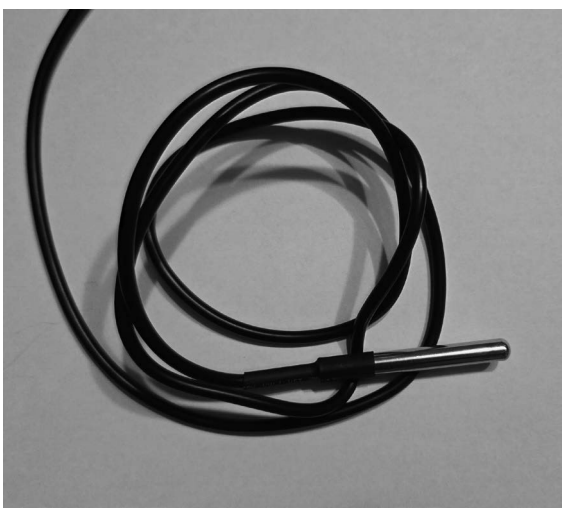

Figure 3. DS18B20 sensor measuring water temperature

Figure 4. Analog liquid turbidity sensor

The concept of a smart aquarium is based on regular measurements taken at specific intervals using the sensors mentioned above. The data is recorded and displayed on the screen and in the mobile app. If the water parameters defined by the user in the app are exceeded, a warning is sent to notify the user of the problem, allowing them to take appropriate action to improve water quality.

4. MONITORING WATER PARAMETERS AND COMMUNICATION WITH THE USER

The concept of a smart aquarium is not limited to passive monitoring of basic water parameters such as temperature, pH, or turbidity. The developed system will operate much more broadly and intelligently. One of the assumptions was that it would analyse the collected data in real time, comparing it with established standards, which would allow it to detect any anomalies before they become a real threat to the organisms in the aquarium.

When certain irregularities occur, such as a sudden drop in water quality, a dangerous change in temperature, or other deviations from the optimal conditions set by the user, the system will react immediately. The user will be notified of the problem in several ways simultaneously. Physical warning signals, such as an LED on the aquarium or a message displayed on the device screen, will allow the problem to be quickly noticed even without using a phone.

At the same time, a detailed notification will be sent to the mobile app, where the user can check the exact nature of the detected anomaly, its possible causes, and recommended actions. This will allow the aquarium owner to know what steps to take to restore the proper conditions in the aquarium as quickly as possible.

This approach not only increases the safety of fish and plants in the aquarium, but also significantly facilitates its maintenance by the user.

Notifications sent to the mobile application will be implemented using Bluetooth technology, which will ensure stable communication between the smart aquarium system and the user's mobile device.
The choice of Bluetooth communication was dictated by the fact that this technology allows for quick device pairing and trouble-free data exchange over short distances, which is the optimal solution for home use. The user receives up-to-date notifications directly in the mobile app, where they can conveniently view the details of the event.

5. MOBILE APPLICATION

The mobile app is the main interface for communication with the user. It allows for real-time monitoring of the aquarium's condition, analysis of water parameters, and quick response to any irregularities. The app presents current data in a clear and intuitive form, allowing the user to quickly check the situation in the aquatic environment. If an anomaly is detected, the system automatically sends a notification that immediately appears on the phone screen.
In addition, the application provides access to detailed information about the detected problems. The user can check which parameter deviates from the norm, when the abnormality occurred, and what actions the system recommends in order to restore optimal conditions in the aquarium. This greatly simplifies things for people who do not have detailed knowledge about aquarium care.

The whole thing has been designed with simplicity and ease of use in mind. The app does not overwhelm the user with excessive information, but focuses on conveying information to the user in a clear manner.

6. USER AND OPERATIONAL ASPECTS OF THE SMART AQUARIUM

The use of a smart aquarium improves the user's comfort of operating the tank and reduces their involvement in its daily control. Automatic monitoring of water parameters and a notification system allow for a quick response in the event of irregularities, thanks to which the fish and plants in the aquarium are much safer and their comfort of life is significantly greater.
Although the implementation of the system involves higher costs at the beginning, it provides better control of the conditions in the aquarium and reduces the risk of fish and plant losses. Using the system is straightforward and mainly involves occasional cleaning of the sensors and operating the mobile application.

The limitations of the solution include dependence on the correct operation of the measuring elements and the range of wireless communication, but despite these imperfections, a smart aquarium significantly increases the safety and stability of the living conditions of aquatic organisms.

Table 1 summarizes all technical and functional aspects in comparison with a traditional aquarium and a smart aquarium [8].

7. SUMMARY

The article presents the concept of a smart aquarium as a modern solution supporting the control of the aquatic environment. The use of an automatic water parameter monitoring system

allows for more effective maintenance of stable living conditions for aquatic organisms compared to traditional aquarium methods.

The biggest advantage of a smart aquarium is the continuous measurement of the most important water parameters, such as temperature, pH, and turbidity, as well as immediate notification of the user about any detected abnormalities. The use of a mobile application and physical notifications increases the safety of fish and plants and reduces the risk of errors resulting from delayed human response.

Despite the higher initial implementation costs, a smart aquarium significantly improves the comfort of tank operation and reduces the user's workload. The automation of the monitoring process and the possibility of remote supervision make this solution particularly attractive for inexperienced users and those who want more control over their aquarium.

Table 1. Summary of two aquarium models

No.	Aspects analysed	Traditional aquarium	Smart aquarium
1.	Water parameter monitoring	Periodic, manual measurement of selected parameters	Continuous, automatic monitoring of multiple parameters
2.	Accuracy of control	Depends on user experience	Independent of the user, based on measurement data
3.	Response to environmental changes	Delayed, manual	Immediate, manual, or automatic
4.	Parameter stability	Limited, susceptible to fluctuations	Limited, susceptible to fluctuations
5.	User workload	High	Low
6.	Risk of human error	High	Limited
7.	Remote monitoring capability	Lack	Yes (mobile app)
8.	Aquarium status notifications	Absent or manual observation	Automatic alerts and signaling
9.	Initial costs	Low	High
10.	Operating costs	Permanent, user-dependent	Optimized through automation
11.	Safety of organisms	Dependent on the regularity of service	Enhanced through constant monitoring

ACKNOWLEDGEMENTS

The work was created as a result of a project carried out as part of project-based learning (PBL) in the 13th competition under the Initiative of Excellence – Research University program, Faculty of Mechanical Engineering, Silesian University of Technology.

BIBLIOGRAPHY

1. M.Sahaya Sheela, S.RaviChand, S. Gopalakrishnan, Shruti Bhargava choubey, M Gopianand, J.Jasmine Hephzipah *Empowering Aquarists aComprehensive Study On IOT-Enabled Smart Aquarium Systems For Remote Monitoring And Control,* Babylonian

Journal of Internet of ThingsVol.2024, pp. 33–43 https://doi.org/10.58496/BJIoT/2024/005

2. Balasubramani S., Aakash Ram S., Akshay Bharadwaj S., Bennet Niffin N. *Smart Aquarium Management System,* 2020, doi:10.3233/APC200196
3. K. Domanus, I. Pietrzkiewicz, *Wpływ pH, metali ciężkich oraz siarczanów występujących w wodach Ojcowskiego Parku Narodowego na życie w oczku wodnym, 2016.*
4. *A Balanced Aquarium – Testing and Analysis*, https://en.zolux.com/tips-from-the-pros/balanced-aquarium [dostęp 16.12.2025].
5. *Ogrzewanie w akwarium – jak zapewnić odpowiednią temperaturę?, https://akwarium.co.pl/poradnik-akwarystyczny/ogrzewanie-w-akwarium-jak-zapewnic-odpowiednia-temperature/ dostęp [16.12.2025].*
6. S. Capel-Cuevas, Poseł Cuéllar, I. de Orbe-Payá, MC Pegalajar, LF Capitán-Vallvey *Full-range optical pH sensor based on imaging techniques,* Analytica Chimica Acta Tom 681, 1–2, 2010, pages 71–81, https://doi.org/10.1016/j.aca.2010.09.033
7. *Jak działa czujnik mętności ? - https://www.boquwater.com/a-how-does-a-turbidity-sensor-work.html [dostęp 16.12.2025].*
8. *https://akwa-pro.pl/akwarium-low-tech-vs-high-tech-ktore-wybrac*

TalentDetector

9th January 2026
Gliwice, Poland

DEPARTMENT OF ENGINEERING MATERIALS AND BIOMATERIALS
FACULTY OF MECHANICAL ENGINEERING
SILESIAN UNIVERSITY OF TECHNOLOGY

INTERNATIONAL STUDENTS SCIENTIFIC CONFERENCE

Structured Methodology for Selecting and Evaluating Distance Sensors in Wearable Obstacle Detection Systems

Wiktoria Głuch[a], Jarosław Paduch[b]

[a] *Student of Silesian University of Technology, Faculty of Automatic Control, Electronics and Computer Science,*
email: wg305182@student.polsl.pl
[b] *Silesian University of Technology, Faculty of Automatic Control, Electronics and Computer Science, Department of Graphics, Computer Vision and Digital Systems*
email: jaroslaw.paduch@polsl.pl

Abstract: A structured methodology for evaluating miniature distance sensors in wearable obstacle detection systems for the visually impaired is presented. Three sensor types (60 GHz radar, VL53L1X, VL53L5CX) were compared based on accuracy, material response, detection angle, and energy consumption. Results demonstrate distinct advantages for each sensor depending on specific application needs. The approach supports informed sensor selection and can be adapted for other devices and real-world testing. This enables the design of future wearable aids driven by experimental data rather than catalogue specifications.

Keywords: wearable devices, distance sensors, obstacle detection, visually impaired, sensor evaluation

1. INTRODUCTION

Blind and visually impaired people, even when highly trained in using a white cane, still often collide with obstacles at torso and head height, such as glass panes, information boards, shop windows, or protruding architectural features [1,2]. The cane provides excellent information about the ground and nearby objects, but does not guarantee early detection of obstacles further away or higher up.

To overcome this limitation, electronic mobility aids are being developed as wearable devices that assist with spatial orientation through vibration or sound. These systems, among others, utilise ultrasonic sensors, cameras, Time-of-Flight (ToF) distance sensors, and millimetre-wave radars. Most research published focuses on designing a specific device and user experience. Meanwhile, the choice of distance sensors is often primarily based on datasheet specifications and the knowledge of the designer [1, 2].

This paper outlines a systematic method for comparing distance sensors used in wearable obstacle-detection systems. Instead of focusing on a specific device shape, three sensors

representing different technologies are analysed, and the experimental results demonstrate their performance in typical pedestrian movement scenarios.

2. AIM, SCOPE AND TESTED SENSORS

It is assumed that the future wearable device should alert the user to obstacles within 0.2–2.0 m, that is, at distances allowing a realistic reaction time while walking. The system should be battery-powered; therefore, alongside accuracy, energy consumption and the potential for pulsed operation are important considerations. Three miniature distance sensors were chosen for the study.

- **60 GHz pulsed radar (Acconeer XM125 with A121 sensor)** – a millimetre-wave radar that measures distance based on reflections of short electromagnetic pulses. It is practically insensitive to lighting and obstacle colour, can operate through thin plastic housings, and at refresh rates of a few hertz exhibits very low average power consumption [10]. A single measurement provides a vector of many amplitude samples as a function of distance.
- **Single-zone ToF sensor VL53L1X** – an optical sensor made by STMicroelectronics. It measures the time-of-flight of a light pulse within a narrow field of view and provides a single distance value, with a maximum range of 4 m and a measurement frequency of up to 50 Hz [8].
- **Multi-zone ToF sensor VL53L5CX** – a newer generation ToF sensor that offers an 8×8 depth map across a wide field of view, with a range of up to 4 m and a measurement frequency of up to 60 Hz [9].

In the literature, similar sensors are mainly discussed in the context of mobile robots, environment mapping, and object property recognition [3, 6]. These studies show, among other things, that low-cost ToF sensors can be used for obstacle detection and the creation of simple depth maps [3], that a programmable region of interest enables the measurement area to be narrowed [4], that sensor configuration significantly affects accuracy, and that accuracy can be enhanced by combining readings or employing multiple devices [5]. Furthermore, ToF data can be utilised to identify object properties within more complex control systems [6].

In this paper, these findings form the basis for designing the distance range, test scenarios, and analysed parameters. The sensors are evaluated from the perspective of a wearable system supporting a user with visual impairment, without specifying any body-mounting method.

3. METHODOLOGY

All three sensors were tested on a standard test bench (as shown in Figure 1) across four types of experiments: distance measurement, material response, angular characteristics, and energy consumption.

3.1 Distance measurements test

The sensors were mounted sequentially on the same rigid holder at a height similar to that of a standing person's torso. The sensor’s axis was horizontal and pointed directly ahead along the measurement line. The room conditions, especially the lighting, remained constant, and no objects apart from the test obstacles were moved during the measurement.

On the floor, along the sensor axis, a sheet of graph paper was laid out with marked points indicating distances of 0.2, 0.4, 0.6, ..., 2.0 m from the sensor. At each of these points, a flat cardboard obstacle was positioned perpendicular to the sensor axis, and the distance was additionally verified with a handheld laser rangefinder. For each sensor and each distance, a series of 50 consecutive readings was recorded. From these, the mean measured distance, the standard deviation, and the mean error relative to the reference distance were calculated. For the VL53L5CX, the central cell of the 8×8 matrix was analysed to ensure the results are comparable with those of single-zone sensors.

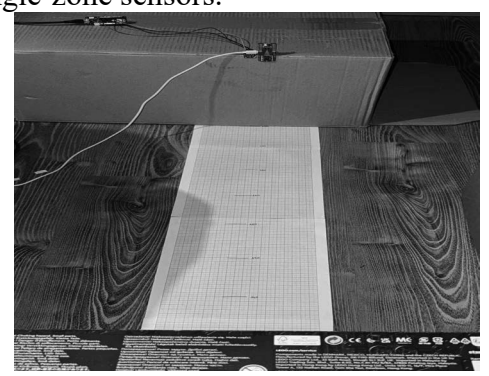

Figure 1. Measurement test bench setup

3.2 Material response test

In the following scenario, the impact of obstacle materials was examined. Instead of the cardboard target, the following flat obstacles were placed along the measurement line: a mirror, a glass pane, and a thin sheet of transparent plastic, each positioned at, for example, 0.5 m or 1.0 m from the sensor. For glass and plastic, an extra series of measurements was performed with a cardboard sheet behind the transparent obstacle. This aimed to determine whether the sensor mainly detects the front material or the object behind it. Based on 50 measurements per setup, the results were categorised as: obstacle detected, partially detected (unstable), or not detected.

3.3 Angular characteristics test

The third type of experiment examined the angular range within which the sensor can reliably detect an obstacle at about 1 m. The sensor remained stationary while the obstacle (a suitcase) was placed at a fixed distance and moved along an arc at angles of 20°, 40°, 60°, 80°, 100°, and 120° relative to the sensor axis (Figure 2). The angular positions were measured using a protractor and a line laser (Figure 3). For each angle, a series of readings was taken to determine whether the sensor still reported a distance close to 1 m (obstacle visible) or mainly measured the distant background.

Figure 2. Setup for measuring angular characteristics

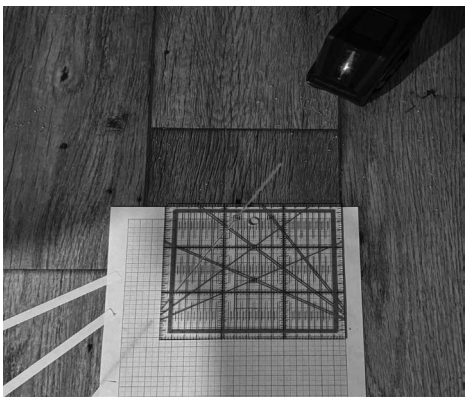

Figure 3. Setting angles with a line laser and grid

3.4 Energy consumption test

The final stage concentrated on energy consumption. Based on datasheets and bench measurements, sleep modes, intermediate states, and active measurement states were analysed for each sensor [8, 9, 10]. Then, the average current was estimated for typical measurement frequencies (e.g., 1Hz) during pulsed operation, where the sensor briefly wakes up, performs a measurement, and returns to a low-power state.

4. TESTS RESULTS

4.1 Results of accuracy and repeatability tests

The comparison of measurement results for the three distance sensors is summarised in the combined plot in Figure 4. The horizontal axis shows the actual distance, while the vertical axis displays the mean distance measured by each sensor. Each point represents the average of 50 samples, and the error bars indicate standard deviations. For reference, the ideal line y = x is also included.

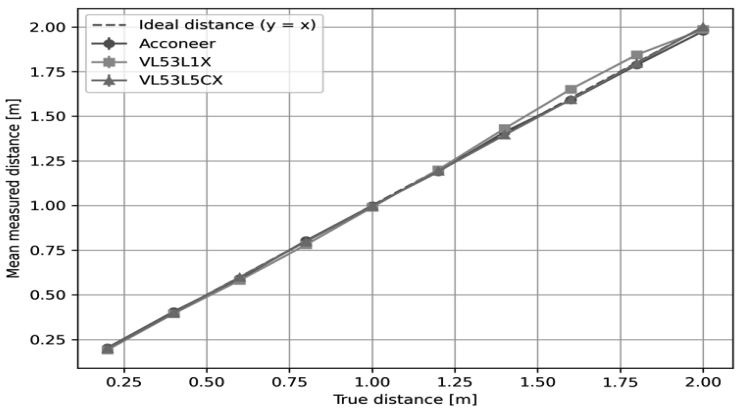

Figure 4. Mean measured distance against actual distance for the three sensors.

The results indicate that all three sensors measure distances within the 0.2–2.0 m range with sufficient accuracy for obstacle detection. The curves stay close to the ideal line, and differences between sensors only become evident when analysing the detailed errors and variations.

The 60 GHz radar produces, in a single measurement, a vector of multiple amplitude samples relative to distance; a typical profile displays several local maxima corresponding to different reflections. To find a single distance value, the central peak should be selected, and smaller peaks disregarded. After this process, the average distance for a specific target position remains close to the reference value. However, the standard deviation, particularly at 0.2 m, is higher than that of the ToF sensors. This suggests a small "dead zone" directly in front of the sensor, with high accuracy above roughly 0.4 m.

The single-zone ToF sensor VL53L1X serves as a reliable rangefinder: for most distances, the 50-point cloud is quite narrow, and average errors are low. However, the plot in Figure 4 indicates that around 1.4–1.8 m, the standard deviation of VL53L1X is slightly higher than that of the other sensors. Even so, the mean values at 0.2, 1.0, and 2.0 m stay close to the y = x line, and the accuracy remains more than adequate for obstacle detection.

The VL53L5CX sensor, analysed within the central matrix cell, achieves comparable or even superior accuracy to VL53L1X locally. At short distances, the spread is minimal. Around 1.4 m, the error margins are noticeably smaller than for VL53L1X, as shown in Figure 4. At 2.0 m, the spread increases but still remains at a level that allows clear obstacle recognition. An added benefit of this sensor is that, apart from the central measurement, it provides data from the other 63 zones, which more advanced algorithms can utilise.

4.2. Results of material tests

In the second stage, the sensors' ability to detect different flat obstacle materials was analysed: a mirror, a thin sheet of transparent plastic, and a glass pane. The qualitative results are summarised in Table 1.

Table 1. Detection of individual obstacles depending on the sensor

Sensor	Mirror	Plastic	Glass
VL53L5CX	yes	partially	yes
VL53L1X	yes	no, distance to cardboard slightly biased	yes
Acconeer	yes	no	yes

Table 1 shows that all three sensors reliably identify both the mirror and the glass. This indicates that a wearable system with these sensors can effectively warn users when approaching glass doors, shop windows, or mirrored surfaces.

The most notable differences occur with the thin plastic sheet. The radar is essentially "blind" to this material – the readings mainly reflect the cardboard behind the sheet. VL53L1X clearly shows biased, less stable distances, indicating that the algorithm sometimes detects the echo from the plastic and sometimes from the cardboard. VL53L5CX detects the plastic only in certain zones, hence the "partially" marking: in the raw data, this appears as the simultaneous presence of near and far distance values. In practice, thin, transparent plastics can be more challenging and may require either additional signal processing (for example, selecting the nearest credible distance) or a suitably designed housing to mitigate this issue.

4.3 Results of angular characteristic tests

The comparison of the angles at which each sensor can reliably detect an obstacle at roughly 1m distance is depicted in Figure 5. The horizontal axis shows the angle relative to the sensor's axis, while the vertical axis lists the three analysed sensors.

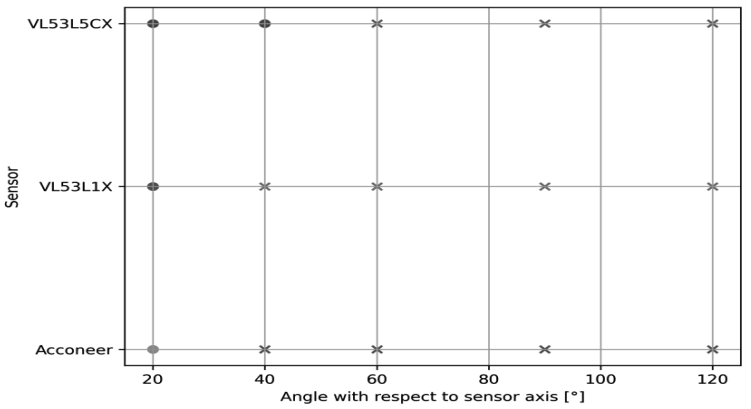

Figure 5. The maximum angle at which each sensor can still reliably detect an obstacle at approximately 1 metre.

The VL53L5CX sensor, due to the wide field of view specified in its datasheet [9], maintains accurate detection even at relatively large angular offsets. VL53L1X, as expected from the manufacturer's data [8], has a noticeably narrower angular range but operates very reliably within this range.

The 60 GHz radar has a relatively wide field of view according to its specification [10]. However, in the experiments, the effective angle of stable detection proved to be noticeably smaller: For larger deviations from the axis, echoes from the room walls dominate, and the obstacle at 1m is no longer clearly visible. This discrepancy between the catalogued field of view and the practical "useful" angle aligns with observations from radar-based human activity recognition, where a significant portion of the signal energy is often distributed over background and clutter [7].

For the designer of a wearable system, this means that the VL53L1X is well-suited as a precise sector sensor, and the VL53L5CX can cover a wide area with a single device. At the same time, the radar, despite a broad nominal field of view, requires careful selection of orientation, operating range, and signal processing strategy to achieve reliable obstacle detection.

4.4 Results of energy consumption tests

From a wearable system perspective, it is important not only how accurately a sensor measures distance but also how much energy it consumes during typical measurement rates. The findings from current measurements were combined with information from the manufacturers' datasheets [8, 9, 10].

For VL53L1X, the typical current during active ranging is approximately 15–20 mA at a supply voltage of around 3 V, depending on the timing budget and measurement frequency [8]. The sensor offers both short- and long-range modes with adjustable timing, enabling a balance between accuracy, range, and energy consumption. In standby, the current drops to a few microamperes, and in a dedicated ultra-low-power mode, the device can operate as a simple presence detector with a current below 0.1 ma. If measurements are performed in a pulsed manner – a single measurement lasting several tens of milliseconds every 0.5-1 s, the average current decreases to a few milliamperes or less, which remains acceptable even with multiple sensors in a single device.

VL53L5CX demands more energy but offers richer spatial data. According to the datasheet, in low-power idle mode, the current is around microamperes; in high-performance idle,

approximately 1–3 mA; and during active measurement of a full 8×8 frame, typically 45–80 mA, depending on configuration and frequency [9]. In continuous operation at a high refresh rate, this results in tens of milliamperes of average current, which is unattractive for wearable devices. However, using pulsed operation-short wake-up, measurement, and return to sleep-significantly reduces average consumption: with one frame per second and a short measurement time, the average current can be lowered to a few milliamperes, which is acceptable given the 64 measurement zones.

The XM125 radar module has a different energy profile. According to its datasheet, for typical distance-measurement configurations, the average power ranges from tenths to hundredths of a milliwatt at refresh rates of about 0.1-1 Hz, and a few milliwatts at 10 Hz [10]. Converted to current at 1.8 V, this equates to average values from hundredths of a milliampere to a few milliamperes. In sleep modes, the current drops to the microampere level. In practice, the radar can therefore be up to ten times more energy-efficient than the multi-zone ToF sensor at similar measurement frequencies, albeit with more complex signal processing.

Comparing the three sensors in terms of energy, VL53L1X offers a good balance between accuracy and power consumption, VL53L5CX requires higher peak currents but, thanks to pulsed operation, can be maintained within a few milliamperes on average, and the XM125 radar has potentially the lowest average power consumption, especially at low refresh rates.

5. DISCUSSION

The experiments show that all three analysed sensors are suitable for wearable obstacle detection systems, although each has a distinct “specialisation”.

The 60 GHz radar is notable for its resilience to lighting and surface colour, its capacity to operate behind thin housings, and its very low average power consumption at low measurement frequencies [7,[10]. However, its data require filtering and identifying a dominant peak, and the effective angular range for reliable detection is narrower than the nominal field of view. Consequently, it is well-suited as a robust, complementary sensor.

The single-zone ToF sensor VL53L1X is a highly reliable and easy-to-understand rangefinder [8]. It is ideally suited for monitoring several narrow sectors in front of the user, with each sensor assigned to a specific direction. Its limitations include a narrow field of view and difficulties with thin, transparent plastics, but overall, the device is relatively lightweight and simple to integrate into a battery-powered system.

The multi-zone VL53L5CX offers accurate and detailed spatial information [9]. A single device can replace multiple single-zone sensors and simultaneously provide data on obstacle direction, supporting the development of more “intelligent” vibrotactile patterns and advanced scene interpretation algorithms, similar to those used in robotics and prosthesis control [6]. However, this necessitates a more powerful microcontroller and a carefully planned energy-saving strategy to maintain the average current draw within acceptable limits.

6. CONCLUSIONS

This paper presents and demonstrates a systematic approach for comparing distance sensors in wearable systems assisting people with visual impairments. Based on the experiments conducted, the following conclusions can be drawn:

- The 60 GHz radar is a highly energy-efficient and durable sensor that resists environmental factors.
- The VL53L1X is a highly accurate rangefinder with a narrow field of view and moderate energy consumption.
- VL53L5CX is the most versatile sensor, especially when information about obstacle direction over a broader field of view is crucial.

The proposed methodology can be applied directly to other sensors and expanded through tests in motion and end-user studies. This approach can support the design of future wearable devices by offering accurate, comparable experimental results instead of relying solely on catalogue parameters.

BIBLIOGRAPHY

1. M. Hersh, *Wearable Travel Aids for Blind and Partially Sighted People: A Review with a Focus on Design Issues*, Sensors, 22(14), 5454, 2022.
2. P. Xu et al., *Wearable Obstacle Avoidance Electronic Travel Aids for Blind and Visually Impaired Individuals: A Systematic Review*, IEEE Access, 11, 66587–66613, 2023.
3. N.Laković et al., *Application of Low-Cost VL53L0X ToF Sensor for Robot Environment Detection*, INFOTEH-Jahorina, 2019.
4. R. M. Jans, A. S. Green, L. J. Koerner, *Characterization of a Miniaturized IR Depth Sensor With a Programmable Region-of-Interest That Enables Hazard Mapping Applications*, IEEE Sensors Journal, 20, 5213–5220, 2020.
5. S.Komarizadehasl et al., *Low-Cost Sensors Accuracy Study and Enhancement Using Multiple Distance Sensors and Arduino Based Data Acquisition System*, Applied Sciences, 12(6), 3186, 2022.
6. K.Baraković et al., *Time-of-Flight Sensing for the Recognition of Object Properties in Prosthesis Control*, proc. konf. IcETRAN.
7. F.Luo, *Applications and Challenges of Radar-Based Human Activity Recognition*, proc. IEEE SmartIoT, 2024.
8. STMicroelectronics, *VL53L1X – A new generation, long distance ranging Time-of-Flight sensor*, Datasheet, DocID031281 Rev. 3, 2018.
9. STMicroelectronics, *VL53L5CX – Time-of-Flight 8×8 multizone ranging sensor with wide field of view*, Datasheet, DS13754 Rev. 1, 2021.
10. Acconeer AB, *XM125 Entry+ Module – Datasheet v1.2*, 2023.

TalentDetector

9th January 2026
Gliwice, Poland

DEPARTMENT OF ENGINEERING MATERIALS AND BIOMATERIALS
FACULTY OF MECHANICAL ENGINEERING
SILESIAN UNIVERSITY OF TECHNOLOGY

INTERNATIONAL STUDENTS SCIENTIFIC CONFERENCE

CoCrMoNi High-Entropy Alloys - A Review of Microstructure, Properties, and Applications

Kacper Górski [a], Natalia Bujak [a], Justyna Czyrw [a], Aleksandra Piechowiak [a], Łukasz Opara [a], Wiktor Łaziński [a], Inez Kredowska [b], Wirginia Pilarczyk [b]

[a] Students of Silesian University of Technology, Faculty of Mechanical Engineering
email: kg303948@student.polsl.pl
[b] Silesian University of Technology, Faculty of Mechanical Engineering, Department of Engineering Materials and Biomaterials
email: wirginia.pilarczyk@polsl.pl

Abstract: High-entropy alloys (HEAs) are a class of metallic materials characterized by the absence of a single dominant element and the presence of multiple principal components in near-equiatomic proportions. Among them, CoCrMoNi system have attracted increasing attention due to their favorable mechanical properties, wear resistance, and corrosion stability, particularly in biomedical applications. This review summarizes current research on CoCrMoNi and related alloy systems, focusing on the relationships between chemical composition, microstructure, processing routes, and resulting properties. Reported studies indicate that FCC-dominated microstructures provide high ductility and toughness, while secondary phases such as BCC and intermetallic compounds contribute to increased hardness and wear resistance. The influence of processing methods, heat treatment, and surface modifications on functional performance is also discussed, highlighting key trends governing the behavior of CoCrMoNi high-entropy alloys.

Keywords: high-entropy alloys, CoCrMoNi, microstructure, biomedical materials,

1. INTRODUCTION

Modern materials engineering constitutes the foundation of technological development across all branches of industry. From electronics, automotive and aerospace engineering to energy and biomedical applications, materials are required to have a combination of high mechanical strength, corrosion resistance, thermal stability, and good processability. The primary group of structural materials consists of metals and their alloys, which have accompanied humanity for centuries, evolving from simple tools of the Bronze Age to advanced alloys used in jet engines and gas turbines [1].

Traditional alloy design is usually based on one dominant element, such as iron in steels or nickel in superalloys, with additional alloying elements added in smaller amounts. While this approach allows for targeted modification of physicochemical properties, it is increasingly

proving insufficient in the face of growing operational and environmental demands [4]. The need to develop materials capable of operating under extreme conditions has led to increased interest in unconventional alloy design strategies, including new classes of materials such as amorphous alloys and high-entropy alloys (HEAs) [8]. This growing research interest is reflected in the steadily increasing number of scientific publications on high-entropy alloys reported over recent years (Figure 1).

In response to these needs, high-entropy alloys were developed, first proposed by Jien-Wei Yeh in 2004 [6]. This concept is based on the use of five or more principal elements in near-equiatomic molar proportions, with each element typically present in the range of 5-35% [2]. Unlike traditional alloys, all elements in HEAs play an equivalent role, leading to a fundamentally new philosophy of materials design [4]. Within this broad class of materials, particular attention has been directed toward CoCrMoNi systems due to their favorable combination of mechanical and corrosion-related properties [2].

The CoCrMoNi alloy system, known from its application in Vitalium-type alloys, plays a key role in biomedical engineering due to its exceptional properties. It is biocompatible and exhibits high strength and ductility, as well as excellent corrosion resistance, ensuring long-term implant durability [14]. These characteristics make it an excellent choice for the production of endoprostheses and other dynamically loaded components.

The aim of this article is to compare available research results, identify trends in materials engineering, and to understand how chemical composition and processing affect the microstructure and properties of materials.

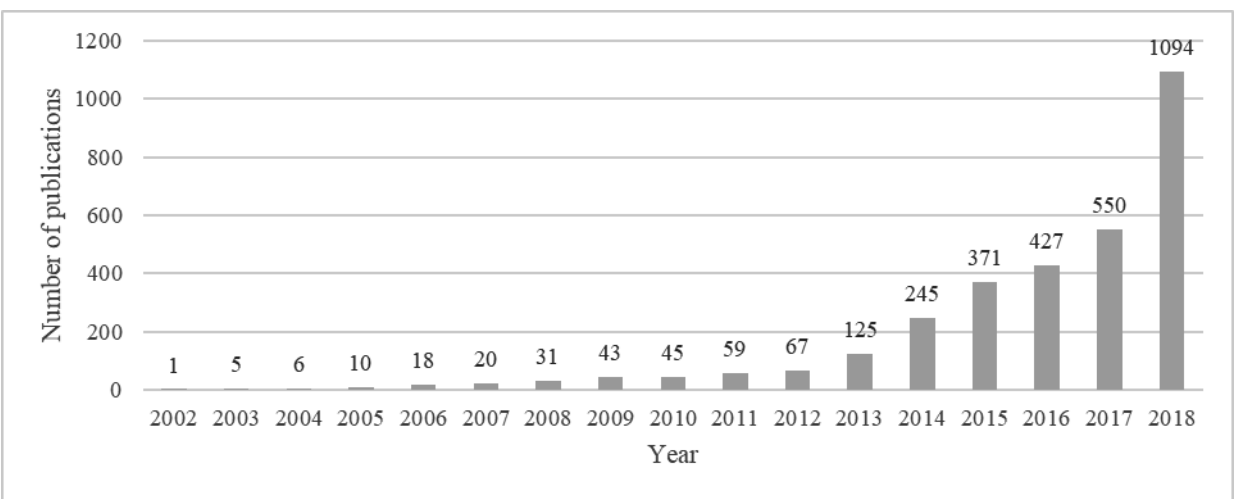

Figure 1. Annual number of publications on high-entropy alloys, showing the increasing research interest over time [2].

2. THEORETICAL BACKGROUND OF HIGH-ENTROPY ALLOYS

2.1. Fundamental concepts and core effects of high-entropy alloys

High-entropy alloys are modern metallic materials that differ from conventional alloys by the absence of a single dominant element [2]. They typically consist of four or more principal elements in similar molar proportions, usually within the range of 5-35%. The unique properties of HEAs arise from the so-called four core effects: high configurational entropy,

severe lattice distortion, sluggish atomic diffusion, and the cocktail effect [4]. These four core effects, which govern the behavior of high-entropy alloys, are schematically illustrated in Figure 2.

The high configurational entropy effect plays a key role in HEA research. It suggests that a high configurational entropy in alloys containing five or more elements in near-equiatomic proportions may promote the formation of solid solutions rather than intermetallic compounds [2]. However, comparisons of configurational entropy with thermodynamic quantities of pure metals or selected compounds are often simplified. They do not account for differences between specific alloy systems. Moreover, both solid solutions and intermetallic phases can exhibit a wide range of stabilities. Therefore, a realistic assessment of the influence of configurational entropy on phase stabilization should be based on classical thermodynamic principles and microstructural data [4].

The lattice distortion effect refers to significant distortions of the crystal lattice in complex, highly concentrated phases caused by differences in atomic sizes of the constituent elements [3]. These distortions are assumed to be more pronounced in high-entropy alloys than in conventional alloys and may influence material properties such as X-ray diffraction peak broadening, increased hardness, and reduced electrical and thermal conductivity [2].

The sluggish diffusion effect assumes that diffusion processes in high-entropy alloys occur more slowly than in traditional alloys. Indirect observations, including the formation of nanocrystalline and amorphous phases during solidification, as well as qualitative interpretations of microstructural stability during cooling, form the basis for this assumption [4].

The cocktail effect, introduced by S. Ranganathan, refers to a synergistic phenomenon in which the properties of a material are superior and less predictable than those expected from a simple rule-of-mixtures approach [2]. This effect has been associated with bulk metallic glasses, highly elastic metals, and high-entropy alloys, all characterized by complex chemical compositions.

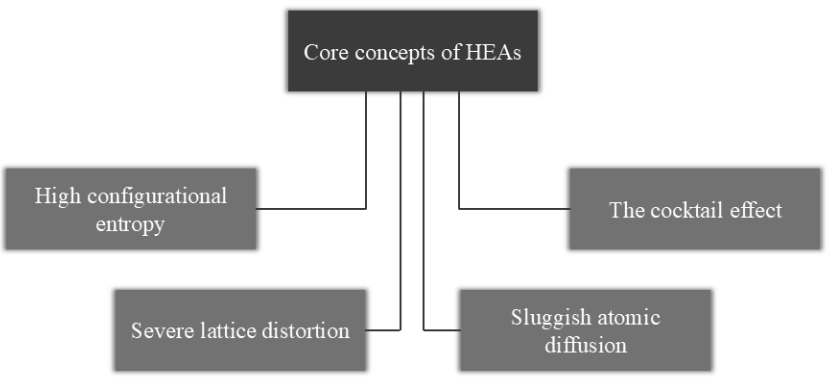

Figure 2. Schematic illustration of the four core effects of high-entropy alloys [2, 6].

2.2. Composition, microstructure, and properties of high-entropy alloys

The chemical composition of high-entropy alloys plays a fundamental role in determining their phase stability, microstructural features, and resulting mechanical and functional properties [4]. Due to the presence of multiple principal elements in comparable concentrations, HEAs commonly form simple solid-solution phases with FCC, BCC, or mixed FCC+BCC crystal structures, rather than complex intermetallic compounds [7].

In general, FCC-dominated microstructures are associated with high ductility, toughness, and resistance to crack propagation, whereas BCC-based structures tend to exhibit higher hardness and strength at the expense of plasticity [3]. The coexistence of multiple phases may provide a balance between strength and ductility; however, excessive phase separation or precipitation of brittle intermetallic phases can negatively affect mechanical performance [4].

Microstructures formed during solidification are often strongly non-equilibrium in nature, which promotes chemical segregation and the formation of dendritic morphologies [4]. The solidification rate and subsequent thermal history significantly influence phase distribution, homogeneity, and long-term stability. Rapid solidification typically leads to refined microstructures and enhanced solid-solution strengthening, while slower cooling favors chemical homogenization and reduced segregation [7].

2.3. Heat treatment effects

Heat treatment conducted above approximately half of the melting temperature significantly affects the microstructure of high-entropy alloys, driving it closer to thermodynamic equilibrium [4]. Studies of alloys examined in both the as-cast and annealed conditions indicate that this process leads to a reduction in the fraction of solid solutions and an increased presence of intermetallic phases. While the precipitation of intermetallic phases enhances hardness and strength, it may also reduce ductility [3]. A microstructure closer to equilibrium provides improved thermal stability and more predictable material behavior.

Heat treatment also influences elemental redistribution and phase stability in high-entropy alloys. Diffusion processes activated at elevated temperatures promote partial homogenization of the chemical composition, while simultaneously enabling the nucleation and growth of secondary phases in energetically favorable regions [4]. As a result, the spatial distribution, morphology, and volume fraction of intermetallic precipitates can be effectively controlled through appropriate selection of annealing temperature and time [2].

The final microstructure obtained after heat treatment therefore reflects a balance between strengthening mechanisms and the preservation of sufficient plasticity. While increased precipitation generally improves hardness and wear resistance, excessive growth or continuous networks of brittle phases may adversely affect fracture resistance [3]. Consequently, heat treatment represents a critical tool for tailoring the microstructural state of high-entropy alloys in accordance with specific performance requirements, enabling more reliable and application-oriented materials design [4].

3. REVIEW OF RESEARCH ON Co-Cr-Mo-Ni ALLOYS

3.1. Microstructure and phase composition

In most reported studies on CoCrMoNi and related alloy systems, the face-centered cubic (FCC) phase is dominant, particularly in alloys containing significant amounts of Ni and Co, and occasionally Mn [12]. The FCC structure is associated with high ductility, good toughness, and strong resistance to crack propagation, although its hardness is generally lower than that of body-centered cubic structures. As a result, FCC-based microstructures are often favored in applications requiring damage tolerance and mechanical reliability [3].

The body-centered cubic (BCC) phase occurs less frequently and is typically observed in alloys with increased molybdenum or chromium content [11]. The presence of the BCC phase

contributes to higher hardness and improved wear resistance; however, it may also reduce ductility depending on its volume fraction and distribution within the microstructure depending on its volume fraction and spatial distribution in the microstructure [3].

Intermetallic phases of the Laves type, such as $CoMo_2$, have been reported primarily in interdendritic regions, particularly in alloys with high Mo and Cr contents. These phases locally increase hardness and wear resistance, but their brittleness can reduce overall ductility and promote crack initiation under mechanical loading [4].

Elemental segregation is a characteristic feature of these alloy systems. Molybdenum and chromium tend to segregate into interdendritic regions, whereas cobalt and nickel are concentrated within the primary dendritic matrix [10]. This segregation behaviour has been consistently observed in both conventionally cast alloys and laser-cladded materials. It therefore appears to be governed primarily by thermodynamic and kinetic factors rather than solely by the processing route [4].

The manufacturing method has a pronounced influence on microstructural development. Conventional casting is characterized by relatively slow cooling rates. This processing route leads to coarse dendritic structures, a more homogeneous matrix, reduced elemental segregation, and a lower volume fraction of Laves-phase precipitates [4]. In contrast, laser cladding involves rapid solidification, resulting in fine dendritic morphologies, ultrafine interdendritic structures, and more pronounced molybdenum segregation [10]. Subsequent heat treatment or aging promotes intermetallic phase precipitation in interdendritic regions, increasing hardness and wear resistance but potentially reducing ductility [11].

Table 1. Typical phases observed in CoCrMoNi alloys and their influence on properties [4].

Phase	Crystal Structure	Typical location	Effect on properties
FCC Solid Solution	FCC	Primary matrix	High ductility and toughness, good crack resistance, moderate hardness
BCC Solid solution	BCC	Matrix or secondary regions	Increased hardness and strength, reduced ductility
Laves phases (e.g. Co-Mo rich)	Intermetallic	Interdendritic regions / precipitates	Enhanced hardness and wear resistance, potential embrittlement
σ / μ phases	Intermetallic	Interdendritic regions / precipitates	Strengthening and thermal stability, reduced fracture toughness if excessive

3.2. Mechanical properties

The mechanical behavior of CoCrMoNi-based alloys is strongly influenced by their phase composition and microstructural features [3]. Hardness is particularly sensitive to the presence of intermetallic phases and carbides, which locally increase local hardness and resistance to abrasive wear. However, excessive precipitation of such phases may lead to a reduction in ductility and toughness [4].

Fracture resistance depends largely on the continuity of the matrix and the extent of elemental segregation. Large and continuous Laves-phase precipitates act as preferential sites for crack initiation, increasing the susceptibility of the material to brittle fracture under mechanical loading [11].

Tribological studies, commonly conducted using the pin-on-disk configuration, indicate that the presence of carbides and a dense, sintered microstructure contributes to a reduction in the friction coefficient and volumetric wear [10]. These effects are attributed to improved load-bearing capacity and enhanced resistance to surface degradation mechanisms.

The evaluation of hardness and wear resistance constitutes a critical step in assessing the functional performance of high-entropy and related multicomponent alloys [4]. It provides insight into their behavior under mechanical load, microstructural stability, and suitability for applications requiring high durability. Vickers hardness testing is widely employed due to its sensitivity to solid-solution strengthening and microstructural homogeneity. In this method, a diamond indenter with a defined geometry is pressed into the material surface under a specified load, and the diagonal lengths of the indentation are measured to determine the hardness value.

Tribological performance is typically assessed using pin-on-disk tests, which enable the evaluation of resistance to abrasive and adhesive wear [10]. During testing, parameters such as friction coefficient, friction force, and contact temperature are monitored, allowing for an assessment of tribological stability over time. Post-test analysis of wear tracks provides additional information on dominant surface degradation mechanisms and differences in material behavior under mechanical stress.

3.3. Corrosion Resistance and Surface Modifications

Beyond bulk mechanical properties, the functional performance of CoCrMoNi alloys is strongly influenced by surface condition and applied surface modification techniques. Tribological performance can be further enhanced through surface modifications [10]. Carbon-based coatings have been shown to significantly reduce friction and wear, particularly in matrices enriched with carbides. Sintered high-entropy alloys often exhibit superior abrasive wear resistance due to their dense, compact microstructure and fine precipitate distribution.

In biomedical environments, CoCrMo-based alloys demonstrate high corrosion resistance, primarily due to the formation of a stable Cr_2O_3 passive layer [14]. This passive film effectively limits anodic dissolution and protects the material against localized corrosion. However, certain surface modifications, such as sodium implantation, may reduce corrosion resistance despite the formation of an amorphous surface layer. In contrast, carbon-based coatings generally increase corrosion potential, reduce anodic current densities, and improve resistance to pitting corrosion, making them particularly attractive for biomedical applications [13].

3.4. Influence of chemical composition on microstructure and properties

The properties of CoCrMoNi-based alloys are governed by the combined effects of their constituent elements. Each of which plays a distinct yet complementary role in determining microstructural stability, mechanical performance, and corrosion resistance. Rather than acting independently, cobalt, chromium, molybdenum, and nickel interact synergistically, leading to a balanced combination of strength, ductility, and environmental resistance [2].

Cobalt serves as a key strengthening element, particularly at elevated temperatures. It enhances high-temperature strength and stabilizes the FCC matrix, contributing to thermal stability [12]. The presence of cobalt also positively influences resistance to oxidation and improves the overall durability of the alloy under thermomechanical loading, which is especially important in both biomedical and high-temperature engineering applications [2].

Chromium plays a dominant role in corrosion resistance through the formation of a stable and protective Cr_2O_3 passive layer [11]. In addition to its corrosion-related function, chromium contributes to oxidation resistance at high temperatures and promotes the formation of carbides,

which can increase hardness and wear resistance. Chromium also affects phase stability, potentially stabilizing ferritic phases depending on its concentration and interaction with other alloying elements [2].

Molybdenum is primarily responsible for improving mechanical strength, hardness, and resistance to localized corrosion [11]. Its strong tendency to form carbides and intermetallic phases, such as σ and μ phases or Mo-rich Laves phases, leads to significant strengthening effects, particularly in interdendritic regions. While these phases enhance wear resistance and high-temperature performance, excessive molybdenum segregation may reduce ductility and increase susceptibility to crack initiation [4]. In nickel-containing systems, molybdenum further improves resistance to pitting corrosion and contributes to solid-solution strengthening [14].

Nickel plays a crucial role in stabilizing the FCC matrix. It enhances ductility and toughness by promoting homogeneous plastic deformation and reducing the tendency to brittle fracture [12]. Its presence supports solid-solution strengthening and contributes to improved structural and chemical stability of the alloy. As a result, nickel is an important alloying element in multicomponent systems, including high-entropy alloys, where it facilitates the formation of stable FCC-based microstructures with favorable mechanical performance [2].

The combined presence of Co, Cr, Mo, and Ni results in a microstructure that balances strength and ductility while maintaining excellent resistance to corrosion and oxidation [2]. The synergistic interactions between these elements enable tailoring of microstructural features, such as phase composition and precipitate distribution, through appropriate control of chemical composition and processing conditions. Consequently, CoCrMoNi-based systems are particularly well suited for demanding applications, including biomedical implants, where mechanical reliability, wear resistance, and long-term corrosion stability are critical [14].

Table 2. General role of alloying elements in CoCrMoNi alloys [2].

Element	Main Effect
Co	Strenghtening, thermal stability
Cr	Corrosion resistance, carbide formation
Mo	Solid-solution & intermetallic tendency, increases hardness and wear resistance
Ni	Stabilising FCC, enhancing ductility

4. CONCLUSIONS

The available literature on CoCrMoNi alloys indicates that their properties are primarily governed by the interplay between chemical composition, microstructure, and processing conditions [4]. A predominantly FCC microstructure provides high ductility, toughness, and resistance to crack propagation, which are essential for applications subjected to cyclic and dynamic loading. In contrast, the presence of secondary phases, such as BCC and Mo-rich intermetallic phases, enhances hardness and wear resistance but may reduce ductility if excessive segregation occurs [11].

Processing routes and post-treatment conditions strongly affect phase distribution and microstructural homogeneity [9]. Rapid solidification techniques promote refined microstructures and increased strength, while conventional casting favors more uniform phase distributions. Subsequent heat treatment enables further tailoring of mechanical and thermal stability through controlled intermetallic precipitation [4].

Surface modification plays a key role in improving functional performance, particularly in biomedical environments [13]. Carbon-based coatings effectively reduce friction and wear while enhancing corrosion resistance through stabilization of passive surface layers. The combined optimization of alloy composition, microstructure, and surface condition enables the development of CoCrMoNi-based materials with a balanced combination of mechanical strength, wear resistance, and corrosion stability, making them promising candidates for advanced biomedical and engineering applications [5].

BIBLIOGRAPHY

1. Dobrzański L. A.: Podstawy nauki o materiałach, Wydawnictwo Politechniki Śląskiej, Gliwice, 2012.
2. Murty B. S., Yeh J.-W., Ranganathan S., Bhattacharjee P. P.: High-Entropy Alloys, Butterworth-Heinemann (Elsevier), second edition, 2019.
3. Zhang Y.: High Entropy Materials, Springer, Beijing, 2016.
4. Miracle D. B., Senkov O. N.: A critical review of high entropy alloys and related concepts, Acta Materialia, 122 (2017) 448–511.
5. Cantor B., Chang I. T. H., Knight P., Vincent A. J. B.: Microstructural development in equiatomic multicomponent alloys, Materials Science and Engineering A, 375–377 (2004) 213–218.
6. Yeh J.-W., Chen S.-K., Lin S.-J., Gan J.-Y., Chin T.-S., Shun T.-T., Tsau C.-H., Chang S.-Y.: Nanostructured high-entropy alloys with multiple principal elements, Advanced Engineering Materials, 6 (2004) 299–303.
7. Zhang Y., Zhou Y. J., Lin J. P., Chen G. L., Liaw P. K.: Solid-solution phase formation rules for multi-component alloys, Advanced Engineering Materials, 10 (2008) 534–538.
8. Sharma P., Dwivedi V. K., Dwivedi S. P.: Development of high entropy alloys, Materials Today: Proceedings, 38 (2021) 1956–1961.
9. Alshataif Y. A., Sivasankaran S., Al-Mufadi F. A., Alaboodi A. S., Ammar H. R.: Manufacturing methods, microstructural and mechanical properties evolutions of high-entropy alloys: A review, Journal of Materials Research and Technology, 8 (2019) 4006–4029.
10. Cui G., Han B., Yang Y., Wang Y., Hua C.: Microstructure and tribological property of CoCrFeMoNi high-entropy alloy treated by ion sulfurization, Journal of Materials Research and Technology, 9 (2020) 12624–12634.
11. Zhao M., Zhang Y., Li Y., Wang X.: Effect of Mo content on the high-temperature properties of CoCrFeNi high-entropy alloys, Journal of Materials Research and Technology, 25 (2025) 173–182.
12. Hiyama K., Nakajima T., Sahara R., Ueda K., Narushima T.: Effect of Ni and Fe content on the plastic deformation behavior of Co–Cr–Fe–Ni–Mo alloys: A combined computational and experimental study, Journal of Alloys and Compounds, 1042 (2025) 183927.
13. Akinwekomi A., Akhtar F.: Microstructural, mechanical, and electrochemical characterization of CrMoNbTiZr high-entropy alloy for biomedical application, Materials, 16 (2023) 5320.
14. Qi J., Ma L., Gong P., Rainforth W. M.: Investigation of the wear transition in CoCrMo alloys after heat treatment to produce an HCP structure, Wear, 518–519 (2023) 204649.

TalentDetector

9th January 2026
Gliwice, Poland

DEPARTMENT OF ENGINEERING MATERIALS AND BIOMATERIALS
FACULTY OF MECHANICAL ENGINEERING
SILESIAN UNIVERSITY OF TECHNOLOGY

INTERNATIONAL STUDENTS SCIENTIFIC CONFERENCE

Laser surface modification of tool steel: remelting and alloying with boron carbide

Kacper Górski [a], Zofia Modlińska [a], Oskar Węgrzyn [a], Wojciech Pakieła [b], Mirosław Bonek [b]

[a] Students of Silesian university of Technology, Faculty of Mechanical Engineering
email: kg303948@student.polsl.pl
[b] Silesian University of Technology, Faculty of Mechanical Engineering, Department of Engineering Materials and Biomaterials
email: miroslaw.bonek@polsl.pl

Abstract: Laser surface remelting (LSR) and laser surface alloying (LSA) with boron carbide (B_4C) were applied to tool steel to compare the microstructural characteristics of the modified surface layers. Microstructural observations using light and scanning electron microscopy (SEM) revealed that laser remelting produced a continuous and relatively homogeneous layer with a fine cellular–dendritic structure. In contrast, laser alloying with B_4C resulted in a heterogeneous, composite-like layer containing ceramic particles mechanically embedded in the metallic matrix. Energy-dispersive X-ray spectroscopy (EDS) confirmed local enrichment in boron and/or carbon within the alloyed layer. The results demonstrate fundamental differences between remelting and ceramic-assisted laser alloying as surface modification strategies.

Keywords: laser surface modification, laser surface remelting, laser surface alloying, boron carbide, tool steel, microstructure, hardness

1. INTRODUCTION

Laser surface modification is an effective method for tailoring the surface layer of engineering materials, enabling local changes in microstructure, chemical composition, and functional properties without significantly affecting the core material. The high energy density of the laser beam and very large temperature gradients promote the formation of non-equilibrium structures characteristic of rapid solidification processes [1]. Such relationships between surface microstructure, processing conditions, and functional properties are fundamental issues in surface engineering and have been widely discussed in the literature [2].

One of the laser surface modification techniques is laser surface alloying, which involves introducing an additional material into the molten pool generated by the laser beam. In contrast to laser surface remelting, this process leads to a deliberate change in the chemical composition of the surface layer, allowing controlled modification of its functional properties [3].

A particularly important group of alloying materials consists of ceramic particles, including boron carbide (B_4C), which is characterized by very high hardness, low density, and excellent wear resistance. Due to its high melting temperature and limited wettability by molten metals, B_4C does not fully dissolve in the metallic matrix, favoring the formation of composite-like surface layers [4].

The aim of this study was to investigate the effect of laser surface alloying with B4C on the microstructure and chemical composition of the surface layer of tool steel. The experiments were carried out at constant energetic process parameters while varying the powder feed rate. The effects of laser alloying were evaluated using light microscopy, scanning electron microscopy, and energy-dispersive X-ray spectroscopy allowing identification of the mechanisms responsible for composite layer formation and assessment of the incorporation of ceramic material into the surface layer.

2. MATERIALS AND EXPERIMENTAL PROCEDURE

The substrate material used in the study was tool steel in the form of flat specimens with a regular geometry of 20 x 10 mm. Prior to laser processing, the samples were mechanically cleaned and degreased to ensure repeatable interaction conditions between the laser beam and the material surface. The process parameters are listed in Table 1.

Laser surface remelting was carried out using variable laser power in the range of 1-3 kW at a constant scanning speed of 20 mm/s. The linear energy input was controlled by adjusting the laser power, which enabled the formation of remelted zones with different depths and widths. The remelting process was performed in the form of single tracks using automated laser head movement. The interaction time of the laser beam with a single track was approximately 3-4 s.

Laser surface alloying was performed at constant energetic process parameters, i.e. a laser power of 2 kW and a scanning speed of 20 mm/s, while varying the powder feed rate in accordance with commonly applied principles of laser surface modification [5]. Boron carbide powder was used as the alloying material and was delivered into the laser–material interaction zone using an automatic powder feeder. The B_4C powder feed rate was set to 1 and 2 g/min, which allowed analysis of the influence of ceramic material content on the characteristics of the formed surface layer. During the process, a thin layer of the substrate material was simultaneously melted and B_4C particles were mechanically introduced into the molten pool.

Table 1. Parameters of LSR and LSA processes.

Sample	Laser power, [kW]	Scanning speed, [mm/s]	Powder feed rate, [g/min]
LSR I	1	20	-
LSR II	2		
LSR III	3		
LSA I	2		1
LSA II	2		2

After laser processing, the samples were prepared for microstructural examination, as illustrated by the prepared metallographic cross-sections shown in Figure 1. The preparation procedure included sectioning to obtain cross-sections, mounting in thermosetting resin, mechanical grinding using abrasive papers with grit sizes of 400, 800, and 1200, followed by

polishing to obtain a mirror-like surface. To reveal the microstructure, the specimens were chemically etched using a Nital solution for several seconds.

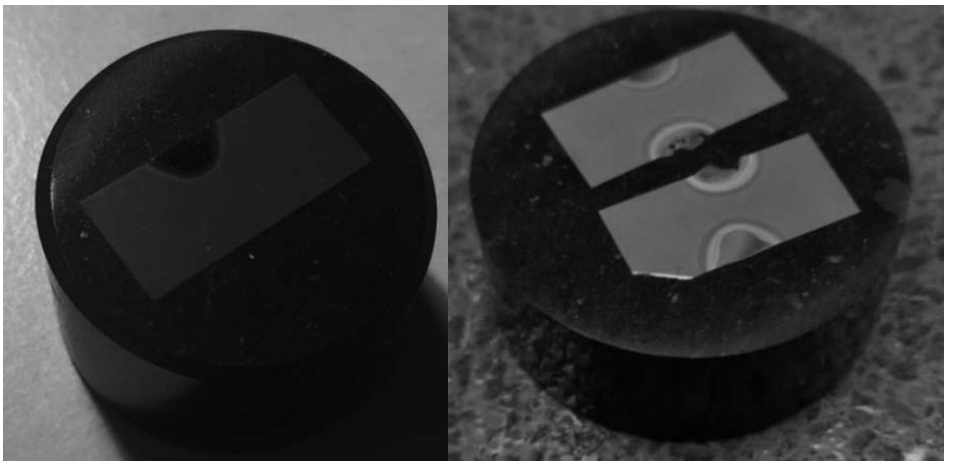

Figure 1. Prepared metallographic cross-sections of samples after laser remelting (left) and laser alloying (right).

Microstructural analysis was carried out using light metallographic microscopy and scanning electron microscopy. SEM observations were performed using secondary electron (SE) and backscattered electron (BSE) detectors, which enabled assessment of the morphology of the remelted and alloyed layers, identification of the heat-affected zone, and evaluation of the distribution of phases and ceramic particles within the metallic matrix.

Chemical composition analysis was performed using EDS coupled with SEM. The measurements were conducted at an accelerating voltage of 15 kV and a magnification of approximately 4000x. Point analyses were carried out in selected micro-areas of the alloyed layer to identify local concentrations of boron and carbon and to evaluate the homogeneity of elemental distribution within the surface layer.

The mechanical properties of the remelted surface layer were evaluated based on Vickers microhardness measurements. The measurements were performed using a 5 x 5 grid of indentation points uniformly distributed over the analyzed surface area. The obtained microhardness values were assigned to their corresponding spatial coordinates, enabling the development of hardness distribution maps and assessment of property uniformity within the surface layer.

3. RESULTS

3.1. Microstructure of modified layers – light microscopy (LM)

Microstructural observations performed using light microscopy enabled evaluation of the geometry and general characteristics of surface layers modified by laser surface remelting and laser surface alloying with boron carbide, as demonstrated by the cross-sectional views shown in Figure 2 and Figure 3. In both cases, a clearly developed modified zone, heat-affected zone, and base material were identified, with distinct boundaries between individual regions visible on the cross-sections of the samples.

For samples subjected to laser surface remelting, the remelted layer exhibited a continuous and homogeneous geometry. A clear increase in the depth and width of the remelted zone was observed with increasing laser power. The microstructure of the remelted layer showed significant refinement, particularly near the remelting boundary, where fine cellular structures predominated. In the central region of the remelted zone, dendritic-type structures were observed, which are typical of rapid solidification of the molten pool.

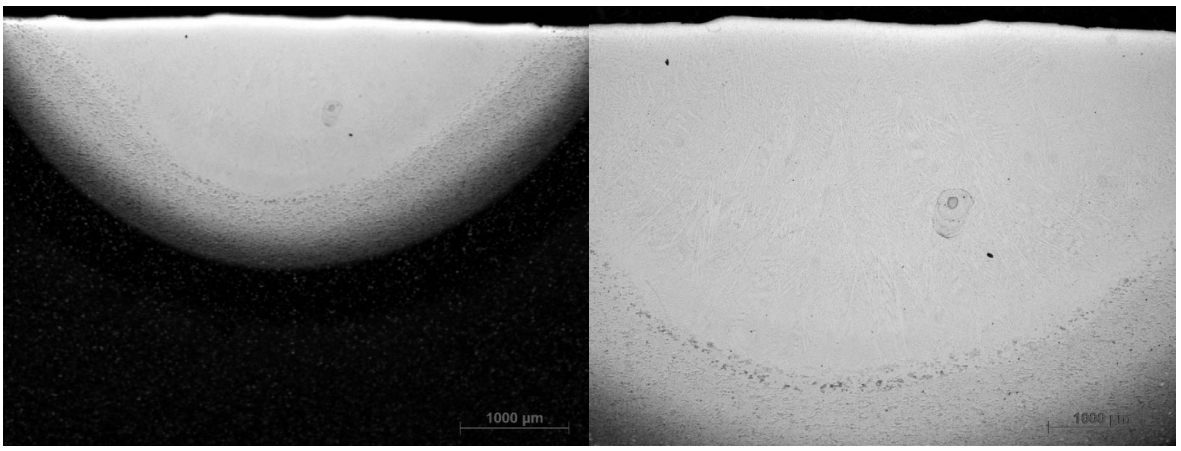

Figure 2. Microstructure of the remelted surface layer of tool steel after LSR at magnifications of 25x (left) and 50x (right) (sample LSR II).

In the case of laser alloyed samples with boron carbide, the microstructure of the surface layer differed significantly from that observed after remelting. The alloyed layer was characterized by pronounced heterogeneity resulting from the presence of ceramic material within the metallic matrix. In regions with lower B_4C powder content, the layer structure was relatively homogeneous, whereas at higher powder feed rates local agglomerations of ceramic particles and areas with diversified morphology were observed.

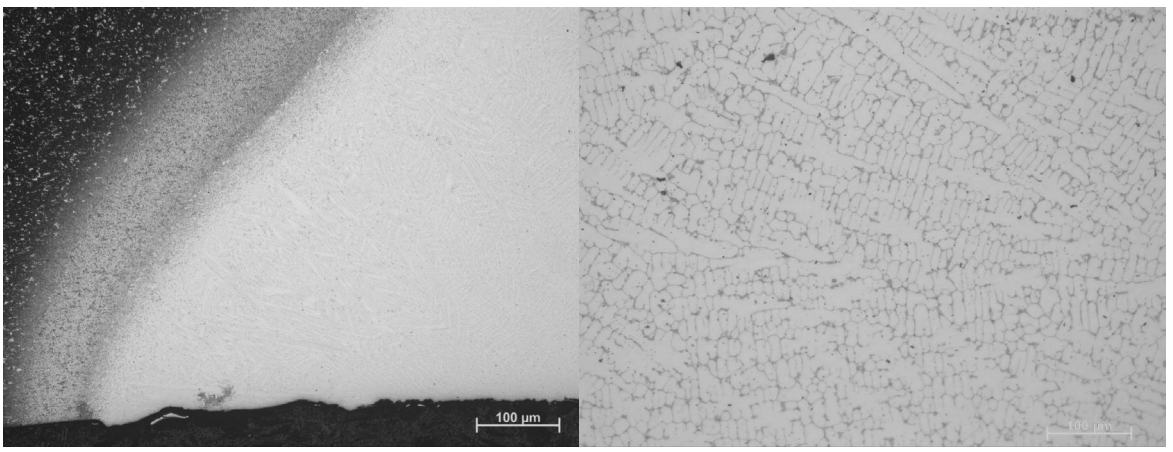

Figure 3. Microstructure of the Surface layer alloyed with B_4C at magnifications of 50x (left) and 500x (right) (sample LSA I).

3.2. Microstructure of modified layers – scanning electron microscopy (SEM)

Detailed microstructural observations carried out using scanning electron microscopy enabled evaluation of the morphology of the modified layers and identification of features not visible in light microscopy.

The layers alloyed with boron carbide exhibited a distinctly composite-like microstructure, as confirmed by the SEM images presented in Figure 4 and Figure 5. The composite character of the layer was less pronounced in regions with lower local B_4C powder content. In the SEM images, B_4C particles were visible as areas with clearly different contrast compared to the metallic matrix. These particles occurred both as individual inclusions and as local agglomerations.

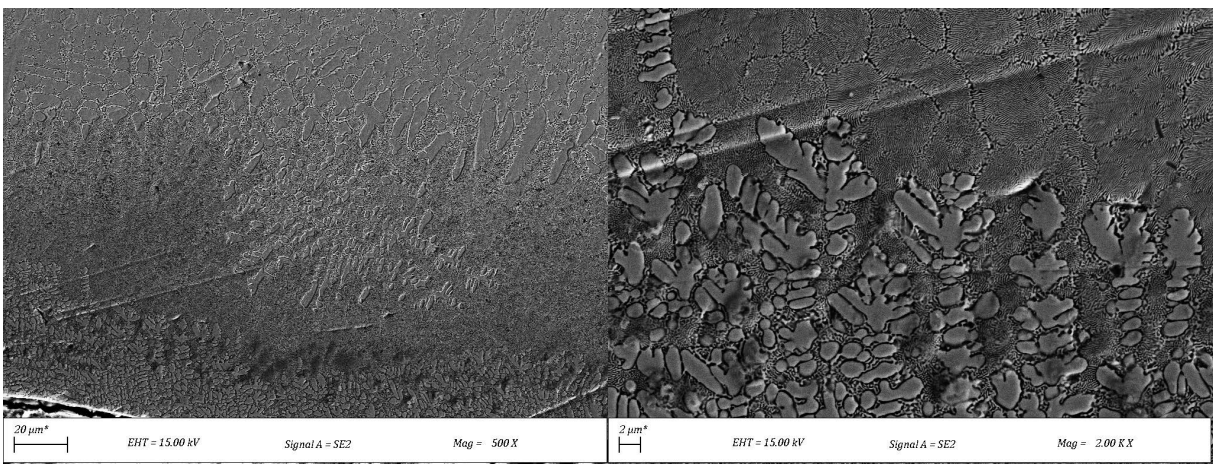

Figure 4. Microstructures of the alloyed layer in regions with lower boron carbide content (sample LSA I).

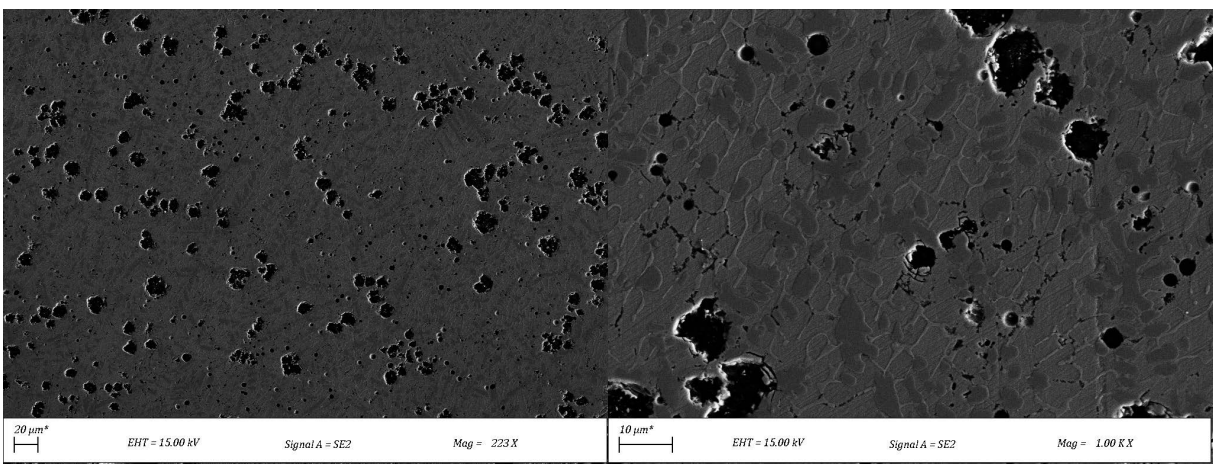

Figure 5. Microstructure of the alloyed layer highly enriched with B_4C particles (sample LSA II).

3.3. Chemical composition analysis of the alloyed layer (EDS)

Chemical composition analysis performed using the EDS technique confirmed the presence of regions locally enriched in boron and carbon in the surface layer alloyed with boron carbide, as demonstrated by the analysis areas marked in Figure 6 and the EDS spectra presented in

Figure 7 and Table 2. The results of point analyses revealed significant chemical heterogeneity within the micro-areas, confirming the composite character of the obtained surface layer.

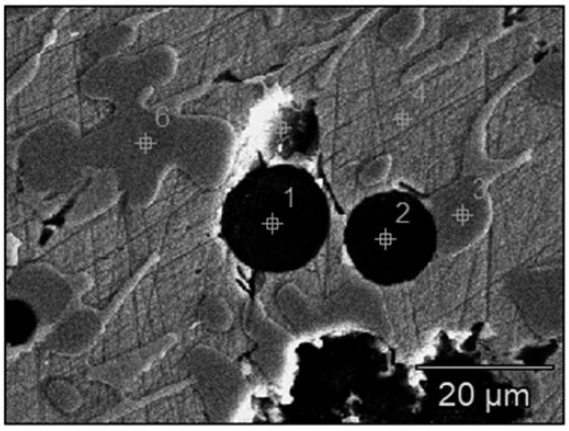

Figure 6. Area of the alloyed surface layer selected for EDS analysis (sample LSA I).

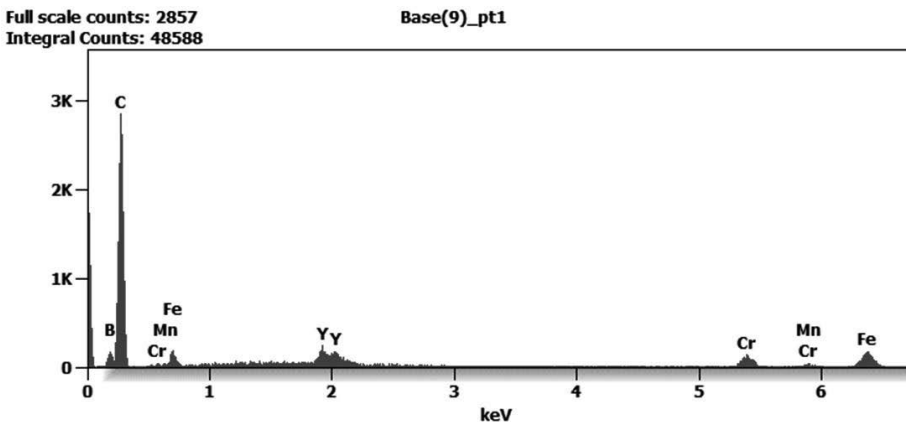

Figure 7. Representative EDS spectra obtained from regions enriched in boron and carbon.

Table 2. Atomic concentrations of elements measured at selected points of the sample.

Point	B	C	O	Si	V	Cr	Mn	Fe	Y	Zr	Mo
1	-	83.76	-	-	-	4.75	1.30	8.63	1.37	-	-
2	-	87.21	-	-	0.31	-	1.84	8.66	1.98	-	-
3	10.87	2.63	-	0.39	1.30	24.35	0.64	59.31	-	-	0.51
4	5.23	3.19	-	-	-	6.31	0.53	84.74	-	-	-
5	-	26.93	3.20	-	-	2.53	-	24.02	-	43.33	-
6	12.58	1.85	-	-	1.52	23.02	0.36	60.37	-	-	0.50

3.4. Microhardness distribution after laser surface remelting

Vickers microhardness measurements revealed a clear variation in mechanical properties within the region subjected to laser surface remelting. The highest microhardness values were observed in the central part of the remelted zone, as clearly illustrated by the microhardness distribution map shown in Figure 8. Toward the edges of the remelted track and within the heat-affected zone, a gradual decrease in hardness was observed.

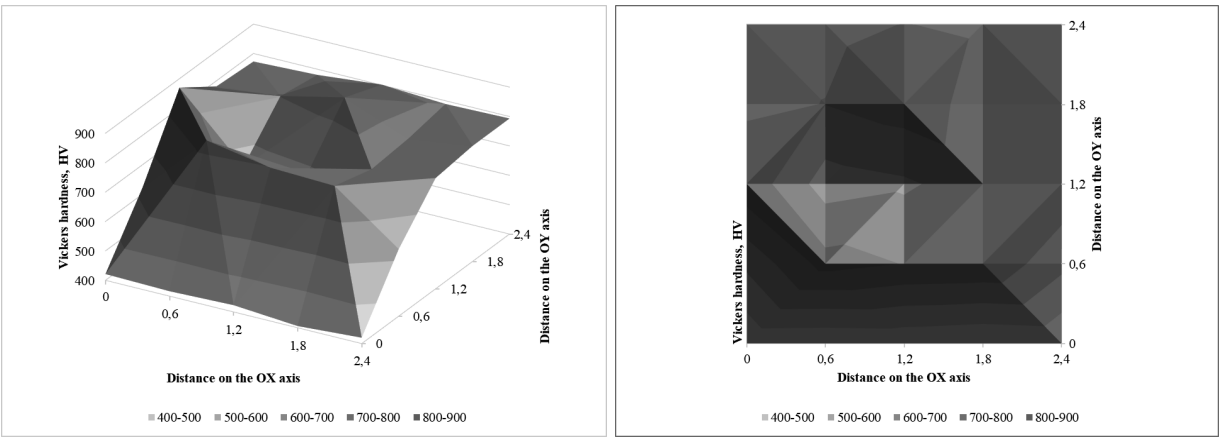

Figure 8. Microhardness distribution map after laser surface remelting of tool steel (sample LSR I).

4. DISCUSSION

The obtained results clearly confirm that laser surface modification of tool steel leads to significant microstructural changes, the nature of which strongly depends on the applied process strategy [1]. Laser surface remelting and laser surface alloying with boron carbide result in the formation of surface layers characterized by fundamentally different formation mechanisms, morphologies, and degrees of structural homogeneity.

In the case of laser surface remelting, the dominant modification mechanism is intensive remelting of a thin surface layer of the substrate material followed by rapid solidification. High temperature gradients and very high cooling rates promote the formation of fine cellular structures near the remelting boundary and dendritic structures in the central part of the molten pool, which is characteristic of laser remelting processes applied to steels and is consistent with literature data [6]. The observed increase in the depth and width of the remelted zone with increasing laser power is a direct consequence of the increased linear energy input of the process.

At the same time, it should be emphasized that laser surface remelting leads to the formation of a layer with a relatively homogeneous microstructure at the scale observed by light and electron microscopy. The absence of an additional material means that modification of surface layer properties results mainly from microstructural refinement and changes in phase morphology rather than from changes in chemical composition, which is typical of laser surface remelting processes described in the literature [7]. This is directly reflected in the microhardness distribution, where the highest values are observed in the central part of the remelted zone. Similar effects of laser surface remelting on microstructural refinement and hardness distribution have also been reported for tool and high-speed steels processed under comparable conditions [10].

A different modification behavior is observed in the case of laser surface alloying with boron carbide. The high melting temperature and limited wettability of B_4C by molten metal prevent complete dissolution of the ceramic material in the molten pool. As a result, a composite-like surface layer is formed, in which boron carbide particles are mechanically entrapped within the metallic matrix during rapid solidification, as commonly reported for laser alloying processes involving ceramic particles [4].

The degree of heterogeneity of the alloyed layer strongly depends on the B_4C powder feed rate. At lower ceramic content, a relatively homogeneous microstructure with locally distributed ceramic particles is observed. In contrast, increasing the powder feed rate leads to the formation of pronounced B_4C agglomerations and local structural discontinuities, including micropores, which has also been reported in previous studies on laser alloying of steels with ceramic phases [8].

The results of EDS analysis confirm the composite nature of the alloyed layer, revealing significant chemical heterogeneity at the microscale. Regions enriched in boron and/or carbon correspond to the locations of boron carbide particles, whereas the metallic matrix retains a chemical composition close to that of the substrate material. The lack of a uniform distribution of light elements indicates that laser surface alloying with B_4C results primarily in mechanical incorporation of the ceramic phase rather than classical alloying in the metallurgical sense, which is consistent with general descriptions of laser surface modification mechanisms [3].

By comparing both modification strategies, it can be concluded that laser surface remelting is an effective method for achieving homogeneous modification of the microstructure and mechanical properties of the surface layer without altering its chemical composition. In contrast, laser surface alloying with boron carbide enables the production of composite-like surface layers, albeit at the expense of increased structural heterogeneity and the potential occurrence of technological defects, which corresponds to general trends described in the literature on laser surface engineering [9].

ACKNOWLEDGEMENTS

The work was created as part of project based learning - PBL, in the 13th competition under the Initiative of Excellence - Research University, Silesian University of Technology, Gliwice, Poland.

BIBLIOGRAPHY

1. Steen W. M., Mazumder J., *Laser Material Processing*, Springer, London, 2010.
2. Dobrzański L. A., *Kształtowanie struktury i własności powierzchni materiałów inżynierskich*, Inżynieria Materiałowa, 5 (2009), 563–576.
3. Kuśiński J., Kac S., Kopia A., Lisiecki A., Major B., *Laser modification of the materials surface layer – a review*, Bulletin of the Polish Academy of Sciences – Technical Sciences, 60(4) (2012), 711–728.
4. Lisiecki A., *Laser surface alloying of steel with ceramic particles*, Archives of Materials Science and Engineering, 44(2) (2010), 93–100.
5. Dobrzański L. A., Dobrzańska-Danikiewicz A. D., *Obróbka powierzchni materiałów inżynierskich*, Open Access Library, Katowice, 2011.
6. Temmler A., Willenberg E., Wissenbach K., *Design surfaces by laser remelting and laser alloying*, Physics Procedia, 12 (2011), 419–430.
7. Bukhari S. S., Khan M. S., Rehman Z. U., *Effect of laser surface remelting on microstructure and mechanical properties of steel*, Applied Physics A, 129 (2023).

8. Ramakrishnan B. P., Lei Q., Misra A., Mazumder J., *Effect of laser surface remelting on the microstructure and properties of Al–Al2Cu–Si ternary eutectic alloy*, Scientific Reports, 7 (2017), 13468.
9. Kuśiński J., *Lasery w inżynierii powierzchni*, Inżynieria Materiałowa, 6 (2010), 685–692.
10. Iwaszko J., *Laser surface remelting of powder metallurgy high-speed steel*, Bulletin of the Polish Academy of Sciences – Technical Sciences, 68(6) (2020).

TalentDetector
9th January 2026
Gliwice, Poland
DEPARTMENT OF ENGINEERING MATERIALS AND BIOMATERIALS
FACULTY OF MECHANICAL ENGINEERING
SILESIAN UNIVERSITY OF TECHNOLOGY
INTERNATIONAL STUDENTS SCIENTIFIC CONFERENCE

Investigation into the Corrosion Resistance of Electrolytically Zinc-Coated Steel via Electro-Assisted Lacquering

[a]Gulsen Guven, [a]Bektas Eker, [a]Berat Ozturk, [a]Cemal Meran

[a] Pamukkale University, Faculty of Engineering, Department of Mechanical Engineering, Denizli-Turkiye, email: cmeran@pau.edu.tr

Abstract: The increasing utilization of metals in industrial applications, corrosion-related material losses have emerged as a major engineering and economic concern. Metallic coatings represent one of the most effective approaches to improving corrosion resistance. This study investigates the effect of current-assisted lacquering (electrophoretic lacquer) on the corrosion behaviour of electrogalvanized steel surfaces. Structural steel specimens were zinc-coated using two different electrolytic baths: cyanide-based and acidic. Following the coating process, Cr^{3+}- and cobalt-based passivation treatments were applied. Selected specimens were subsequently subjected to current-assisted lacquering as an additional protective layer. Corrosion performance was evaluated by immersing the prepared samples in a 3.5 wt.% NaCl solution for 168 hours in accordance with ASTM G31-21 standards. The corrosion behaviour was assessed based on mass loss measurements and variations in coating thickness. The results demonstrated that specimens coated in both acidic and cyanide-based baths and treated with current-assisted lacquering were unable to fully preserve coating integrity under severe corrosion conditions. The findings of this study provide insight into the influence of current-assisted lacquering on corrosion resistance and comparatively evaluate the effectiveness of different passivation systems applied to electrogalvanized coatings

Keywords: Corrosion, electro-galvanization, current-assisted lacquering, passivation

1. INTRODUCTION

Metals are increasingly utilized across various industrial sectors, and consequently, material losses due to corrosion are steadily rising. To address corrosion, metallic coatings have been developed. Metallic coatings have become a crucial and necessary method not only to enhance existing properties of the substrate material but also to impart surface characteristics that the base material lacks, such as wear, corrosion, and oxidation resistance [1].

Among metallic coatings, zinc-based coatings play a significant role in improving corrosion resistance. One of the most widely used methods for zinc coatings is electro galvanization. In electrogalvanized coatings, zinc is deposited onto the metal surface through the application of electric current. This type of coating is typically applied to small mechanical or decorative parts. The coating thickness usually ranges between 5 and 25 μm, resulting in a smooth and

bright surface. Compared to hot-dip galvanizing, electro galvanization produces a thinner coating layer, making it more suitable for subsequent forming or forging processes in engineering and manufacturing units [2]. However, electrogalvanized coatings may sometimes fail to provide the desired level of corrosion resistance.

To enhance the performance of the coating, additional post-coating surface treatments are often employed. In recent years, lacquering has emerged as one of the most common techniques for this purpose. In particular, current-assisted lacquering significantly improves corrosion resistance by forming an additional barrier layer on the surface of electrogalvanized coatings.

Corrosion is defined as the destructive and unintentional attack on a metal; it is electrochemical and ordinarily begins at the surface. The problem of metallic corrosion is significant; in economic terms, it has been estimated that approximately 5% of an industrialized nation's income is spent on corrosion prevention and the maintenance or replacement of products lost or contaminated because of corrosion reactions [3].

Electrolytic metal plating is the process of forming a metallic film on the surface of a metallic or non-metallic material using electrochemical methods. Current density, concentration and agitation, temperature, distribution power, the nature of the base metal and electrolyte, pH factors are factors that affect the quality of the electrolytic coating [4].

Steel is cathodic, while zinc coatings are anodic, sacrificing themselves to protect the metal, which is why they are widely used. The protective properties of zinc coating stem from its uniformity and good adhesion, its high resistance to atmospheric corrosion, and the tight adhesion of corrosion products formed under various atmospheric conditions, such as Zn(OH)2, ZnCO3, and ZnCl2, other than ZnSO4, to the surface. Although acidic and basic salt baths have traditionally been widely used for zinc plating, cyanide-containing and cyanide-free alkaline baths have become more common in recent years.

The passivation process is also a method applied to improve the coating quality in zinc plating. In zinc plating, the passivation process not only removes invisible imperfections on the surface but also gives the coating a vibrant appearance; it increases the durability of the yellow-green or blue color (passivation color) that forms on it [5].

Lacquer is essentially a combination of one or more synthetic and/or natural resins or "plastics," one or more solvents, and one or more plasticizers (softeners). This combination gives lacquers their transparency. Varnish is generally in the form of a pure solution, sometimes an emulsion, and sometimes a suspension, depending on its intended use. When using varnish, the basic principle is this: The solvent evaporates, leaving a homogeneous thin layer of resin or "plastic" on the work, along with a small amount of plasticizer [6].

2. MATERIAL AND METHOD

Structural steel specimens with dimensions of 20 × 20 × 100 mm were used in this study. Prior to testing, the specimens were subjected to the preparation and cleaning procedures illustrated to remove oil, grease, and surface contaminants, in Figure 1a-b. Subsequently, the specimens were cleaned in a degreasing bath to remove surface contaminants and to eliminate particles adhering to the surface during grinding. Finally, the specimens were mounted on racks to complete the preliminary preparations for the surface cleaning procedures.

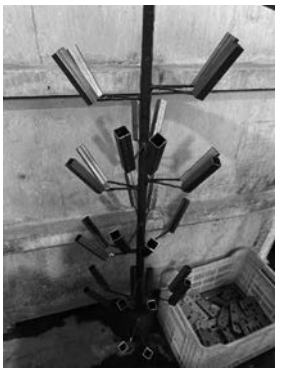

a) Preparation of the specimens

b) Degreasing bath used for surface cleaning specimens

Figure 1: The preparation and cleaning procedures of samples before coating

The specimens underwent a preliminary cleaning treatment by immersion in a chemical bath containing cyanide, sodium hydroxide (caustic), and soda for approximately one minute. During this process, a cathodic cleaning method was applied, which effectively removed the oily layer and accumulated contaminants from the surface. In order to achieve coatings that are typically fine-grained, adherent, and uniform in thickness across the entire surface of the substrate, parameters such as current density, bath concentration, temperature, and the use of additives are carefully controlled. Plating baths can be classified into various types, including sulphate, cyanide, chloride, perchlorate, and phosphate baths, as well as solutions containing precious metals [7].

2.1. Cyanide-Based Zinc Plating

The specimens were subjected to cyanide-based zinc plating for 20 minutes in a bath maintained at a temperature of 25 °C and a current density of 2 A/dm². The resulting deposition rate in the bath was approximately 2 µm/min. Upon completion of the plating process, the specimens were removed from the bath, thoroughly rinsed, and the cyanide-based zinc plating procedure was concluded.

2.2. Acidic Zinc Plating

After the rinsing step, the specimens were immersed in a degreasing bath for 1–2 minutes and subsequently rinsed again. Next, the specimens were treated in a hydrochloric acid bath followed by a further rinsing process. Upon completion of these pre-treatment stages, the specimens were plated for 20 minutes in a stirred acidic zinc plating bath, operating at a current density of 2 A/dm², with pH maintained between 4.9 and 5.5, and temperature controlled within 25–35 °C. After plating, the specimens were removed from the bath, rinsed, and subjected to final processing steps.

2.3. Passivation Treatments

2.3.1. Cr^{3+} Passivation

After the completion of the zinc plating processes, the specimens were first rinsed in a pre-passivation water bath, and then subjected to treatment in a Cr^{3+} passivation bath. Following the

passivation procedure, the specimens were rinsed again, resulting in a Cr^{3+}-passivated surface and the completion of this final treatment step.

2.3.2. Cobalt Passivation

Upon completion of zinc plating, the specimens were rinsed in pre-passivation water and subsequently treated in a cobalt-based passivation bath. After the passivation process, the specimens were thoroughly rinsed, thus obtaining a cobalt-passivated surface and concluding the final treatment step.

2.4. Current-Assisted Lacquering

Zinc-coated specimens were first subjected to the first and second rinsing stages in the lacquering chamber. Prior to lacquering, the surfaces were pre-cleaned using citric acid to remove residual contaminants. To eliminate acid residues, the specimens were rinsed with water and deionized water, and then transferred to the lacquering bath. The specimens underwent current-assisted lacquering for approximately 35 seconds at a current of 35–40 A. After the lacquering process, the specimens were first rinsed in a solvent-containing water bath, followed by rinsing in deionized water to complete the surface treatment. After the completion of all treatment processes, the specimens were placed in an oven for drying.

3. CORROSION TESTS

3.5 wt.% sodium chloride (NaCl) solution in deionized water was prepared as the test medium. The solution was prepared in accordance with the conditions specified in ASTM G31-21. The standard requires the pH of the solution to be in the range of 6.5–7.2. The prepared solution was measured to have a pH of 6.8. During the experiments, the solution temperature was maintained at room temperature.

Specimens for the corrosion tests were prepared following the procedures outlined in ASTM G31-21. During the cleaning stage, any possible oxide layers and foreign residues on the surface were removed by washing the specimens with deionized water. The surface roughness of each specimen was then measured to verify the suitability of the surface conditions for testing. To establish the initial condition, all specimens were weighed using a precision balance, and the coating thicknesses were recorded. The prepared specimens were fixed to support rods using threads in a manner that allowed complete immersion in the solution. The samples were tested for 168 hours in a solution containing 3.5% NaCl in accordance with the ASTM G31-21 standard. During the corrosion tests, the specimens were removed from the solution every 24 hours and dried to remove any residual liquid from their surfaces. At the same intervals, the solution was stirred to provide slight flow and to redistribute any particles that had settled at the bottom. The mass and coating thickness of the specimens were measured during this process, and all obtained values were recorded systematically. Every 48 hours, the solutions were refreshed, and their pH values were measured. After 7 days, the specimens were removed from the solution and cleaned in accordance with ASTM G1. To remove corrosion products, the specimens were immersed in a hydrochloric acid and deionized water solution.

4. RESULTS AND DISCUSSION

The electrophoretic lacquer coating applied in this study formed an additional protective film, enhancing the resistance of the plating system to external factors. The lacquer significantly increased the initial total coating thickness, Table 1, and Figure 2. The lacquer also supported the zinc plating and passivation layers against mechanical, moisture, and chemical effects, with its barrier effect limiting exposure to corrosion-inducing environmental factors.

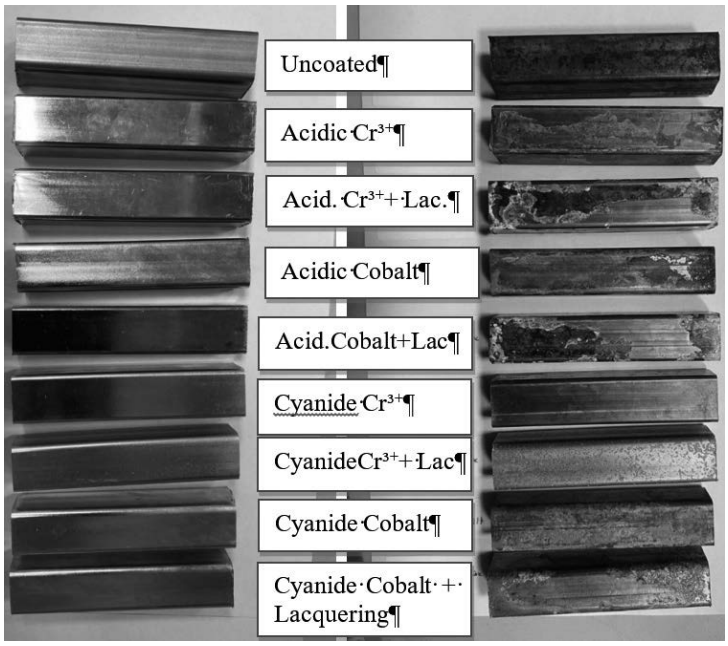

Figure 2: The view fs specimens before and after corrosion test

Daily mass change data show that lacquered specimens remained more stable over 168 hours compared to uncoated ones. Data analysis confirms that lacquer slows corrosion and extends the service life of the zinc coating, while also improving surface brightness and visual integrity, offering aesthetic advantages for industrial applications.

Table 1. Coating thickness changes in corrosive atmosphere depend on day

	Coating Thickness (µm)							
Measurement Days	**Initial**	**1.**	**2.**	**3.**	**4.**	**5.**	**6.**	**7.**
Cyanide Cr^{3+}	6,4	6,2	6	6	5,6	5,5	5,1	0
Cyanide Cr^{3+} + Lacquering	24,15	23,8	19	17,8	16,95	16,63	16,1	15,03
Cyanide Cobalt	9,5	7,9	7,4	7,25	6	5,7	5,5	5
Cyanide Cobalt + Lacquering	22,9	18,1	17,7	16,3	14,7	13,8	12,6	11,2
Acidic Cr^{3+}	8,4	8,3	7,8	7,5	7,3	7	6,3	5,5
Acidic Cr^{3+} + Lacquering	11,5	10,7	10,4	9,9	9,3	8,8	8,45	7,6
Acidic Cobalt	11,8	11,35	10,4	9,73	9,1	8,23	7,68	7,25
Acidic Cobalt + Lacquering	13,9	13,3	12,75	12,3	11,6	11,4	9,25	8,4

ACKNOWLEDGEMENTS

Within the scope of this study, electroplating was carried out at the Ona Nikelaj company in Denizli. We would like to express our gratitude to Bekir Ona for his contributions.

BIBLIOGRAPHY

1. Gülçelik, A G. (2019). Elektrolitik çinko kaplamalı plakalarda hızlandırılmış korozyon testi uygulaması. İstanbul.
2. Umer Draz, M. W. (2025). Asit klorür elektrolit çözeltisi kullanılarak elektrokaplama yoluyla çinko kaplamanın karakterizasyonu ve korozyon analizi.
3. Callister, W. D., & Rethwisch, D. G. (2014). Materials Science and Engineering, p683.
4. Uyanık, M. (2012). SiC Nanopartikül İlaveli Asitli Çinko Kaplama Banyolarında Yapılan Kaplamaların Malzemenin Korozyon Direnci ve Mekanik Özelliklerine Etkisinin Araştırılması, p38-41.
5. T.C. Çevre ve Şehircilik Bakanlığı. (2020). Yüzey işlemleri sektörel uygulama kılavuzu. https://webdosya.csb.gov.tr/db/sanayihavarehberi/icerikler//27_yuzey-islemler--20200103075115.pdf
6. Kushner, J. B. (1974). Electroplating know how II (Chapter 12). Joseph B. Kushner Electroplating School.
7. Çelik, K. (2006). Elektrolitik Çinko Kaplama Ve Işletme Parametrelerinin Kaplama Kalitesine Etkisi, Anadolu Üniversitesi Fen Bilimleri Enstitüsü, Yüksek Lisans Tezi, p21-22,

TalentDetector
9th January 2026
Gliwice, Poland
DEPARTMENT OF ENGINEERING MATERIALS AND BIOMATERIALS
FACULTY OF MECHANICAL ENGINEERING
SILESIAN UNIVERSITY OF TECHNOLOGY
INTERNATIONAL STUDENTS SCIENTIFIC CONFERENCE

Microstructural investigation of hybrid coatings combining PVD and ALD techniques using scanning electron microscopy

Jakub Gwóźdź[a], Vladyslav Makar[a], Daniel Pakuła[b], Marcin Staszuk[b]

[a] Students of the 5th Secondary School named after Andrzej Struga in Gliwice, Górnych Wałów 29, 44-100 Gliwice, Poland
[b] Silesian University of Technology, Faculty of Mechanical Engineering, Department of Engineering Materials and Biomaterials, Konarskiego 18A, 44-100 Gliwice, Poland
*email: marcin.staszuk@polsl.pl

Abstract: This paper was prepared as part of a project-based learning (PBL) initiative entitled "What the eye cannot see… the engineer will observe under an electron microscope. Applications of microscopy in materials engineering." The aim of the study was to investigate the microstructure of CrN–Cr_2O_3/TiO_2_500 and AlTiCN–DLC coatings deposited by combined PVD/ALD techniques on stainless steel and tool steel substrates. The morphology of the coatings was examined using scanning electron microscopy (SEM) and atomic force microscopy (AFM). In addition, the chemical composition of the coatings was analyzed by energy-dispersive X-ray spectroscopy (EDS).

Keywords: DLC, SEM, EDS, PVD, ALD

1. INTRODUCTION

In recent decades, the rapid development of advanced surface engineering technologies has significantly expanded the possibilities for tailoring the functional properties of materials, particularly in the fields of microelectronics, cutting tool technology, and biomedicine. Increasing demands for resistance to wear, friction, dynamic loading, and aggressive chemical environments have rendered conventional surface modification methods insufficient in many applications. As a response to these challenges, thin film deposition techniques have gained prominence, enabling precise control over chemical composition, microstructure, thickness, and physicochemical properties of surface layers.

Among these technologies, Physical Vapor Deposition (PVD) and Atomic Layer Deposition (ALD) play a particularly important role. PVD processes involve the evaporation or sputtering of a source material under vacuum conditions, followed by its condensation on the substrate surface. This technique allows for the production of metallic, ceramic, and composite coatings characterized by high hardness and a wide range of structural modifications, making it a standard solution for cutting tools and components exposed to severe wear. However, PVD processes may also lead to the formation of microdroplets or craters, which can affect the functional performance of the coatings in certain cases.

In contrast, ALD is based on sequential, self-limiting chemical reactions, enabling the deposition of ultrathin, highly uniform layers. This feature is particularly advantageous for micro- and nanoelectronic applications, barrier coatings, and protective layers on substrates with complex geometries. The combination of PVD and ALD into hybrid coating systems allows the advantages of both techniques to be synergistically integrated, resulting in enhanced durability and functionality of the surface layers [1–10].

2. MATERIALS AND METODOLOGY

Stainless steel and tool steel substrates were coated with hybrid layers using Physical Vapor Deposition (PVD) and Atomic Layer Deposition (ALD) technologies. The CrN–Cr_2O_3/TiO_2_500 and AlTiCN–DLC coatings were deposited on appropriately prepared steel substrates.

The crack structure and surface topography of the investigated materials were analyzed using scanning electron microscopy (SEM). The observations were carried out with an HRSEM SUPRA 35 microscope operating at an accelerating voltage of 15 kV in SE mode, with magnifications ranging from 1,000× to 20,000×. The chemical composition of selected micro-areas of the coatings was examined using energy-dispersive X-ray spectroscopy (EDS). Additionally, surface topography measurements were performed using atomic force microscopy (AFM).

3. RESULTS

SEM analysis revealed that both CrN–Cr_2O_3/TiO_2 and AlTiCN–DLC coatings are continuous and exhibit strong interlayer adhesion. The CrN–Cr_2O_3 coating consists of alternating CrN and Cr layers with a surface Cr_2O_3 layer, forming a columnar grain structure consistent with the Thornton zone T growth model [1,3]. The ALD-deposited titanium oxide layer uniformly covers the underlying PVD coating, effectively sealing potential discontinuities and confirming the effectiveness of the hybrid PVD/ALD concept (Fig. 1a). Surface analysis of the hybrid coatings showed a morphology typical of PVD processes while maintaining homogeneity and continuity.

Cross-sectional observations of the AlTiCN–DLC coating clearly indicate a multilayer architecture. The top DLC layer is continuous and uniform, while the underlying AlTiCN layer exhibits a columnar structure and serves as a load-bearing layer. The interfaces between individual layers are well defined, indicating good control of the deposition process. No voids or delamination were observed at the coating–substrate interface (Fig. 1b).

a) b)

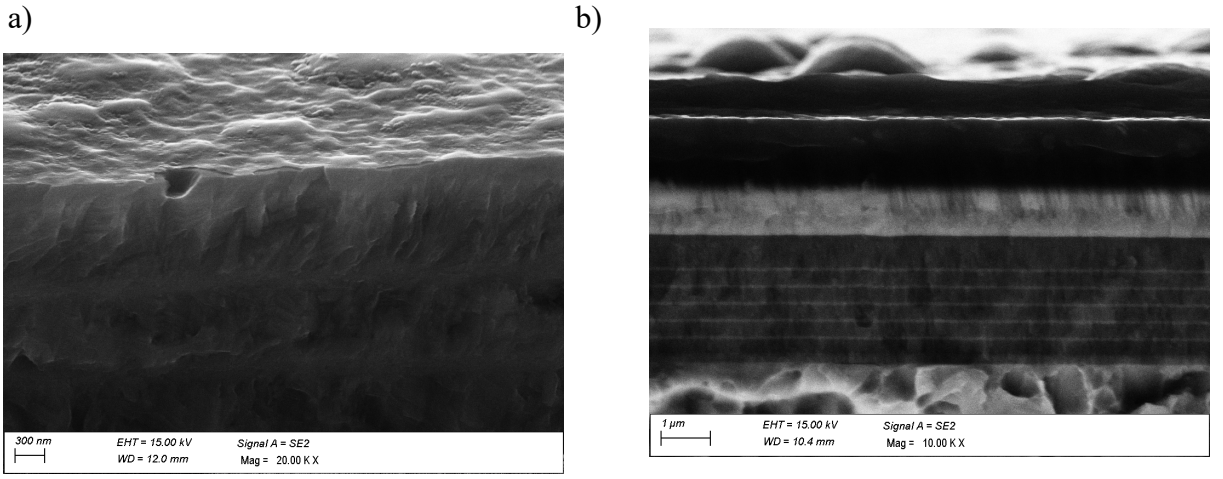

Figure 1. Structure of the: a) CrN+Cr_2O_3/TiO_2 coating, b) AlTiCN-DLC coating

Microcraters with diameters ranging from 0.5 μm to 10 μm for CrN–Cr_2O_3/TiO_2 and from 0.5 μm to 2 μm for AlTiCN–DLC were formed as a result of metal droplet coagulation during the PVD process. The ALD layers accurately replicate the morphology of the underlying PVD coatings, as confirmed by SEM and AFM observations. At the nanometer scale, the CrN–Cr_2O_3/TiO_2 coating exhibits a granular morphology (Fig. 2).

The AlTiCN–DLC coating shows a homogeneous structure with minor point defects and localized protrusions, which are characteristic of arc-based PVD processes. Occasional droplets of varying sizes were observed, distributed randomly across the surface. The absence of cracks or extensive surface damage confirms the continuity of the top DLC layer (Fig. 3).

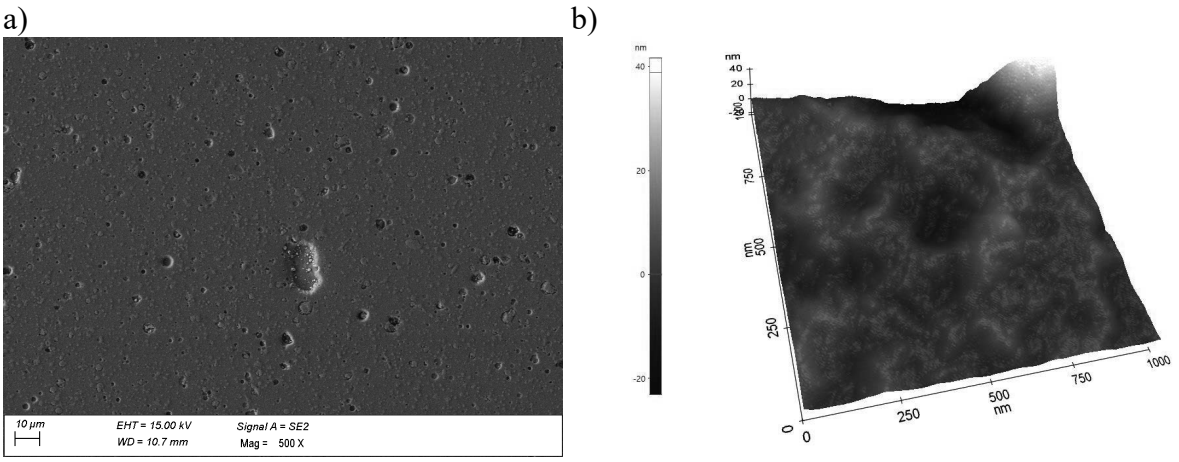

Figure 2. Surface topography of the CrN+Cr_2O_3/TiO_2 coating, a) SEM b) AFM

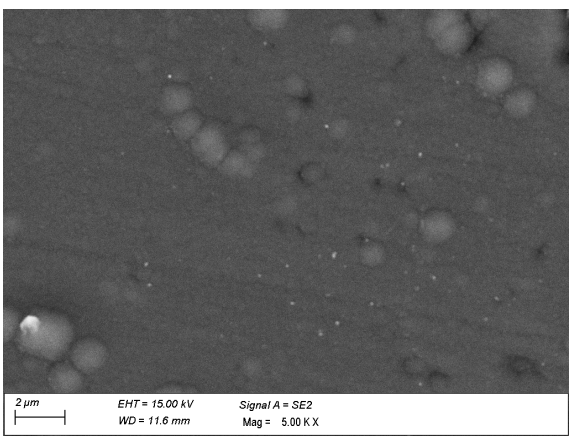

Figure 3. Surface topography of the AlTiCN-DLC coating (SEM)

EDS analysis confirmed the presence of elements characteristic of the investigated coatings, including chromium, titanium, oxygen, and nitrogen (Fig. 4).

a)

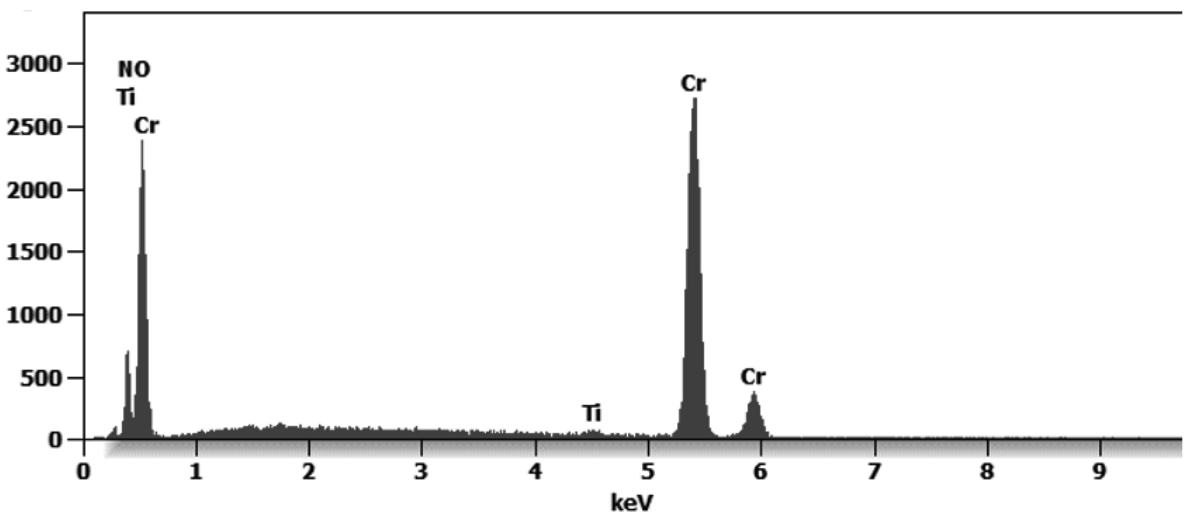

b)

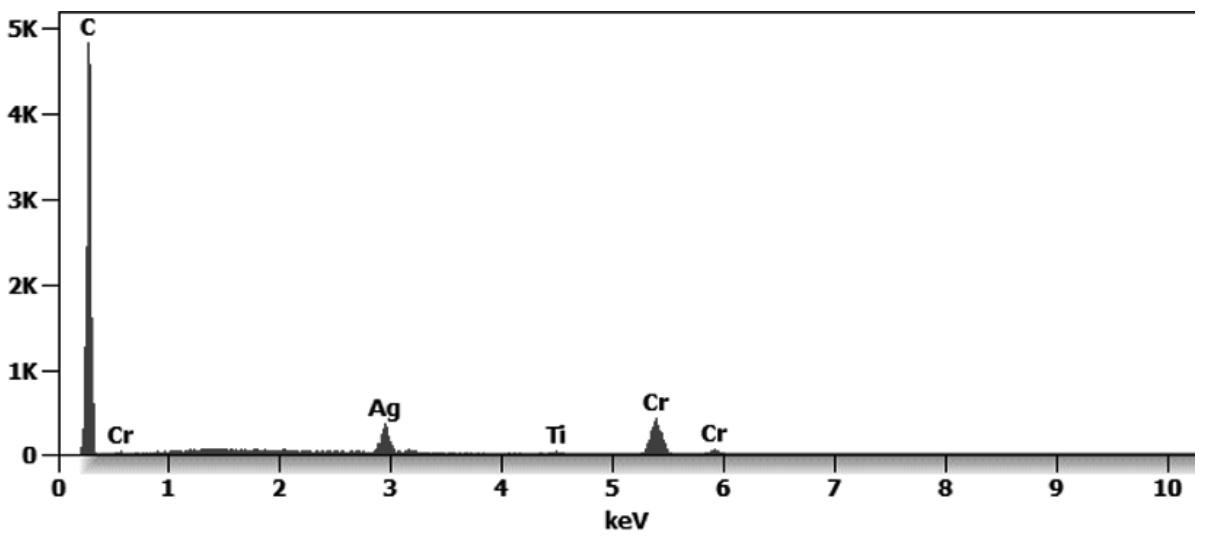

Figure 4. EDS analysis from the CrN+Cr_2O_3/TiO_2 coating

4. CONCLUSIONS

Based on the conducted investigations, the following conclusions can be drawn:

- Hybrid PVD/ALD CrN–Cr_2O_3/TiO_2 and AlTiCN–DLC coatings were deposited uniformly, without discontinuities or delamination, and exhibited strong adhesion to both the substrate and adjacent layers.
- The surface topography is typical of PVD coatings, with the presence of microcraters formed as a result of metal droplet deposition.

- The absence of cracks and delamination in the AlTiCN–DLC coating indicates excellent adhesion of the coating to the substrate.
- A distinct interface between the AlTiCN and DLC layers confirms effective functional separation: the AlTiCN layer provides load-bearing capacity, high hardness, and thermal resistance, while the DLC layer enhances tribological properties, enabling a balance between wear resistance and low friction.

ACKNOWLEDGEMENTS

This work was produced as part of the project implemented within the framework of project-oriented education - PBL project implemented with secondary school students, in the VI competition under the Excellence Initiative - Research University program, at the Silesian University of Technology.

BIBLIOGRAPHY

1. M. Staszuk Investigations of $CrN+Cr_2O_3/TiO_2$ coatings obtained in a PVD/ALD hybrid method on austenitic 316L steel substrate, Vacuum 207 (2023) 111653.
2. M. Staszuk, D. Pakuła, Ł. Reimann, A. Kloc-Ptaszna, M. Pawlyta, A. Kríž, Structure and Properties of TiO_2/nanoTiO_2 Bimodal Coatings Obtained by a Hybrid PVD/ALD Method on 316L Steel Substrate. Materials 14 (2021) 4369.
3. M. Staszuk, D. Pakuła, Ł. Reimann, A. Kloc-Ptaszna, K. Lukaszkowicz, Structure and properties of the TiN/ZnO coating obtained by the hybrid method combining PVD and ALD technologies on austenitic Cr-Ni-Mo steel substrate, Surfaces and Interfaces 37 (2023) 102693.
4. C.X. Shan, Xianghui Hou, Kwang-Leong Choy, Patrick Choquet, Improvement in corrosion resistance of CrN coated stainless steel by conformal TiO_2 deposition, Surface and Coatings Technology 202 (2008) 2147–2151.
5. E. Marin, L. Guzman, A. Lanzutti, L. Fedrizzi, M. Saikkonen, Chemical and electrochemical characterization of hybrid PVD+ALD hard coatings on tool steel, Electrochemistry Communications 11/10 (2009) 2060–2063.
6. M. Yazici, H. Kovacı, A.F. Yetim, A. Çelik, Structural, mechanical and tribological properties of Ti and TiN coatings on 316L stainless steel, Ceramics International 44/12 (2018) 14195-14201.
7. L. Shan, Y. Wang, J. Li. X. Jiang. J. Chen, Improving tribological performance of CrN coatings in seawater by structure design, Tribology International 82/A (2015) 78–88.
8. J. Leppäniemi, P. Sippola, M. Broas, J. Aromaa, H. Lipsanen, J. Koskinen, Corrosio protection of steel with multilayer coatings: Improving the sealing properties of physical vapor deposition CrN coatings with Al_2O_3/TiO_2 atomic layer deposition nanolaminates, Thin Solid Films 627 (2017) 59–68.
9. M. Staszuk, Ł. Reimann, D. Pakuła, M. Pawlyta, M. Musztyfaga-Staszuk, P. Czaja, P. Benes, Investigations of TiO_2/nanoTiO_2 bimodal coatings obtained by a hybrid PVD/ALD method on Al-Si-Cu alloy substrate, Coatings 12 (2022) 338.
10. S. Jannat, H. Rashtchi, M. Atapour, M.A. Golozar, H. Elmkhah, M. Zhiani, Preparation and performance of nanometric Ti/TiN multi-layer physical vapor deposited coating on 316L stainless steel as bipolar plate for proton exchange membrane fuel cells, J. Power Sources 435 (2019) 226818.

TalentDetector

9th January 2026
Gliwice, Poland

DEPARTMENT OF ENGINEERING MATERIALS AND BIOMATERIALS
FACULTY OF MECHANICAL ENGINEERING
SILESIAN UNIVERSITY OF TECHNOLOGY

INTERNATIONAL STUDENTS SCIENTIFIC CONFERENCE

Overview of Hydrogen Embrittlement in Weld Joints of High-Strength Steels: Mechanisms, Risks and Mitigation

Branislav Hajas[a*], Denisa Straková[a]

[a] University of Žilina in Žilina, Faculty of Mechanical Engineering, Department of Materials Engineering, Univerzitná 8215/1, 010 26 Žilina, Slovak Republic
* Corresponding author: hajas@stud.uniza.sk

Abstract: This review article systematically analyses the issue of hydrogen embrittlement (HE) in weld joints, with a focus on high-strength steels. Hydrogen embrittlement is a degradation mechanism in which the diffusion and accumulation of hydrogen lead to a significant decrease in the ductility and toughness of metals. The article elaborates on the main mechanisms such as HELP (Hydrogen Enhanced Localized Plasticity) and HEDE (Hydrogen Enhanced Decohesion), which explain the interaction of hydrogen with the crystal lattice. Special attention is devoted to the sources and the heterogeneous distribution of hydrogen in the Heat-Affected Zone (HAZ) of weld joints. In conclusion, the article summarizes the key factors influencing the susceptibility of high-strength steels to hydrogen-assisted cracking (HAC) and proposes strategies for minimizing the risk.

Keywords: hydrogen, high-strength steels (AHSS), hydrogen embrittlement (HE), weld joints, HELP, HEDE, hydrogen diffusion.

1. INTRODUCTION

High-strength steels are key materials for modern structures in the automotive, energy, and petrochemical industries, where they provide an optimal strength-to-weight ratio. The reliability of these structures is often limited by the integrity of their weld joints.

Hydrogen embrittlement (HE) represents one of the most serious threats that can lead to premature and catastrophic failure, particularly in high-strength steels, which are more susceptible to this phenomenon [1], [2], [3].

Weld joints are inherently prone to HE due to the presence of microstructural heterogeneities, various phases, non-metallic inclusions, and residual stresses, which create ideal conditions for the accumulation and diffusion of hydrogen [4]. HE is defined as a process in which hydrogen atoms penetrating the spatial lattice of the metal cause a reduction in ductility and toughness, leading to premature material failure [1].

The aim of this review article is to systematically summarize and analyse current knowledge on the theoretical mechanisms of HE, the influence of hydrogen on the microstructure of weld joints, and an overview of key measures for minimizing the risk of weld cracking (HAC).

2. THEORETICAL OVERVIEW: INTERACTION OF HYDROGEN WITH METALS

The susceptibility of a material to HE is directly related to the ability of the metal to absorb hydrogen and to its subsequent distribution and interaction with the crystal lattice.

2.1. Diffusion and accumulation of hydrogen

The solubility of hydrogen in a metal depends on temperature, pressure, the type of crystal lattice, and the microstructure. Hydrogen, as the element with the smallest atomic radius, easily diffuses through interstitial sites and crystalline defects [5].

Diffusing hydrogen is trapped in so-called hydrogen traps (Fig. 1), which are classified into reversible and irreversible [6]:

- Reversible traps: sites from which hydrogen can easily escape when the temperature increases. These include dislocations and grain boundaries.
- Irreversible traps: sites where hydrogen is bound more strongly and its release requires higher energy. These are mainly non-metallic inclusions (e.g., MnS, Al_2O_3) and precipitates.

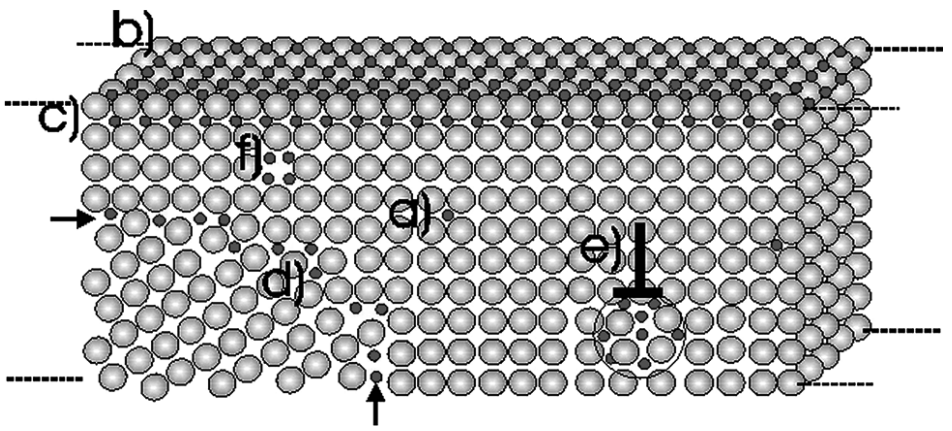

Figure 1. Schematic representation of hydrogen accumulation and trapping in a metal at the atomic level (the red atom represents hydrogen): a) interstitial lattice positions; b) absorbed H on the surface; c) penetrated H below the surface; d) along the grain boundary; e) H in the dislocation core; f) vacancies [7], [8].

The accumulation of hydrogen in hydrogen traps leads to an increase in the local hydrogen concentration, which is a key prerequisite for the development of hydrogen embrittlement.

2.2. Mechanisms of hydrogen embrittlement (HELP and HEDE)

Despite extensive research, no scientific consensus has been reached on a single universally valid mechanism. It is currently recognized that material failure under the influence of hydrogen is the result of a synergy of several mechanisms [5]. The most widely accepted mechanisms are:

a) HELP mechanism (Hydrogen Enhanced Localized Plasticity)
b) HEDE mechanism (Hydrogen Enhanced Decohesion)
c) Synergy of HELP and HEDE mechanisms

The HELP mechanism (Fig. 2) assumes that hydrogen locally weakens atomic bonds and alters the crystal lattice, thereby increasing dislocation mobility. This "softening" of the material at the nanoscale promotes the concentration of plastic deformation in weakened regions ahead of the crack tip. Although HELP appears to increase local plasticity, it in fact accelerates crack growth through ductile fracture (microvoid coalescence, MVC) [9], [10].

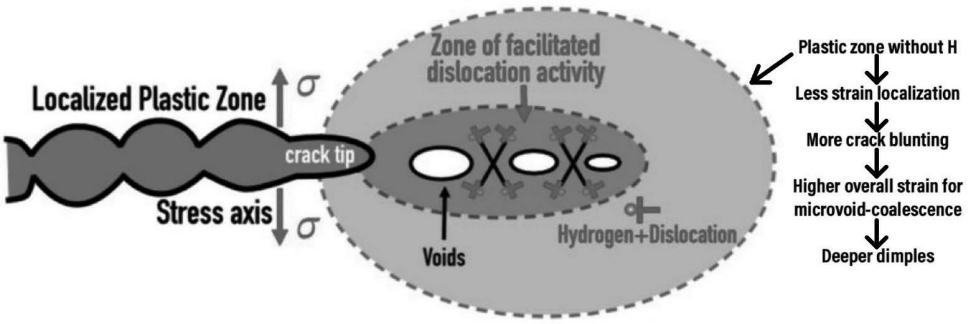

Figure 2. Schematic representation of the HELP mechanism [8], [9].

The HEDE mechanism (Fig. 3) is based on the assumption that hydrogen accumulates in regions of high hydrostatic stress (e.g., ahead of the crack tip or at interfaces between secondary phases and the matrix). The accumulation of hydrogen in these locations causes a weakening of the cohesive bonds between metal atoms. When the local stress reaches a critical level, decohesion (separation) occurs, leading to brittle fracture (intergranular IG or transgranular TG fracture) [9].

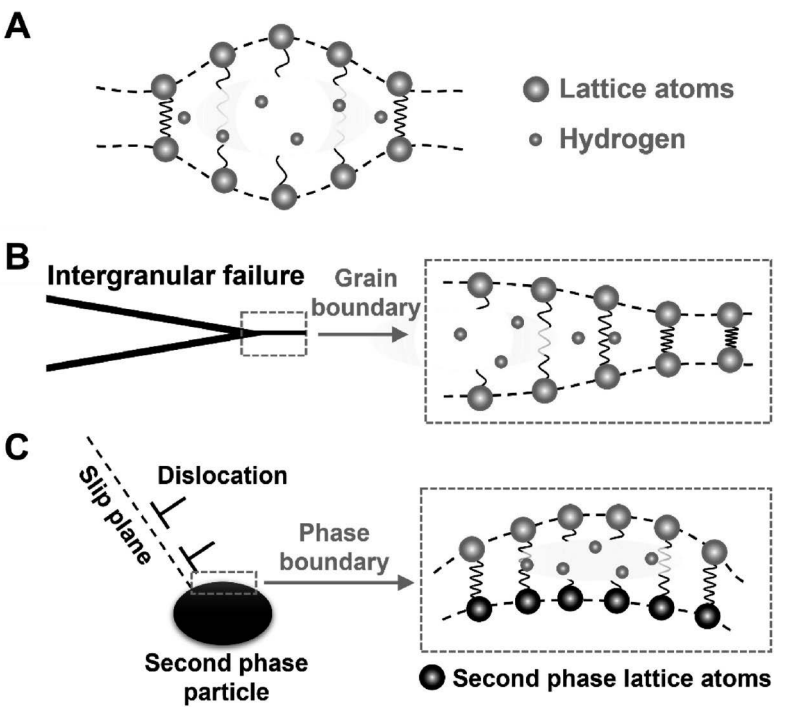

Figure 3. Schematic representation of the HEDE mechanism: A - in the crystal lattice, B - in the crack, C - at the phase interface [5], [9].

Newer models, such as the HELP+HEDE coexistence model (Fig. 4) proposed by Djukic et al. [11], [12], assume that both mechanisms act simultaneously and that their dominance depends on the local hydrogen concentration in the metal:

- At low hydrogen concentration (HELP dominates): Hydrogen primarily facilitates dislocation motion.
- At higher hydrogen concentration (HEDE dominates): Accumulation of hydrogen at traps leads to decohesion and brittle fracture.

It is important that HELP can facilitate the activity of HEDE by promoting local accumulation of stress and hydrogen.

Explanation of abbreviations for Fig. 4:

- MVC microvoid coalescence,
- TG - transgranular fracture,
- IG - intergranular fracture.

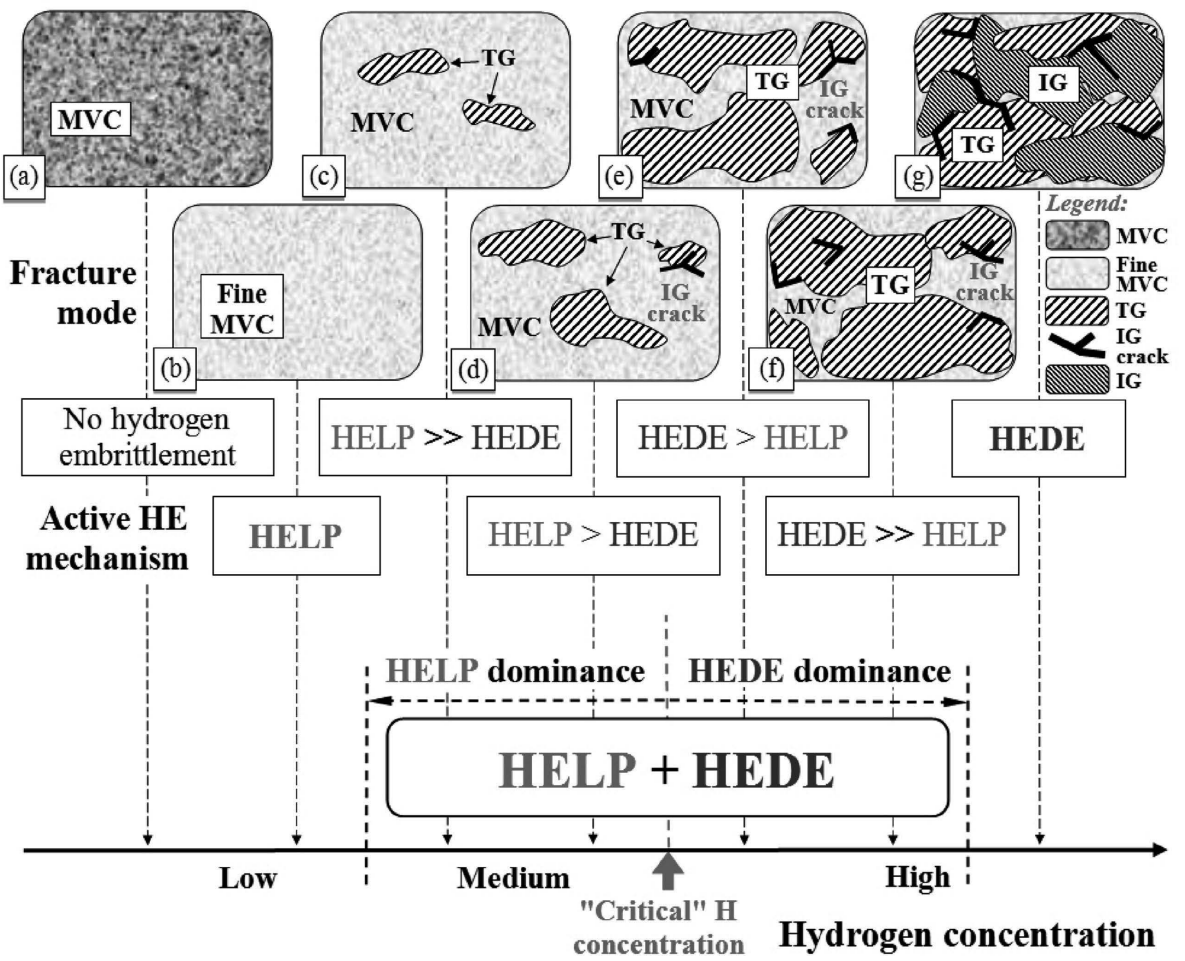

Figure 4. Schematic representation of the coexistence of HELP + HEDE mechanisms, depending on the overall hydrogen concentration in low-carbon steels [13].

3. HYDROGEN IN THE WELD JOINT ENVIRONMENT

Weld joints of high-strength steels are particularly susceptible to hydrogen-assisted cracking (HAC). The main sources of hydrogen during welding include [6]:

- *Moisture*: in electrode coatings, filler materials, or fluxes.
- *Surface contamination:* oil, grease, corrosion, or coating residues on the base material surface that decompose at high temperatures and release hydrogen atoms.
- *Shielding gases*: hydrogen produced by the decomposition of the shielding gas.

The distribution of hydrogen in the weld joint is heterogeneous. During cooling, due to phase transformations, the solubility of hydrogen in the metal decreases. This leads to its migration from the weld metal into the Heat-Affected Zone (HAZ) (Fig. 5), where the martensitic-bainitic microstructure has a higher sensitivity to hydrogen trapping [14], [6]. The zones most susceptible to HAC are particularly [15]:

- ICHAZ Intercritically Heat-Affected Zone
- SCHAZ Subcritically Heat-Affected Zone

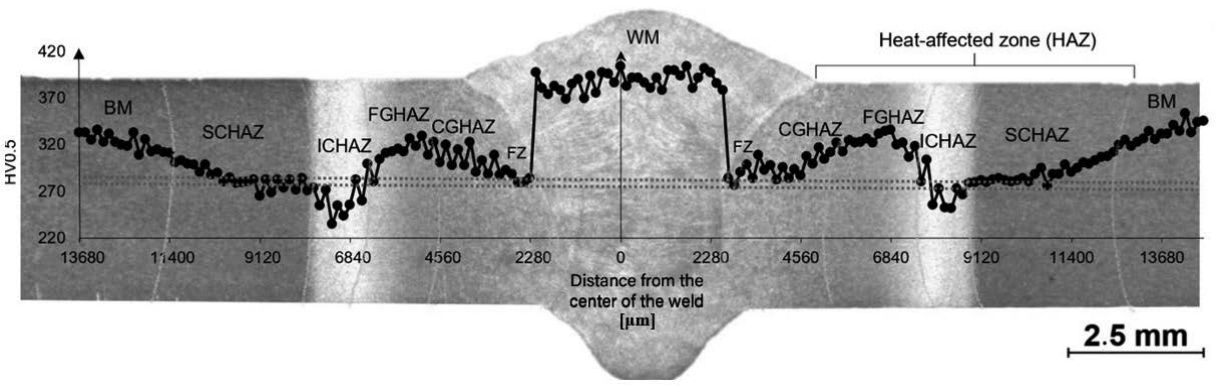

Figure 5. Schematic representation of the zone distribution in a butt weld joint of S960MC steel [16].

High-strength steels in the HAZ form a fine-grained, more brittle martensitic or bainitic microstructure that is rich in dislocations and grain boundaries, and thus also in hydrogen traps. A high hydrogen concentration combined with residual stresses arising from non-uniform cooling during welding significantly increases the risk of HAC [6].

4. STRATEGIES FOR MINIMIZING THE RISK OF HYDROGEN EMBRITTLEMENT

To ensure the reliability of weld joints, it is essential to implement preventive measures aimed at minimizing internal stresses and the hydrogen content in the weld metal.

Key strategies include [6], [17]:

- Control of hydrogen sources: use of low-hydrogen welding materials and thorough drying of electrodes and fluxes.
- Material preparation: thorough removal of surface contamination (oil, rust, coatings) from the surfaces to be welded.

- Optimization of the thermal cycle:
  - preheating of the base material: reduces the cooling rate and facilitates the diffusion of hydrogen away from the joint before cooling to a critical temperature, thereby minimizing residual stresses.
  - controlled cooling: controlled post-weld cooling, or heat treatment if necessary, can reduce the hardness of the HAZ and allow hydrogen to escape.
- Optimization of welding parameters: selecting an appropriate heat input that does not lead to excessively rapid cooling and the formation of brittle microstructures.
- Selection of filler material: use of filler materials with suitable chemical composition that reduce weld metal hardness and thereby increase its tolerance to hydrogen.

5. CONCLUSION

Hydrogen embrittlement represents a complex problem for weld joints of high-strength steels. This review article has confirmed that degradation is governed by the synergy of the HELP mechanism (localized plasticity) and the HEDE mechanism (decohesion), with the accumulation of hydrogen in critical microstructural traps (e.g., in the ICHAZ and SCHAZ zones) being a key factor. Therefore, ensuring the long-term reliability of structures exposed to hydrogen requires a comprehensive approach involving control of hydrogen sources, management of welding processes, and optimization of the microstructure.

ACKNOWLEDGEMENTS

The article was created as part of the joint Slovak-Polish project TalentDetector 2026 as a result of cooperation between the Silesian University of Technology, Gliwice and the Faculty of Mechanical Engineering, University of Žilina and project KEGA č. 033ŽU-4/2026.

REFERENCES

1. MCEVILY, A., J. - MAY, I., LE. 1991. Hydrogen-Assisted Cracking. In: Materials Characterization [online]. 1991, roč.26, č. 4, s. 253-268.
2. DONG, C., F. et al. 2009. Effects of hydrogen-charging on the susceptibility of X100 pipeline steel to hydrogen-induced cracking. In: International Journal of Hydrogen Energy [online]. 2009, roč.34, č. 24, s. 9879-9884.
3. LOVICU, G. et al. 2012. Hydrogen Embrittlement of Automotive Advanced High-Strength Steels. In: Metallurgical and Materials Transactions A [online]. 2012, roč. 43, s. 4075-4087.
4. ZHENG, W. et al. 2018. Hydrogen diffusion mechanism of the single-pass welded joint in welding considering the phase transformation effects. In: Journal of Manufacturing Processes [online]. 2018, roč. 36, s.126-137.
5. YI-SCHENG, CH. et al. 2024. Hydrogen trapping and embrittlement in metals -A review. In: International Journal of Hydrogen Energy [online]. 2024.
6. PADHY, G. - KOMIZO, Y. 2013. Diffusible hydrogen in steel welds - A status review. In: Transactions of JWRI [online]. 2013, roč. 42.

7. CAVALIERE, P. et al. 2024. Modelling of hydrogen diffusion leading to embrittlement in austenitic stainless steels. In: International Journal of Pressure Vessels and Piping, [online]. 2024, roč. 208.
8. XINFENG, L. et al. 2020. Review of Hydrogen Embrittlement in Metals: Hydrogen Diffusion,Hydrogen Characterization, Hydrogen Embrittlement Mechanism and Prevention. In: Acta Metallurgica Sinica (English Letters) [online]. 2020, roč. 33, s. 759-773.
9. TUNES, M., A. et al. 2024. Limitations of Hydrogen Detection After 150 Years of Research on Hydrogen Embrittlement. In: Advanced Engineering Materials [online]. 2024, roč. 26, s. 18.
10. BINIYAM, A., A. - ALTUNCU, E. 2024. A Review on hydrogen embrittlement behavior of steel structures and measurement methods. In: INTERNATIONAL ADVANCED RESEARCHES and ENGINEERING JOURNAL [online]. 2024, roč. 08, č. 02, s. 91-101.
11. DJUKIC, M.,B. et al. 2015. Hydrogen damage of steels: A case study and hydrogen embrittlement model. In: Engineering Failure Analysis [online]. 2015, roč. 58., s. 485-498
12. DJUKIC, M.,B. et al. 2016. Hydrogen Embrittlement of Industrial Components: Prediction, Prevention, and Models. In: CORROSION [online]. 2016, roč. 72, č. 7, s. 943-961
13. WASIM, M. - DJUKIC,M. 2022. External corrosion of oil and gas pipelines: A review of failure mechanisms and predictive preventions. In:Journal of Natural Gas Science and Engineering [online]. 2022, roč. 100.
14. YANG, Z. et al. 2024. Control strategy of reducing hydrogen enrichment in heat-affected zone during welding for ultra-high strength steels. In: International Communications in Heat and Mass Transfer [online]. 2024, roč.159.
15. XUE, J. et al. 2024. In-depth understanding in the effect of hydrogen on microstructural evolution, mechanical properties and fracture micro-mechanisms of advanced high-strength steels welded joints. In: Corrosion Science [online]. 2024, roč.233.
16. MEDVECKÁ, D. et al. 2022. Microstructural changes in HAZ of weld joints of S960 MC steel. In: MATERIALS TODAY-PROCEEDINGS [online]. 2022, roč.62, s. 2214-7853
17. Rudzinskas, V. 2024. The Role of Welding Parameters in Hydrogen Embrittlement Mitigation: A Case Study in Steel. In: RESEARCH REVIEW International Journal of Multidisciplinary [online]. 2024, roč. 9, č. 3.

TalentDetector
9th January 2026
Gliwice, Poland
DEPARTMENT OF ENGINEERING MATERIALS AND BIOMATERIALS
FACULTY OF MECHANICAL ENGINEERING
SILESIAN UNIVERSITY OF TECHNOLOGY
INTERNATIONAL STUDENTS SCIENTIFIC CONFERENCE

Forming the tiny-crystalic metals' structure via innovative laser processing

Krzysztof Hlubek, Michał Kopciowski, Mirosław Bonek

[a] Students of the 5th Secondary School named after Andrzej Struga in Gliwice, ul. Górnych Wałów 29, 44-100 Gliwice, Poland
[b] Silesian University of Technology, Faculty of Mechanical Engineering, Department of Engineering Materials and Biomaterials, ul. Konarskiego 18A, 44-100 Gliwice, Poland

Abstract: This article will discuss the material and technological aspects of the process of laser remelting of the metallic materials surface layers. The topics related to the design of such a processing method, to the material effects of its influence on tribological and strength properties will be discussed.

Key words: laser, surface processing, computer support of the process, PVD and CVD coatings, finished elements method

1. INTRODUCTION

Nowadays industry creates constantly growing requirements towards the quality and versatility of materials used in responsibility-demanding constructions, as well as elements ensuring durability during the exploitation. Throughout constant degradation - materials are affected by various factors. Specified elements must fulfill given functions, e.g. hard and resistant to abrasion external layer, and a plastic core. Some however must possess high stiffness or good weldability. Many aspects are exclusive to specific branches of industry, where modern engineering imposes a need for extreme precision in the creation process, further processing, and traits obtained as a result of alteration. In response to mentioned prerequisites, quality systems are striving for reinforcement of the materials' manufacturing processes with very advanced, reflecting realistic conditions - simulation programmes, in order to ensure required properties. The manufacturing process, as well as the design process - conducted in the described way provides great exactitude and precision of emerging materials and final products.

One of the methods that have been gaining popularity in recent years, consists of assigning the traits of the final product through modification of the material's external layer. There exists a number of possibilities for alteration of the surface, among others: surface hardening, hardfacing, thermal spraying, coating with PVD and CVD, remelting and metal alloying. The above methods enable assigning superior properties of the external layer in relation to the material of the base. It gives useful economical opportunities, because it is possible to coat a

relatively cheap material with only a handful of slightly expensive material - ensuring sufficient operational traits.

2. STRUCTURE AND OPERATION OF A LASER

A laser is a generator of optical radiation, comprising an optical amplifier utilizing the phenomenon of stimulated emission, a feedback system, and a power supply system. Lasers are capable of generating optical radiation within the visible spectrum (i.e. light), as well as ultraviolet and infrared radiation. The generation of optical radiation occurs when both the amplitude and phase conditions are fulfilled. The role of the feedback system is performed by an optical resonator, which is responsible for the properties of the radiation source, such as high temporal and spatial coherence. Optical radiation amplification may also be achieved by means of, among others, parametric amplification [1]. The basic structure of a laser consists of elements such as the active medium, the optical resonator, and the pumping system. The active medium is a specific substance (e.g. a collection of atoms, ions, or molecules) capable of amplifying an electromagnetic wave; it may also be realized in the form of a semiconductor material. The excited active medium is located between mirrors forming the optical resonator, where the radiation emitted by the excited medium is amplified. The pumping system is responsible for exciting the active medium to higher energy states. Assuming that the active medium remains in a state of thermodynamic equilibrium, the energy levels are described by the Boltzmann distribution. In such a case, an inverse proportionality exists between the energy levels and the number of atoms occupying them [2]. A simplified diagram illustrating the structure of a laser is presented in Figure 1.

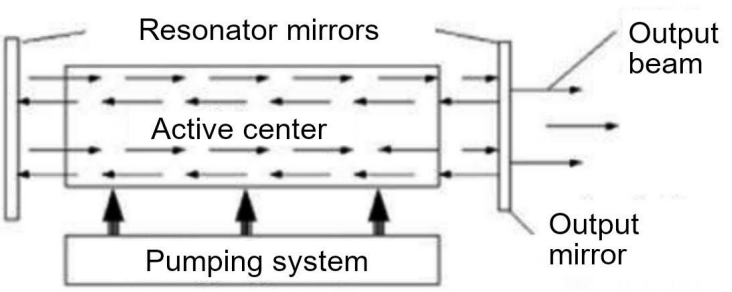

Figure 1. Simplified schematic of the laser structure [3]

It should also be noted that a cooling system is required, as the temperature of the active medium may increase significantly during laser operation. The most commonly applied cooling media include continuous flow of laser gas and the installation of heat exchangers surrounding the resonator. The fundamental objective of these solutions is the efficient dissipation of excess heat [4, 5]. Lasers can be classified according to their power, operating mode, wavelength, active medium, and application. Classification according to the active medium includes:

- gas lasers (e.g. argon laser),
- solid-state lasers (e.g. ruby laser),
- liquid lasers (e.g. dye laser),
- semiconductor lasers (e.g. junctionless lasers).

According to their application, lasers may be distinguished as:
- special-purpose lasers producing ultraviolet radiation of the shortest possible wavelength (e.g. KrCl laser),
- medical lasers (e.g. ruby laser).

Depending on the radiation spectrum, lasers are classified as:
- infrared lasers,
- visible-light lasers,
- ultraviolet lasers.

An additional classification is based on the power of the generated laser beam:
- low-energy lasers (in medicine: biostimulation lasers),
- medium-energy lasers (in medicine: therapeutic lasers),
- high-energy lasers (in medicine: surgical lasers) [6].

The application of lasers in various fields has been steadily increasing. They are widely used in medicine, particularly as surgical lasers; in industry, for applications such as laser cutting of metals, product marking tools, and measuring devices. Military technologies also exploit the potential of lasers, both in the form of directed-energy weapons and guidance systems. Laser printers are becoming increasingly widespread and are readily used in modern printing technologies, while lasers are also employed in artistic fields specializing in visual laser-based performances. Owing to the wide range of laser types and configurations, numerous disciplines are able to utilize them in diverse ways [6]. In industrial applications, the principal disadvantages of laser technology include its high cost and the considerable expenses associated with training qualified personnel to operate laser equipment. Additionally, material limitations may occur, such as restrictions related to the maximum thickness of the processed material. The positive aspects of this technology include the ability to produce accurately manufactured components with precision reaching up to 0.001 mm. It is a fast and highly precise solution that can be fully automated, thereby significantly improving production efficiency. Low noise emission further reduces occupational hazards at the workplace. A comparative analysis of laser cutting and mechanical cutting demonstrates another advantage of laser technology in industry—namely, the reduction of material waste [1].

3. TECHNOLOGIES OF PROCESSES RELATED TO SHAPING BY LASER REMELTING OF STEEL

The development of laser technologies, particularly high-power lasers introduced in the 1980s, has enabled the use of lasers as tools for producing enhanced surface layers. Laser-based processes for modifying metal layers—such as hardening, alloying, laser ablation, remelting, and cladding—are increasingly replacing traditional surface treatment methods previously in widespread use [7]. Laser techniques enable the modification, enhancement, or alteration of the surface structure of a material by exposing its outer layer to laser radiation with specific properties. They allow for the execution of numerous highly precise technological operations on materials that are difficult to machine, including soft, brittle, and structurally complex materials, achieving accuracy and efficiency that significantly exceed those of conventional machining methods [8]. Additive manufacturing processes frequently utilize laser technology during the sintering and melting of metal powders, owing to the ability to precisely heat designated structural elements. This enables accurate deposition of material onto a surface

while significantly reducing material consumption. The most commonly encountered laser-based additive manufacturing technologies include Selective Laser Sintering (SLS) and Selective Laser Melting (SLM). These technologies differ in terms of the properties of the manufactured products, including porosity, density, and mechanical strength [9].

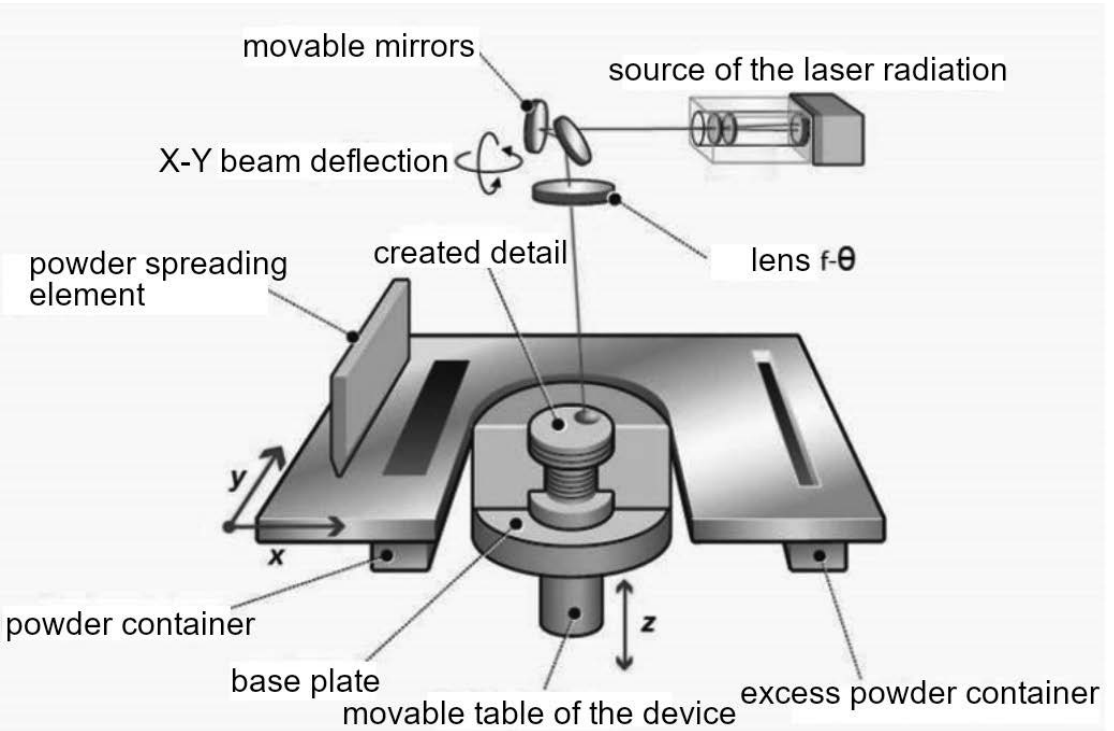

Figure 2. Schematic and principle of operation of additive powder sintering manufacturing equipment [9]

Laser-based additive manufacturing involves depositing a thin layer of powdered metal onto a build platform or substrate, which is subsequently subjected to sintering or melting processes. This procedure is repeated multiple times, with each sintered or melted layer contributing to the formation of the final component. By selecting appropriate methods, powder types, and process parameters, it is possible to achieve the desired properties and microstructure of the manufactured object. Complete modification of the surface structure may also be achieved through laser remelting processes, during which the metal surface is exposed to a laser beam of sufficient power to melt the outer layer of the material. The molten layer undergoes rapid self-quenching due to thermal interaction with the remaining part of the component, resulting in the formation of exceptionally fine martensitic grains [10].

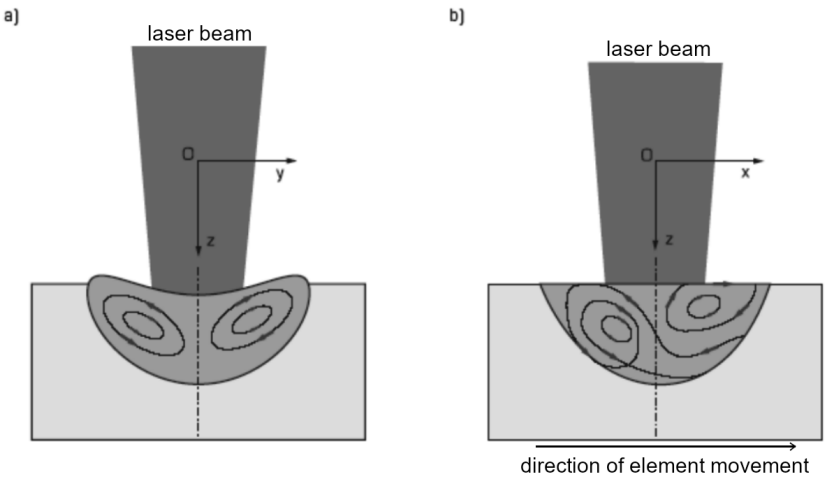

Figure 3. Schematic of convective motion in the laser melt pool: a) cross-section perpendicular (z0y) to the direction of sample (or beam) movement, b) cross-section parallel (z0x) to the direction of sample (or beam) movement

Remelting only a thin surface layer followed by rapid quenching leads to a surface layer characterized by low plasticity, high hardness, and increased surface roughness. Numerous factors influence the quality of the modified structure during remelting; however, the laser scanning speed has the most significant effect on changes occurring in the surface layer.

One of the more recent variants of surface structure modification by remelting is Selective Laser Polishing (SLP), which—unlike conventional remelting—involves the precise application of a laser over a very small area (approximately 0.1 mm²) on a selected material. This technique enables accurate remelting of metal to a depth of less than 25 micrometers and significantly reduces surface roughness compared to standard laser remelting processes [12].

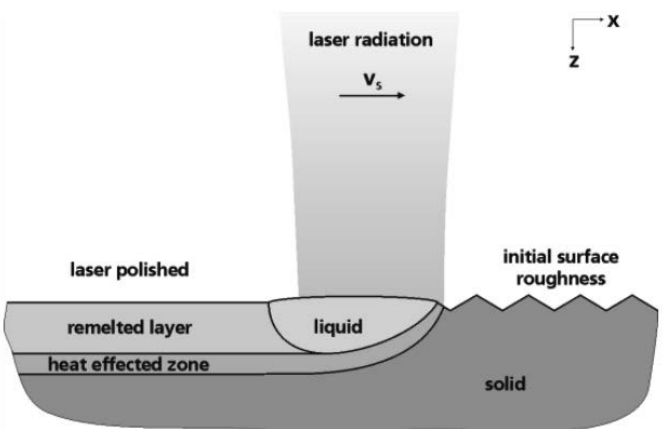

Figure 4. Schematic of laser polishing by melting a thin surface layer using continuous laser radiation [12]

Due to the surface tension of the molten material, surface roughness is smoothed during the remelting process. As a result, the liquid metal surface solidifies without cracks, pores, or hidden stresses and structural defects [13].

4. PROPERTIES OF LASER-REMELTED STEEL SURFACE LAYERS COMPARED TO PVD AND CVD COATINGS

Laser surface remelting is a highly dynamic process occurring over a very short time interval, during which only a small fraction of the absorbed thermal energy penetrates into the bulk of the material. This results in a substantial temperature gradient between the molten surface layer and the remaining material, leading to rapid solidification. The remelted surface layer exhibits high resistance to corrosion, erosion, and abrasive wear, without altering the chemical composition of the material, while maintaining a chemically homogeneous, fine-grained surface structure [14–16]. PVD coatings are applied not only in mechanical engineering but also in microelectronics, biomedicine, automotive, and construction industries. In the PVD method, the deposited coating is formed from a stream of ionized plasma directed onto the substrate. Coating deposition is carried out on substrates that are either unheated or heated to temperatures ranging from 200 to 500°C. In PVD techniques, variations in process parameters have a significant impact on coating structure. Key parameters influencing the structure include substrate temperature, energy of bombarding ions, gas pressure, and substrate characteristics such as chemical composition, microstructure, and surface topography, all of which determine the mechanical properties of the coating. The most critical property of PVD coatings is adhesion, i.e. the bond strength between the coating and the substrate; insufficient adhesion may result in the complete loss of coating functionality. The CVD method involves the introduction of coating precursors that deposit onto the substrate, where chemical reactions occur, forming a thin material layer on the object's surface. This is a high-temperature process, with temperatures reaching up to 1100°C. In CVD processes, the atmospheric components may be activated thermally (APCVD, LPCVD) or by plasma (PACVD) [17].

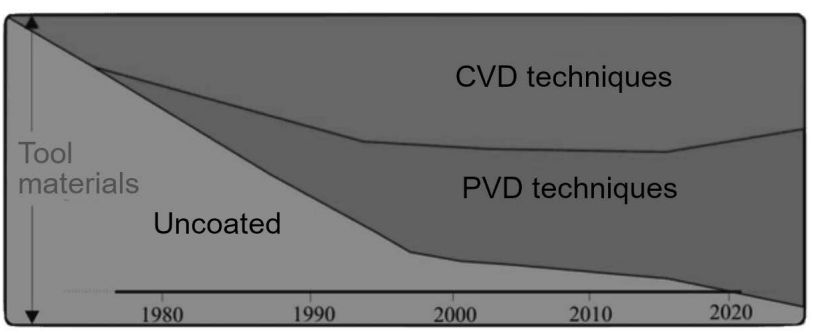

Figure 5. Forecast of the development of PVD and CVD techniques [18]

The surface properties obtained by laser remelting and by PVD/CVD coatings are largely comparable; both methods yield high surface hardness and resistance to abrasive wear. However, each technique also presents certain disadvantages. The primary drawback of the CVD method is the necessity of high processing temperatures, low efficiency, or limited possibilities for final dimensional correction. Despite these limitations, CVD technology has found application in electronics for semiconductor material deposition and in optical coatings, such as those used for eyeglasses [20]. In the case of PVD, disadvantages include the relatively slow coating deposition rate compared to other coating processes, the use of complex and costly equipment, and limitations when processing substrates with complex geometries.

PVD technologies are employed for the production of magnetic coatings, decorative coatings and jewelry applications, high-hardness coatings resistant to wear and corrosion made of composite materials, as well as metallic coatings that impart semiconductor properties to substrates that originally did not possess them [21]. Surface remelting processes often lead to the formation of tensile stresses due to non-uniform heating and cooling of the treated layer [15]. Improper selection of process parameters may also result in evaporation of the surface layer; therefore, accurate parameter selection is of critical importance. Above all, the choice and adaptation of an appropriate technology to the intended manufacturing objectives is essential, as each surface treatment technology has its advantages and limitations, which should ultimately determine the selection process.

5. POSSIBILITIES OF FEM ANALYSIS IN LASER PROCESSING

Numerical methods are commonly used tools for evaluating changes in the material state of machine components subjected to external forces or thermal processes. The Finite Element Method (FEM) provides valuable information regarding the material condition during processing, as well as changes in properties after process completion. However, FEM has certain limitations due to the necessity of applying assumptions that often depend on the material state during processing or are difficult to measure, such as laser energy absorption during phase transformations, which may lead to inaccuracies in calculations. Furthermore, numerical descriptions rely on models that approximate real phenomena. Compared to analytical methods, numerical methods are less labor-intensive and, even if they introduce certain inaccuracies, in most cases these errors can be minimized or eliminated [22]. Accurate input of material data, accounting for changes due to temperature variations and external factors, is decisive for the precision of numerical calculations. In particular, the correct definition of boundary conditions plays a crucial role in result accuracy. Calculations performed using appropriate numerical methods can be verified against experimental results. Experimental methods are also susceptible to errors; however, such errors can be estimated and reduced using statistical techniques. The accuracy of phenomenon description can be improved through appropriate experimental design, selection of parameter variability levels, formulation of suitable mathematical models, application of proper measurement methodologies, and elimination of input variables with negligible influence on the studied phenomenon [23].

The application of FEM analysis enables the acquisition of information on microstructural changes in materials subjected to laser beam interaction processes. Results obtained using numerical methods may explain material transformations occurring during processing, as well as the formation of microstructures after cooling. The process and its outcomes can be more precisely identified through the combined use of analytical and experimental approaches.

FEM analysis is particularly effective in situations where appropriate experimental equipment is unavailable. Conducting laser processing studies using the Finite Element Method offers numerous advantages [24]:

- reduced development time of the investigated object,
- decreased number of prototypes (cost reduction),
- analysis of thermal stresses during laser processing,
- acquisition of information on generated heat quantities,
- assessment of temperature influence on the behavior of the investigated object.

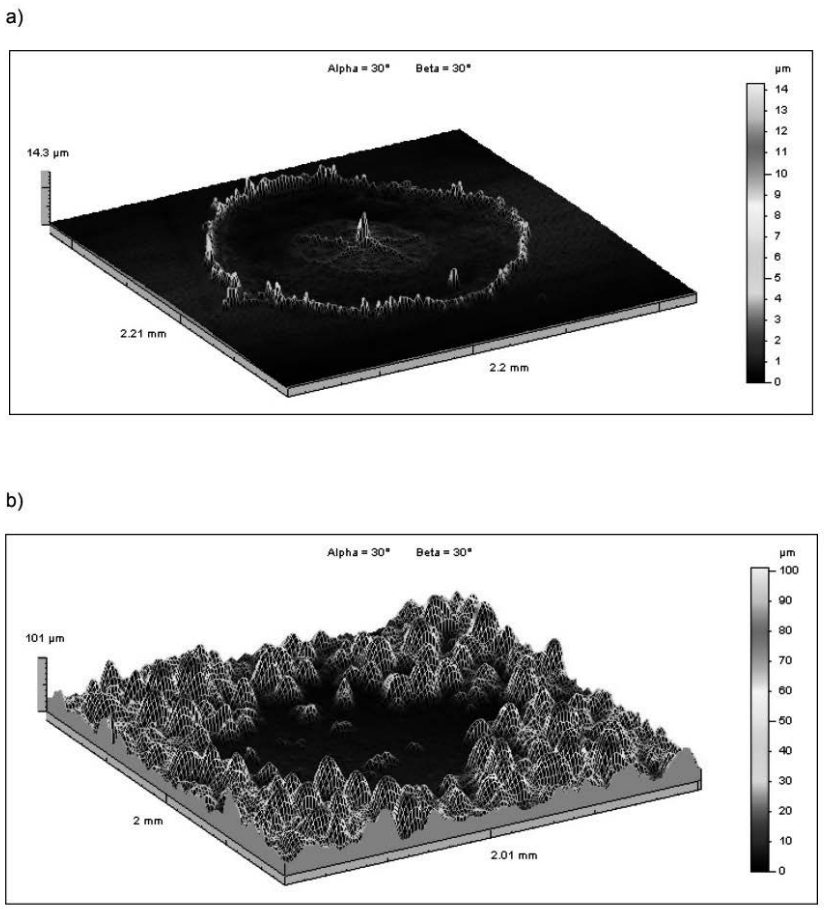

Figure 6. Example of FEM simulation in laser processing [22]

7. CONCLUSIONS

Numerous literature sources demonstrate the broad scope of laser material processing within industrial applications. Currently, many industrial sectors benefit from the advantages and methods based on laser surface treatment, continuously improving this technology through the aforementioned and briefly characterized process-supporting techniques. Computer-based modernization and simulation of these processes contribute significantly to material and time savings during component design and initial manufacturing trials. Such software also assists in selecting appropriate process parameters, including laser power, scanning speed, and the type of protective atmosphere used. The high precision of laser processing methods underscores the extensive range of contemporary industrial applications and the continual development of new surface modification techniques, particularly those involving laser remelting.

ACKNOWLEDGEMENTS

This work was created as part of the project implemented within the framework of project-orientated education, the PBL project implemented with secondary school students, in the VI competition under the Excellence Initiative - Research University programme, at the Silesian

University of Technology and as part of project of Students Scientific Circle of Laser Surface Treatment under the Initiative of Excellence - Research University, Silesian University of Technology, Gliwice, Poland.

BIBLIOGRAPHY

[1] J. Pluciński, „Lasery w medycynie", Gdańsk, 2015.
[2] Kujawski A., Szczepański P. „Lasery Podstawy fizyczne", Oficyna Wydawnicza Politechniki Warszawskiej, Warszawa, 1999.
[3] Cenian A., Zaremba E., Frankowski M., Materiały do kursu „Lasery w medycynie", http://www.implaser.pl/nasze_wyklady/fizyczne_podstawy/med_main.htm dostęp: 13.05.22r.
[4] Czupryński A., Rzeźnikiewicz A., „Specjalne technologie spawalnicze w ćwiczeniach laboratoryjnych", Wydawnictwo Politechniki Śląskiej, Gliwice, 2020.
[5] Startton J.A., „Electromagnetic theory", Wiley, New Jersey, 2007.
[6] Fidytek R., „Rodzaje laserów i ich zastosowanie", http://cami-antiaging.eu/STRONA%20W%20BUDOWIE%20-%20WWB/08%20-%20LASERY/01.-LASERY%20W%20TEORII/R.Fidytek_RodzajeLaser%C3%B3wiichZastosowanie.pdf dostęp 13.05.2022r.
[7] J. Radziejewska, Laserowa modyfikacja właściwości warstwy wierzchniej wspomagana nagniataniem, Instytut Podstawowych Problemów Techniki Polskiej Akademii Nauk, Warszawa, 2011
[8] L.A. Dobrzański, E. Jonda, A. Klimpiel, A. Lisiecki, Wpływ laserowego przetapiania i stopowania na strukturę i własności warstw wierzchnich stali X40CrMoV5-1
[9] A. Mazurkiewicz, B. Nędzi, Ocena jakości wykonania wybranego elementu z proszków metali metodą laserowego wytwarzania przyrostowego, Instytut Naukowo-Wydawniczy „SPATIUM", 2016
[10] L.A. Dobrzański, A.D. Dobrzańska-Danikiewicz, Obróbka powierzchni materiałów inżynierskich, Internarional OCSCO World Press, 2011
[11] K. Radziejewska, W. Kalita, B.Nowicki, Laserowo-mechaniczna modyfikacja warstwy wierzchniej stali, Przegląd Mechaniczy, Tom 7-8, 2006
[12] A. Temmler, Designing Surfaces by Laser Remelting, 2001
[13] E. Willenborg, Polishing by laser radiation, Fraunhofer Institute for Laser Technology, 2003
[14] L.A. Dobrzański, T. Tański, A.D. Dobrzańska-Danikiewicz, M. Król, S. Malara, J. Domagała-Dubiel, Laserowa obróbka powierzchniowa stopów Mg-Al-Zn
[15] J.Radziejewska, Laserowa modyfikacja właściwości warstwy wierzchniej wspomagana nagniataniem
[16] https://technolutions.pl/chemical-vapour-deposition-cvd/
[17] L.A. Dobrzański, Podstawy nauki o materiałach i metaloznawstwo, Wydawnictwa Naukowo-Techniczne, 2003.
[18] W. Kwaśny, Prognozowanie własności powłok PVD i CVD na podstawie wielkości fraktalnych opisujących ich powierzchnie, Instytut Materiałów Inżynierskich I Biomedycznych Politechnika 2009
[19] K. Bohusz, Badanie mikrostruktury powłok azotku chromu wytworzonych metodą PAMOCVD z zastosowaniem 2-etyloheksanianu chromu III, Politechnika Warszawska 2010
[20] http://zasoby.open.agh.edu.pl/~11sashot/stronae375.html?t=tw&h=cvd&v=

[21] https://www.atriainnovation.com/en/physical-vapor-deposition-pvd/
[22] W. Napadek, K. Kosiuczenko, „Symulacja numeryczna laserowego umacniania udarowego stopu tytanu Ti-6Al-2Cr-2Mo" Prace instytutu elektrotechniki, zeszyt 237, 2008
[23] Szargut J.: Modelowanie numeryczne pól temperatury. WNT, Warszawa (1992).
[24] Bień A., Dacko A., Osiński J., Szot A.: Modelowanie numeryczne procesu laserowej obróbki. Przegląd Mechaniczny 6 (2004) 16÷19.
[25] Capanidis, Dymitry, and Piotr Kowalewski. "Przegląd systemów wspomagania procesów konstruowania i wytwarzania." Zeszyty Naukowe Dolnośląskiej Wyższej Szkoły Przedsiębiorczości i Techniki. Studia z Nauk Technicznych 1 (2012): 25-42.
[26] https://extrudesign.com/category/cad-cae-cam/ dostęp: 15.05.2022
[27] Chlebus E., Techniki komputerowe CAx w inżynierii produkcji, Wydawnictwa Naukowo-Techniczne, Warszawa, 2000
[28] Stanisławski M., Historia komputerowych systemów wspomagających projektowanie, wytwarzanie i analizy inżynierskie, 2009
[29] Stanisławski M., Komputerowe wspomaganie projektowania i analiz, CADblog.pl, t. 8, 7, 2009, s. 71–85
[30] https://yeswebim.wordpress.com/2015/01/15/history-of-computer-aided-design/ dostęp: 15.05.2022
[31] https://solidexpert.com/3dexperience/catia/ dostęp: 15.05.2022
[32] Sydor M., Wprowadzenie do CAD. Podstawy komputerowo wspomaganego projektowania, PWN, Warszawa, 2009.
[33] https://www.intechopen.com/chapters/57728 dostęp: 15.05.2022
[34]https://home.agh.edu.pl/~zmsz/pl/pliki/os/OS_symulacja_przeplywu.pdf dostęp: 15.05.2022
[35] Miecielica M., Kaszkiel G., Komputerowe wspomaganie wytwarzania CAM, ZNI Nicom, Warszawa, 1999.
[36] Skawiński P., Systemy CAM – narzędzia technologicznego przygotowania produkcji, „Mechanik", 11, 2009, s. 953.
[37] https://it.edgecam.com/2009R2 dostęp: 15.05.2022

TalentDetector
9th January 2026
Gliwice, Poland
DEPARTMENT OF ENGINEERING MATERIALS AND BIOMATERIALS
FACULTY OF MECHANICAL ENGINEERING
SILESIAN UNIVERSITY OF TECHNOLOGY
INTERNATIONAL STUDENTS SCIENTIFIC CONFERENCE

Secondary Aluminium Alloys for Sustainable Electric Mobility: Production Routes, Limitations and Future Perspectives

Edita Illichmanová[a], Zuzana Straková[a], Eva Tillová[a], Lenka Kuchariková[a]

[a] University of Žilina, Faculty of Mechanical Engineering, Department of Materials Engineering, Univerzitná 8215/1, 010 26 Žilina, Slovak Republic
*email: edit.illichmanova@fstroj.uniza.sk

Abstract: Secondary aluminium production is becoming a cornerstone of sustainable development in the aluminium industry because it enables a substantial reduction in energy demand and CO_2 emissions compared with primary production. Increasing scrap availability and intensified decarbonisation targets further strengthen the role of secondary aluminium alloys, especially in sectors that require high material efficiency - most notably the automotive industry and electric mobility. However, secondary aluminium alloys exhibit greater variability in chemical composition and are prone to impurity build-up, particularly iron (Fe). This adversely affects microstructure and mechanical performance through the formation of Fe-rich intermetallic phases, thereby limiting application potential and increasing the risk of downcycling. This paper compares primary and secondary aluminium routes from the perspectives of energy and environmental performance, evaluates the quality constraints of currently used secondary casting alloys, and discusses prospects for a new generation of Fe-tolerant and "recycle-friendly" alloys. Particular attention is paid to their relevance for aluminium castings used in electric vehicles, where mechanical requirements, casting technologies, and sustainability of material flows must be reconciled.

Keywords: secondary aluminium, recycling, aluminium alloys, carbon footprint.

1. INTRODUCTION

Aluminium is among the most important structural materials in modern engineering, primarily due to its combination of low density (≈ 2.7 g/cm³), good electrical and thermal conductivity, high corrosion resistance, excellent formability, and a favourable strength-to-weight ratio. Aluminium alloys provide a wide range of mechanical properties; in particular, precipitation-hardenable systems can be formed in a soft condition and subsequently heat treated to achieve a significant increase in strength, which supports their use in structurally demanding applications. Owing to its non-toxicity and the ability to be repeatedly recycled without a fundamental loss of properties, aluminium is considered a circular material and a key enabler of the transition to a low-carbon and circular economy. Globally, aluminium is the

second most consumed metal after steel, and its importance is growing especially in sectors critical to CO_2 reduction, such as transportation, construction, and packaging [1, 2].

Although aluminium is the most abundant metal in the Earth's crust, its isolation in elemental form was only achieved in the 19th century, and the first production methods were extremely costly, which historically led to aluminium being perceived as a luxury material. Industrial expansion of aluminium became possible through the combined development of the Bayer process (production of alumina from bauxite) and the Hall-Héroult process (electrolytic reduction of Al_2O_3), which established the technological basis of modern primary aluminium production [3, 4].

2. ALUMINIUM PRODUCTION

Current aluminium production is therefore divided into primary production based on bauxite and secondary production based on scrap and residual materials; the differences between these two routes fundamentally affect energy consumption, emissions, and production economics [3, 5].

2.1 Primary aluminium production

Primary aluminium is produced by the Hall-Héroult process, in which alumina is dissolved in molten cryolite and reduced to liquid aluminium, while significant amounts of CO_2 and other greenhouse gases are generated at carbon anodes. A substantial share of the energy demand of primary production is already associated with the Bayer process, which requires high temperatures and pressures and includes several energy-intensive steps such as clarification, precipitation, and calcination [1, 4].

Despite research efforts aimed at replacing carbon anodes with inert alternatives, a solution that is reliably applicable at industrial scale has not yet been established, which constrains the decarbonisation potential of primary aluminium production [1].

2.2 Secondary aluminium production

Secondary aluminium production represents an environmentally and economically advantageous alternative because it utilises technological, commercial, and post-consumer wastes and significantly reduces the need for bauxite mining as the primary raw material for aluminium production [1, 5].

Secondary Aluminium Production (SAP) requires approximately 10-15 times less energy than primary aluminium production. Recycling of metal scrap is beneficial in terms of conserving aluminium resources and reducing costs associated with landfilling. SAP is particularly advantageous for countries that are fully dependent on imports of primary aluminium, because scrap can be used to recover aluminium and partially satisfy domestic demand. The importance of SAP is increasing globally due to an exponential growth in aluminium demand (Figure 1) and the rising amount of aluminium scrap becoming available [6, 10].

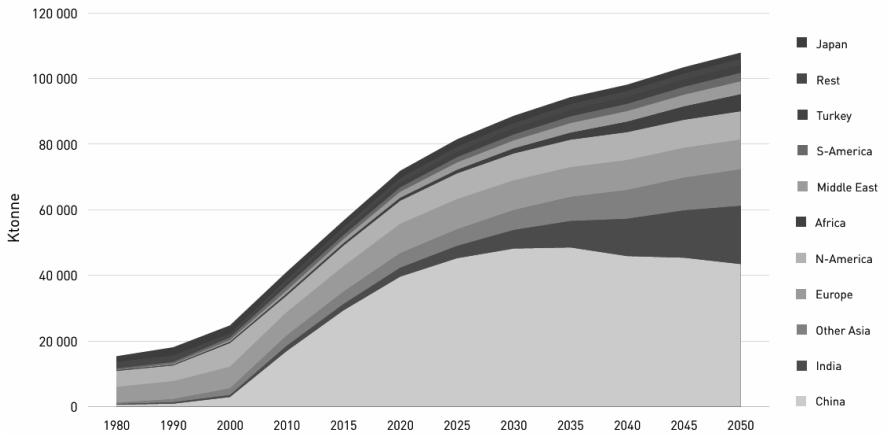

Figure 1. Demand for primary aluminium 1980 - 2050 [6]

At present, approximately 36 % of total aluminium production is based on recycling, i.e., secondary production. By 2050, this share may reach up to 50 % of European Union demand and help avoid approximately 39 million tonnes of CO_2 per year. Supporting secondary production can also reduce EU dependence on aluminium imports from other regions, such as China, which produces more than 55 % of global primary aluminium [4].

The feedstock for secondary production is aluminium scrap, typically classified into pre-consumer (production) and post-consumer (end-of-life) scrap. Pre-consumer scrap is usually chemically more homogeneous and enables the production of recycled alloys with higher added value, whereas post-consumer scrap is a heterogeneous mixture of alloys and contaminants. From a volume perspective, post-consumer scrap has the greatest potential for future recycling growth. However, its processing requires demanding sorting and chemical composition control. Insufficient sorting leads to the accumulation of impurities - especially iron - which negatively affects the mechanical properties of secondary alloys [2, 4].

2.3 Quality of secondary aluminium and scrap processing

The main limiting factor of secondary production is the accumulation of undesirable elements and contaminants, which makes most scrap-derived aluminium unsuitable for applications requiring high purity [1, 11].

To address this issue, strategies such as dilution of secondary aluminium with primary metal or downcycling (production of lower-grade alloys) are applied; however, these approaches may also lead to economic challenges for secondary production [1, 5].

Key steps in aluminium recovery include:

1. Physical separation, covering methods such as magnetic separation, air separation, eddy current separation, sink/float separation, and optical colour sorting.
2. Refining processes, including the Hoopes process, fluxing, gas fluxing, and related treatments. Figure 2 integrates the various recovery processes used in SAP.

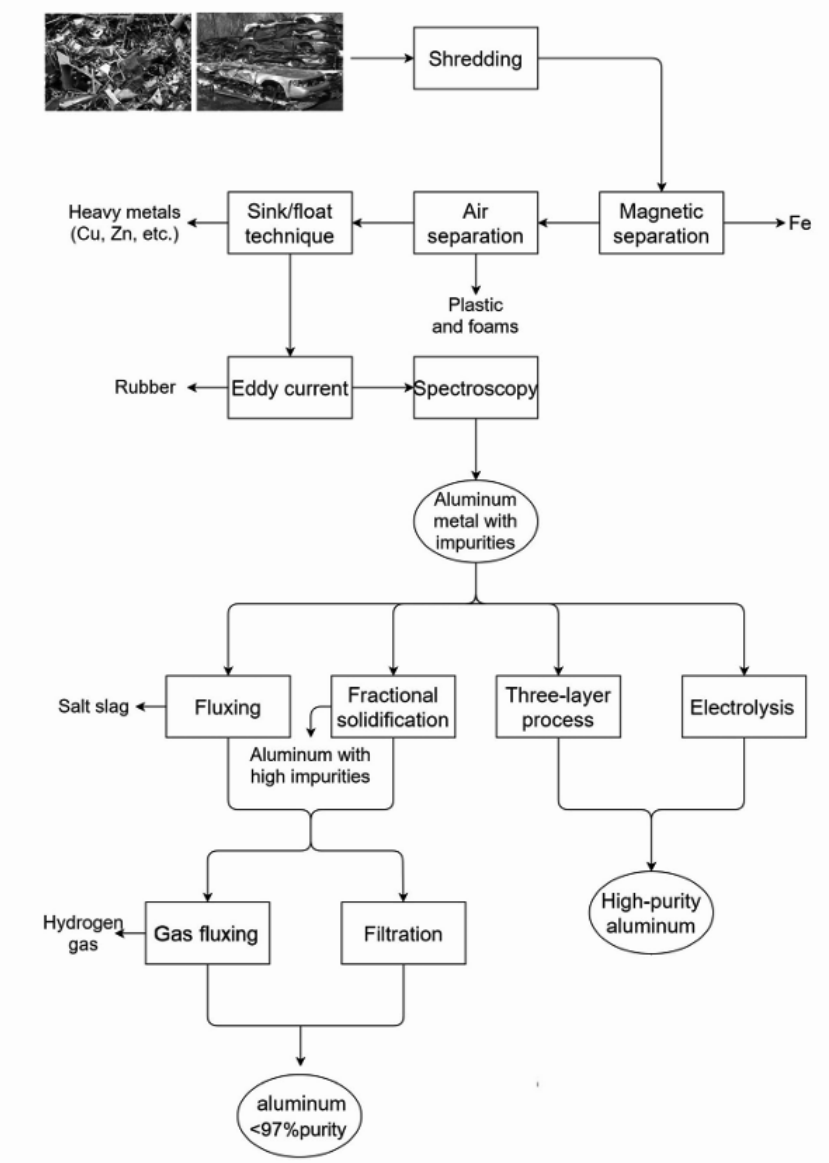

Figure 2. Flowsheet of aluminium recovery using various recovery processes from scrap [5]

3. ALUMINIUM RECYCLING

It is more than certain that due to the energy crisis and increasing electricity prices, primary aluminium production will decline, whereas secondary production will increase. Secondary aluminium also has the advantage of significantly lower energy demand and thus a substantially lower carbon footprint, making it a decisive material for achieving the climate targets of the European Union [2, 6].

From an environmental perspective, aluminium recycling offers the greatest potential for reducing CO_2 emissions within the aluminium sector. European scenarios indicate that replacing imported primary aluminium with recycled aluminium could lead to a significant emissions reduction by 2030, as quantified in Figure 3, which shows avoided CO_2 emissions by comparing 2019 and 2030 [2, 11].

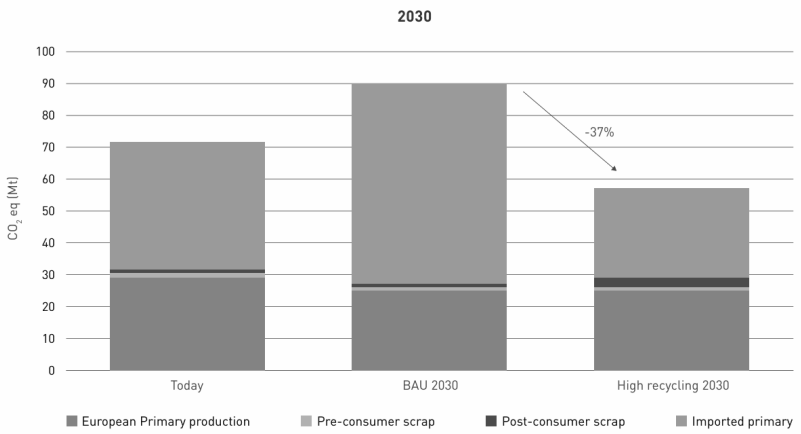

Figure 3. CO_2 emissions avoided by replacing import of primary aluminium with recycled aluminium in Europe [2]

4. APPLICATIONS OF ALUMINIUM

The transport sector is the most significant and fastest-growing area of aluminium use in Europe and globally (Figure 4). The increasing share of electric vehicles (EVs) drives demand for lightweight structural materials, because mass reduction directly affects driving range, energy efficiency, and battery system sizing [7, 8].

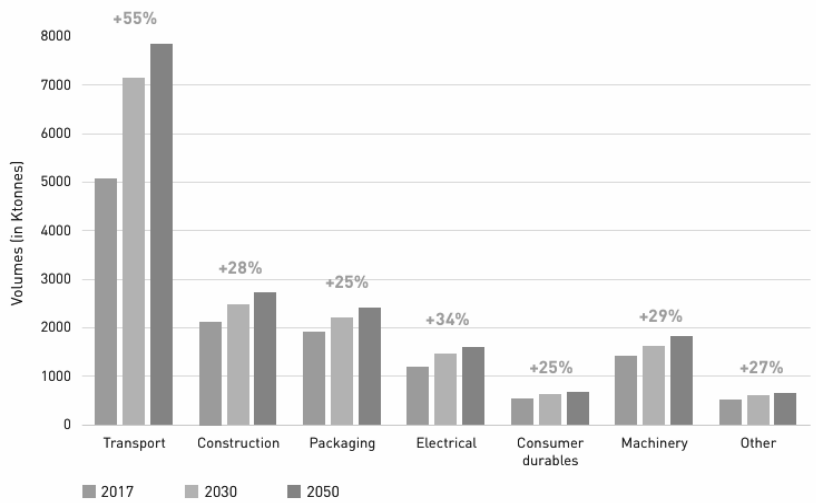

Figure 4. Demand for semi-finished aluminium in Europe per sector [2]

The transition from internal combustion engines to electric powertrains fundamentally changes demand patterns for aluminium castings. While engine blocks and transmissions dominated in conventional vehicles, EVs increasingly require castings for battery enclosures, electric motor housings, and power electronics casings [7].

Figure 5 shows that in Europe, by 2025, the mass of cast aluminium demand for combustion powertrains is expected to decrease by approximately 16 %, whereas cast aluminium demand for battery systems is expected to increase by approximately 19 %. Globally, cast aluminium demand is also projected to rise further due to expanding electric mobility.

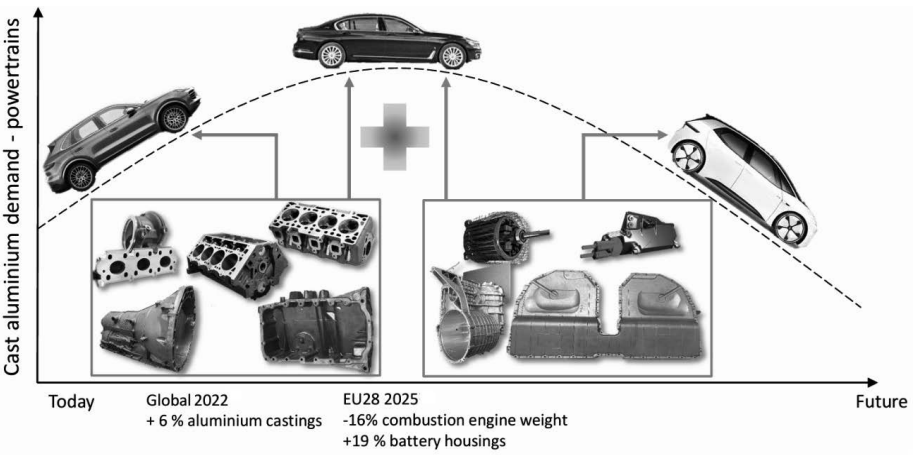

Figure 5. Cast aluminium demand - powertrain [7]

4.1 Secondary alloys used today

In industrial practice, secondary casting alloys are dominated by Al-Si, Al-Si-Mg, and Al-Si-Cu systems, suitable for gravity casting, low-pressure casting, and high-pressure die casting (HPDC). Common alloys include AlSi7Mg0.3, AlSi9Cu3(Fe), and AlSi12, used for housings, wheels, engine blocks, cylinder heads, and various structural castings. Their advantages include good castability and the possibility to tailor properties by heat treatment; however, they remain sensitive to Fe content [4].

Repeated remelting cycles of secondary aluminium alloys lead to pronounced microstructural changes and degradation of mechanical properties. During remelting, some alloying elements are lost - especially eutectic silicon modifiers - while impurity levels, particularly iron, increase. For the AlSi9Cu alloy (Figures 6, 7), a decline in tensile strength and elongation has been observed already after the fourth remelting cycle, correlating with an increasing Fe content [4].

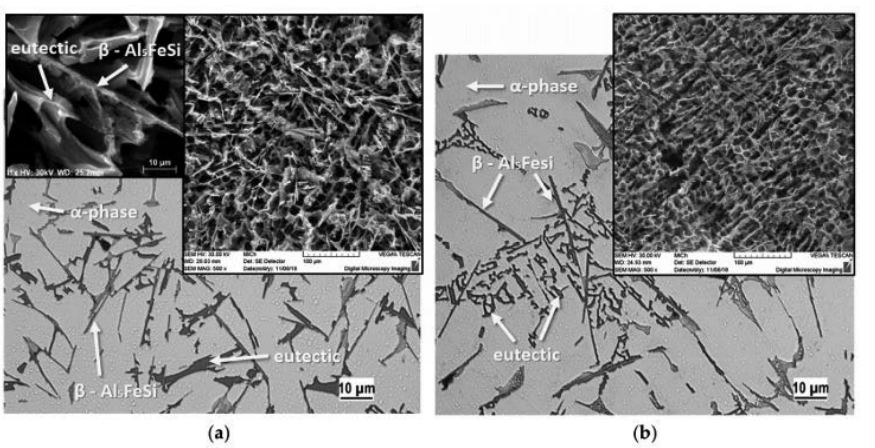

Figure 6. Microstructures of the AlSi9Cu alloy after: (a) one cycle of remelting, (b) three cycles of remelting [9]

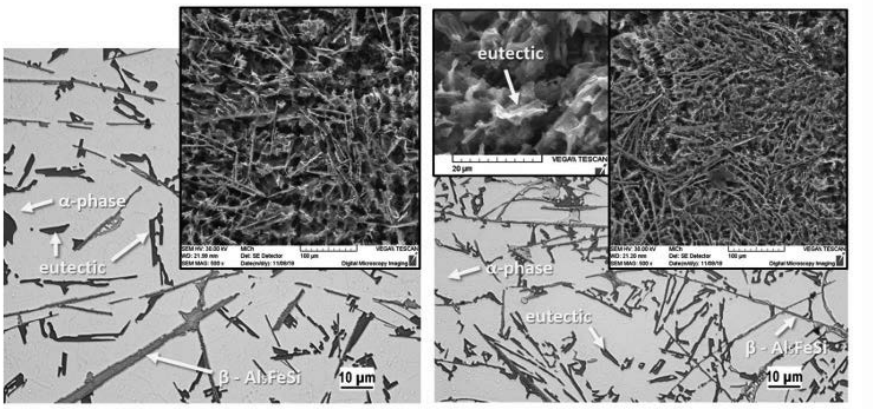

Figure 7. Microstructures of the AlSi9Cu alloy after: (c) five cycles of remelting, and (d) seven cycles of remelting [9]

Iron is among the most critical impurities in secondary aluminium alloys. At higher concentrations, it promotes the formation of Fe-rich intermetallic phases, particularly the needle-like β-Al5FeSi, which increases brittleness, reduces ductility, and supports crack initiation - this is a major driver of downcycling. From a metallurgical standpoint, Fe behaviour is significantly influenced not only by its absolute level but also by ratios such as Si/Fe and (Fe, Mn)/Si, cooling rate, and casting technology. Therefore, addressing Fe cannot rely solely on tightening chemical limits; it also requires targeted alloy design and optimisation of solidification conditions [4].

4.2 New generation of Fe-tolerant secondary alloys

With increasing post-consumer scrap volumes and pressure to raise recycled content, research is shifting toward Fe-tolerant secondary alloys capable of accommodating higher Fe contents without major loss of mechanical performance. One key strategy is transforming harmful β phases into less detrimental α-Al(Fe,Mn)Si phases via microalloying (especially Mn, potentially Cr) and composition optimisation [4].

The automotive aluminium roadmap explicitly highlights the need to develop structural HPDC alloys with higher allowable Fe levels to enable broader use of secondary aluminium in load bearing and safety-relevant components. This approach is commonly described as "recycle-friendly alloy design", representing a shift from purity maximisation toward functional performance optimisation under recycled input constraints [8].

In addition to modified Al-Si systems, alternative alloy families are being explored to better tolerate recycled feedstock. A promising direction involves alloys with combined Zn-Si-Mg additions, potentially providing higher strength and improved Fe tolerance. An example is the experimental alloy AlZn10Si8Mg, investigated as a potential substitute for the widely used AlSi7Mg0.3 in specific applications. The aim is to achieve comparable or superior mechanical properties at higher recycled input shares [4, 8].

CONCLUSION

Secondary aluminium production is the most effective route for reducing energy demand and CO_2 emissions in the aluminium industry, and its importance will continue to increase over

the coming decades due to constraints on primary production and growing scrap availability. The key technical limitation for wider deployment of secondary alloys remains the quality of scrap feedstock and the associated accumulation of Fe, which degrades mechanical properties and increases downcycling risks. Future progress will therefore depend not only on stricter chemistry limits but on a combined strategy of advanced scrap sorting, process optimisation, and development of Fe-tolerant "recycle-friendly" alloys. In the context of electric mobility - where demand is rising for aluminium castings used in battery systems and electric powertrains - such alloy concepts represent a critical prerequisite for sustainable, material-efficient use of secondary aluminium in structurally and safety-demanding applications.

ACKNOWLEDGEMENTS

This paper was prepared within the framework of the joint Slovak-Polish project TalentDetector 2026 as a result of collaboration between the Silesian University of Technology (Poland) and the University of Žilina (Slovakia), and was supported by the projects VEGA 1/0461/24 and KEGA 033ŽU-4/2026.

BIBLIOGRAPHY

1. X. Lian, H. Gao, L. Shen, Y. Yu, Y. Wang, Z. Peng, Life Cycle Assessment of Primary Aluminum Production, Processes 13 (2025) 419.
2. European Aluminium, Circular Aluminium Action Plan: A Strategy for Achieving Aluminium's Full Potential for Circular Economy by 2030, European Aluminium, Brussels, (2020).
3. Aluminum and Aluminum Alloys, *ASM Subject Guide*, ASM International, Materials Park, Ohio, (2015).
4. H. Nunes, O. Emadinia, R. Soares, M.F. Vieira, A. Reis, Adding Value to Secondary Aluminum Casting Alloys: A Review on Trends and Achievements, Materials 16 (2023) 895.
5. S.K. Padamata, A. Yasinskiy, P. Polyakov, A Review of Secondary Aluminum Production and Its Byproducts, JOM 73 (9) (2021) 2603-2614.
6. European Aluminium, Vision 2050 - European Aluminium's Contribution to the EU's Mid-Century Low-Carbon Roadmap, European Aluminium, Brussels, (2019).
7. J. Steglich, L. Marzoli, I. Zerbin, Cast alloys for electric vehicle powertrains, Conference presentation, EAC Düsseldorf, Germany, (2019).
8. The Aluminum Association, Roadmap for Automotive Aluminum: Driving Industry Innovation and Collaboration, The Aluminum Association, Washington, DC, (2021).
9. J. Kasińska, D. Bolibruchová, M. Matejka, The Influence of Remelting on the Properties of AlSi9Cu3 Alloy with Higher Iron Content, Materials 13 (2020) 575.
10. K.N. Maung, T. Yoshida, G. Liu, C.M. Lwin, D.B. Müller, S. Hashimoto, Assessment of secondary aluminum reserves of nations, Resources, Conservation & Recycling 126 (2017) 34-41.
11. S. Al-Alimi, N.K. Yusuf, A.M. Ghaleb, M.A. Lajis, S. Shamsudin, W. Zhou et al., Recycling aluminium for sustainable development: A review of different processing technologies in green manufacturing, Results in Engineering 23 (2024) 102566.

TalentDetector

9th January 2026
Gliwice, Poland

DEPARTMENT OF ENGINEERING MATERIALS AND BIOMATERIALS
FACULTY OF MECHANICAL ENGINEERING
SILESIAN UNIVERSITY OF TECHNOLOGY

INTERNATIONAL STUDENTS SCIENTIFIC CONFERENCE

Design and construction of an automatic vertical hammer for impact strength testing in accordance with IEC 60068-2-75

Tomasz Janica [a], Kamil Kohut[b], Dawid Osińczuk[b], Dominik Szlichcin[a], Daniel Wala[a], Mariola Jureczko [c]

[a] Students, Silesian University of Technology, Faculty of Mechanical Engineering, Mechanics, and Machine Construction
[b] Students, Silesian University of Technology, Faculty of Mechanical Engineering, Industrial Automation and Robotics
[c] Silesian University of Technology, Faculty of Mechanical Engineering, Department of Theoretical and Applied Mechanics
email: mjureczko@polsl.pl

Abstract: This paper describes the comprehensive design and construction of an automated vertical hammer specifically designed for impact strength testing, in strict compliance with the IEC 60068-2-75 standard. The research focused on increasing the repeatability of the test procedures by integrating advanced mechanical components with an automatic feedback control system. The optimal design, with two guide shafts and two lead screws (Concept 3), was selected through a weighted multi-criteria evaluation to ensure maximum perpendicularity and favorable load distribution. The use of a Siemens S7-1200 PLC and KTP700 HMI enables fully automated measurement cycles and a drop height accuracy of ±1%, effectively minimizing human factors. Furthermore, the device incorporates a precise linear motion system and stringent safety features, including a PILZ PNOZ X3 relay compliant with Category 4 PL e and SIL 3 standards. The final device provides a robust testing tool, guaranteeing high repeatability and operational safety in a variety of industrial applications.

Keywords: vertical hammer, impact testing, IEC 60068-2-75, automation, PLC

1. INTRODUCTION

The objective of this study was the comprehensive design and physical implementation of a fully functional, automated vertical hammer, specifically engineered for impact testing in accordance with the stringent requirements of the IEC 60068-2-75 standard [1]. A pivotal stage of the project, fundamental to ensuring operational safety and reliability, involved conducting detailed structural strength calculations. Simultaneously, precise analyses of the forces acting on test specimens at the moment of impact were performed, which is essential to ensure the credibility of results and full compliance with the testing procedures specified in the aforementioned standard.

Based on the data derived from these engineering analyses, the mechanical structure was designed and manufactured using an optimized configuration of twin guide shafts and twin lead screws (Concept 3), ensuring maximum ram perpendicularity and favorable load distribution. A fundamental aspect of the project was the integration of advanced automation systems with mechanical components, which significantly enhanced the repeatability of testing procedures compared to manual solutions available on the market. The implementation of a programmable logic controller (PLC - Siemens S7-1200) and specialized sensors enabled precise control over test parameters and full automation of measurement cycles. This approach effectively minimized the human factor, which is critical for obtaining reproducible and reliable laboratory data. The completed work resulted in a robust testing device that not only complies with international standards but also guarantees advanced control, high reproducibility, and the highest safety standards for component durability verification.

2. CHOOSING THE BEST CONCEPT

At the beginning of the project, a criteria-based assessment of three different mechanical setups was performed to choose the optimal solution:

- Twin guide shafts and a single lead screw (fig.1.a. – concept 1);
- Twin lead screws only (fig.1.b. – concept 2);
- Twin guide shafts and twin lead screws (fig.1.c. – concept 3).

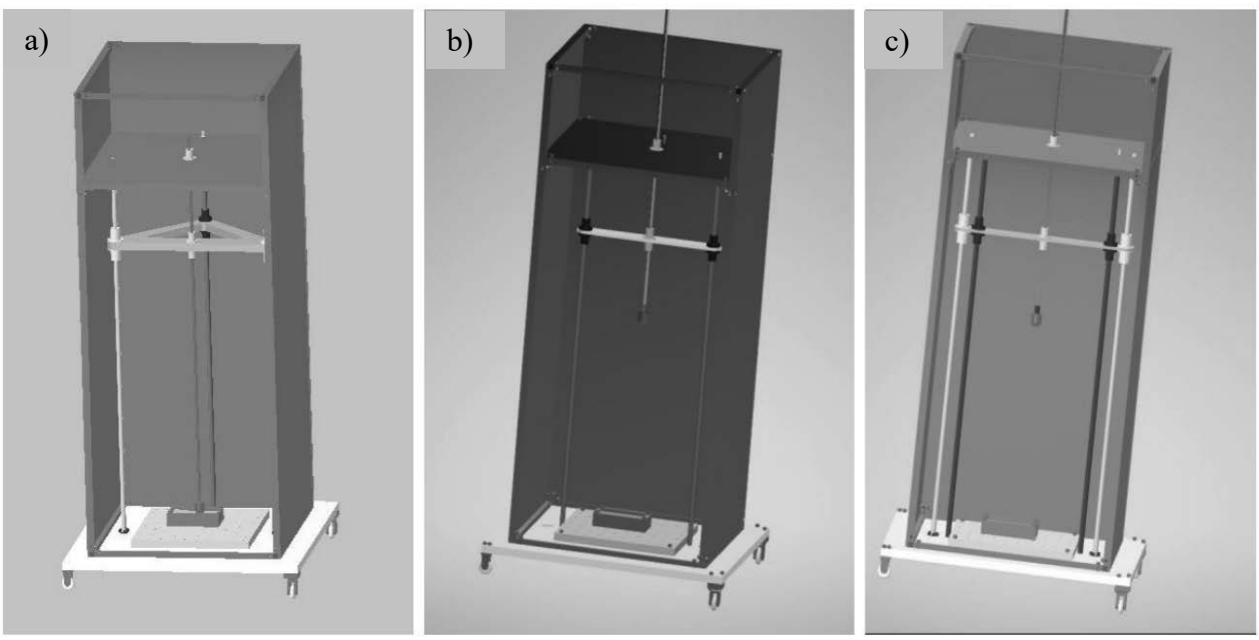

Figure 1. Developed test stand concepts

A weight scoring technique was used to select the best concept. The procedure for selecting the best concept using the weighted multi-criteria assessment was carried out in the following stages:

1. Criteria weighting: To reflect the technical priorities of the project, such as measurement precision and compliance with the IEC 60068-2-75 standard, the criteria were assigned a rank on a scale of 1-3, where 3 was very important, 2 was important, and 1 was other criteria.

For selecting the best test bench concept, the following ranks were assigned to the criteria considered:

- Perpendicularity and Parallelism (rank 3): Critical to test reliability and meeting standard requirements.
- Weight and Load Distribution (rank 2): Critical to device durability and result repeatability.
- Ease of Installation (rank 1): A secondary criterion, secondary to the technical quality of the device.

2. Calculations and Ranking: The synthetic score (U) is calculated as the sum of the products of weights (r_i) and partial scores.

$$(u_i),\ U = \sum_{i=1}^{5} r_i \cdot u_i$$

Table 1. Weighted multi-criteria assessment of design concepts

Criteria	weights (r_i)	Concept 1	Concept 2	Concept 3
Perpendicularity of the impact to the test specimen	**3**	5	3.5	5
Parallelism of the impactor to the guide elements	**3**	5	5	5
Ease of assembly	**1**	3.5	5	3.5
Weight distribution	**2**	3	4	5
Uniform load distribution across guide elements	**2**	1	4	5
The synthetic score		**41.5**	**46.5**	**53.5**

The highest synthetic score (U = 53.5 points) was achieved by Concept 3, featuring twin guide shafts and twin lead screws. Although this configuration entails greater assembly complexity, it demonstrates superior performance in criteria of the highest strategic importance (ranks 2 and 3), specifically in ensuring perfect perpendicular alignment and optimal load distribution. The selection of this design facilitates the realization of a testing apparatus with maximum precision, which directly addresses the fundamental research goals: minimizing the human factor and significantly enhancing the repeatability of impact tests.

3. COMPETITIVE ADVANTAGES AND MARKET DIFFERENTIATION

The primary advantage of the developed impact test stand is its implementation as a fully automated test stand, ensuring strict compliance with the IEC 60068-2-75 standard. To the best of the authors' knowledge, this is a unique application of a Siemens S7-1200 PLC-controlled system that enables the execution of tests with significantly higher precision and repeatability than currently available manual solutions.

A secondary objective of the project was the minimization of the human factor in the testing process. In typical market solutions, tests are performed manually, making the results highly dependent on the operator's qualifications and experience. In the proposed conceptual solution, the human role is limited exclusively to specifying the required impact force level through

a Siemens KTP700 Basic HMI panel, after which the system automatically executes the programmed cycle.

While existing competitive products often utilize PETG tubes for gravity-fed "weight" drops, this solution incorporates an automated, high-precision linear motion system based on ball-screw drives. This advancement allows for durability stress testing with exceptional accuracy and repeatable positioning, verified by a stepper motor servo controller with an encoder to compensate for any potential "lost steps".

4. VERTICAL HAMMER - AUTOMATION

Modern industry is increasingly transitioning from manual control toward advanced autonomous systems. Automation is no longer merely a convenience but has become a technical and economic necessity. This process involves the integration of mechanical assemblies with digital control architectures, facilitating real-time regulation of machine operations and ensuring exceptional precision. A primary component for configuring the critical parameters of the impact strength testing process - including the number of automatic cycles, height adjustment, and real-time measurement of forces applied by the selected load - is the Siemens KTP700 Basic HMI (Human-Machine Interface) panel. This interface also manages auxiliary functions, such as the activation of lighting for precise monitoring of test progress and the implementation of a manual operation mode.

Ensuring rigorous safety standards in accordance with the Machinery Directive 2006/42/EC [2, 3] was a fundamental requirement of the project described. To achieve this, a PILZ PNOZ X3 774310 safety relay was integrated, meeting the requirements of Category 4 PL e [4] and SIL 3 [5]. This safety system provides continuous monitoring of the emergency stop buttons, located at both the front and rear of the machine, as well as the front door limit switch, which prevents operation while the doors are open. In the event of an uncontrolled situation endangering the operator, the relay facilitates an immediate interruption of the working cycle upon activation of any emergency stop input. The "heart" of this automation system is the Siemens S7-1200 1214C PLC, which transforms the mechanical structure into a high-precision research tool. By implementing complex control logic, the PLC manages the positioning of the ball-screw drives and coordinates the stepper motor servo controller. This integration allows the device to achieve superior repeatability by compensating for potential "lost steps" via an encoder system, thereby minimizing the influence of the human factor on the final test results.

5. SAMPLE CALCULATIONS

To ensure high operational reliability and precise positioning of the test platform, an analysis of the drive parameters of the lifting system was conducted. These calculations were crucial for the correct selection of the stepper motor and for verifying the mechanical efficiency of the selected screw gears. Due to the selection of Concept 3 (a system with two lead screws), the total torque T_{total} was determined as the sum of the torques required to drive both screws simultaneously.

The analysis takes into account the effect of the variable friction coefficient μ on the system efficiency η and the required motor load. Assuming different values of μ (from 0.10 to 0.15) allows for the potential wear of friction elements or changes in guide lubrication, which is

essential for maintaining the safety and repeatability of tests during long-term operation of the device. The amount of motor torque needed to lift the entire load:

- For $\mu = 0.10$:
  $\eta_1 = 0.527$ (52.7%)
  Torque for each screw $T_1 \approx 0.311$ Nm
  T_total ≈ 0.622 Nm

- For $\mu = 0.12$:
  $\eta_2 \approx 0.481$ (48.1%)
  $T_1 \approx 0.341$ Nm
  T_total = 0.681 Nm

- For $\mu = 0.15$:
  $\eta_3 \approx 0.426$ (42.6%)
  $T_1 \approx 0.385$ Nm
  T_total = 0.769 Nm

6. NORMATIVE FORCE TABLE

The IEC 60068-2-75 standard establishes standardized energy levels to ensure that impact test results are directly comparable across different laboratory environments. This framework is essential for maintaining global consistency in durability assessments, as it allows researchers to conduct tests using identical energy values. The following table (Table 2) illustrates the specific combinations of equivalent mass and fall height required to achieve these normative thresholds.

To ensure the credibility of the test results, the fall height must be maintained with a precision of ± 1%, which in this project is facilitated by the automated high-precision linear motion system and PLC control. This integration of advanced automation significantly enhances the repeatability of the tests, minimizing the variations typically associated with manual testing methods.

Table 2. Energy levels and corresponding impact parameters according to IEC 60068-2-75

Energy (J)	Equivalent mass (kg)	Falls (mm ± 1%)
0,14 J	0,25 kg	56 mm
0,2 J	0,2 kg	100 mm
0,2 J	0,25 kg	80 mm
0,3 J	0,2 kg	150 mm
0,35 J	0,25 kg	140 mm
0,4 J	0,2 kg	200 mm
0,5 J	0,2 kg	250 mm
0,5 J	0,25 kg	200 mm
0,7 J	0,25 kg	280 mm
1 J	0,25 kg	400 mm

2 J	0,5 kg	400 mm
5 J	1,7 kg	300 mm
10 J	5 kg	200 mm
20 J	5 kg	400 mm
50 J	10 kg	500 mm

The precision of these heights (±1%) is guaranteed by the PLC control system and the stepper motor encoder, which distinguishes the device from the competition.

7. CONCLUSIONS

The shift in modern industry from manual control towards advanced autonomous systems makes automation a technical and economic necessity. Thanks to the integration of mechanical systems with digital PLC control, the developed automatic vertical hammer is widely used in sectors requiring the highest precision and repeatability of impact tests. The device's main application areas include:

- Research laboratories and certification bodies – the device is dedicated to facilities performing impact resistance tests in accordance with the stringent requirements of the IEC 60068-2-75 standard. The use of a Siemens S7-1200 controller and a precise linear motion system based on ball screws allows for a drop height accuracy of 1%, guaranteeing the comparability of test results between different laboratories.
- Automotive industry – in this sector, the device is used to verify the durability of components. A key aspect is minimizing the influence of the human factor on test results; The operator simply selects the impact force level on the HMI panel, eliminating errors resulting from inexperienced personnel and ensuring the reliability of laboratory data necessary for assessing the durability of vehicle parts.
- Defense and military industries – companies in this sector require rigorous stress and impact resistance analysis under extreme operating conditions. Operator safety during such intensive testing is guaranteed by an advanced protection system based on the PILZ PNOZ X3 safety relay, meeting Category 4 PL e, and SIL 3 requirements, allowing for immediate interruption of the work cycle in hazardous situations.
- Medical device production – medical device manufacturers, striving to deliver the highest quality devices, utilize automatic hammers to precisely verify the mechanical resistance of housings and sensitive components. Full automation of measurement cycles and the ability to monitor parameters in real time ensure the highest quality control standards, which is critical in the medical industry.

The project successfully achieved its primary objective: the comprehensive development and physical realization of a fully functional automatic vertical hammer for impact testing in accordance with the IEC 60068-2-75 standard [1]. The final device provides an important level of control, repeatability, and safety, surpassing traditional manual market solutions. The implementation of a multi-criteria assessment, specifically the weighted point rating technique, was crucial in selecting the optimal mechanical configuration. Concept 3, featuring twin guide shafts and twin lead screws, emerged as the superior solution, ensuring perfect perpendicular alignment of the impactor and optimal load distribution across guide elements.

This design choice directly translates to the credibility and precision of the strength testing results.

A significant technological advantage of the developed stand is the integration of an advanced automation system based on the Siemens S7-1200 PLC and KTP700 Basic HMI panel. This transition from manual control to an autonomous system effectively minimized the human factor, as the operator's role is limited to selecting the required force level. Furthermore, the use of a high-precision linear motion system with ball-screw drives and a stepper motor with encoder feedback ensures exceptional positioning repeatability and eliminates the issue of "lost steps".

Safety and operational reliability were confirmed through detailed structural strength calculations and precise impact force analysis. Compliance with the Machinery Directive 2006/42/EC was achieved by integrating a PILZ PNOZ X3 safety relay, providing Category 4 PL e and SIL 3 protection. In conclusion, the designed vertical hammer represents a high-precision research tool that meets modern industrial requirements for automation and rigorous testing standards.

BIBLIOGRAPHY

1. The IEC standard for "Environmental testing - Part 2-75: Tests - Test Eh: Hammer tests", IEC 60068-2-75:2014 © IEC 2014
2. The Machinery Directive 2006/42/EC (MD)
3. Acarnley, P. (2002). Stepping Motors: A Guide to Theory and Practice. 4th ed. London: IET.
4. Mastering EN ISO 13849-1: Key Principles for Safe Control Systems
5. The Polish/European standard for functional safety of machine control systems PN-EN IEC 62061

TalentDetector

9th January 2026
Gliwice, Poland

DEPARTMENT OF ENGINEERING MATERIALS AND BIOMATERIALS
FACULTY OF MECHANICAL ENGINEERING
SILESIAN UNIVERSITY OF TECHNOLOGY

INTERNATIONAL STUDENTS SCIENTIFIC CONFERENCE

Kinetyka przemian fazowych w stopach metali - podstawy teoretyczne analizy termiczno-derywacyjnej

Ewa Jędryka[a], Mateusz Kuźnik[a], Franciszek Bednarz[a], Mariusz Krupiński[b]

[a]Politechnika Śląska, Wydział Mechaniczny Technologiczny, Mechanika i Budowa Maszyn
[b]Politechnika Śląska, Wydział Mechaniczny Technologiczny, Katedra Materiałów Inżynierskich i Biomedycznych, 44-100 Gliwice, ul. Konarskiego 18a
email: mariusz.krupinski@polsl.pl

Streszczenie: W pracy omówiono teoretyczne podstawy analizy termiczno-derywacyjnej. Analiza termiczno-derywacyjna umożliwia określenie przebiegu krystalizacji stopu w zależności od składu chemicznego oraz fazowego. W ramach opracowania przeprowadzono szczegółową analizę literatury przedmiotu, na podstawie której sklasyfikowano metody TDA i DTDA oraz zdefiniowano kluczowe parametry kinetyki krzepnięcia. W pracy przedstawiono termodynamiczne ujęcie procesu z wykorzystaniem newtonowskiego modelu chłodzenia oraz metodologię wyznaczania linii bazowej, niezbędnej do obliczeń kalorymetrycznych. Teoretyczne rozważania poparto przykładem zastosowania metody do analizy stopów z układu Zn-Al, wskazując na wpływ modyfikatorów na charakterystyczne punkty temperaturowe oraz końcową mikrostrukturę odlewu.

Abstract: The paper discusses the theoretical foundations of thermal-derivative analysis. Thermal-derivative analysis enables the determination of the alloy crystallization process depending on its chemical and phase composition. As part of the study, a detailed literature review was conducted, based on which TDA and DTDA methods were classified and key solidification kinetics parameters were defined. The work presents a thermodynamic approach to the process using the Newtonian cooling model and the methodology for determining the baseline necessary for calorimetric calculations. Theoretical considerations were supported by an example of applying the method to the analysis of Zn-Al system alloys, indicating the influence of modifiers on characteristic temperature points and the final casting microstructure.

Słowa kluczowe: Analiza termiczno-derywacyjna, kinetyka krystalizacji, Newtonowski model chłodzenia

1. WPROWADZENIE

Analiza termiczna i derywacyjna procesu krzepnięcia metali i stopów znajduje coraz większe zastosowanie w przemyśle odlewniczym i metalurgicznym. Metody te są stosowane jako techniki umożliwiające szybką i całkowitą ocenę przebiegu krystalizacji oraz pośrednią ocenę składu chemicznego stopu. Dzięki wysokiej czułości na zmiany cieplne zachodzące w

materiale pozwalają one na identyfikację charakterystycznych etapów krzepnięcia oraz przemian fazowych występujących podczas chłodzenia ciekłego metalu [1].

Zaletą analizy termicznej i derywacyjnej jest możliwość jednoczesnej oceny kinetyki krystalizacji pierwotnej i wtórnej - wyznaczenie temperatur charakterystycznych, czasu trwania krystalizacji oraz przebiegu pochodnej temperatury. Umożliwia analizę intensywności wydzielania ciepła krystalizacji i mechanizmów wzrostu faz stałych. W literaturze naukowej, parametry te są powiązane z właściwościami mechanicznymi metali i stopów. Wykazano, że wybrane parametry krzywych ATD mogą być wykorzystywane do oceny właściwości użytkowych materiałów, takich jak wytrzymałość mechaniczna, plastyczność czy skłonność do powstawania wad odlewniczych. Krótki czas uzyskiwania wyników umożliwia natychmiastową korektę parametrów technologicznych procesu, co sprzyja wysokiej jakości produkcji oraz ograniczeniu strat materiałowych. Możliwość ciągłej obserwacji przebiegu krystalizacji stanowi istotne narzędzie zarówno badawcze, jak i technologiczne. Analiza termiczna i derywacyjna pozwala na właściwy dobór warunków sterowania procesem krzepnięcia, prowadzący do uzyskania pożądanej struktury i wysokiej jakości wyrobów metalowych [1-3].

2. METODY ANALIZY-TERMICZNO DERYWACYJNEJ

W przemyśle stosuje się dwa podstawowe typy analizy termiczno-derywacyjnej:

- klasyczną analizę termiczno-derywacyjną (TDA) – polegającą na rejestracji krzywej chłodzenia T(t) oraz jej pierwszej pochodnej dT/dt w jednym punkcie próbki. Jest to metoda ogólnie stosowana w warunkach przemysłowych do kontroli składu chemicznego, przebiegu krystalizacji oraz jakości ciekłego metalu [1, 2].
- różnicową analizę termiczno-derywacyjną (DTDA) – opartą na pomiarze temperatury w kilku punktach próbki lub na porównaniu próbki badanego stopu z próbką odniesienia. Umożliwia ona dokładniejszą analizę efektów cieplnych, ilości wydzielonego ciepła krystalizacji oraz lokalnej kinetyki przemian fazowych. Metoda ta jest stosowana głównie w badaniach technologicznych i laboratoriach przemysłowych [1, 2].

3. KINETYKA KRYSTALIZACJI STOPÓW METALI

Kinetyka krystalizacji stopów metali może być opisana za pomocą szeregu wielkości fizycznych i strukturalnych, które wzajemnie na siebie oddziałują i decydują o przebiegu procesu krzepnięcia oraz ostatecznej mikrostrukturze odlewu. Do najważniejszych parametrów charakteryzujących kinetykę krystalizacji należą [1, 2, 5]:

- szybkość stygnięcia ciekłego metalu,
- szybkość chłodzenia w trakcie krystalizacji,
- szybkość wydzielania ukrytego (utajonego) ciepła krystalizacji,
- gęstość ziarna, utożsamiana z gęstością powstających zarodków krystalizacji,
- udział frakcji stałej w wykrystalizowanym stopie,
- zmiany stężenia składników stopowych w pozostałej fazie ciekłej,
- charakterystyczne odległości między składnikami strukturalnymi oraz parametry opisujące ich kształt i rozmiar.

Proces chłodzenia ciekłego stopu przebiega od temperatury zalewania do osiągnięcia linii likwidus, odpowiadającej początkowi krystalizacji. Następnie zachodzi krystalizacja faz pierwotnych oraz eutektycznych, aż do momentu osiągnięcia linii solidus, czyli stanu pełnego zakrzepnięcia stopu, zgodnie z odpowiednimi diagramami równowagi fazowej [2, 3]. W trakcie tego procesu na krzywej chłodzenia pojawiają się charakterystyczne punkty załamania i przegięcia, będące efektem reakcji egzotermicznych (wydzielanie ciepła podczas krystalizacji) lub endotermicznych, związanych z przemianami fazowymi. Na podstawowej krzywej chłodzenia nie zawsze jest możliwe jednoznaczne wyznaczenie temperatur krystalizacji poszczególnych faz. Stosuje się analizę pierwszej pochodnej temperatury względem czasu, czyli analizę termiczno-pochodną (TDA), zwaną również analizą derywacyjną [2, 3]. Krzywa pochodna uwidacznia efekty cieplne zachodzące podczas krzepnięcia w postaci wyraźnych ekstremów, przegięć oraz zmian nachylenia. Położenie tych charakterystycznych punktów, pole powierzchni pod krzywą derywacyjną oraz jej ogólny kształt pozwalają na identyfikację rodzaju krystalizującej eutektyki oraz kolejności powstawania faz. Kształt krzywej pochodnej, odzwierciedlający przebieg krystalizacji w charakterystycznych punktach temperaturowych, pozwala na dokładne obliczenie ilości wydzielonego ciepła utajonego krystalizacji poszczególnych faz [2]. Przyjmując założenie, że wydzielone ciepło krystalizacji jest proporcjonalne do ilości (udziału objętościowego lub masowego) danej fazy w stopie, analiza TDA umożliwia również określenie udziału poszczególnych faz krystalizujących w trakcie krzepnięcia stopu. Dodatkowo, sumując pole pod krzywą derywacyjną pomiędzy punktami T_L (likwidus) a T_{Sol} (solidus), możliwe jest precyzyjne określenie stopnia krystalizacji stopu, czyli wyznaczenie ilości materiału, który skrzepł w przedziale od 0 do 100%.Charakterystyczne punkty widoczne na krzywych chłodzenia i krzywych pochodnych odzwierciedlają efekty cieplne zachodzące w stopie i są silnie uzależnione od składu chemicznego stopu, szybkości chłodzenia, intensywności wydzielania ciepła krystalizacji oraz temperatury ciekłego metalu w chwili zalewania formy. Parametry te mają bezpośredni wpływ na morfologię faz, wielkość ziarna oraz rozmieszczenie składników strukturalnych w mikrostrukturze odlewu (rys. 1) [1-4].

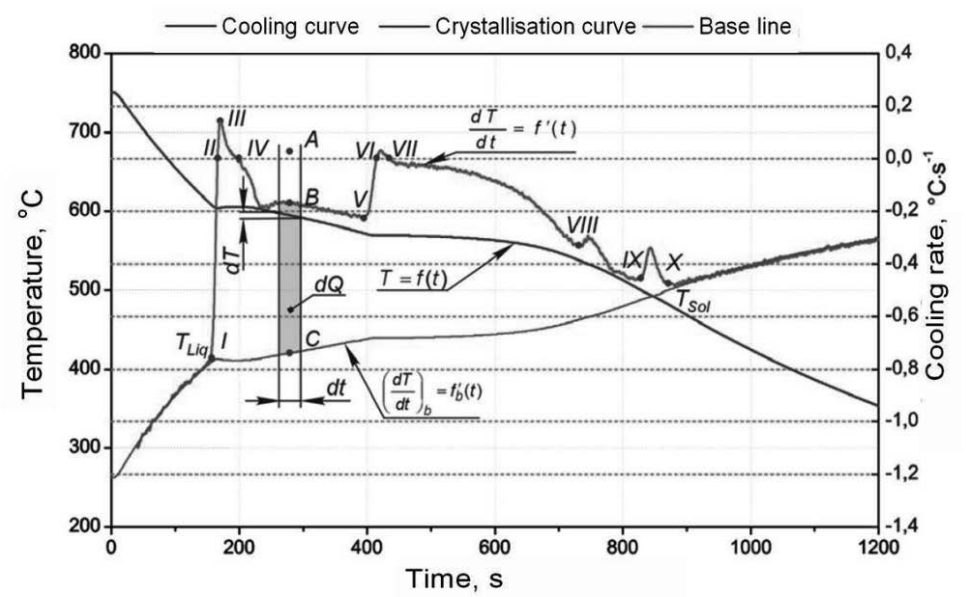

Rysunek 1. Krzywa chłodzenia, krzywa derywacyjna oraz krzywa kalorymetryczna stopu Al-Si-Cu [4].

Wszystkie wymienione wielkości są funkcjami czasu krystalizacji oraz współrzędnych geometrycznych odlewu, co oznacza, że proces krzepnięcia ma charakter niejednorodny w całej objętości odlewu. Pełna i ilościowa charakterystyka kinetyki krystalizacji może zostać uzyskana poprzez sprzężenie równań opisujących procesy krystalizacji z równaniami wymiany ciepła. Wydzielające się ciepło krystalizacji stanowi czynnik łączący oba te zagadnienia i jest bezpośrednio zależne od udziału wykrystalizowanych składników strukturalnych oraz dynamiki ich wzrostu [2].

4. TERMODYNAMICZNA ANALIZA PROCESU KRZEPNIĘCIA

W celu wyznaczenia i obliczenia parametrów procesów cieplnych zachodzących podczas krzepnięcia, należy przeprowadzić odpowiednie obliczenia termodynamiczne. Bardzo ważnym narzędziem w tej analizie jest krzywa szybkości chłodzenia z wyznaczoną linią bazową. Obliczenie równania linii bazowej wymaga, aby rozważany układ termiczny (tj. próbka stopu) spełniał wymagania Newtonowski'ego modelu chłodzenia. Oznacza to, że:

- temperatura wewnątrz układu musi być przestrzennie jednolita.
- gradient temperatury w dowolnym kierunku wewnątrz układu musi być pomijalny w każdym momencie procesu chłodzenia [5].

Ogólny współczynnik przenikania ciepła opiera się na całkowitym oporze cieplnym między temperaturą krzepnącej próbki (T_c) a temperaturą otoczenia (T_∞). Przy powyższych założeniach, bilans energii można zapisać następująco:

$$\frac{\rho C_p V\left(d(T_c - T_\infty)\right)}{dT} = -UA(T_c - T_\infty) + \frac{dQ_L}{dt}$$

Natomiast równanie linii bazowej w przypadku, gdy nie zachodzi żadna reakcja metalurgiczna (tj. gdy ciepło krystalizacji $Q_L = 0$), powyższe równanie można sprowadzić do formy, która pozwala wyznaczyć równanie linii bazowej:

$$\frac{dT_c}{dt} = \left(-\frac{UA}{\rho C_p V}\right)(T_c - T_\infty)$$

Oznaczenia parametrów:
Q_L - ciepło krystalizacji stopu, C_p - ciepło właściwe materiału, U – współczynnik przenikania ciepła, A – powierzchnia wymiany ciepła, V – objętość odlewu, ρ – gęstość stopu, dTc/dt - pochodna temperatury po czasie (szybkość chłodzenia), Tc – temperatura krzepnącego stopu, T_∞ – temperatura otoczenia, $\rho C_p V$ – człon pojemności cieplnej układu

5. PRZYKŁAD ZASTOSOWANIA ANALIZY TERMICZNO-DERYWACYJNEJ DO STOPÓW Zn-Al

Na rysunku przedstawiono krzywe chłodzenia oraz odpowiadające im krzywe derywacyjne (TDA) stopu Zn–Al–Cu w stanie niemodyfikowanym oraz po modyfikacji dodatkami Sr oraz Ti–B. Analizę termiczno-derywacyjną wykonano w celu określenia wpływu dodatków modyfikujących na przebieg krystalizacji, temperatury charakterystycznych przemian fazowych oraz kinetykę wydzielania ciepła krystalizacji. Zastosowanie dodatków stopowych

powoduje przesunięcia temperatur likwidus i solidus oraz zmiany intensywności efektów cieplnych widocznych na krzywych pochodnych, co świadczy o modyfikacji mechanizmu krzepnięcia i prowadzi do rozdrobnienia mikrostruktury oraz zmiany morfologii faz krystalizujących [6].

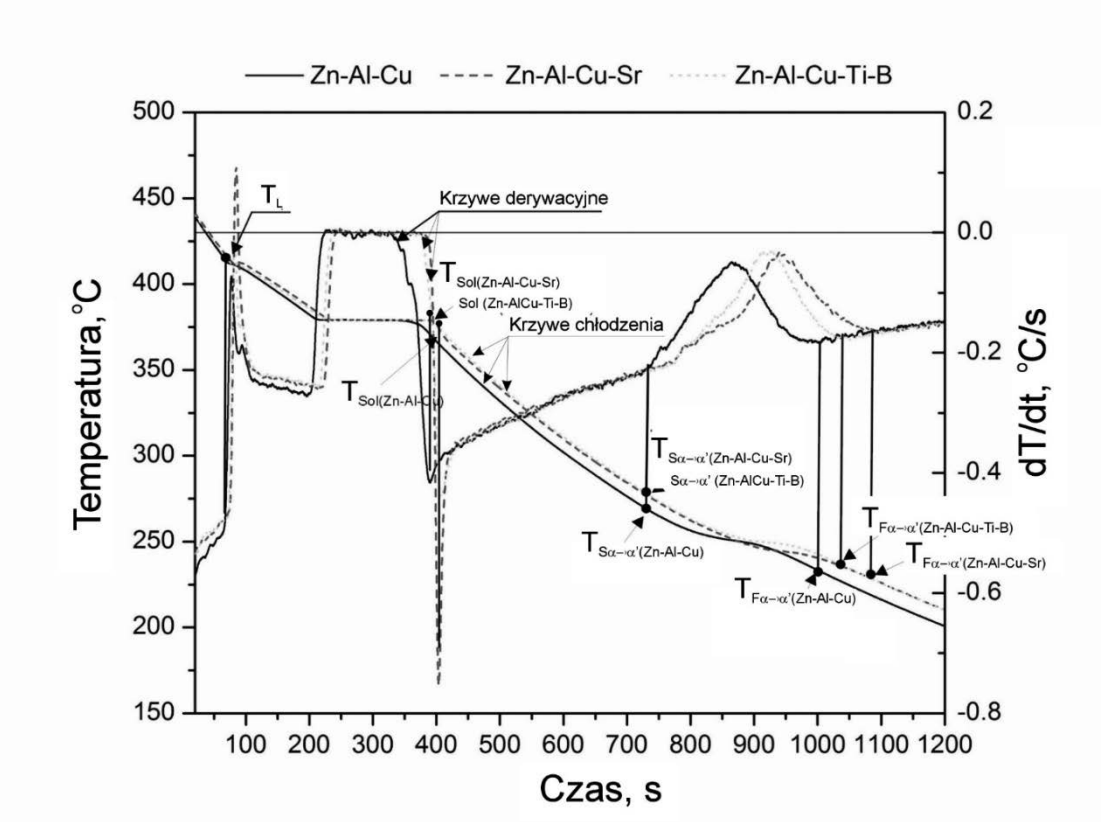

Rysunek 2. Zestawienie krzywych chłodzenia oraz krzywych derywacyjnych dla stopów Zn-Al-Cu, Zn-Al-Cu-Sr oraz Zn-Al-Cu-Ti-B [6].

6. PODSUMOWANIE

Analiza termiczno-derywacyjna (TDA) jest metodą służącą do badania kinetyki krystalizacji stopów metali poprzez rejestrację krzywej chłodzenia T = f(t) oraz jej pierwszej pochodnej dT/dt = f(t). Umożliwia ona identyfikację przemian fazowych zachodzących podczas krzepnięcia oraz ocenę efektów cieplnych towarzyszących tym przemianom.

Na wykresach TDA możliwe jest wyznaczenie temperatury początku krystalizacji - temperatura likwidus (T_L) oraz temperatur reakcji eutektycznych oraz temperatury końca krystalizacji - temperatura solidus (T_{Sol}). Przegięcia i ekstrema krzywej pochodnej odzwierciedlają intensywność wydzielania ciepła krystalizacji i pozwalają na ocenę kolejności krystalizacji faz oraz wpływu składu chemicznego stopu na przebieg krzepnięcia. Analiza kształtu krzywych derywacyjnych umożliwia pośrednią ocenę kinetyki przemian fazowych, stopnia przechłodzenia ciekłego metalu oraz przewidywanie zmian mikrostruktury i właściwości stopów metali.

PODZIĘKOWANIA

Praca powstała w wyniku realizacji projektu „Kinetyka krystalizacji stopów Zn-Al modyfikowanych magnezem" w ramach kształcenia zorientowanego projektowo – PBL, w XIII konkursie Programu Inicjatywa Doskonałości – Uczelnia Badawcza, Wydział Mechaniczny Technologiczny, Politechnika Śląska.

BIBLIOGRAFIA

1. E. Fraś, Krystalizacja metali, Wydawnictwa Naukowo-Techniczne (WNT), Warszawa, 2003, s. 17–30.
2. L.A. Dobrzański, M. Krupiński, K. Labisz, Derivative thermo analysis of the near eutectic Al-Si-Cu alloy, Archives of Foundry Engineering, vol. 8, no. 4, 2008, s. 37–40.
3. L. Andberg, L. Backerud, G. Chai, J. Tamminen, Solidification characteristics of aluminum alloys. 3rd ed. Illinois: AFS; 1996
4. R. Maniara, Crystallization kinetics and the structure of Al-Si-Cu casting alloys, rozprawa doktorska, 2006.
5. W.T. Kierkus, J.H. Sokolowski, Recent advances in cooling curve analysis: a new method for determining the 'base line' equation. AFS Trans.1999;107.
6. M. Krupiński, B. Krupińska, Z. Rdzawski, K. Labisz, T. Tański, Additives and thermal treatment influence on microstructure of nonferrous alloys, Journal of Thermal Analysis and Calorimetry, vol. 120, 2015, s. 1573–1583.

TalentDetector

9th January 2026
Gliwice, Poland

DEPARTMENT OF ENGINEERING MATERIALS AND BIOMATERIALS
FACULTY OF MECHANICAL ENGINEERING
SILESIAN UNIVERSITY OF TECHNOLOGY

INTERNATIONAL STUDENTS SCIENTIFIC CONFERENCE

Analiza wpływu promieniowania jonizującego beta i gamma na polimerowe materiały kompozytowe na bazie żywicy epoksydowej

Magdalena Jureczko[a], Paweł Kałusek[b], Bartosz Kępski[b], Hubert Pyśk[a], Mariola Jureczko[c], Tomasz Bury[d], Maciej Mrówka[e]

[a] Studenci, Politechnika Śląska, Wydział Automatyki, Elektroniki i Informatyki
[b] Studenci, Politechnika Śląska, Wydział Energetyki i Inżynierii Środowiska
[c] Politechnika Śląska, Wydział Mechaniczny Technologiczny, Katedra Mechaniki Teoretycznej i Stosowanej
email: mjureczko@polsl.pl
[d] Politechnika Śląska, Wydział Inżynierii Środowiska i Energetyki, Katedra Techniki Cieplnej
email: tbury@polsl.pl
[e] Politechnika Śląska, Wydział Inżynierii Materiałowej i Cyfryzacji Przemysłu, Laboratorium Innowacji Materiałowych
email: mmrowka@polsl.pl

Streszczenie: Niniejsze badania dotyczą zdolności materiałów kompozytowych na bazie żywicy epoksydowej wzmocnionej różnymi wypełniaczami do tłumienia promieniowania jonizującego (Cs-137). W artykule przedstawiono proces wytwarzania próbek metodą odlewania grawitacyjnego i szczegółowo scharakteryzowano użyte wypełniacze, w tym montmorylonit, diatomit, haloizyt, saponit, pył cynkowy i popioły przemysłowe. Analiza eksperymentalna wykazała, że odpady przemysłowe, a w szczególności popiół z elektrowni i popiół cynkowy, wykazują najwyższą skuteczność ekranowania przy niskim stężeniu wypełniacza wynoszącym 1%, co czyni je ekonomiczną alternatywą dla komercyjnych absorberów. Co istotne, odpadowy popiół cynkowy wykazał lepsze właściwości tłumiące w porównaniu z czystym pyłem cynkowym. W przypadku saponitu szczytową skuteczność zaobserwowano przy stężeniu 1%, a następnie spadek przy wyższych stężeniach, prawdopodobnie z powodu aglomeracji cząstek. Z kolei haloizyt wymagał wyższego stężenia (10%), aby uzyskać znaczące efekty ekranowania. Wyniki potwierdzają, że wypełniacze pochodzące z odpadów mogą być skutecznie stosowane w celu poprawy właściwości ekranujących kompozytów polimerowych.

Abstract: This study investigates the ionizing radiation (Cs-137) attenuation capability of composite materials based on an epoxy resin matrix reinforced with various fillers. The paper presents the sample fabrication process via gravity casting and provides a detailed characterization of the fillers used, including montmorillonite, diatomite, halloysite, saponite, zinc dust, and industrial ashes. The experimental analysis revealed that industrial waste materials, specifically power plant ash and zinc ash, exhibit the highest shielding efficiency at a low filler loading of 1%, making them a cost-effective alternative to commercial absorbers. Notably, waste zinc ash demonstrated superior attenuation properties compared to pure zinc dust. In the case

of saponite, a peak efficiency was observed at 1% concentration, with a subsequent decrease at higher loadings likely due to particle agglomeration. Conversely, halloysite required a higher concentration (10%) to achieve significant shielding effects. The results confirm that waste-derived fillers can be successfully utilized to enhance the radiation shielding properties of polymer composites.

Słowa kluczowe: promieniowanie jonizujące, polimery, żywica epoksydowa, kompozyty, absorpcja promieniowania

1. WPROWADZENIE

Polimerowe materiały kompozytowe, w szczególności te oparte na osnowie żywic epoksydowych, znajdują kluczowe zastosowanie w ekstremalnych środowiskach inżynieryjnych. Są one wykorzystywane w przemyśle jądrowym (izolacje, uszczelnienia) [1, 2, 3], systemach kriogenicznych [1] oraz w sektorze lotniczym i kosmicznym [4]. Wybór żywicy epoksydowej jako osnowy wynika z jej doskonałych właściwości elektroizolacyjnych oraz łatwości formowania skomplikowanych kształtów, co jest kluczowe przy budowie osłon radiacyjnych i uszczelnień w reaktorach [5, 6]. Promieniowanie jonizujące oddziałuje z materią poprzez procesy jonizacji i wzbudzenia atomów, co w przypadku polimerów prowadzi do modyfikacji struktury molekularnej, w tym sieciowania lub degradacji łańcuchów [5, 6]. Kwalifikacja polimerów do pracy w tych warunkach stanowi poważne wyzwanie inżynierskie, ponieważ stałe narażenie na promieniowanie może skutkować katastrofalną utratą kluczowych właściwości mechanicznych. Głównym celem modyfikacji polimerów jest zwiększenie ich zdolności do absorpcji lub rozpraszania kwantów gamma i neutronów bez pogorszenia parametrów konstrukcyjnych.

W niniejszej pracy skupiono się na ocenie, jak wprowadzenie różnych wypełniaczy mineralnych i odpadowych wpływa na współczynnik osłabienia promieniowania pochodzącego z izotopu Cezu-137.

2. METODYKA BADAŃ I MATERIAŁY

Za pomocą licznika Geigera ustawionego na 900V oraz przygotowanego stanowiska pomiarowego (rys. 1) przechodzące przez niego promieniowanie jonizujące zlicza wszystkie impulsy przez 60 sekund. Początkowo zliczano promieniowania tła bez źródła promieniowania jonizującego, następnie wartość tą odejmuje się od zarejestrowanej ilości impulsów z **Cs-137**. Średnia wartość tła w pomiarach wyniosła 11174 impulsów na minutę. Ostatnim etapem jest zmierzenie impulsów dla danej próbki materiału kompozytowego, o danym procencie użytego wypełniacza oraz wyliczeniem wartości osłabienia.

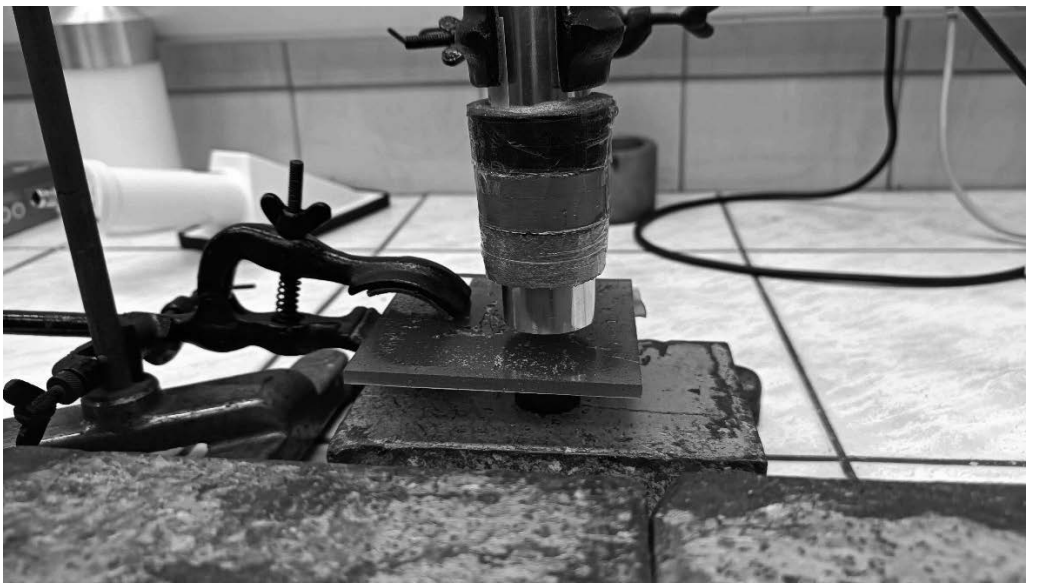

Rysunek 1. Stanowisko badawcze służące do pomiaru promieniowania

2.1. Materiał kompozytowy

Próbki kompozytowe wykonano metodą grawitacyjnego odlewania, łącząc żywicę epoksydową, utwardzacz oraz wybrany wypełniacz. Zastosowano następujące napełniacze: montmorylonit (M), diatomit (D), haloizyt (H), popiół z elektrowni (PE), popiół z cynkowni (ZA), pył cynkowy (ZD) oraz saponit (S). Każdy z wymienionych wypełniaczy został wprowadzony do matrycy epoksydowej w czterech zdefiniowanych wariantach stężeniowych: 1%, 3%, 5% oraz 10% wag., co pozwoliło na wytypowanie kompozytów o optymalnych parametrach ochronnych. Jako materiał odniesienia (referencyjny) odlano próbkę z czystej żywicy, pozbawioną dodatków modyfikujących.

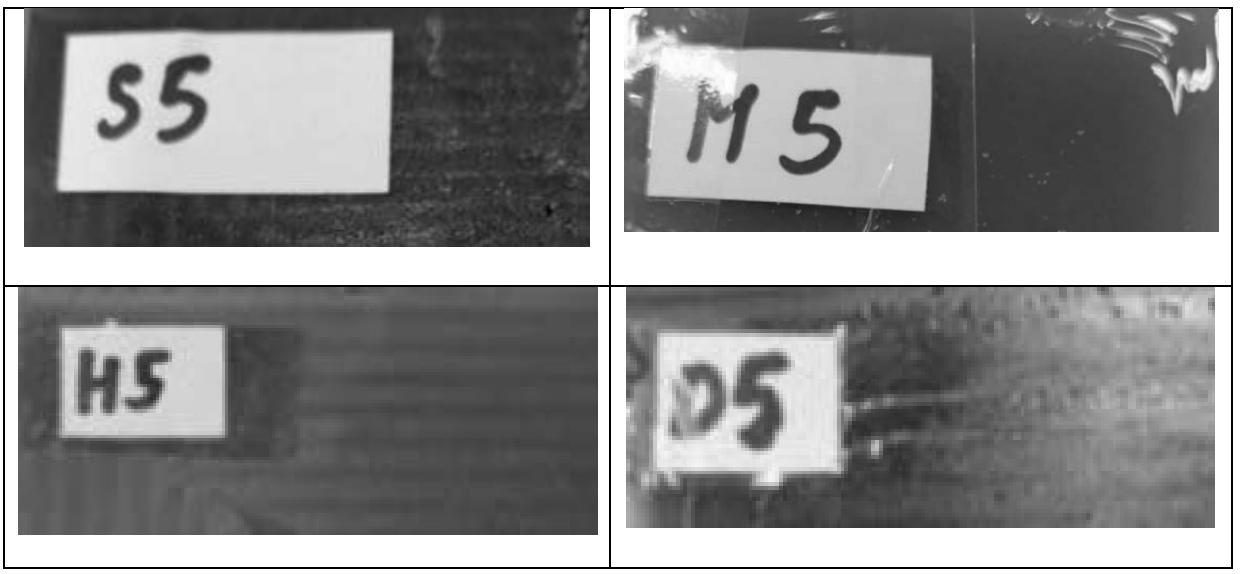

Rysunek 2. Przykładowe próbki badanych kompozytów

2.2. Charakterystyka wypełniaczy

W doborze materiałów kierowano się ich specyficznymi właściwościami fizykochemicznymi:

- Saponit - to absorber o wysokiej pojemności wymiany kationowej, którego właściwości fizykochemiczne okazały się kluczowe przy wyborze go jako materiału sorpcyjnego używanego w oczyszczaniu środowiska po katastrofie w elektrowni atomowej w Czarnobylu.
- Haloizyt charakteryzuje się nanometryczną strukturą rurkowa, która sprawia, że można go uznać za naturalny nano-pojemnik, który cechuje się dużą powierzchnią właściwą, osiągającą nawet 200 m^2/g. Ta właściwość jest istotna w procesach selektywnej sorpcji oraz w projektowaniu kompozytów polimerowych.
- Diatomit charakteryzuje się rozwiniętą, porowatą strukturą, która odpowiada za doskonałe właściwości filtracyjne, które znajdują zastosowanie w wielu obszarach przemysłu.
- Montmorylonit jest kluczowym składnikiem bentonitów i wyróżnia się wysokim potencjałem pęcznienia w kontakcie z wodą. Ta cecha została wykorzystana w tworzeniu barier uszczelniających, które mają na celu minimalizowanie migracji zanieczyszczeń, w tym radionuklidów, takich jak Cs-137.
- Pył cynkowy to wartościowy produkt rynkowy, charakteryzujący się wyjątkowo wysoką czystością, przekraczającą 99% Zn, oraz bardzo drobnym uziarnieniem poniżej 0,01 mm. Stosuje się go jako surowiec w procesach chemicznych i metalurgicznych, gdzie wymagana jest wysoka jednorodność i kontrolowany skład.
- Popiół cynkowy stanowi cenne źródło surowców wtórnych. Zawartość cynku w popiele zawiera się w zakresie od około 30 do 80%, natomiast resztę stanowią odpady metalurgiczne o zmiennym składzie. Utrudnia to proces odzyskiwania czystego cynku oraz znalezienie mu zastosowania w różnych gałęziach przemysłu.
- Popiół z elektrowni powstający w procesie spalania węgla kamiennego to produkt powstający w milionach ton w Polsce. Ponieważ jego skład fazowy oraz chemiczny ulegają zmianom w zależności od pochodzenia węgla czy warunków jego spalania to znalezienie mu uniwersalnego zastosowania jest bardzo trudne. Pewna jego ilość stosowana jest w budownictwie, natomiast nie rozwiązuje to problemu z dużą ilością popiołów zalegającą przy elektrownianych hałdach.

3. WYNIKI

Na rys. 3 przedstawiono zależności pomiędzy stężeniem napełniaczy a osłabieniem promieniowania.

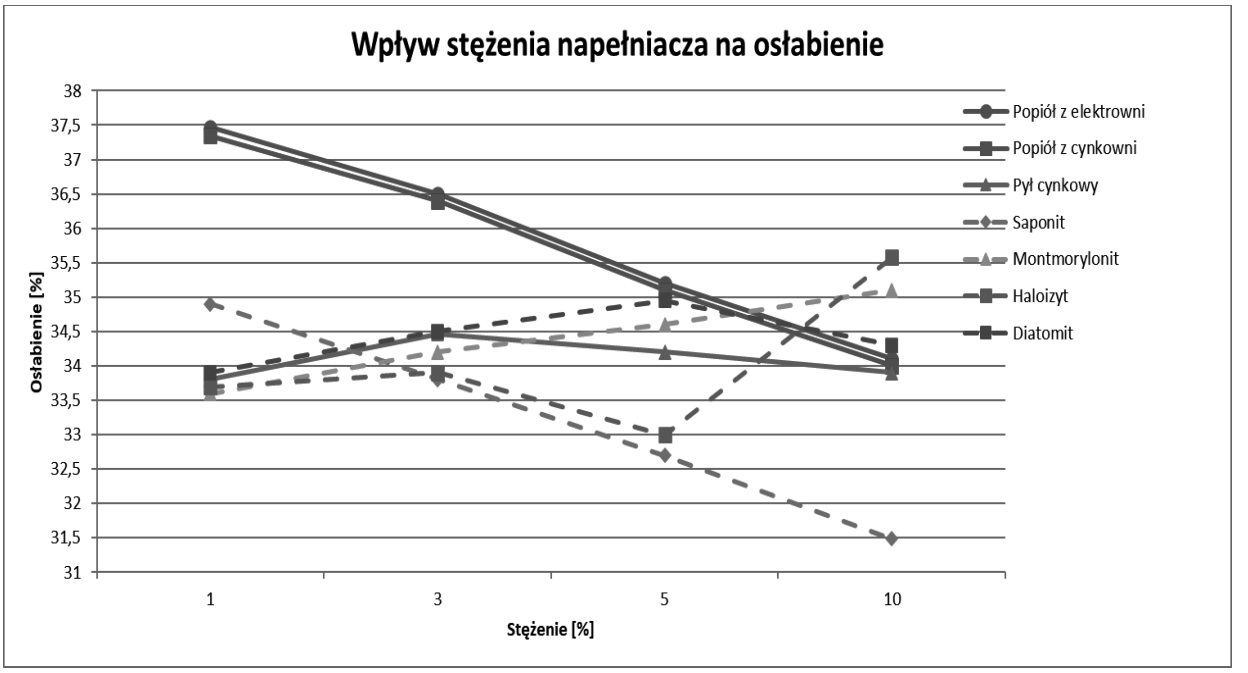

Rysunek 3. Zależności pomiędzy stężeniem napełniaczy a osłabieniem promieniowania.

Analiza porównawcza zależności współczynnika osłabienia od stężenia napełniacza ujawniła fundamentalne różnice w mechanizmach działania poszczególnych grup materiałowych. Najbardziej znaczącym obserwowanym trendem jest wysoka efektywność surowców odpadowych – popiołów z elektrowni oraz z cynkowni – które osiągają swoje maksimum skuteczności (powyżej 37%) już przy minimalnym, 1% udziale masowym. Wraz ze wzrostem stężenia tych wypełniaczy następuje wyraźny spadek zdolności osłonowych, co sugeruje, że w przypadku materiałów o nieregularnej geometrii cząstek, ich nadmierna ilość prowadzi do zaburzenia jednorodności struktury kompozytu i tworzenia lokalnych defektów przepuszczalnych dla promieniowania. Analogiczną charakterystykę wykazuje saponit, dla którego również odnotowano optimum przy stężeniu 1%, po czym następuje gwałtowny spadek efektywności, prawdopodobnie wynikający z tendencji tego minerału do aglomeracji w osnowie epoksydowej.

Przeciwną tendencję zaobserwowano w przypadku montmorylonitu, gdzie zdolność tłumienia promieniowania rośnie monotonicznie wraz ze wzrostem zawartości wypełniacza, co wskazuje na odmienny mechanizm dyspersji i budowania bariery radiacyjnej, bardziej zależny od masy wprowadzonego glinokrzemianu. Istotnym wnioskiem płynącym z badań jest również przewaga odpadowego popiołu cynkowego nad komercyjnym pyłem cynkowym o wysokiej czystości. Odpad, dzięki złożonemu składowi chemicznemu, wykazuje znacznie lepsze właściwości absorpcyjne, szczególnie w zakresie niskich stężeń, podczas gdy czysty metal charakteryzuje się płaską krzywą osłabienia. Uzupełnieniem analizy jest zachowanie materiałów o specyficznej mikrostrukturze: porowaty diatomit osiąga punkt nasycenia i maksymalną efektywność przy 5%, natomiast rurkowy haloizyt wymaga znacznego, 10% nasycenia kompozytu, aby struktura napełniacza zaczęła dominować w procesie tłumienia promieniowania.

W celu ostatecznej klasyfikacji badanych materiałów, spośród siedmiu analizowanych grup kompozytowych (z których każda obejmowała cztery warianty stężenia napełniacza) wyselekcjonowano po jednym reprezentancie charakteryzującym się najwyższą efektywnością osłonową. Wytypowane próbki o optymalnych parametrach zestawiono następnie z materiałem

odniesienia, którym była czysta osnowa epoksydowa (Rysunek 4). Pomiary dla próbki referencyjnej wykazały bazowy poziom osłabienia promieniowania wynoszący 33,50%.

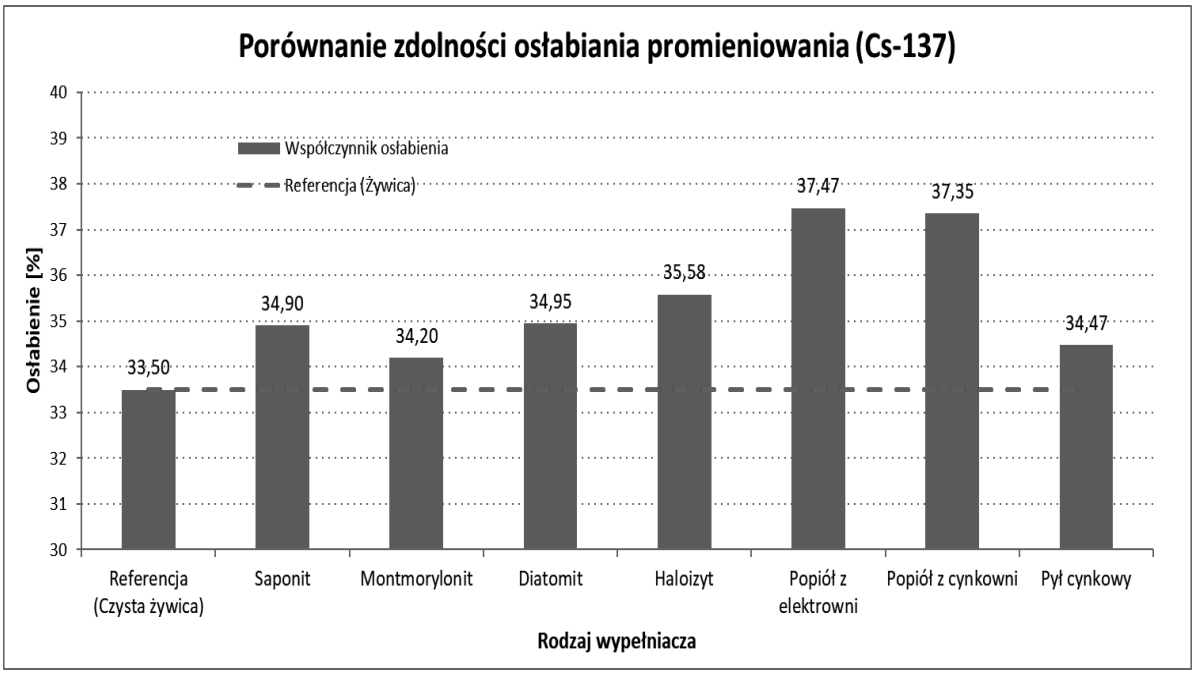

Rysunek 4. Porównanie zdolności osłabiania promieniowania Cs - 137

Szczegółowa analiza danych pomiarowych pozwoliła na sformułowanie następujących spostrzeżeń:

- W przypadku popiołów przemysłowych najwyższą efektywność odnotowano dla popiołu z elektrowni (37,47%) oraz popiołu z cynkowni (37,35%) przy zawartości zaledwie 1%. Stanowi to wzrost ochrony o blisko 4 punkty procentowe względem czystej żywicy. Popiół z cynkowni okazał się skuteczniejszy niż czysty pył cynkowy, co wskazuje na korzyści płynące z wykorzystania surowców wtórnych o złożonym składzie chemicznym. Wzrost zawartości tych wypełniaczy powyżej 5% powodował jednak spadek zdolności osłabiania;
- w przypadku saponitu, zaobserwowano interesującą korelację: najwyższe osłabienie (34,9%) wystąpiło przy 1% zawartości, a następnie malało wraz ze wzrostem ilości wypełniacza (31,49% przy 10% zawartości). Zjawisko to może wynikać ze składu pierwiastkowego saponitu (Si, Al, Mg, domieszki Fe). Wprowadzenie tych atomów zwiększa prawdopodobieństwo zderzeń fotonów gamma z elektronami (rozpraszanie). Spadek efektywności przy wyższych stężeniach sugeruje aglomerację cząstek, co pogarsza jednorodność bariery;
- w przeciwieństwie do saponitu, montmorylonit wykazywał tendencję wzrostową osłabienia wraz ze zwiększaniem zawartości wypełniacza. Może to być związane z obecnością glinu, pierwiastka cięższego od magnezu dominującego w saponicie. Tworzenie się skupisk glinu w strukturze kompozytu może wpływać na zmianę charakterystyki pochłaniania promieniowania;
- W przypadku diatomitu maksymalną wartość osłabienia uzyskano przy stężeniu 5%. Diatomit jest materiałem porowatym; żywica wnikająca w mikroskopijne pory może zmieniać gęstość efektywną kompozytu. Dalsze dodawanie wypełniacza nie poprawiało

właściwości osłonowych, co sugeruje, że za tłumienie odpowiada w dużej mierze gęstość samej żywicy;

- Haloizyt wymagał najwyższego stężenia (10%), aby osiągnąć osłabienie na poziomie 35,58%, co czyni go mniej efektywnym ekonomicznie w porównaniu do popiołów. Specyficzna, rurkowata struktura haloizytu sprawia, że przy niższych stężeniach żywica wypełnia puste przestrzenie. Dopiero przy przesyceniu (10%) sam materiał wypełniacza zaczyna dominować w procesie osłabiania.

Analiza porównawcza (Rys. 4) jednoznacznie wskazuje, że najwyższy przyrost zdolności ochronnych względem referencji uzyskano dla kompozytów napełnionych 1% wag. popiołów odpadowych.

4. WNIOSKI

Przeprowadzona analiza porównawcza materiałów kompozytowych wykazała, że surowce odpadowe, w szczególności popiół z elektrowni oraz popiół z cynkowni, charakteryzują się najwyższą efektywnością osłabiania promieniowania jonizującego Cs-137. Najkorzystniejsze parametry ochronne dla tych materiałów uzyskano już przy minimalnym, 1% stężeniu napełniacza, co czyni je wysoce atrakcyjną alternatywą ekonomiczną dla rozwiązań komercyjnych. Istotnym spostrzeżeniem jest fakt, że odpadowy popiół z cynkowni wykazał lepsze właściwości absorpcyjne niż czysty pył cynkowy, co sugeruje, że złożony skład chemiczny odpadu sprzyja efektywniejszemu rozpraszaniu fotonów gamma. W przypadku saponitu zaobserwowano nieliniową zależność, gdzie najwyższą skuteczność bariery również odnotowano przy zawartości 1%, natomiast dalsze zwiększanie udziału fazy rozproszonej prowadziło do spadku zdolności osłonowych, najprawdopodobniej na skutek aglomeracji cząstek zaburzającej jednorodność struktury.

Odmienną charakterystykę wykazał montmorylonit, dla którego zdolność tłumienia promieniowania wykazywała tendencję wzrostową wraz ze zwiększaniem stężenia, co wynika z różnic w składzie pierwiastkowym (dominacja glinu) oraz odmiennej dyspersji w osnowie epoksydowej względem saponitu. Analiza pozostałych minerałów wskazuje na ich mniejszą efektywność w badanym zakresie; haloizyt ze względu na swoją rurkowatą nanostrukturę wymagał znacznego nasycenia kompozytu (10%), aby sam materiał wypełniacza zaczął dominować nad żywicą w procesie osłabiania, co obniża jego opłacalność. Z kolei diatomit osiągnął swoje maksimum efektywności przy stężeniu 5%, co jest ściśle powiązane z jego porowatą morfologią i zjawiskiem infiltracji żywicy w mikropory szkieletu okrzemkowego.

BIBLIOGRAFIA

1. F. Akman, H. Oğul, Interaction Parameters of Some Polymers Used in Nuclear Power Plants with Ionizing Radiation, Produced Secondary Radiations and Radiation Damages, *Macro Molecular Materials and Engineering*, Vol. 310, no. 3, 2025, https://doi.org/10.1002/mame.202400326
2. C. L. Hanks, D. J. Hamman , Radiation effects design. Section 3. Electrical Insulating Materials and Capacitors, National Aeronautics and Space Administration (NASA), Washington, D.C., Handbook. NASA-CR-1787, 1971

3. E. Hałasa, Radioliza nieutwardzonych i utwardzonych dianowych żywic epoksydowych, *Polimery*, T. 45, nr 1, s. 1-9, 2000
4. R. Adeli, S. P. Shirmardi, S. J. Ahmadi, Neutron Irradiation Tests on B4C/Epoxy Composite for neutron Shielding Application and the Parameters Assay. *Radiation Physics and Chemistry*, Vol. 127. P. 140-146, 2016. Doi: 10.1016/j.radphyschem.2016.06.026
5. V. P. Larichewa, Effect of ionizing radiation on epoxy oligomers of different structures and manufacture of new promising materials on their base. *Radiation Physics and Chemistry*, Vol 77, no.1, p. 29-33,2008, doi: https://doi.org/10.1016/j.radphyschem.2007.02.033
6. X. Coqueret, Radiation-induced cross-linking polymerization: Recent developments for coating and composite applications, *Nukleonika*, Vol. 69, p. 37-44, 2024. doi: 10.2478/nuka-2024-0006

TalentDetector

9th January 2026
Gliwice, Poland

DEPARTMENT OF ENGINEERING MATERIALS AND BIOMATERIALS
FACULTY OF MECHANICAL ENGINEERING
SILESIAN UNIVERSITY OF TECHNOLOGY

INTERNATIONAL STUDENTS SCIENTIFIC CONFERENCE

Study of the effect of Al doping on the properties of ZnO:Al nanoparticles used in electronics and photovoltaics

Emilia Krajewska[a], Jakub Kuta[a], Adrian Ścieszka[a], Jakub Rusinek[a],
Magdalena Szindler[b], Marek Szindler [c]

[a] Student of the Silesian University of Technology
[b] Silesian University of Technology, Faculty of Mechanical Engineering, Department of Engineering Materials and Biomaterials
[c] Silesian University of Technology, Faculty of Mechanical Engineering, Didactic Laboratory of Nanotechnology and Material Technologies, Gliwice, Poland

email: marek.szindler@polsl.pl

Abstract: Aluminum-doped zinc oxide (ZnO:Al) nanoparticles with an aluminum content of 2 at.% were synthesized using the sol–gel method and systematically characterized to evaluate the influence of Al doping on their structural and optical properties. Scanning electron microscopy revealed uniformly distributed nanoparticles with regular oval morphology and particle sizes below 50 nm. Energy-dispersive X-ray spectroscopy confirmed the presence of Zn, O, and Al, indicating successful incorporation of aluminum into the ZnO lattice. UV–Vis spectroscopy showed strong absorption in the ultraviolet region and high transparency in the visible range, with an absorption edge located at approximately 370 nm. The optical band gap energy was estimated to be about 3.35 eV from the absorption edge. The results demonstrate that aluminum doping effectively modifies the optical properties of ZnO nanoparticles, making them promising candidates for applications in electronics and photovoltaic devices.

Keywords: ZnO:Al nanoparticles, sol–gel synthesis, optical band gap

1. INTRODUCTION

Zinc oxide (ZnO) is a II–VI compound semiconductor that has attracted significant attention due to its wide direct bandgap of approximately 3.37 eV at room temperature and its high exciton binding energy of about 60 meV, which enable efficient optical and electronic performance at ambient conditions [1-2,3]. These properties, combined with high transparency in the visible range, chemical stability, low cost, and environmental friendliness, make ZnO a promising material for applications in electronics, optoelectronics, and photovoltaic devices [2,4]. ZnO-based materials are widely investigated for use in transparent conductive oxides, thin-film transistors, light-emitting devices, photodetectors, and solar cells, where both optical transparency and electrical conductivity are required [4,5].

However, intrinsic ZnO typically exhibits limited electrical conductivity due to relatively low carrier concentration and the presence of native defects, which restrict its performance in advanced electronic and photovoltaic systems [3]. To overcome these limitations, intentional doping with group III elements such as aluminum (Al), gallium (Ga), or indium (In) is commonly employed to enhance the electrical properties of ZnO [5]. Among these dopants, aluminum is particularly attractive because of its low cost, abundance, and compatibility with large-scale fabrication processes [5]. Aluminum-doped zinc oxide (ZnO:Al or AZO) is therefore considered a viable alternative to indium tin oxide (ITO), especially for transparent electrodes in solar cells and flexible electronics [3-5].

Aluminum doping modifies the electrical, optical, and structural properties of ZnO by substituting Zn^{2+} ions with Al^{3+} ions in the wurtzite lattice, which introduces additional free electrons and increases n-type conductivity [3,6,7]. At the same time, the difference in ionic radii between Al^{3+} and Zn^{2+} leads to lattice distortion, which can influence crystallite size, defect concentration, and carrier mobility [2,3]. In nanostructured ZnO, these effects become even more pronounced due to the high surface-to-volume ratio, making ZnO:Al nanoparticles particularly sensitive to dopant concentration and synthesis conditions [4]. The effect of aluminum addition on the structure and electrical properties of zinc oxide is presented in Table 1.

Table 1. Influence of Al doping on selected properties of ZnO nanoparticles (based on literature data) [2,3,5].

Al content (at.%)	**Crystallite size (nm)**	**Optical bandgap (eV)**	**Electrical conductivity (S/cm)**
0	30÷40	3.25÷3.30	10^{-3}÷10^{-4}
1÷2	25÷35	3.30÷3.35	10^{-2}÷10^{-3}
3÷5	20÷30	3.35÷3.40	10^{-1}÷10^{-2}

2. MATERIALS AND METHODOLOGY

Aluminum-doped zinc oxide (ZnO:Al) nanoparticles were synthesized using the sol–gel method due to its effectiveness in producing nanomaterials with controlled composition, high chemical homogeneity, and relatively low processing temperatures. All reagents were of analytical grade and used as received. Zinc acetate dihydrate ($Zn(CH_3COO)_2 \cdot 2H_2O$) was employed as the zinc precursor, while aluminum nitrate nonahydrate ($Al(NO_3)_3 \cdot 9H_2O$) served as the aluminum dopant source. Absolute ethanol (C_2H_5OH) was used as the solvent, acetic acid (CH_3COOH) as a stabilizing agent, and deionized water to initiate hydrolysis. In a typical synthesis, zinc acetate dihydrate was dissolved in absolute ethanol under continuous magnetic stirring at room temperature until a clear solution was obtained. The molar concentration of the zinc precursor was fixed at 0.5 $mol \cdot L^{-1}$. Subsequently, an appropriate amount of aluminum nitrate nonahydrate was added to the solution to achieve an aluminum doping level of 2 at.% relative to zinc. The mixture was stirred for 30 minutes to ensure complete dissolution and uniform distribution of Al^{3+} ions within the sol. Acetic acid was then added dropwise to the solution to stabilize the system and control the hydrolysis and condensation reactions. After stabilization, a controlled amount of deionized water was introduced slowly to initiate the sol–gel transition. The resulting solution was continuously stirred for 2 hours at room temperature, leading to the formation of a transparent and homogeneous sol. The sol was subsequently aged for 24 hours to promote polymerization and improve network formation.

The obtained sol was dried in an air oven at 100 °C for 12 hours to remove solvents and obtain a xerogel precursor. The dried material was gently ground into a fine powder and then subjected to thermal treatment in air to achieve crystallization of ZnO:Al nanoparticles. Calcination was performed at 500 °C for 2 hours in a muffle furnace, with heating and cooling rates of 5 °C·min^{-1}. This thermal treatment removed organic residues, decomposed nitrate and acetate groups, and facilitated the formation of crystalline wurtzite ZnO with aluminum ions incorporated into the lattice.

2. RESULTS AND DISCUSSION

The surface morphology of the synthesized ZnO:Al nanoparticles was examined using scanning electron microscopy (SEM) (Figure 1a). The SEM image recorded at a magnification of 200,000× in in-lens mode reveals a uniform distribution of nanoparticles with a regular, predominantly oval morphology. The particles are well separated, with no significant agglomeration observed, indicating effective control of the sol–gel synthesis process. The average particle diameter does not exceed 50 nm, confirming the successful formation of nanostructured ZnO:Al material.

Elemental composition analysis was performed using energy-dispersive X-ray spectroscopy (EDS) (Figure 1b). The EDS spectrum confirms the presence of zinc (Zn), oxygen (O), and aluminum (Al), which originate from the ZnO:Al nanoparticles, verifying successful aluminum incorporation into the zinc oxide matrix. In addition, a silicon (Si) signal is detected, which is attributed to the silicon-based substrate used during SEM/EDS measurements. No other impurity-related elements were observed, indicating high chemical purity of the synthesized nanoparticles.

a) b)

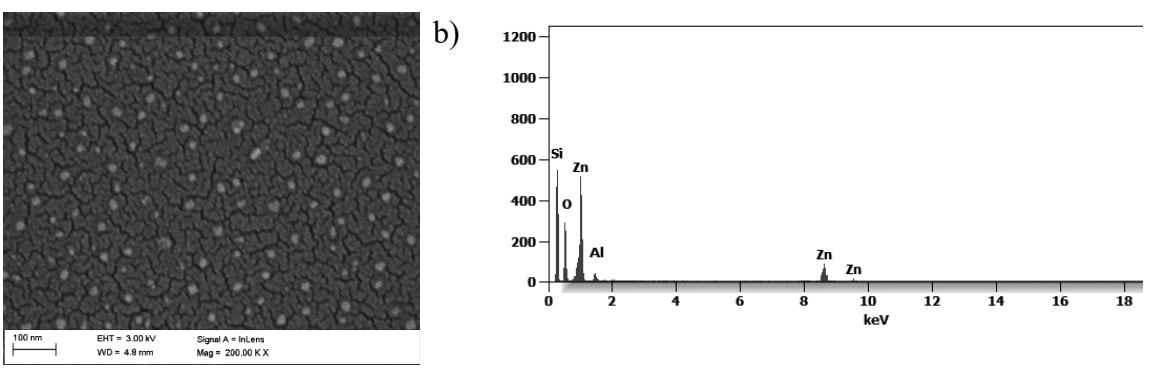

Figure 1. SEM micrograph (a) and Energy-dispersive X-ray spectroscopy (EDS) spectrum (b) of ZnO:Al (2 at.%) nanoparticles synthesized by the sol–gel method after calcination at 500 °C, showing particle morphology and size distribution.

Figure 2 shows the UV–Vis absorbance spectrum of ZnO:Al (2 at.%) nanoparticles recorded in the wavelength range from 250 to 950 nm, starting from the shortest wavelength. The spectrum exhibits strong absorption in the ultraviolet region, followed by a rapid decrease in absorbance toward the visible and near-infrared ranges. Such behavior is characteristic of ZnO-based nanomaterials and indicates high optical transparency in the visible region. A pronounced absorption edge is observed in the near-UV region, confirming the semiconducting nature of the synthesized ZnO:Al nanoparticles. The gradual decrease of absorbance with increasing

wavelength suggests a well-defined electronic transition without significant sub-bandgap absorption, indicating good optical quality of the nanoparticles. The observed spectral profile is consistent with previous reports on aluminum-doped ZnO nanostructures and confirms the suitability of the material for optoelectronic and photovoltaic applications.

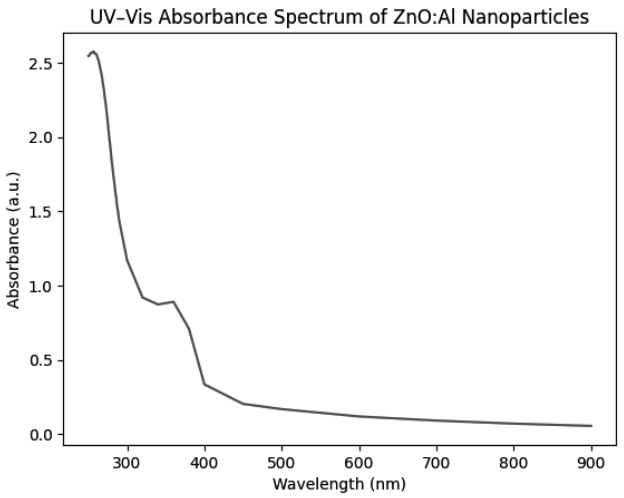

Figure 2 The UV–Vis absorbance spectrum of ZnO:Al (2 at.%) nanoparticles

The optical band gap energy (E_g) of the ZnO:Al nanoparticles was estimated using the absorption edge method. The wavelength corresponding to the onset of strong absorption was determined from the UV–Vis spectrum to be approximately **370 nm**. The band gap energy was calculated using the relation:

$$Eg = \frac{1240}{\lambda\, edg}$$

where λ_{edg} is the absorption edge wavelength expressed in nanometers. Substituting the experimental value yields:

$$Eg = \frac{1240}{370} = 3.35eV$$

4. SUMMARY AND CONCLUSIONS

In this study, aluminum-doped zinc oxide (ZnO:Al) nanoparticles with an aluminum concentration of 2 at.% were successfully synthesized using the sol–gel method. The applied synthesis route enabled good control over particle morphology, chemical composition, and optical properties, while maintaining relatively low processing temperatures, making it suitable for scalable fabrication of functional nanomaterials. SEM analysis revealed uniformly distributed nanoparticles with a regular, predominantly oval morphology and average particle diameters not exceeding 50 nm. The absence of significant agglomeration indicates effective control of nucleation and growth during the sol–gel process. EDS measurements confirmed the presence of Zn, O, and Al elements originating from the ZnO:Al nanoparticles, verifying successful aluminum incorporation into the ZnO matrix. The detected silicon signal was attributed solely to the substrate used during analysis, while no impurity-related elements were observed. Optical

characterization using UV–Vis spectroscopy showed strong absorption in the ultraviolet region and high transparency in the visible range, which are desirable features for optoelectronic applications. A well-defined absorption edge was observed at approximately 370 nm. The optical band gap energy estimated from the absorption edge was about 3.35 eV, indicating a slight widening compared to bulk ZnO. This behavior can be attributed to aluminum doping and nanoscale size effects. Overall, the optical results suggest that Al doping effectively modifies the electronic structure of ZnO nanoparticles. In conclusion, the synthesized ZnO:Al nanoparticles exhibit controlled morphology, high chemical purity, and tunable optical properties, making them promising candidates for applications in electronics, transparent conductive materials, and photovoltaic devices. The presented results demonstrate that aluminum doping is an effective approach to tailoring the properties of ZnO nanomaterials for advanced optoelectronic applications

BIBLIOGRAPHY

1. S. Ranjan, S. Balaji, R. A. Panella, and B. E. Ydstie, “Silicon solar cell production,” *Comput. Chem. Eng.*, vol. 35, pp. 1439–1453, 2011, doi: 10.1016/j.compchemeng.2011.04.017.
2. Ü. Özgür, Y. I. Alivov, C. Liu, A. Teke, M. A. Reshchikov, S. Doğan, V. Avrutin, S. J. Cho, and H. Morkoç, “A comprehensive review of ZnO materials and devices,” *J. Appl. Phys.*, vol. 98, no. 041301, 2005, doi: 10.1063/1.1992666.
3. D. C. Look, “Recent advances in ZnO materials and devices,” *Mater. Sci. Eng. B*, vol. 80, pp. 383–387, 2001, doi: 10.1016/S0921-5107(00)00604-8.
4. C. Klingshirn, “ZnO: Material, physics, and applications,” *ChemPhysChem*, vol. 8, pp. 782–803, 2007, doi: 10.1002/cphc.200700002.
5. T. Minami, “Transparent conducting oxide semiconductors for transparent electrodes,” *Semicond. Sci. Technol.*, vol. 20, pp. S35–S44, 2005, doi: 10.1088/0268-1242/20/4/004.
6. J. G. Lu, Z. Z. Ye, Y. Z. Zhang, Q. L. Liang, L. P. Zhu, B. H. Zhao, and J. Y. Huang, “Structural, electrical, and optical properties of Al-doped ZnO films,” *J. Appl. Phys.*, vol. 100, no. 073714, 2006, doi: 10.1016/j.jcrysgro.2004.04.098.
7. C. G. Van de Walle, “Hydrogen as a cause of doping in zinc oxide,” Phys. Rev. Lett., vol. 85, pp. 1012–1015, 2000, doi: 10.1103/PhysRevLett.85.1012.

TalentDetector
9th January 2026
Gliwice, Poland
DEPARTMENT OF ENGINEERING MATERIALS AND BIOMATERIALS
FACULTY OF MECHANICAL ENGINEERING
SILESIAN UNIVERSITY OF TECHNOLOGY
INTERNATIONAL STUDENTS SCIENTIFIC CONFERENCE

Comparison of different heat treatment types of amorphous metallic materials

Inez Kredowska [a], Wirginia Pilarczyk [a], Kacper Górski [b], Oskar Węgrzyn [b]

[a] Silesian University of Technology, Faculty of Mechanical Engineering, Department of Engineering Materials and Biomaterials
[b] Students of Silesian University of Technology, Faculty of Mechanical Engineering
email: inez.kredowska@polsl.pl

Abstract: This article presents a comparison between conventional heat treatment methods and laser-based modification of amorphous metallic materials. Key differences between both approaches are discussed, including the working area, heating time, cooling rate, and process precision. Special attention is given to the influence of thermal parameters on the stability of the amorphous structure and the risk of undesired crystallization. The study also characterizes three types of lasers: Nd:YAG, CO_2, and fiber lasers, highlighting their suitability for processing metallic glasses, their potential for re-amorphization, and their typical application areas. The analysis shows that laser heat treatment, due to its localized heating, extremely high cooling rates, and high precision, is a promising method for modifying amorphous metallic materials, enabling the preservation or restoration of their unique structure and properties.

Keywords: heat treatment, laser heat treatment, amorphous materials, metallic glasses, material modification

1. INTRODUCTION

Heat treatment is one of the most common material modification used in engineering, playing an important role in optimizing the properties of various alloys and metals. The concept of heat treatment dates back to ancient times, with early traces of humans heating metals like copper and iron to improve their strength and malleability, marking one of the earliest important advancements in material science [1]. In modern times, it is used to tailor the mechanical, thermal, and chemical properties of a wide variety of materialsincluding more modern material groups, such as amorphous metallic materials known also as metallic glasses), which have unique structural characteristics compared to conventional crystalline metals.

Unlike traditional alloys, which possess a regular and symmetrical atomic structure, amorphous metals lack long-range atomic order, giving them a unique combination of properties [2]. These include high strength, elasticity, and wear resistance, but also desirable thermal and electrical characteristics [3-5]. However, due to their non-crystalline nature, amorphous metals pose distinct challenges in terms of processing and performance. Particularly

when it comes to tailoring their properties for industrial applications. Heat treatment processes, e.g. annealing, quenching, or controlled crystallization are important for modifying the structure and properties of these materials, offering possibilities to enhance their mechanical behaviour, thermal stability, and overall performance. As interest in metallic glasses continues to grow for applications in fields ranging from aerospace to electronics, understanding the effects of different heat treatment methods is important stage of development for this group of alloys.

However, heat treatment of amorphous metals is a particularly challenging process, as these materials are highly sensitive to temperature and time [6,7]. Even slight deviations in temperature or duration can lead to unwanted crystallization, which diminishes their characteristic properties, such as strength and elasticity [6]. The heat treatment process requires precise control of process parameters. Too much heat or too long an exposure can lead to a loss of the amorphous state and start crystallization in the structure, which typically results in a significant reduction in performance. On the other hand, insufficient heat treatment can prevent the desired modifications, leaving the material in an undesirable state. Therefore, controlling the heat treatment conditions is very important factor for achieving the optimal balance between maintaining the unique benefits of amorphous metals while enhancing their mechanical and thermal properties.

2. CONVENTIONAL HEAT TREATMENT VS HT WITH LASER

Heat treatment may significantly influence the final properties of amorphous metallic materials, including hardness, strength, and structural integrity. To improve the performance of these materials, several heat treatment approaches have been developed, among which conventional furnace-based heat treatment (conventional HT) [8] and laser-based modification [9] are the most commonly applied. While both methods are intended to modify the microstructure in order to enhance mechanical and physical properties, they differ in their processing principles and thermal characteristics. This section presents a comparison between conventional heat treatment and laser-based modification based on key parameters such as the treated area, heating time, cooling rate, process cost, and the ability to preserve or restore the amorphous structure, as well as the associated risk of deformation. The comparison is summarized in Table 1.

Table 1. Comparison of conventional and laser heat treatment.

Parameter	**Heat Treatment Type**	
	Conventional HT	**Laser modification**
Area of working	Whole material	Local
Heating time	Minutes-Hours	Microseconds-milliseconds
Cooling speed	Low (hours)	High (10^6-10^8 K/s)
Possibility of obtain amorphous structure	Hard	Possible (re-amorphization)
Process precision	Low	High
Risk of deformation	High	Low
Atmosphere during process	Argon or vacuum	Argon or vacuum
Cost	Lower	High

The entire material is heated during a conventional heat treatment, which usually takes several minutes to hours. In contrast to the quick procedures required in laser treatment, this slow heating and the cooling phase that follows take hours. Although the entire material can be heated uniformly via conventional heat treatment, the process's accuracy is typically low, making it more difficult to achieve the appropriate structural changes in the material [10]. Additionally, there is a significant chance of deformation during this process because of the extended exposure to heat. In order to avoid oxidation and other unwanted reactions, the atmosphere during the process frequently needs controlled conditions, like argon or a vacuum [11]. However, traditional HT is less expensive than laser-based methods, making it a more cost-effective choice, especially for processing large materials.

However, laser modification is a more sophisticated method in which the material is heated locally. This technique, which usually calls for heating periods between micro- and milliseconds, enables far more precise control over the heat-affected zone [12]. Rapid cooling rates, between 10^6 and 10^8 K/s [13], are one of the distinguishing characteristics of laser modification and have a major impact on the material's structure. Due to these high cooling rates, it is possible to obtain or preserve an amorphous structure [14]. In contrast to traditional HT, laser therapy provides high precision, allowing for more selective treatment of the material. Because of the localized heating, the risk of deformation is significantly reduced, and unlike with traditional heat treatment, the environment does not need to be strictly controlled [12]. However, because laser modification requires advanced technology, it is more expensive, particularly when it comes to setup costs.

3. TYPES OF LASER HEAT TREATMENT

As discussed in Chapter 2, laser heat treatment has benefits over traditional heat treatment techniques. Different laser types, e.g. Nd:YAG, CO2, and fiber lasers, have their distinct qualities that affect the treatment's results in different ways [12]. These variances include differences in absorption, the possibility of achieving an amorphous structure, accuracy, and the danger of crystallization. The main characteristics and uses of each laser types will be examined in this part, giving a better understanding of how each might be applied to maximize the heat treatment of amorphous metallic materials. Such a comparison allows for a more effective selection of the appropriate technology for certain applications and guarantee the best outcomes in terms of material qualities and performance by knowing of the advantages and disadvantages of each kind of laser. Main comparison is presented in Table 2.

Laser heat treatment offers a variety of methods for modifying the properties of materials, particularly amorphous metallic materials. This technique, depending on the type of laser used, can be fine-tuned for specific applications, influencing factors such as heat affected zone (HAZ), the risk of crystallization, and the precision of the process. In the context of laser heat treatment, the choice of laser type, such as Nd:YAG, CO_2, or fiber lasers, is important in determining the outcome of the treatment.

Table 2. Comparison of types of lasers used for heat treatment.

Parameter	Laser type		
	Nd:YAG	**CO_2**	**Fiber**
Lengthwave [nm]	1064	10640	1070
Absorption	Good	Weak	Very good
HAZ	Medium	High	Low
Risk of Crystallization	Medium	High	Low
Level of possibility of obtain amorphous structure	Medium	Low	High
Level of process precision	Medium	Low	High
Ablation	Medium	Low	High
Risk of chipping	Medium	High	Low
Most suitable application	Texturizing, surface modification	Macroheating,	Cutting,
HAZ – heat affected zone			

3.1. Nd:YAG laser type

The Nd:YAG laser, operating at a wavelength of 1064 nm, is characterized by good absorption in a wide range of metallic materials, which makes it an effective tool for surface texturizing and modification of amorphous metals [12]. This type of laser provides a balanced combination of energy density and beam quality, enabling controlled heating of the surface layer without excessive thermal penetration into the bulk material.

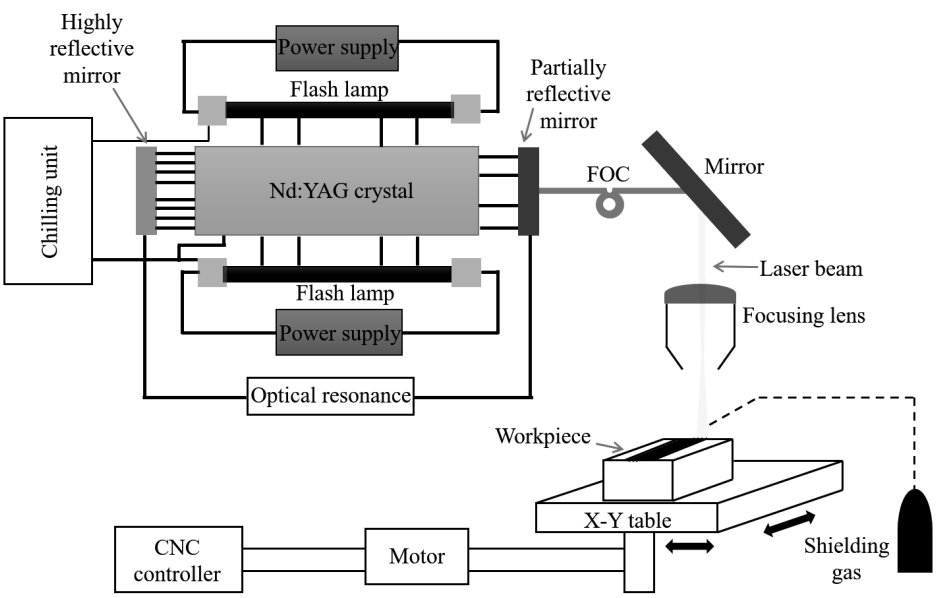

Figure 1. Scheme of Nd:YAG laser method [12].

As a result, Nd:YAG lasers are associated with a medium risk of crystallization, which is a key consideration in processes aimed at preserving or partially enhancing the amorphous structure of the treated material. The achievable level of process precision is moderate, making this laser

type suitable for applications where controlled but not extremely fine modification of material properties is required [15].
Figure 1, the Nd:YAG laser system is presented. Such construction allows for focused delivery of laser energy onto the material surface, resulting in a localized heat-affected zone and relatively uniform thermal distribution.
On the other hand, the Nd:YAG laser involves a medium risk of ablation and chipping, which may lead to unintended surface damage if processing parameters are not carefully optimized. Therefore, proper selection of laser power and interaction time is essential to achieve the desired modification effects while minimizing adverse phenomena.

3.1. CO_2 laser type

CO_2 lasers, on the other hand, emit radiation at a longer wavelength of 10 640 nm (10.64 μm), which is characterized by weaker absorption in most metallic materials compared to Nd:YAG lasers [16]. As a result, CO_2 lasers generally require higher energy input or longer interaction times to achieve comparable thermal effects, which limits their applicability in processes demanding high precision or rapid heating, particularly in the treatment of non-crystalline alloys.
The relatively large heat-affected zone generated during CO_2 laser processing increases the risk of crystallization, which may lead to partial loss of the amorphous structure and degradation of the desired material properties [17]. For this reason, CO_2 lasers are less suitable for applications where strict control of microstructural transformations is required.
Additionally, the higher risk of chipping and surface defects associated with CO_2 laser treatment may be problematic in applications requiring high surface quality. Nevertheless, CO_2 lasers remain useful in selected industrial applications where large-scale heating and process simplicity are prioritized over microstructural control.
As schematically presented in Figure 2, CO_2 laser systems typically involve a broader laser beam and less concentrated energy delivery to the material surface. This configuration makes them more appropriate for macroheating processes, where uniform heating of larger areas is required and high spatial precision is not a critical factor.

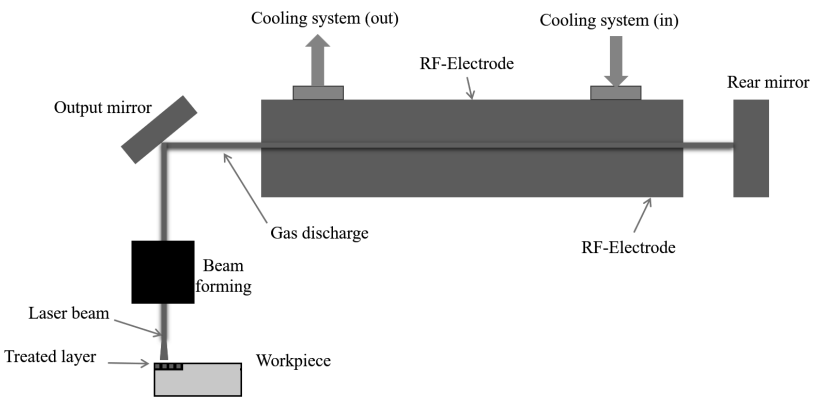

Figure 2. Scheme of CO_2 laser method [16].

3.3. Fiber laser type

Fiber lasers, with a wavelength of approximately 1070 nm, offer very good absorption characteristics in metallic materials, which results in high process efficiency and effective

energy transfer during heat treatment [18]. Due to their stable beam quality and the possibility of precise control of laser power and scanning parameters, fiber lasers enable accurate and repeatable processing conditions.

This type of laser is associated with a relatively low risk of crystallization, mainly as a result of localized heating and high cooling rates, which are crucial factors in preserving the amorphous structure of metallic glasses. For this reason, fiber lasers are particularly effective in applications that require cutting, surface remelting, or precision material removal while maintaining the structural integrity of the treated material.

As illustrated in Figure 3, the fiber laser system is based on the generation and amplification of laser radiation within an optical fiber, followed by precise focusing of the beam on the material surface. Such a configuration allows for efficient energy delivery, a small and well-defined heat-affected zone, and high process stability.

Additionally, fiber lasers are characterized by low risks of ablation and chipping, which minimizes surface damage and reduces the formation of defects in the heat-affected zone [19]. Their high reliability, compact design, and suitability for industrial-scale applications make fiber lasers a promising and widely used tool in the laser processing of amorphous metallic materials.

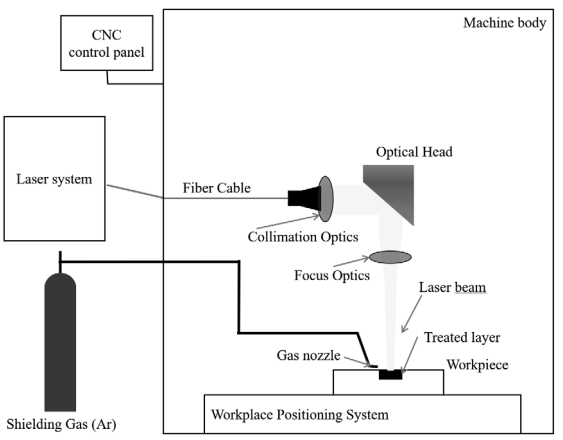

Figure 3. Scheme of Fiber laser method [18].

Each type of laser offers distinct advantages depending on the specific application and processing requirements. Nd:YAG lasers are particularly suitable for surface modification processes requiring a moderate level of precision and controlled thermal input. In contrast, CO_2 lasers are primarily applied in macroheating operations, where large treatment areas and uniform heating are more important than high spatial accuracy. Fiber lasers, on the other hand, demonstrate the highest effectiveness in applications involving cutting, surface remelting, and high-precision material processing.

Consequently, the selection of an appropriate laser type should be based on the specific requirements of the material treatment process, including the desired level of precision, the acceptable risk of crystallization, and the targeted material properties.

4. CONCLUSIONS

The conducted analysis indicates that laser-based heat treatment methods offer significant advantages over conventional techniques when applied to amorphous metallic alloys. Localized

heating, extremely high cooling rates, and precise control of process parameters contribute to minimizing the risk of crystallization and preserving the disordered atomic structure characteristic of metallic glasses.

Among the analyzed laser technologies, fiber lasers appear to be the most promising solution for the modification of amorphous alloys, primarily due to their small heat-affected zone and low susceptibility to structural transformations. Nevertheless, the final selection of the heat treatment method and laser type should always be adjusted to the specific material, geometry, and required properties.

The presented comparison confirms that modern laser-based technologies constitute an effective and flexible tool for the processing of amorphous metallic materials and may play an important role in the further development of advanced engineering applications.

BIBLIOGRAPHY

1. Scott, D. A., Metallography and Microstructure of Ancient and Historic Metals, Getty Conservation Institute in association with Archetype Books, Marina del Rey (CA), 1991.
2. Hu, Z.-Q., Wang, A.-M., & Zhang, H.-F., Amorphous Materials, Modern Inorganic Synthetic Chemistry, 2017, 641–667. doi:10.1016/b978-0-444-63591-4.00022-7
3. Löffler, J. F., Bulk metallic glasses, Intermetallics, 11(6), 2003, 529–540. doi:10.1016/s0966-9795(03)00046-3
4. Trexler, M. M., & Thadhani, N. N., Mechanical properties of bulk metallic glasses, Progress in Materials Science, 55(8), 2010, 759–839. doi:10.1016/j.pmatsci.2010.04.002
5. Zakharenko, M. I., Kalnysh, T. V., & Semen'ko, M. P., Interrelation between the electrical resistance of amorphous alloys and their atomic and electronic structures, Physics of Metals and Metallography, 113(8), 2012, 762–770.
6. Janovszky, D., Sveda, M., Sycheva, A. et al., Amorphous alloys and differential scanning calorimetry (DSC), Journal of Thermal Analysis and Calorimetry, 147, 2022, 7141–7157. doi:10.1007/s10973-021-11054-0
7. Jiaqiang, G., Yating, W., Lei, L., Bin, S., & Wenbin, H., Crystallization temperature of amorphous electroless nickel–phosphorus alloys, Materials Letters, 59(13), 2005, 1665–1669. doi:10.1016/j.matlet.2004.11.064
8. Minić, D. M., Structural transformations of $Fe_{81}B_{13}Si_4C_2$ amorphous alloy induced by heating, Journal of Magnetism and Magnetic Materials, 323, 2011, 400–404.
9. Kapustynskyi, O.; Višniakov, N. The Influence of Heat Treatment and Laser Alternative Surface Treatment Methods of Non-Alloy Steels: Review. *Photonics* **2025**, *12*, 207. https://doi.org/10.3390/photonics12030207
10. Heat Treating of Tool Steels, in: Metals Handbook Desk Edition, 2nd ed., J. R. Davis (ed.), ASM International, 1998, 1019–1025. doi:10.31399/asm.hb.mhde2.a0003202
11. Nemenyi, R., Controlled Atmospheres for Heat Treatment: The Pergamon Materials Engineering Practice Series, Elsevier, 2013.
12. Babu, P. D., Balasubramanian, K. R., & Buvanashekaran, G., Laser surface hardening: a review, International Journal of Surface Science and Engineering, 5(2/3), 2011, 131. doi:10.1504/ijsurfse.2011.041398

13. Brown, M. S., & Arnold, C. B., Fundamentals of Laser-Material Interaction and Application to Multiscale Surface Modification, in: Sugioka, K., Meunier, M., Piqué, A. (eds.), Laser Precision Microfabrication, Springer Series in Materials Science, vol. 135, Springer Berlin Heidelberg, 2010, 91–120. doi:10.1007/978-3-642-10523-4_4
14. Balla, V. K., & Bandyopadhyay, A., Laser processing of Fe-based bulk amorphous alloy, Surface and Coatings Technology, 205(7), 2010, 2661–2667. doi:10.1016/j.surfcoat.2010.10.029
15. Mishra, Y. K., & Mishra, S., A comprehensive review on Nd:YAG and CO_2 laser drilling of fiber-reinforced composites: mechanisms, defects, and optimization, Engineering Research Express, 7(2), 2025, 025560. doi:10.1088/2631-8695/addb9a
16. Schüttler, J., 3D Modeling of a Planar Discharge in a CO_2 Laser Using a Multilevel Approach, 2016.
17. Zhao, W., Yu, J., Hu, M., Hu, H., & Luo, J., Effect of forced cooling on the microstructure and properties of Fe-based amorphous composite coatings prepared by laser remelting, Intermetallics, 145, 2022, 107552. doi:10.1016/j.intermet.2022.107552
18. Nandam, S., Rao, A., Gokhale, A., & Joshi, S., Laser Surface Remelting in Single-Crystal Nickel-based Superalloy using a Continuous Wave Fiber Laser, Lasers in Manufacturing and Materials Processing, 10, 2023, 1–37. doi:10.1007/s40516-023-00219-4
19. Li, C., Zhang, Y., Zhai, J., Li, C., & Kou, S., Effects of heat treatment on microstructure and properties of Fe-based amorphous composite coatings, Materials Science and Technology, 39(15), 2023, 2168–2178. doi:10.1080/02670836.2023.2195750

TalentDetector

9th January 2026
Gliwice, Poland

DEPARTMENT OF ENGINEERING MATERIALS AND BIOMATERIALS
FACULTY OF MECHANICAL ENGINEERING
SILESIAN UNIVERSITY OF TECHNOLOGY

INTERNATIONAL STUDENTS SCIENTIFIC CONFERENCE

Properties of materials used for punches and dies produced via additive manufacturing

Mariusz Król[a], Juraj Beniak[b],

[a] Silesian University of Technology, Faculty of Mechanical Engineering, Department of Engineering Materials and Biomaterials, e-mail: mariusz.krol@polsl.pl
[b] Slovak University of Technology in Bratislava, Faculty of Mechanical Engineering, Bratislava

Abstract: The study focuses on the properties of materials, in particular maraging steels, used for the production of punches and dies by Additive Manufacturing (AM) using the Selective Laser Melting (SLM) technique. This method enables the production of complex and almost solid metal components used in many industries, including the automotive and tool industries. The paper characterizes the W722 alloys and the newly designed M789 steel, based on the 250 martensitic grade, which are characterized by an optimal combination of high strength and impact resistance. In addition, M789 AMPO steel is presented, which is a new grade combining the desirable mechanical properties of 1.2709 steel with the corrosion resistance of 17-4 PH steel.

Keywords: additive manufacturing, SLM, 3d printing, materials characterization,

1. INTRODUCTION

Additive manufacturing of components from metal powders offers a wide range of possibilities for obtaining finished components or products that require only minor additional finishing, details with complex and complicated shapes, precise and homogeneous elements that cannot be produced by other methods using various engineering materials, which are widely used in many industries. One of the additive manufacturing techniques that can be used to produce almost solid metal components is the Selective Laser Melting (SLM) method. This technique has great potential for applications in the automotive, aerospace, dental, and medical industries [1-4].

Additive manufacturing of metal components involves the uniform application of thin layers of powdered metal onto a moving machine table, where the part is formed. The table is lowered by the thickness of the powder layer applied each time before the laser beam is applied. The laser beam then bonds the metal particles within the area representing the flat cross-section of the manufactured part. A thin, homogeneous metallic layer is formed, which resembles the process of surfacing. The procedure is repeated layer by layer until the entire element is obtained. The thicknesses of individual layers may vary, ranging from 20μm to 150μm. This size is closely related to the gradation of the powder. The possibilities for the application of

laser additive manufacturing technology are very broad. The production of highly complex parts using modern metal alloys opens up new opportunities for many industries [5-8].

Typical applications include:

- production of high-quality functional prototypes, including tool components and machine parts (Figure 1),
- manufacturing of biocompatible components or components with very complex geometric shapes,
- small-batch production of metal parts with complex shapes from special materials,
- production of injection molds and freedom to design shapes that enable efficient conformal cooling during a single process,
- manufacturing of personalized prostheses or implants used in dentistry, prosthetics, and other advanced medical applications,
- thin-walled, high-efficiency heat exchangers,
- precious metal components used in jewelry.

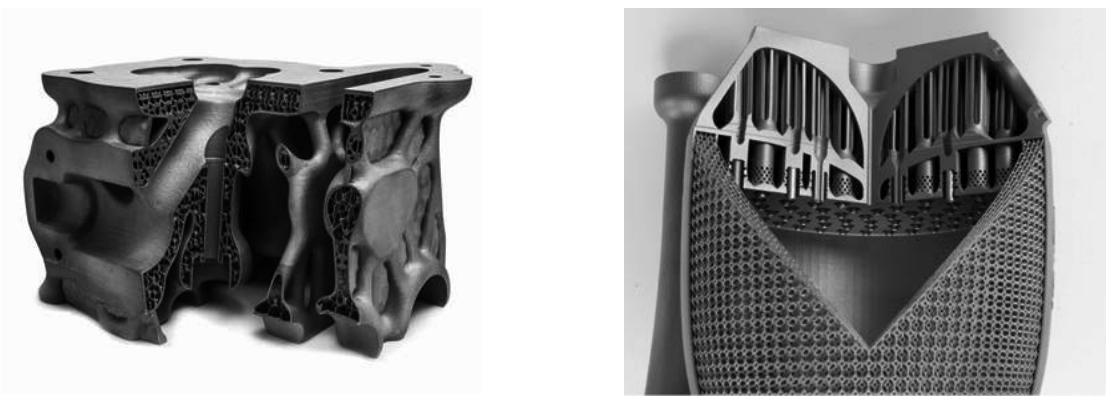

Figure 1. Examples of components manufactured using SLM technology

2. EXPERIMENT

The most commonly used material, apart from austenitic alloys AISI 316L or AISI 304, is martensitic steel 18wt.-% Ni X3NiCoMoTi18-9-5. Well-balanced properties of hardness, strength, ductility, and plasticity, in addition to ease of processing using the SLM method, make this alloy one of the most commonly produced steel powders for the SLM method. However, X3NiCoMoTi18-9-5 steel is not corrosion resistant due to the lack of chromium, which could form a protective passive layer on the surface. If corrosion resistance is required in specific applications, designers and engineers involved in additive manufacturing must change their choice of materials to austenitic or precipitation-hardened corrosion-resistant steels such as X5CrNiCuNb17-4-4. These steels, however, exhibit lower strength and hardness compared to X3NiCoMoTi18-9-5.

The study examined W722 steel as well as a newly developed iron alloy based on Voestalpine's 250 martensitic steel, commercially known as M789 steel.

Maraging steel based on nickel martensite, precipitation hardened, offering a good combination of strength and impact resistance. It can be printed very easily without the need for additional heating of the work platform or chamber. With an achievable hardness of 55 HRC, this material is a versatile solution for tooling applications where conformal cooling is required, such as in die casting molds. As mentioned earlier, this alloy must be heat treated to achieve the most favorable characteristics in accordance with the manufacturer's recommendations, i.e., annealing at a minimum temperature of 820 °C, heating time: 1 hour / air, gas with aging at a minimum temperature of 490 °C for 6 hours / air.

Proper heat treatment will enable the following mechanical properties to be achieved:

- tensile strength (Rm) (MPa) 1960 to 2100
- yield strength ($Rp_{0,2}$) (MPa) 1880 to 2020
- elongation (%) 4 to 8
- hardness (HRC) 51 to 55
- impact strength (Iso-V) (J) 16 to 20.

Steel designated as M789 AMPO is a newly developed maraging steel combining the mechanical properties of 1.2709 steel with the corrosion resistance of 17-4 PH steel. This patented grade can be easily printed without preheating and, after appropriate simple heat treatment, achieves a hardness of up to approx. 52 HRC. In addition, this material has excellent polishability, making it ideal for conformal cooling inserts in injection molds where high surface quality of the molded part is required, and in any other application where high hardness and corrosion resistance are required.

In order to obtain the mechanical properties declared by the manufacturer, such as:

- tensile strength (Rm) (MPa) 1800 to 1900
- yield strength ($RP_{0,2}$) (MPa) 1670 to 1770
- elongation (%) 4 to 8
- hardness (HRc) 51 to 53
- impact strength (ISO-V) (J) 6 to 14.

heat treatment should be carried out as shown in Figure 2.

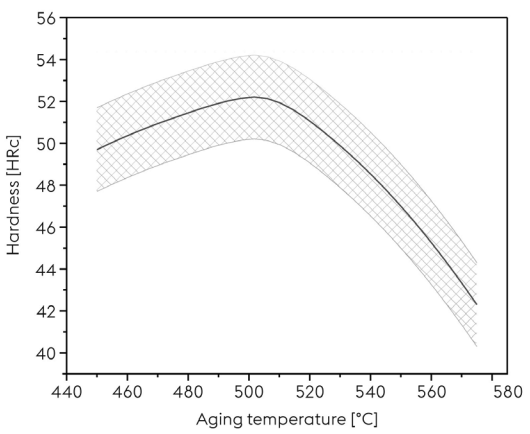

Figure 2. Recommended heat treatment.

Heat treatment to obtain optimal properties: annealing: 1000°C / 1h heating time / air cooling to room temperature with aging: 500°C / 3h heating time / air cooling.

The selected materials belong to the group of precipitation-hardened steels. These steels are characterized by a good combination of strength and impact resistance. Due to their properties, these materials can be used for the construction of critical mechanical parts as well as cold-working injection molds or hot-working casting molds. After heat treatment (saturation and aging), parts made from these materials achieve a hardness of 52-55 HRC [9].

3. RESULTS

The materials used for testing were W722 and M789 steel powders, whose chemical composition is presented in Table 1. The average grain size of the powders used ranged from 15 to 45 μm (Fig. 3).

Table 1.
Chemical composition of W722 steel used wt. %

Mo	Ni	Co	Ti	Al
4,9	18	9,3	1,1	-
Chemical composition of the M789 steel used wt. %				
Mo	Ni	Cr	Ti	Al
1,0	10,0	12,2	1,0	0,6

a) *b)*

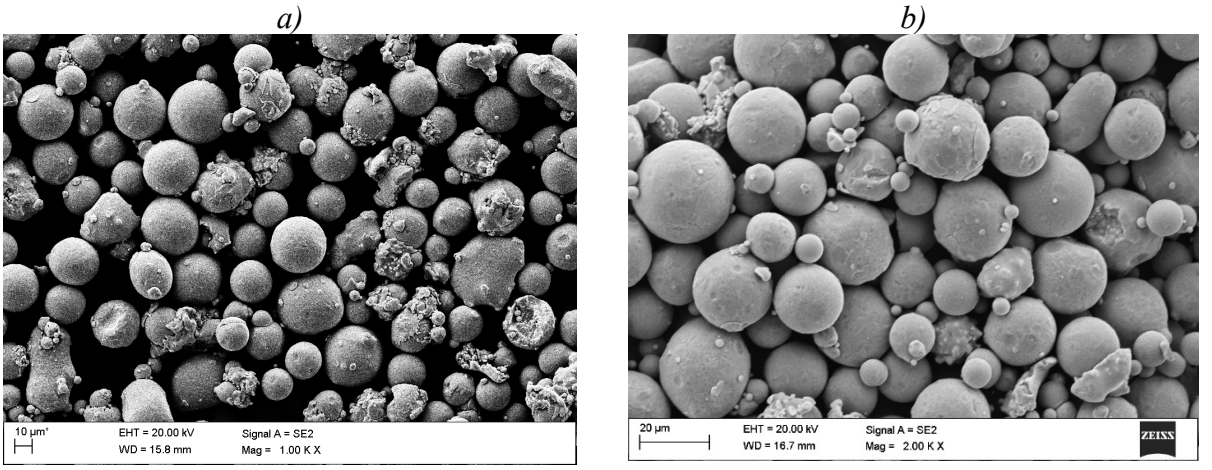

Figure. 3. Morphology of steel powder a) W722 and b) M789

The particle size distribution analysis is listed below Figure 4 and 5.

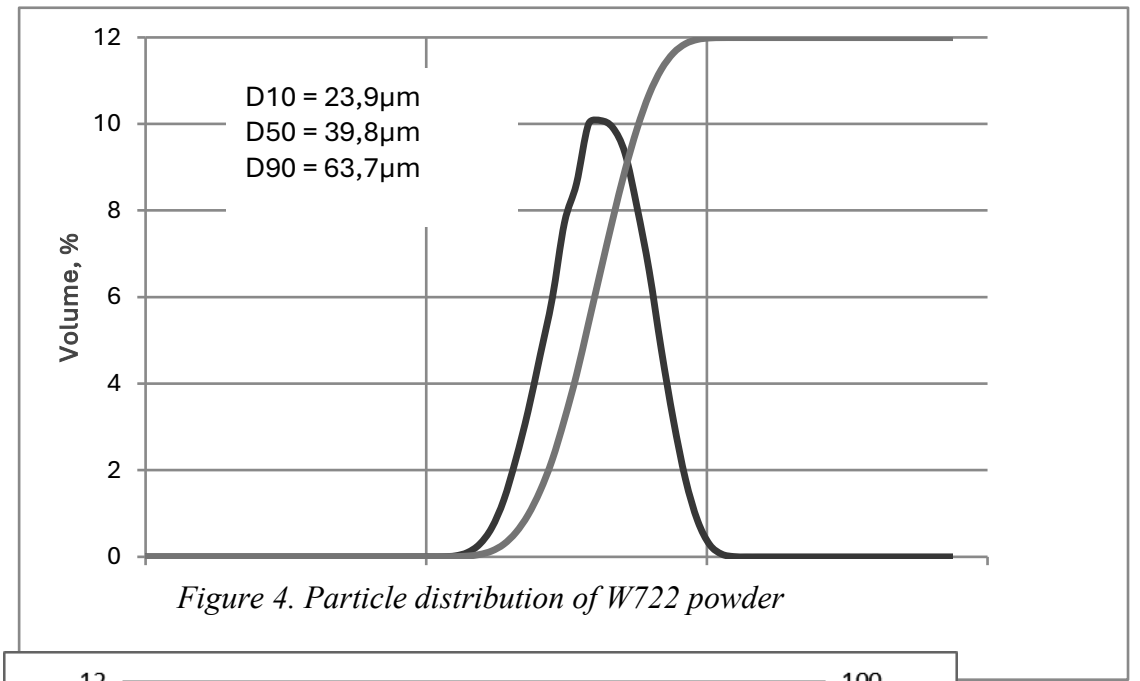

Figure 4. Particle distribution of W722 powder

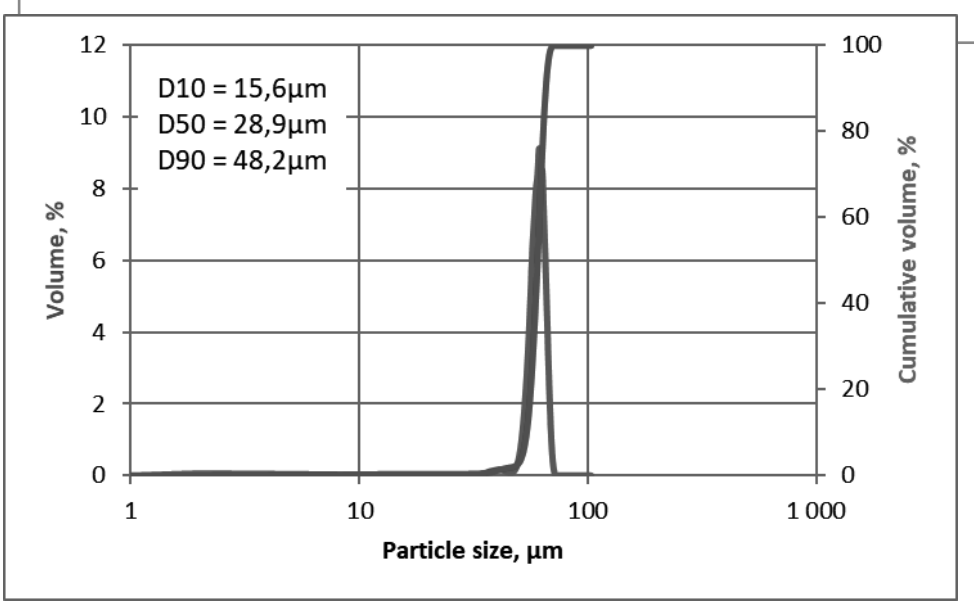

Figure 5. Particle distribution of M789 powder

Chemical composition of analysed powders used for production of tools for punches and dies (Figure 6 and 7).

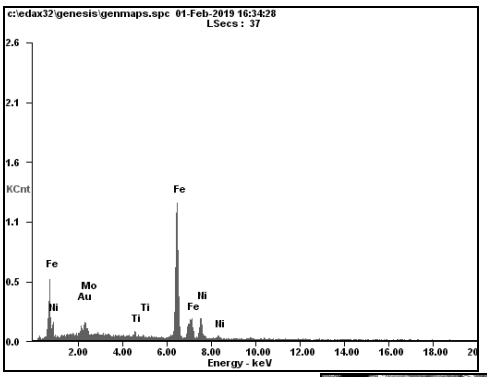

Element	*Wt%*	*At%*
AuM	05.02	01.52
MoL	05.20	03.24
TiK	01.21	01.51
FeK	70.06	74.91
NiK	18.50	18.81
Matrix	Correction	ZAF

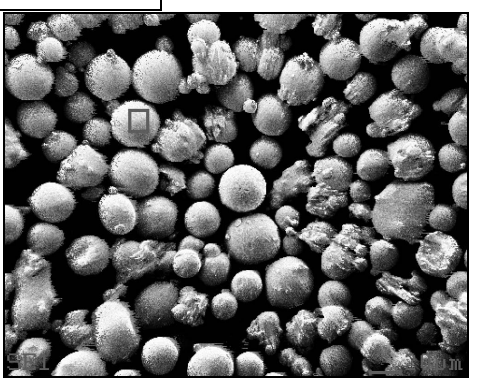

Figure 6. Chemical composition of analysed W722 powder

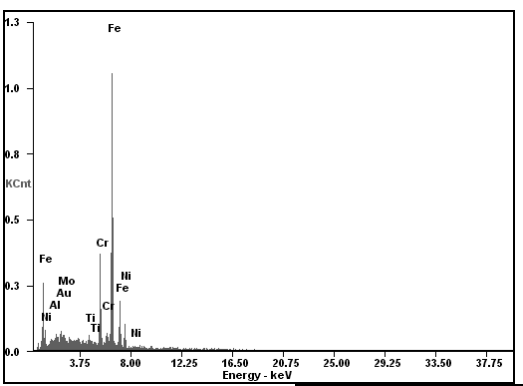

Element	*Wt%*	*At%*
AlK	00.81	01.72
AuM	04.22	01.22
MoL	01.35	00.80
TiK	01.37	01.63
CrK	13.00	14.25
FeK	69.68	71.10
NiK	09.56	09.28
Matrix	Correction	ZAF

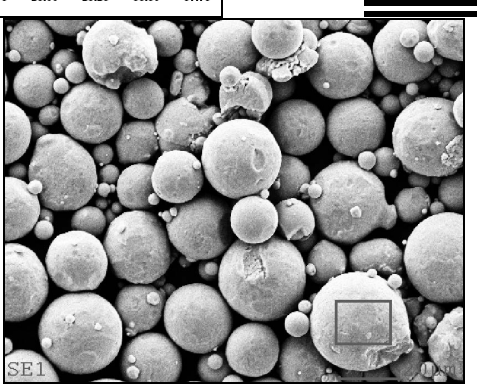

Figure 7. Chemical composition of analysed M789 powder

4. CONCLUSION

The research focused on the use of Selective Laser Melting (SLM) for the production of tools such as punches and dies, with particular emphasis on maraging steel. The SLM technique enables the creation of almost solid metal components with very complex shapes, finding wide application in the aerospace, automotive, and medical industries. In addition to the standard austenitic alloys (e.g., AISI 316L) and martensitic steel X3NiCoMoTi18-9-5, which has balanced mechanical properties but is not corrosion resistant, it was crucial to investigate newer, high-performance materials.

The study analyzed W722 and M789 (Voestalpine) alloys, which belong to the maraging (precipitation hardened) steel group. These steels are characterized by an optimal combination of strength and impact resistance. The M789 AMPO alloy is a patented grade that combines the high hardness of 1.2709 steel with the corrosion resistance of 17-4 PH steel, making it a versatile solution. These materials can be easily printed using SLM technology, often without the need for preheating.

A key stage in obtaining optimal properties is heat treatment. After a properly conducted process (saturation and aging), components made of the tested materials achieve a hardness in the range of 52–55 HRC. For M789 AMPO steel, heat treatment, consisting of annealing at 1000°C and aging at 500°C, allows tensile strength of up to 1900 MPa and hardness of up to 53 HRC to be achieved.

Thanks to these parameters, these steels are ideal for tooling applications, including the production of conformal cooling inserts in injection molds, where high surface quality and wear resistance are required.

ACKNOWLEDGEMENT

The scholar would like to acknowledge the International Visegrad Fund for the financial support during the realization of the research project. The most thanks are directed to prof. MSc. Juraj Beniak, PhD. from the Institute of Production Engineering and Quality, Faculty of Mechanical Engineering, Slovak University of Technology in Bratislava for friendship and invaluable help while doing the research.

Visegrad Fund

BIBLIOGRAPHY

1. Groover, M. P. (2010). Fundamentals of modern manufacturing: materials, processes, and systems. John Wiley & Sons.
2. ASM International. (1990). Tool Steels (4th ed.). Materials Park, OH: ASM International.
3. Roberts, G. A., Kennedy, R., & Krauss, G. (1998). Tool Steels: Properties and Performance. In G. Krauss (Ed.), Tool Materials. ASM International.
4. Thelning, K. E. (1984). Steel and its heat treatment: handbook. Butterworth-Heinemann.
5. Totten, G. E., & Howes, M. A. H. (1997). Handbook of residual stress and deformation of steel. ASM International.

6. Krauss, G. (1990). Principles of Heat Treatment of Steel. ASM International.
7. Chandler, H. (1995). Heat Treater's Guide: Practices and Procedures for Irons and Steels (2nd ed.). ASM International
8. Vaezi, M., Seitz, H., & Yang, S. (2013). A review on three-dimensional micro-additive manufacturing technologies. The International Journal of Advanced Manufacturing Technology, 67(5-8), 1721-1754.
9. https://www.bohler.pl

TalentDetector
9th January 2026
Gliwice, Poland
DEPARTMENT OF ENGINEERING MATERIALS AND BIOMATERIALS
FACULTY OF MECHANICAL ENGINEERING
SILESIAN UNIVERSITY OF TECHNOLOGY
INTERNATIONAL STUDENTS SCIENTIFIC CONFERENCE

Zabezpieczenie antykorozyjne profili stalowych

Amelia Krupińska[a], Laura Raczek[a], Tomasz Szeliga[a], Beata Krupińska[b],

[a] Zespół Szkół Chemiczno-Medycznych i Ogólnokształcących w Tarnowskich Górach, uczniowie klasy o profilu Technik Analityk
[b] Silesian University of Technology, Faculty of Mechanical Engineering, Department of Engineering Materials and Biomaterials
email: beata.krupinska@polsl.pl

Streszczenie: Celem niniejszego projektu było omówienie i analiza nanoszenia powłok ochronnych na powierzchnię profili stalowych. Wykonano badania korozyjne oraz badania własności mikrostruktury. Zbadano własności mechaniczne otrzymanych warstw wierzchnich. Wykonano analizę wyników badań mikrostrukturalnych oraz wybranych własności mechanicznych w zależności od zastosowanych pokryć.
Abstract: The aim of this project was to discuss and analyze the application of protective coatings to the surfaces of steel profiles. Corrosion and microstructural tests were performed. The mechanical properties of the resulting surface layers were examined. The results of microstructural tests and selected mechanical properties were analyzed depending on the coatings used.

Keywords: materials, protective coatings, copper plating, galvanizing, corrosion

1. WSTĘP

Najczęściej stosowane metody zabezpieczania antykorozyjnego profili stalowych to cynkowanie (ogniowe lub galwaniczne) oraz nakładanie powłok malarskich (mokrych lub proszkowych), które to tworzą barierę izolującą stal od wszelkiego rodzaju szkodliwych czynników atmosferycznych [1-4].

Cynkowanie to jedna z najskuteczniejszych i najtrwalszych metod ochrony stali przed korozją. Polega na pokryciu jej cienką, silnie przylegającą warstwą cynku w celu ochrony przed korozją powodowaną działaniem powietrza i wody. Cynkowanie jest stosowane powszechnie w wielu gałęziach gospodarki, np. w przemyśle samochodowym, budowlanym, lotniczym [1-4].

Cynkowanie ogniowe to proces, który polega na zanurzeniu elementów stalowych w kąpieli ciekłego cynku o temperaturze około 450°C. Powstała powłoka cynkowa będzie działała zarówno jako bariera fizyczna, jak i anoda protektorowa (ochrona katodowa), co oznacza, że cynk będzie korodował w pierwszej kolejności, chroniąc stal nawet w przypadku miejscowego

uszkodzenia powłoki. Wymaga przygotowania specjalnych otworów technologicznych w profilach, by cynk mógł swobodnie przepływać [1-4].

Cynkowanie galwaniczne (elektrolityczne) polega na wytwarzaniu cieńszej i bardziej estetycznej powłoki niż w przypadku cynkowania ogniowego, często stosowaną w mniej agresywnych środowiskach lub jako podkład pod malowanie [1-4].

Galwanizacja to z kolei proces polegający na elektrochemicznym pokrywaniu powierzchni materiału, zazwyczaj metalowego, cienką warstwą metalu. Proces ten zachodzi w roztworze elektrolitycznym, w którym zanurzone elektrody poddawane są działaniu prądu stałego. W efekcie powstaje różnica potencjałów między katodą a anodą, co prowadzi do przemieszczania się jonów metalu zawartych w elektrolicie oraz ich osadzania na powierzchni galwanizowanego elementu [1,5,6].

2. MATERIAŁ I METODYKA BADAWCZA

Do procesu galwanizacji zastosowano profile o przekroju kwadratowym o wymiarach 15x15x1,5 mm i długości 50 mm i cynkowane o wymiarach 20x20x1,5 i długości 150 cm - wykonane ze stali konstrukcyjnej S235 (PN-EN 10025-2) o składzie chemicznym podanym w tabeli 1. Profile miały różną chropowatość powierzchni uzyskaną za pomocą papierów ściernych o różnych gradacjach.

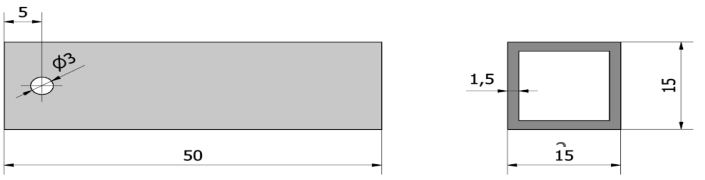

Rys.1. Wymiary profili stalowych zastosowanych do galwanizacji

Tabela 1. Skład chemiczny stali S235 według PN-EN 10025-2

Fe	C	Mn	P	S	N
reszta	<0,17	<1,4	<0,045	<0,045	<0,012

Przygotowanie próbek do procesu elektrochemicznego obejmowało obróbkę mechaniczną powierzchni, odtłuszczanie i trawienie. Pomiędzy każdym etapem obróbki przygotowawczej próbki płukano w wodzie i suszono.

Proces miedziowania galwanicznego przeprowadzano w kąpieli z siarczanem miedzi o temperaturze pokojowej.

Cynkowanie (wykonano w firmie E-Galwan Carbon w Tarnowskich Górach). Polegało na: odtłuszczaniu elektrochemicznym (istotne jest natężenie prądu). Następnie płukaniu gorącą wodą. Trawieniu w kwasie solnym z inhibitorem trawienia. Kolejnym płukaniu. Cynkowaniu słabokwaśne. Płukaniu. Chromianowaniu niebieskim cienkopowłokowe CrIII. Płukaniu. Suszeniu w temperaturze do 60°C. Kontroli jakości.

Otrzymane próbki poddano badaniom korozyjnym w komorze solnej CC450iP firmy Ascott na Politechnice Śląskiej. Testy korozyjne polegają nz odtwarzaniu lub przyspieszaniu różnych warunków. Test jest przydatny dla przewidywania możliwości eksploatacji materiałów i elementów poddanych testowi. Badania tego typu zyskały szeroką akceptację, szczególnie w przemyśle motoryzacyjnym, gdzie wielu producentów opracowało swoje własne normy CCT.

Komora solna Ascott CC 450iP może pracować w trzech trybach: mgły solnej, kondensacji wilgotności, oraz suszenia. Próbki pozostały w komorze solnej przez 72h w 5% solance NaCl.

a) b) c)

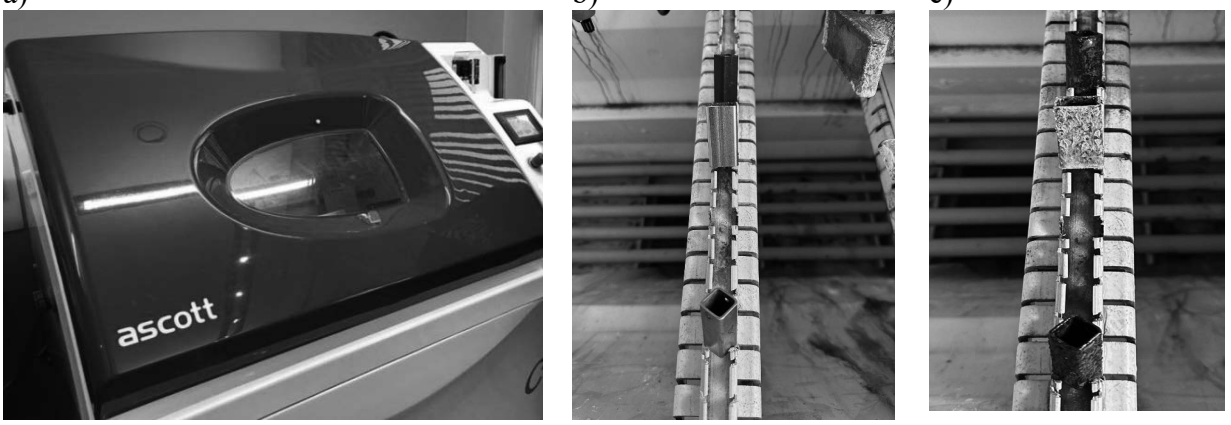

Rys. 2. a) Komora solna CC450iP firmy Ascott, b) próbki przed badaniem korozyjnym, c) próbki po badaniu korozji

Następnie uzyskane próbki poddano badaniom struktury i własności. W celu przygotowania próbek do badań wykonano szlifowanie z wykorzystaniem papierów o gradacjach 220, 500, 800, 1500 i 2000 oraz polerowanie z wykorzystaniem zawiesiny diamentowej 1μm.

a) analiza mikrostruktury - obserwacje mikrostruktury przeprowadzono z wykorzystaniem mikroskopii świetlnej z wykorzystaniem mikroskopu Axio Observer firmy ZEISS. Obserwacje prowadzone były prowadzone z wykorzystaniem powiększeń x100, x200, x500 i x1000.
b) analiza składu i grubości powłoki pod mikroskopem skaningowym.
c) badania mikrotwardości - pomiar z wykorzystaniem mikrotwardościomierza to metoda badania twardości bardzo cienkich powłok, małych elementów lub mikrostruktur materiałów. Opiera się na wciskaniu diamentowego wgłębnika (np. Vickers'a lub Knoop'a) pod niewielką siłą i pomiarze powstałego odcisku.

2. WYNIKI BADAŃ

Ocenę jakości powłok miedzianych naniesionych w procesie galwanizacji oraz powłok cynkowych wykonano za pomocą mikroskopu świetlnego i zestawiono na rysunkach 3 oraz 4. Średnia grubość powłoki miedzianej uzyskana w wyniku obserwacji mikrostruktury to 5,5 μm, jednak warstwa była bardzo nierównomierna, natomiast dla powłoki cynkowej grubość wyniosła 21,6μm – powłoka była równomierna. Dla próbki z powłoką cynkową wykonano również badania składu chemicznego, którego wyniki widzimy na rysunku 5.

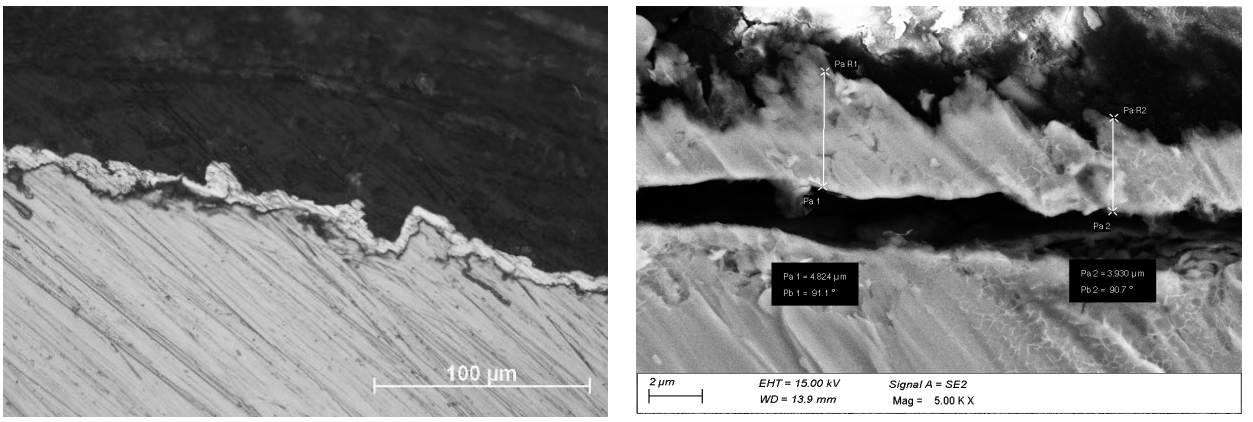

Rys. 3. Mikrostruktura i pomiar grubości powłoki na próbce miedziowanej

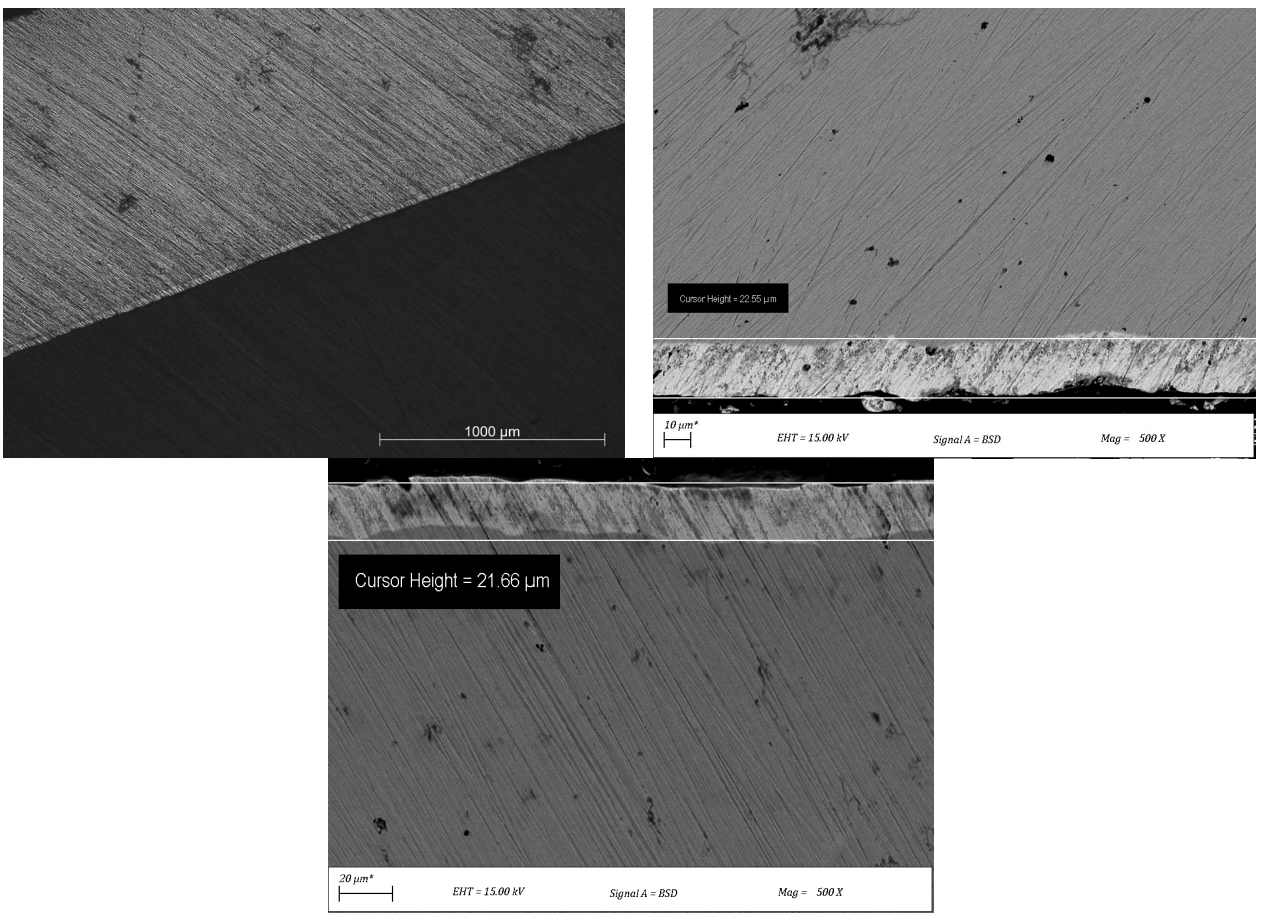

Rys. 4. Mikrostruktura i pomiar grubości na próbce cynkowanej

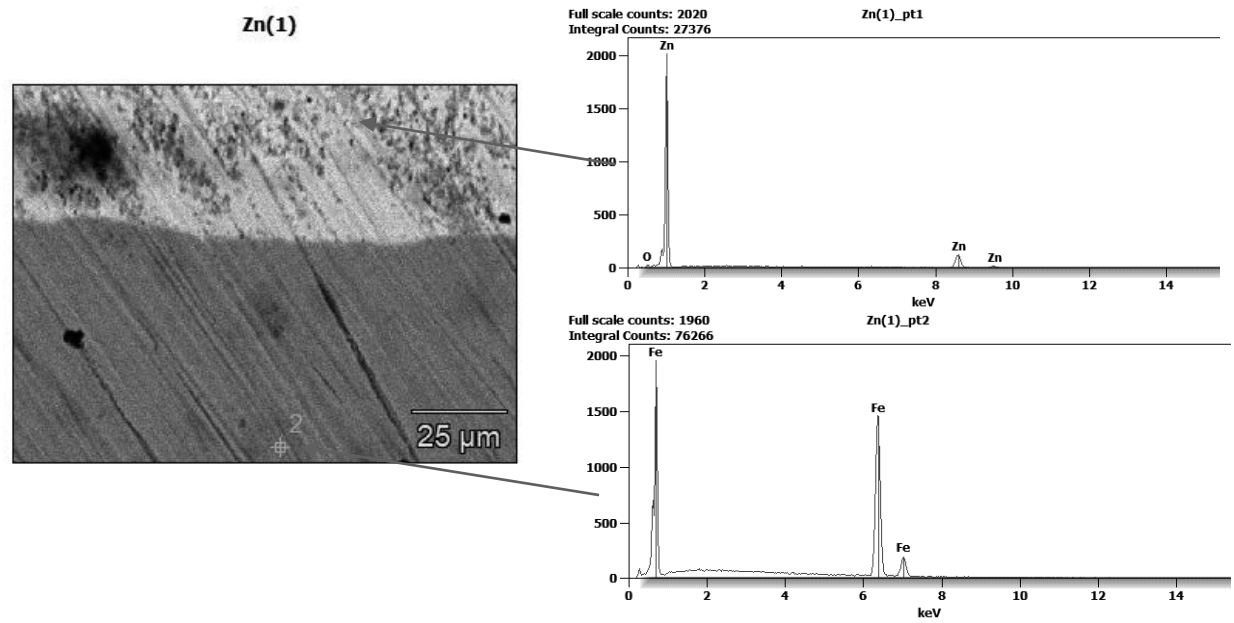

b)

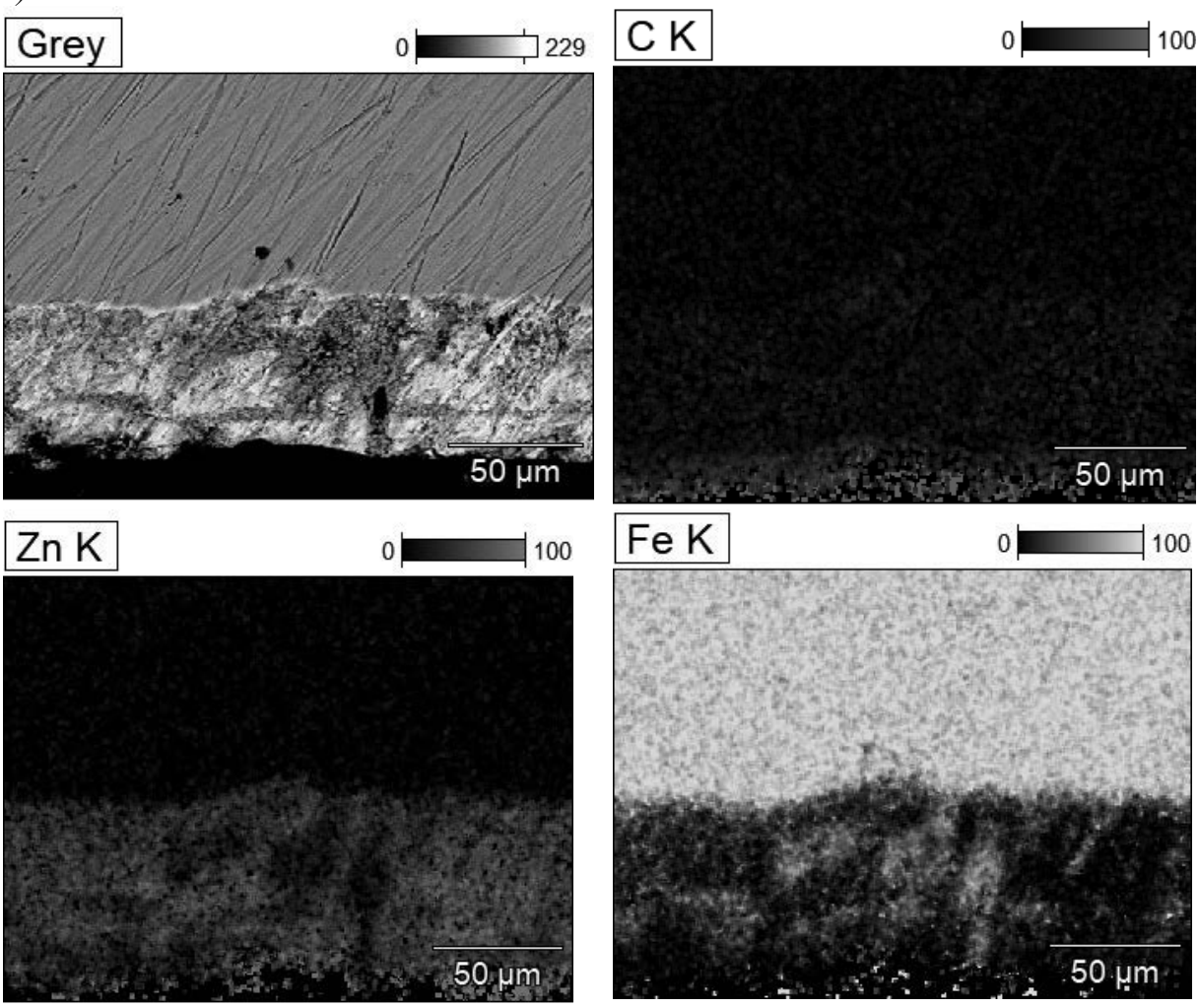

Rys.5. Analiza składu chemicznego próbki cynkowanej a)punktowa, b)powierzchniowa

Powierzchnię profili stalowych z powłokami cynkową i miedzianą zbadano mikrotwardościomierzem FUTURE–TECH FM–ARS9000, pod obciążeniem 50 gf (ok. 0,5 N) przez 10 sekund. Analiza mikrotwardości próbek wykazała, że wartości mikrotwardość próbki z powłoką miedzianą wynosi 132HV, a z powłoką cynkową 127 HV.
Wyniki badań antykorozyjnych przedstawiono w tabeli 1. Najmniejszy ubytek masy próbki zaobserwowano w próbce z powłoką miedzianą. Na rysunku 6 pokazano jak wyglądała powierzchnia próbek po badaniu korozyjnym.

Tabela 2. Zestawienie wyników badań korozji

MASA PRÓBEK PRZED BADANIEM: Próbka wzorcowa (bez powłoki) – 22,3798 g Próbka cynkowana – 33,1197 g Próbka miedziowana – 21,7893 g	UBYTEK MASY PRÓBKI: Próbka wzorcowa– 0,14278 g Próbka cynkowana – 0,1749 g Próbka miedziowana – 0,0137 g
MASA PRÓBEK PO BADANIU KOROZYJNYM: Próbka wzorcowa (bez powłoki) – 22,2371 g Próbka cynkowana – 32,9448 g Próbka miedziowana – 21,77573 g	

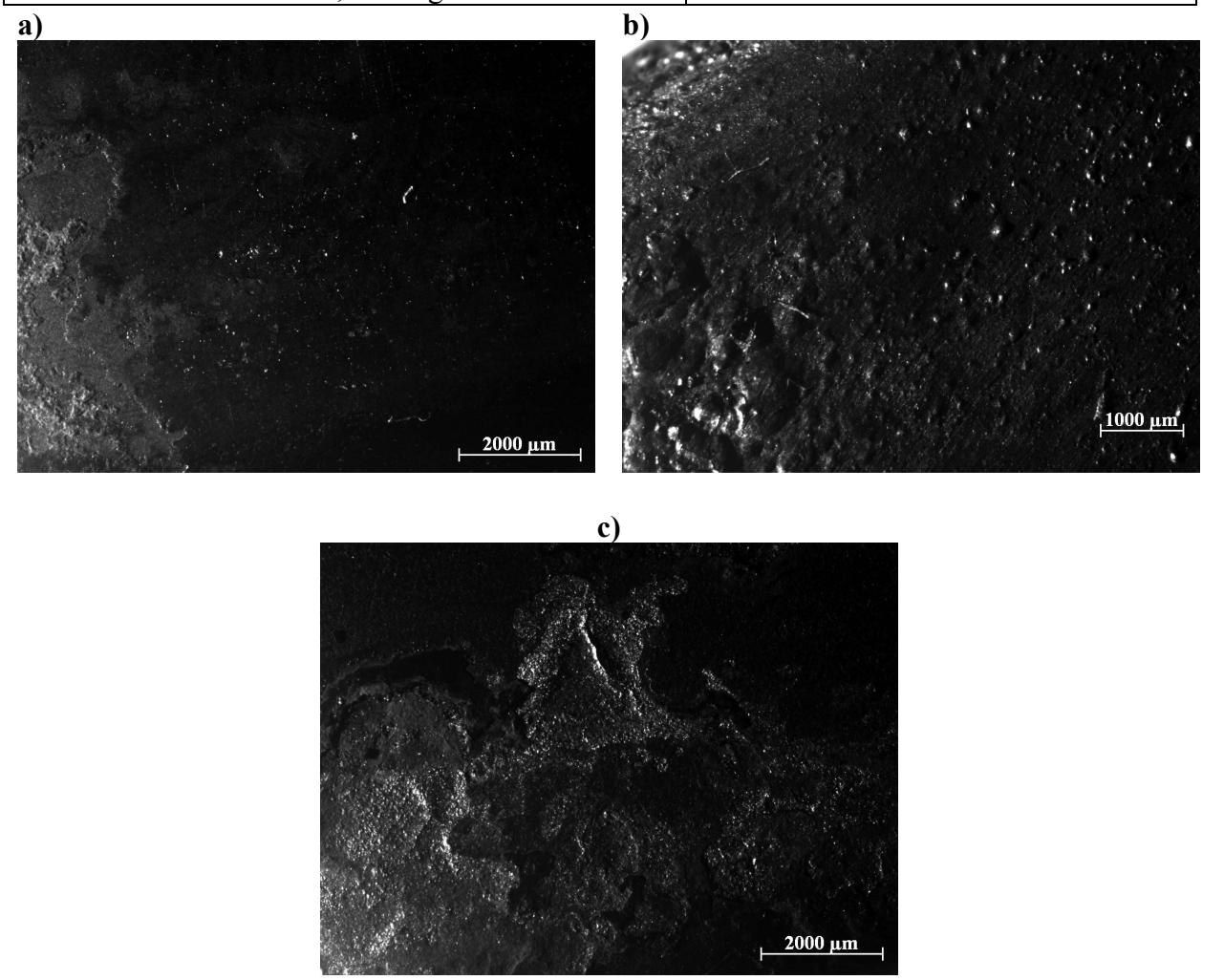

Rys.6. a) Próbka cynkowana – powierzchnia po korozji; b) próbka miedziowana – powierzchnia po korozji; c) próbka stalowa bez powłoki

4. PODSUMOWANIE

Wykonano analizę wyników badań oraz określono wpływ pokrycia warstwą ochronną na odporność korozyjną (która okazała się największa dla próbki miedziowanej), mikrostrukturę i wybrane własności takie jak twardość (najwyższa dla próbki miedziowanej) i grubość warstwy ochronnej (najwyższa dla próbki cynkowej).

Cynkowanie chroni stal przed korozją, nawet jeśli warstwa zostanie lekko uszkodzona (ochrona katodowa), jest ekonomiczne. Warstwa charakteryzuje się dużą trwałością w warunkach zewnętrznych (wilgoć, deszcz). Z kolei warstwa powstała w wyniku miedziowania posiada bardzo dobre przewodnictwo elektryczne, dobrą przyczepność dla kolejnych powłok (niklowania, chromowania), dobrą obrabialnością. Natomiast nie jest warstwą chroniącą przed korozją.

PODZIĘKOWANIA

Praca powstała w wyniku realizacji projektu „*Zabezpieczenia antykorozyjne profili stalowych*” w ramach kształcenia zorientowanego projektowo – PBL, w V konkursie Programu Inicjatywa Doskonałości – Uczelnia Badawcza, Wydział Mechaniczny Technologiczny, Politechnika Śląska

Podziękowania dla Elektrocarbon Galwan Sp. z o.o. w Tarnowskich Górach za pomoc w wykonaniu próbek cynkowanych.

LITERATURA

1. L.A. Dobrzański, A.D. Dobrzańska - Danikiewicz, Obróbka powierzchni materiałów inżynierskich, Open Access Library, Volume 5, 2011.
2. K.Kurski, Cynkowanie ogniowe, WNT,1970.
3. M. Jaśniok, Zabezpieczenie stali zbrojeniowej przed korozją w betonie metodą cynkowania ogniowego, „Przegląd Budowlany”, R. 89, nr 2, 2018, ISSN 0033-2038.
4. https://egalwan.eu/
5. Poradnik Galwanotechnika – Praca zbiorowa, Wydawnictwa Naukowo-Techniczne, Warszawa, 1985.
6. W. Golec, J. Zorychta, A. Krupińska, A. Zaleska, S. Topolska, Galwaniczne nakładanie powłok ochronnych, W: TalentDetector2025_Winter : International Students Scientific Conference / Bonek Mirosław (red.), Prace Katedry Materiałów Inżynierskich i Biomedycznych, 2025, Gliwice, Katedra Materiałów Inżynierskich i Biomedycznych. Wydział Mechaniczny Technologiczny. Politechnika Śląska, s.511-517, ISBN 978-83-65138-42-2

TalentDetector
9th January 2026
Gliwice, Poland
DEPARTMENT OF ENGINEERING MATERIALS AND BIOMATERIALS
FACULTY OF MECHANICAL ENGINEERING
SILESIAN UNIVERSITY OF TECHNOLOGY
INTERNATIONAL STUDENTS SCIENTIFIC CONFERENCE

Wpływ składu chemicznego na krystalizację stopów metali

Amelia Krupińska[a], Tomasz Szeliga[a], Beata Krupińska[b]

[a] Zespół Szkół Chemiczno-Medycznych i Ogólnokształcących w Tarnowskich Górach, uczniowie klasy o profilu Technik Analityk
[b] Silesian University of Technology, Faculty of Mechanical Engineering, Department of Engineering Materials and Biomaterials
email: beata.krupinska@polsl.pl

Streszczenie: Do badań zastosowano stop aluminium 42100 oraz miedź jako modyfikator stopu bazowego. Stop przed i po modyfikacji miedzią poddano analizie termiczno-derywacyjnej za pomocą urządzenia UMSA-MT5 (Universal Metallurgical Symulator and Analyzer). Wykonano badania mikrostruktury z zastosowaniem mikroskopii świetlnej oraz pomiar twardości. W wyniku wykonanych badań wyznaczono temperaturę T_L oraz T_{sol} oraz twardość.
Abstract: The 42100 aluminum alloy was used for the tests, with copper as a base alloy modifier. The alloy, both before and after copper modification, was subjected to thermal and derivative analysis using a UMSA-MT5 (Universal Metallurgical Simulator and Analyzer). Microstructural examinations were performed using light microscopy and hardness measurements. As a result, the T_L and T_{sol} temperatures, as well as hardness, were determined.

Słowa kluczowe: ATD, stopy aluminium, miedź

1. WSTĘP

W dzisiejszych czasach możemy zauważyć zwiększającą się liczbę konstrukcji przy jednoczesnym wzroście wymagań panujących na rynku. Mając powyższe na uwadze, prowadzone są różnorodne i niejednokrotnie czasochłonne badania mające na celu stworzenie i opracowanie nowych i co raz to bardziej optymalnych materiałów i technologii. Drugim co do popularności najczęściej używanym materiałem na produktu są stopy aluminium, wykorzystywane głównie w przemyśle motoryzacyjnym i lotniczym [1-5].

Głównym celem obu branży jest redukcja emisji dwutlenku węgla, co w rosnącym tempie szeroko rozumianego przemysłu ma nadrzędne znacznie w ochronie środowiska. Najwięksi producenci samochodów (Stany Zjednoczone, Chiny, Europa) prześcigają się w innowatorskich pomysłach co do zastosowania lżejszych, trwalszych materiałów celem zmniejszenia emisji CO_2 do atmosfery [1-5].

Stopy aluminium, które łączą niską gęstość oraz wysoką wytrzymałość są coraz częściej stosowane w różnego rodzaju projektach, w których redukcja wagi komponentów jest

niezbędna i opłacalna, co wiąże się bezpośrednio z obniżeniem kosztów. Przewiduje się że użycie aluminium będzie rosło mimo silnej konkurencji polimerów i kompozytów [1-5].

Znajomość procesu krystalizacji oraz wpływ obróbki ciekłego i półstałego metalu na mikro i makrostrukturze ma pierwszorzędny wpływ na stan odlewu. Analiza termiczna jest bardzo ważna w badaniach naukowych jak i w praktyce przemysłowej. Może być wykonana przed odlaniem do formy, aby zadbać o składniki stopowe poprawiające jakość wykonanego procesu. W związku z tym analiza termiczno-derywacyjna to najlepszy i najkorzystniejszy sposób na zwiększenie jakości w odlewni oraz zmniejszenie negatywnego wpływu na maszyny wykorzystywane w zakładzie produkcyjnym [1-5].

2. BADANY MATERIAŁ ORAZ METODOLOGIA

Materiałem wykorzystanym do badań był odlewniczy stop aluminium EN 42100 należący do stopów typu Al-Si-Mg, do którego dodano miedź w celu analizy wpływu składu chemicznego na kinetykę krystalizacji oraz własności. Skład chemiczny badanych stopów został przedstawiony w tablicy 1.

Tablica 1. Skład chemiczny badanych stopów aluminium.

Stężenie masowe pierwiastków, %												
	Si	Fe	Mn	Mg	Cr	Ni	Zn	Pb	Sn	Ti	Al	Cu
AlSi7Mg0,3	7	0,14	0,02	0,3	0,01	0,01	0,02	0,01	0,01	0,13	reszta	-
AlSi7Cu2Mg0,3	7	0,14	0,02	0,3	0,01	0,01	0,02	0,01	0,01	0,13	reszta	2

W celu określenia zależności pomiędzy składem chemicznym a mikrostrukturą i twardością wykonano następujące badania:

- Analiza Termiczno-Derywacyjna wykonana z wykorzystaniem UMSA MT5 (Universal Metallurgical Symulator and Analyzer) z wygrzewaniem w temp. 750 °C w czasie 5 minut, a następnie swobodnego chłodzenia. Pomiar temperatury wykonano poprzez termoparę umieszczoną w próbce. Zastosowano termopary typu K.

- Analiza mikrostruktury wykonano z wykorzystaniem mikroskopu optycznego Axio Observer firmy ZEISS z wykorzystaniem powiększeń x100, x200, x500 i x1000.

- Pomiary twardości przeprowadzone zgodnie z normą PN-EN ISO 6508-1:2016-10, z wykorzystaniem wgłębnika diamentowego o kącie wierzchołkowym 120° i promieniu zaokrąglenia 0,2mm. Dla skali HRA (siła obciążająca - 60 N).

Rysunek 1. Stanowisko UMSA; 1 – zespół cewka – dysze chłodzące; 2 – komputer sterujący; 3 – układ sterujący mocą grzania; 4 – układ sterujący szybkością chłodzenia [6].

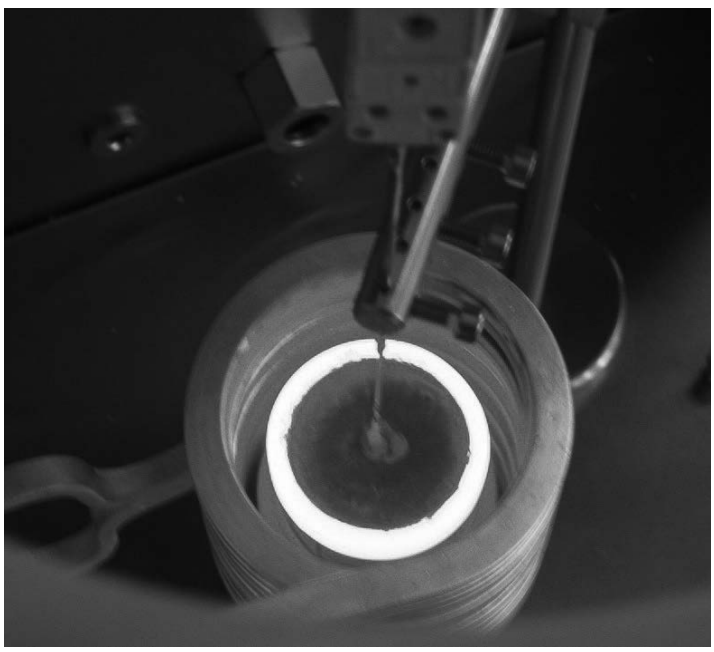

Rysunek 2. Próbka podczas doświadczenia w urządzeniu UMSA MT5 (Universal Metallurgical Symulator and Analyzer)

3. WYNIKI

Analiza Termiczno-Derywacyjna wykonana z wykorzystaniem UMSA MT5 (Universal Metallurgical Symulator and Analyzer) pozwoliła określić temperatury T_L i T_{sol} (Rys.3,4, tab. 2) dla każdej z próbek.

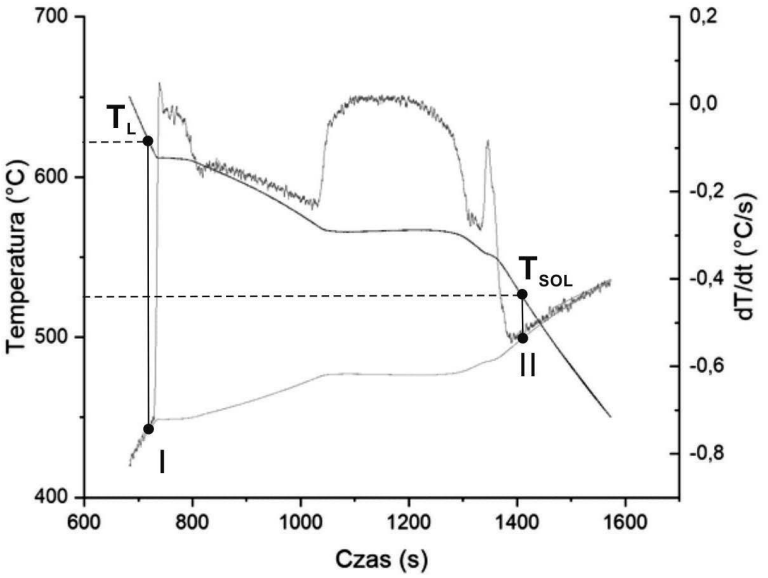

Rysunek 3. Wykres szybkości chłodzenia od temperatury dla próbki AlSi7Mg0,3 (zielona – krzywa chłodzenia, niebieska – krzywa derywacyjna, czerwona – krzywa bazowa).

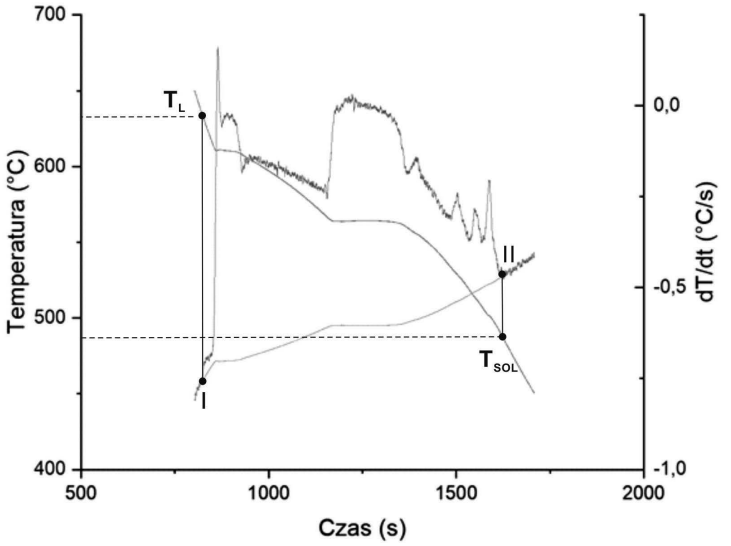

Rysunek 4. Wykres szybkości chłodzenia od temperatury dla próbki AlSi7Mg0,3Cu2 (zielona – krzywa chłodzenia, niebieska – krzywa derywacyjna, czerwona – krzywa bazowa).

Tablica 2. Wyznaczone temperatury likwidus i solidus badanych stopów.

	AlSi7Mg0,3	AlSi7Mg0,3Cu2
Szybkość chłodzenia	0,11°C/s	0,19°C/s
T_L	610°C	625°C
T_{SOL}	530°C	490°C

Analiza mikrostruktury - obserwacje mikrostruktury przeprowadzono z wykorzystaniem mikroskopii świetlnej z wykorzystaniem mikroskopu Axio Observer firmy ZEISS (Rys.5,6)

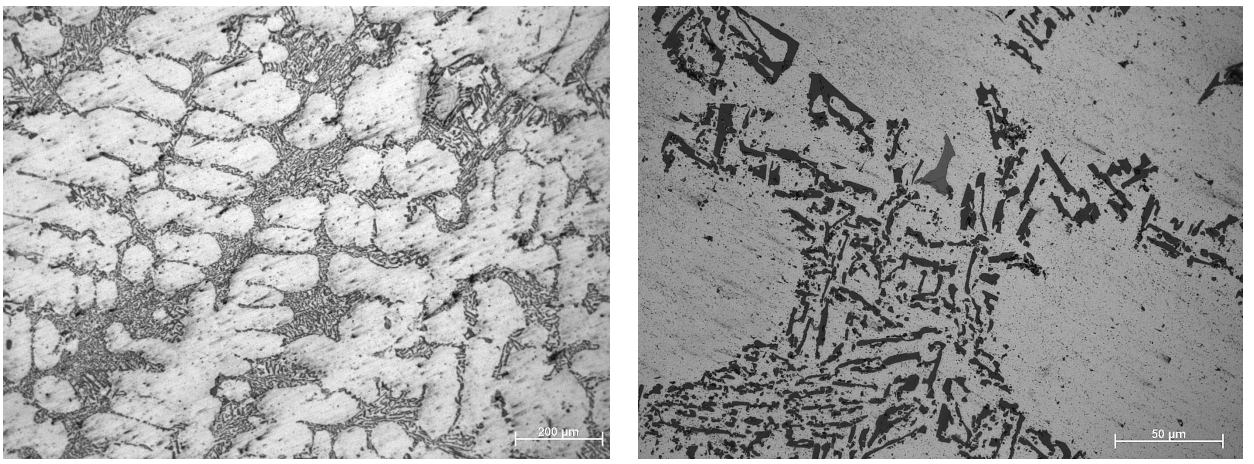

Rysunek 5. Mikrostruktura stopu AlSi7Mg0,3 –ATD

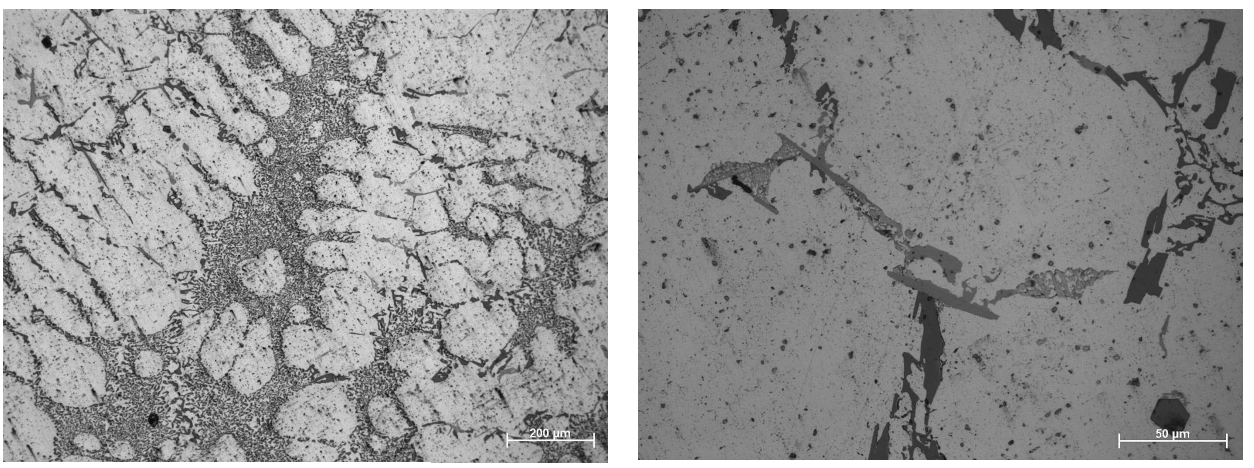

Rysunek 6. Mikrostruktura stopu AlSi7Mg0,3Cu2 - ATD

Wyniki pomiarów twardości zamieszczono w tablicy 3.

Tablica 3. Wyniki pomiaru twardości

	Twardość HRA
AlSi7Mg0,3	56
AlSi7Mg0,3Cu2	64

WNIOSKI

W wyniku wykonanych badań sformułowano następujące wnioski:

1. Modyfikacja stopu AlSi7Mg0,3 miedzią podniosła temperaturę T_L z 610°C do 625°C czyli o ok. 2%, natomiast temperatura T_{sol} dla stopu AlSi7Mg0,3Cu2 obniżyła się z 530°C do 490°C czyli o ok 7% , co oznacza że temperatura przesycania dla próbki AlSi7Mg0,3 powinna być wyższa niż dla próbki AlSi7Mg0,3Cu2 – pozwala to na bardziej efektywne określenie parametrów możliwej obróbki cieplnej w celu dalszej optymalizacji własności stopu.

2. W stopie z Cu wystąpił wzrost twardości z 56HRA na 64HRA czyli o ok 12%.

PODZIĘKOWANIA

Praca powstała w wyniku realizacji projektu „*Wpływ składu chemicznego na krystalizację stopów metali*" w ramach kształcenia zorientowanego projektowo – PBL, w VI konkursie Programu Inicjatywa Doskonałości – Uczelnia Badawcza, Wydział Mechaniczny Technologiczny, Politechnika Śląska

LITERATURA

1. K. Oczoś, A. Kawalec, Shaping of light metal, Wydawnictwo Naukowe PWN, Warszawa, 2012.
2. S.J. Skrzypek, K. Przybyłowicz, Engineering of metals and their alloys, Wydawnictwo AGH, Kraków, 2012..
3. L.A. Dobrzański, Podstawy nauki o materiałach, Wydawnictwo WNT, Warszawa, 2002.
4. W. Miller, L. Zhuang, J. Bottema, A.J. Wittebrood, P. De Smet, A. Haszler, A. Vieregge, Recent Development in Aluminium Alloys for the Automotive Industry, Materials Science and Engineering A280, 2000, 37–49.
5. P.E. Smolarczyk , M. Krupiński, Thermal-Derivative Analysis and Precipitation Hardening of the Hypoeutectic Al-Si-Cu Alloys, Archives of Foundry Engineering, Vol.19(1), 2019, 41-46.
6. L.A. Dobrzański, T. Tański, A.D. Dobrzańska-Danikiewicz, M. Król, S. Malara, J. Domagała-Dubiel, Struktura i własności stopów Mg-Al-Zn, Volume 5 (11) 2012, OPEN ACCESS LIBRARY.

TalentDetector

9th January 2026
Gliwice, Poland

DEPARTMENT OF ENGINEERING MATERIALS AND BIOMATERIALS
FACULTY OF MECHANICAL ENGINEERING
SILESIAN UNIVERSITY OF TECHNOLOGY

INTERNATIONAL STUDENTS SCIENTIFIC CONFERENCE

Umocnienie wydzieleniowe stopu Al-Si-Cu stosowanego na elementy silników pojazdów samochodowych

Mateusz Krupiński[a], Dominik Hatlapa[a], Szymon Kocot[a], Mariusz Krupiński[b]

[a]Wieloprofilowy Zespół Szkół, 42-600 Tarnowskie Góry, ul. Sienkiewicza 6
[b]Politechnika Śląska, Wydział Mechaniczny Technologiczny, Katedra Materiałów Inżynierskich i Biomedycznych, 44-100 Gliwice, ul. Konarskiego 18a
email: mariusz.krupinski@polsl.pl

Streszczenie: W artykule opisano wpływ obróbki cieplnej na mikrostrukturę i własności stopów Al-Si-Cu stosowanych na elementy spalinowych i elektrycznych silników samochodowych. Do badań zastosowano stop EN AC-AlSi7Cu3Mg. Wykonano analizę termiczno-derywacyjną na urządzeniu UMSA-MT5. Obróbkę cieplną składającą się z procesów przesycania i starzenia wykonano na urządzeniu Nabertherm P330. W wyniku umocnienia wydzieleniowego fazą θ” nastąpił wzrost twardości stopu.
Abstract: This article describes the effect of heat treatment on the microstructure and properties of Al-Si-Cu alloys used in automotive internal combustion and electric engine components. The EN AC-AlSi7Cu3Mg alloy was used for testing. Thermal derivation analysis was performed on a UMSA-MT5 device. Heat treatment, consisting of solution heat treatment and aging, was performed on a Nabertherm P330 heat treatment unit. As a result of precipitation hardening with the θ" phase, the alloy's hardness increased.

Słowa kluczowe: Stopy Al-Si-Cu, obróbka cieplna, analiza termiczno-derywacyjna

1. WSTĘP

Redukcja masy pojazdów, a tym samym emisja zanieczyszczeń zarówno skoncentrowana jak i rozproszona, skłania do stosowania metali lekkich w tym aluminium do produkcji odlewanych podzespołów samochodowych (rys. 1, rys. 2). Jednocześnie mniejsza wytrzymałość stopów metali lekkich w porównaniu ze stalą i żeliwem zmusza producentów do stosowania technologicznych metod podnoszenia własności wytrzymałościowych w tym po przez obróbkę cieplną [1-3].

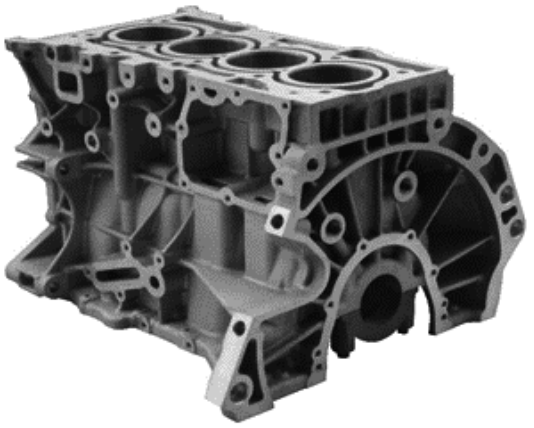

Rysunek 1. Blok silnika spalinowego [4]

Rysunek 2. Obudowa silnika elektrycznego [5]

2. MATERIAŁ DO BADAŃ I METODYKA

Do badań wpływu obróbki cieplnej na mikrostrukturę i własności zastosowano stop aluminium EN AC-AlSi7Cu3Mg o składzie chemicznym wg normy PN-EN 1706 pokazanym w tabeli 1. Obróbkę cieplną wykonano przy zastosowaniu pieca Nabertherm P330. Parametry obróbki cieplnej pokazano w tabeli 2.

Tabela 1. Skład chemiczny stopu

Stężenie masowe pierwiastków, %							
Si	Cu	Mg	Mn	Fe	Ti	Zn	Ni
6.5-8	3-4	0.3-0.6	0.2-0.65	≤0.8	≤0.25	≤0.65	≤0.3

Tabela 2. Parametry obróbki cieplnej

Temperatura przesycania, °C	Czas przesycania, h	Temperatura starzenia, °C	Czas starzenia, h
475	5	175	4

Do badań mikrostruktury stopów aluminium przygotowano zgłady metalograficzne przy użyciu półautomatycznej szlifierko-polerki STRUERS LaboPol-5 z głowicą LaboForce-3 oraz zawiesin diamentowych (1µm) oraz sukna do polerowania MD-Nap. Próbki ze stopu AlSi7Cu3Mg były trawione w wodnym roztworze NaOH. Badania mikrostruktury przy powiększeniach 25-500x realizowano za pomocą mikroskopu świetlnego Axio Observer firmy Zeiss wraz z dedykowanym oprogramowaniem do analizy obrazu struktur metalograficznych. Wykonano również analizę składu chemicznego w mikroobszarach przy użyciu spektroskopii dyspersji energii (EDS) oraz analizę rozmieszczenia pierwiastków przy użyciu skaningowego mikroskopu elektronowego Zeiss Supra 35. Badania twardości metodą Rockwell'a zrealizowano przy użyciu twardościomierza Zwick ZHR 4150.

3. WYNIKI BADAŃ

Wykonana obróbka cieplna składająca się z przesycania w temperaturze 475°C (poniżej temperatury solidus - T_{Sol}) (rys. 3) dla badanego stopu (rys. 4a; 5a), powoduje rozpuszczenie składnika umacniającego, a następne starzenie w temperaturze 175°C wydzielenie się w osnowie α fazy umacniającej θ" (rys. 4 b; 5 b, c; 6; tab. 3). Wydzielenie się w osnowie aluminium fazy umacniającej, w wyniku wykonanej obróbki cieplnej powoduje wzrost twardości dla badanego stopu AlSi7Cu3Mg o ok. 69% (tab. 4).

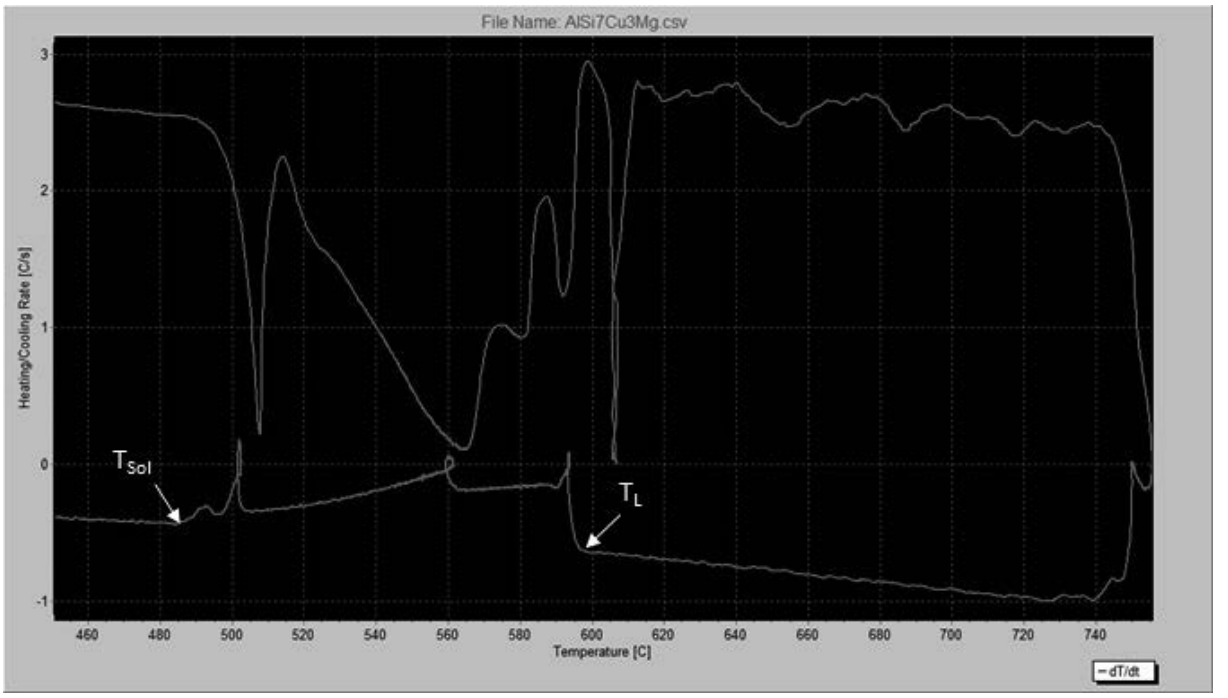

Rysunek 3. Krzywa derywacyjna dla stopu AlSi7Cu3Mg, chłodzonego swobodnie z szybkością 0.1°C/s, temperatura T_L = 598°C, temperatura T_{Sol} = 485°C.

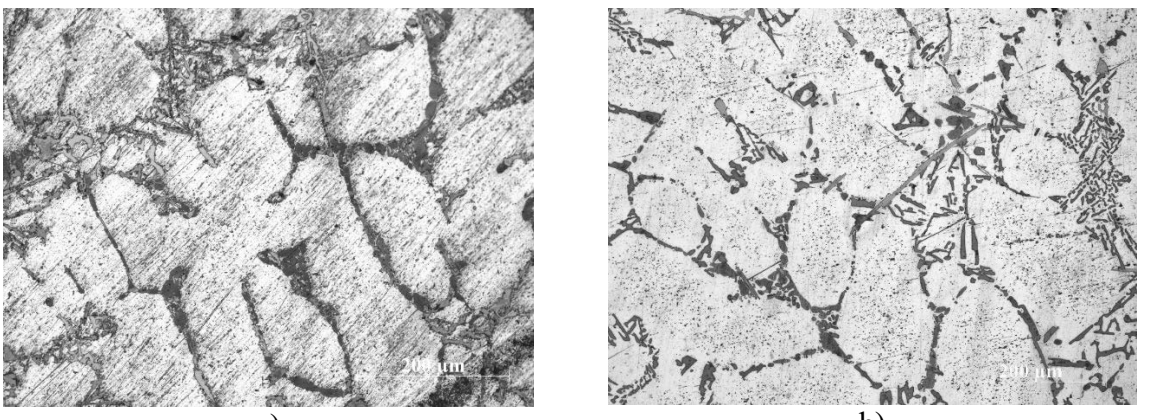

a) b)

Rysunek 4. Struktura odlewniczego stopu AlSi7Cu3Mg: a) stan odlany; b) stan obrobiony cieplnie

Obserwacje wykonane za pomocą skaningowego mikroskopu elektronowego, oraz badania składu chemicznego wykonane z zastosowaniem rentgenowskiej mikroanalizy ilościowej, potwierdzają obecność w badanych stopach składników chemicznych stopu w postaci Si, Cu, Mg, Fe, Mn (rys. 5 a, b) wraz z zaznaczonymi punktami pomiarowymi P1-P4 (rys. 5 c) oraz stężeniem masowym pierwiastków w badanych punktach (tab. 3). Na rysunku 4 przedstawiono rozkład powierzchniowy pierwiastków będących składnikami struktury stopu.

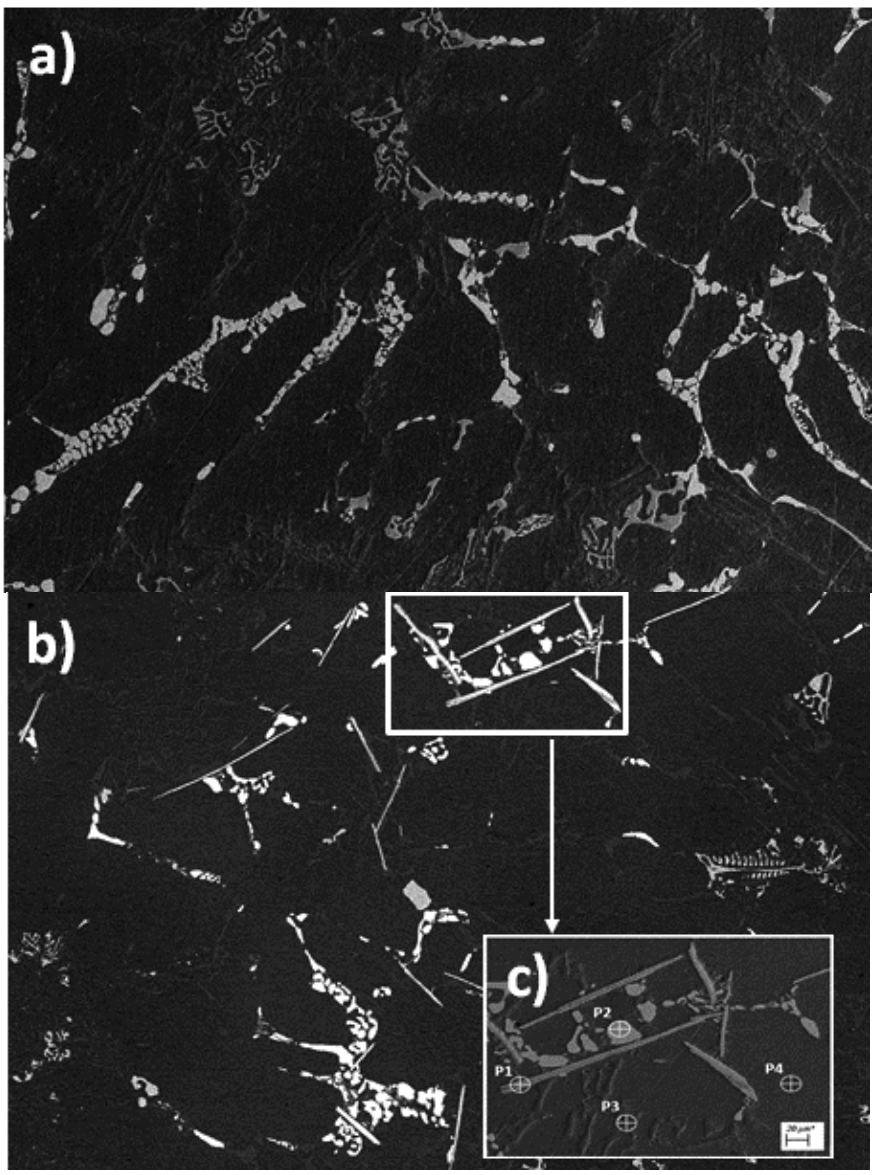

Rysunek 5. Struktura odlewniczego stopu AlSi7Cu3Mg: a) stan odlany; b, c) stan obrobiony cieplnie

Tabela 3. Wyniki ilościowej analizy EDS składu chemicznego stopu AlSi7Cu3Mg wykonane w miejscach zaznaczonych na rys. 5 c.

Punkt pomiaru	Stężenie masowe pierwiastków, %					
	Mg	Al	Si	Mn	Fe	Cu
P1	0.2	52.9	14.3	3.4	28.8	0.4
P2	0.4	46.0	0.5	-	-	53.1
P3	0.1	60.4	36.9	-	-	2.6
P4	0.4	94.7	0.2	-	-	4.7

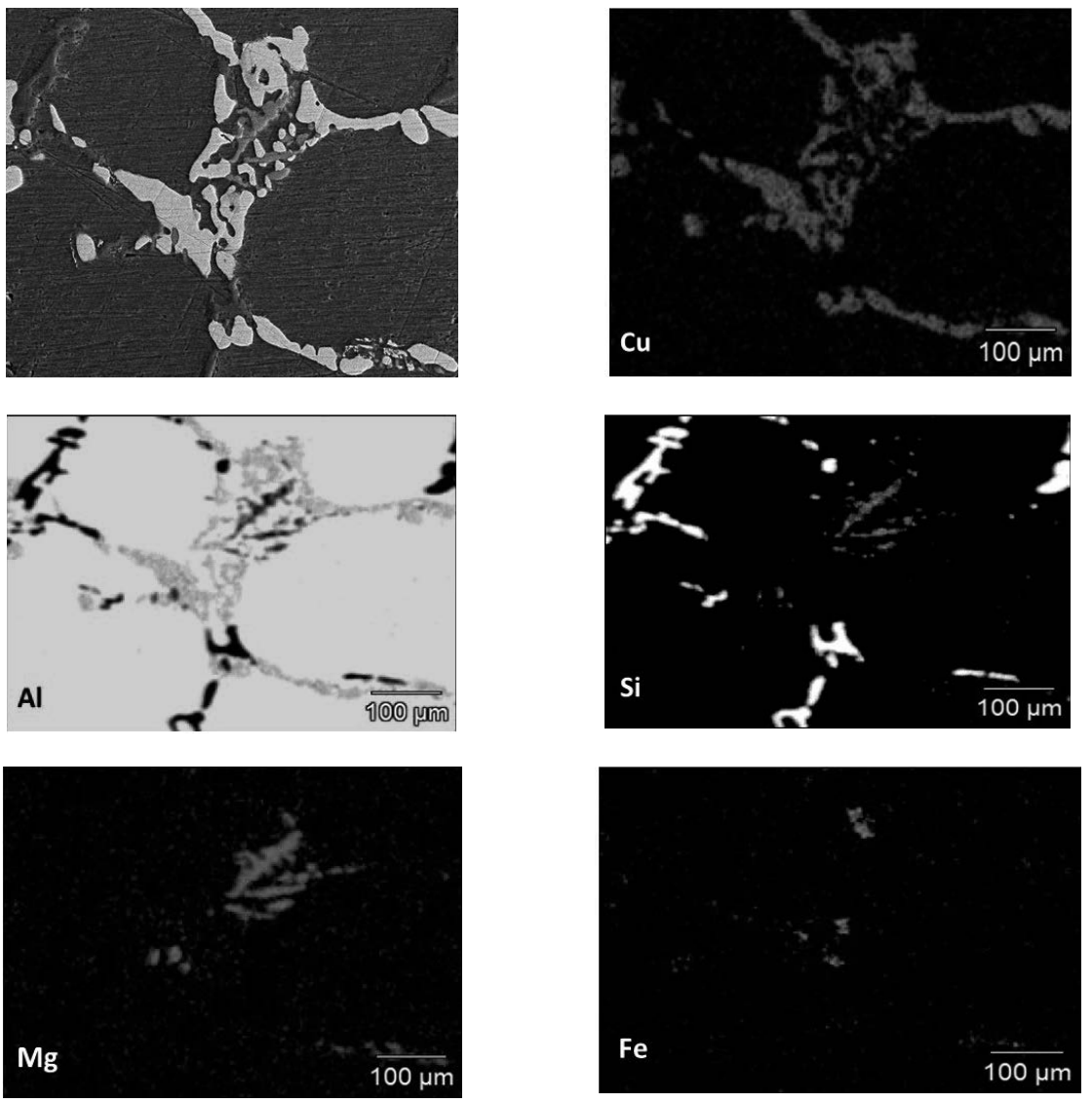

Rysunek 6. Struktura odlewniczego stopu AlSi7Cu3Mg chłodzonego z szybkością 0.1℃/s, obraz mapy rozmieszczenia pierwiastków

Tabela 3. Statystyczne opracowanie wartości pomiarów twardości badanego stopu

Stan stopu	Twardość, HRB	Odchylenie standardowe
Odlany	43.9	3.7
Przesycony i starzony	74.1	3.2

4. PODSUMOWANIE

Wykonana obróbka cieplna składająca się z przesycania w temperaturze 475°C (poniżej temperatury solidus - T_{Sol}) (rys. 3) dla badanego stopu, powoduje rozpuszczenie składnika umacniającego, a następne starzenie w temperaturze 175°C wydzielenie się w osnowie α fazy umacniającej θ". Wydzielenie się w osnowie aluminium fazy umacniającej, w wyniku wykonanej obróbki cieplnej powoduje wzrost twardości dla badanego stopu AlSi7Cu3Mg o ok. 69%.

PODZIĘKOWANIA

Praca powstała w wyniku realizacji projektu „Stopy metali nieżelaznych stosowane na elementy silników spalinowych i elektrycznych w pojazdach samochodowych" w ramach projektu realizowanego z uczniami szkoły ponadpodstawowej Programu Inicjatywa Doskonałości – Uczelnia Badawcza, Wydział Mechaniczny Technologiczny, Politechnika Śląska.

LITERATURA

1. M. Krupiński, M. Król, R. Maniara, Heat treatment of Al-Si-Cu alloys, Solid State Phenomena, 2018, vol. 275, s.15-29.
2. S. Pietrowski, Siluminy. Wyd. Politechniki Łódzkiej, Łódź 2001.
3. A. Jarco, Właściwości mechaniczne stopów EN AC-45000 (AlSi6Cu4) i AlSi17CuNiMg po obróbce cieplnej, Inżynieria Maszyn, 2017, R. 22, z. 1, 58-64.
4.http://pl.zhdlen.com/cast-aluminum-engine-block-ne15-product
5.http://pl.fendadiecasting.com/custom-aluminum-alloy-die-cast-electric-vehicle-motor-housing-die-casting-auto-parts-product/

TalentDetector

9th January 2026
Gliwice, Poland

DEPARTMENT OF ENGINEERING MATERIALS AND BIOMATERIALS
FACULTY OF MECHANICAL ENGINEERING
SILESIAN UNIVERSITY OF TECHNOLOGY

INTERNATIONAL STUDENTS SCIENTIFIC CONFERENCE

Design and Implementation of an Active Self-Leveling Chassis for a Mobile Exploration Rover

Michał Lasak[a], Kamil Moszumański[a], Franciszek Borgosz[b], Dariusz Myszor[c]

[a] Silesian University of Technology, Faculty of Automatic Control, Electronics and Computer Science, SKN SpaceCoffee
email: Michal.Lasak@student.polsl.pl, km322442@student.polsl.pl
[b] Silesian University of Technology, Faculty of Automatic Control, Electronics and Computer Science, SKN SpaceCoffee, SKN vFly
email: fborgosz@spacecoffee.net
[c] Silesian University of Technology, Faculty of Automatic Control, Electronics and Computer Science, Department of Algorithmics and Software
email: Dariusz.Myszor@polsl.pl

Abstract: This paper presents the design specification and the initial proof-of-concept implementation of an active self-leveling chassis intended for a mobile rover operating on uneven planetary terrain. The project is motivated by the stringent requirements of in-situ operations, specifically subsurface sample collection using a drilling mechanism. Standard mobility systems often result in a tilted chassis when traversing slopes, which poses significant risks to drilling tools, including shear stress, borehole misalignment, and potential fracture. To validate the feasibility of mitigating these risks, a simplified experimental testbed was constructed. The prototype utilizes four independently controlled linear DC actuators to actively adjust the suspension geometry, ensuring the main platform remains horizontal relative to the gravity vector. The paper details the mechanical concept, the electronic control architecture based on high-current motor drivers, and the preliminary testing of the fundamental leveling logic required for safe drilling operations.

Keywords: self-leveling chassis, mobile rover, active suspension, linear actuators, proof of concept, mechatronic design

1. INTRODUCTION

The exploration of extraterrestrial bodies, such as Mars or the Moon, has evolved from simple imaging missions to complex scientific operations requiring physical interaction with the environment. Modern mission profiles often require rovers not only to traverse rugged terrain but also to perform delicate tasks such as robotic manipulation and deep-soil drilling [1]. A significant engineering challenge arises when these operations must be conducted on inclined surfaces. Planetary terrain is rarely flat; craters, dunes, and rocky outcrops present constant

navigational challenges, often limiting the efficacy of traditional passive suspension systems [4, 2]. For a drilling mechanism rigidly mounted to a rover's chassis, the angle of the rover directly dictates the angle of penetration. Drilling into the regolith at an oblique angle introduces detrimental lateral forces. These forces can lead to drill bit jamming, increased power consumption, excessive heat generation due to friction against the borehole wall, or catastrophic tool failure. Consequently, the ability to decouple the chassis orientation from the terrain gradient is a critical operational requirement, a challenge shared by planetary landers which require similar stabilization for safe touchdown and operation [7].

This paper describes the development of the MPER (Multi-Purpose Exploration Rover) chassis concept (Fig. 1). The study focuses on the validation of an active suspension system designed to stabilize the rover's payload. A functional prototype (proof-of-concept) has been built to test the electromechanical integration and the fundamental control strategies required to achieve a stable, level platform using accessible, off-the-shelf components [10, 11].

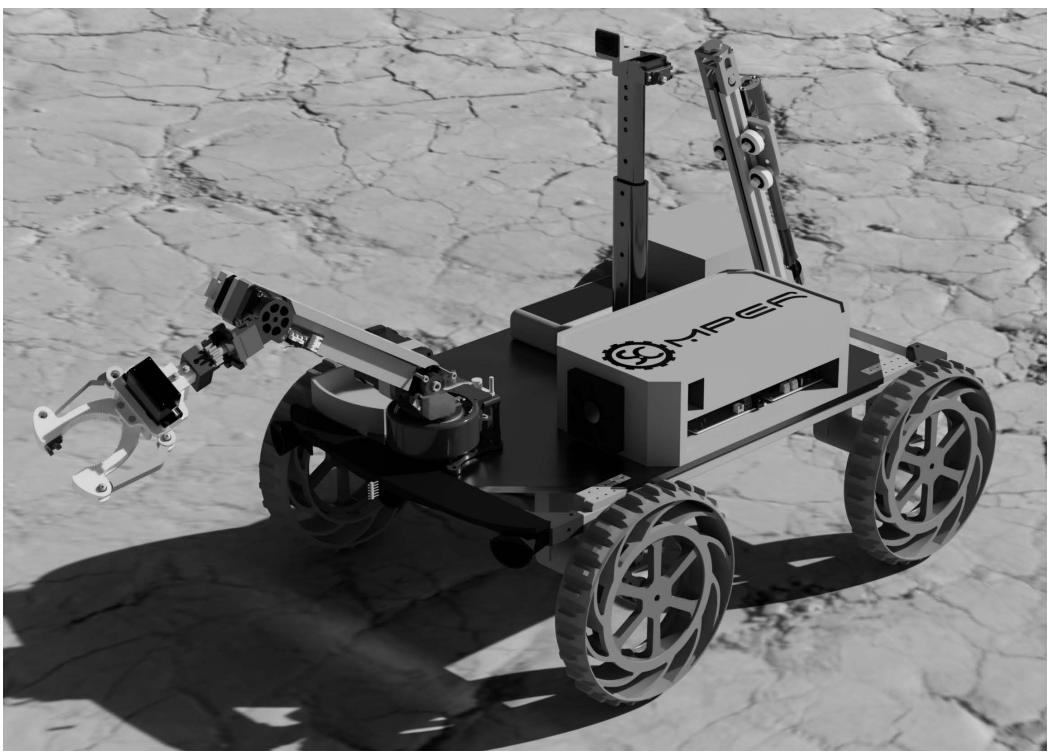

Figure 1: Conceptual design of the MPER system. The active chassis is designed to stabilize the central platform for the manipulator and drill.

2. KINEMATIC ANALYSIS AND MECHANICAL DESIGN

The mechanical architecture of the MPER chassis was driven by two conflicting requirements: sufficient ground clearance for obstacle traversal and a rigid, stable base for drilling operations. The design process was divided into the theoretical kinematic specification and the practical implementation of the testbed.

2.1. Suspension Kinematics Concept

The target design utilizes an independent control arm configuration. In this topology, each wheel unit is attached to a pivoted suspension arm located beneath the main chassis. The linear actuator connects the central frame to a specific hardpoint on the control arm. This active approach contrasts with passive rocker-bogie mechanisms, which average the terrain irregularities but cannot alter the chassis inclination [3]. While hydraulic systems offer high force capabilities for off-road leveling [8], they are often too heavy and complex for small-scale planetary rovers, making electromechanical actuators a more suitable choice for this application.

Mathematically, the system can be modeled as a closed kinematic chain where the actuator acts as a variable-length link (L_{act}). By extending or retracting the actuator, the system changes the angle of the control arm (θ_{arm}), which results in a change in the vertical position (z_{wheel}) of the wheel contact point relative to the chassis frame. This arrangement allows for the independent control of three degrees of freedom (DOF) of the chassis:

1. Heave: Uniform vertical lifting of the entire platform.
2. Pitch: Rotation around the lateral axis (nose up/down).
3. Roll: Rotation around the longitudinal axis (tilt left/right).

This design decouples the lateral structural loads—handled by the robust control arms—from the vertical height adjustment mechanism [6].

2.2. Prototype Construction Details

To validate this kinematic concept without incurring the cost and machining time of a full aerospacegrade chassis, an experimental testbed was assembled.

Actuation: The prototype employs 12V DC linear actuators with a stroke length of 150 mm. These actuators were selected specifically for their lead-screw mechanism, which provides a high self-locking force. Unlike servo-driven systems that require continuous power to hold a position against gravity, the lead-screw allows the actuators to be powered down once the target level is achieved. This is a crucial feature for energy efficiency during the drilling phase.

Structural Integration: The wheels are attached to the actuators and control arms via customdesigned brackets. Given the high shear loads generated during skid-steering maneuvers and the reaction forces during lifting, standard 3D printing materials were deemed insufficient. Therefore, these key structural components were manufactured using FDM technology with PCTG filament reinforced with 10% carbon fiber (PCTG-CF10). This material choice offers a superior stiffnessto-weight ratio compared to standard PET-G or ABS.

Chassis Base: To facilitate rapid reconfiguration of the electronic layout during the testing phase, the prototype chassis utilizes a composite baseplate structure (combining aluminum profiles with a rigid mounting plate) rather than the final fully welded frame. This allows for easy access to the motor drivers and wiring harness during troubleshooting.

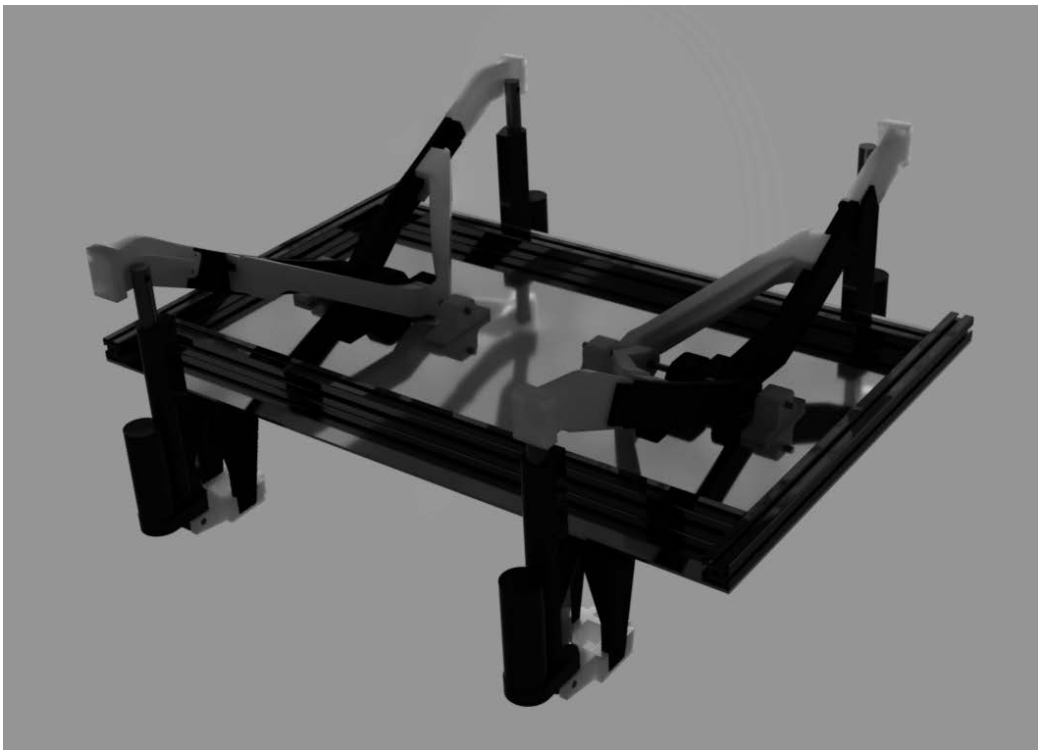

Figure 2: Undercarriage view of the design illustrating the independent suspension arm configuration.

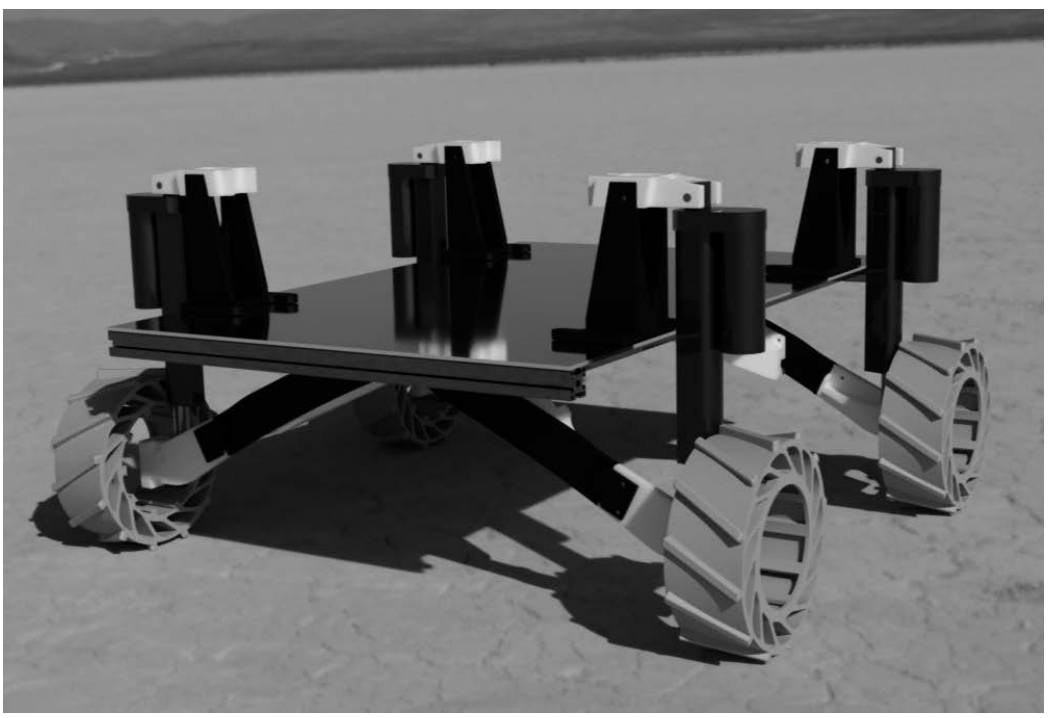

Figure 3: Mechanical configuration of the chassis. The linear actuators adjust the angle of the suspension control arms.

3. PHYSICS OF DRILLING ON INCLINED TERRAIN

The primary driver for the active leveling capability is the physics of the onboard drilling subsystem. Drilling into consolidated soil or rock dictates strict alignment tolerances to ensure sample quality and tool longevity.

Consider a scenario where the rover is positioned on a slope with an inclination angle α. If the chassis is parallel to the slope, the drill bit enters the ground at angle α relative to the gravity vector $\vec{g}$. When a thrust force F_{thrust} is applied along the drill axis, it decomposes into two orthogonal components relative to the vertical plane:

$$F_{vertical} = F_{thrust} \cdot \cos(\alpha) \tag{1}$$

$$F_{lateral} = F_{thrust} \cdot \sin(\alpha) \tag{2}$$

The component $F_{lateral}$ (shear force) is particularly problematic. Research on mobile manipulator stability indicates that lateral forces on inclined terrain significantly increase the risk of tip-over and mechanical stress [9]. Specifically, this leads to:

1. Bending Moment: It creates a bending moment on the drill shaft, which can exceed the elastic limit of the tool steel, leading to permanent deformation.

2. Borehole Ellipticity: The lateral force causes the bit to "walk" or scrape against the side of the borehole, increasing friction and potentially jamming the bit.

3. Rover Stability: The reaction force tends to push the rover down the slope. If $F_{lateral}$ exceeds the static friction force of the wheels (μF_{normal}), the rover will slip, shearing the drill bit inside the ground.

By utilizing the active chassis to drive $\alpha \rightarrow 0$, the term $\sin(\alpha)$ vanishes, and $F_{lateral}$ is minimized. This ensures that the entire thrust force is directed into penetration, optimizing energy use and safety.

4. ELECTRONIC SYSTEM ARCHITECTURE

The electronic control system for the proof-of-concept is designed to be robust and capable of handling high current loads, while maintaining a simplified logic structure appropriate for an initial prototype using low-cost embedded systems [10].

4.1. Power Distribution and Actuation

The power system is supplied by a high-discharge Li-Ion source. A critical component selection was the motor driver units. The four leveling actuators, under load, can draw significant current, especially during the initial phase of lifting the chassis. Standard L298N drivers were deemed insufficient due to their voltage drop and thermal limitations.

Instead, the prototype utilizes two Cytron MDD10A dual-channel DC motor drivers. These drivers utilize NMOS H-Bridge technology, which allows for continuous currents up to 10A per channel without active cooling. This ensures that the system can handle the peak currents required to lift the rover's weight. The drivers are interfaced via PWM (Pulse Width Modulation) and DIR (Direction) signals, allowing for bidirectional control (extension and retraction) of the actuators.

4.2. Sensor Fusion and Signal Processing

To determine the rover's orientation in 3D space, a 6-axis Inertial Measurement Unit (IMU) is employed, consisting of a 3-axis accelerometer and a 3-axis gyroscope. The IMU is mounted at the geometric center of the chassis to minimize the influence of centrifugal accelerations during rover rotation.

Raw accelerometer data is susceptible to high-frequency noise and mechanical vibrations caused by the traction motors. To address this, a complementary filter is implemented in the microcontroller firmware [13]. The estimated pitch (θ_{est}) is calculated as:

$$\theta_{est} = \alpha \cdot (\theta_{gyro} + \omega \cdot dt) + (1 - \alpha) \cdot \theta_{accel} \tag{3}$$

Where α is a weighting factor (typically 0.98), ω is the angular velocity, and θ_{accel} is the angle derived from the gravity vector. This filtered data forms the feedback loop for the leveling controller.

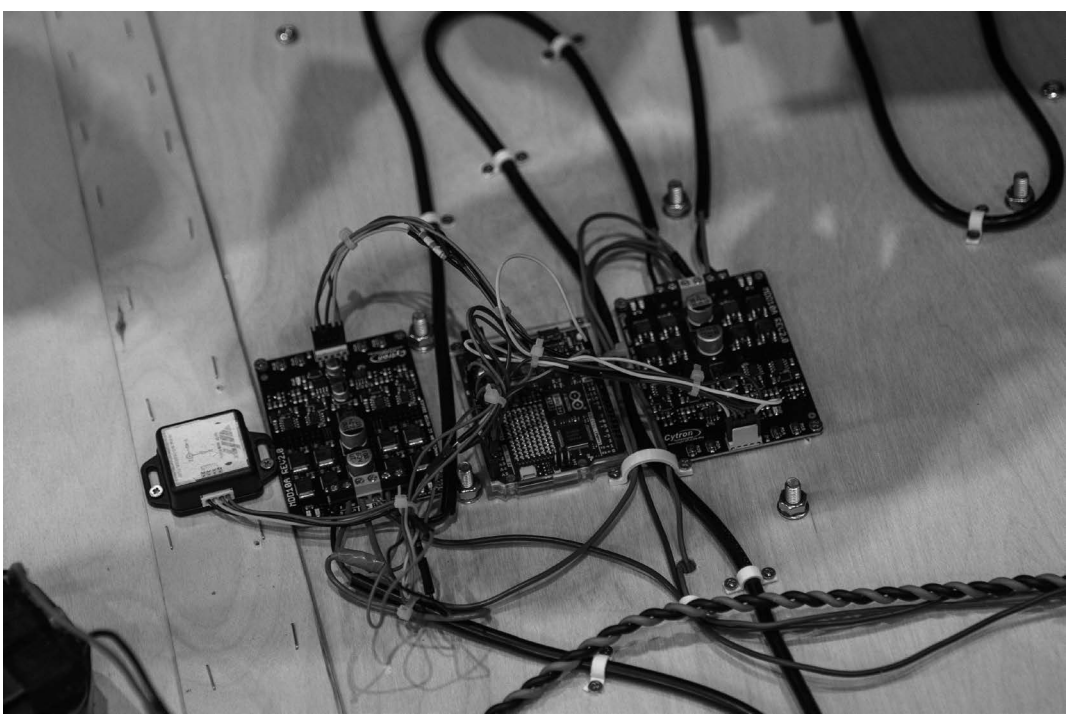

Figure 4: *View of the electronics, showing the microcontroller, Cytron MDD10A drivers, and wiring harness.*

5. CONTROL STRATEGY IMPLEMENTATION

For this stage of development, the focus was on validating the mechanical capability of the system to self-level. Therefore, a fundamental closed-loop control strategy was implemented.

5.1. Control Logic

The control algorithm operates on a "Bang-Bang" principle with hysteresis. This approach was chosen for its simplicity and robustness in the absence of absolute position encoders on the linear actuators, a common practice in early-stage educational rover prototyping [11]. The control loop executes the following sequence:

1. Data Acquisition: The system reads the filtered pitch (ϕ) and roll (ψ) angles from the IMU.

2. Error Calculation: The system calculates the deviation from the horizontal plane (0°).

3. Threshold Comparison: The error is compared against a defined deadband (tolerance) of $\pm 0.5^\circ$. This deadband is essential to prevent "hunting"—a phenomenon where the motors continuously oscillate back and forth trying to achieve an impossibly perfect zero angle.

4. Actuation:
• If $\text{Error}_{\text{pitch}} > +0.5^\circ$ (Nose Up): The rear actuators extend and/or the front actuators retract.
• If $\text{Error}_{\text{pitch}} < -0.5^\circ$ (Nose Down): The front actuators extend and/or the rear actuators retract.
• Similar logic is applied simultaneously to the Roll axis using left/right pairs.

5. Hold State: Once the error falls within the $\pm 0.5 \circ$ window, the motors are powered down. The mechanical self-locking of the lead screws holds the platform in position.

6. PRELIMINARY VALIDATION AND RESULTS

The assembled proof-of-concept device was subjected to initial functional testing to verify the integration of the mechanical structure, the PCTG-CF10 mounts, and the control logic.

6.1. Test Setup

The testing procedure involved placing the rover on a variable-angle ramp. The ramp angle was incrementally increased from 0° to 25°. At each increment, the auto-leveling sequence was triggered, and the final platform angle was measured using an external digital inclinometer for verification.

6.2. Observations

The tests confirmed that the electromechanical system successfully interprets IMU data and drives the actuators in the correct direction to counteract the slope.
• **Load Capacity:** The Cytron MDD10A drivers and selected actuators demonstrated sufficient torque to lift the chassis under its own weight (approx. 10 kg for the prototype) without stalling.

• **Range of Motion:** The system successfully leveled the platform on slopes up to approximately 20° . Beyond this angle, the stroke length of the linear actuators (150 mm) became the limiting factor, as the actuators reached their mechanical end-stops.

• **Stability:** The structural rigidity provided by the PCTG-CF10 brackets proved sufficient. No significant deflection or plastic deformation was observed in the mounts during the lifting cycles.

These results validate the fundamental design premise: that a simple, modular active suspension can effectively create a stable workspace for drilling operations, even with a simplified control architecture.

7. CONCLUSION AND FUTURE WORK

This paper presented the design specification and the initial prototyping of an active self-leveling chassis for the MPER project. The constructed testbed confirms that a relatively simple architecture using linear actuators and inertial feedback can effectively maintain a horizontal platform orientation, significantly mitigating the risks associated with drilling on inclined terrain.

Future development of the MPER chassis will focus on transitioning from this proof-of-concept to a fully autonomous field rover. Key planned improvements include:

• **Feedback Integration:** Installing linear potentiometers or optical encoders on the actuators to enable more sophisticated control strategies, such as adaptive control algorithms [14], allowing for proportional speed adjustment and smoother motion compared to the current bang-bang approach.

• **Structural Optimization:** Replacing the prototype baseplate with the final welded aluminum chassis frame to reduce weight and increase torsional stiffness.

• **Predictive Leveling:** Researching the integration of LiDAR or depth cameras to scan the terrain ahead. This would allow the rover to adjust its suspension preemptively (Feed-Forward control) rather than reacting to tilt after it occurs.

BIBLIOGRAPHY

1. M. Rudnicka, M. Lasak, I. Puchała, P. Bartosz, D. Bereta, & D. Myszor (2024, June). Sample collection and containment system for a compact planetary exploration rover. International Students Scientific Conference TalentDetector2024_Summer: 417-422
2. S. Rajath and N. D. Shivakumar, “Rovers with Rocker-Bogie Mechanisms: A review of progress and innovations in design, manufacturing, and control,” Proceedings of the Institution of Mechanical Engineers, Part C, 2024.
3. A. Alexandrov, “Mathematical Model and Kinematic Analysis of Rocker-Bogie Suspension Design for UGV Applications,” Bulgarian Academy of Sciences, 2025.

4. J. Gao, Y. Li, J. Jin, Z. Jia, and C. Wei, “Design, Analysis and Control of Tracked Mobile Robot with Passive Suspension on Rugged Terrain,” Actuators, vol. 14, no. 8, p. 389, 2025.
5. S. Han, H. S. Kim, S. Ryu, and T. W. Seo, “Design and robust control of track-based active suspension for rough terrain robots,” International Journal of Control, Automation, and Systems, 2025.
6. S. Ravi and V. Krishnan, “Self-leveling suspension design for autonomous exploration rovers using linear actuators,” IEEE Access, vol. 11, pp. 67214–67226, 2023.
7. R. Manca, M. Puliti, S. Circosta, R. Galluzzi, and S. Salvatore, “Design and Optimization of an Active Leveling System Actuator for Lunar Lander Application,” Actuators, vol. 11, no. 9, p. 263, 2022.
8. P. Cavallone and R. Romano, “Hydropneumatic and Electro-Hydraulic Active Suspension Systems for Off-Road Vehicles,” Vehicle System Dynamics, vol. 58, no. 9, pp. 1410–1428, 2020.
9. H. Jiang, G. Xu, W. Zeng, F. Gao, and K. Chong, “Lateral stability of a mobile robot utilizing an active adjustable suspension,” Applied Sciences, vol. 9, no. 20, p. 4410, 2019.
10. D. Kim and S. Lee, “Design of a Modular Terrain-Adaptive Rover Using Low-Cost Embedded Systems,” IEEE Access, vol. 10, pp. 56213–56224, 2022.
11. B. Frazer, R. Borden, J. Howard, and R. Lueg, “Self-leveling rover using Arduino microcontroller and DC actuator system,” Senior Design 2, University of Central Florida, 2014.
12. P. Kiviluoma, P. Kuosmanen, and T. Otto, “Prototyping and Validation of a Modular Mechatronic Self-Leveling Platform,” Proceedings of the 5th Baltic Mechatronics Symposium, Espoo, Finland, 2020.
13. A. Saini and D. Sharma, “Arduino-controlled tilt stabilization system for educational robotics platforms,” International Journal of Mechanical Engineering and Robotics Research, vol. 12, no. 4, pp. 233–241, 2023.
14. S. Jain and M. J. Nigam, “Adaptive Control of Semi-Active Suspension Systems in Autonomous Ground Vehicles,” IEEE Transactions on Intelligent Transportation Systems, vol. 23, no. 11, pp. 21157–21167, 2022.

TalentDetector

9th January 2026
Gliwice, Poland

DEPARTMENT OF ENGINEERING MATERIALS AND BIOMATERIALS
FACULTY OF MECHANICAL ENGINEERING
SILESIAN UNIVERSITY OF TECHNOLOGY

INTERNATIONAL STUDENTS SCIENTIFIC CONFERENCE

Microstructural study of molybdenum silicide using scanning electron microscopy

Lew Lewandowski[a], Emilia Jackow[a], Mikołaj Łysień[a], Roland Fabiańczyk[a], Radosław Szklarek[b], Daniel Pakuła[c], Marcin Staszuk[c]

[a] Student of Silesian University of Technology, Faculty of Mechanical Engineering, Konarskiego 18A, 44-100 Gliwice, Poland
[b] Łukasiewicz Research Network – Institute of Aviation, 110/114 Krakowska Avenue, 02-256 Warsaw, Poland
[c] Silesian University of Technology, Faculty of Mechanical Engineering, Department of Engineering Materials and Biomaterials, Konarskiego 18A, 44-100 Gliwice, Poland
email: marcin.staszuk@polsl.pl

Abstract: This paper presents a study of the microstructure of molybdenum with a silicon coating deposited using the CVD (chemical vapor deposition) method. The basic properties of molybdenum and the operating principle of silicon coatings, which significantly improve oxidation resistance, are discussed. Microstructural analysis of the coatings revealed the presence of microcracks throughout the entire coating thickness.

Keywords: silicon coating, molybdenum, scanning electron microscope, SiO_2

1. INTRODUCTION

Molybdenum belongs to the group of refractory metals and is characterized by a favorable set of physical and mechanical properties, such as a very high melting point, good thermal conductivity, and resistance to creep at elevated temperatures [3,9].

This metal has a body-centered cubic (bcc) crystal structure and a melting point of approximately 2622 °C [3]. Low thermal expansion combined with high structural stability allows molybdenum to retain its mechanical properties even under significant temperature gradients. For this reason, the material is used in aircraft engine components, nozzles, and rocket engine parts, where operating temperatures can reach 2000–3000 °C depending on the type of fuel and oxidizer [5,7].

A limitation of using molybdenum in an air atmosphere is its susceptibility to high-temperature oxidation, which begins above 400 °C. At temperatures above 600 °C, volatile molybdenum trioxide (MoO_3) is formed, leading to intense surface degradation [4,6].

One of the most effective methods of limiting this process is the use of silicon coatings, which form a diffusion barrier between the metallic substrate and the atmosphere. High-temperature

operation of molybdenum coated with a silicon layer leads to the formation of a protective silica layer that limits oxygen access to the substrate [1,2,8,10,11].

Molybdenum is used in industries that require high temperature resistance, including aviation, space technology, and the energy sector [3,5]. In rocket engine and turbojet combustion chambers, temperatures can reach 2000–3000 °C [5,7], while in steam and gas turbines as well as turbochargers they range from 500 to 1000 °C.

Without a protective coating, molybdenum undergoes rapid degradation due to surface oxidation [4]. A silicon coating deposited using the CVD method acts as an effective barrier that limits oxygen diffusion and significantly extends the service life of components operating at high temperatures [2,8].

The aim of this study is to present the results of investigations of a molybdenum sample coated with a silicon layer, with particular focus on its microstructure and surface morphology. The analysis was carried out using scanning electron microscopy (SEM) combined with energy-dispersive X-ray spectroscopy (EDS).

2. MATERIAL AND RESEARCH METHODOLOGY

The investigations were carried out on a technically pure molybdenum sample with a molybdenum silicide coating deposited using a diffusion method [1,11].

Coating consisted mainly of intermetallic phases such as $MoSi_2$, as well as transition phases with reduced silicon content in the zone adjacent to the substrate [5,7]. This type of layer structure reduces thermal stresses and improves coating adhesion [1,9,11].

The studies were performed using a Zeiss Supra 35 scanning electron microscope (SEM) equipped with a Thermo Scientific energy-dispersive X-ray spectroscopy (EDS) analyzer for local chemical composition analysis. The observations were conducted using secondary electron (SE) detection at an accelerating voltage of 15 kV.

3. RESULTS

Surface topography studies carried out using a scanning electron microscope confirmed that the produced silicon layers exhibit a rough structure typical of this type of coating. The structure is uniform and has a mound-like appearance (Fig. 1a). Cracks characteristic of silicon coatings were observed on the surface of all siliconized substrates. The cracking may also be influenced by the large difference in brittle–ductile transition temperature between the silicon coating and the substrate. Cracks in the silicon layer may cause loss of coating tightness and thus negatively affect its functional properties. Microstructural observations of cross-sections (Fig. 1b) confirmed a dense columnar structure and crystal growth perpendicular to the substrate material.

Figure 2 and Table 1 present the results of the microanalysis of the coating chemical composition. The analysis confirmed the presence of chemical elements typical for the investigated type of coating.

Table 1. Chemical composition of the sample's silicon coating

Element	Weight %	Atom %
Si	35,38	65,16
Mo	64,62	34,84

a) b)

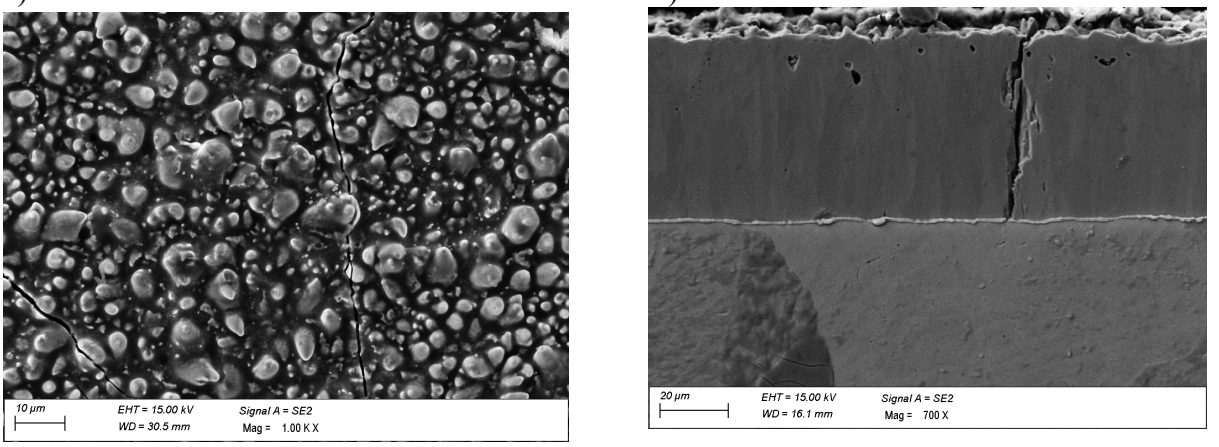

Figure 1. a) Surface topography of the investigated silicon coating, b) cross-sectional structure of the molybdenum silicide coating on a molybdenum substrate

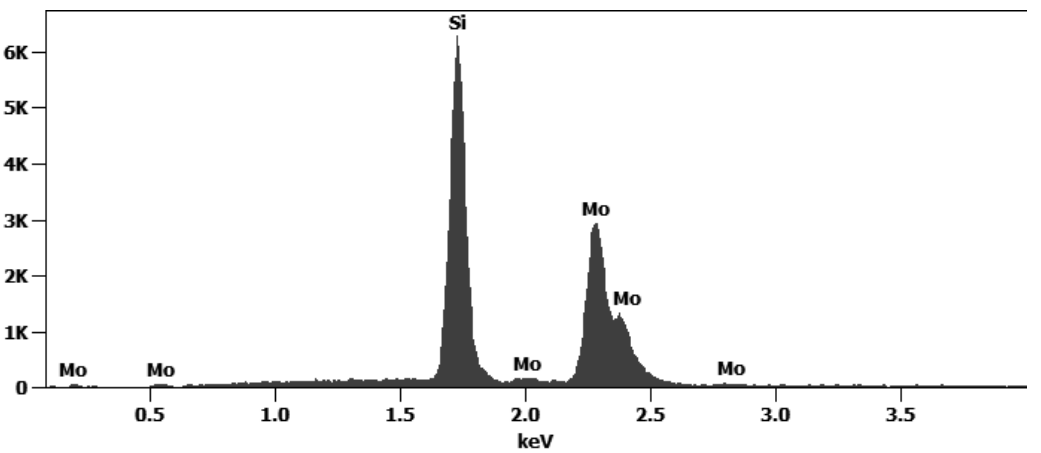

Figure 2. Chemical composition of the sample's silicon coating.

4. CONCLUSIONS

Based on the conducted studies, the following conclusions can be drawn:

1. The diffusion-deposited molybdenum silicide coating on technically pure molybdenum is characterized by a dense, columnar microstructure with $MoSi_2$ as the dominant phase.
2. The coating surface exhibits a uniform, rough topography with cracks typical for silicon layers, which may result from differences in the thermal properties of the coating and the substrate and could potentially reduce its functional performance.

ACKNOWLEDGEMENTS

This work was carried out as part of a project conducted within project-based learning (PBL) during the 13th edition of the "Excellence Initiative – Research University" program at the Silesian University of Technology.

REFERENCES

1. R. Szklarek, Investigation of the Structure and Properties of Silicon Layers Produced on Molybdenum and Niobium Substrates, PhD dissertation, Silesian University of Technology, Gliwice, 2023.
2. H.S. Nalwa (red.), Handbook of Thin Film Materials. Vol. 1: Deposition and Processing of Thin Films, Academic Press, San Diego, 2002.
3. T.Ya. Kosolapova (red.), Handbook of High-Temperature Compounds, Hemisphere Publishing, New York, 1990.
4. Z. Bao, X. Liu, Y. Zhang et al., Study on High Temperature Oxidation Properties of Molybdenum-based Alloys, Journal of Physics: Conference Series, vol. 1789, 2021.
5. J.J. Petrovic, $MoSi_2$ and other silicides as high-temperature structural materials, Materials Science and Engineering A, vol. 155, 1992.
6. R. Mitra, Mechanical behavior and oxidation resistance of $MoSi_2$ and $MoSi_2$-based composites, Materials Science and Engineering A, vol. 261, 1999.
7. Y. Yao, J. Stiglich, T. Sudarshan, Molybdenum silicide based materials and their properties, Journal of Materials Engineering and Performance, vol. 8, no. 3, 1999.
8. L. Zhang, X. Wu, Oxidation behavior of $MoSi_2$ coatings at high temperatures, Surface and Coatings Technology, vol. 201, 2006.
9. R. Asthana, A. Kumar, N. Dahotre, Materials Processing and Manufacturing Science, Elsevier, 2006.
10. AZoM, Molybdenum Disilicide ($MoSi_2$) – Properties and Applications, AZoM Materials Database.
11. R. Szklarek, T. Tański, B. Mendala, M. Staszuk, Ł. Krzemiński, P. Nuckowski, K. Sobczak, High temperature resistance of silicide-coated niobium. Bulletin of the Polish Academy of Sciences Technical Sciences, 69(5), 2021, e137416.

TalentDetector
9th January 2026
Gliwice, Poland
DEPARTMENT OF ENGINEERING MATERIALS AND BIOMATERIALS
FACULTY OF MECHANICAL ENGINEERING
SILESIAN UNIVERSITY OF TECHNOLOGY
INTERNATIONAL STUDENTS SCIENTIFIC CONFERENCE

3D-printed prosthetic foot prototype

Mateusz Liszka[a], Oliwier Lukoszek[a], Maik Bialas[a], Dominik Meisner[a], Jakub Kruk[a], Szymon Pala[a], Mateusz Konsek[b] Magdalena Polok-Rubiniec[c], Anna Włodarczyk-Fligier[c], Aneta Kania[c]

[a]Silesian University of Technology, Faculty of Mechanical Engineering, Students of Mechanical Engineering
[b]Silesian University of Technology, Faculty of Mechanical Engineering, Student of Industrial Mechatronics
[c]Silesian University of Technology, Faculty of Mechanical Engineering, Department of Engineering Materials and Biomaterials
email: ml316665@student.polsl.pl

1. INTRODUCTION

3D printing is one of the rapid prototyping techniques increasingly used in science and engineering, enabling the creation of customized, client-specific designs. In recent years, additive manufacturing technologies have gained popularity and user-friendliness, while the financial barrier to entry has significantly decreased. Despite persisting drawbacks, such as visible layering or anisotropy, this technology allows for relatively fast and advanced prototyping, as well as the production of functional models. 3D printing is based on additive manufacturing, which involves depositing successive layers of material. One of the greatest advantages of this method is minimal material waste, in contrast to subtractive manufacturing, which relies on removing material layers. The design will be simplified relative to an actual human foot while maintaining mechanical functionality [1,2].

The model will be developed in a CAD environment using **Autodesk Inventor**. It is an engineering-grade 3D software that enables 3D design visualization and the generation of technical documentation. Furthermore, it is a solid modelling program, meaning it can determine mass by assigning specific material properties to the model. It also allows for performing structural stress simulations (FEA). Utilizing a CAD environment significantly minimizes the number of physical iterations and, in some cases, allows for a successful 3D print on the first attempt.

The objective of the project was to design and print a prototype of a prosthetic foot using **FDM (Fused Deposition Modelling)** technology. This process involves additive manufacturing of polymer components, where semi-molten material is deposited in layers through a heated nozzle [2]. The print will serve as a demonstration model for a person with a disability facing the choice of a daily-use prosthesis. The prosthesis is intended to enable walking; therefore, its application will be based on simulating the behaviour of a human foot during a normal gait cycle.

2. DESIGN OF A PROSTHETIC FOOT PROTOTYPE

The design of the prosthetic foot model necessitated an analysis of the gait cycle and the key elements that are essential for the correct interaction between the foot and the rest of the human body's mechanics. The foot serves as a fundamental support for the body, and its geometry directly influences postural balance; therefore, its appropriate shaping is crucial [3]. The process was initiated with the establishment of a skeletal framework of the foot's motion system. The fundamental supposition underlying this endeavour entailed the conceptualisation and fabrication of a prosthesis endowed with a component that emulates the functional characteristics of the ankle joint. The objective of this undertaking was to facilitate movement in a manner analogous to that of a natural human gait (Fig. 1).

Fig.1. 3D model of the first concept.

Following the execution of the initial model, it was determined that the adopted solution did not accurately represent the gait process. Gait is comprised of two primary phases: the stance phase and the swing phase. These two phases are further subdivided into four sub-phases [4]. Consequently, in the second iteration, a mechanism designed to simulate the toe-flexion mechanism was incorporated (Fig.2).

The return of the foot to its neutral position is facilitated by a spring element with welded bushings, mounted on the fastening bolts (Fig. 3). The heel component has been engineered to deflect under load. In order to achieve this effect, a thin-walled structure was developed, which was filled with resilient EVA foam in order to provide shock absorption during heel-strike. In order to optimise the 3D printing process and enable movement, the model was divided into three separate parts, which were secured with bolted joints. This solution also facilitates the reprinting of components that may be damaged during testing or fail to meet design requirements.

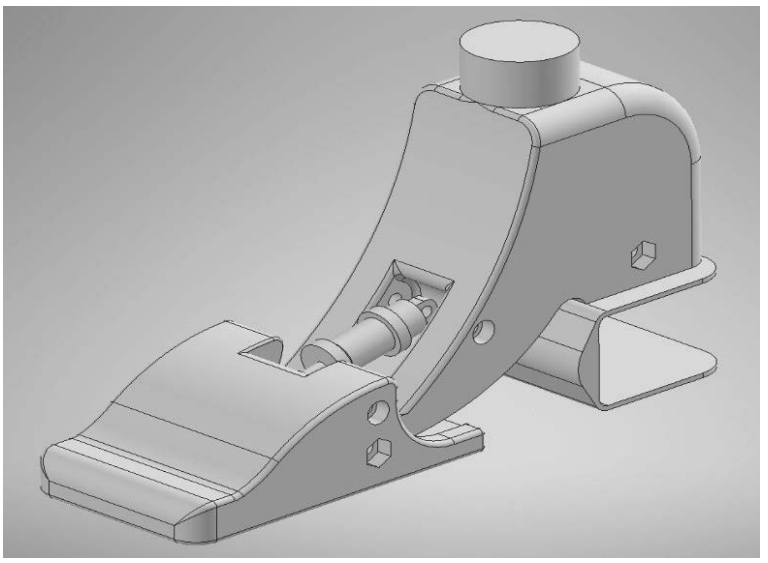

Fig.2 3D model of the second concept

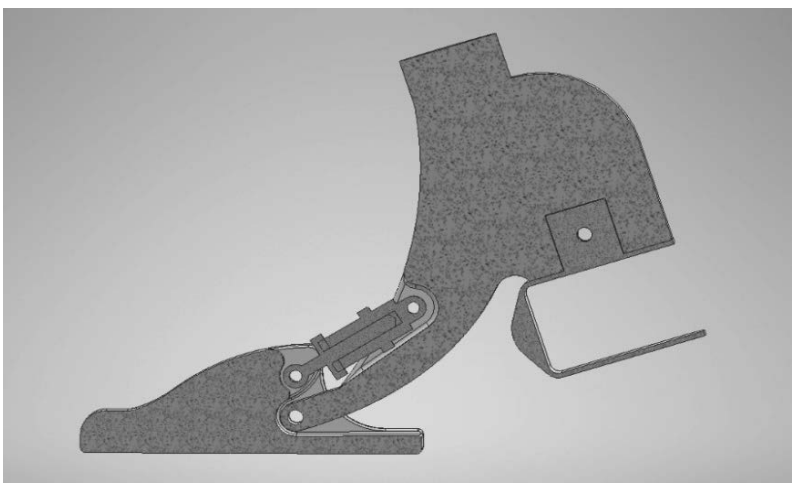

Fig.3 The following illustration is a cross-section of an assembly of a prosthetic foot.

3. MATERIALS APPLIED

The prosthetic foot model was printed using a PET-G filament, a material that combines key mechanical and biological properties, making it a noteworthy material for prosthetic applications. In comparison to other polymers used in 3D printing, this material is characterised by high strength, impact resistance, flexibility, and creep resistance. The combination of these properties with low print anisotropy is key to ensuring the stability of the print's mechanical properties under constant load, thereby extending the service life of the prosthesis. Another advantage of the selected polymer is its biocompatibility, which is a requirement for prostheses in direct contact with the skin [5]. Moreover, the material's low level of toxicity facilitates the development of subcutaneous implants.

A cavity was designed into the heel area to accommodate foam that provides cushioning during heel strike. The selection of EVA foam for this application was made on the basis of its proven superiority in terms of shock-absorbing properties and low compression set.

4. 3D PRINTING PROCESS OF A PROSTHETIC FOOT PROTOTYPE

The foot design was produced through the utilisation of a 3D printer, specifically the 'Original Prusa MK3S+' model. The model was prepared for printing using PrusaSlicer 2.9.3. The orientation of the components on the build plate was determined during the design phase to ensure that the layer deposition prevents the forces generated during prosthetic operation from having a negative effect on interlayer adhesion. The printing parameters are presented in Table 1.

Table 1. The printing parameters [6].

Wall line count	1.6 mm
Infill pattern	Gyroid
Infill density	15%
Support structures	Organic

The printed components necessitated manual post-processing, involving the removal of supports and the deburring of sharp edges using a deburring tool and a heat gun.

5. ASSEMBLING THE PROSTHETIC FOOT PROTOTYPE DESIGN

The spring responsible for actuating the movable finger mechanism was MIG-welded to sleeves, which were subsequently secured to the prosthesis using M6 bolts. The prosthesis incorporates specially designed through-holes that facilitate this process. Each bolt is designed to pass through the designated holes and the sleeve, thus extending through the entire prosthesis. The bolts are then secured with a nut on the opposite side. The remaining components were also affixed using M6 bolts. Hexagonal counterbores were incorporated into the design with a view to facilitating the assembly process. M6 socket head cap screws (SHCS) in lengths of 60mm and 80mm were utilised, tightened with hexagonal nuts. The EVA foam was bonded to the structure using cyanoacrylate adhesive

6. SUMMARY

The resulting model was found to be in accordance with the design specifications (Fig. 5). The application of FDM technology has been demonstrated to be an effective method for the initial prototyping stage. The 3D-printed prosthetic foot model functions as a demonstrative

prototype of the foot's mechanical operation for an individual with a disability. This prototype will provide the basis for the development of a functional foot prosthesis.

a) b)

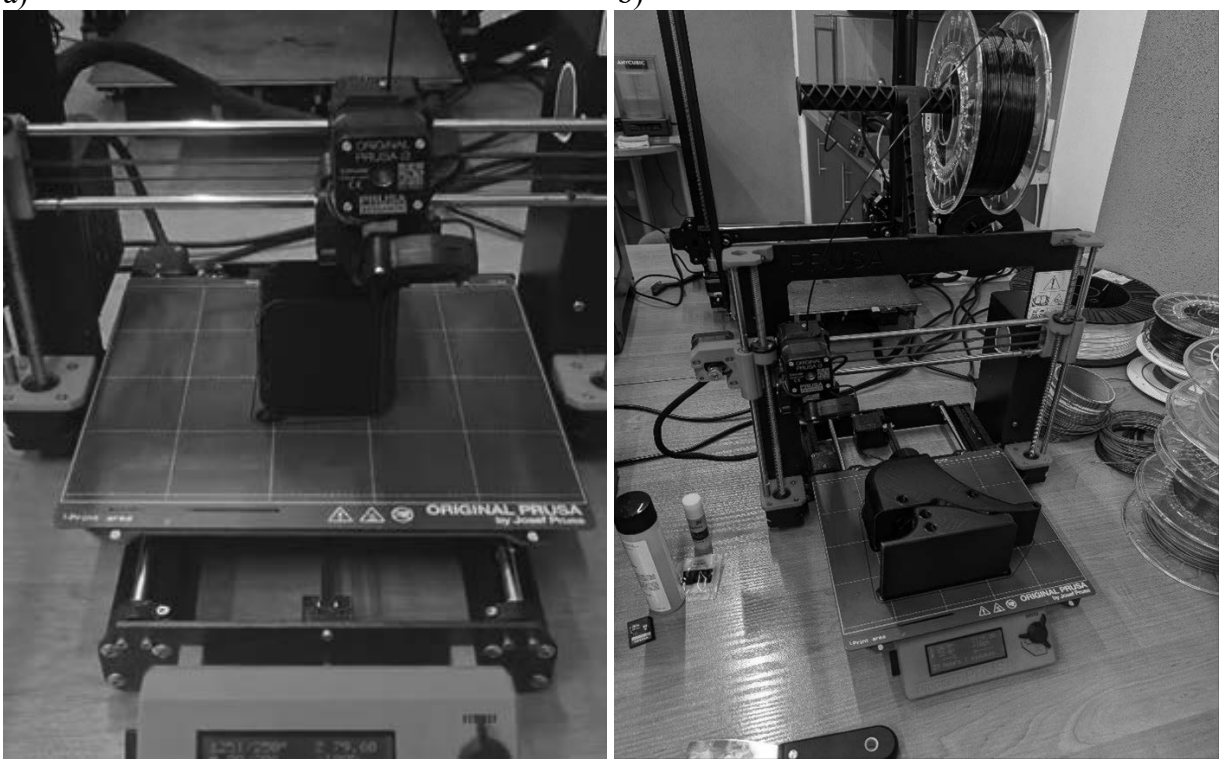

Fig.4. 3D printed a) heel, b) foot and toe modules

Fig.5. Prosthetic foot assembly

BIBLIOGRAPHY

1. https://yadda.icm.edu.pl/baztech/element/bwmeta1.element.baztech-178f94ef-112c-4397-a777-97253b8777a9
   data dostępu: 12.12.2025 godz. 12:26
2. http://www.protetstomatol.pl/pdf-100246-32257?filename=%20Zastosowanie%20i.pdf
   data dostępu: 12.12.2025 godz. 14.21
3. https://fizjoterapeuty.pl/anatomia/stopa-stawy-wiezadla-i-miesnie.html
   data dostępu: 9.12.2025 godz.20:47;
4. https://fizjoterapeuty.pl/kinezyterapia/fazy-chodu.html#elementor-toc__heading-anchor-1
   data dostępu: 9.12.2025 godz.20:44;
5. https://www.sciencedirect.com/science/article/pii/S2666138123000592
   data dostępu 12.12.2025 godz 16:35
6. https://help.prusa3d.com/pl/filament-material-guide?fbclid=IwY2xjawOkFWNleHRuA2FlbQIxMABicmlkETBrVlVzbkFuSDBqT1o2U3B2c3J0YwZhcHBfaWQQMjIyMDM5MTc4ODIwMDg5MgABHtZt4NUTK5Exzgk52WRMDBL1ODD90OkslCG5gGLCyy1R44bVAh9XBGBZYHFi_aem_G6oDjUeNvKb55fFxV4tRNw
   data dostępu: 8.12.2025 godz.21:53;

TalentDetector
9th January 2026
Gliwice, Poland
DEPARTMENT OF ENGINEERING MATERIALS AND BIOMATERIALS
FACULTY OF MECHANICAL ENGINEERING
SILESIAN UNIVERSITY OF TECHNOLOGY
INTERNATIONAL STUDENTS SCIENTIFIC CONFERENCE

Microstructure and adhesion of TiAgN coating deposited by PVD technology

Paulina Lukaszkowicz[a], Jozef Sondor[b], Krzysztof Lukaszkowicz[c], Klaudiusz Gołombek[d]

[a] Medical University of Silesian in Katowice, Faculty of Pharmaceutical Sciences in Sosnowiec, Student Scientific Club at the Department of Inorganic Chemistry
email: s86990@365.sum.edu.pl
[b] LISS, a.s., Dopravni 2603, 756 61 Roznov pod Radhostem, Czech Republic
email:j.sondor@liss.cz
[c] Silesian University of Technology, Faculty of Mechanical Engineering, Department of Engineering Materials and Biomaterials
email: przysztof.lukaszkowicz@polsl.pl
[d] Silesian University of Technology, Faculty of Mechanical Engineering, Materials Research Laboratory
email: klaudiusz.golombek@polsl.pl

Abstract: The research subject was the microstructural and adhesion characterisation of the TiAgN coating deposited by PVD. The TiAgN coating was characterised using scanning electron microscopy (SEM), energy-dispersive spectroscopy (EDS), and the scratch test method for morphological, chemical composition, and adhesion studies, respectively.

Keywords: TiAgN coating, PVD, SEM, scratch test

1. INTRODUCTION

Titanium nitride (TiN) is a well-known hard coating widely used due to its excellent properties, including good chemical stability, high hardness, and corrosion resistance [1]. TiN coating is often used on biomedical implants because it combines the advantages of increased mechanical stability and high corrosion resistance with biocompatibility [2].

A promising approach to improving the properties of TiN coatings is the addition of silver (Ag). Silver has many unique properties, such as high strength combined with excellent plasticity, very high electrical and thermal conductivity, resistance to oxidation, high light reflectivity, and antibacterial properties [3-4].

TiAgN is an advanced hard coating, often applied to medical implants or cutting tools, that combines the hardness of titanium nitride (TiN) with the potent antibacterial properties of silver (Ag), resulting in surfaces that resist wear, corrosion, and bacterial growth, making them ideal for orthopedic equipment (such as implants/screws) and specific medical instruments, balancing biocompatibility with infection prevention [5-7].

2. MATERIALS AND METHODS

The tests were performed on samples of the X6CrNiMoTi17-12-2 austenitic stainless steel and on a polished silicon wafer deposited by a PVD process with a TiAgN coating. The coating deposition process was performed in a device using the cathodic arc evaporation method in an Ar and N_2 atmosphere. Cathodes containing pure metals (Ti ang Ag) were used during the deposition process.

The morphology, cross-section, and chemical composition of the investigated coating were examined using a high-resolution scanning electron microscope, HRSEM SUPRA 35 by Zeiss, equipped with an EDS detector. Chemical composition analyses in micro-areas were performed using the EDS detector with Pathfinder software.

Adhesion of the deposited coating to the substrate material was investigated using the Revetest RST scratch tester from Anton Paar by moving the diamond indenter across the examined specimen's surface under progressively increasing load. The tests were made using the following parameters: load range: 0–100 N; indenter sliding speed: 10 mm/min; load increase rate: 100 N/min; acoustic emission detector's sensitivity AE: 5.

3. RESULTS AND DISCUSSION

The morphology of the produced coatings is characterised by high heterogeneity, with numerous drop-shaped or spherical particles on the surface (Fig. 1a), which is related to the PVD arc evaporation deposition process. This is caused by metallic droplets sprayed from the target into the plasma, which participate in coating formation. The size of the drop-shaped particles varies from a few tenths of a micrometre to about 2 μm. In most cases, their diameter ranges from 0.5 to 1 μm. The cross-section image of the TiAgN coating is presented in Fig. 1b. The film produced by the cathodic arc evaporation technique characterizes a compact structure without any delamination or defects. TiAgN shows columnar growth. The measured thickness of the TiAgN is approximately 1.3 μm.

a) b)

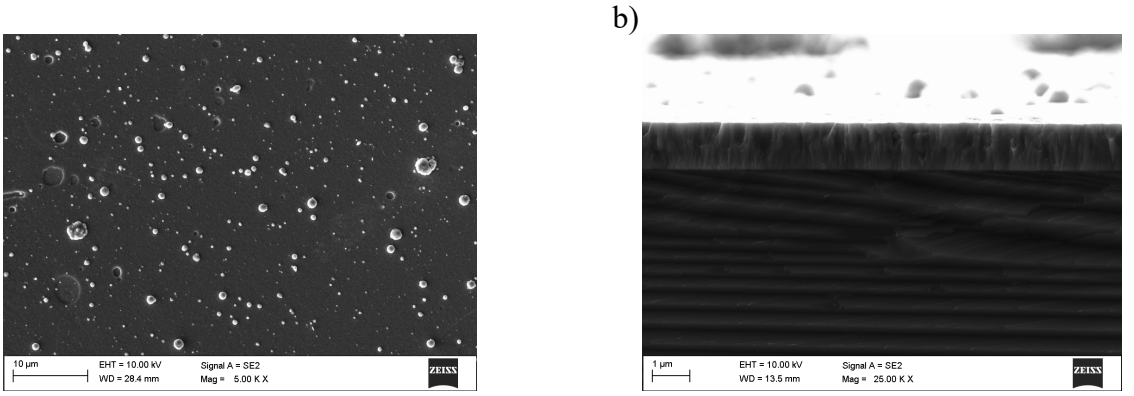

Figure 1. TiAgN coating deposited on the silicon wafer: a) surface morphology image (SEM), b) cross-section image (SEM)

The chemical composition tests performed using the EDS detector confirmed the presence of individual elements included in the analysed TiAgN coating (Fig. 2). The results of the EDS

analysis of the chemical composition demonstrate the high chemical quality of the investigated coating. The chemical composition of the TiAgN is presented in Table 1.

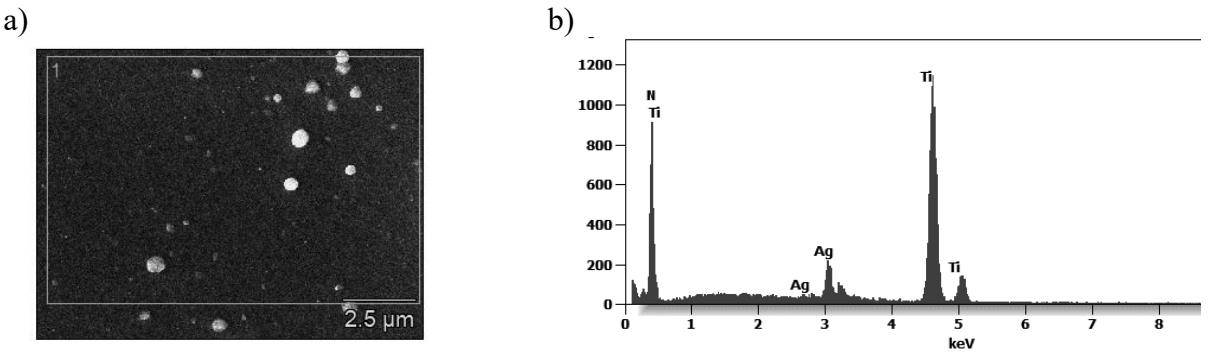

Figure 2. TiAgN coating: a) surface morphology image (SEM), b) EDS spectrum of the area as in fig. a

Table 1. Chemical composition of TiAgN coating

Element	Weight %	Atomic %
N	26,3	57,4
Ti	61,3	39,1
Ag	12,4	3,5

In order to characterize the adhesion of the TiAgN coating to the substrate, the critical load values L_{C1} and L_{C2} were determined by the scratch test method (Fig. 3).

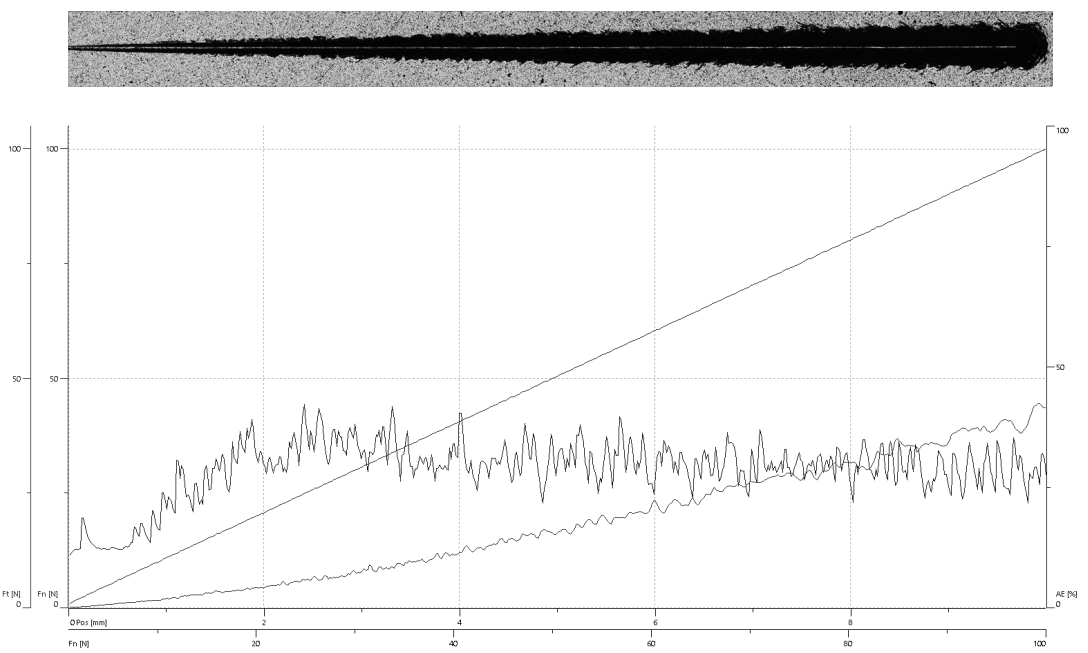

Figure 3. Optical image of the scratch-test tracks and diagram of the dependence of the acoustic emission (AE) and friction force Ft on the load for the TiAgN coating deposited on the X6CrNiMoTi17-12-2 steel substrate

The load at which the first damage to the coating occurs is referred to as the first critical load L_{C1}. The first weak acoustic emission signal represents this damage. The value of the first critical load corresponds to cohesive damage from material spalling within the coating, without exposing the substrate. The second critical load L_{C2} is characterised by complete coating damage. This damage is treated as the breaking point of the rising friction force curve on the graph. This point corresponds to the first contact of the diamond indenter with the substrate, when extensive spalling of the coating occurs. In this work, the first critical load L_{C1} occurred at 3 N, while the second L_{C2} occurred at 31 N.

4. CONCLUSION

The TiAgN coating was successfully deposited on the substrate material. A compact microstructure, free of visible delamination, was observed by SEM. Analysis of the chemical composition, based on EDS tests, indicates the high chemical quality of the coatings. The TiAgN coating exhibits strong adhesion to the substrate. The coating adhesion scratch tests revealed the cohesion and adhesion properties of the tested coatings. The next step in analysing the TiAgN coating will be to assess its antibacterial property using the bacterial adhesion test.

BIBLIOGRAPHY

1. U. Mahajan, M. Dhode, K. Sahu, P. Ghosh, P.M. Shirage, Titanium nitride (TiN) as a promising alternative to plasmonic metals: a comprehensive review of synthesis and application, Materials Advences 5 (2024) 846-895.
2. C. Moseke, U. Gbureck, P. Elter, P. Drechsler, A. Zoll, R. Thull, A. Ewald, Hard implant coatings with antimicrobial properties, Journal of Materials Science: Materials in Medicine 22 (2011) 2711-2720
3. N. Babacan, F. Kochta, V. Hoffmann, T. Gemming, U. Kuhn, L. Giebeler, A. Gebert, J. Hufenbach, Effect of silver additions on the microstructure, mechanical properties and corrosion behavior of biodegradable Fe-30Mn-6Si, Materials Today Communications 28 (2021) 102689.
4. J. Konieczny, Z. Rdzawski, Antibacterial properties of copper and its alloys, Archive of Materials Science and Engineering 56/2 (2021) 53-60.
5. C.P. Priyanka, K.K. Krishnan, U. Sudeep, K.K. Ramachandran, Osteogenic and antibacterial properties of TiN-Ag coated Ti-6Al-4V bioimplants with polished and laser textured surface topography, Surface and Coatings Technology 474 (2023) 130058.
6. A. Al-Rjoub, A. Cavaleiro, F. Fernandes, Influence of Ag alloying on the morphology, structure, mechanical properties, thermal stability and oxidation resistance of multilayered TiSiN/Ti(Ag)N films, Materials and Design 192 (2020) 108703.
7. K. Piotrowska, M. Madej, Tribological properties of silver doped titanium nitride coatings, Tribologia 3 (2023) 43-51.

TalentDetector
9th January 2026
Gliwice, Poland
DEPARTMENT OF ENGINEERING MATERIALS AND BIOMATERIALS
FACULTY OF MECHANICAL ENGINEERING
SILESIAN UNIVERSITY OF TECHNOLOGY
INTERNATIONAL STUDENTS SCIENTIFIC CONFERENCE

Research on solar cells with and without anti-reflective coatings

Jakub Madej [a], Urszula Rudzińska [a], Tomasz Stokłosa [a], Jakub Wydra [a], Paweł Gajek [a], Mikołaj Skorupa [b], Wojciech Filipowski [a], Aleksandra Drygała [c] , Małgorzata Musztyfaga-Staszuk [c]

[a] Silesian University of Technology, Faculty of Automatic Control, Electronics and Computer Science, Akademicka 16, 44-100 Gliwice, Poland
[b] Silesian University of Technology, Faculty of Biomedical Engineering, Roosevelta 40, 41-800 Zabrze, Poland
[c] Silesian University of Technology, Faculty of Mechanical Engineering, Konarskiego 18A, 44-100 Gliwice, Poland
email: malgorzata.musztyfaga-staszuk@polsl.pl

Abstract: This paper presents the results of investigations into solar cells with and without an anti-reflective coating. The photovoltaic conversion efficiency was evaluated based on current–voltage characteristic measurements performed using a solar simulator. In addition, microstructural analysis was conducted using a scanning electron microscope (SEM) to assess the surface morphology and chemical composition of the samples

Keywords: solar cell, anti-reflective coating, ARC

1. INTRODUCTION

The primary objective of optimizing crystalline silicon photovoltaic cells is to maximize photovoltaic conversion efficiency. This efficiency is influenced by all components of the solar cell. One of the most fundamental elements is a high-quality silicon wafer with the lowest possible defect density. Equally important is the treatment of the front surface of the cell to create a textured structure that reduces light reflection. A critical step in the fabrication process is the formation of the emitter layer, which creates the p–n junction responsible for separating charge carriers generated by incident photons. An important stage in the fabrication process is also the formation of the back surface field (BSF). Research on diffusion doping processes has been the subject of numerous scientific studies [1] [2]. The subsequent step involves the deposition of an anti-reflective coating (ARC), which significantly reduces optical reflection losses [3]. The most commonly used materials for anti-reflective layers are silicon dioxide, titanium dioxide, and silicon nitride.

The silicon dioxide (SiO_2) layer on photovoltaic cells is formed through the thermal oxidation of silicon. This process involves annealing silicon wafers at temperatures ranging from 900 to 1100 °C in an oxygen or water vapor atmosphere. As a result, a chemical reaction occurs between silicon and the oxidizing agent, leading to the formation of a SiO_2 layer that grows directly from the silicon substrate. This process ensures high structural and electrical

quality of the oxide. In solar cell structures, silicon dioxide is most commonly used to protect the silicon surface; however, when sufficiently thick, it can also serve as an effective anti-reflective layer.

An anti-reflective coating made of silicon nitride (Si_3N_4) exhibits a refractive index of n = 2, which lies between that of air (n = 1) and silicon (n = 3.4). This layer is chemically stable and provides an excellent protective barrier against moisture and mechanical damage such as scratches. It is deposited using the plasma-enhanced chemical vapor deposition (PECVD) method. In the case of Si_3N_4, the process involves depositing a silicon nitride layer onto a thin silicon dioxide layer.

Another material that can be used as an anti-reflective coating is titanium dioxide (TiO_2), which is deposited on the front surface of the cell covered with a thin protective silicon dioxide layer. Titanium dioxide is typically deposited using the chemical vapor deposition (CVD) process.

The final fabrication step involves the formation of conductive electrodes. The front grid electrode for the n-type emitter layer is most commonly made of silver, while the rear electrode for the p-type base material is typically fabricated from aluminum.

2. MATERIALS AND METHODOLOGY

Within the scope of this study, crystalline silicon solar cells without an anti-reflective coating and with an anti-reflective coating, as shown in Figure 1, were subjected to experimental investigation and measurements.

The current–voltage characteristics of the solar cells were measured using a solar simulator, model SS150AAA, shown in Figure 2. The simulator generates artificial light that closely matches the standard solar spectrum, which is commonly used as a reference in photovoltaic research. This enables reliable evaluation of the tested devices under conditions comparable to real solar irradiation.

The system provides stable light intensity and uniform illumination over the measurement area, as well as high measurement repeatability. These features are essential for accurate analysis of solar cells and for meaningful comparison of experimental results. The described solar simulator is used to determine key electrical parameters of photovoltaic cells, including current–voltage characteristics, open-circuit voltage, short-circuit current, fill factor, maximum power point, and photovoltaic conversion efficiency.

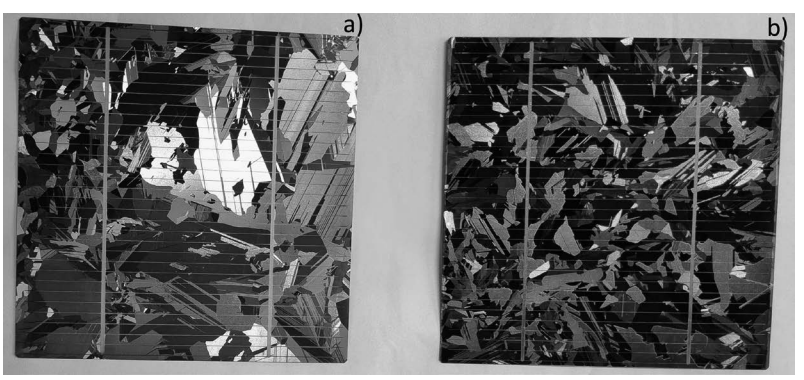

Figure 1. Crystalline silicon solar cells: a) without an anti-reflective coating, b) with an anti-reflective coating

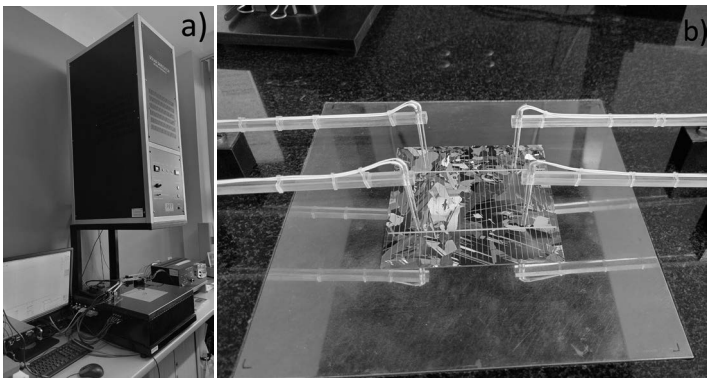

Figure 2. Measurement setup used for current–voltage characterization: a) SS150AAA solar simulator, b) measurement table and electrical probes

The topography and cross-section of the silicon were analyzed using a Zeiss Supra 35 scanning electron microscope (SEM) (Fig. 3). Microchemical analyses of selected areas on the front of the solar cells were conducted using the same microscope, which is equipped with an energy-dispersive X-ray (EDS) spectrometer.

Figure 3. Photos of scanning electron microscope (SEM) Zeiss Supra 35 equipped with an EDS spectrometer

The Sherescan (Fig. 4) device, also created by SunLab in partnership with Mechatronics, was used to assess key electrical parameters of the solar cell, including the sheet resistance (R_p) of the silicon wafer, as well as the surface resistance (R_p) and resistivity (ρ) of the metallic layer forming the front electrode of the photovoltaic cell. The measurements were carried out using a setup equipped with a probe head featuring a four-point linear probe.

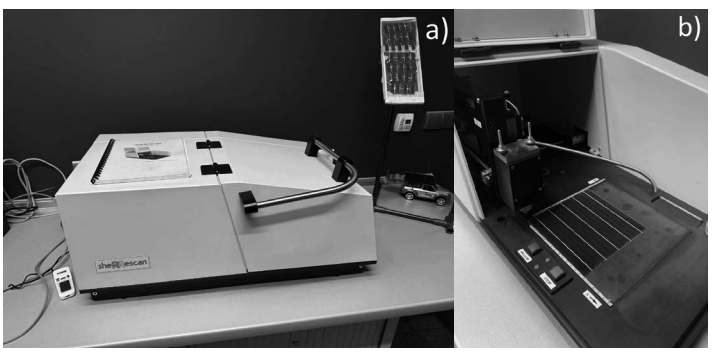

Figure 4. Sharescan device: a) entire device, b) center with a probe head featuring a four-point linear probe

Similarly, the Correscan (Fig. 5) device, developed by SunLab in collaboration with Mechatronics, was employed to evaluate selected electrical parameters of the solar cell, such as the resistivity (ρ) of the emitter layer and the contact resistance of the emitter layer (R_{cont}). The Core scan mode in the software was utilized for this purpose. Measurements were performed using a probe consisting of a single-point contact probe.

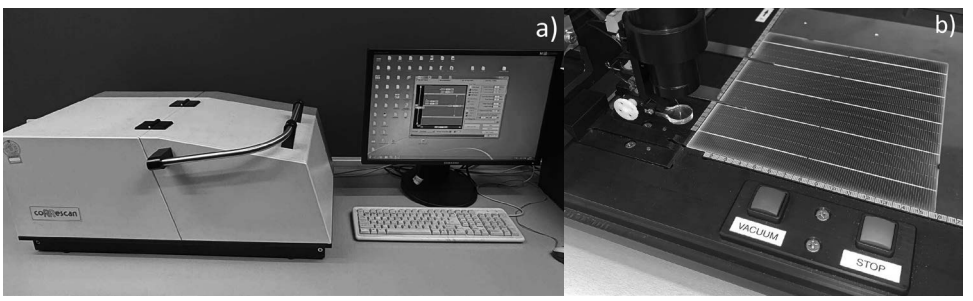

Figure 5. Correscan device: (a) complete device, (b) center with probe consisting of a single point contact probe

The phase composition of the silicon surface topography of the selected photovoltaic cell was analyzed using X-ray diffraction in the Bragg–Brentano technique.

3. RESULTS ANALYSIS

The results of the current–voltage characteristic measurements are presented in Figure 6. Cell (a), without an anti-reflective coating (ARC), exhibits a distinctly lower short-circuit current density of 25.4 mA/cm² compared to the short-circuit current density of 30.97 mA/cm² observed for cell (b) with an ARC. In addition, the open-circuit voltage of cell (a) is lower than that of cell (b), amounting to 546.6 mV and 615.5 mV, respectively. The fill factor of the current–voltage characteristic is 61.9% for cell (a) and 65.9% for cell (b). The anti-reflective coating clearly has a beneficial influence on the performance parameters of the solar cell.

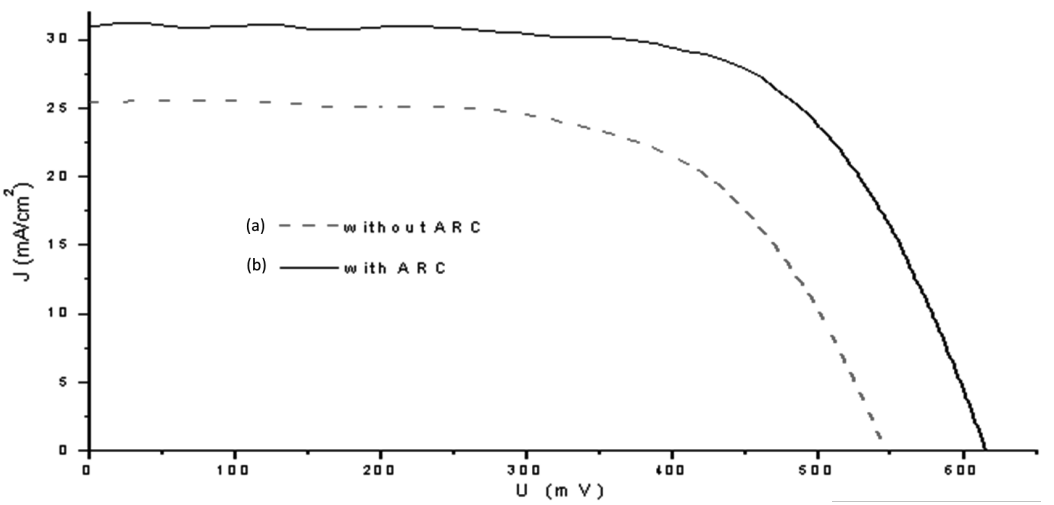

Figure 6. Current–voltage characteristics of the investigated solar cells.

The EDS results for the chemical composition of selected fragments of solar cell are provided in Table 1 and Figure 7.

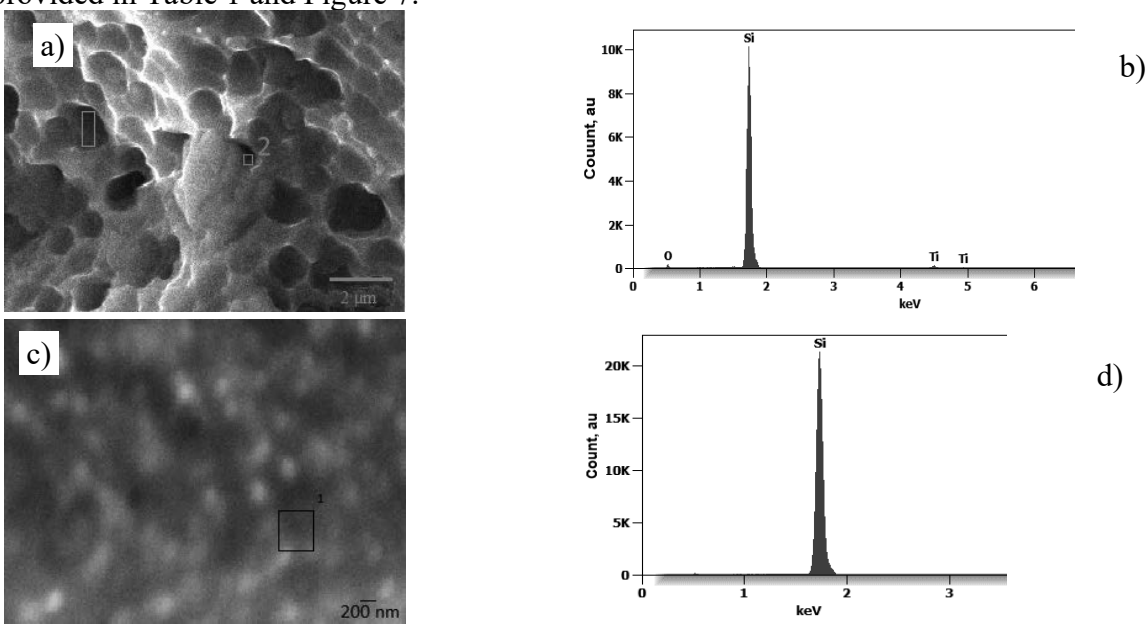

Figure 7. (a), (c) Energy-dispersive X-ray spectroscopy (EDS) analysis of selected micro-areas of the solar cells; (b), (e) EDS spectra from micro-area 1 (Si), 2 (TiO_x). (a, b) –Textured solar cell with an ARC layer; (c, d) – Non-textured solar cell without an ARC layer.

The results indicate that area 1 in the textured solar cell with an ARC layer is composed mainly of silicon, titanium, and oxygen. In the case of the non-textured solar cell without an ARC layer, mainly silicon was identified.

Table 1. Selected Chemical composition of selected locations within the solar cell

Type of sample	The substrate area	Weight fraction of elements,%		
		O	Ti	Si
Textured solar cell with an ARC layer	1	4.53	4.78	90.69
Non-textured solar cell without an ARC layer	1	-	-	100

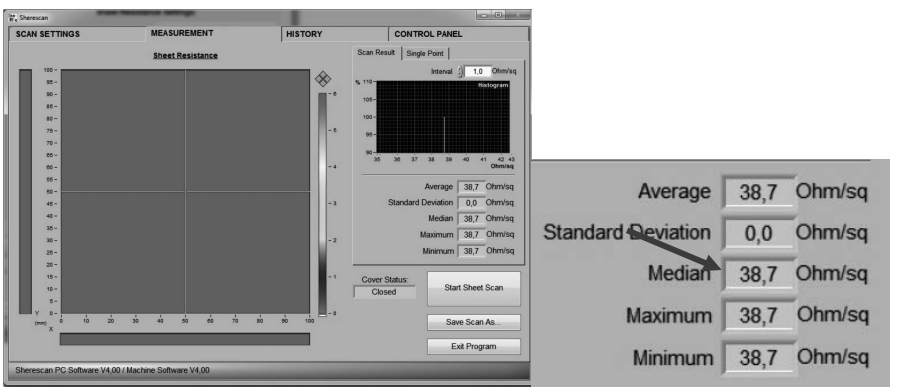

Figure 8. The view of the tab "Measurement"

Figure 8 shows the screen view after activating the "MEASUREMENT" tab and selecting the sheet resistance measurement mode, along with the entered measurement process parameters. The average sheet resistance was found to be 38.7 Ω/□, with the standard deviation, median, maximum, and minimum values also all equal to 38.7 Ω/□. The value of the sheet resistance of the diffusion layer depends on the temperature, the diffusion process duration, and the concentration of components in the applied doping atmosphere. The measurement of the sheet resistance of the doped layer is performed after the formation of the junction, e.g., n^+- p.

As a result of the measurement, the surface resistivity (R_p) was found to be 0.19 mΩ/□, and the resistivity of the front electrode of the photovoltaic cell (ρ) was 0.27 μΩ·cm (Figure 10). In the distribution of actual measurement points, some deviations from the parabolic curve can be observed (Figure 10). This indicates that errors were made during the formation of the front electrode, related to improper thermal treatment of the conductive paste applied to the surface of the cell during the screen printing process [4].

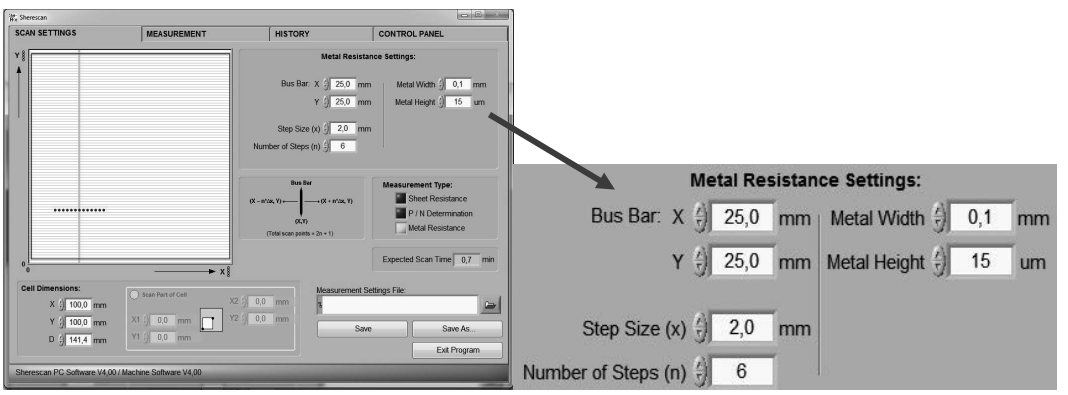

Figure 9. Settings of scanning process parameters in "Metal Resistance" measurement mode

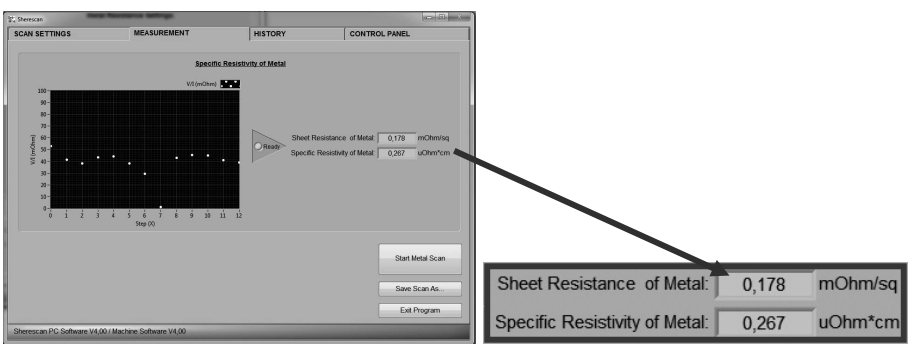

Figure 10. Measurement results of the front metal electrode's sheet resistance and resistivity are presented as a graph with selectable data values.

Figure 11 shows the measurement results of the electrical parameters, namely the resistivity (ρ) of the emitter layer and the contact resistance of the emitter layer in a solar cell with a textured surface without an antireflection coating.

The measurements gave a resistivity (ρ) of 6,4 Ω·cm and an emitter layer contact resistance (R_{cont}) of 77 mΩ·cm². This indicates that the tested photovoltaic cell exhibited

a low resistivity value for the connection between the front silver electrode and the silicon substrate. Both 2D maps and 3D images allow a detailed analysis of the parameter variations across different regions of the photovoltaic cell, which can be used to draw conclusions regarding the manufacturing technology of individual solar cell components [5].

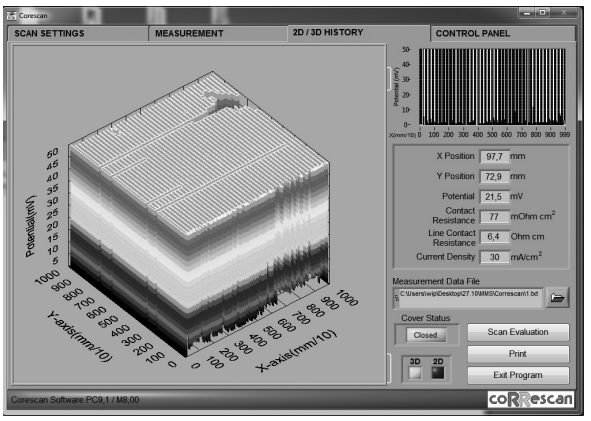

Figure 11. Part from the "2D/3D Measurement History" tab showing the measurement results of the parameters R_{cont} and ρ in the form of a 3D image

Phase composition analyses of chosen silicon surface topography of a solar cell done using the XRD method (Figure 12). The qualitative analysis of the phase composition performed using X-ray diffraction (Figure 12) confirms that the layer on the silicon substrate contains the SiO_2 phase, which is likely a passivating layer. Furthermore, a preferred orientation with respect to the {133} planes can be observed.

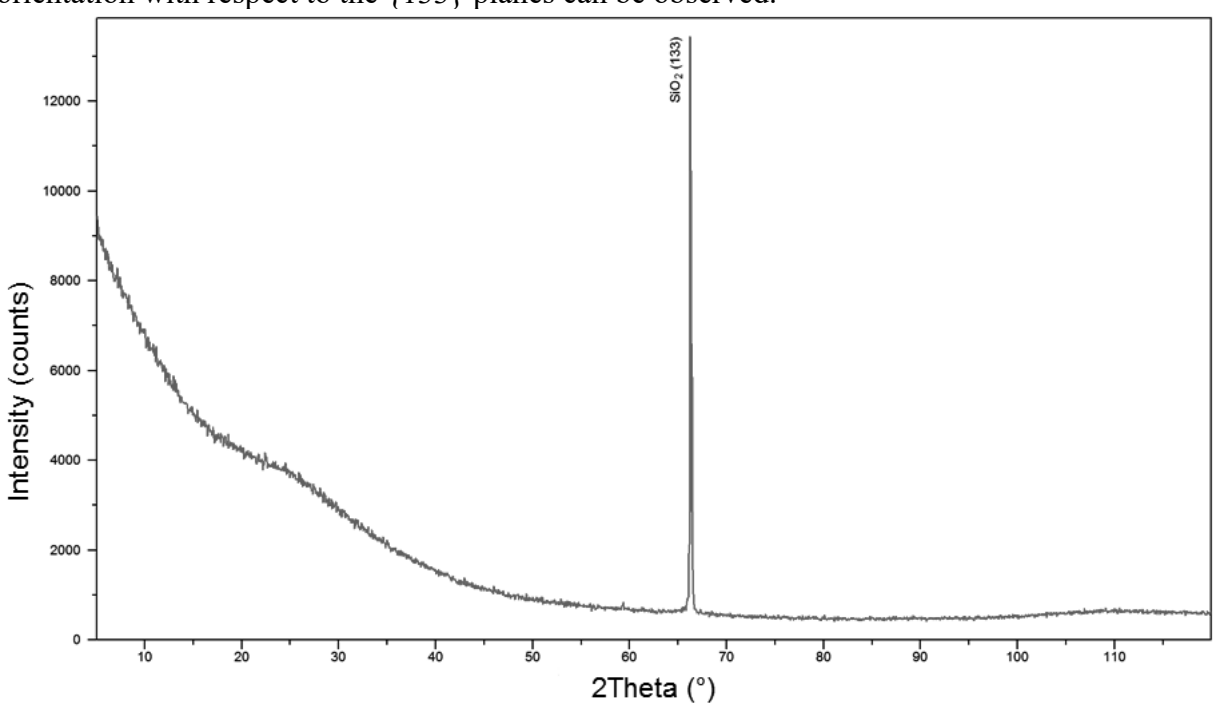

Figure 12. X-ray diffraction pattern of the textured surface topography of a solar cell without an ARC layer(chosen example)

4. SUMMARY

The results of the electrical measurements indicate a clearly higher photovoltaic conversion efficiency for the cell equipped with an anti-reflective coating (ARC). This observation confirms the effective increase in the number of photons absorbed by the cell as a result of reduced reflection from its front surface. Consequently, this enhancement is primarily reflected in the cell current, which is proportional to the number of photons generating electron–hole pairs within the p–n junction region.

The surface morphology of the investigated silicon solar cells indicates that the samples have a distinctly textured surface, as confirmed by SEM metallographic observations.

Comparison of the samples indicates that the presence of an ARC layer in the textured solar cell introduces titanium and oxygen in addition to silicon, whereas the non-textured cell without an ARC layer consists almost entirely of silicon.

The sheet resistance measurements confirm a uniform result of 38.7 Ω/□, with no variation observed among the statistical parameters.

The obtained results indicate that the surface resistivity of 0.19 mΩ/□ and the electrode resistivity of 0.27 μΩ·cm suggest a generally good electrical performance of the front contact. However, the deviations from the ideal parabolic distribution point to irregularities in the electrode formation process, most likely caused by improper thermal treatment of the conductive paste during screen printing.

Resistivity and contact resistance measurements confirm a low-resistance front electrode–silicon contact, while 3D analysis reveals local variations relevant to cell quality.

X-ray diffraction analysis indicates that the SiO_2 layer on the silicon substrate likely acts as a passivating layer with a preferred {133} orientation.

ACKNOWLEDGEMENTS

This work was completed as part of a project-based learning (PBL) initiative under the XIII competition of the Excellence Initiative – Research University program at the Silesian University of Technology.

BIBLIOGRAPHY

[1] Filipowski, W., Drabczyk, K., Wróbel, E., Sobik, P., Waczynski, K., & Waczynska-Niemiec, N. (2018). Borosilicate spray-on glass solutions for fabrication silicon solar cell back surface field. Microelectronics International, 35(3), 172-176.

[2] Filipowski, W., Wrobel, E., Drabczyk, K., Waczynski, K., Kulesza-Matlak, G., & Lipinski, M. (2017). Spray-on glass solution for fabrication silicon solar cell emitter layer. Microelectronics International, 34(3), 149-153.

[3] Swatowska, B., Stapinski, T., Drabczyk, K., & Panek, P. (2011). The role of antireflective coatings in silicon solar cells–the influence on their electrical parameters. Optica Applicata, 41(2), 487-492.

[4] Musztyfaga-Staszuk M., (2025) Basic diagnostics of electrical and structural properties of solar cells, Acta Physica Polonica A, vol. 147, nr 3, p. 270-279. DOI:10.12693/aphyspola.147.270.

[5] Musztyfaga-Staszuk M. (2022) Application of the Transmission Line Method (TLM) to Measure the Resistivity of Contacts: Monograph, vol. 955, Silesian University of Technology Publishing House, 92 pages, ISBN 978-83-7880-861-9.

TalentDetector
9th January 2026
Gliwice, Poland
DEPARTMENT OF ENGINEERING MATERIALS AND BIOMATERIALS
FACULTY OF MECHANICAL ENGINEERING
SILESIAN UNIVERSITY OF TECHNOLOGY
INTERNATIONAL STUDENTS SCIENTIFIC CONFERENCE

Procesy nanoszenia powłok ochronnych stosowanych na elementy maszyn i robotów przemysłowych

Marta Marianek[a], Beata Krupińska[b]

[a] Politechnika Śląska, Wydział Mechaniczny Technologiczny, Kierunek Mechanika i Budowa Maszyn, sem. VII
[b] Politechnika Śląska, Wydział Mechaniczny Technologiczny, Katedra Materiałów Inżynierskich i Biomedycznych

Streszczenie: Współczesna automatyzacja procesów wytwórczych wymaga stosowania materiałów o wysokiej niezawodności eksploatacyjnej. W niniejszym artykule przedstawiono analizę procesu wytwarzania ochronnych powłok fosforanowych na stali S235, dedykowanych dla elementów maszyn i robotów przemysłowych. Praca łączy zagadnienia inżynierii materiałowej z wymogami stawianymi przez robotyzację, takimi jak stabilność wymiarowa, odporność na korozję w agresywnym środowisku oraz odporność na zużycie ścierne. Na podstawie badań mikrostrukturalnych (LM, SEM) oraz pomiarów mikrotwardości wykazano, że odpowiednio uformowana warstwa fosforanowa stanowi skuteczną barierę ochronną, przyczyniając się do wydłużenia czasu bezawaryjnej pracy (MTBF) zautomatyzowanych linii produkcyjnych.
Abstract: Modern automation of manufacturing processes requires the use of materials with high operational reliability. This article presents an analysis of the process of producing protective phosphate coatings on S235 steel, dedicated to industrial machine and robot components. The work combines material engineering issues with the requirements of robotization, such as dimensional stability, corrosion resistance in aggressive environments and abrasion resistance. Based on microstructural studies (LM, SEM) and microhardness measurements, it has been shown that a properly formed phosphate layer provides an effective protective barrier, contributing to the extension of the mean time between failures (MTBF) of automated production lines.

Słowa kluczowe: automatyzacja, robotyzacja, stal S235, fosforanowanie, powłoki konwersyjne, inżynieria powierzchni, utrzymanie ruchu

1. WSTĘP

1.1. Wyzwania eksploatacyjne w automatyzacji przemysłowej

Dynamiczny rozwój koncepcji Przemysłu 4.0 wymusza na inżynierach ciągłe poszukiwanie rozwiązań zwiększających efektywność i niezawodność systemów produkcyjnych. Roboty przemysłowe, manipulatory oraz zautomatyzowane systemy transportu

bliskiego są fundamentem nowoczesnych fabryk. Jednakże, ich bezawaryjna praca jest ściśle uzależniona od kondycji fizycznej poszczególnych komponentów mechanicznych [1].
Elementy takie jak chwytaki, prowadnice liniowe, korpusy czy elementy złączne, pracują często w skrajnie niekorzystnych warunkach. Czynniki degradujące obejmują [1-3]:

- **Środowisko korozyjne:** Obecność wilgoci, zmiennych temperatur oraz oparów chemicznych (np. chłodziw i smarów w obróbce CNC) sprzyja korozji elektrochemicznej.
- **Zużycie tribologiczne:** Cykliczna praca robotów (powtarzalność rzędu milionów cykli) prowadzi do zużycia ściernego w węzłach tarcia, co skutkuje powstawaniem luzów i utratą precyzji pozycjonowania (powtarzalności) robota.

Awaria nawet drobnego elementu konstrukcyjnego, wynikająca z korozji, może prowadzić do zatrzymania całej linii produkcyjnej, generując straty nieproporcjonalnie wysokie w stosunku do kosztu samego elementu. Dlatego też, w procesie projektowania systemów zrobotyzowanych, kluczową rolę odgrywa dobór odpowiednich technologii zabezpieczenia powierzchni [4].

1.2. Charakterystyka i mechanizm tworzenia powłok konwersyjnych

Fosforanowanie, znane w inżynierii powierzchni jako fosfatyzacja, należy do grupy procesów wytwarzania powłok konwersyjnych (przemianowych). Istotą tego procesu jest chemiczna lub elektrochemiczna reakcja metalu podłoża ze środowiskiem kąpieli, w wyniku której na powierzchni wytwarza się nowa, trwale związana warstwa, będąca integralną częścią materiału rodzimego, a nie tylko nałożoną "koszulką" (jak w przypadku lakierowania) [5-10].

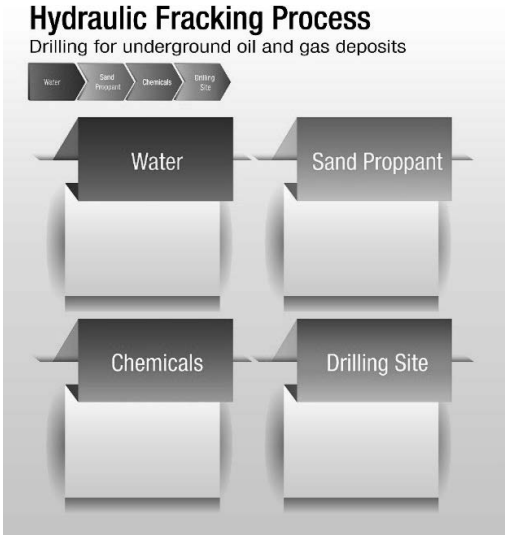

Rys. 1 Proces szczelinowania hydraulicznego [10]

Mechanizm tworzenia powłoki fosforanowej na stali S235 jest procesem wieloetapowym i dynamicznym, opierającym się na reakcjach kwasowo-zasadowych oraz procesach redoks. Gdy stalowy element zostaje zanurzony w kwaśnym roztworze fosforanującym (zawierającym jony metali takich jak Zn^{2+}, Mn^{2+} lub Fe^{2+} oraz kwas fosforowy H_3PO_4), następuje natychmiastowy atak chemiczny na powierzchnię metalu [1, 7].
Proces ten można opisać sekwencją następujących zjawisk fizykochemicznych:

1. Trawienie anodowe (rozpuszczanie podłoża): W mikrostrefach anodowych powierzchni dochodzi do utleniania żelaza zgodnie z reakcją: $Fe \rightarrow Fe^{2+} + 2e^{-}$. Proces ten uwalnia kationy żelaza do warstwy granicznej roztworu.
2. Depolaryzacja katodowa: W strefach katodowych następuje redukcja jonów wodorowych, co prowadzi do wydzielania gazowego wodoru: $2H^{+} + 2e^{-} \rightarrow H_2\uparrow$.
3. Lokalna zmiana pH i krystalizacja: Zużycie jonów wodorowych (H^{+}) w reakcji katodowej powoduje gwałtowny wzrost pH w warstwie dyfuzyjnej bezpośrednio przylegającej do metalu. To naruszenie równowagi chemicznej roztworu powoduje przekroczenie iloczynu rozpuszczalności dla fosforanów trzeciorzędowych. W rezultacie następuje zarodkowanie i wzrost trudno rozpuszczalnych kryształów (np. hopeitu $Zn_3(PO_4)_2 \cdot 4H_2O$ lub foszofilitu $Zn_2Fe(PO_4)_2 \cdot 4H_2O$) bezpośrednio na siatce krystalicznej stali.

Z punktu widzenia automatyzacji i robotyzacji, wytworzona w ten sposób powłoka posiada unikalny zespół cech, trudny do uzyskania innymi metodami [1, 7]:

- Właściwości trybologiczne i retencja oleju: Powłoka fosforanowa nie jest idealnie gładka – posiada strukturę mikroporowatą i kapilarną. Ta cecha, która w innych zastosowaniach mogłaby być wadą, w mechanice precyzyjnej jest zaletą. Przestrzenie międzykrystaliczne działają jak mikrozbiorniki (rezerwuary), które dzięki siłom kapilarnym trwale wiążą olej lub smar stały. W elementach ruchomych robotów (prowadnice, łożyska ślizgowe, przeguby) zapewnia to doskonałe smarowanie w warunkach granicznych, np. podczas rozruchu maszyny (*start-up*) lub przy nagłych zmianach kierunku ruchu, eliminując niebezpieczne zjawisko *stick-slip* (drgania cierne).
- Pasivacja i ochrona korozyjna: Fosforany są solami nieorganicznymi o właściwościach dielektrycznych (są izolatorami elektrycznymi). Warstwa ta skutecznie hamuje przepływ prądów korozyjnych pomiędzy mikrouniwami na powierzchni stali, zapewniając ochronę barierową przed agresywną atmosferą przemysłową (wilgoć, mgła olejowa, opary kwasów). Jest to kluczowe dla zachowania integralności strukturalnej ramion robotów i korpusów maszyn przez cały cykl życia produktu (*Life Cycle*).
- Stabilność wymiarowa: Proces fosforanowania jest procesem addytywnym, ale o bardzo małym przyroście masy (rzędu g/m²), co przekłada się na grubości powłok w zakresie 1–15 μm. Pozwala to na zabezpieczanie precyzyjnych elementów maszyn bez ryzyka przekroczenia tolerancji pasowania, co jest krytyczne przy montażu zrobotyzowanych gniazd produkcyjnych.

1.3. Uwarunkowania eksploatacyjne i wymagania tribologiczne dla węzłów kinematycznych robotów przemysłowych

W procesie projektowania i eksploatacji zrobotyzowanych systemów produkcyjnych, kluczowym wyzwaniem inżynierskim jest zapewnienie długotrwałej niezawodności węzłów kinematycznych. Elementy takie jak prowadnice liniowe, łożyska ślizgowe, przeguby manipulatorów oraz systemy chwytakowe pracują w reżimie obciążeń cyklicznych, które determinują rygorystyczne wymagania dla warstwy wierzchniej materiałów konstrukcyjnych, takich jak stal S235.

Analiza warunków pracy robotów w przemyśle 4.0 pozwala wyodrębnić trzy krytyczne zjawiska degradacyjne, które uzasadniają konieczność stosowania powłok konwersyjnych [1-7]:

1. Niestabilność ruchu: Zjawisko Stick-Slip (Drgania cierne)

W precyzyjnych układach pozycjonowania robotów, fundamentalnym problemem jest zjawisko stick-slip (pol. drgania cierne). Występuje ono w fazie rozruchu lub przy bardzo małych prędkościach przemieszczania, gdy wartość tarcia statycznego (T_s) jest znacząco wyższa od tarcia kinetycznego (T_k).
Dla niezabezpieczonej stali S235, która wykazuje tendencję do sczepiania się z materiałem współpracującym, różnica ta jest znaczna. Prowadzi to do skokowej pracy napędów, powstawania drgań rezonansowych w ramieniu robota oraz błędów pozycjonowania końcówki robota (TCP – Tool Center Point).
Zastosowanie powłoki fosforanowej eliminuje ten problem poprzez mechanizm smarowania granicznego. Krystaliczna struktura fosforanów działa jak matryca kapilarna, utrzymująca film olejowy nawet w stanie spoczynku. Dzięki temu przejście z tarcia statycznego do kinetycznego jest płynne (zmniejszenie amplitudy drgań), co jest warunkiem koniecznym dla precyzji operacji montażowych.
2. Degradacja powierzchni: Zużycie adhezyjne i fretting

Węzły kinematyczne robotów są narażone na dwa specyficzne typy zużycia:

- Zużycie adhezyjne (Galling): W przypadku braku warstwy rozdzielającej, dochodzi do bezpośredniego kontaktu metal-metal. Miękka stal S235 (ferrytyczno-perlityczna) ulega lokalnemu sczepianiu (zimne spawy), a następnie wyrywaniu cząstek materiału.
- Korozja cierna (Fretting): Wiele połączeń w robotach (np. wpusty, mocowania narzędzi) poddawanych jest mikrodganiom o małej amplitudzie. Powoduje to powstawanie tlenków żelaza, które działają jak twarde ścierniwo, przyspieszając degradację złącza.

Warstwa fosforanowa pełni rolę separatora niemetalicznego. Zapobiega ona bezpośredniemu kontaktowi metalicznych powierzchni współpracujących (*anti-galling agent*), a w przypadku zużycia, produkty ścierania fosforanów są miękkie i nie powodują rysowania gładzi, w przeciwieństwie do tlenków żelaza.
3. Synergia korozji i zużycia (Tribokorozja)
W środowisku przemysłowym roboty często pracują w atmosferze agresywnej chemicznie (obecność wilgoci, mgły olejowej z chłodziw obróbkowych). W takich warunkach zachodzi zjawisko tribokorozji – procesu, w którym uszkodzenie mechaniczne warstwy pasywnej przyspiesza korozję, a produkty korozji przyspieszają zużycie ścierne2222.
Fosforanowanie stali S235 przerywa ten destrukcyjny cykl. Nawet w przypadku lokalnego przerwania ciągłości powłoki na skutek tarcia, sąsiednie obszary fosforanowe zapewniają ochronę katodową lub barierową, a nasiąknięta olejem struktura powłoki wypiera wilgoć z strefy kontaktu. Jest to kluczowe dla zachowania geometrii elementów robotów przez cały przewidywany okres eksploatacji (LCA – Life Cycle Assessment).

2. MATERIAŁ I METODYKA BADAWCZA

Głównym celem pracy była ocena wpływu parametrów procesu fosforanowania (czasu i temperatury) na jakość warstwy wierzchniej stali S235 oraz analiza przydatności tak zabezpieczonych elementów w systemach zrobotyzowanych. Badania zrealizowano w ramach projektu PBL "Ochronne powłoki fosforanowe na powierzchni stali". Zakres pracy obejmował wytworzenie powłok oraz ich charakterystykę z wykorzystaniem zaawansowanych metod inżynierii materiałowej, ze szczególnym uwzględnieniem analizy pod kątem wymagań automatyzacji (trwałość, twardość, precyzja wymiarowa).

2.1. Przygotowanie materiału badawczego

Próbki wykonano z profili stalowych o przekroju kwadratowym 15x15x1,5 mm ze stali S235. Proces przygotowania powierzchni jest kluczowy dla adhezji powłoki i obejmował [6, 8]:

1. **Obróbkę mechaniczną:** Szlifowanie papierami ściernymi o dobranej gradacji w celu usunięcia zgorzeliny walcowniczej i ujednolicenia stanu powierzchni.
2. **Odtłuszczanie chemiczne:** Kąpiel w roztworze NaOH w celu usunięcia zanieczyszczeń organicznych (smarów, olejów konserwujących).
3. **Trawienie aktywujące:** Krótkotrwałe zanurzenie w roztworze kwasu w celu odsłonięcia "świeżej" powierzchni metalicznej, niezbędnej do nukleacji kryształów fosforanów.

2.2. Proces nakładania powłok

Proces właściwy prowadzono w roztworach fosforanujących, zmieniając parametry procesowe (zmienne decyzyjne) [6]:

- **Czas ekspozycji:** Zmieniany w zakresie od kilku do kilkunastu minut, co pozwala na sterowanie grubością warstwy.
- **Temperatura procesu:** Badano wpływ temperatury pokojowej oraz podwyższonej (ok. 60°C) na kinetykę wzrostu kryształów.

2.3. Metody analityczne

Do oceny jakości powłok wykorzystano aparaturę badawczą Politechniki Śląskiej [8]:

- **Mikroskopia świetlna (LM):** Mikroskop **Axio Observer (Zeiss)** posłużył do oceny makroskopowej ciągłości powłoki oraz detekcji ewentualnych wad powierzchniowych.
- **Skaningowa Mikroskopia Elektronowa (SEM):** Mikroskop **Zeiss Supra 35** z analizatorem EDS wykorzystano do obserwacji morfologii kryształów przy dużych powiększeniach oraz precyzyjnego pomiaru grubości powłoki na przekrojach poprzecznych. Jest to badanie kluczowe dla oceny precyzji wymiarowej elementów.

3. WYNIKI BADAŃ

3.1. Charakterystyka mikrostrukturalna i morfologia powłok (SEM)

W celu oceny morfologii wytworzonych warstw ochronnych wykorzystano skaningową mikroskopię elektronową (SEM). Analiza obrazów wykazała, że proces fosforanowania doprowadził do wytworzenia na powierzchni stali S235 ciągłej powłoki.

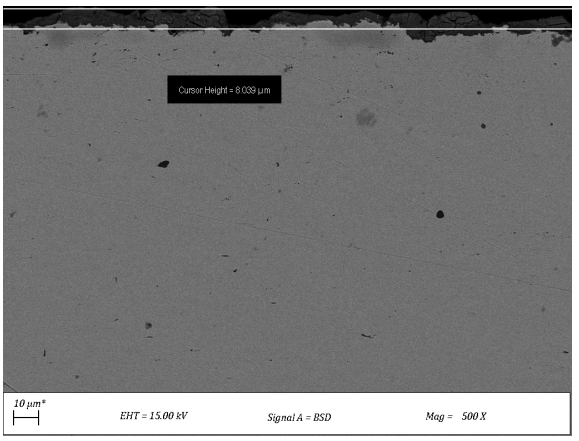

Rys. 2 Mikrostruktura powłoki fosforanowej na podłożu stalowym

Z punktu widzenia automatyzacji procesów przemysłowych, zaobserwowana struktura ma kluczowe znaczenie. W układach ruchowych robotów pozwala na utrzymanie filmu smarnego nawet przy dużych obciążeniach, co minimalizuje ryzyko awarii i wydłuża czas bezawaryjnej pracy maszyn (MTBF).

3.2. Analiza grubości powłok

Analiza przekrojów poprzecznych oraz pomiary grubości wykazały, że wytworzone powłoki charakteryzują się grubością w przedziale od 1 do 15 μm. Jest to parametr krytyczny dla komponentów zrobotyzowanych, takich jak precyzyjne prowadnice czy elementy chwytaków. Niewielki przyrost wymiarowy pozwala na zabezpieczenie antykorozyjne bez konieczności korygowania tolerancji pasowania elementów mechanicznych, co znacznie upraszcza proces technologiczny montażu automatycznych linii produkcyjnych.

3.3. Analiza składu chemicznego (EDS)

Potwierdzeniem prawidłowości przeprowadzonego procesu konwersyjnego są wyniki punktowej analizy składu chemicznego. Poniżej (tabela 1) przedstawiono wyniki udziałów masowych dla kluczowych pierwiastków budujących powłokę.

Tabela 1. Udział masowy pierwiastków (Weight %) w wybranych punktach pomiarowych.

Próbka	Tlen (O) [%]	Fosfor (P) [%]	Żelazo (Fe) [%]	Cynk (Zn) [%]	Inne (Ca, Cl, Na)
s 02_pt1	26.34	15.53	19.32	37.44	Si, Cl, K, Ca
s_pt1	6.77	4.08	78.81	10.34	-
A(1)_pt1	29.33	15.74	14.34	39.58	Cl, Ca
A(2)_pt1	30.25	14.89	10.54	43.18	Cl

Wysoka zawartość fosforu i cynku w badanych punktach potwierdza powstanie trwałej warstwy fosforanowej. Obecność sygnału pochodzącego od żelaza (Fe) w niektórych obszarach (np. próbka s_pt1) świadczy o niewielkiej grubości warstwy, co jest zjawiskiem pożądanym przy zachowaniu wysokiej szczelności powłoki.

4. DYSKUSJA: IMPLIKACJE DLA AUTOMATYZACJI I ROBOTYZACJI

Analiza uzyskanych wyników w kontekście Automatyzacja i robotyzacji pozwala na wyciągnięcie istotnych wniosków wdrożeniowych [4, 8].

1. **Niezawodność i Redukcja Przestojów (Reliability & Maintenance):** Korozja jest "cichym zabójcą" w automatyce. Skorodowany trzpień siłownika pneumatycznego może uszkodzić uszczelnienia, prowadząc do wycieków i spadku ciśnienia, a w konsekwencji do zatrzymania maszyny. Powłoki fosforanowe, jako warstwa konwersyjna, szczelnie izolują stal S235, drastycznie zmniejszając ryzyko takich awarii. Wprowadzenie fosforanowania jako standardu dla elementów stalowych w budowie maszyn jest działaniem prewencyjnym, wpisującym się w strategię *Predictive Maintenance*.
2. **Trybologia w Układach Ruchowych:** W robotach przemysłowych kluczowa jest płynność ruchu. Zjawisko *stick-slip* (drgania przy ruszaniu) negatywnie wpływa na precyzję pozycjonowania i żywotność serwonapędów. Struktura fosforanów, zdolna do retencji oleju, zapewnia obecność filmu smarnego nawet w warunkach granicznych

(duże obciążenia, małe prędkości), co stabilizuje procesy tarcia w przegubach i prowadnicach.

3. **Standaryzacja i Powtarzalność:** Badania wykazały, że proces fosforanowania jest sterowalny. Możliwość uzyskania powtarzalnej grubości i struktury powłoki jest kluczowa dla seryjnej produkcji komponentów automatyki. Pozwala to na projektowanie elementów z uwzględnieniem naddatku na powłokę, bez ryzyka przekroczenia tolerancji wymiarowych.

5. PODSUMOWANIE

Na podstawie przeprowadzonych badań oraz analizy literaturowej sformułowano następujące wnioski:

1. Fosforanowanie stali S235 jest skuteczną metodą modyfikacji warstwy wierzchniej, umożliwiającą wytworzenie powłok o właściwościach ochronnych i tribologicznych, niezbędnych w nowoczesnych systemach zrobotyzowanych.
2. Parametry procesu (czas, temperatura) mają bezpośredni wpływ na morfologię i grubość powłoki, co pozwala na optymalizację procesu pod kątem konkretnych zastosowań (np. cienkie powłoki pod malowanie vs. grube powłoki olejowane do pracy w tarciu).
3. Zastosowanie badanych powłok przyczynia się do zwiększenia niezawodności elementów maszyn poprzez eliminację ognisk korozji oraz redukcję zużycia ściernego.
4. Realizacja projektu PBL pozwoliła na praktyczną weryfikację założeń teoretycznych i potwierdzenie przydatności stali S235 z powłoką fosforanową w konstrukcjach maszyn i urządzeń automatyki.

PODZIĘKOWANIA

Praca powstała w wyniku realizacji projektu „Ochronne powłoki fosforanowe na powierzchni stali” w ramach kształcenia zorientowanego projektowo – PBL, w XIII konkursie Programu Inicjatywa Doskonałości – Uczelnia Badawcza, Wydział Mechaniczny Technologiczny, Politechnika Śląska.

LITERATURA

1. T. Burakowski, T. Wierzchoń, Inżynieria powierzchni metali, Wydawnictwa Naukowo-Techniczne, Warszawa 1995.
2. J. Demydems, Orange Data Mining – Visual Programming User Guide, University of Ljubljana, 2024. Dostępne online: https://orangedatamining.com/docs/.
3. L.A.Dobrzański, A.D. Dobrzańska-Danikiewicz, Obróbka powierzchni materiałów inżynierskich, Open Access Library, Volume 5, 2011.
4. J. Honczarenko, Roboty przemysłowe. Budowa i zastosowanie, Wydawnictwa Naukowo-Techniczne, Warszawa 2010.
5. D.T. Larose, Metody i modele eksploracji danych, Wydawnictwo Naukowe PWN, Warszawa 2008.

6. PN-EN 10025-2:2019-11: Wyroby walcowane na gorąco ze stali konstrukcyjnych. Część 2: Warunki techniczne dostawy stali niestopowych konstrukcyjnych.
7. Poradnik Galwanotechnika – Praca zbiorowa, Wydawnictwa Naukowo-Techniczne, Warszawa 1985.
8. J. Sikora, K. Michalik, J. Hasiński, M. Nowak, B. Krupińska, M. Staszuk, Właściwości powłoki miedzianej nakładanej w procesie galwanizacji, Materiały konferencyjne TalentDetector, Gliwice 2025.
9. J. Żytkow, Systemy uczące się i odkrywanie wiedzy, Akademicka Oficyna Wydawnicza PLJ, Warszawa 2000.
10. www.123fr.com

TalentDetector
9th January 2026
Gliwice, Poland
DEPARTMENT OF ENGINEERING MATERIALS AND BIOMATERIALS
FACULTY OF MECHANICAL ENGINEERING
SILESIAN UNIVERSITY OF TECHNOLOGY
INTERNATIONAL STUDENTS SCIENTIFIC CONFERENCE

Optymalizacja wybranych procesów inżynierii powierzchni

Marta Marianek[a], Beata Krupińska[b], Mateusz Krupiński[c]

[a] Politechnika Śląska, Wydział Mechaniczny Technologiczny, Kierunek Mechanika i Budowa Maszyn, sem. VII
[b] Politechnika Śląska, Wydział Mechaniczny Technologiczny, Katedra Materiałów Inżynierskich i Biomedycznych
[c] Wieloprofilowy Zespół Szkół w Tarnowskich Górach, klasa IV Technik elektryk

Streszczenie: Opracowanie przedstawia interdyscyplinarne podejście do optymalizacji procesów inżynierii powierzchni, wykorzystujące paradygmat systemów bazujących na wiedzy (Knowledge-Based Systems). Na przykładzie procesu fosforanowania stali konstrukcyjnej S235, przedstawiono metodykę zbierania, przetwarzania i analizy danych eksperymentalnych. Głównym celem pracy była implementacja środowiska Orange Data Mining do wykrywania ukrytych korelacji między parametrami wejściowymi procesu (czas, temperatura, przygotowanie powierzchni), a właściwościami wynikowymi powłoki (grubość, mikrotwardość). Wykazano, że zastosowanie wizualnych metod eksploracji danych pozwala na efektywniejsze wnioskowanie o jakości produktu i wspomaga procesy decyzyjne technologa, ograniczając konieczność stosowania metody prób i błędów.
Abstract: The article presents an interdisciplinary approach to the optimization of surface engineering processes using the paradigm of knowledge-based systems. Using the example of the phosphating process of S235 structural steel, the methodology of acquisition, processing and analysis of experimental data is presented. The main objective of the work was to implement the Orange Data Mining environment to detect hidden correlations between the input parameters of the process (time, temperature, surface preparation) and the resulting properties of the coating (thickness, microhardness). It was demonstrated that the use of visual data mining methods allows for more effective conclusions about product quality and supports the technologist's decision-making processes, reducing the need for trial and error.

Słowa kluczowe: systemy bazujące na wiedzy, Data Mining, Orange, fosforanowanie, stal S235, analiza danych, inżynieria materiałowa

1. WSTĘP

1.1. Transformacja cyfrowa w inżynierii materiałowej (Industry 4.0)

W dobie Czwartej Rewolucji Przemysłowej dane stają się kluczowym zasobem przedsiębiorstwa, często określanym mianem "ropy naftowej XXI wieku". Tradycyjna inżynieria materiałowa, opierająca się na intuicji eksperta i analizie pojedynczych przypadków,

ewoluuje w kierunku inżynierii sterowanej danymi (*data-driven engineering*). W nowoczesnym podejściu, każdy eksperyment laboratoryjny traktowany jest nie jako izolowane zdarzenie, ale jako rekord w bazie wiedzy, który może posłużyć do trenowania modeli predykcyjnych i systemów ekspertowych.

Procesy obróbki powierzchniowej, takie jak fosforanowanie, charakteryzują się dużą złożonością fizykochemiczną. Właściwości końcowe produktu – grubość powłoki, jej jednorodność czy mikrotwardość – zależą od nieliniowej interakcji wielu zmiennych procesowych (czas, temperatura, stężenie kąpieli, przygotowanie podłoża). Analiza tych zależności przy użyciu klasycznych metod statystycznych bywa czasochłonna i nie zawsze ujawnia wielowymiarowe wzorce zachowań materiału [2, 5].

1.2. Systemy bazujące na wiedzy i proces KDD

Systemy bazujące na wiedzy (KBS – Knowledge Based Systems) to systemy informatyczne, które naśladują zdolność eksperta do podejmowania decyzji, wykorzystując zgromadzoną bazę faktów i reguł wnioskowania. Fundamentem KBS jest proces Odkrywania Wiedzy z Baz Danych (KDD – Knowledge Discovery in Databases) [1, 3].

Proces ten składa się z sekwencji kluczowych etapów [1, 3]:

1. **Selekcja:** Wybór odpowiedniego zbioru danych (dataset) z dostępnych zasobów.
2. **Preprocessing (Wstępne przetwarzanie):** Czyszczenie danych, usuwanie szumów i błędów pomiarowych, uzupełnianie brakujących wartości.
3. **Transformacja:** Normalizacja lub dyskretyzacja danych, aby były "zrozumiałe" dla algorytmów.
4. **Data Mining (Eksploracja Danych):** Zastosowanie algorytmów w celu znalezienia wzorców (np. drzewa decyzyjne, sieci neuronowe, klasteryzacja).
5. **Ewaluacja i Interpretacja:** Ocena przydatności znalezionej wiedzy przez eksperta dziedzinowego.

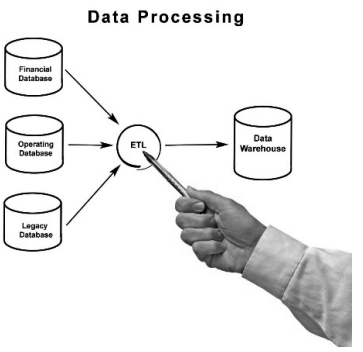

Rys. 1 Przykładowy schemat przetwarzania danych [3].

W kontekście inżynierii produkcji, Data Mining pozwala na realizację zadań takich jak [3]:

- **Klasyfikacja:** Przypisanie próbek do kategorii jakościowych (np. "zgodna z normą" / "brak").
- **Regresja:** Przewidywanie wartości liczbowej (np. grubości powłoki w mikrometrach) na podstawie parametrów procesu.
- **Klasteryzacja:** Grupowanie próbek o podobnych właściwościach fizycznych w celu znalezienia optymalnych okien technologicznych.

1.3. Środowisko Orange Data Mining jako narzędzie inżynierskie

Narzędziem umożliwiającym realizację procesu KDD bez konieczności zaawansowanego programowania w językach Python czy R jest środowisko Orange Data Mining. Jest to

platforma typu *open-source*, rozwijana przez Uniwersytet w Lublanie, oparta na paradygmacie programowania wizualnego.
Użytkownik buduje ścieżki przetwarzania danych (*workflows*), łącząc ze sobą graficzne komponenty zwane widżetami (widgets). Każdy widżet realizuje określoną funkcję: od wczytania pliku, przez filtrację danych, aż po trenowanie modeli uczenia maszynowego i wizualizację wyników. Taka architektura pozwala inżynierom materiałowym skupić się na istocie problemu badawczego, a nie na składni kodu programistycznego [2].

1.4. Charakterystyka domeny problemowej

Przedmiotem analizy w niniejszej pracy jest proces nakładania powłok fosforanowych na stal S2351. Fosforanowanie jest procesem konwersyjnym, w którym na powierzchni stali tworzy się trudno rozpuszczalna warstwa fosforanów, pełniąca funkcję ochronną i tribologiczną.
Zmienne decyzyjne w tym procesie, które będą stanowiły wejście do systemu KBS, to [2,3]:

- Czas ekspozycji w kąpieli (t).
- Temperatura procesu (T).
- Rodzaj obróbki wstępnej powierzchni.

Zmiennymi wyjściowymi (celem predykcji) są parametry fizyczne powłoki: grubość warstwy oraz jej mikrotwardość [2,3].

2. MATERIAŁ I METODYKA BADAWCZA

2.1. Eksperyment fizyczny (Data Acquisition)

Baza wiedzy została zbudowana w oparciu o dane rzeczywiste, uzyskane w ramach projektu PBL. Materiałem badawczym były profile ze stali S235 o wymiarach 15x15x1,5 mm. Próbki poddano procesowi przygotowania powierzchni (szlifowanie papierami o różnej gradacji, odtłuszczanie alkaliczne, trawienie kwasowe), a następnie fosforanowaniu w różnych wariantach czasowych i temperaturowych. Eksperyment zaplanowano tak, aby pokryć szeroki zakres zmiennych wejściowych, co jest kluczowe dla jakości trenowania systemu bazującego na wiedzy [2,5,6].

2.2. Pomiary laboratoryjne (Feature Extraction)

Aby przekształcić fizyczne próbki w cyfrowe rekordy danych, przeprowadzono serię badań instrumentalnych:
Pomiary mikroskopowe: Wykorzystano mikroskop świetlny Axio Observer oraz skaningowy mikroskop elektronowy (SEM) **Zeiss Supra 35** z analizą EDS. Pozwoliło to na precyzyjny pomiar grubości powłoki z dokładnością do nanometrów oraz ocenę morfologii kryształów.
Pomiary twardości: Wykonano badania mikrotwardości metodą Vickersa (HV0.05) przy użyciu twardościomierza **FUTURE-TECH FM-ARS 9000**. Każda próbka została zmierzona w kilku punktach, a wynik uśredniony, aby zminimalizować błąd losowy.
Wyniki te posłużyły do utworzenia ustrukturyzowanego zbioru danych (Dataset), w którym każda próbka stanowi pojedynczą instancję, a parametry procesu i wyniki badań są atrybutami (cechami) [7, 8].

3. IMPLEMENTACJA PROCESU ANALITYCZNEGO W ŚRODOWISKU ORANGE

W ramach pracy zaprojektowano i zaimplementowano kompletną ścieżkę przetwarzania danych (*pipeline*) w środowisku Orange. Poniżej omówiono szczegółowo poszczególne etapy analizy.

3.1. Wczytanie i definicja ról zmiennych (Widget: File)

Pierwszym krokiem było zaimportowanie zbioru danych w formacie .CSV (Comma Separated Values). W widżecie *File* zdefiniowano semantykę poszczególnych zmiennych, co jest kluczowe dla poprawnego działania algorytmów [4, 8]:

- **Features (Cechy):** Czas procesu [min], Temperatura [°C], Gradacja ścierniwa. Są to zmienne niezależne, na podstawie których system będzie wnioskował.
- **Target (Cel):** Grubość powłoki [µm], Mikrotwardość [HV]. Są to zmienne zależne, które chcemy przewidywać lub analizować.
- **Meta:** Numer próbki (dane informacyjne, nie biorące udziału w obliczeniach statystycznych).

3.2. Wstępne przetwarzanie danych (Widget: Preprocess)

Surowe dane eksperymentalne rzadko nadają się do bezpośredniej analizy. Zastosowano widżet *Preprocess* w celu wykonania dwóch kluczowych operacji [4]:

Imputacja brakujących danych: W przypadku próbek, dla których pomiar był niemożliwy (np. uszkodzenie próbki), zastosowano algorytm zastępowania braku średnią wartością z danej klasy.

Normalizacja: Czas procesu (zakres 5-15 min) i twardość (zakres 100-200 HV) operują na zupełnie innych skalach liczbowych. Algorytmy oparte na odległościach (jak k-Nearest Neighbors czy k-Means) błędnie interpretowałyby twardość jako cechę ważniejszą tylko dlatego, że ma wyższe wartości liczbowe. Zastosowano normalizację do przedziału [0,1], co zrównuje wagi wszystkich atrybutów.

3.3. Eksploracyjna analiza danych (Widget: Scatter Plot & Distributions)

W celu zrozumienia charakterystyki statystycznej danych, wykorzystano narzędzia wizualizacji. Widżet *Distributions* (Rozkłady) pozwolił na wygenerowanie histogramów dla poszczególnych atrybutów. Pozwoliło to na identyfikację wartości odstających (*outliers*), które mogły wynikać z błędów grubych (np. trafienie wgłębnikiem twardościomierza w inkluzję niemetaliczną).

Kluczowym narzędziem był widżet *Scatter Plot* (Wykres punktowy), który posłużył do wizualizacji korelacji wielowymiarowych. Umożliwił on nałożenie na siebie wymiaru czasu (oś X) i grubości powłoki (oś Y), z dodatkowym kodowaniem kolorem dla temperatury procesu.

3.4. Ranking ważności cech (Widget: Rank)

Aby odpowiedzieć na pytanie, który parametr procesowy ma największy wpływ na jakość powłoki, użyto widżetu *Rank*. Wykorzystuje on zaawansowane miary statystyczne, takie jak:

- **Information Gain (Zysk Informacyjny):** Mierzy, jak bardzo znajomość danej cechy (np. temperatury) zmniejsza entropię (niepewność) co do klasy wynikowej.
- **ReliefF:** Algorytm oceniający jakość atrybutów na podstawie ich zdolności do rozróżniania próbek znajdujących się blisko siebie w przestrzeni cech.

Analiza ta pozwala inżynierowi skupić się na ścisłej kontroli parametrów krytycznych (o wysokim rankingu), ignorując te, które mają marginalny wpływ na wynik końcowy (szum informacyjny) [4, 8].

4. WYNIKI BADAŃ

4.1. Akwizycja danych morfologicznych (SEM)

W ramach procesu akwizycji wiedzy o produkcie, przeprowadzono badania morfologii powierzchni z wykorzystaniem skaningowej mikroskopii elektronowej (SEM). Obrazy te stanowią dane wejściowe do oceny jakości procesu optymalizacji.

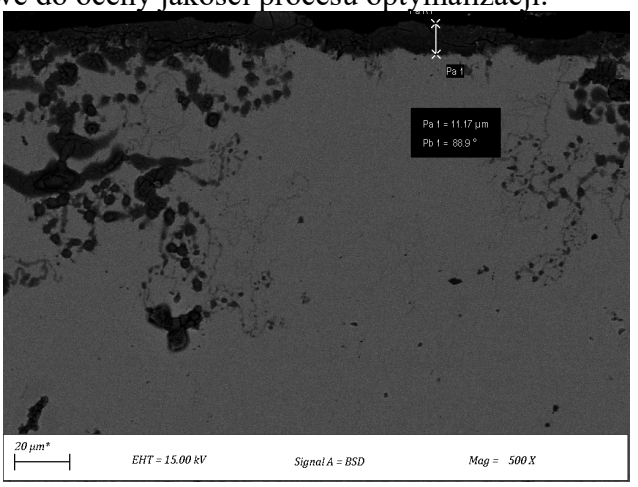

Rys. 2 Powłoka fosforanowa na stali S235

Analiza wykazała, że struktura krystaliczna powłoki jest powtarzalna, co pozwala na parametryzację cech powierzchniowych w systemach doradczych. Zidentyfikowana porowatość międzykrystaliczna została sklasyfikowana jako kluczowa cecha wpływająca na retencję środków smarnych w zautomatyzowanych systemach mechanicznych.

3.2. Eksploracja składu chemicznego (EDS)

Dane chemiczne pozyskane metodą EDS posłużyły do weryfikacji stabilności procesu fosforanowania. Wykorzystanie wizualnych metod eksploracji danych pozwala na szybką identyfikację pierwiastków kluczowych dla jakości powłoki.

Tabela 1. Udział masowy pierwiastków jako zmienne procesowe.

PUNKT POMIAROWY	O [%]	P [%]	FE [%]	ZN [%]	INNE PIERWIASTKI
s 02_pt1	26.34	15.53	19.32	37.44	Si, Cl, K, Ca
A(1)_pt1	29.33	15.74	14.34	39.58	Na, Cl, Ca

Obecność cynku (Zn) i fosforu (P) na poziomie powyżej 15% (P) i 35% (Zn) w próbach optymalizowanych potwierdza poprawność przyjętego modelu technologicznego.

3.3. Analiza korelacji grubości i twardości

W toku badań stwierdzono, że grubość powłoki (1–15 µm) skorelowana jest z czasem ekspozycji próbek w kąpieli. Dane te, wprowadzone do środowiska Orange Data Mining, pozwalają na przewidywanie właściwości wynikowych bez konieczności kosztownych powtórzeń eksperymentów. Wzrost mikrotwardości powierzchniowej potwierdza skuteczność optymalizacji parametrów kąpieli fosforanowej.

5. PODSUMOWANIE

Integracja klasycznej inżynierii materiałowej z nowoczesnymi narzędziami analizy danych i systemami bazującymi na wiedzy przynosi wymierne korzyści w procesie badawczym i produkcyjnym. Przeprowadzona analiza pozwala na sformułowanie następujących wniosków:

1. **Efektywność Analizy:** Środowisko Orange Data Mining umożliwia szybką, wizualną analizę wielowymiarowych zbiorów danych bez konieczności pisania złożonego kodu programistycznego. Pozwala to inżynierom materiałowym na samodzielną eksplorację wyników badań i szybsze wyciąganie wniosków.
2. **Obiektywizacja Decyzji:** Systemy bazujące na wiedzy pozwalają na podejmowanie decyzji technologicznych (np. precyzyjny dobór czasu procesu w celu uzyskania zadanej grubości) w oparciu o twarde dane statystyczne i wykryte trendy, a nie tylko na podstawie subiektywnej intuicji eksperta.
3. **Optymalizacja Procesu:** Wykryte korelacje, w tym zjawisko nasycenia grubości powłoki w czasie, pozwalają na optymalizację kosztową procesu fosforanowania, eliminując zbędne wydłużanie czasu operacji w skali produkcji masowej.
4. **Zgodność z trendami Industry 4.0:** Realizacja projektu potwierdziła, że dla stali S235 możliwe jest stworzenie cyfrowego modelu procesu (*Digital Twin*), łączącego parametry wejściowe z jakością powłoki, co stanowi wstęp do budowy inteligentnych systemów sterowania w nowoczesnych galwanizerniach.

PODZIĘKOWANIA

Praca powstała w wyniku realizacji projektu „Ochronne powłoki fosforanowe na powierzchni stali” w ramach kształcenia zorientowanego projektowo – PBL, w XIII konkursie Programu Inicjatywa Doskonałości – Uczelnia Badawcza, Wydział Mechaniczny Technologiczny, Politechnika Śląska.

LITERATURA

1. T. Burakowski, T. Wierzchoń, Inżynieria powierzchni metali, Wydawnictwa Naukowo-Techniczne, Warszawa 1995.
2. J. Demydems, Orange Data Mining – Visual Programming User Guide, University of Ljubljana, 2024. Dostępne online: https://orangedatamining.com/docs/.
3. L.A.Dobrzański, A.D. Dobrzańska-Danikiewicz, Obróbka powierzchni materiałów inżynierskich, Open Access Library, Volume 5, 2011.
4. D.T. Larose, Metody i modele eksploracji danych, Wydawnictwo Naukowe PWN, Warszawa 2008.
5. PN-EN 10025-2:2019-11: Wyroby walcowane na gorąco ze stali konstrukcyjnych. Część 2: Warunki techniczne dostawy stali niestopowych konstrukcyjnych.
6. Poradnik Galwanotechnika – Praca zbiorowa, Wydawnictwa Naukowo-Techniczne, Warszawa 1985.
7. J. Sikora, K. Michalik, J. Hasiński, M. Nowak, B. Krupińska, M. Staszuk, Właściwości powłoki miedzianej nakładanej w procesie galwanizacji, Materiały konferencyjne TalentDetector, Gliwice 2025.
8. J. Żytkow, Systemy uczące się i odkrywanie wiedzy, Akademicka Oficyna Wydawnicza PLJ, Warszawa 2000.

TalentDetector

9th January 2026
Gliwice, Poland

DEPARTMENT OF ENGINEERING MATERIALS AND BIOMATERIALS
FACULTY OF MECHANICAL ENGINEERING
SILESIAN UNIVERSITY OF TECHNOLOGY

INTERNATIONAL STUDENTS SCIENTIFIC CONFERENCE

Protective Efficiency of Wax and Ceramic Coatings on Automotive Paints: A Comparative Study

Magdalena Markiewicz [b], Bartłomiej Wątroba [b], Julia Wawrzynek [b], Maciej Nogieć [b], Mateusz Sadowski [b], Wojciech Tokarz [b], Daniel Bujara [b], Marta Fizia [b], Marek Kremzer [a]

[a] Silesian University of Technology, Faculty of Mechanical Engineering, Scientific and Didactic Laboratory of Nanotechnology and Materials Technology
email: Marek.Kremzer@polsl.pl

[b] Silesian University of Technology, Faculty of Mechanical Engineering
email:mm305639@student.polsl.pl,bw305635@student.polsl.pl, jw305636@student.polsl.pl, mn303954@student.polsl.pl, ms303956@student.polsl.pl, wt303939@student.polsl.pl, db303946@student.polsl.pl, mf309372@student.polsl.pl

Abstract: This work compares the protective performance of waxes and ceramic coatings used on automotive paint systems. Their mechanisms of action, key advantages, and practical limitations are discussed. Aluminium substrates with a representative multilayer coating system consisting of a primer, an acrylic basecoat, and a clear coat were prepared and treated with waxes or ceramic coatings, alongside an untreated reference. The specimens were then subjected to accelerated tests simulating service conditions to evaluate protection efficacy and the impact of the treatments on surface appearance.

Keywords: waxes, automotive paint protection, ceramic coatings, hydrophobicity, wear, coating durability

1. INTRODUCTION

In today's world, environmental protection is of fundamental importance, and efforts should be made to minimise the impact of human activity on the environment. One step in this direction was the introduction of Directive 2004/42/EC of the European Parliament and of the Council on the limitation of emissions of volatile organic compounds, VOC, which has compelled manufacturers to modify coating technologies [1]. Conventional solvent-borne paints are increasingly being replaced by water-borne systems, which are substantially safer for both the environment and workers. Despite their unquestionable benefits, modern automotive coating systems pose significant challenges in long-term service. The scientific literature indicates that the use of water-borne coatings requires much stricter quality control, and application errors may reduce coating uniformity and negatively affect visual appearance [2]. As reported in [3], page 201, scratch resistance is a key challenge for clear coats, and damage

generated during mechanical vehicle washing leads to gloss loss and is a frequent cause of customer complaints. The same authors also highlight the risk of chemical degradation caused by factors such as acid rain and bird droppings. They note that, historically, manufacturers' efforts to increase solids content to reduce VOC emissions had an adverse effect on resistance to chemical degradation [3]. It is also important that vehicle manufacturers increasingly apply thinner paint layers to reduce costs. Taken together, these factors strongly support the use of additional protective coatings by vehicle owners. The improvement in surface appearance achieved with such treatments is also an important consideration. A traditional method of surface protection is the use of waxes. In practice, both natural and synthetic polymer-based waxes are used. Waxes form a physical barrier layer that fills microscopic surface irregularities, enhances gloss, and provides hydrophobicity, reflected by a high contact angle. However, this layer is not durable because it does not form chemical bonds with the substrate; it also exhibits limited thermal resistance and is susceptible to removal by detergents [4]. In response to the limitations of wax-based protection, ceramic coatings have become widespread in the automotive sector. These systems are based on resins and solvents, while their protective performance is primarily attributed to a high content of silica, SiO2, often supplemented with titanium dioxide, TiO2, which improves resistance to ultraviolet radiation [4]. The most recent generation of protective coatings in the automotive industry includes hybrid graphene–ceramic coatings, which form a thin, glossy, and strongly hydrophobic protective layer. They can provide a higher contact angle and greater flexibility, which reduces brittleness and limits local heat accumulation compared with conventional ceramic coatings [5]. Studies published in 2025 indicate that selecting an appropriate graphene concentration is crucial for achieving the most desirable performance [6].
Overall, a wide range of protective coatings is available, and manufacturers often claim exceptional properties in promotional materials; however, independent studies confirming these claims are frequently limited. The aim of this work is to analyse the protective and aesthetic properties of six selected coatings.

1.1. Research methodology

1.1.1 Surface protection procedure

The specimens were made of 100 × 100 mm aluminium sheets coated with a standard automotive multilayer system comprising a reactive wash primer, an acrylic primer, a DYNA COAT acrylic basecoat (Akzo Nobel), and a DYNA COAT clear coat (Akzo Nobel). The protective coatings and waxes listed in Table 1 were then applied. Application was carried out in accordance with the manufacturer's recommendations for each product. The products were applied to a clean, dry, and degreased surface using dedicated applicators, ensuring uniform coverage over the entire specimen surface. After the recommended initial curing time, excess material was buffed off with a soft microfiber cloth to obtain a homogeneous finish. To ensure comparable conditions, all specimens were prepared in the same manner, and an untreated control specimen without any additional protective layer was used as the reference.

Table 1 Description and indication of used protection coatings

Indication	Product	Description
Waxes		
1	Dark Angel	A wax intended for dark and black paintwork, providing protection for up to 6 months. It contains a blend of natural oils and waxes that enhances colour depth, masks minor scratches, and leaves a durable, glossy protective layer with pronounced hydrophobic behaviour.
2	Soft 99 Fusso	A hard protective wax based on fluoropolymers, valued for strong hydrophobic properties. Depending on operating conditions and maintenance, the protective layer can last up to approximately one year.
Coatings		
3	Ultracoat Skyline	A ceramic–graphene coating for paint protection that provides long-term durability and enhances colour depth. According to the manufacturer, it can last up to 3 years and is formulated with SiO_2 and SiC compounds as well as graphene flakes.
4	Ultracoat Aurora	A universal ceramic–graphene spray coating protecting paintwork for up to 9 months, intended for various exterior surfaces such as paint, wheels, and plastics. Owing to its high SiO_2 content and graphene additives, it can be used as a stand-alone product or as a maintenance product for previously applied coatings.
5	Carpro D-quartz	A "nano-diamond" ceramic coating designed to increase the mechanical resistance of the surface. The manufacturer emphasises its focus on reducing micro-scratches and improving resistance to damage.
Top-up products		
6	Ultracoat – Ceramic Q-detailer	A quick detailer with a high SiO_2 content for rapid maintenance of paintwork and other exterior components. It can serve as short-term protection or as a product for regular refreshing and boosting the properties of ceramic coatings, including gloss, slickness, and hydrophobicity.
Referenced specimen		
7	Uncoated sample	Reference specimen without any protective coating.

1.1.2 Simulation of Service Conditions

a) Coating resistance to abrasive blasting erosion

The resistance of the coatings to abrasive jet erosion was evaluated using previously prepared aluminium panels. The aim of the test was to reproduce mechanical effects similar to those occurring during vehicle service, particularly the impact of solid particles on the painted surface. Identical exposure conditions were applied for all variants to enable a direct comparison of coating degradation.

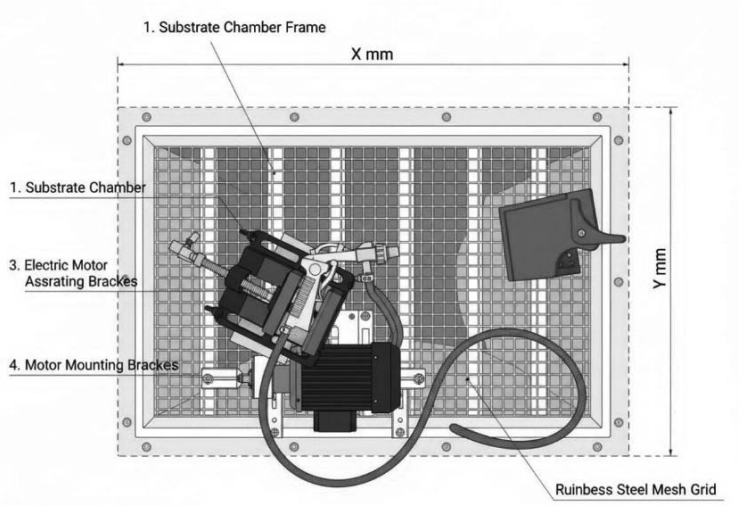

Figure 1 Schematic diagram of the sandblasting test setup

The schematic of the test setup is shown in Fig. 1. The device is based on a steel chamber housing, which serves as the load-bearing structure and protective enclosure. It provides sufficient rigidity during operation at pressures of up to 200 kPa and limits operator exposure to abrasive particles suspended during the test. A stainless-steel mesh grid located at the bottom of the chamber supports the specimen and enables separation of the spent abrasive for reuse. The drive system, in the form of a vibration unit, was attached to the frame using assisting brackets, ensuring stable mounting and maintaining the target vibration amplitude to promote a uniform distribution of the abrasive. Additional mounting brackets limited lateral movement of the drive unit during operation and improved alignment. The abrasive stream was directed onto the test surface via a grit feed nozzle assembly positioned at an angle of 45 ± 1° relative to the specimen surface, ensuring compliance with the required particle impingement angle. During testing, each specimen was sandblasted for 1 min at an operating pressure of approximately 0.8 bar using abrasive media with a particle size of 0.5–1 mm

b) Resistance to mechanical wear during washing

The hydrophobic properties of the investigated surfaces were assessed qualitatively based on the behaviour of a water droplet on the specimen, including wetting, droplet formation, and droplet retention on the surface. Photographic documentation of specimens coated with the individual products is presented in Figs. 2–7, while the uncoated reference specimen is shown in Fig. 8. In the surface-tension test images (Figs. 2–8), water droplets maintain a near-spherical shape, indicating limited wetting and the presence of a hydrophobic effect. At the same time, differences in droplet size and stability are observed between specimens, which may indicate varying degrees of surface-energy reduction achieved by the applied coatings. The uncoated specimen (Fig. 8) served as a reference point for further evaluation of the effect of repeated soiling and washing on surface properties.

To simulate service conditions associated with road contamination and cyclic vehicle washing, a mixture of clay, salt, and water was applied to the specimen surfaces (Fig. 9). The specimens were left for 24 h at room temperature to allow the mixture to dry and the deposit to form, as confirmed by the uniform dried film visible in the photograph (Fig. 9). Next, a pre-wash was performed using a Traffic Film Remover, TFR, from KiurLab diluted 1:9 with water. The

specimens were then rinsed and subjected to the main wash using KiurLab Bubble Fruit car shampoo with neutral pH. The purpose of the test was to evaluate changes in coating performance after successive soiling and cleaning cycles, including susceptibility to contamination build-up and visible signs of surface wear. The procedure was repeated three times, each cycle consisting of application of the mixture and 24 h deposition, followed by TFR pre-wash, rinsing, and the main wash. In addition, to further approximate real service conditions, the specimens were blown with compressed air after selected stages to remove loose water droplets and non-adhered contaminants. The specimen condition after the first cleaning cycle, following compressed air blowing, is shown in Fig. 10, and after the third cycle in Fig. 11. Comparison of the photographs after successive cycles indicates a gradual emergence of differences between coatings in terms of ease of soil removal and the character of post-wash residues, such as spot marks and local deposits. This provides a basis for further assessment of the durability and resistance of the investigated protective treatments under conditions approximating real-world use.

Figure 2 Specimen coated with Dark Angel wax – surface tension test

Figure 3 Specimen coated with Soft 99 Fusso wax – surface tension test

Figure 4 Specimen coated with Ultracoat Skyline – surface tension test

Figure 5 Specimen coated with Ultracoat Aurora – surface tension test

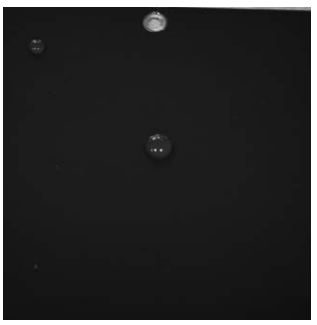

Figure 6 Specimen coated with CarPro D-quartz – surface tension test

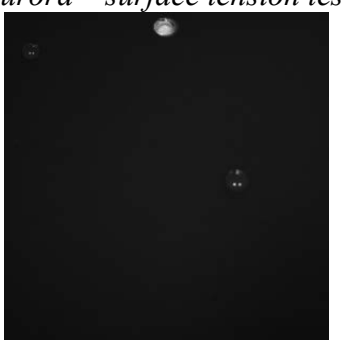

Figure 7 Specimen treated with Ultracoat Ceramic Q-Detailer – surface tension test

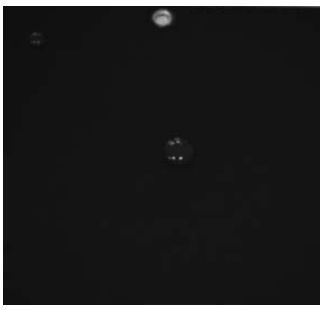

Figure 8 Uncoated specimen – surface tension test

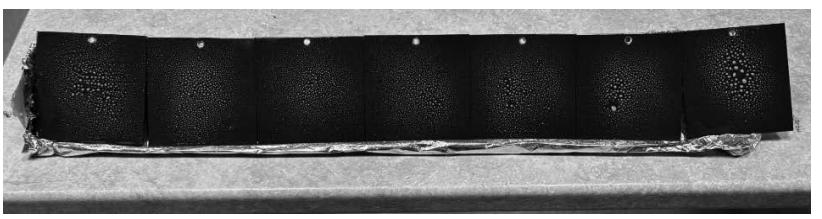

Figure 9. Specimens coated with a clay–salt–water mixture

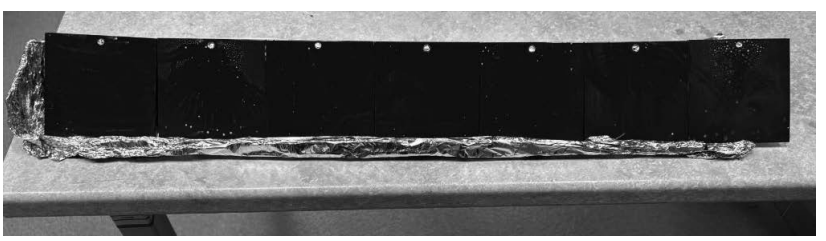

Figure 10. Specimens after the first cleaning cycle, subjected to a compressed-air jet

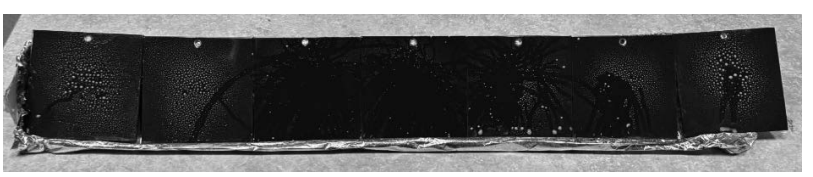

Figure 11. Specimens after the third cleaning cycle, subjected to a compressed air jet

c) Evaluation of coating degradation under UV irradiation

UV irradiation of the wax and ceramic coatings was used to simulate long-term solar exposure under accelerated conditions.

Figure 12 UV test setup

Ultraviolet radiation is one of the primary factors responsible for material ageing; therefore, exposure under controlled laboratory conditions makes it possible to evaluate coating durability and stability and to observe changes that would occur gradually during vehicle service under natural conditions. The use of a UV lamp enables direct comparison of different protective systems under identical conditions and assessment of their resistance to prolonged exposure. To ensure consistent conditions for each specimen, a dedicated test rig was constructed, as shown in Fig. 12. It consisted of UV lamps placed in containers lined with aluminium foil.

d) Spectrophotometer measurements

The specimens were analysed using a UV–Vi's spectrophotometer, Thermo Scientific Evolution 220, to characterise the optical properties of the investigated coatings. Measurements were performed over the 250–950 nm range, covering ultraviolet radiation, visible light, and the near-infrared region. The first measurement mode was reflectance. This mode is used to analyse the interaction of light with the specimen surface and allows evaluation of the effect of the coating on aesthetic attributes, optical transparency, and gloss. Subsequently, absorbance measurements were carried out to determine the coating's ability to attenuate incident radiation, which is a direct indicator of the effectiveness of paint protection against photodegradation processes, as shown in Fig. 13.

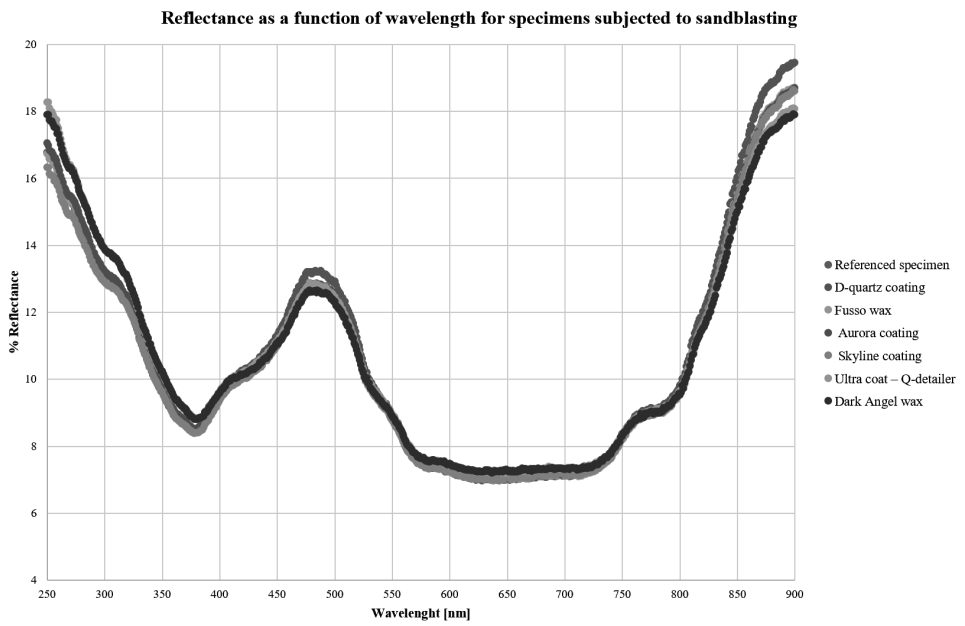

Figure 13 Plot showing the dependence of percent reflectance on wavelength

CONCLUSIONS

Based on qualitative observations of water droplet shape, all applied waxes and coatings improved surface hydrophobicity compared with the unprotected reference. The strongest hydrophobic effect was observed for CarPro D-quartz and Ultracoat Aurora, for which droplets exhibited the most spherical shape. Dark Angel, Ultracoat Ceramic Q-Detailer, and Soft 99 Fusso provided a comparable, moderately high level of hydrophobicity. In contrast, Ultracoat Skyline produced a more flattened droplet profile, indicating a weaker hydrophobic effect relative to the best-performing variants.

After drying with compressed air, an increasing amount of fine residual contamination was observed on the surfaces as the number of washing cycles increased. This indicates a gradual reduction in protective performance, manifested by a decreasing ability to shed and release contaminants during cleaning.

After 250 h of UV exposure, no visible changes in the specimen surfaces were detected under the applied test conditions. The results obtained after extended UV exposure will be reported in subsequent publications.

The reflectance spectra of sandblasted specimens exhibited very similar overall profiles. This suggests that, following abrasive blasting, the measured optical response is governed primarily by the post-blasting surface condition rather than by the coating type. In the 600–730 nm range, the curves almost overlap, indicating comparable reflectance and only minor differences between variants. The largest deviations occur at the spectral extremes, particularly above approximately 820 nm, where reflectance increases markedly. The highest reflectance values, especially in the 850–900 nm range, were obtained for CarPro D-quartz, which may indicate superior retention of surface properties after abrasive blasting. The lowest reflectance values were recorded for Dark Angel wax, whose curve remained consistently lowest, particularly at longer wavelengths.

The lower persistence of hydrophobic behaviour for the quick detailer relative to protective coatings after washing can be attributed to differences in adhesion to the substrate. Quick detailers, primarily formulated as conditioners to enhance surface appearance, typically exhibit limited resistance to degradation under alkaline or acidic cleaning agents and are prone to rapid desorption during routine maintenance. In contrast, long-term coatings are designed to provide a more durable modification of paint surface energy.

A key factor differentiating the investigated systems is their resistance to mechanical and chemical degradation. Spectrophotometric analysis after abrasive blasting supports the superior performance of ceramic-based technology. CarPro D-quartz achieved the highest reflectance in the 850–900 nm range, suggesting that its structure most effectively mitigates permanent surface dulling. Conversely, natural waxes such as Dark Angel demonstrated the lowest resistance, reflected by a pronounced reduction in reflectance after erosive exposure.

Overall, CarPro D-quartz outperformed graphene-based solutions in terms of mechanical protection and the preservation of optical properties under aggressive service-like conditions. Ultracoat Aurora represents an effective option where maximising hydrophobicity is prioritised, showing performance comparable to D-quartz in this respect. Ultracoat Skyline appears to prioritise long-term durability at the expense of slightly reduced self-cleaning performance, reflected by lower hydrophobicity.

BIBLIOGRAPHY

[1] Parlament Europejski i Rada Unii Europejskiej, Dyrektywa 2004/42/WE w sprawie ograniczeń emisji lotnych związków organicznych w wyniku stosowania rozpuszczalników

organicznych w niektórych farbach i lakierach oraz produktach do odnawiania pojazdów. Dziennik Urzędowy Unii Europejskiej L 143, 2004.
[2] Akafuah, N.K.; Poozesh, S.; Salaimeh, A.; Patrick, G.; Lawler, K.; Saito, K. Evolution of the Automotive Body Coating Process—A Review. Coatings 2016, 6, 24. https://doi.org/10.3390/coatings6020024
[3] Streitberger H.-J., Dössel K.-F., Automotive Paints and Coatings, Weinheim, Wiley-VCH Verlag GmbH & Co. KGaA, 2008.
[4] Nirmal U, Musa MA, Yuhazri MY, Ahmad MMHM. Development of Car Coating Materials over the Past Decade for Paint Protection Applications—An Overview on the Different Types of Paint Protections. Polymers. 2025; 17(23):3114. https://doi.org/10.3390/polym17233114
[5] Priyadharshini R, Xavier JR. Recent Advances in Graphene-Based Nanocomposite Coatings for Corrosion Resistance in the Automotive Industry and Their Smart Functional Applications. Journal of Bio- and Tribo-Corrosion. 2025; 11:113.
[6] BUI, Huyen TT; HOANG, Anh Nguyet; LE, Cuong Manh. Study on the Effect of Graphene on Characteristics of Inorganic Polymer Paint. ACS omega, 2025, 10.6: 5503-5516.

ACKNOWLEDGEMENTS

The research was conducted within design-oriented research projects using the Project Based Learning (PBL) approach, in collaboration with the Department of Mechanical and Manufacturing Engineering, Trinity College Dublin, Ireland.

TalentDetector

9th January 2026
Gliwice, Poland

DEPARTMENT OF ENGINEERING MATERIALS AND BIOMATERIALS
FACULTY OF MECHANICAL ENGINEERING
SILESIAN UNIVERSITY OF TECHNOLOGY

INTERNATIONAL STUDENTS SCIENTIFIC CONFERENCE

Mechanical Characteristics of Selected Engineering Materials

Mateusz Marzec[a], Jan Popiołkiewicz[a], Sabina Lesz[b*]

[a] Upper-Secondary Schools of Communications in Gliwice, Warszawska 35, 44-100 Gliwice
[b] Silesian University of Technology, Faculty of Mechanical Engineering, Department of Engineering Materials and Biomaterials, Konarskiego 18a, 44-100 Gliwice
*email: sabina.lesz@polsl.pl

Abstract: In this paper, static hardness measurement methods were described. The results of tests on the mechanical properties (hardness/strength) of selected materials, along with their analysis, are presented. The mechanical characterization of selected engineering materials is of fundamental practical importance, both in the design and manufacture of machine and tool components.

Keywords: mechanical characteristics, steel, hardness, strength

1. INTRODUCTION

Mechanical characterization of engineering materials is one of the pivotal stages in the design, manufacture, and operation processes of machine and tool components. With accurate knowledge of mechanical properties, material selection for specific use conditions can be made correctly, and their reaction to external and environmental stresses can also be predicted [1–2].

A variety of experimental methods are used to ascertain the mechanical properties of metals and their alloys. The most common methods are tensile, compression, torsion, shear tests, and hardness measurements. In these methods, hardness testing is of particular practical significance due to its simplicity, short duration of the test, and the possibility of a non-destructive nature of the test [1–2].

Hardness measurement methods are generally routine in the testing of metals and their alloys, as well as polymers and composites. Their virtues are low test costs, no need for specially prepared surfaces of the specimen, and performance of tests without major interference with material structures. That is why such methods are widely used both in research laboratories and industrial production quality control [1–2].

An important aspect of hardness measurements is the empirical correlation between hardness and tensile strength, particularly in the case of structural steels. This relationship allows for the approximate determination of strength parameters based on hardness measurement results, making this method an extremely useful diagnostic and control tool in materials engineering [1-2].

The main objective of hardness testing is the quantification of the material's resistance to plastic deformation caused by the penetration of an indenter of a specified shape under a given load. Hardness is an indirect measure of the strength of a material, and therefore, its determination allows the mechanical properties of different materials to be compared [1-2].

Different hardness measurement methods are differentiated: static, dynamic, and special. Static hardness testing involves applying a static load to the surface of the material being tested by an indenter. Dynamic testing is associated with the impact deformation of the material. It is mostly static tests that are performed [1–2].

With static measurements, the indenter of the hardness tester forcibly pushes the material surface with a certain force, thus creating an indentation whose depth or size determines the hardness of the material. The less the depth or the smaller the size of the indentation, the harder it is for the tested material. The correct selection of a particular method depends on the tested material type and its geometry, hardness, specimen thickness, as well as measurement purpose, for instance, quality control, comparative studies, or analysis of structural changes due to heat treatment. The most widely used methods for static hardness measurements are Brinell (HBW), Rockwell (HR), and Vickers (HV) methods [1–2].

1.1. Brinell method

The Brinell method of hardness measurement is performed with an indenter in the form of a composite ball made of sintered carbides (previous standards permitted the use of a steel ball). In the Brinell hardness test, the diameter of the indentation left by the indenter is measured (Fig.1). The measurement procedure is specified in the PN-EN ISO 6506-1:2014-12 standard [3].

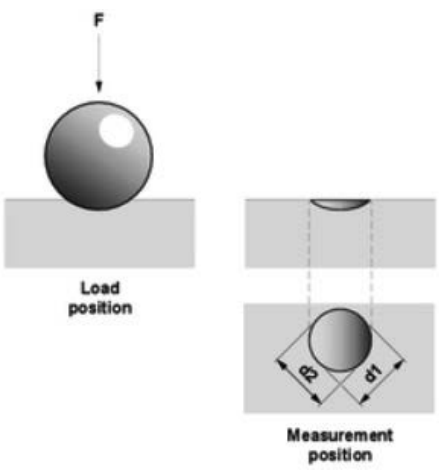

Figure 1. Diagram of hardness measurement using the Brinell method [5]

The ball diameter may be 1, 2.5, 5, or 10 mm; the loading time may be 10, 15, or 20 seconds; and the applied force may range from 9.807 to 29420 N (1–3000 kgf). All parameters are dependent on the material and the thickness of the specimen [3–5].

Hardness is a measure of the ratio of the applied force to the surface area of the indentation and is obtained using the following formula [3]:

$$HBW = \frac{0{,}204F}{\pi D\left(D-\sqrt{D^2-d^2}\right)} \quad (1)$$

F – applied force [N], D – indenter diameter [mm], d – indentation diameter [mm].

1.2. Rockwell method

The indenter in the Rockwell method is either a diamond cone with an apex angle of 120° and a rounding radius of 0.2 mm or a steel ball with a diameter of 1.5875 mm (1/16”) or 3.175 mm (1/8”) [6–8].

The depth of the penetration made by the indenter is the parameter that is measured in this method (Fig. 2). The measurement procedure is described in the ISO 6508-1:2023 standard [6].

At first, the preliminary load F_0 is used to press the indenter into the material. After that, the main load Fm is put on for the time specified by the standard. The indenter goes the deepest under this load. The total force F is the summation of the two forces. Hardness is expressed as the difference in penetration depth before and after the total test force application [6–8].

a) b)

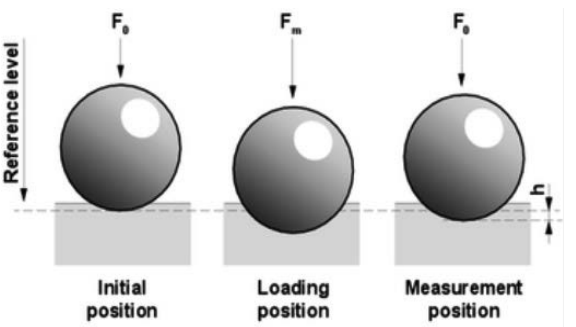

Figure 2. Hardness tester (a) and measurement diagram (b) using the Rockwell method [8]

1.3. Vickers method

In the Vickers hardness test, the metal surface is subjected to pressure by a diamond pyramid with a square base and an apex angle of 136°. Then, after removing the loading force, the lengths of the diagonals of the indentation formed on the surface are measured (Fig. 3) [9–11].

Numerical hardness is the ratio of the force applied to the surface area of the indentation [9]:

$$HV = \frac{0{,}1891F}{d^2} \quad (2)$$

F – applied test force [N], d – indentation diagonal [mm].

The duration of the test force is typically 10–15 seconds. The test forces used in this method are usually lower than those used in the Brinell method. For the macro range, 49, 98, 196, 294, 490, and 980 N are used. The measurement procedure is described in the ISO 6507-1:2023 standard [9].

a) b)

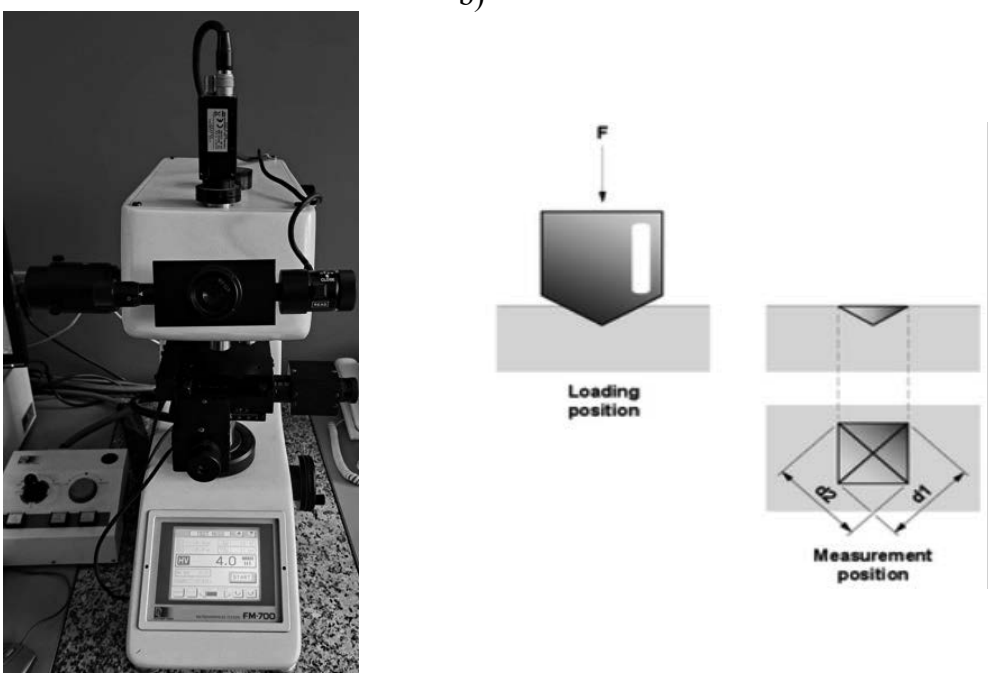

Figure 3. Hardness tester (a) and measurement diagram (b) using the Vickers method [11]

1.4. Hardness and strength

The value of hardness obtained as a result of measurement is an indirect indication of resistance to plastic deformation and damage of the surface by a material. Apart from the homogeneity of the material structure, the presence of thermal or technological defects, and the effectiveness of the applied heat or thermochemical treatment processes, these can also be determined on the basis of hardness test results [1-2].

In the case of structural and low-alloy steels, a well-defined correlation can be found between hardness and tensile strength (Rm). This relationship is of an empirical nature and serves as a rough material strength indication without the need for a full tensile test. For most carbon and low-alloy steels, the following rough relationship may be considered:

$$R_m \approx k \cdot HBW \quad (3)$$

The proportionality coefficient value k, which depends on hardness, is 3.33 for steels with hardness in the range of 125–175 HB and 3.53 for steels with hardness above 175 HB.

Determining hardness across the cross-section of a component also makes it possible to assess the depth of the layer that has been hardened, e.g., after carburizing, nitriding, or surface quenching, and the degree of its uniformity. When it comes to coatings and thin layers, Vickers hardness with a small load makes it possible to determine surface microhardness with high accuracy [1-2].

1.5. Measurement errors and factors affecting test results

The precision of the hardness measurement results depends on many metrological, material, and technological factors. The most important of them are:

- Surface condition of the specimen - roughness, oxidation, or contamination may alter readings; thus, the surface should be both smooth and clean.
- Specimen thickness - an excessively thin specimen may experience local deformation or perforation, thus resulting in incorrect outcomes.
- Loading conditions - the wrong selection of the test force or its duration may cause deviations in the results.
- Shape and condition of the indenter - wear or contamination of the indenter leads to distortion of the indentation and lessens measurement precision.
- Local material inhomogeneities - non-metallic inclusions, pores, or structural variations may cause the scatter of the results.
- Reading errors - in optical methods (Brinell, Vickers), inaccuracy in measuring the diameter or diagonals of the impression is one of the main sources of uncertainty.

To get rid of the effect of these factors, it is advisable to carry out a number of measurements at points different from one another on the specimen and then compute the average. In laboratory practice, it is also very important to keep the constant measurement conditions and perform periodical calibrations of the hardness tester [1-2].

2. MATERIALS AND METHODS

The tests involved steel specimens with varying carbon contents. According to the Polish standard PN-EN ISO 683-1:2018-09 [12], steel can be defined as a material that contains more iron by mass than any other element, with a carbon content of less than 2%, and that also contains other elements. The test specimens also comprised C45 steel in different technological states (before heat treatment - as-received condition, after normalizing, and after quenching). The chemical composition of C45 steel is shown in Table 1. Normalizing is used after different metal processing and joining operations (forging, welding, and machining). Heating metal and other metals to the quenching temperature and then cooling them rapidly is what makes metal stronger; however, less prone to plastic deformation is the quenched steel.

The hardness of the materials was measured by Brinell, Rockwell, and Vickers methods in accordance with the relevant standards [3, 6, 9]. The strength of the materials was calculated from the hardness data through the use of relationship (3). In the Brinell hardness test, a load of F = 29,420 N and a loading time of 15 s were used. The ball indenter diameter was D = 10 mm. In the Vickers hardness test, loads of 300 gf and 500 gf with loading times of 15 s and 20 s were used. Rockwell hardness tests were performed on scales B and C. The loading times for F_0 and F were 1-8 s and 2-6 s, respectively.

Table 1. The chemical composition of the C45 steel [12-13]

Element	Mass concentration [%]
Carbon	0.42 – 0.50
Silicon	0.10 – 0.40
Manganese	0.50 – 0.80
Chromium	>0.40
Nickel	>0.40
Molybdenum	>0.10
Sulfur	>0.04
Phosphorus	>0.04

3. RESULTS

3.1. Brinell method

For steels with different carbon contents (0.1, 0.2, 0.3, 0.45, 0.55, and 0.9 wt.% C) Brinell hardness measurements were made. A 10 mm diameter indenter and a load of 29,420 N were the main tools used in the experiment. With the help of a scale (in mm) and a magnifying glass, the diameters of the indentations were determined. The obtained values were used in formula (1). The hardness values that have been calculated are displayed in Fig. 4a. The strength of the tested materials was determined based on the hardness results using the relationship (3) and illustrated in Fig. 4b.

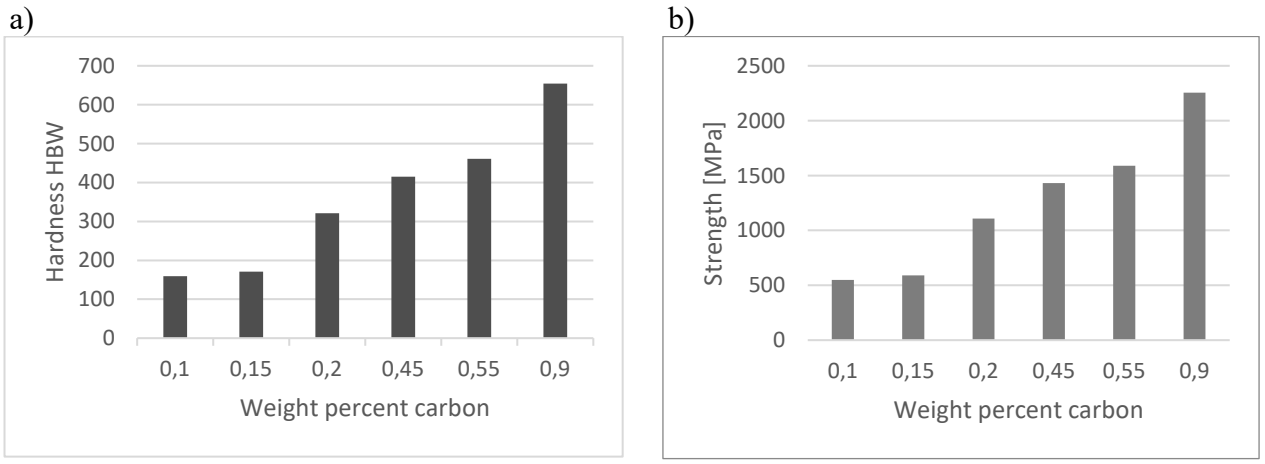

Figure 4. Graphs showing changes in HBW hardness (a) and strength (b) as a function of weight percent carbon in steel.

3.2. Rockwell method

Rockwell hardness test results for C45 steel in three states: as-received condition, after normalizing, and after quenching were 94.5 HRB, 94.6 HRB, and 62 HRC, respectively. The photographs of the instrument, on which sample hardness values were recorded, are shown in Fig. 5a and 5b.

a) b)

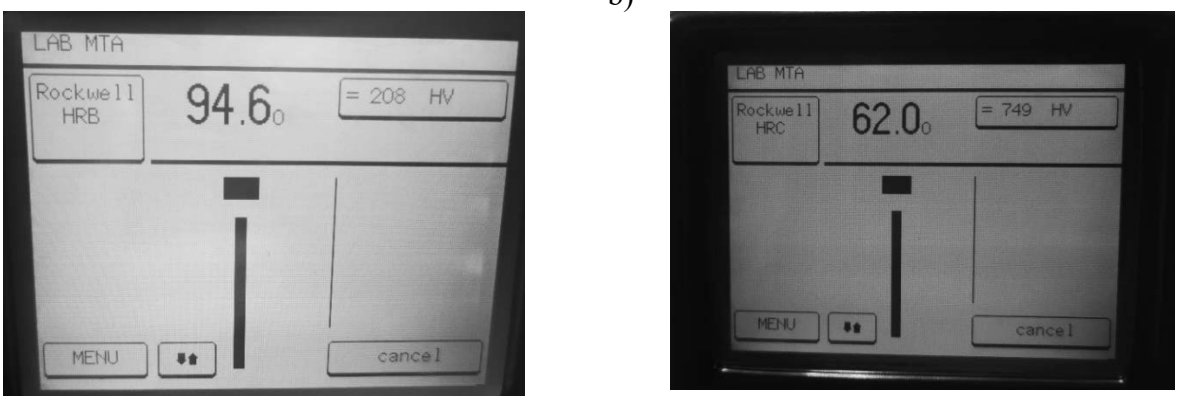

Figure 5. Example of Rockwell hardness data for a C45 steel sample in as-received condition (a) and after quenching (b).

3.3. Vickers Method

Vickers hardness testing results for C45 steel in three states are the as-received condition, after normalizing annealing, and after quenching are presented in Fig. 6. Fig. 6b, c show the metal structure and the indentation left by the indenter, respectively (Fig. 6b, c).

a) b)

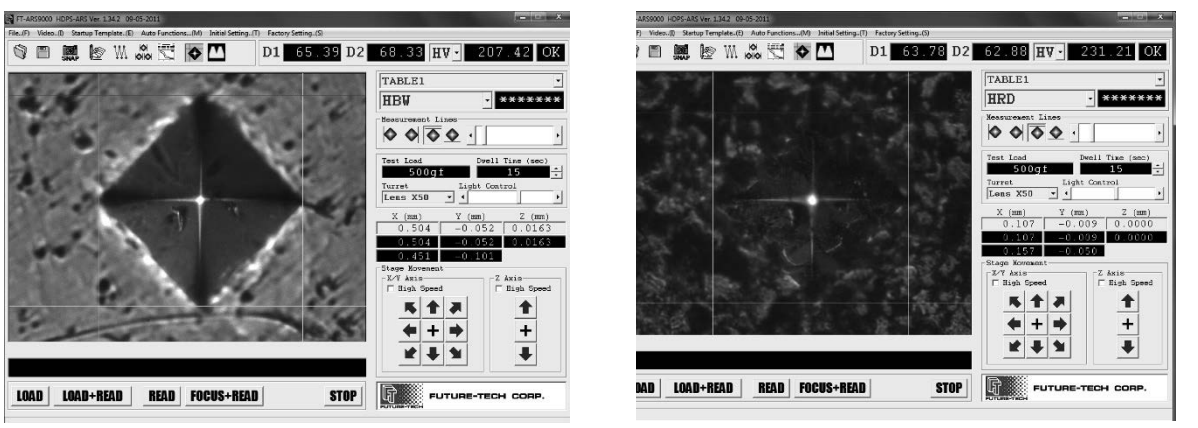

c)

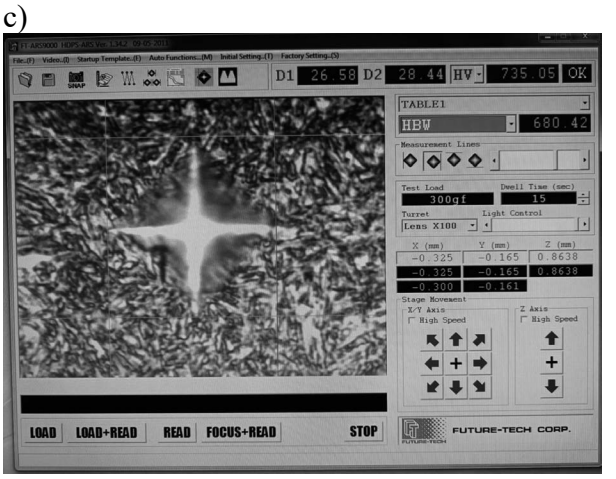

Figure 6. Example of Vickers hardness data for a C45 steel sample in as-received condition (a), after normalizing (b), and after quenching (c), presented in the FT-ARS9000 software.

4. CONCLUSIONS

The mechanical properties of engineering materials are those that depict their reaction to external forces and include not only strength and hardness, but also ductility and impact toughness. In addition, these properties are supplemented with elasticity, plasticity, fatigue resistance, and resistance to creep and wear. The specific combination of these properties determines the suitability of a material for a given application.

Key mechanical properties (hardness and strength) of selected engineering materials have been determined based on the measurements performed. There was observed a relationship between the chemical composition and the hardness of the material obtained. The analysis of the results reveals that the samples that were quenched, as well as those that had higher carbon content, showed substantially higher hardness than the other samples. Thus, depending on the usage and working conditions (e.g., high loads), the right technological processes are chosen to change the mechanical properties (hardness and strength) of metals and alloys in the solid state by bringing about structural changes.

ACKNOWLEDGMENT

This paper is the result of a project carried out with secondary school students under the Excellence Initiative - Research University program (6th competition), Silesian University of Technology.

BIBLIOGRAPHY

1. L.A. Dobrzański, Materiały inżynierskie z podstawami technologii procesów materiałowych, Wydawnictwo Naukowe PWN, 2024.
2. L.A. Dobrzański, Metaloznawstwo: z podstawami nauki o materiałach, Wydawnictwa Naukowo Techniczne WNT, 1996.
3. EN ISO 6506-1:2014-12. Metallic materials – Brinell hardness test. Part 1: Test method
4. https://pl.wikipedia.org/wiki/Skala_twardo%C5%9Bci_Brinella
5. https://www.zwickroell.com/pl/branze/metal/normy-metal/brinell-badanie-iso-6506/
6. ISO 6508-1:2023. Metallic materials — Rockwell hardness test. Part 1: Test method
7. https://pl.wikipedia.org/wiki/Skala_twardo%C5%9Bci_Rockwella
8. https://www.zwickroell.com/pl/branze/metal/normy-metal/rockwell-badanie-iso-6508/
9. ISO 6507-1:2023 Metallic materials — Vickers hardness test. Part 1: Test method
10. https://pl.wikipedia.org/wiki/Skala_twardo%C5%9Bci_Vickersa
11. https://www.zwickroell.com/pl/branze/metal/normy-metal/vickers-badanie-iso-6507/
12. PN-EN ISO 683-1:2018-09. Quenched and tempered steels - Part 2: Technical delivery conditions for unalloyed quality steels.
13. https://www.kronosedm.pl/stal-stal-c45-1-0503/

TalentDetector
9th January 2026
Gliwice, Poland
DEPARTMENT OF ENGINEERING MATERIALS AND BIOMATERIALS
FACULTY OF MECHANICAL ENGINEERING
SILESIAN UNIVERSITY OF TECHNOLOGY
INTERNATIONAL STUDENTS SCIENTIFIC CONFERENCE

Direct conversion of solar energy into electricity using solar cells

Adrian Mateja[a], Maksymilian Kwitek[a], Jakub Budzynowski[b], Oskar Górka[b], Eva Tillová[c], Peter Palček[c] Sabina Lesz[d], Aleksandra Drygała[d]

[a] Pupil, Complex of Secondary Vocational Schools No. 2, Szpitalna 29, 44-194 Knurów, Poland
[b] Student, Silesian University of Technology, Faculty of Mechanical Engineering, Konarskiego 18a, 44-100 Gliwice, Poland
[c] University of Zilina, Faculty of Mechanical Engineering, Department of Materials Engineering, Univerzitná 1 Str., 010 26 Zilina, Slovak Republic
[d] Silesian University of Technology, Faculty of Mechanical Engineering, Department of Engineering Materials and Biomaterials, Konarskiego 18a, 44-100 Gliwice, Poland
email: aleksandra.drygala@polsl.pl

Abstract: In this work, the electrical properties of monocrystalline silicon solar cells are presented. Solar energy is one of the most important forms of renewable energy on Earth and a key element of strategies for energy transition and economic decarbonization. Solar cells enable the direct conversion of solar radiation into electricity through the photovoltaic effect occurring in semiconductors. The determination of the electrical properties of solar cells is fundamental to assessing their quality, efficiency, and reliability.

Keywords: renewable energy sources, photovoltaics, solar cell, silicon, current–voltage characteristic

1. INTRODUCTION

Photovoltaic (PV) technologies are a key element of the energy transition and obtaining energy from renewable sources. Solar cells enable the direct conversion of sunlight into electricity, increasing the share of clean, emission-free energy. Approximately 89 PW reach the Earth's surface, which translates to an average of approximately 180 W/m². This power is not evenly distributed, as an area illuminated by light incident perpendicularly from above can receive up to 1000 W/m². The total energy reaching a horizontal surface throughout the year ranges from 600 kWh/m² in Scandinavian countries to over 2500 kWh/m² in Central Africa. In Poland, it is approximately 1100 kWh/m² per year. The total power used by humans is approximately 18 TW, or about 0.02% of the solar radiation power [1]. Technological advances are lowering production costs, reducing dependence on fossil fuels, and supporting the energy transition towards sustainable, local, and environmentally friendly energy systems. Photovoltaic modules used both in ground-mounted installations and in buildings, where solar cells are integrated into the building structure (BIPV) [2]. Advances in materials, design, and measurement methods are making these devices increasingly efficient and durable [3].

1.1. Classification of solar cells

Solar cells are commonly classified into three main generations, which differ in the materials used, manufacturing technologies, optical properties, and achievable power conversion efficiency. The first generation includes monocrystalline and polycrystalline silicon solar cells, which are based on classic p–n junction technology. Modern monocrystalline silicon solar cells manufactured using PERC, TOPCon or heterojunction technologies currently reach efficiencies in the range of 24–26% in laboratory conditions, while commercial modules typically achieve 21–23 % [4, 5]. Polycrystalline silicon, composed of multiple crystalline grains, exhibits lower structural order. As a result, solar cells made from this type of silicon achieve efficiencies that are a few percent lower (17÷19 %). Their industrial relevance has been decreasing in recent years due to lower performance compared to monocrystalline structures [4, 6].

The second generation consists of thin-film solar cells, which include technologies based on CdTe, CIGS (Copper Indium Gallium Selenide), and amorphous silicon. These solar cells are characterized by the deposition of absorber layers with thicknesses of only a few micrometers or less, which significantly reduces the consumption of raw materials and lowers production costs. Modern CdTe modules reach efficiencies of 22–23 % in laboratory conditions, whereas CIGS structures attain 23–24 %, representing the highest values among commercial thin-film technologies [7, 8]. Amorphous silicon remains the least efficient, typically achieving 10 ÷ 12 %, but it is used where low cost and flexibility are required [7].

The third generation of solar cells includes innovative technologies beyond traditional silicon cells, such as dye-sensitized solar cells (DSSCs), perovskite solar cells, quantum dot solar cells, and various tandem and multi-junction configurations, which aim to significantly increase efficiency while reducing production costs. Perovskite single-junction solar cells have recently surpassed 26 % efficiency in laboratory tests, showing the fastest development among all photovoltaic technologies [9]. Organic solar cells currently reach efficiencies of 19–20% for non-fullerene acceptors, benefiting from low-temperature processing and high mechanical flexibility, although their long-term stability remains a challenge [10]. The most promising technology in this group is perovskite-silicon tandem solar cells, which in 2024–2025 reached record efficiencies exceeding 33.7 %, surpassing the theoretical limit for single-junction silicon devices and establishing new performance benchmarks for the photovoltaic industry [9, 11].

1.2. Solar cell structure and operation

A typical solar cell consists of several distinct functional layers, each of which plays a role in converting light into electricity. The basic element of a solar cell is a silicon wafer, made of monocrystalline or polycrystalline silicon. It is most often p-doped (e.g., with boron), which means holes predominate as charge carriers. A thin layer of n-doped silicon (usually with phosphorus) is formed on the substrate surface. This creates a p-n junction, a key element enabling the separation of electron-hole pairs generated by solar radiation. A thin antireflection layer, most often made of silicon nitride (SiN_x), is applied to the top surface of the solar cell. Its purpose is to reduce light reflection from the solar cell surface and increase the amount of radiation penetrating the silicon. Additionally, passivating and protective layers are often used to prevent surface recombination, stabilize the semiconductor surfaces, and protect the device

from environmental degradation. On the top side, where the light enters, there is usually a grid of electrical contacts consisting of busbar electrodes and series of collecting tracks. Their task is to receive electrons with minimal shading of the active surface of the solar cell. The back side of the solar cell is covered with a metallic layer, which provides electrical contact for the p-type region and acts as a reflector, increasing the optical path of light in the material. The silicon surface is textured, which reduces light reflection and increases its effective absorption in the silicon [2].

The operation of a solar cell is based on the photovoltaic effect. Photons with energy equal to or greater than the semiconductor bandgap are absorbed within the active material, leading to the excitation of electrons from the valence band to the conduction band and the simultaneous creation of electron–hole pairs. The p–n junction formed within the semiconductor generates an internal electric field in the depletion region, which efficiently separates the photogenerated charge carriers. Electrons are driven toward the n-type region, while holes are transported toward the p-type region and collected by the corresponding electrical contacts. When the external circuit is closed, the directional movement of charge carriers gives rise to an electric current. In this way, the energy of incident solar radiation is directly converted into electrical energy, with the output power depending on factors such as the intensity and spectral distribution of sunlight, as well as the material properties and design of the solar cell [3].

1.3. Electrical properties of solar cells

The electrical behavior of a solar cell is mainly described by its current-voltage (I-V) characteristic, which is measured under Standard Test Conditions (STC). The STC were defined to standardize the measurement of solar cell parameters and to enable direct comparison across different laboratories, manufacturers, and technologies. The STC are defined as an irradiance of 1000 W/m², a solar cell temperature of 25°C, and a solar spectrum defined as Air Mass AM 1.5. The I-V curve supplies the necessary information about the behavior of the solar cell while irradiated, reflecting the processes going on inside the device, such as charge carrier generation, recombination, and resistive losses [12, 13].

From the I-V characteristic, several basic electrical parameters can be extracted. The open-circuit voltage (V_{oc}) is the maximum voltage generated when no current flows, and it reflects the quality of the photovoltaic junction. The short-circuit current I_{sc} is the maximum current generated under illumination when the external circuit is shorted, and it is directly related to the device's ability to absorb photons and collect charge carriers. Power at the maximum power point P_{mpp} is the operating condition for which the solar cell delivers its highest output power and is obtained by multiplying the voltage and current at the optimal operating point. The total conversion efficiency, η, is the ratio of electrical power at the MPP to the intensity of incident solar radiation and serves as the primary metric for comparing different photovoltaic technologies. Another important parameter is the fill factor, which indicates how closely the current–voltage (I–V) characteristic approaches an ideal rectangular shape. It is defined as the ratio of the maximum obtainable power (P_{mpp}) to the product of the open-circuit voltage (V_{oc}) and the short-circuit current (I_{sc}). A high fill factor indicates low internal resistive losses and efficient carrier transport within the material, making it a key indicator of the cell's quality and performance. These parameters together give a full representation of the electrical performance of the solar cells and form the basis for assessing technological process, quality of operation, and possibilities of their further exploitation [12, 14].

1.4. Future development outlook

The future of photovoltaics is expected to be shaped by advances in materials, device architectures, and system integration, all aimed at increasing efficiency, sustainability, and economic competitiveness. Research is increasingly focused on novel materials, such as halide perovskites, tandem solar cells, and organic–inorganic hybrids, which offer the potential to combine high efficiency with low production costs [4, 5]. In parallel, developments in recycling and reuse of photovoltaic components, along with the use of abundant and non-toxic elements, contribute to reducing the environmental impact and enhance the sustainability of PV technologies [14]. Emerging applications, such as building-integrated photovoltaics (BIPV), agrivoltaics, and flexible or portable solar devices, are likely to broaden the reach of solar energy and create new opportunities for energy production in diverse environments. Coupled with the development of smart energy systems and improved energy storage solutions, these innovations are expected to play a key role in meeting future energy demands sustainably and cost-effectively [13-15].

The potential of solar cells can be assessed by examining their conversion efficiency, cost-effectiveness, and suitability for specific applications. Key factors include local solar irradiance, climate conditions, installation type (rooftop, ground-mounted, or BIPV), and material properties. By analyzing these aspects, it is possible to estimate the energy yield, economic viability, and environmental impact of PV systems, guiding decisions on deployment and optimization [13].
In this work, the electrical properties of monocrystalline silicon solar cells are determined.

2. MATERIALS AND METHODS

Five monocrystalline silicon solar cells of unknown origin, measuring 5 cm x 5 cm, with one main busbar, were used for the tests. To determine the electrical properties of monocrystalline silicon solar cells, a special PV Test Solutions System SS I V CT 02 was used (Fig.1).

The test station includes a solar simulator, a measurement system with a data acquisition system, a measuring table equipped with probes, and a table temperature control unit. The solar simulator meets the requirements of the measurement class AAA. It provides uniform light intensity over a 15 x 15 cm area. Combined with an I-V characteristic measurement system, the simulator enables accurate testing of the current-voltage characteristics of solar cells under standard test conditions (STC), i.e., a temperature of 25°C, a solar irradiance of 1000 W/m², and an AM1.5 spectrum.

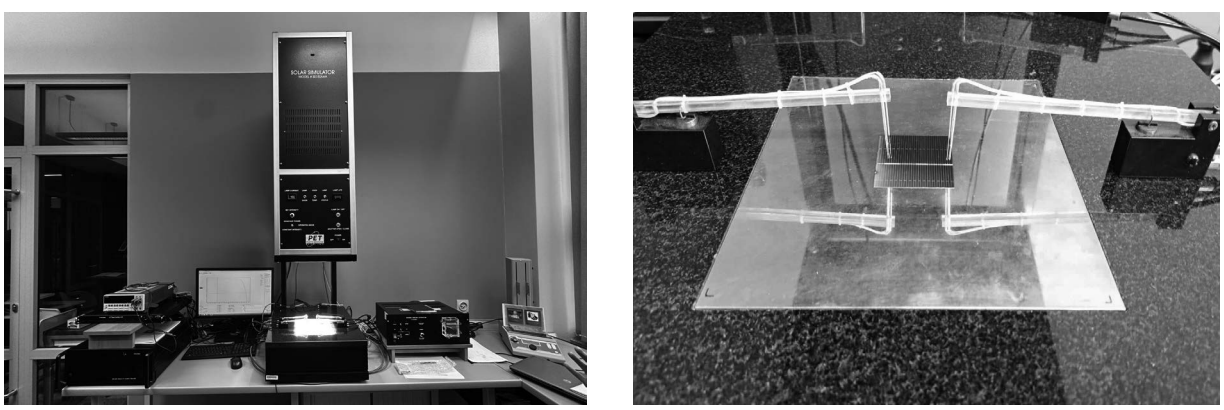

Figure 1. SS I-V CT-02 System for measuring of current-voltage characteristics of solar cells

3. RESULTS

This study examined the electrical properties of five monocrystalline solar cells. Macroscopic observations revealed a grid of electrical contacts on the front surface of the device, including one busbar and a series of collecting fingers (Fig. 2). Silver (Ag) in the form of screen-printed paste is primarily used for its fabrication due to its excellent electrical conductivity, good adhesion to silicon, and chemical stability. Despite the high cost of silver, its properties enable the achievement of low contact resistance and high solar cell efficiency [16]. Furthermore, the solar cells are navy blue, which indirectly indicates that an antireflection layer, e.g., silicon nitride (Si_3N_4) or titanium dioxide (TiO_2) [17], is applied to the surface.

It has been observed that the rear electrode covers the entire surface of the solar cell (Fig.3). Additionally, each device is equipped with a rear connection contact. The rear electrode of the solar cell is most commonly made of aluminium, which is characterized by good electrical conductivity, low cost, and ease of application, for example by screen printing. The rear connection contact provides a durable and electrically stable connection between the rear electrode and the subsequent components of the circuit within the photovoltaic module [18].

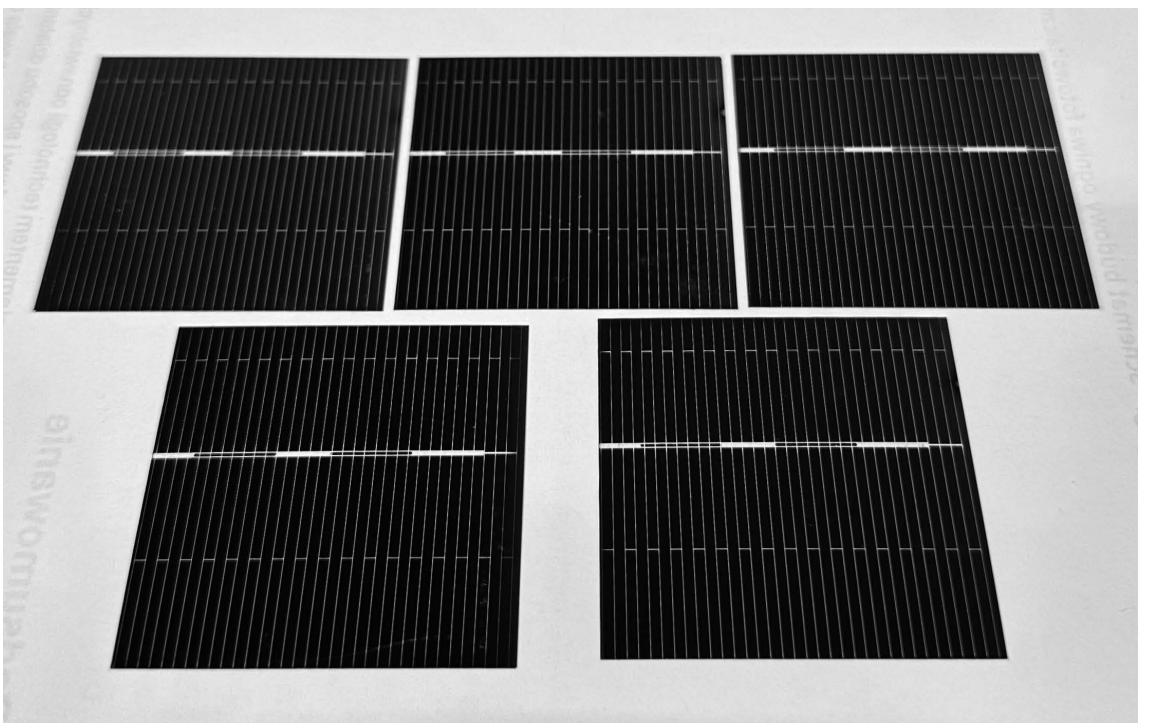

Figure 2. The front surface of monocrystalline silicon solar cells of unknown origin subjected to electrical property tests.

The Figure 4 shows the current-voltage characteristics of the five tested monocrystalline silicon solar cells, based on which the electrical properties were determined (Table 1). The current voltage characteristics of each of the five solar cells are very similar. The average efficiency of the tested solar cells is 19.84 %, with the highest (20.10 %) and lowest (19.67 %) values obtained for solar cells No. 4 and No. 1, respectively. The small differences in electrical properties indicate a high repeatability of the solar cell manufacturing process.

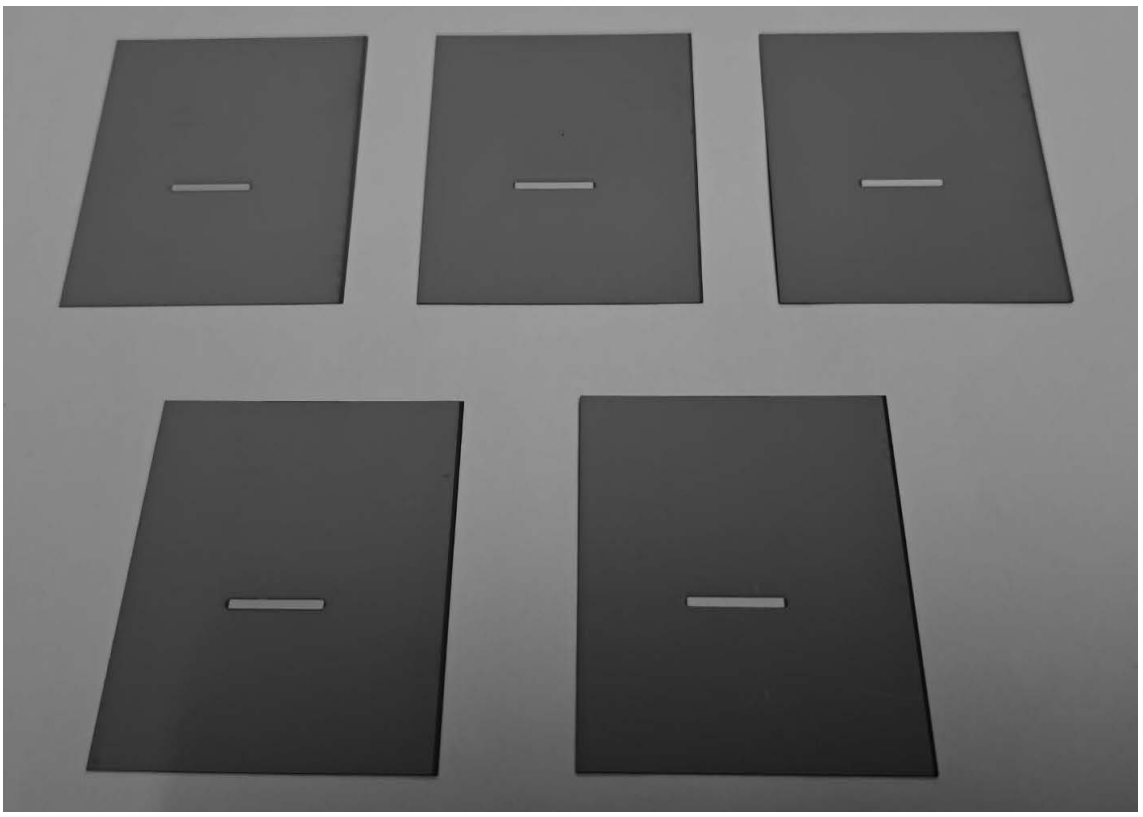

Figure 3. The back surface of monocrystalline silicon solar cells of unknown origin subjected to electrical property tests.

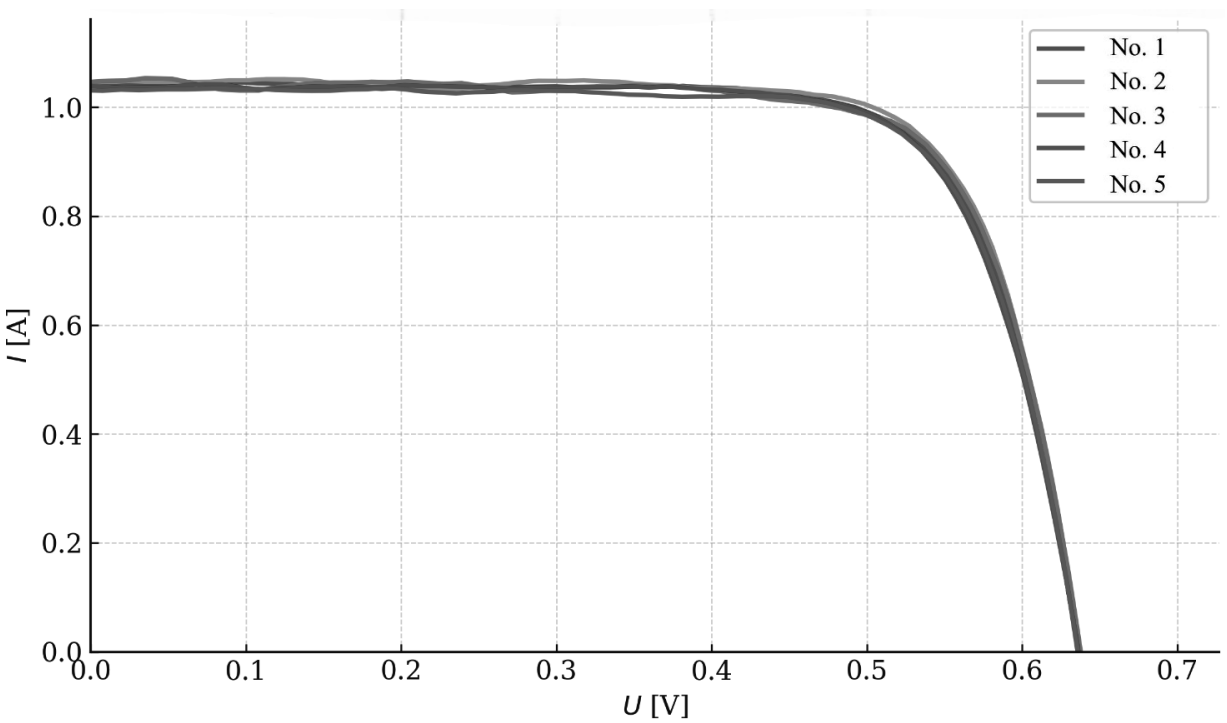

Figure 4. Current-voltage characteristics of the tested solar cells

Table 1. Test results of electrical properties of monocrystalline silicon solar cells

Solar cell	I_{sc} [A]	V_{oc} [V]	I_m [A]	V_m [V]	P_m [W]	FF [-]	E_{ff} [%]
No. 1	1.033	0.636	0.964	0.514	0.496	0.76	19.67
No. 2	1.038	0.636	0.972	0.512	0.498	0.75	19.70
No. 3	1.049	0.638	0.962	0.522	0.502	0.75	19.90
No. 4	1.045	0.638	0.980	0.518	0.508	0.76	20.10
No. 5	1.042	0.636	0.970	0.516	0.501	0.76	19.84

4. CONCLUSIONS

Solar energy is the primary energy source on Earth. It influences temperature, climate, and processes occurring in the atmosphere and hydrosphere. It enables photosynthesis, which is the foundation of plant life and entire ecosystems. Solar energy is also a source that humans can utilize in environmentally friendly way. Solar cells directly convert solar energy into electricity, allowing for electricity generation without burning fuels or emitting polluting emissions. They reduce energy costs and increase energy independence. They play a crucial role in the development of renewable energy sources while simultaneously reducing the negative impact of human activity on the climate. It was found that the average efficiency of the tested monocrystalline silicon solar cells is 19.84%. They exhibit good and consistent electrical parameters, which is important for their future performance in photovoltaic modules.

Solar cells possess significant potential for contributing to sustainable energy generation. Their ability to directly convert solar energy into electricity offers a clean, renewable alternative to fossil fuels, reducing greenhouse gas emissions and dependence on non-renewable resources. The continuous advancements in solar cell efficiency, materials engineering, and module integration enable wider application in residential, commercial, and industrial sectors. Furthermore, the scalability of PV technology - from small rooftop installations to large utility-scale photovoltaic power plants - provides flexibility in energy planning and grid integration. Given the global push toward decarbonization and the decreasing cost of solar technologies, solar cells are poised to play a key role in future energy systems, supporting both energy security and environmental sustainability.

BIBLIOGRAPHY

1. hydroglob.pl/energetyka-sloneczna-wykorzystywanie-i-perspektywy-rozwoju.
2. A. Herez, H. Jaber, H. El Hage, T. Lemenand, M. Ramadan, M. Khaled, A review on the classifications and applications of solar photovoltaic technology, AIMS Energy, 11(6) (2023) 1102–1130.
3. E.K. Solak, E. Irmak, Advances in organic photovoltaic cells: a comprehensive review of materials, technologies, and performance, RSC Advances, 13 (2023) 12244–12269.
4. M.A. Green, E.D. Dunlop, J. Hohl-Ebinger, M. Yoshita, N. Kopidakis, X. Hao, Solar cell efficiency tables (Version 64), Progress in Photovoltaics 32 (2024) 425-441.
5. International Technology Roadmap for Photovoltaic (ITRPV), 2024. Available: https://www.itrpv.org.

6. Fraunhofer ISE, Photovoltaics Report, 2024. Available: https://www.ise.fraunhofer.de/en/publications/studies/photovoltaics-report.html.
7. First Solar, Technology Overview and Performance Roadmap, 2023–2024.
8. P. Mwenda, , W. Njoroge, S. Mirenga, D. Kinyua, Review: Advances in the CIGS Thin Films for Photovoltaic Applications. Smart Grid and Renewable Energy 13 (2022) 75-87.
9. National Renewable Energy Laboratory (NREL), Best Research-Cell Efficiencies Chart, 2025. Available: https://www.nrel.gov/pv/cell-efficiency.html.
10. L. Zhu, M. Zhang, Z. Zhou, W. Zhong, T. Hao, S. Xu, R. Zeng, J. Zhuang, X. Xue, H. Jing, Y. Zhang, F. Liu, Progress of organic photovoltaics towards 20% efficiency, Nature Reviews Electrical Engineering 1 (2024) 581-596.
11. J. Liu, Y. He, L. Ding, et al., Perovskite/silicon tandem solar cells with bilayer interface passivation, Nature 635 (2024) 596-603.
12. M. Prokopiuk vel Prokopowicz, M. Szindler, L. Dobrzański, A. Drygała, Wyznaczanie własności elektrycznych krzemowych ogniw fotowoltaicznych, w: SO-KÓŁ'14, Prace Studenckich Kół Naukowych, Instytut Materiałów Inżynierskich i Biomedycznych, Politechnika Śląska 29 (2014) 63–68.
13. P. Sharama, R. K. Mishra, Comprehensive study on photovoltaic cell's generation and factors affecting its performance: A Review, Materials for Renewable and Sustainable Energy, 14 (2025) 21.
14. E. Gerold, H. Antrekowitsch, Advancements and Challenges in Photovoltaic Cell Recycling: A Comprehensive Review, Sustainability, 16(6) (2024) 2542.
15. M. Noman, Z. Khan, S.T. Jan, A comprehensive review on the advancements and challenges in perovskite solar cell technology, RSC Advances, 14 (2024) 5085–5131.
16. J.D. Fielsds, Md. I. Ahmad, V.L. Pool, J. Yu, D.G. B. Campen, P.A. Parilla, M.F. Toney, M.F.A.M. van Hest, The formation mechanism for printed silver-contacts for silicon solar cells, ature Communications 7 (2016) 11143.
17. A. Diaw, A. Dieye, O Ngom, M. Diagne, N. Mbenque, O.A. Niase, B. Ba, Optimization of Antireflective Layers of Silicon Solar Cells: Comparative Studies of the Efficiency Between Single and Double Layer at the Reference Wavelength, American Journal of Physics and Applications, 9(6) (2021) 133-138.
18. H.M. Lee, Y.J. Kim, Preparation of size-controlled fine Al particles for application to rear electrode of Si solar cells, Solar Energy Materials and Solar Cells 95(12) (2011) 3352-3358.

TalentDetector

9th January 2026
Gliwice, Poland

DEPARTMENT OF ENGINEERING MATERIALS AND BIOMATERIALS
FACULTY OF MECHANICAL ENGINEERING
SILESIAN UNIVERSITY OF TECHNOLOGY

INTERNATIONAL STUDENTS SCIENTIFIC CONFERENCE

Investigation of mechanical damage to aircraft landing gear components

Dawid Matuszak[a], Piotr Kubica[a], Marianna Muszyńska[a], Daniel Pakuła[b], Marcin Staszuk[b]

[a] Student of Silesian University of Technology, Faculty of Mechanical Engineering, Konarskiego 18A, 44-100 Gliwice, Poland
[b] Silesian University of Technology, Faculty of Mechanical Engineering, Department of Engineering Materials and Biomaterials, Konarskiego 18A, 44-100 Gliwice, Poland
email: marcin.staszuk@polsl.pl

Abstract: The article presents an analysis of the causes of damage to an aircraft landing gear sleeve made of high-strength 30HGSNA steel. The research methodology, including verification of the chemical composition and a detailed fractographic analysis of the fracture surface using scanning electron microscopy (SEM), is described. Based on the observed morphological features, the failure mechanism was identified as a fatigue process. The paper characterizes two main fracture zones: the zone of transcrystalline fatigue crack propagation, characterized by the presence of flat areas and steps, and the zone of ductile fracture with a dimpled structure, formed as a result of the rapid rupture of the component following critical weakening of the effective cross-section.

Keywords: 30HGSNA steel, material fatigue, SEM

1. INTRODUCTION

In post-accident investigations and engineering analyses, fracture morphology constitutes a key diagnostic tool, enabling the precise distinction between failures resulting from a single overload and processes of long-term degradation. Immediate failure occurs when the applied load exceeds the material strength, which, depending on the temperature and loading rate, can proceed according to two extreme mechanisms. Brittle fracture is a sudden and violent process occurring with negligible macroscopic plastic deformation through the direct breaking of bonds in cleavage planes. Once the crack reaches a critical size, its propagation proceeds uncontrollably at a speed close to that of elastic waves, leaving a bright and shiny fracture surface. This mechanism dominates particularly at low temperatures and in the presence of notches, which favor stress concentration. The opposite of this phenomenon is ductile fracture, a highly energy-absorbing process typical for materials undergoing significant plastic deformation before final separation. This process involves the nucleation and coalescence of microvoids around non-metallic inclusions and shearing in slip planes, which macroscopically manifests as the occurrence of necking and a matte, fibrous fracture structure [1].

A separate and extremely important failure mechanism in aviation engineering is material fatigue, defined as structural degradation under the influence of cyclic variable loads occurring at stresses significantly lower than the yield point. The entire fatigue failure process proceeds in three characteristic and consecutive stages. The first of these is crack nucleation, which is most often initiated on the component surface in areas with stress concentrators, such as geometric defects, slip bands, or defects like extrusions and intrusions. After the crack is initiated, the stage of its stable growth follows, consisting of transcrystalline propagation into the material. Each load cycle results in a microscopic increase in crack length, which is reflected on the microstructural scale in the form of characteristic fatigue striations visible on the fracture surface. The last stage is the final fracture, which has the character of sudden immediate failure. It occurs when the remaining, undamaged effective cross-section of the element becomes too small to carry the applied load, leading to a rapid exceeding of the rupture strength and the final failure of the component [2].

2. MATERIAL AND RESEARCH METHODOLOGY

The subject of the research is a damaged structural component identified as an aircraft landing gear sleeve (Fig. 1). It was manufactured from 30HGSNA steel – a high-quality low-alloy grade dedicated to operation under extreme loading conditions (Table 1) [3]. The key distinguishing feature of this material compared to its more popular equivalent, 30HGSA, is the addition of nickel. This element performs a dual role: it ensures deep hardenability, enabling a homogeneous martensitic structure to be obtained throughout the component's cross-section, and significantly lowers the brittleness threshold. The latter characteristic is critical for landing gear components, which cyclically absorb violent impacts during landing [4].

Figure 1. Aircraft landing gear sleeve

To confirm the steel grade, a qualitative analysis of the chemical composition was performed using an EDS spectrometer (Fig. 2). The analysis involved identifying the elements constituting the material based on the obtained spectrum and comparing it with normative requirements. The tests confirmed the presence of all characteristic alloying elements.

Table 1. Chemical composition of 30HGSNA steel according to PN-H-84035[5]

Standard	Steel Grade	C	Mn	Si	P	S	Cr	Ni	Cu
PN	30HGSNA	0.27 - 0.34	1.0 - 1.3	0.9 - 1.2	<0.030	<0.025	0.9 - 1.2	1.4 - 1.8	<0.20

The investigated 30HGSNA steel grade is characterized by a set of high mechanical properties. Tensile strength exceeding 1620 MPa combined with a yield point above 1375 MPa minimizes the risk of operational deformations. An important parameter is also the impact strength (>59 J), indicating resistance to dynamic fracture, and relative elongation above 9%. This indicates the maintenance of a safe plasticity reserve, allowing for partial deformation of the element before the occurrence of critical failure [5].

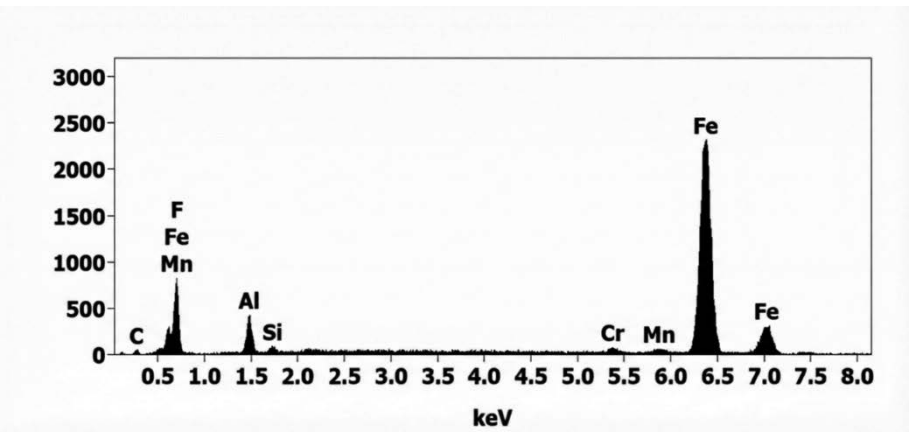

Figure 2. Analysis of the chemical composition of the tested steel using an EDS spectrometer

3. RESEARCH RESULTS

The analysis of fracture surfaces was performed using a scanning electron microscope (SEM). This method allows for the observation of failure surface morphology with high accuracy, which is crucial for the identification of fracture micromechanisms. Prior to placement in the microscope vacuum chamber, the fracture surface (Fig. 3) required careful cleaning of contaminants that could mask key morphological features [6].

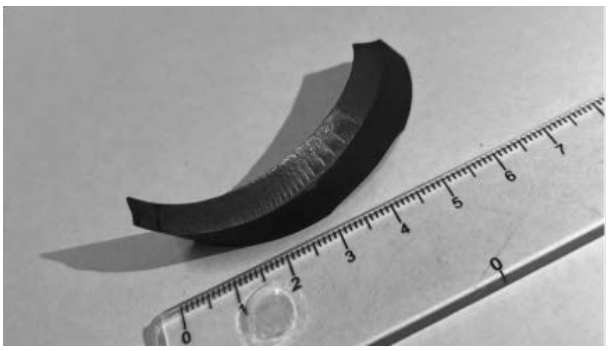

Figure 3. The investigated element.

Based on observations made using scanning electron microscopy (SEM), the presence of fatigue striations was observed on the fracture surface of the tested steel. Their visibility even at a relatively low magnification of the order of 20× may indicate the involvement of a low-cycle fatigue (LCF) mechanism, associated with the action of elevated variable stresses close to the material's yield point (Fig. 4).

.

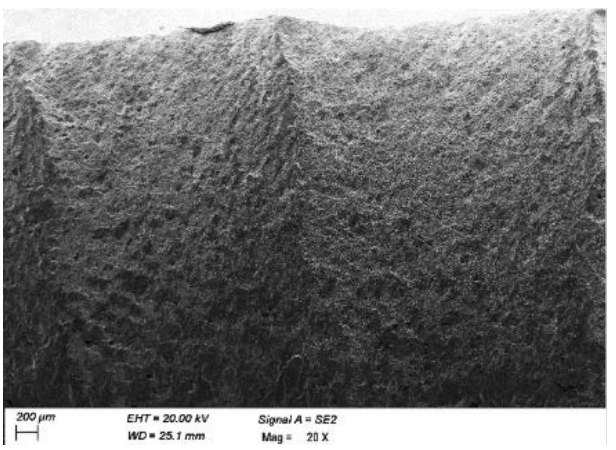

Figure 4. Fatigue fracture surface of 30HGSNA steel (20× mag.) with characteristic fatigue striations

Analysis of the fracture morphology revealed that the damaged component is characterized by the presence of two clearly distinguished, interconnected failure zones (Fig. 5). The first of these is the fatigue fracture zone, encompassing a relatively flat fracture area where local crack growth steps and material delamination are observed, which are typical for stable crack propagation under cyclic loading conditions. The second zone is the area of final fracture of a ductile nature, distinguished by a dimpled fracture morphology, indicating rapid immediate failure after exceeding the load-bearing capacity of the remaining effective cross-section.

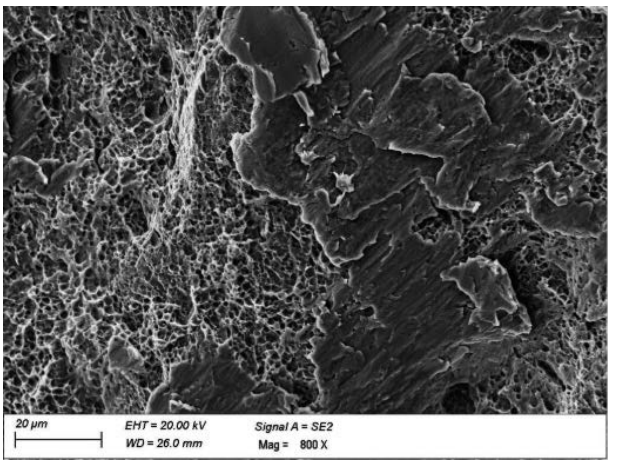

Figure 5. Fatigue fracture surface of 30HGSNA steel (800× mag.)

The fatigue damage zone is characterized by the occurrence of relatively flat fracture areas with local crack growth steps and delaminations, which corresponds to transcrystalline fatigue crack propagation. Such a morphology, combined with the presence of traces of friction on the fracture surface, reflects the cyclic nature of material degradation. This indicates that the damage did not result from a single overload but developed gradually during the component's operation (Fig. 6a).

The ductile damage zone reveals a typical dimpled fracture morphology. The observed numerous, irregular dimples indicate a plastic fracture mechanism occurring in the area of final overload, accompanied by intense material deformation and significant energy absorption. The formation of this zone was a consequence of the critical weakening of the effective cross-section of the component due to prior fatigue crack propagation. At the moment when the remaining undamaged part of the material was no longer able to carry the applied loads, a rapid rupture of the component occurred (Fig. 6b) [7- 9].

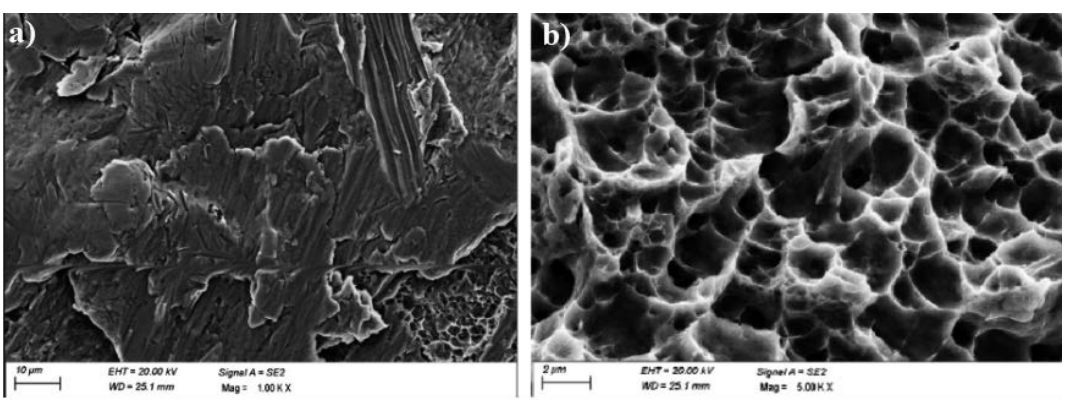

Figure 6. Surface of the a) fatigue fracture zone and b) ductile fracture zone

4. CONCLUSIONS

The conducted material examinations of the damaged aircraft landing gear sleeve, including chemical composition analysis and fracture morphology observations, indicate that the component

was made of steel corresponding to the 30HGSNA grade. The obtained results allowed for the identification of the failure mechanism as a process of a fatigue nature, with dominant transcrystalline crack propagation through the material grains. The fracture surface analysis revealed a two-stage failure process, including a fatigue zone characterized by gradual crack growth and the presence of fatigue striations, as well as a final zone of a ductile nature. The presence of numerous dimpled fracture forms in the area of final rupture indicates a plastic failure mechanism that occurred under overload conditions following the critical weakening of the component's effective cross-section. The entirety of the obtained results suggests that the failure was of a long-term fatigue process nature and was not the result of a single mechanical impact.

ACKNOWLEDGMENTS

This work was created as part of a project carried out within the framework of Project Based Learning (PBL), in the 13th edition of the "Excellence Initiative – Research University" program competition at the Silesian University of Technology.

BIBLIOGRAPHY

1. J. Adamczyk, Theoretical Metallurgy. Part 2: Plastic Deformation, Work Hardening, and Fracture, Silesian University of Technology Publishing House, 1999.
2. Changzeng Fan, Zejian Xu, Yang Han, Yan Liu, Fenglei Huang, Loading rate effect and failure mechanisms of ultra-high-strength steel under mode II fracture, International Journal of Impact Engineering 171 (2022) 104374.
3. Lei Song, Chunping Yan, Mao Yang, Gan Tu, Investigation on the Cutting Performance of High-Speed Dry Milling for 30CrMnSiNi2A Steel, The International Journal of Advanced Manufacturing Technology 125, (2024),1-23.
4. J. Hucińska, W. Serbiński, J. Łabanowski et al., Metallurgy: Materials for Laboratory Exercises, Gdańsk University of Technology Publishing House, 1995.
5. Virgamet, https://virgamet.pl/oferta/30hgsna-30hgsn2a-30chgsn2a-30hgsn2ma-30chgsn2ma-stal-stopowa, (access: 13.12.2025)
6. J. Sokołowski, B. Pluta, M. Nosiła, Scanning Electron Microscope: Principles of Operation and Applications, Silesian University of Technology Publishing House, 1980.
7. S. Kłysz, J. Lisiecki Strength testing and analysis of fatigue crack growth in selected aircraft materials, Fatigue of Aircraft Structures 2009 (2009) 74-83.
8. Keyence International (Belgium), https://www.keyence.eu/plpl/ss/products/microscope/vhx-casestudy/automobile/fracture-surface.jsp, (access: 13.12.2025)
9. M. Kurek, A. Kurek, T. Łagoda, Fatigue Processes and Fracture Mechanics Opole University of Technology Publishing House, 2020.

TalentDetector

9th January 2026
Gliwice, Poland

DEPARTMENT OF ENGINEERING MATERIALS AND BIOMATERIALS
FACULTY OF MECHANICAL ENGINEERING
SILESIAN UNIVERSITY OF TECHNOLOGY

INTERNATIONAL STUDENTS SCIENTIFIC CONFERENCE

Using Smart City components to develop a free city-centre transport system

Aleksandra Mikuła[a], Marek Sroka[b]

[a] Silesian University of Technology, Faculty of Organization and Management
email: am320737@student.polsl.pl
[b] Silesian University of Technology, Faculty of Mechanical Engineering, Department of Engineering Materials and Biomaterials, Konarskiego 18a, 44-100 Gliwice, Poland

Abstract: In this article, based on the analysis of the distribution of public transport routs in the city of Gliwice, the analysis of vehicle traffic intensity and the analysis of the distribution of public utility places in the city center of Gliwice, a concept of a free city center transport system consisting of small buses of the "A0" line, running in a loop (turning only right) around the city center and a part of the existing "A4" bus line was proposed.

Keywords: public transport, integration of the city center, transport management, smart city conceptions, metropolis management.

1. INTRODUCTION

Intelligent transport systems encompass not only new solutions for autonomous vehicles and traffic control systems, but also, above all, organizational and systemic solutions for public transport. These must be closely linked to the functions of individual city areas and take into account the specificity and constraints of a given city/agglomeration [1, 2]. The road system in Gliwice city center is primarily a result of historical conditions, is characterized by limited space, and is not fully adapted to the communication functions of the city center [3]. Bus transportation is the only mode of public transport that integrates regionally and internally. Rail transportation in Gliwice, on the other hand, has a regional and supraregional character. The bus system is therefore the basis for organizing public transport within the city. An alternative to this form of transportation is car transportation. Reducing the city center's traffic congestion from individual cars depends on the good organization of bus transportation. The aim of this work is to use the analysis of the distribution of public transport lines in the city of Gliwice, the analysis of vehicle traffic intensity and the analysis of the distribution of public places in the city centre of Gliwice to propose a coherent concept of a free city centre transport system consisting of small buses designed for the needs of this study on the "A0" line, running in a loop (turning only to the right) around the city centre and a section of the existing "A4" line.

2. METHODOLOGY

Analyses of the Gliwice public transport system were conducted, including analyses of bus route alignments. Analysis of the distribution of public spaces and other traffic-generating locations within the Gliwice city center was conducted. Traffic volume analyses in the Gliwice city center were conducted based on Google Maps data and also on data from the ITS system. Data for this system is continuously updated and collected in real time from a range of sensors and devices installed at all intersections with traffic lights, main thoroughfares, and on public transport buses. Images from ITS surveillance cameras (Fig. 1) and traffic volume data were used in the analyses. In addition, a number of site visits were carried out to assess traffic flow, potential threats resulting from the condition of the road infrastructure and the geometric features of individual intersections. Based on the analysis of the collected data, a diagram of the new "A0" bus line was designed, along with sections of the existing "A4" line.

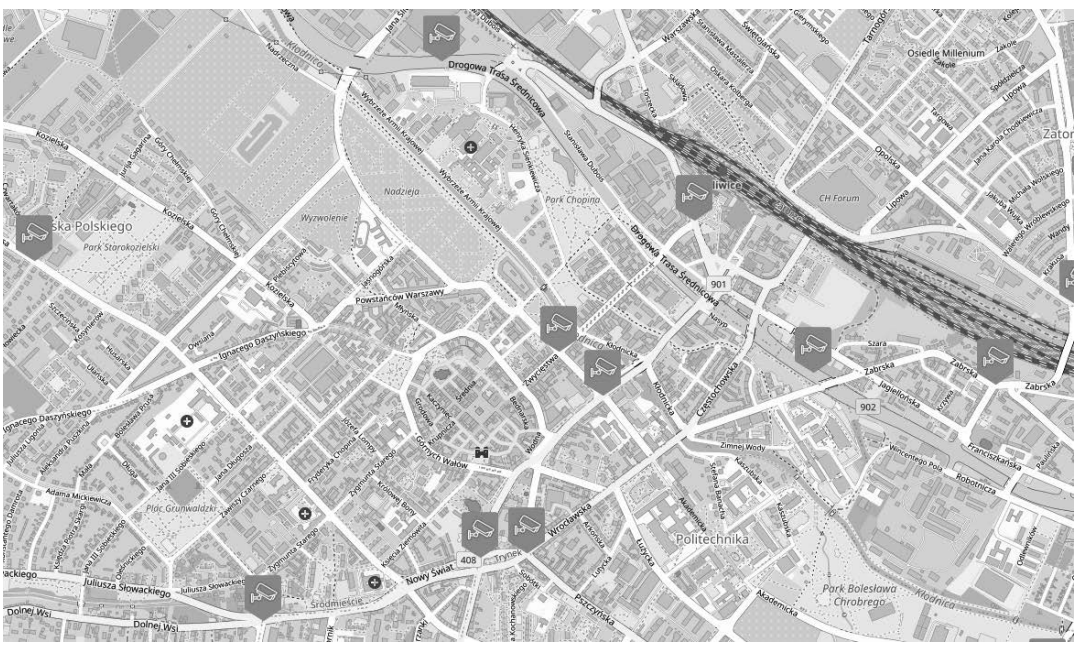

Fig. 1. Publicly available ITS system interface with a visible layer of publicly available ITS Gliwice cameras used in the conducted analyses [5].

3. ANALYSIS RESULTS

Based on source data and analyses, it was concluded that the bus system in Gliwice is centric, with almost all bus lines leading to/through the transfer center or Piastów Square [4]. Public transportation provides access to the city center, but getting around the city center without a car is difficult. City center residents seeking to run errands elsewhere in the city center typically use a car today, as the city center is largely disconnected from public transportation. An additional incentive for city center residents to travel by car is the resident parking card, which allows parking throughout the extensive Paid Parking Zone (SPP). Currently, there is no attractive rotational connection around the western part of the city center. The area along Kościuszki Street is particularly difficult to access by public transportation. This area was previously completely excluded from public transportation, and the new route of line

676 did not solve the problem. Kościuszki Street, which has become a regional center for the judiciary, legal services, and healthcare, and is also home to the Municipal Public Library and the District Office, is practically excluded from the public transportation system. In 2025, route 676 was re-routed along Sobieskiego and Kościuszki Streets, but its alignment (from Toruńska Street to Lipowa Street) prevents it from achieving the goal of integrating the city center. A free city center bus system has been proposed, consisting of small A0 buses running in a loop (turning only right) around the city center and a section of the existing A4 line. The bus can rotate only on the right side, and thanks to its relatively short ring route and right-hand turn, it can also be attractive for trips to previous stops. The A0 Line concept is met by one or two vehicles. The entire loop, including stops, takes about 15 minutes, or about 20 minutes in heavy traffic. The diagram of the designed downtown transport system is shown in Fig. 4. The route was deliberately designated via Mikołowska Street and not Jana Pawła Street due to the permanent traffic jam in the right lane of Dworcowa Street and then Jana Pawła Street (Fig. 2, 3).

a) b)

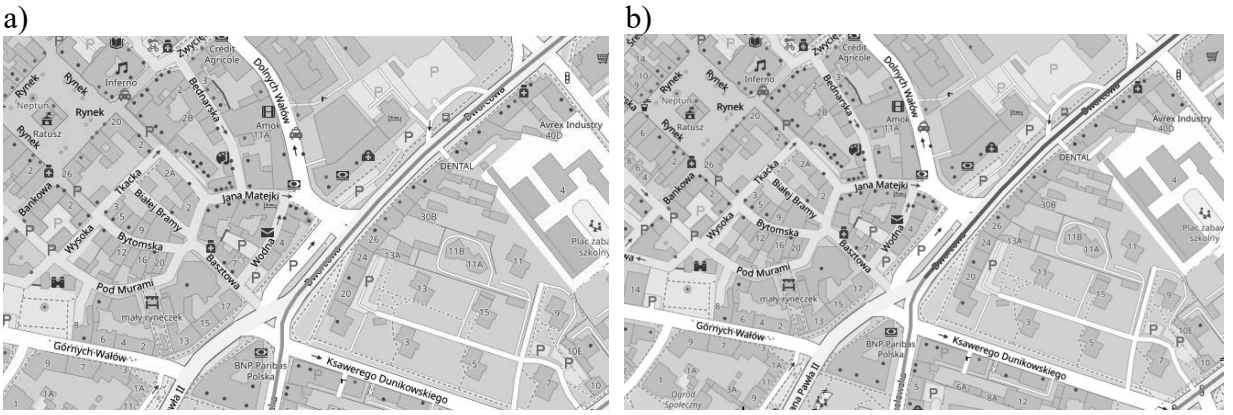

Fig. 2. Traffic volume on Dworcowa Street, a) 9:30 p.m., non-working day; b) 10:30 a.m., working day. Green indicates no traffic disruptions, orange indicates medium traffic intensity (may cause minor disruptions), red indicates high traffic intensity (possible disruptions) [5].

a) b)

Fig. 3 Traffic flow image from the ITS monitoring system, Rybnicka Street / Nowy Świat Street; a) 9:30 p.m., non-working day; b) 10:30 a.m., working day.

The designated "A0" route (Fig. 4) is optimal in terms of travel time and connection to the most important points of the downtown district, but there may be limitations that cannot be eliminated by selecting the right rolling stock. In the event of technical problems resulting in the inability to turn from Kościuszki onto Sobieskiego Street, a route via Daszyńskiego Street or Styczyńskiego Street may be considered (in which case there will be one left turn onto Jasnogórska Street, but from Styczyńskiego Street it is worth returning via Kozielska Street to Jasnogórska Street, as the route along the uninhabited part of Styczyńskiego Street / Orlickiego Street significantly limits the advantages of the proposed "A0" line).

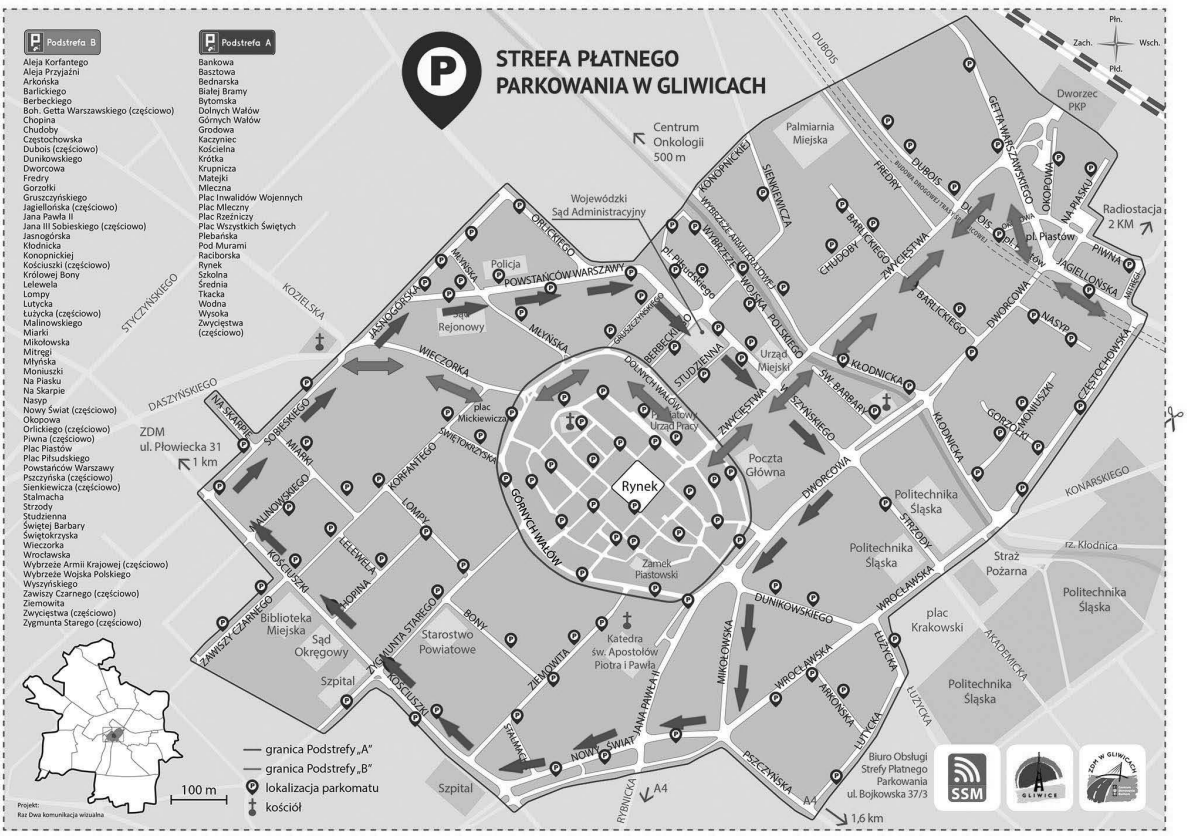

Fig. 4. Concept of a free city centre public transport system consisting of small A0 line buses running in a loop (turning only right) around the city centre and a section of the existing A4 line. The planned "A0" line is marked in red, while the section of the existing "A4" line running through the city centre is marked in blue. Own work based on diagram [6].

3. CONCLUSIONS

The solution proposed in this article, which involves the "A0" bus circling the city center (plus the existing "A4" line), offers a "3-in-1" benefit:

- Offering city center residents a way to reach every part of the city center;
- Providing access to the thriving institutional area of Kościuszki Street;
- Providing residents of housing estates and districts who reach the city center by public transportation with the ability to quickly and conveniently travel around the city center.

Moreover, the proposed solution may have a positive impact on road safety due to the reduction in the number of individual vehicles in the city centre in favour of public transport. The designated route was deemed optimal in terms of travel time and connection to the most important points of the city center, but there may be limitations that cannot be eliminated by selecting the right rolling stock. Based on the conducted analyses, it is also recommended to expand the existing research to develop a concept for amending the current Paid Parking Zone system in the city of Gliwice. The purpose of introducing the Paid Parking Zone was to force vehicle rotation and enable short-term parking in sensitive areas of the city, particularly (as can be seen from the price list analysis) in Subzone A – the Old Town Zone. In Gliwice, residents of both Subzones A and B can obtain a "Resident's Subscription," entitling them to parking throughout the city, regardless of where they are registered. Despite the solution proposed in this paper, this still constitutes a significant incentive for downtown residents to use individual vehicles. Proposing changes in this area will complement the concept presented in this article.

BIBLIOGRAPHY

1. T. Bradecki, N. Dymarska, and M. Sanigórska, Eds., Modele struktury miasta Gliwice: Nowe Gliwice, dzielnica akademicka. Modele przestrzeni publicznych, modele fizyczne, 3D, w rzeczywistości rozszerzonej i wirtualnej, Augmented and Virtual Reality. Gliwice: Silesian University of Technology, 2022, DOI: 10.34918/83377.
2. M. B. Dębowska-Mróz and A. Rogowski, Optymalizacja transportu publicznego, Autobusy, Vol. R. 20, Art. No. 12, 2019, DOI: 10.24136/atest.2019.221.
3. B. Tracz, Gliwice. Biografia miasta, Museum in Gliwice, Publ. V, Gliwice 2022.
4. Kamil Pniewski, Anna Urbanek, Ocena układu tras i linii komunikacyjnych w Gliwicach oraz koncepcja zmian, Komunikacyjny Związek Komunalny Górnośląskiego Okręgu Przemysłowego, Report, 2012, DOI: 10.13140/RG.2.2.20191.46247.
5. Analytical data and visual images of the ITS system, City of Gliwice, https://its.gliwice.eu/.
6. Paid Parking Zone Diagram, publication: Śląska Sieć Metropolitarna, https://parkowaniegliwice.pl/mapa/.

WYDAWNICTWO POLITECHNIKI ŚLĄSKIEJ
ul. Akademicka 5, 44-100 Gliwice
tel. (32) 237-13-81
wydawnictwo@polsl.pl
www.wydawnictwopolitechniki.pl

UIW 48600

Sprzedaż i Marketing
tel. (32) 237-18-48
wydawnictwo_mark@polsl.pl

Nakł. 130 + 22 Tom 1: 24 arkusze wydawnicze (24,25 arkuszy drukarskich)

Monografia 1098